SCUOLA NORMALE SUPERIORE DI PISA



TESI DI PERFEZIONAMENTO IN CHIMICA

Green synthesis of magnetic nanostructures suitable as recoverable nanocatalysts and conductive nanomaterials

Relatore
Prof. Vincenzo Barone

Candidato
Elisa Bertolucci

Supervisore Esterno
Prof.ssa Anna Maria Raspolli Galletti

Anno accademico 2016/2017

To my family and my grandparents

The Experimental work of this PhD thesis was carried out in the Department of Chemistry and Industrial Chemistry of the University of Pisa, in the École nationale supérieure des ingénieurs en arts chimiques et technologiques of Toulouse and in the Departement Toso Montanari of University of Bologna.

ACKNOWLEDGE

First, I wish to thank all the people that in my life have helped me to reach this important goal. In particular, I would like to thank my supervisors, Prof. Vincenzo Barone and Prof. Anna Maria Raspolli Galletti, which give me the support and the inspiration that drive me in this experience.

I wish to thank Prof. Philippe Serp, Dr. Rosa Axet and their research group for their help, skill and patience during my period at the INP-ENSIACET of Toulouse.
I would like to extend my thanks to Prof. Fabrizio Cavani of University of Bologna and his research group for their advice during my period at the University of Bologna.

I would like to thank Prof. Bernardo Tellini and Ing. Mirko Marracci of University of Pisa for their help and competence in making magnetic and electrical tests. I whish to thank Prof. Guido Pampaloni of University of Pisa for his collaboration in the preparation of some of my catalysts.
I gratefully acknowledge the contributions of Prof. Tiziana Funaioli, Prof. Fabio Bellina of University of Pisa and Dr. Gabriella Garbarino of University of Genova for their help and expertise in making catalytic tests.

I owe a thank you to our laboratory technician Marco Martinelli for his support and advices.

I would like to offer special thanks to my laboratory colleagues and all the colleagues and friends that I met during this experience.

Finally, I would like to extend my special thanks to my family, Nicola, Ettore and all my "friends" for their support and constant encouragement.

INDEX

1. INTRODUCTION 13

1.1 Introduction 13

2. NANOCATALYSIS IN GREEN CHEMISTRY 17

2.1 Green chemistry principles 17

2.2 Nanocatalysis 18

2.3 Magnetic nanomaterials as recoverable nanocatalysts 23
2.3.1 Magnetic nanomaterials 23
2.3.2 Iron oxides 27

2.4 References 31

3. METHODOLOGIES FOR THE SYNTHESIS OF MAGNETIC IRON OXIDE NANOPARTICLES 32

3.1 Introduction 32

3.2 Synthesis of iron oxide nanoparticles: the co-precipitation approach 34

3.3 Synthesis of iron oxide nanoparticles: the solvolthermal approach 36

3.4 Synthesis of iron oxide nanoparticles: the microemulsion approach 39

3.5 Synthesis of iron oxide nanoparticles: the polyol approach 41

3.6 Synthesis of iron oxide nanoparticles: metal areosol/vapour approaches 42

3.7 Synthesis of iron oxide nanoparticles: the electrochemical approach 43

3.8 Synthesis of iron oxide nanoparticles: microwave or ultrasound assisted approaches 44

3.9 References 48

4. SYNTHESIS OF NANOSTRUCTURED IRON OXIDES 51

4.1 Synthesis of iron oxides: the microwave assisted co-precipitation technique 52

4.2 Synthesis of magnetite: Microwave assisted hydrothermal procedure 61

4.3 References 69

5. SYNTHESIS OF MAGNETIC NANOCATALYSTS 72

5.1 Synthesis of magnetic palladium nanocatalysts 74
5.1.1 Palladium nanoparticles anchored over iron oxide nanocrystal 74

5.2 Synthesis of ruthenium magnetic nanocatalysts 91

5.3 Synthesis of palladium magnetic nanocatalysts 99

5.4 Synthesis of magnetic copper oxides nanocatalysts **104**

5.5 References **112**

6. ELECTRICAL AND MAGNETIC PROPERTIES OF MAGNETITE NANOPOWDERS **115**

6.1 Magnetic characterization of magnetite nanopowders **115**

6.2 Electrical characterization of magnetite nanopowders **131**

6.3 References **137**

7. SYNTHESIS OF MAGNETIC NANOCOMPOSITES **138**

7.1 Synthesis of acid magnetic nanocomposites: the microwave assisted precipitate approach **140**

7.2 Synthesis of magnetic nanocomposites: the microwave assisted hydrothermal approach **146**

7.2 References **155**

8. SYNTHESIS OF MAGNETIC CARBON NANONOCATALYSTS **158**

8.1 Carbon nanostructures **159**

8.2 Synthesis of mono and bimetallic carbon nanocatalyts by Microwave assisted procedure **166**

8.3 References **181**

9. SYNTHESIS OF COPPER NANOOBJECTS **184**

9.1 Introduction **184**

9.2 Synthesis of copper nanoparticles **185**

9.3 Synthesis of copper nanowires by sugar assisted growth **190**

9.4 References **204**

10. STUDY OF THE SELECTIVE HYDROGENATION OF CYNNAMALDEHYDE TO HYDROCINNAMALDEHYDE IN THE PRESENCE OF THE MAGNETIC PALLADIUM CATALYSTS **205**

10.1 Introduction **205**

10.2 The effect of the palladium loading on hydrogenation rate **207**

10.4 The effect of temperature on the hydrogenation rate 214

10.5 Recyclability tests 216

10.6 Conclusion **218**

10.7 References....218

11. STUDY OF THE SELECTIVE OXIDATION OF 1-PHENYLETHANOL TO ACETOPHENONE IN THE PRESENCE OF THE MAGNETIC RUTHENIUM CATALYSTS.... 221

11.1 Introduction....221

11.2 Results and discussion....222

11.3 Conclusion....228

11.4 References....229

12. THE USE OF RUTHENIUM, PLATINUM AND PALLADIUM MAGNETIC NANOCATALYSTS IN THE SELECTIVE OXIDATION OF HMF TO FDCA231

12.1 Introduction....231

12.2 Oxidation of HMF catalysed by magnetic ruthenium nanocatalysts....234

12.3 Oxidation of HMF catalysed by magnetic platinum nanocatalyst....242

12.4 Oxidation of HMF catalysed by magnetic palladium nanocatalyst....247

12.5 Conclusion....257

12.6 References....258

13. STUDY OF THE CROSS-COUPLIG REACTIONS USING MAGNETIC PALLADIUM NANOCATALYSTS.... 260

13.1 Introduction....260

13.2 The Suzuki-Miyaura reaction catalysed by magnetic palladium catalyst....262

13.3 The Heck-Mizoroki reaction catalysed by magnetic palladium catalyst....268

13.4 Cassar-Heck reaction catalysed by magnetic palladium catalyst....272

13.5 Arylation of N-Methyl-1-*H*-imidazole catalysed by magnetic palladium catalyst....276

13.6 Conclusion....279

13.7 References....280

14. THE OXIDATION/CONDENSATION OF ETHANOL 283

14.1 Introduction....283

14.2 Effect of the catalytic support on reaction pathways....285

14.3 The effect of the residence time on reaction pathway....289

14.4 The effect of the temperature on the reaction products....292

14.5 Conclusion....293

14.6 References....294

15. THE SELECTIVE HYDROGENATION OF 1-CHLORONITROBENZENE TO 1-CHLOROANILINE 296

15.1 Introduction....296

15.2 The effect of temperature on the hydrogenation of pCNB....297

15.3 The effect of solvent on hydrogenation of pCNB....298

15.4 The effect of catalytic support on hydrogenation of pCNB....300

15.5 The Effect of catalyst pre-treatment the hydrogenation of pCNB.... 302

15.6 Recycling test....306

15.7 HYDROGENATION OF OTHER NITROAROMATICS 308

15.8 Conclusion....309

15.8 References....310

16. CONCLUSION 312

17. EXPERIMENTAL SECTION 314

17.1 Chemicals....314

17.2 Instrumentations....317

17.3 Synthesis of nanostructured iron oxides....322

17.4 Synthesis of magnetic nanocatalysts....322

17.5 Preparation of magnetic nanocomposites 323

17.6 Preparation of ruthenium and/or magnetic carbon nanomaterial....323

17.7 Preparation of copper nanoobjects....323

17.8 Catalytic reactions.... 325

1. INTRODUCTION

1.1 Introduction

Magnetic iron oxide nanoparticles (MNPs) attract huge interest thanks to their striking physicochemical properties. These materials are suitable candidates for a wide range of uses in many different areas of science and technology. In particular, they are attractive in biomedicine and biotechnology for the production of implantable devices, such as biosensors, drug delivery systems, catheters and micro dialysis probes, magnetic resonance imaging and hyperthermia therapy. In industry, MNPs are used for nanocatalysis, magnetic membranes, sensors and storage devices. In industrial catalysis in particular, magnetic nanoparticles find an increasing interest because they are able to summarize the advantages of traditional homogeneous and heterogeneous catalysts. Their small nano-size in fact increases the exposed surface area of the active component of the catalyst, enhancing the contact between reactants and catalyst, leading to higher reaction yield typical of traditional homogeneous catalysis. Moreover, thanks to peculiar magnetic properties, MNPs are easily and efficiently recovered from the reaction mixture.

Magnetic separation in fact can be considered a strategic sustainable alternative to traditional separation methods, which are usually expensive, unsustainable, energy, solvent and time consuming.

It is important to underline that MNP catalytic properties strongly depend on particle size shape and stability; therefore, high control of these parameters during their nanosynthesis is highly desired.

In literature, numerous synthetic approaches for the preparation of magnetic iron oxides are described: co-precipitation, solvothermal, microemulsion, polyol, metal aerosol/vapour, electrochemical etc. Among these, co-precipitation and solvothermal techniques are the most commonly used. Both these techniques lack in size and shape particle control and usually require environmentally unfriendly auxiliaries. The co-precipitation method for example involves hazardous reducing and stabilizing agents to reach an acceptable size and shape control, whereas the solvothermal method deals with extremely high temperatures and pressures, which are dangerous, expensive and unsustainable for industrial scale up.

In view of tightened environmental standards and social sensitivity towards environmental protection, a new re-design of MNP preparation has become essential.

In this context, the aim of my PhD work is to develop more sustainable and greener synthetic approaches to produce well-defined magnetic nanostructured catalysts. In particular, two new synthetic approaches were developed following the green chemistry principles as "design rule". The new precipitation and hydrothermal procedures were optimized to obtain good particle size and shape control. Both these innovative methodologies are characterized by:

- The use of aqueous ethanol as a solvent;
- The use of monomode or multimode microwave irradiation, which are highly energy efficient heating sources;
- The absence of polymeric stabilizers, which could lead to the MNP surface passivation, decreasing both magnetic properties and catalytic activity;
- A single reaction step;
- Short reaction time.

The correlations between the obtained nanostructure characteristics and the main synthetic parameters (such as temperature, heating sources, pH, precursor concentration and reaction time) were deeply investigated. These relationships are fundamental and permit us to drive the nanoparticles synthesis to obtain nanocatalysts with the desired properties. In fact, thanks to these studies it was possible to prepare diverse kinds of magnetic nanocatalysts, which are listed in Scheme 1.

The numerous magnetic nanostructures obtained were subsequently employed in strategic industrial reactions such as:

- Hydrogenation of cinnamaldheyde to hydrocinnamaldheyde;
- Oxidation of 1-phenylethanol to acetophenone;
- Oxidation of hydroxymethylfurfural to furan dicarboxylic acid;
- Suzuki-Miyaura cross-coupling;
- Heck-Mizoroki cross-coupling;
- Cassar-Heck cross-coupling;
- Direct arylation of 1-methyl-1-H-imidazole and 4-iodioanisole;
- Hydrogenation of *p*chloronitrobenzene to *p*chloroaniline

Moreover, in this PhD work, the effects of the main reaction parameters (such as solvent, temperature and pressure) on MNP catalytic performances were intensely investigated. All these studies were performed in the liquid phase using a Parr Autoclave.

In order to expand the potential catalytic applications of magnetic nanocatalysts, MNPs were also employed in the gas phase oxidation/condensation of ethanol using a continuous flow reactor.

The promising catalytic results confirm the high control reached during nanocatalyst preparations and their wide range of possible industrial uses.

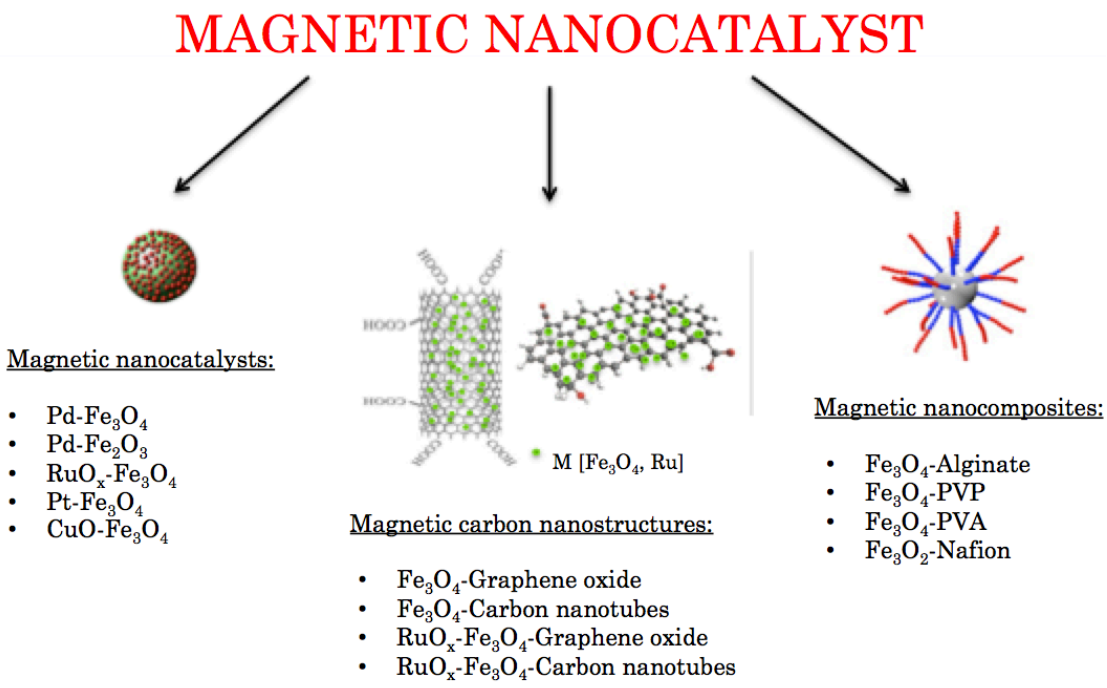

Scheme 1 Diverse magnetic nanostructured systems prepared during this PhD work

The accurate control of nanoparticle properties, reached by adopting new precipitation and hydrothermal procedures, guarantees not only that MNPs can be used as nanocatalysts or catalytic supports but also as electrostatic sensors and nanoconductors. In particular, for these last applications an extensive study of the effects of particle size and composition on magnetic and electrical properties was performed.

Finally, in order to produce better nanoconductors and electrostatic sensors, other interesting nanostructures were studied. Generally, for these applications different nanostructured metals and their compounds are used. Among them copper and copper oxides show promising electrical properties, which strongly depend on nanostructure size, shape and geometry.

The accurate and efficient control of particle properties is extremely important for the application of nanomaterials in sensor and conductor science; therefore, a well-defined and reproducible synthetic procedure is highly desired.

Several synthetic methods for the preparation of copper and copper oxides nanostructures are reported in literature. Unfortunately, these techniques show poor control of particle size and composition resorting in the use of hazardous and unfriendly stabilizing agents.

In this context, a new sustainable approach was developed following green chemistry principles. This new seed mediated growth method is characterized by the use of water as solvent, short reaction time and mild reaction conditions. It is important to underline that this new procedure allows the selection of diverse copper nanostructure geometries simply by tuning the synthetic parameters such as kind of stabilizing agent or reaction time.

2. NANOCATALYSIS IN GREEN CHEMISTRY

2.1 Green chemistry principles

The Green Chemistry concept was introduced by Anastas in 1990 [1]. Green chemistry can be defined as the design of chemical products and processes to reduce or eliminate the use and the generation of hazardous substances. It can be summarized in twelve principles.

1. Waste prevention instead of remediation;
2. Atom efficiency;
3. Less hazardous/toxic chemicals;
4. Safer products by design;
5. Innocuous solvents and auxiliaries;
6. Energy efficient by design;
7. Preferably renewable raw materials;
8. Shorter syntheses (avoid derivatization);
9. Catalytic rather than stoichiometric reagents;
10. Design products for degradation;
11. Analytical methodologies for pollution prevention;
12. Inherently safer processes.

These principles have been extensively adopted for the optimization and the design of a wide range of processes from laboratory scale to industrial plant scale.

The green chemistry approach attracts huge industrial and scientific interest due to tightened environmental standards and growing social sensitivity towards environmental protection.

In this context the catalytic processes become more relevant, allowing: [2]

- A lower amount of fresh reagents, reducing both resource depletion and recycling of the unreacted stream.
- Mild reaction conditions, such as lower temperature and pressure, and almost neutral pH. These aspects are particularly important because they reduce the hazards and risks connected to the industrial plant.
- Higher yield, reducing the separation, purification and recycle stages.

Generally, industrial catalysts are chosen and evaluated through different parameters such as: catalytic activity, selectivity, lifetime, catalyst regeneration, toxicity and price.
Catalytic activity (A) is the reaction rate defined as product number of moles over catalyst volume per hour. It can also be expressed as Turnover Frequency (TOF) calculated as product number of moles over catalyst number of moles per hour.
Selectivity (S) is a factor that shows the amount of reagent converted to the desired product. It is one of the most important parameters that drives the catalyst selection; in particular, if the selectivity is high the formation of by-products will be lower, thus making the purification, separation and recycle stages easier.
The catalyst lifetime refers to the utilization time of the catalyst; in particular, it is defined as years of use before catalyst disposal or as amount of product over amount of catalyst. In addition, this factor is very important because it is strongly connected to the economic and environmental process costs. A high catalyst lifetime allows less need of fresh catalyst minimizing the production of hazardous waste.
Catalyst regeneration is the procedure applied to reactivate the catalytic site after each reaction cycle, in order to guarantee the same catalytic activity. Fast and easy regeneration procedures result in a longer catalytic lifetime, and in the reduction of the economic cost of the entire process.
Finally, toxicity is an important factor that quantifies the environmental hazard and health risks connected to the use of a certain material.
One of the most important aspects of Green Chemistry is the concept of design applied to chemical products and processes. In fact Green Chemistry is characterized by the careful planning of chemical synthesis and molecular design to reduce adverse consequences, adopting the twelve principles as "design rules"[3].
The new magnetic nanocatalysts described in this work were developed taking into account all of these principles, with the purpose to design new sustainable catalytic tools for industrial processes.

2.2 Nanocatalysis

Nanocatalysis is a field of catalysis in which nanoobjects are used to catalyse reactions; this field has undergone an exponential growth during the last few years, as can be seen in Figure 1, which reports the increment of the number of publications on this issue per year.

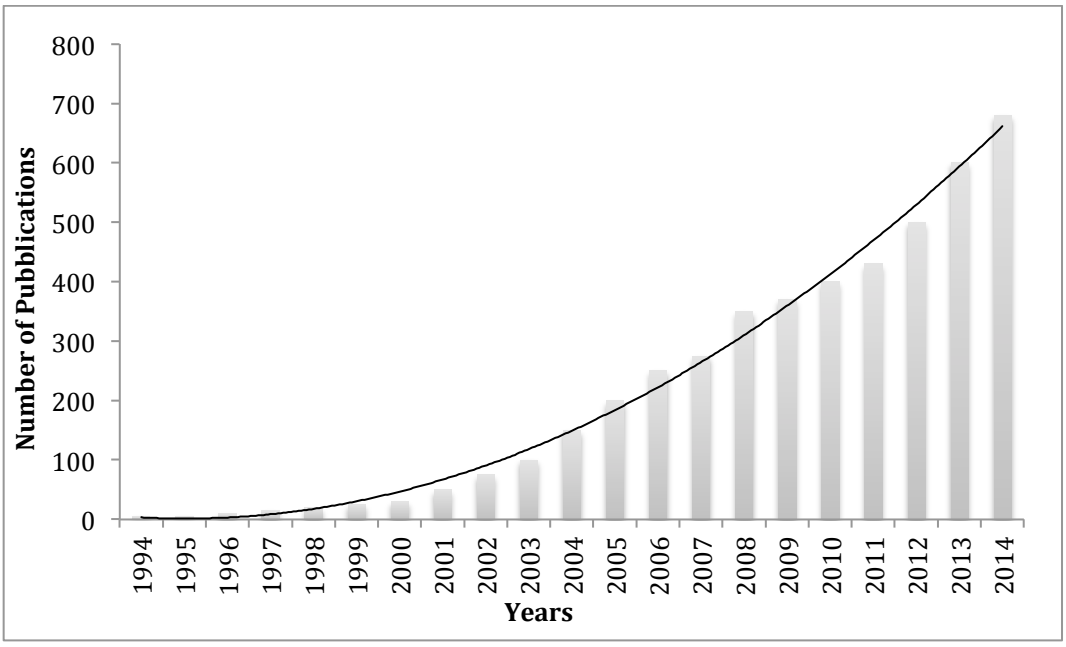

Figure 1 Number of publications dealing with nanocatalysis per year extracted from the ISI Web of Science (Thomson Reuters) database, searched with the combined keywords nano and catalysis

Nanocatalysis, as traditional catalysis, can be divided in two categories[4]:

- Homogeneous nanocatalysis when the catalyst is a colloidal dispersion of nanoparticles.
- Heterogeneous nanocatalysis when the catalyst is a nanopowder supported on polymers or inorganic compounds.

Traditional homogeneous catalysis shows high catalytic activity and selectivity thanks to the straight contact between reagents and active catalytic sites. On the other hand, homogeneous catalysts are difficult to recover and recycle leading to unsustainable and expensive purification steps. On the other hand, traditional heterogeneous catalysis allows an easy recovery and recycle of the catalysts but requires hard reaction conditions to reach an acceptable reaction yield.

In this context nanocatalysis has emerged as a sustainable alternative to conventional catalysis, summing up the advantage of traditional homogeneous and heterogeneous systems[5]. The nanomaterials are characterized by a high surface/volume ratio that increases the exposed surface area of the active component of the catalyst, enhancing the contact between reactants and catalyst thus mimicking the homogeneous catalysis. Moreover, the insolubility of the catalytic nanoparticles assures the separation and recovery which are typical of heterogeneous systems.

Homogeneous nanocatalysis uses colloidal dispersion of transition metal nanoparticles as catalysts. In particular, the nanoparticles are dispersed in an organic or water solution and stabilized to prevent their agglomeration. The better the stabilization of colloidal nanoparticles, the lower the catalytic activity of the entire system because the active surface sites will be better protected.

Generally, colloidal dispersions are prepared by reducing a transitional metal precursor in the presence of a good stabilizing agent. The common reducing and stabilizing agents employed in homogeneous nanocatalyst preparations are reported in Table 1.

Table 1 References to the common reducing and stabilizing agents used to prepare homogenous nanocatalysts

Nanoparticles colloidal dispersions	
Reducing agents	alcohols, hydrogen gas, sodium borohydride, hydrazine, sodium citrate, thermal reduction, photochemical reduction, sonochemical reduction, metal vapour condensation of organometallics, metal vapour condensation, electrochemical reduction
Stabilizers	polymer, block copolymers, dendrimers, surfactants, other ligands

These homogeneous nanocatalysts were generally employed in diverse reactions such as:

- Suzuki cross-coupling reactions;
- Heck cross-coupling reactions;
- Electron-transfer reactions;
- Hydrogenations;
- Oxidations.

However, colloidal nanocatalysts are difficult to recover from the reaction mixture due to their small size. Generally, the purification and recovery of metal nanoparticles involve extremely expensive procedures such as ultracentrifugation, electrophoresis and osmosis separation.

On the other hand, heterogeneous nanocatalysis uses transition metal nanoparticles supported on various matrices such as polymeric or inorganic compounds.

Generally heterogeneous nanocatalysts are prepared following three diverse methods: the impregnation of nanoparticles onto supports, the grafting of nanoparticles onto supports or lithographic techniques.

These catalytic systems were usually employed in diverse reactions such as:

- Fuel cell reactions;
- Oxidations;
- Hydrogenations;
- Reduction reactions;
- Decompositions.

The recovery and recycle of heterogeneous nanocatalysts are also quite hard tasks and require long filtration and centrifugation stages.

The introduction of magnetic nanostructured materials as catalytic support or catalysts could be a strategic choice to improve the recoverability of these promising nanostructured systems.

It is well known that the catalytic performances of nanomaterials are strongly connected to their chemical physical properties. Therefore, it is possible to address the activity and selectivity of nanocatalysts by tailoring size, shape, composition and morphology of the nanoobjects. For this reason an accurate nanocatalyst design becomes fundamental, taking into account the dependence between catalytic activity and nanoparticles structure (shape and size). In particular, Somorjai et al.[6] and Che et al.[7] demonstrated the relationships between size and catalytic activity for selected catalysts and reactions, classifying these reactions into four primary groups (see Figure 2):

- Positive size-sensitivity reactions;
- Negative size-sensitivity reactions;
- Size-insensitivity reactions;
- Mix of negative and positive sensitivity.

Positive size-sensitivity reactions are those for which turnover frequency increases with the decrease of particle size, as shown by ethane hydrogenolysis over Pt/SiO_2 (the adopted model reaction). Moreover, this positive size-sensitivity behaviour is commonly observed in reactions in which the activation of σ-bond is the rate-limiting step.

Negative size-sensitivity reactions are those for which turnover frequency increases with the increase of particle size, as shown by CO hydrogenation on Ru/Al_2O_3. In this class of reactions, the formation or the dissociation of π-bond is the rate-limiting step.
Size-insensitivity reactions are those for which turnover frequency is not significantly dependent on particle size, as shown by benzene hydrogenation over Pt/SiO_2.
Finally, the mix of negative and positive-sensitivity are those for which turnover frequency has a local maximum or minimum at a particular nanoparticle size.

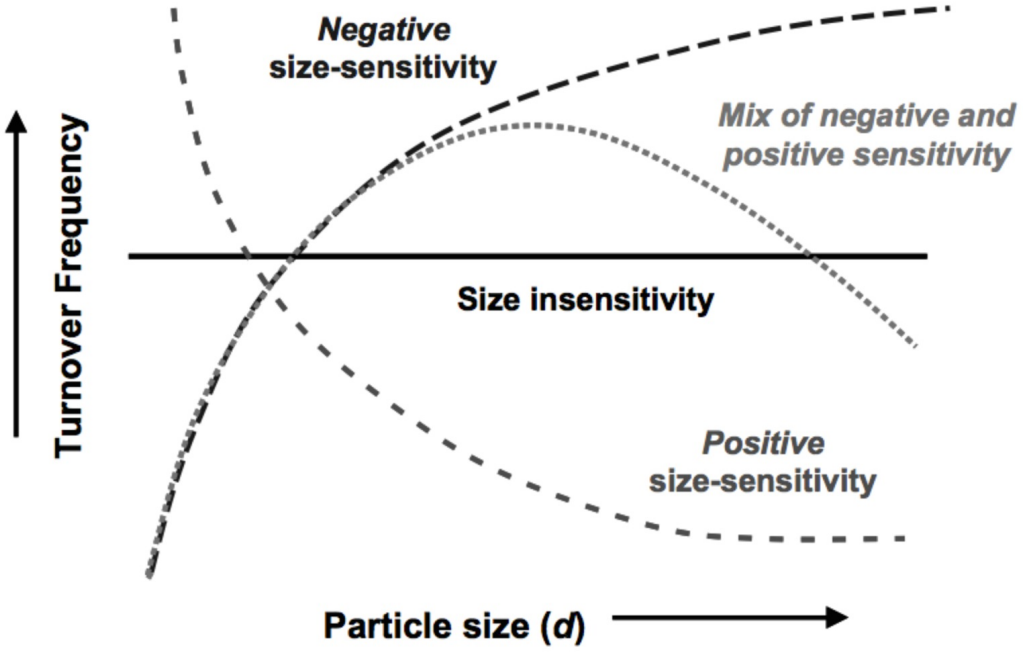

Figure 2 Major classes of sensitivity, which describe the relationships between NP size and turnover frequency for a given combination of reaction and NP catalyst

Transition metal nanoparticles can be synthetized in diverse shapes that are characterized by peculiar atomic arrangements and electronic configurations.[8] Nanomaterial shape and geometry influence the catalytic activity of the entire catalytic systems, in fact the position of the surface atoms and the electronic arrangement can determine the availability or the inhibition of the active catalytic sites [9].
Consequently the design of new sustainable synthetic procedures able to control nanocatalyst shape and size is highly desired and could assure good selectivity and high yields in determined reactions.

2.3 Magnetic nanomaterials as recoverable nanocatalysts

In the last few years, the use of magnetic nanoparticles (MNPs) as nanocatalysts or catalytic supports for metal nanoparticles has seen an extraordinary growth. Thanks to their reduced-size and magnetic properties, MNPs combine the high catalytic activity of nanostructures, discussed above, with the efficiency of magnetic separation. Usually nanoparticle separation is characterized by elevated solvent, time and energy consumption and involves complex techniques such as filtration, electrophoresis, osmosis, inverse osmosis, centrifugation, ultracentrifugation and dialysis.

On the other hand MNPs can be easily recovered using a simple external magnet[10]. The separation and recycle of catalysts is important not only from an environmental point of view but also for the economical balance of the industrial process.

Generally the catalytic systems are composed of transition or noble metals (which are very expensive and sometimes environmentally dangerous materials) and must be efficiently recovered and recycled. For these reasons, MNPs are becoming a strategic choice for industrial processes, opening the road to the future employment of nanomaterials in catalytic industrial plants.

2.3.1 Magnetic nanomaterials

Magnetic properties of materials arise from the spin and orbital angular moment of the electrons contained in the compound. The main measurements that allow the characterization and classification of magnetic materials are magnetic permeability, magnetic retentivity and magnetization of saturation as shown in the magnetic hysteresis curve reported in Figure 3.

Magnetic permeability μ is a function of the magnetic field which shows the ability of the material to let the magnetic field flow (See equation 1).

$$B = \mu H \qquad (1)$$

Where B is the induced magnetic field and H is the magnetic field force.

Materials characterized by permeability values less than 1 are defined as diamagnetic, those that show permeability near to 1 are called paramagnetic; finally, materials with permeability higher than 1 are classified as ferromagnetic.

Magnetic retentivity is the ability of the material to maintain magnetization after the external magnetic field has been removed. Retentivity is a typical property of

ferromagnetic materials, which are able to maintain dipole magnetic orientation after the removal of the external field.

Finally, magnetic saturation M_0 is the maximum magnetization value that a material can reach when its magnetic domains are completely oriented in parallel to the magnetic field. The complete orientation of the material magnetic domains leads to the formation of a unique big Weiss domain. At this point, when improving the magnetic force *H*, the magnetization does not change. The M_0 value arises from the atomic magnetic moment *m* and the number of the atoms *n* that form the material (See equation 2):

$$M_0 = nm \tag{2}$$

All these properties are represented in the hysteresis curves which show the influence of the magnetizing force *H*, and magnetization *M*, on the induced magnetic field *B* (see Equation 3).

$$B = \mu_0 (H + M) \tag{3}$$

As it is possible to observe from the hysteresis curves showed in Figure 3, when the material has been driven to saturation, the magnetizing field can be dropped to zero and the material will retain most of its magnetization (retentivity).

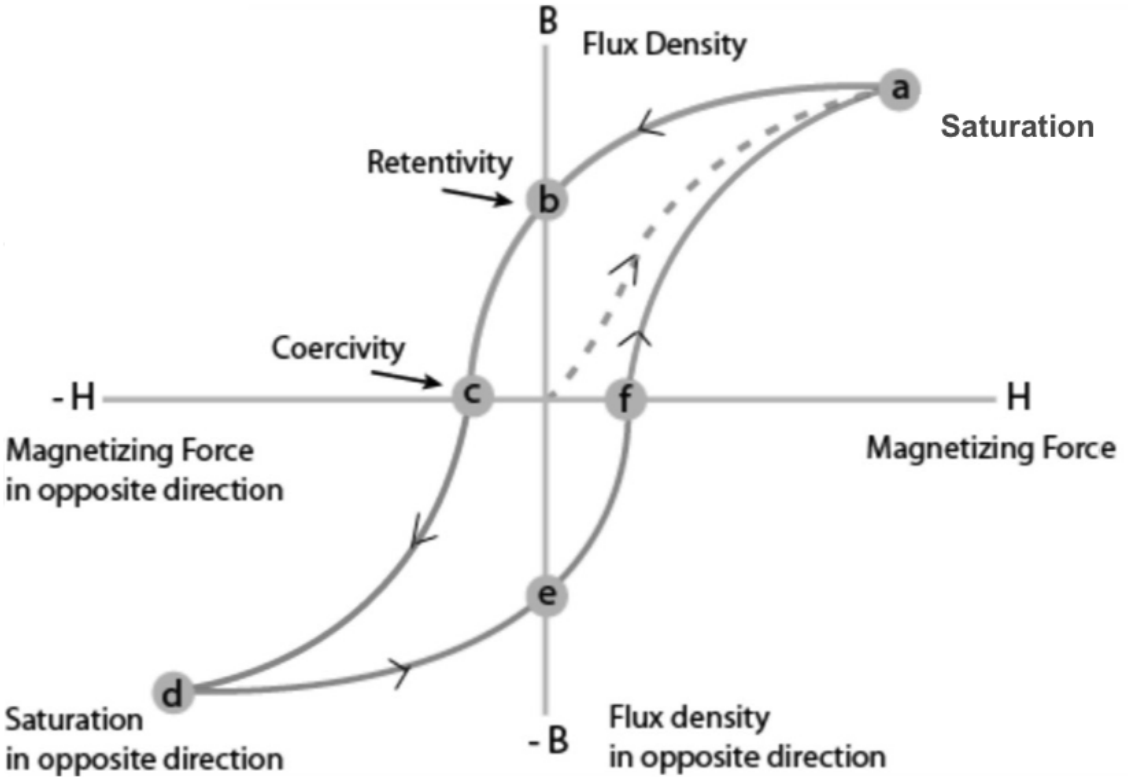

Figure 3 Typical magnetic hysteresis curves where a is the saturation point M_0, and b is the retentivity curve

Depending on magnetic properties and behaviours it is possible to classify materials as diamagnetic, paramagnetic, ferromagnetic and antiferromagnetic (see Figure 4).

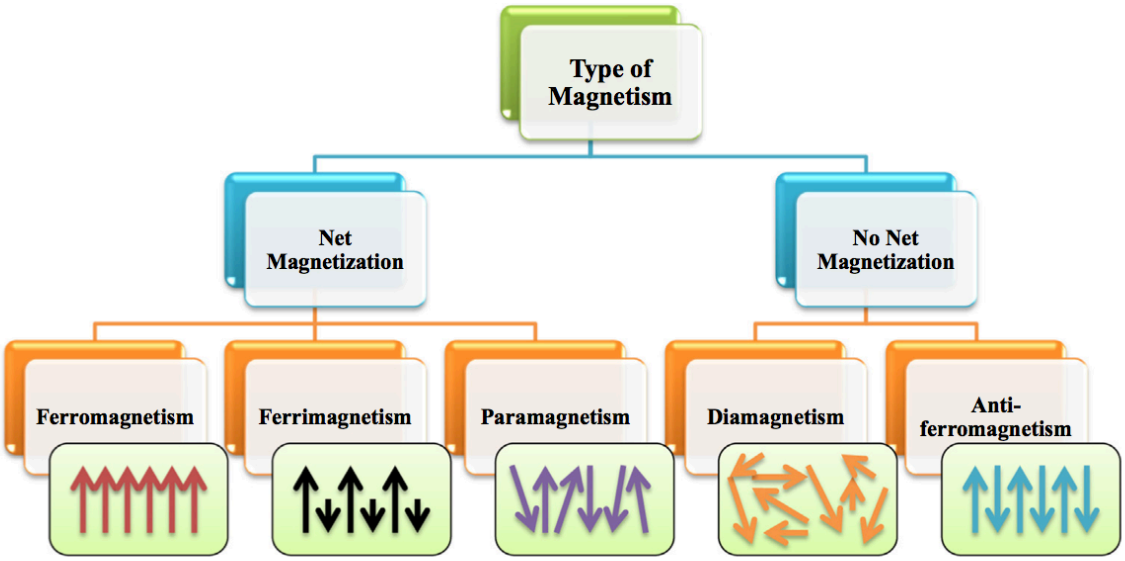

Figure 4 Types of magnetism with the schematic representation of typical atom dipole orientation.

Diamagnetic materials do not show permanent magnetic atomic moment but if these materials are placed in a magnetic field, an atomic magnetic moment opposite this magnetic field is created.

Paramagnetic materials are those materials characterized by magnetic atomic moments randomly oriented. When these materials are placed in a magnetic field all the atomic magnetic moments can be arranged and oriented in the same way.

Ferromagnetic materials are characterized by Weiss domains (represented in Figure 5), which are areas bigger than 100 nm where the atomic magnetic moments are oriented in the same direction. When ferromagnetic materials are placed in a magnetic field all the Weiss domains are oriented in the magnetic field direction and this orientation is maintained also when the magnetic field is removed.

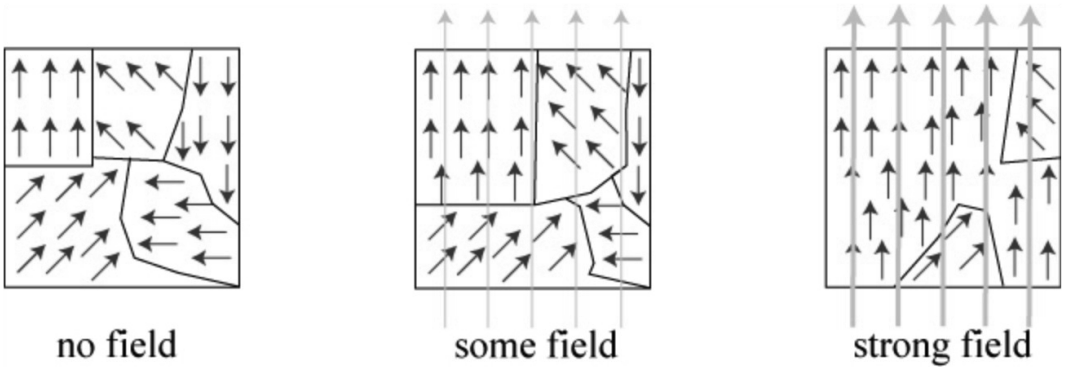

Figure 5 Weiss domain inside a ferromagnetic material and the progressive orientation of a magnetic moment with an external magnetic field

Small ferromagnetic nanoparticles characterized by size smaller than 100 nm contain only a single Weiss domain and show a particular magnetic behaviour defined as superparamagnetism. The superparamagnetic materials are single domain particles with a giant atomic moment composed of the magnetic moments of the atoms that form the particles. The orientation of this giant magnetic moment could change rapidly to contrast an external magnetic field as observed by Goussin et al[11].

It is important to underline that the magnetic behaviour of a material depends also on the temperature so the analysis of material magnetic behaviour should be performed at the temperature of utilization.

Ferromagnetic behaviour in fact can be observed only below the Curie temperature; over this temperature, magnetic permeability decreases and the material behaves like diamagnetic one.

Ferromagnetic materials are divided into hard ferromagnetic if characterized by a coercivity higher than 10 KA/m and soft ferromagnetic materials if characterized by a coercivity below 1 KA/m.

Finally, antiferromagnetic materials are characterized by domains analogous to the ones of ferromagnetic materials but in which atomic magnetic moments are oriented in antiparallel way and the resultant magnetic moment is zero.

Several transition metals and their oxides or compounds show interesting ferromagnetic and paramagnetic properties such as (Co, Fe, Fe_2O_3 Fe_3O_4, $NiFe_2O_3$, $CuOFe_2O_3$, $MgOFe_2O_3$, MnBi, Ni, MnSb, $MnOFe_2O_3$, $Y_3Fe_5O_{12}$, CrO_2, MnAs, Gd, Dy, EuO)[12]. Among them, iron oxides are the most interesting materials that produce sustainable magnetic nanocatalysts. Iron oxides in fact are the most common minerals on Earth. Moreover magnetic iron oxides such as maghemite and magnetite due to their low cost, high biocompatibility and negligible toxicity[13] have been extensively investigated for

biomedical applications[14]. For all these reasons, magnetic iron oxides can be considered interesting and promising suitable candidates as greener nanocatalysts.

2.3.2 Iron oxides

With the term iron oxides, sixteen iron compounds (oxides and hydroxides) are commonly indicated. Among them, the most interesting species studied in this work are hematite α-Fe_2O_3, maghemite γ-Fe_2O_3 and magnetite Fe_3O_4.

Hematite is a red semiconductor mineral with a compact rhombohedral structure formed by octahedral planes of FeO_6 (see Figure 6). This mineral is the thermodynamic stable isomer of maghemite. Consequently, if maghemite nanoparticles are thermally stressed they are easily converted to hematite as reported by X. Ye et al[15].

Hematite shows a peculiar magnetic behaviour, in fact at room temperature (273 K) it is weakly ferromagnetic, under 270 K it becomes antiferromagnetic and over its Curie temperature (965 K) it is paramagnetic.

Maghemite is a semiconductor red brick mineral with a compact cubic structure where the octahedral and tetrahedral sites are not completely filled by iron ions (See Figure 6). Maghemite shows a ferromagnetic behaviour until its Curie temperature (700-800K) at which it is converted into hematite.

Finally, magnetite is a semiconductor black mineral with the typical formula of inverse ferrite spinel MO • Fe_2O_3 (where M is Fe^{II}). Magnetite shows a compact cubic crystalline structure analogous to maghemite, where the octahedral sites are occupied by Fe^{II} ions and the tetrahedral sites are occupied by Fe^{III} ions (See Figure 6)[16]. Thanks to this inverse spinel structure, magnetite shows a ferromagnetic behaviour until its Curie temperature (850 K), over this value magnetite can be classified as antiferromagnetic.

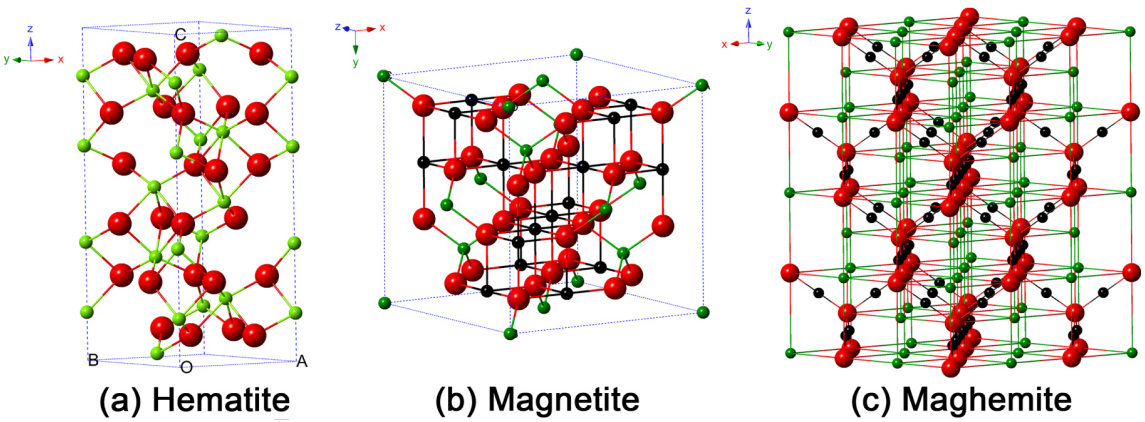

Figure 6 Crystalline structures of hematite magnetite and maghemite

Below the Curie temperature both maghemite and magnetite crystals show the typical Weiss domain of ferromagnetic materials. If the crystals of these iron oxides are characterized by a nanometric size (< 100 nm) their magnetic behaviour is classified as superparamagnetic.

It is important to underline that the iron oxide phases presented above are at the equilibrium phase, in fact by changing the environmental condition (such as temperature, pressure and pH) it is possible to transform one iron oxide into the other. A scheme of the numerous complex reactions involved in this equilibrium is reported in Figure 7. This complex reaction scheme is extremely important in order to verify the possibility of employing a specific iron oxide as catalyst or catalytic support under determinate conditions.

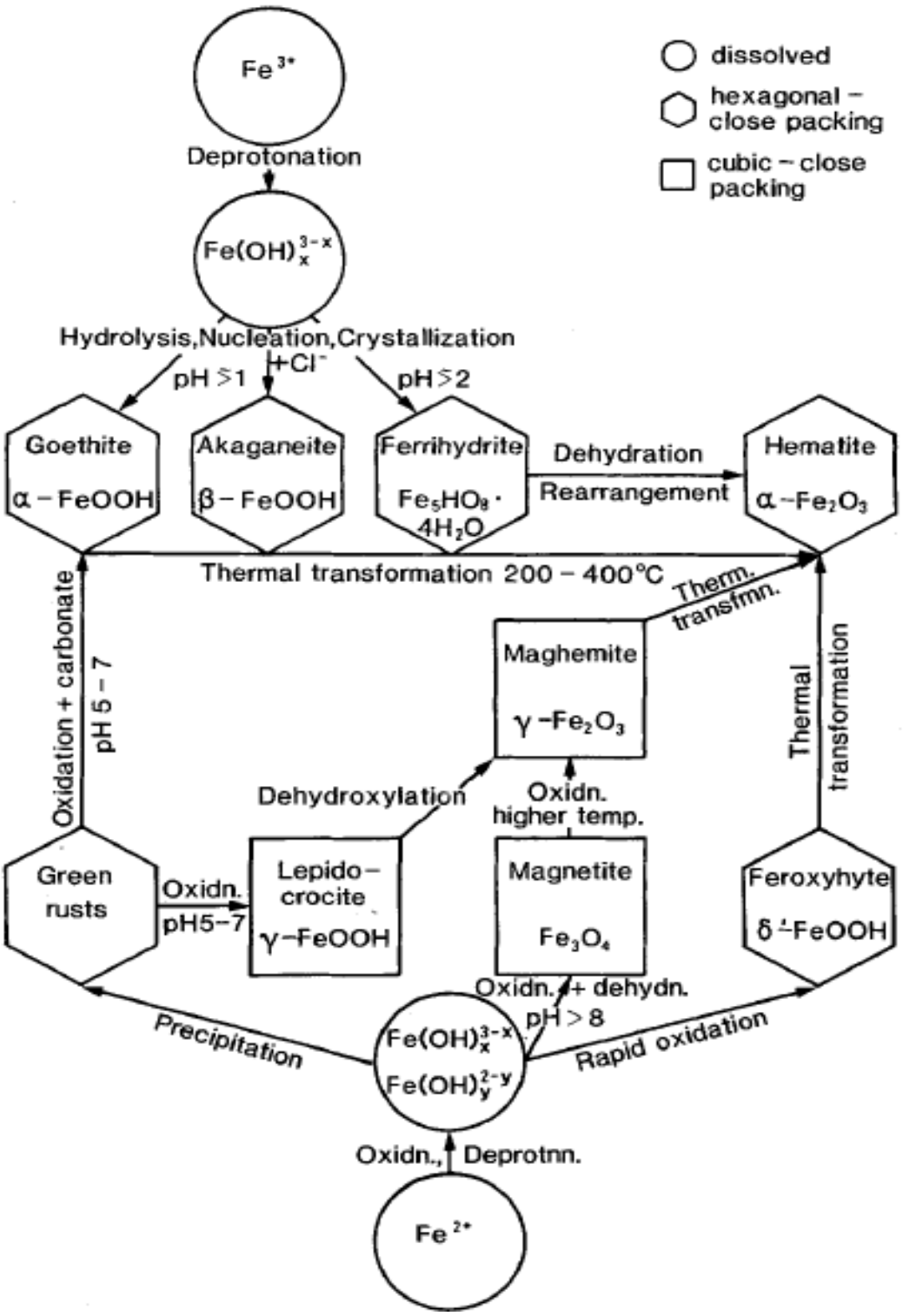

Figure 7 Scheme of the reaction involved in iron oxide phase transformations[17]

The preparation of nanoparticles composed of a single stable iron oxide phase is quite a hard task; therefore accurate phase identification is fundamental to ascertain the composition of the obtained nanomaterial.

As described by Schwertmann et al. it is possible to identify and characterize the diverse iron oxides through their physical chemical properties.[18] In particular the main distinctive aspects are:

- Mineral Colour
- Mineral crystalline structure
- Magnetic properties

Colour analysis can be a simple visual analysis or a specific colorimetric analysis using a CIELAB colorimeter or a Spectrophotometer UV-VIS.

The crystalline structure of the mineral is the unique digital footprint for each iron oxide. The crystalline parameters, the kind of Fe-O bond and the dimensions of the crystalline cell of each iron compound can be determined by using diverse techniques: X-Ray diffractometry, Raman spectrometry and FT-IR spectroscopy.

Finally, the magnetic properties, such as the peculiar hysteresis curves, can be investigated by using a Vibrating Sample Magnetometer (VSM) or Superconducting Quantum Interface Device (SQUID).

Mineral colour, crystalline structure and magnetic properties allows to clearly identify hematite, maghemite and magnetite as shown in Table 2.

Table 2 Main characteristics of hematite, maghemite and magnetite

Mineral	Colour	UV band (nm)	Crystal shape	FT-IR band	Raman	Magnetic properties
Hematite	Red	884,649, 529,444, 404,380, 319, 270	Rhombohedral	540,470	224,290, 408,607, 656,1316	Weak
Maghemite	Red brick	934,666, 510,434, 370,315, 250	Cubic	450,470, 570,590, 630	308,375, 513,640, 712,1316	Medium
Magnetite	Black	1400,300	Cubic	590	290,408, 518,672, 1316	Strong

2.4 References

[1] a) N. Rajendran, *International Journal of Scientific Engineering and Research* **2015**, *3*, 47-49; b) R. A. Sheldon, I. W. C. E. Arends and U. Hanefeld in *Introduction: Green Chemistry and Catalysis*, *Vol.* Wiley-VCH Verlag GmbH & Co. KGaA, **2007**, pp. 1-47.
[2] G. Centi and S. Perathoner, *Catalysis Today* **2003**, *77*, 287-297.
[3] P. Anastas and N. Eghbali, *Chemical Society Reviews* **2010**, *39*, 301-312.
[4] C. Burda, X. Chen, R. Narayanan and M. A. El-Sayed, *Chemical Reviews* **2005**, *105*, 1025-1102.
[5] V. Polshettiwar and R. S. Varma, *Green Chemistry* **2010**, *12*, 743-754.
[6] R. A. Van Santen, *Accounts of Chemical Research* **2009**, *42*, 57-66.
[7] M. Che and C. O. Bennett in *The Influence of Particle Size on the Catalytic Properties of Supported Metals*, *Vol. Volume 36* Eds.: H. P. D.D. Eley and B. W. Paul), Academic Press, **1989**, pp. 55-172.
[8] R. Schlögl and S. B. Abd Hamid, *Angewandte Chemie International Edition* **2004**, *43*, 1628-1637.
[9] K. Philippot and P. Serp in *Concepts in Nanocatalysis*, *Vol.* Wiley-VCH Verlag GmbH & Co. KGaA, **2013**, pp. 1-54.
[10] L. M. Rossi, N. J. S. Costa, F. P. Silva and R. Wojcieszak, *Green Chemistry* **2014**, *16*, 2906-2933.
[11] Yves Gossuin, Pierre Gillis, Aline Hocq, Quoc L Vuong and A. Roch, *Nanomedicine and Nanobiotechnology* **2009**, *1*, 299-310.
[12] C. Kittel in *Introduction to Solid State Physics, 7th Edition*, *Vol.* (Ed. Wiley-VCH), **1996**, pp. 333-485.
[13] A. Seabra and P. Haddad in *Cytotoxicity and Genotoxicity of Iron Oxides Nanoparticles*, *Vol.* Eds.: N. Durán, S. S. Guterres and O. L. Alves), Springer New York, **2014**, pp. 265-279.
[14] a) D. Ling, N. Lee and T. Hyeon, *Accounts of Chemical Research* **2015**, *48*, 1276-1285; b) L. Gutierrez, R. Costo, C. Gruttner, F. Westphal, N. Gehrke, D. Heinke, A. Fornara, Q. A. Pankhurst, C. Johansson, S. Veintemillas-Verdaguer and M. P. Morales, *Dalton Transactions* **2015**, *44*, 2943-2952; c) R. Jin, B. Lin, D. Li and H. Ai, *Current Opinion in Pharmacology* **2014**, *18*, 18-27.
[15] Y. Xisheng, L. Dongsheng, J. Zhengkuan and Z. Lide, *Journal of Physics D: Applied Physics* **1998**, *31*, 2739.
[16] W. Wei, W. Zhaohui, Y. Taekyung, J. Changzhong and K. Woo-Sik, *Science and Technology of Advanced Materials* **2015**, *16*, 023501.
[17] U. Schwertmann and R. M. Cornell in *The Iron Oxides*, *Vol.* Wiley-VCH Verlag GmbH, **2007**, pp. 5-18.
[18] R. M. Cornell and U. Schwertmann in *Characterization*, *Vol.* Wiley-VCH Verlag GmbH & Co. KGaA, **2004**, pp. 139-183.

3. METHODOLOGIES FOR THE SYNTHESIS OF MAGNETIC IRON OXIDE NANOPARTICLES

3.1 Introduction

Magnetic iron oxide nanoparticles (MNPs) find smart and increasing applications in many strategic fields thanks to their striking physicochemical properties[1]. These materials are suitable candidates for a wide range of uses in many different areas of science and technology. In particular, they are attractive in biomedicine and biotechnology for the production of implantable devices, such as biosensors, drug delivery systems, catheters and micro dialysis probes[2], magnetic resonance imaging[3] and hyperthermia therapy[4]. In industry MNPs are applied for nanocatalysis[5], magnetic membranes[6], sensors[7] and storage devices[8]. In particular, magnetic nanocatalysts are becoming a strategic choice for industrial processes, not only from an economic point of view but also for the eco-sustainability of the entire process, because the magnetic recovery of MNPs from the reaction mixture is simpler and more efficient than conventional separation methods[9].

It is important to underline that nanoparticle catalytic performances are strongly connected to their size, shape, composition, surface structure and stability, and these parameters are strongly influenced by the synthetic procedure adopted for nanoparticles preparation.

In particular, taking into account that most of MNPs peculiar properties are strongly connected to their size and shape, good particle stability against aggregation results fundamental[10].

Generally, metal nanoparticles are only kinetically stable and tend to aggregate with time, especially when inter-particle distance is short enough to permit particle attraction and aggregation due to Van der Waals forces. However, the stability of colloidal dispersion can be achieved by using specific stabilizing agents able to generate repulsive forces opposed to Van der Waals ones.

Nanoparticle stabilization can be explained using the Derjiaguin-Landau-Verwey-Overbeek theory (DLVO theory)[11], and described through the charge and steric interaction at particle surface. In particular, it is possible to identify three kinds of stabilization: electrostatic stabilization, steric stabilization and electrosteric stabilization.

Electrostatic stabilization is based on the use of ionic compounds and deals with the adsorption of ions on the particle surface. The absorption of ions causes the formation of an electrical double layer around the particles that generates the Coulombic repulsion between them. If the Coulombic repulsion is higher than Van der Waals attraction forces this electrostatic repulsion will prevent particle aggregations. However, this kind of stabilization is very sensitive to the chemical environment, and any parameter which influences the colloidal dispersion (such as temperature, ionic strength and concentration) can result in electrical double layer disruption and consequently particles aggregation.

Steric stabilization is based on the particle surface coating with sterically bulky compounds such as polymers, dendrimers, amines, thiols, phosphine, silanes and aminosilanes. This large protective layer is able to limit the movement of the particles thus preventing particles aggregation. Moreover, if two particles are near enough to interpenetrate their protective layer, an osmotic repulsion force occurs. This osmotic force pushes the solvent between the particles re-establishing the initial solvent concentration.

Finally, electrosteric stabilization is a combination of the above stabilizations and is based on the use of ionic surfactants. In particular, particle surfaces are coated with long and sterically bulky molecules characterized by a polar group and a long carboxylate chains that provide electrostatic and steric stabilization.

In conclusion, to obtain well-defined stable MNPs an accurate design of the synthetic approach is required.

The methodologies for the preparation of MNPs are divided into the “Top-Down” and the “Bottom-Up” techniques represented in Figure 1. The “Top-Down” approaches involve thermal, chemical or mechanical disintegration of large bulk material into nanostructures.

The “Bottom-Up” approaches are chemical techniques which involve first the generation of metal atoms from salt or organometallic precursors and then their growth and agglomeration until a determined nano-size. Commonly, Bottom-Up approaches involve specific reducing agents such as dihydrogen, sodium borohydride, amineboranes, hydrazine, alcohols or diols and stabilizing agents such as polymers, dendrimers and surfactants to control nanoparticle agglomeration.

For the preparation of MNPs the most common “ Bottom-Up” synthetic techniques are:

- Co-precipitation;
- Hydrothermal;
- Microemulsion;

- Polyol;
- Areosol/vapour pyrolysis;
- Electrochemical;
- Microwave or sonochemical assisted approaches.

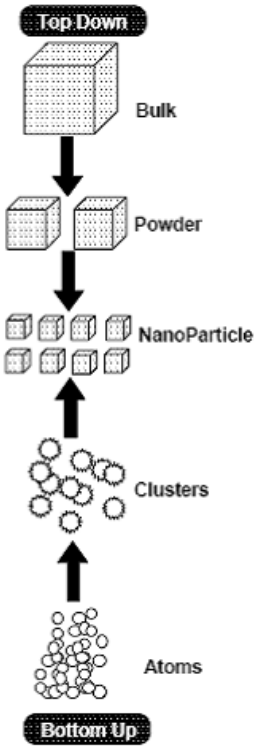

Figure 1 Schematic representations of Top-Down and Bottom-Up approaches for the preparation of nanoparticles

Among them co-precipitation and hydrothermal methods are the most extensively used. In this work the relationship between the diverse synthetic parameters and the final textural particle properties were studied to better optimize and customise the synthetic procedures.

3.2 Synthesis of iron oxide nanoparticles: the co-precipitation approach

The traditional co-precipitation technique is based on two steps, the nucleation of nanoparticle seeds and their subsequent growth. In particular, the nucleation stage starts when the concentration of the constituent species reaches critical saturation point, then the obtained seeds start to grow by diffusion of solutes from the solution. This mechanism was described by La Mer et al.[12] and represented in Figure 2. The main disadvantage of this approach is the lack in nanoparticle size and shape controls. In fact, only by keeping the

nucleation stage well separated from the growth stage is it possible to achieve narrow particle size distribution.

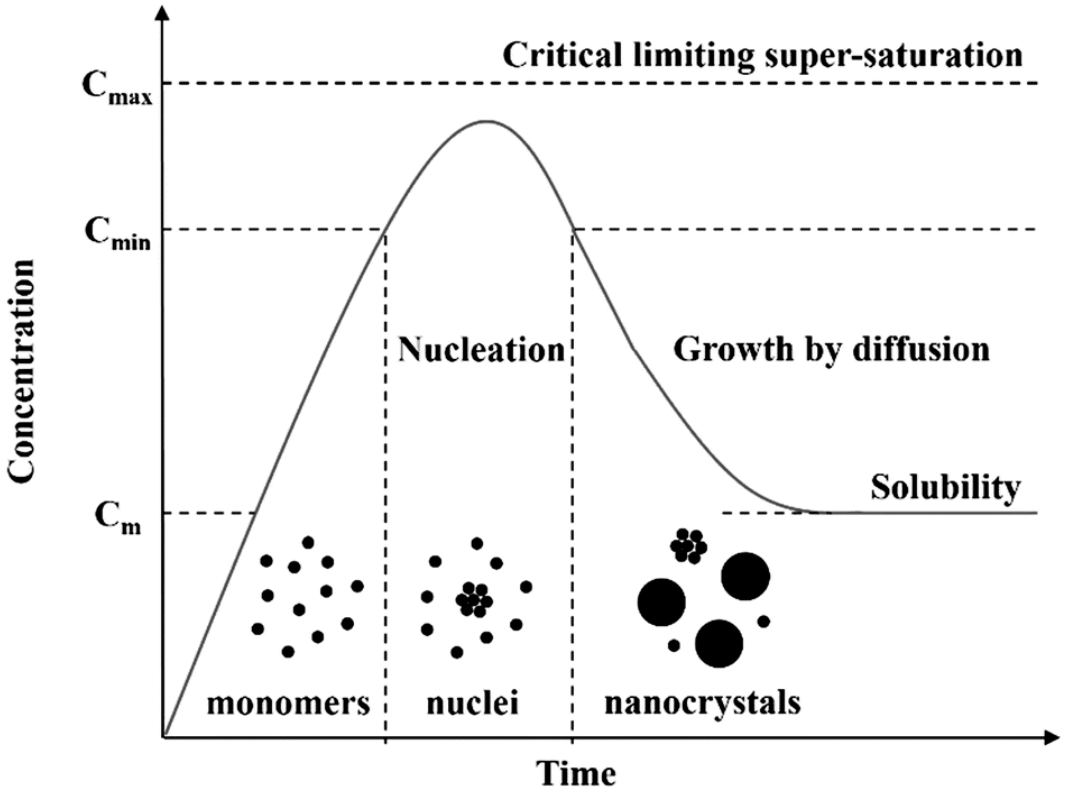

Figure 2 La Mer schematic mechanisms of nanoparticle nucleation and growth

Co-precipitation is a common technique for producing magnetic iron oxides, and is based on the dissolution of Fe^{II} and Fe^{III} salts in aqueous media and the subsequent precipitation of iron oxide nanoparticles by increasing the pH up to 8-14 (see Scheme 1). This approach leads to the preparation of diverse iron oxides such as hematite, maghemite and magnetite. For example, Ramaya et al. showed the preparation of diverse pure iron oxide phases and their mixtures by changing the reaction conditions[13].

$$1Fe^{2+} + 2Fe^{3+} + 8OH^- \longrightarrow Fe_3O_4 + 4H_2O$$

$$Fe_3O_4 + 2H^+ \longrightarrow \gamma\text{–}Fe_2O_3 + Fe^{2+} + H_2O$$

Scheme 1 Scheme of the reactions involved in the co-precipitation of iron oxide

Nanoparticle size, shape, magnetic properties and catalytic activity are strongly connected to the adopted synthetic conditions such as the type of precursor, the Fe^{II}/Fe^{III} molar ratio, reaction temperature, pH value and the ionic strength of the solvent.

By selecting the right reaction conditions it is possible to produce well-defined iron oxide nanoparticles, as described also by E. Rafiee et al.[14] who reported the preparation of maghemite (γ-Fe_2O_3) nanoparticles. In more specific detail, their procedure involved the dissolution of iron chlorides salts. NH_4OH 6 M and NH_4OH at 25% wt. were then added to this solution and heated at boiling temperature under reflux for 1h. S. Keshavarz et al.[15], instead, described the preparation of magnetite, Fe_4O_3 nanoparticles characterized by an average diameter of 10 nm. These small particles were obtained starting from an iron aqueous solution characterised by a Fe^{II}/Fe^{III} molar ratio of 2/1. Then 20 wt.% of polyacrilic acid was added to this solution and it was heated up to 95°C. When this temperature was reached, the pH of the resulting solution was increased up to 10 by adding NaOH. After 3 h the magnetite nanoparticles were collected by centrifugation.

Finally, K. C. Souza et al.[16] showed the preparation of magnetite nanoparticles through precipitation of $FeSO_4$ under aqueous alkaline pH obtained by adding KOH.

Several other co-precipitation procedures are reported in the literature involving different kinds of iron salts such as chlorides[17], sulfates[18] and nitrates[19] , numerous alkaline precipitation auxiliaries such as sodium hydroxide[20], ammonia[21], ammonium monobasic phosphate[22] and hydrazine[23] and organic stabilizing agents like polyvinylalcohol[24], polyacrilic acid[15], citric acid[25], oleic acid and other organic compounds[26].

The use of diverse kinds of hazardous and unfriendly auxiliaries strongly discouraged the use of co-precipitation as an industrial process to produce MNPs. In fact, the growing interest in environmental protection and tightened environmental standards lead to re-design the classical preparations. Moreover, efficient particle size control and high purity iron oxide are difficult to obtain when adopting co-precipitation methods. For these reasons in this work, a new, greener and efficient precipitation approach to produce well-defined nanoparticles is proposed.

3.3 Synthesis of iron oxide nanoparticles: the solvolthermal approach

The solvolthermal method involves the use of solvents under moderate to high pressure (typically between 1 atm and 1000 atm) and temperature (typically over 100 °C). These harsh conditions facilitate the interaction between metal precursors during synthesis. The

most common metal precursors adopted for solvothermal preparations are metal salts or organometallic compounds (such as chlorides, nitrates and acetates).

In the solvothermal approach, solvent characteristics, such as ionic product, density, thermal conductivity, viscosity, heat capacity and the dielectric constant are extremely important. All these peculiar characteristics are strongly dependent on the adopted pressure and temperature.

For example, the dielectric constant of solvents drastically changes with the temperature (see Figure 3), and rapresents a very important parameter because it determines the solubility of polar and ionic species, which are usually employed as precursors in the solvothermal preparation.

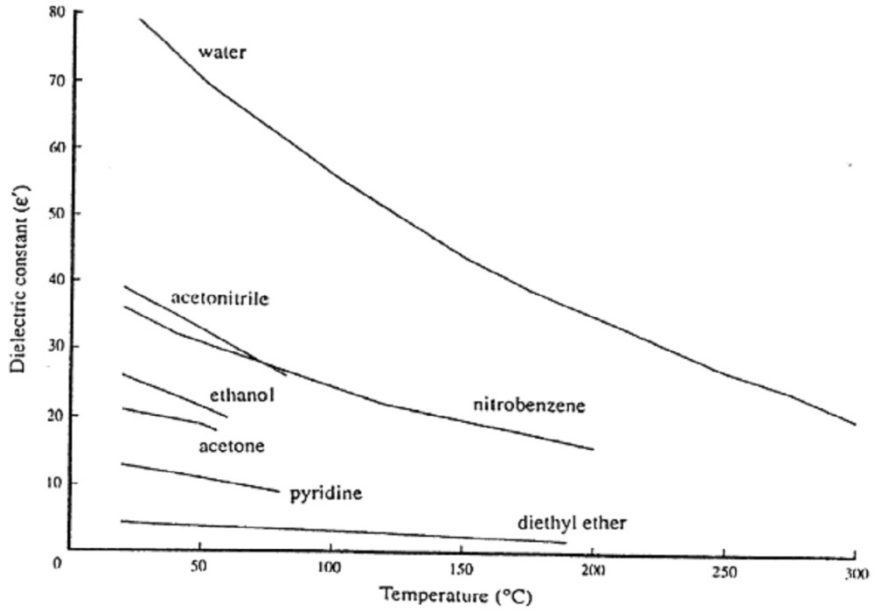

Figure 3 Dielectric constant vs temperature for diverse solvents

Specific nanoparticle characteristics can be obtained simply by tuning the reaction conditions, as pressure, temperature and kind of solvent.

T. Adschiri et al.[27] reported the classical hydrothermal mechanism for the preparation of metal oxides from a salt aqueous solution. The hydrothermal mechanism, as can be observed in Scheme 2, is divided into two steps: salt hydrolysis and its subsequent dehydration.

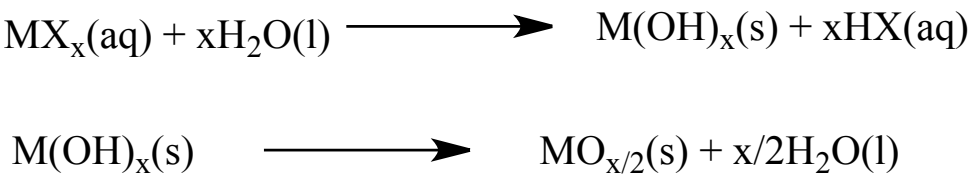

Scheme 2 Classical hydrothermal reaction mechanism proposed for the preparation of metal oxides from a salt solution where M is the metal and X is the anion of the metal salt.

In particular, the first step deals with the hydrolysis of the metal salts to produce the metal hydroxide, while the second step is the dehydration of metal hydroxides to metal oxides. However, the mechanism that controls the reaction is not completely understood, in fact the intermediate hydroxides are not stable and their structure and formation are not fully cleared.

Furthermore, the hydrothermal synthesis can also start from organometallic precursors, in this case the decomposition of the organic part of the metal precursor must be considered as shown in Scheme 3. The partial oxidation of Fe(II) to Fe(III) is guarantee by a complex balance between the oxidizing power of the oxygen dissolved in the water medium and the reducing power of the adopted alcohol.

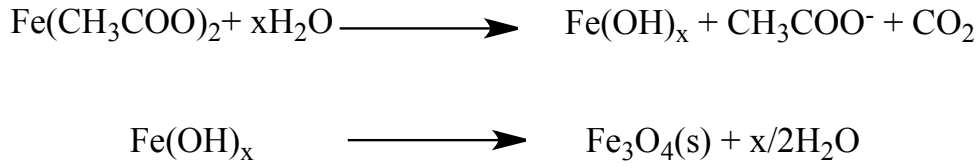

Scheme 3 Hydrothermal reaction mechanism proposed for the preparation of magnetite from organometallic precursors

Several authors report MNP preparation through solvothermal procedures, L. Hu et al.[28] for example, described the preparation of diverse iron oxides through the hydrothermal treatment of iron chlorides in an aqueous ethanol solution. In particular, by changing the precursor concentration, temperature, pH and reaction time it was possible to obtain the different single iron oxide phases or their mixture. Y.H Zheng et al.[29] showed the preparation of magnetite nanoparticles utilizing iron(III) nitrate in an aqueous medium.

M. Gotić et al.[30], instead, showed the synthesis of magnetite nanoparticles by adopting hydrothermal decomposition of the iron(III) acetate.

The iron oxidation state control is a fundamental task for the solvothemical approach, because it can drive the synthesis toward the desired pure ion oxide. As explained in Chapter 2, there are a lot of complex balances between the iron(II) and iron(III) species, which could occur in the preparation of diverse pure iron oxides or iron oxide mixtures.

Hydrothermal processes can be used to prepare diverse nanostructured geometries such as sphere (0D) rod or wire (1D) and sheet (2D), controlled by manipulating solvent supersaturation and metal precursor concentration. However, efficient size, shape and composition control is difficult to reach and generally requires the addition of different stabilizing agents such as oleic acid[31], oleylamine[32], pyrrolidone[33], polyethilene glycol[34], and long reaction times. The adsorption of these stabilizing compounds on nanoparticle surfaces generates a protective layer, which lead to the catalyst surface passivation, reducing the catalytic activity. Moreover, this protective layer can act as a magnetic shield by decreasing the final magnetic behaviour of MNPs. For all these reasons, in this work a greener hydrothermal procedure, able to assure narrow particle size and good magnetic behaviour, is proposed.

3.4 Synthesis of iron oxide nanoparticles: the microemulsion approach

Microemulsion is a thermodynamically stable dispersion of two immiscible liquids, where the microdomains are stabilized by the presence of surfactant. For example, in water-in-oil microemulsions, the aqueous phase is organized as a micelles surrounded by a monolayer of surfactant in a continuous hydrocarbon media. It is possible to control the micelle size and shape simply by choosing the right kind of surfactant and water/surfactant molar ratio as showed in Figure 4.

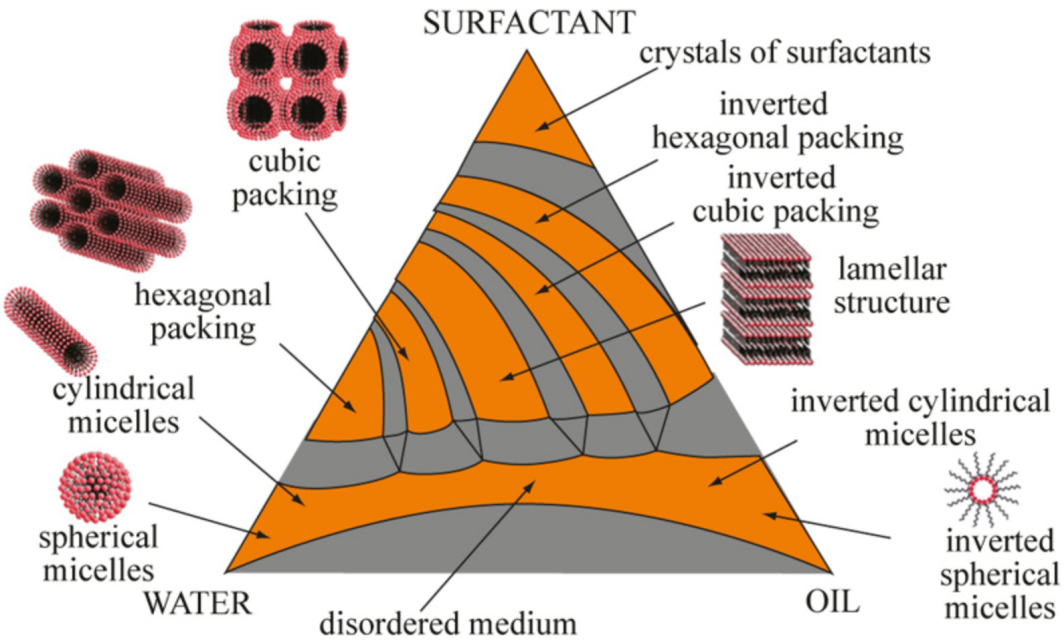

Figure 4 Water-in-oil microemulsion phase diagram with the diverse micelle geometries

The micelles can be used as a microreactor for metal particle synthesis and their size and shape strongly influences particle growth. By adding metal salts to water-in-oil microemulsion, the salts selectively enter into the water micelle leading to the nucleation of nanoparticles. The nanoparticle can grow into this microdomain reaching the maximum micelle size and shape. At the end of the growth process, it is possible to precipitate nanoparticles destabilizing the water-in-oil microemulsion by adding a polar solvent. The microemulsion schematic process is shown in Figure 5.

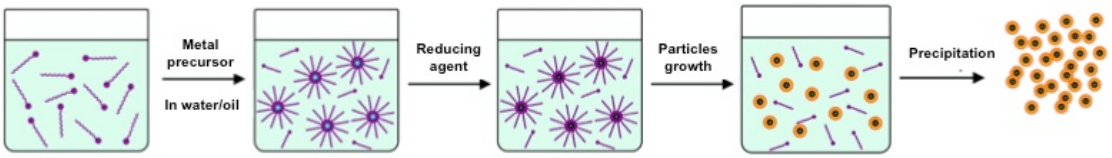

Figure 5 Schematic representation of water-in-oil microemulsion preparation of MNPs

Housaindokht et al.[35] reported the study of the dependence between particle size and surfactant hydrophilic-lipophilic balance. The surfactant hydrophilic-lipophilic balance is an important concept related to the interfacial packing of surfactants that are connected with the micelle geometry and structure.

This technique allows the preparation of many types of magnetic nanoparticles characterized by a relatively wide range of controlled size and shape that strongly depend on the micelle structures. C. Okoli et at.[36] for example reported the preparation of magnetite through water-in-oil microemulsion and its inverse system underlining the marked difference in particle textural properties. In particular, oil-in-water systems lead to smaller particles characterized by the highest surface area.

Moreover, magnetite nanoparticles with around 10 nm diameter have been prepared by Z. L. Liu et al.[37] by adopting controlled hydrolysis of $FeCl_2$ and $FeCl_3$ aqueous solutions within a reverse micelles generated using sodium dodecyl benzene sulphonate (DBS) as surfactant and toluene as the continues oil phase. Numerous analogous procedures have been reported for the microemulsion production of magnetic nanoparticles although the working windows for the microemulsion synthesis is quite narrow and the nanoparticles production yield is usually low if compared with those reached with the other techniques. In conclusion, this process is not really sustainable either from an economical and

environmental point of view being characterized by low process efficiency and extensive energy and solvent consumption.

3.5 Synthesis of iron oxide nanoparticles: the polyol approach

The Polyol technique is based on the use of liquid polyols acting as reaction medium, solvent, reducing agent and in some cases, as complexing agents for the metallic precursors. The metallic salts are dissolved or suspended in polyol and the final metal o metal oxide is precipitated under stirring and heating. The general reaction mechanism of polyol process is shown in scheme 4.

$$OHCH_2CH_2OH \longrightarrow CH_3CHO + H_2O$$

$$Fe^{3+} + 2OH^- + 2CH_3CHO \longrightarrow CH_3COCOCH_3 + Fe^{2+} + 2H_2O$$

$$1Fe^{2+} + 2Fe^{3+} + 8OH^- \longrightarrow Fe_3O_4 + 4H_2O$$

Scheme 4 MNPs preparation by polyol synthesis

Numerous polyol procedures have been reported in the literature adopting different types of polyols. F. Fievet et al.[38], for example, described the use of ethylene glycol and polyethylene glycol as reducing agent and reaction medium. H. L. Liu et al.[39] reported the preparation of magnetite nanoparticles utilizing iron(III) acetylacetonate dispersed in 1,2 hexandecanediol, octyl ether, polyvinylpirrolidone and then heated up to 120°C for 1 h. Analogously J. Wan et al.[40] showed the preparation of magnetite nanoparticles through thermal decomposition of iron(III) acetylacetonate in triethylene glycol and D. Arndt et al.[41] described the same reaction in diethylene glycole.

By adopting this procedure it is possible to control size and shape of nanoparticles by selecting the kinetic profile of the precipitation and the kind of polyol involved.[42]

C. Cheng et al.[43] studied the effect of two polyols, ethylene glycol and propylene glycol on nanoparticle size distribution. A better control of nanoparticle size distribution can be achieved keeping nucleation and growth stages well separate. For example, it is possible to seeds the reactive medium with well-defined metal seeds (small nanoparticles), which start to grow up all together at the same time, reaching almost the same size.

However, this technique is not extensively adopted because it requires high temperatures and un-sustainable organic compounds.

3.6 Synthesis of iron oxide nanoparticles: metal areosol/vapour approaches

Spray and laser pyrolysis are two metal aerosol/vapour techniques based on the pyrolysis of metal solution droplets. In particular, spray pyrolysis allows the preparation of solid nanoparticles by spraying a solution into a furnace. The obtained aerosol droplets undergo evaporation of the solvent and thermolysis leading to the formation of solid nanoparticles. On the other hand, laser pyrolysis involves the heating of a flowing mixture of gases with a continuous wave carbon dioxide laser, which initiates and sustains the chemical reaction. At certain pressure and laser power, a critical concentration of metal is reached, which leads to homogeneous nucleation of particles. These particle nuclei then grow and are collected in a filter. The laser and spray pyrolysis schemes are represented in Figure 6.

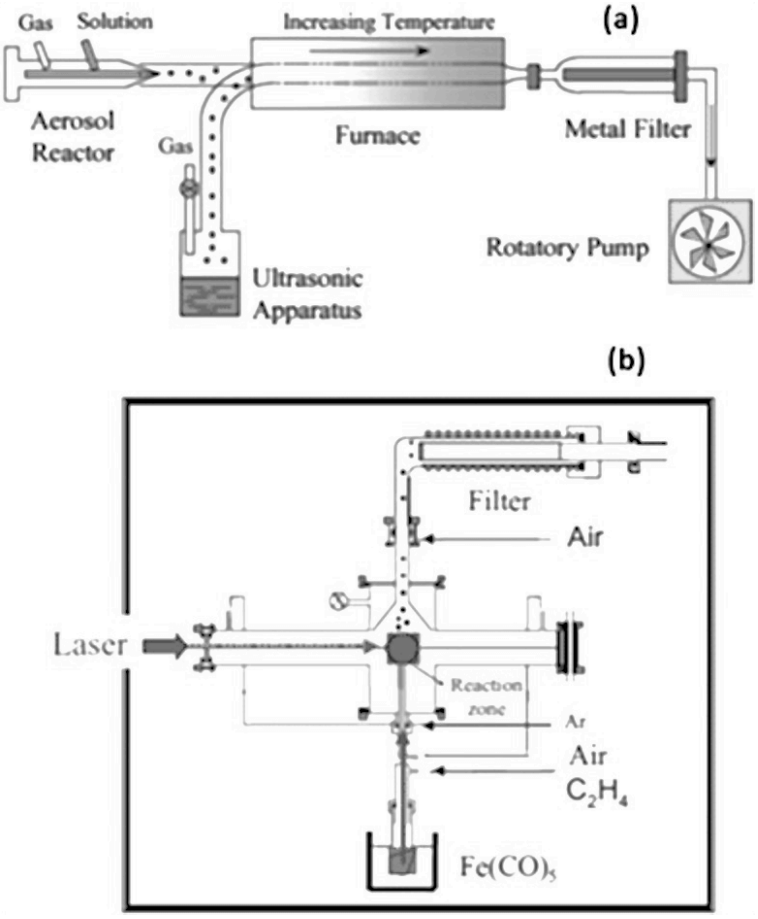

Figure 6 Schematic representation of: a) the spray pyrolysis device and b) the laser pyrolysis device both used for nanoparticle preparation

In conclusion, the main difference between spray and laser pyrolysis is the final state of the obtained nanostructures. In particular, in spray pyrolysis the particles are generally more aggregated than in laser pyrolysis.

In fact J. N. Wang et al.[44] evidenced the degree of aggregation of the magnetite particles obtained by spray pyrolysis, and O. B. Miguel et al.[45] obtained very narrow size distributed magnetite nanoparticles with the laser pyrolysis method. Aerosol/vapour techniques do not allow good control of particle composition, therefore the MNPs obtained could contain traces of other iron oxides, with detrimental consequences on the magnetic and catalytic properties.

3.7 Synthesis of iron oxide nanoparticles: the electrochemical approach

The electrochemical synthesis of iron oxides uses a sacrificial iron anode as the metal source. The anode is immersed in an electrolytic solution of a quaternary ammonium salt and oxidized in the presence of a stabilizing agent. The oxidation of the sacrificial iron anode results in the formation of reactive cations that form an oxygenated species in the electrolytic solution. The oxygenated species can subsequently aggregate and precipitate. The fundamental steps of this technique are:

1. Oxidative dissolution of the sacrificial anode;
2. Migration of the reactive cations obtained;
3. Reaction between cations and oxygenated species present in the electrolytic solution leading to nanoparticle nucleation;
4. The end of nanoparticle growth and their stabilization with surfactant molecules;
5. Precipitation of nanostructured iron oxides.

The reactions involved in the electrochemical preparation of iron oxide nanoparticles are reported in Scheme 5. It important to remark that by selecting the oxidizing condition it is possible to prepare magnetite nanoparticles or maghemite nanoparticles as discussed by H. R. Khan et al.[46]

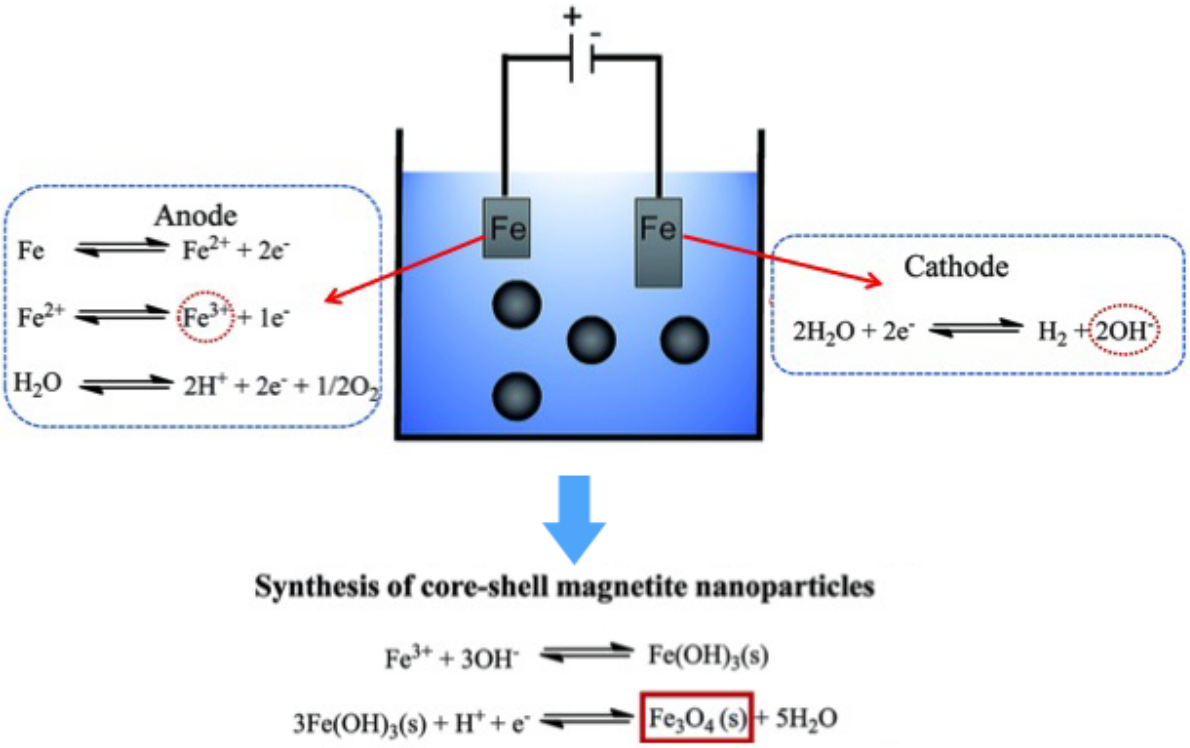

Scheme 5 Electrochemical mechanism of iron oxide nanoparticle synthesis

Recently, the electrochemical procedure was adopted also for the preparation of core-shell magnetic nanoparticles, where the magnetite is coated by a polymeric shell[47].

The electrochemical method presents several advantages: the absence of nanoparticles contamination by by-products and the control of particle size by varying the current density. Despite these positive aspects, this approach presents also some drawbacks, such as high energy consumption and the difficulties connected with the scale-up.

3.8 Synthesis of iron oxide nanoparticles: microwave or ultrasound assisted approaches

Microwave (MW) and ultrasonic irradiation are two alternative green energy sources that can facilitate chemical reactions.

Microwave heating is a strategic tool for the design of greener and more sustainable nanosynthesis, in fact it allows a shorter reaction time, reduced energy consumption and higher product yields[48]. Microwave heating is based on the interaction between the electromagnetic radiation and the dipole moment of the molecules; therefore only polar

solvents and molecules characterized by dipole moments can be heated by MW-irradiation[49].

Microwaves are electromagnetic waves characterized by a low frequency ($3 \times 10^2 - 3 \times 10^4$ MHz) able to cause the movement of particle charges. These rotation and migration movements result in molecular polarization. The dipoles of the molecules try to align themselves with the rapidly changing electric field of microwaves ($2{,}4 \times 10^9$ per second) and this causes the heating of the solution. The extent of microwave heating is connected to the relative permittivity ε' that is a measure of the ability of a molecule to be polarized by an electric field, and the dielectric loss ε'' that is indicative of the ability of the medium to convert dialectic energy into heat. The dependence between permittivity, dielectric loss and heating rate is described in equation 1.[50]

$$\tan \delta = \varepsilon' / \varepsilon'' \qquad (1)$$

Where tan δ is the dielectric loss tangent and defines the ability of the substrate to transform electromagnetic energy into thermal energy. Each polar solvent or compound shows a different tan δ.

Thanks to its characteristics, microwave heating shows numerous benefits if compared to traditional heating:

- Fast or almost instantaneous heating;
- Lower energy consumption;
- Homogeneous in-core heating, avoiding the wall effect commonly present in traditional thermal heating;
- Selective heating based on the ability of a certain substrate to interact with microwaves;
- Overheating effect that allows an overheating of polar solvents in a range of 13-26°C over their boiling point[51].

Conventional heating occurs through contact with a hot surface leading to a temperature profile that progressively decreases with the distance from the heat source, on the contrary microwave heating acts directly on the molecules, allowing an uniform temperature profile inside the reactor (see Figure 7).

The rapid, selective and homogeneous heating assured by MW-irradiation is an extremely important factor in nanoparticle synthesis. In particular, a homogeneous temperature can lead to uniform nanoparticle nucleation and growth, thus resulting in narrow particle size distribution.

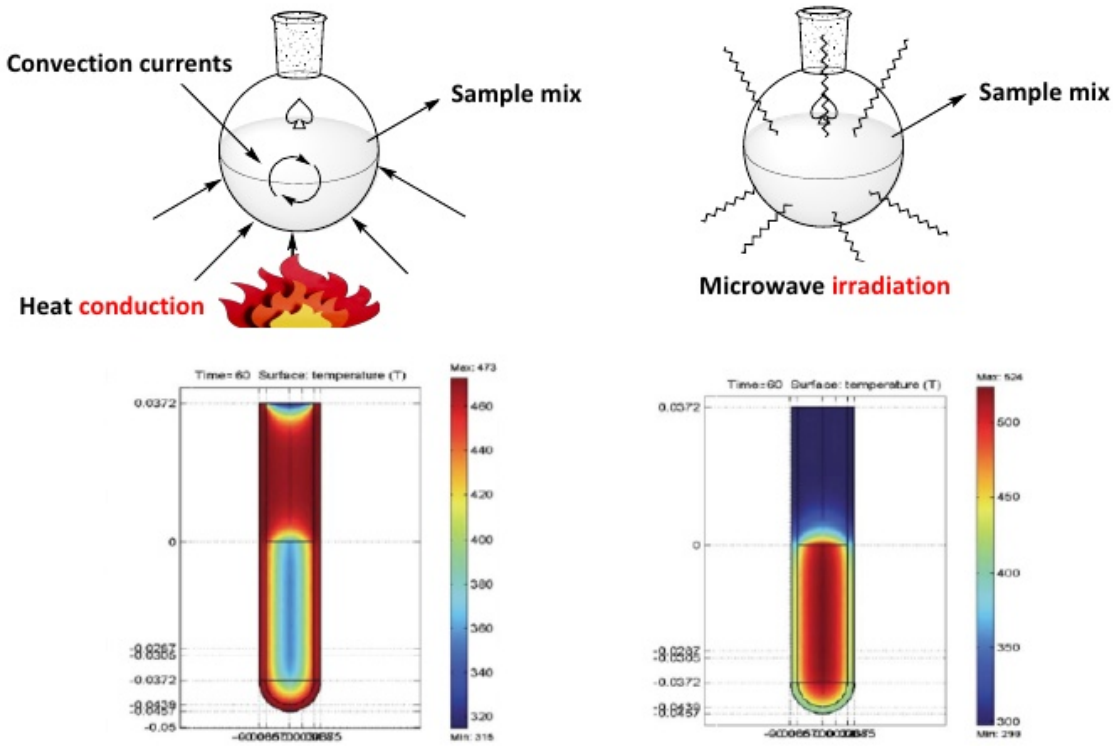

Figure 7 Temperature profile of conventional heating source and microwave heating system

Another peculiar aspect of microwave heating is the overheating effect that brings solvents over their boiling point. This effect is more significant when large amounts of ions are present.

These microwave characteristics provide the uniform nucleation and growth of the nanoparticles, leading to nanomaterials characterized by a wide range of geometries such as polygonal plates, rods, wires, parallelepipeds, shells and spheres.

Recently the interest in microwave-assisted synthesis has grown quickly and several classical iron oxide preparations have been optimized adopting microwaves as the energy source with promising results.

O. Pascu et al.[52] compared iron oxide nanoparticles obtained via classical thermal decomposition with the ones obtained through microwave assisted decomposition, underlining the diverse morphologies reached with these two approaches. In detail, the microwave-assisted decomposition permits the adoption of a softer reaction conditions leading to the formation of nanoparticles with higher catalytic activity.

Nowadays almost all classical iron oxide synthetic methodologies (such as co-precipitation, solvothermal, microemulsion and polyol) were reproduced by optimizing the processes with the use of microwave heating [18, 21-23, 29, 53].

The ultrasonic approach is another important tool for nanostructure synthesis. Ultrasound heating occurs through the acoustic cavitation effect that causes the formation, growth and collapse of bubbles (i.e. cavities) in the liquid media. This cavitational implosion is very localized and transient, characterized by a temperature above 5000 K and a pressure above 1000 bar. The bubbles can overgrow and collapse in a very short time leading to a heating and cooling rate of about 10^{10} K/second. The sonochemical synthesis of metal nanoparticles has advantages over other traditional reduction methods because the cavitational effect permits the reduction of metal salts without chemical reducing agents. In particular, the sonochemical reduction of metal salts involves three steps (see Scheme 6): sonochemical formation of active species such as radicals, hydrolysis of the metal precursors (salts or organometallic compounds) and finally nucleation and growth of metal particles.

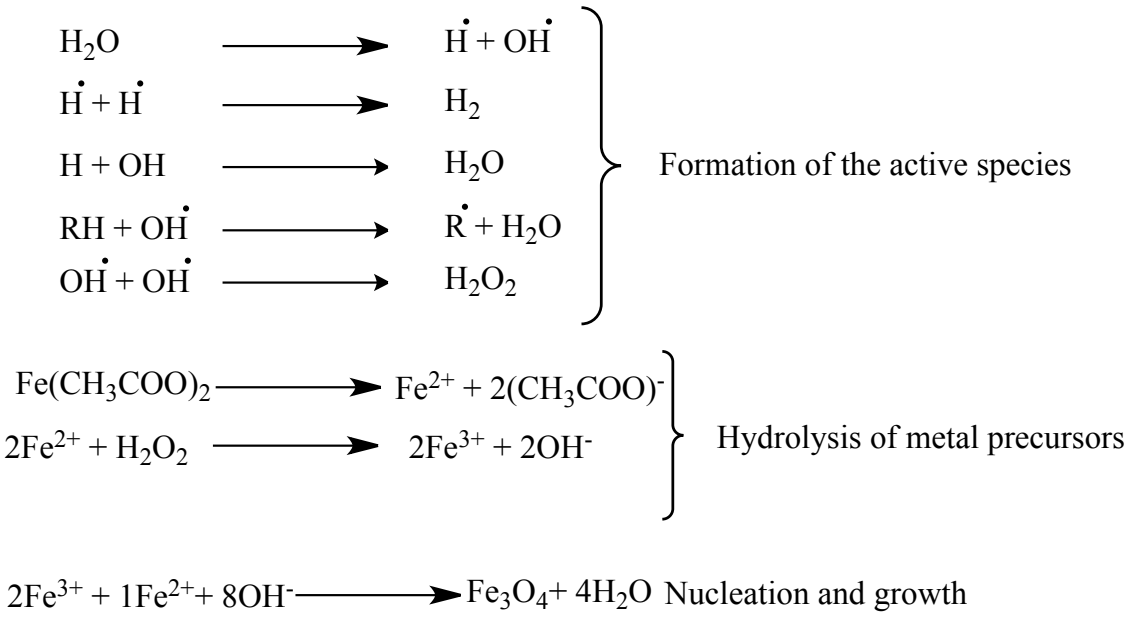

Scheme 6 Sonochemical synthesis of metal nanoparticles

Ultrasounds permits us to achieve small particles characterized by controlled shape and good crystallinity[54]. For example, R. Vijayakumar et al.[55] described the synthesis of magnetite nanoparticles through the sonochemical reduction of iron(II) acetate in water. Similarly C. Marchegiani et al.[56] showed the sonochemical treatment of iron(II) chlorine using di and tri ethylene glycol as stabilizing agents to obtain stable colloidal dispersion.
Microwaves and ultrasounds can be considered sustainable tools to design innovative and greener iron oxide nanosynthesis. Moreover, both these techniques lead to a reduction of

reaction time maintaining good particle size control. For this reason, MW-irradiation is extensively used as an energy source in this work.

3.9 References

[1] B. Issa, I. Obaidat, B. Albiss and Y. Haik, *International Journal of Molecular Sciences* **2013**, *14*, 21266-21305.

[2] a) Wahajuddin and S. Arora, *International Journal of Nanomedicine* **2012**, *7*, 3445-3471; b) A. Joshi, S. Solanki, R. Chaudhari, D. Bahadur, M. Aslam and R. Srivastava, *Acta Biomaterialia* **2011**, *7*, 3955-3963.

[3] H. Y. Yoon, G. Saravanakumar, R. Heo, S. H. Choi, I. C. Song, M. H. Han, K. Kim, J. H. Park, K. Choi, I. C. Kwon and K. Park, *Journal of Controlled Release* **2012**, *160*, 692-698.

[4] M. Bañobre-López, A. Teijeiro and J. Rivas, *Reports of Practical Oncology & Radiotherapy* **2013**, *18*, 397-400.

[5] a) D. Cantillo, M. M. Moghaddam and C. O. Kappe, *The Journal of Organic Chemistry* **2013**, *78*, 4530-4542; b) M. Gawande, A. Rathi, P. Branco and R. Varma, *Applied Sciences* **2013**, *3*, 656-674; c) M. B. Gawande, P. S. Branco and R. S. Varma, *Chemical Society Reviews* **2013**, *42*, 3371-3393; d) V. Polshettiwar, R. Luque, A. Fihri, H. Zhu, M. Bouhrara and J.-M. Basset, *Chemical reviews* **2011**, *111*, 3036-3075; e) C. S. Gill, B. A. Price and C. W. Jones, *Journal of Catalysis* **2007**, *251*, 145-152.

[6] a) W. Karboul-Trojet, Y. Roussigné, D. Faurie and S. M. Chérif, *The European Physical Journal B* **2012**, *85*, 1-7; b) J. Gass, P. Poddar, J. Almand, S. Srinath and H. Srikanth, *Advanced Functional Materials* **2006**, *16*, 71-75.

[7] a) N. V. Long, Y. Yang, M. Yuasa, C. M. Thi, Y. Cao, T. Nann and M. Nogami, *RSC Advances* **2014**, *4*, 6383-6390; b) M.-H. Wu, H.-W. Yang, M.-Y. Hua, Y.-B. Peng and T.-M. Pan, *Biosensors and Bioelectronics* **2013**, *47*, 99-105.

[8] J. M. Haberl, A. Sánchez-Ferrer, A. M. Mihut, H. Dietsch, A. M. Hirt and R. Mezzenga, *Advanced Materials* **2013**, *25*, 1787-1791.

[9] L. M. Rossi, N. J. S. Costa, F. P. Silva and R. Wojcieszak, *Green Chemistry* **2014**, *16*, 2906-2933.

[10] M. Zahmakran and S. Ozkar, *Nanoscale* **2011**, *3*, 3462-3481.

[11] M. Yang, C. M. Neubauer and H. M. Jennings, *Advanced Cement Based Materials* **1997**, *5*, 1-7.

[12] V. K. LaMer and R. H. Dinegar, *Journal of the American Chemical Society* **1950**, *72*, 4847-4854.

[13] S. I. S. Ramya and C. K. Mahadevan, *Materials Letters* **2012**, *89*, 111-114.

[14] E. Rafiee and S. Eavani, *Green Chemistry* **2011**, *13*, 2116-2122.

[15] S. Keshavarz, Y. Xu, S. Hrdy, C. Lemley, T. Mewes and Y. Bao, *Magnetics, IEEE Transactions on* **2010**, *46*, 1541-1543.

[16] K. C. Souza, G. Salazar-Alvarez, J. D. Ardisson, W. A. A. Macedo and E. M. B. Sousa, *Nanotechnology* **2008**, *19*, 185603.

[17] A. Bandhu, S. Mukherjee, S. Acharya, S. Modak, S. K. Brahma, D. Das and P. K. Chakrabarti, *Solid State Communications* **2009**, *149*, 1790-1794.

[18] X. Du, C. Wang, M. Chen, Y. Jiao and J. Wang, *The Journal of Physical Chemistry C* **2009**, *113*, 2643-2646.

[19] I. U. Haq and F. Haider, *Journal of the Chinese Chemical Society* **2010**, *57*, 174-179.

[20] R. Hong, J. Li, J. Wang and H. Li, *China Particuology* **2007**, *5*, 186-191.

[21] R. Y. Hong, J. H. Li, H. Z. Li, J. Ding, Y. Zheng and D. G. Wei, *Journal of Magnetism and Magnetic Materials* **2008**, *320*, 1605-1614.
[22] X. Hu and J. C. Yu, *Advanced Functional Materials* **2008**, *18*, 880-887.
[23] W.-W. Wang, Y.-J. Zhu and M.-L. Ruan, *Journal of Nanoparticle Research* **2007**, *9*, 419-426.
[24] J. Lee, T. Isobe and M. Senna, *Colloids and Surfaces A: Physicochemical and Engineering Aspects* **1996**, *109*, 121-127.
[25] Y. Sahoo, A. Goodarzi, M. T. Swihart, T. Y. Ohulchanskyy, N. Kaur, E. P. Furlani and P. N. Prasad, *The Journal of Physical Chemistry B* **2005**, *109*, 3879-3885.
[26] Y. Sahoo, H. Pizem, T. Fried, D. Golodnitsky, L. Burstein, C. N. Sukenik and G. Markovich, *Langmuir* **2001**, *17*, 7907-7911.
[27] T. Adschiri, K. Kanazawa and K. Arai, *Journal of the American Ceramic Society* **1992**, *75*, 1019-1022.
[28] L. Hu, A. Percheron, D. Chaumont and C.-H. Brachais, *Journal of Sol-Gel Science and Technology* **2011**, *60*, 198-205.
[29] Y.-h. Zheng, Y. Cheng, F. Bao and Y.-s. Wang, *Materials Research Bulletin* **2006**, *41*, 525-529.
[30] M. Gotić and S. Musić, *European Journal of Inorganic Chemistry* **2008**, *2008*, 966-973.
[31] F. Y. Jiang, C. M. Wang, Y. Fu and R. C. Liu, *Journal of Alloys and Compounds* **2010**, *503*, L31-L33.
[32] B. Sarah, L. Sophie, V. Marjorie, E. Luce Vander, P.-M. David and N. M. Robert, *Nanotechnology* **2013**, *24*, 055705.
[33] Z. Li, Q. Sun and M. Gao, *Angewandte Chemie International Edition* **2005**, *44*, 123-126.
[34] K. A. Porter, Barnhardt, Keller E. in *Synthesis and use of intermetallic iron palladium nanoparticle composition*, *Vol.* United States, **2012**, pp. 1-13.
[35] M. R. Housaindokht and A. Nakhaei Pour, *Journal of Chemistry* **2013**, *2013*, 10.
[36] C. Okoli, M. Sanchez-Dominguez, M. Boutonnet, S. Järås, C. Civera, C. Solans and G. R. Kuttuva, *Langmuir* **2012**, *28*, 8479-8485.
[37] Z. L. Liu, X. Wang, K. L. Yao, G. H. Du, Q. H. Lu, Z. H. Ding, J. Tao, Q. Ning, X. P. Luo, D. Y. Tian and D. Xi, *Journal of Materials Science* **2004**, *39*, 2633-2636.
[38] F. Fievet, J. P. Lagier, B. Blin, B. Beaudoin and M. Figlarz, *Solid State Ionics* **1989**, *32–33, Part 1*, 198-205.
[39] H.-L. Liu, S. P. Ko, J.-H. Wu, M.-H. Jung, J. H. Min, J. H. Lee, B. H. An and Y. K. Kim, *Journal of Magnetism and Magnetic Materials* **2007**, *310*, e815-e817.
[40] J. Wan, W. Cai, X. Meng and E. Liu, *Chemical Communications* **2007**, 5004-5006.
[41] D. Arndt, V. Zielasek, W. Dreher and M. Bäumer, *Journal of Colloid and Interface Science* **2014**, *417*, 188-198.
[42] R. J. Joseyphus, D. Kodama, T. Matsumoto, Y. Sato, B. Jeyadevan and K. Tohji, *Journal of Magnetism and Magnetic Materials* **2007**, *310*, 2393-2395.
[43] C. Cheng, F. Xu and H. Gu, *New Journal of Chemistry* **2011**, *35*, 1072-1079.
[44] J. N. Wang, L. Zhang, F. Yu and Z. M. Sheng, *The Journal of Physical Chemistry B* **2007**, *111*, 2119-2124.
[45] O. B. Miguel, M. P. Morales, C. J. Serna and S. Veintemillas-Verdaguer, *Magnetics, IEEE Transactions on* **2002**, *38*, 2616-2618.
[46] H. R. Khan and K. Petrikowski, *Journal of Magnetism and Magnetic Materials* **2000**, *215–216*, 526-528.
[47] E. Mazario, J. Sanchez-Marcos, N. Menendez, P. Herrasti, M. Garcia-Hernandez and A. Munoz-Bonilla, *RSC Advances* **2014**, *4*, 48353-48361.

[48] R. Varma, *Sustainable Chemical Processes* **2014**, *2*, 1-8.
[49] A. Loupy, *Comptes Rendus Chimie* **2004**, *7*, 103-112.
[50] S. A. Galema, *Chemical Society Reviews* **1997**, *26*, 233-238.
[51] A. de la Hoz, A. Diaz-Ortiz and A. Moreno, *Chemical Society Reviews* **2005**, *34*, 164-178.
[52] O. Pascu, E. Carenza, M. Gich, S. Estradé, F. Peiró, G. Herranz and A. Roig, *The Journal of Physical Chemistry C* **2012**, *116*, 15108-15116.
[53] a) V. Sreeja and P. A. Joy, *Materials Research Bulletin* **2007**, *42*, 1570-1576; b) Y. Li, H. Li and R. Cao, *Journal of the American Ceramic Society* **2009**, *92*, 2188-2191; c) M. Baghbanzadeh, L. Carbone, P. D. Cozzoli and C. O. Kappe, *Angewandte Chemie International Edition* **2011**, *50*, 11312-11359; d) V. Polshettiwar, M. N. Nadagouda and R. S. Varma, *Chemical Communications* **2008**, 6318-6320; e) X. Hu, J. C. Yu, J. Gong, Q. Li and G. Li, *Advanced Materials* **2007**, *19*, 2324-2329; f) H. Zhang, X. Zhong, J.-J. Xu and H.-Y. Chen, *Langmuir* **2008**, *24*, 13748-13752; g) Z. Ai, K. Deng, Q. Wan, L. Zhang and S. Lee, *The Journal of Physical Chemistry C* **2010**, *114*, 6237-6242; h) F. Y. Jiang, C. M. Wang, Y. Fu and R. C. Liu, *Journal of Alloys and Compounds* **2010**, *503*, L31-L33.
[54] J. H. Bang and K. S. Suslick, *Advanced Materials* **2010**, *22*, 1039-1059.
[55] R. Vijayakumar, Y. Koltypin, I. Felner and A. Gedanken, *Materials Science and Engineering: A* **2000**, *286*, 101-105.
[56] G. Marchegiani, P. Imperatori, A. Mari, L. Pilloni, A. Chiolerio, P. Allia, P. Tiberto and L. Suber, *Ultrasonics Sonochemistry* **2012**, *19*, 877-882.

4. SYNTHESIS OF NANOSTRUCTURED IRON OXIDES

The synthesis of nanostructured iron oxides is an extremely important key issue because the final properties of nanostructured materials strongly depend on the synthetic conditions adopted during their preparation. In the catalytic application of nanostructures in particular, good control of morphology, size distribution and stability is fundamental[1].

As extensively discussed in chapter 3, the traditional techniques used to prepare nanostructured iron oxides are: co-precipitation, solvothermal, microemulsion, electrochemical, and polyol approach. Among them co-precipitation and solvothermal are the most commonly used thanks to their practicability and reproducibility.

Despite these positive aspects, co-precipitation and hydrothermal methods are poorly sustainable from an environmental point of view. In fact in order to achieve good control on particle characteristics the co-precipitation technique requires the use of different sometimes hazardous stabilizing agents such as oleic acid[2], oleylamine[3], pyrrolidone[4], polyethilen glycol[5] and reducing agents such as hydrazine[6]. The solvothermal method, instead, involves hard reaction conditions such as high temperature, elevated pressure and long reaction times [7].

Furthermore, both these methods require the use of a steric stabilizing agent, which could cause particle surface passivation leading to the inhibition of catalytic sites, and the reduction of magnetic properties.

Taking into account all these aspects, during this PhD work two efficient and greener microwave-assisted procedures for the synthesis of MNPs have been developed. The first approach was based on the precipitation method, and permits the synthesis of different iron oxides (maghemite γ-Fe_2O_3 and hematite α-Fe_2O_3). The second technique is a hydrothermal method that leads to the preparation of pure magnetite particles (Fe_3O_4). Both these procedures can represent a valid sustainable improvement compared to the traditional synthesis, being characterized by a one-step reaction in an alcoholic aqueous medium as solvent, the absence of hazardous reducing agents, short reaction times and the use of microwaves as an efficient heat source. The iron oxides obtained were characterized by X-Ray Diffraction (XRD), Fourier Transform Infrared

Spectroscopy (FT-IR), Auger electron spectroscopy (AES), X-Ray Photoelectron Spectroscopy (XPS), Raman spectroscopy, Transmission Electron Microscopy (TEM), Atomic Force Microscopy (AFM), Vibrating Sample Magnetometer (VSM), BET surface analysis (BET) and Inductively coupled plasma-optical emission spectrometer (ICP-OES).

4.1 Synthesis of iron oxides: the microwave assisted co-precipitation technique

In a typical experiment $FeCl_3 \cdot 1.5H_2O$ (1g) and the proper amount of NaOH (see Table 1) were dissolved in EtOH 96 wt% (44 mL) under stirring. As soon as the base was added the mixture became darker. The resulting mixture was treated by monomode microwave (CEM discovery S-class equipped with the 80 mL glass vessel) at 160°C for 15 minutes at 250W under inert atmosphere. At the end of the treatment, particles were collected using centrifuge at 1500 rpm for 5 minutes, washed three times with EtOH 96 wt% (40 mL) and dried under vacuum for 12 h. They were stored under argon.

It is well known that the precipitation method involves complex balances between numerous iron oxide and hydroxide phases that are strongly influenced by pH, temperature and electrochemical potential. Therefore, by changing the reaction conditions it is possible to drive the diverse species involved into the desired iron oxide phase[8]. The effect of Fe(III)/NaOH molar ratio on the synthesis of the different iron oxides is summarized in Table 1.

Table 1 Precipitation of iron oxide nanoparticles under different Fe(III)/NaOH molar ratio

Sample	Fe(III)/NaOH molar ratio	Iron oxide phase
A	0.31	Hematite
A bis	0.31	Hematite
B	0.17	Maghemite
B bis	0.17	Maghemite
C	0.08	Hematite and Maghemite
C bis	0.08	Hematite and Maghemite

Reaction conditions: EtOH: 44 ml, $FeCl_3 \cdot 1.5H_2O$: 5.29 mmol, MW irradiation conditions: temperature 160 °C, power 250 W, reaction time 15 min.

The obtained nanoparticles were characterized by Raman, FT-IR and XRD analyses.[9] All these techniques together allow the identification of the nature of the different iron oxides.

Figure 1 shows the Raman spectra of samples A, B and C synthetized adding different sodium hydroxide concentrations.

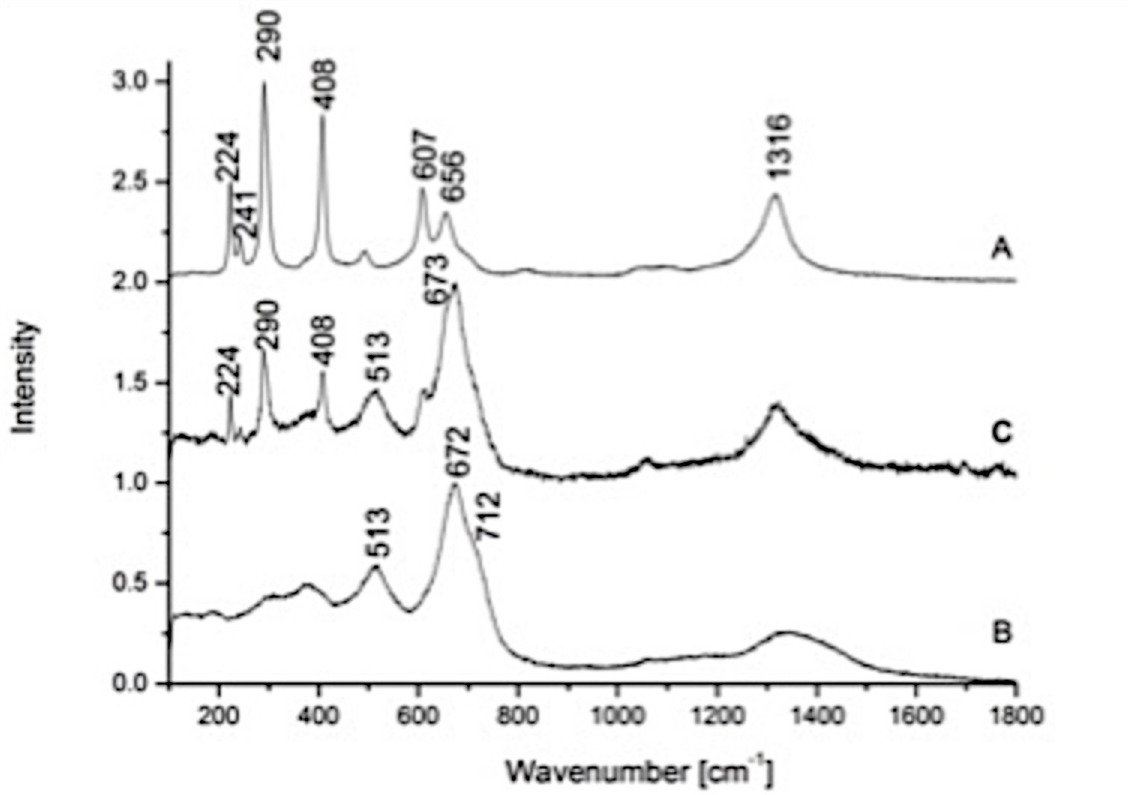

Figure 1 Raman spectra of Sample A: hematite; Sample B: maghemite; Sample C: a mixture of hematite and maghemite

As it is possible to observe in Figure 1, sample A shows the typical Raman peaks of the hematite phase at 656, 607, 408, 290, 241, 224 1/cm. The spectrum of sample B has a main peak at 672 1/cm with a bump at 712 1/cm and a broad peak at 513 1/cm, proper to the maghemite phase. Finally, sample C shows both the typical peaks of hematite and maghemite phases[9c].

The repeated samples showed the identical spectra confirming the complete reproducibility of this method. The identification of iron oxide phases was also confirmed by FT-IR analysis. Figure 2 shows the FT-IR spectra of samples A, B and C.

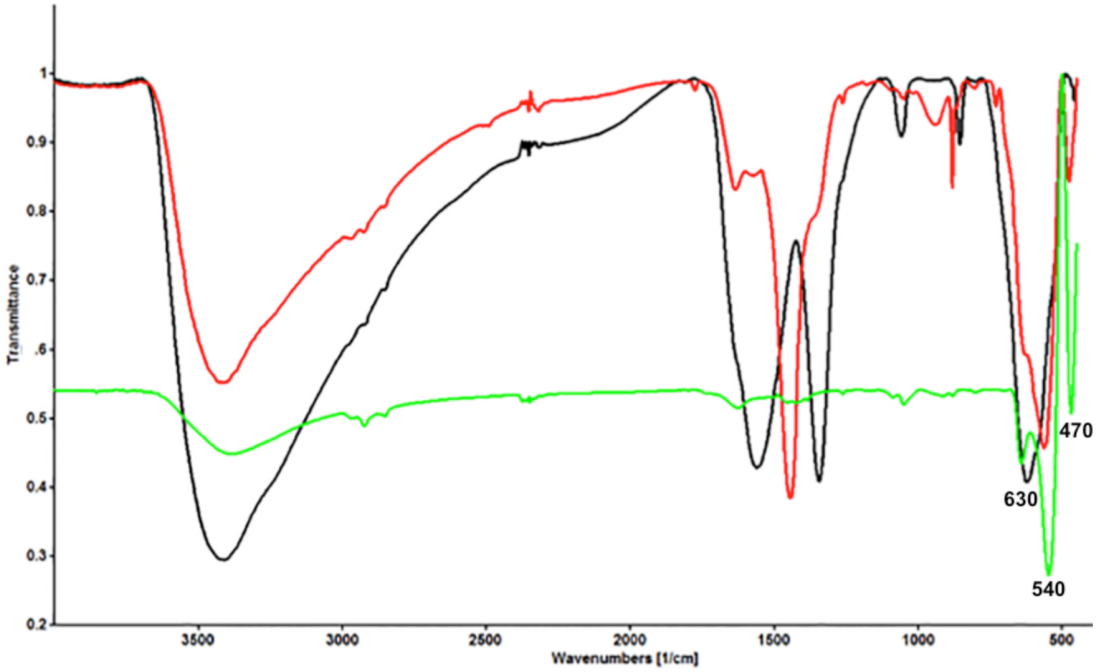

Figure 2 FT-IR spectra of a) Sample A: hematite (green); b) sample B: maghemite (black); c) sample C: a mixture of hematite and maghemite (red)

As reported in Figure 2, sample A shows the adsorption bands at 470 and 540 1/cm corresponding to hematite, while sample B shows an adsorption peak at 630 1/cm which evidences the presence of maghemite. Finally, sample C shows both hematite and maghemite adsorption bands and this means that by using the highest sodium hydroxide concentration a mix of iron oxides was obtained. Moreover, in all the FT-IR spectra the peak of carbonate around 1400 1/cm is present, as this species is an impurity introduced with the used sodium hydroxide. This impurity was more abundant in samples B and C because their preparation involved a higher base concentration. In all spectra there is a broad band at 3000-3500 1/cm, which is due to hydroxyl stretching vibration of ethanol and water molecules trapped in iron oxide nanoparticles. In addition, the FT-IR spectroscopy confirmed the reproducibility of this synthetic procedure.

The iron oxides are also characterized by different colours and magnetic behaviours, which give further support to oxide phase identification[10]. In particular, hematite (sample A) is red and does not respond to a permanent neodymium magnet, whereas maghemite (sample B) is brick red and follows the magnet very well, and sample C is reddish and reacts worst to the magnet (see Figure 3).

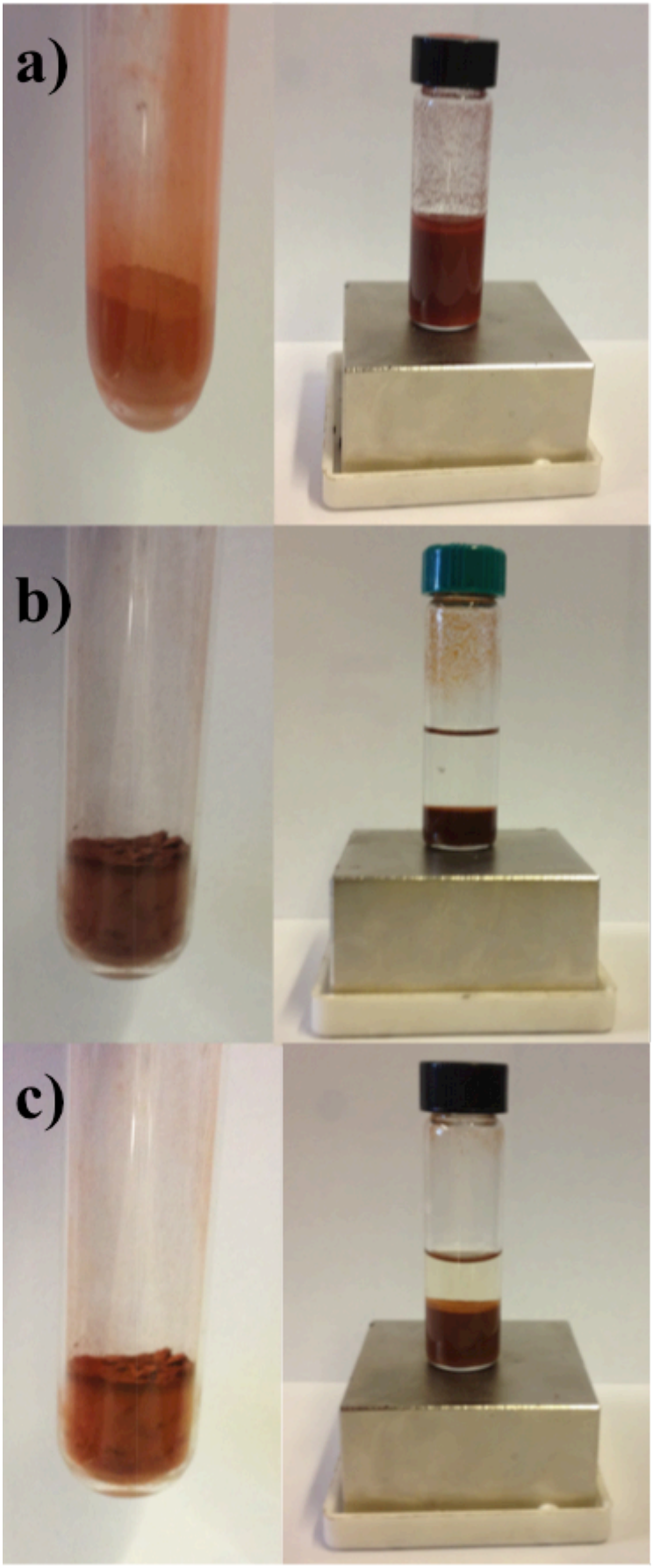

Figure 3 Photographs of samples as powder and colloidal dispersion: a) sample A, hematite b) sample B maghemite and c) sample C a mixture of hematite and maghemite

Depending on the Fe(III)/NaOH molar ratio, different iron oxide phases are obtained: hematite at 0.31 Fe(III)/NaOH molar ratio, nearly pure maghemite at 0.17 molar ratio and a mixture of hematite and maghemite at 0.08 molar ratio. According to literature, these results can be explained by taking into account the different competitive reactions that take place. The addition of base to a hydrolysed Fe(III) solution causes the precipitation of the iron (III) ions as goethite (α-FeOOH) releasing acid species, which consume the OH^- ions. At the end of this process, goethite is easily thermally dehydrated to hematite. However, under peculiar conditions able to partially reduce Fe(III) to Fe(II), goethite is converted to magnetite that is instable and can be quickly oxidized to maghemite. At this point, if the hydroxide ion concentration is extremely high, other reactions become competitive, in particular maghemite can be re-dissolved and converted to hematite. In conclusion all these reactions are competitive and the result is strongly dependent on OH^- concentration and temperature[11].

On the basis of these statements it is possible to rationalize the observed effect of Fe(III)/NaOH molar ratio on the final pH mixture and the resulting oxide phases. In particular, when sample A was synthesized adopting a Fe(III)/NaOH molar ratio of 0.31 (sample A, Table 1) a marked decrease of pH was observed from the initial value of 14 to the final one of 2.2, favouring the hematite formation as reported in literature[11c]. On the contrary when the Fe(III)/NaOH molar ratio of 0.17 was employed (sample B, Table 1) it was not possible to appreciate the pH decrease due to the OH^- saturation in the mixture and a pure maghemite phase was obtained. This result can be explained by the partial reducing conditions guaranteed by the alkaline aqueous ethanol heated with MW-irradiation, which cause the transformation of goethite to magnetite. However, under the adopted conditions due to the presence of oxygen dissolved in the adopted commercial aqueous ethanol, magnetite is rapidly converted to maghemite. This approach allows the synthesis of a nearly pure maghemite adopting an eco-friendly, faster and greener procedure than those previously reported. Finally, when an extremely low Fe(III)/NaOH molar ratio was employed (sample C, Table 1) a mixture of hematite and maghemite was obtained according to the literature: in fact, under this condition, maghemite can be re-dissolved and partially converted to the more stable hematite[11a].

Taking into account the promising magnetic behaviour of maghemite samples, these were further characterized by XRD, AES, TEM, AFM, BET and VSM analyses.

Figure 4 reports the collected X-ray powder diffraction pattern of sample B and the reference card for γ-Fe_2O_3 (Card No. 01-089-5894). Due to the close match between the expected diffraction peaks of γ-Fe_2O_3 and the observed ones of the sample B, we can assert that the powder under investigation is a phase possessing the crystal structure of maghemite, in fact the sample B patterns can be indexed as Miller indexes of γ-Fe_2O_3 maghemite like structure (311), (201), (116), (206), (009), (109), (119), (226) (219), (0012), (3010), (2215), (1115), (2015), (2115), (4012), (2018), (3315).

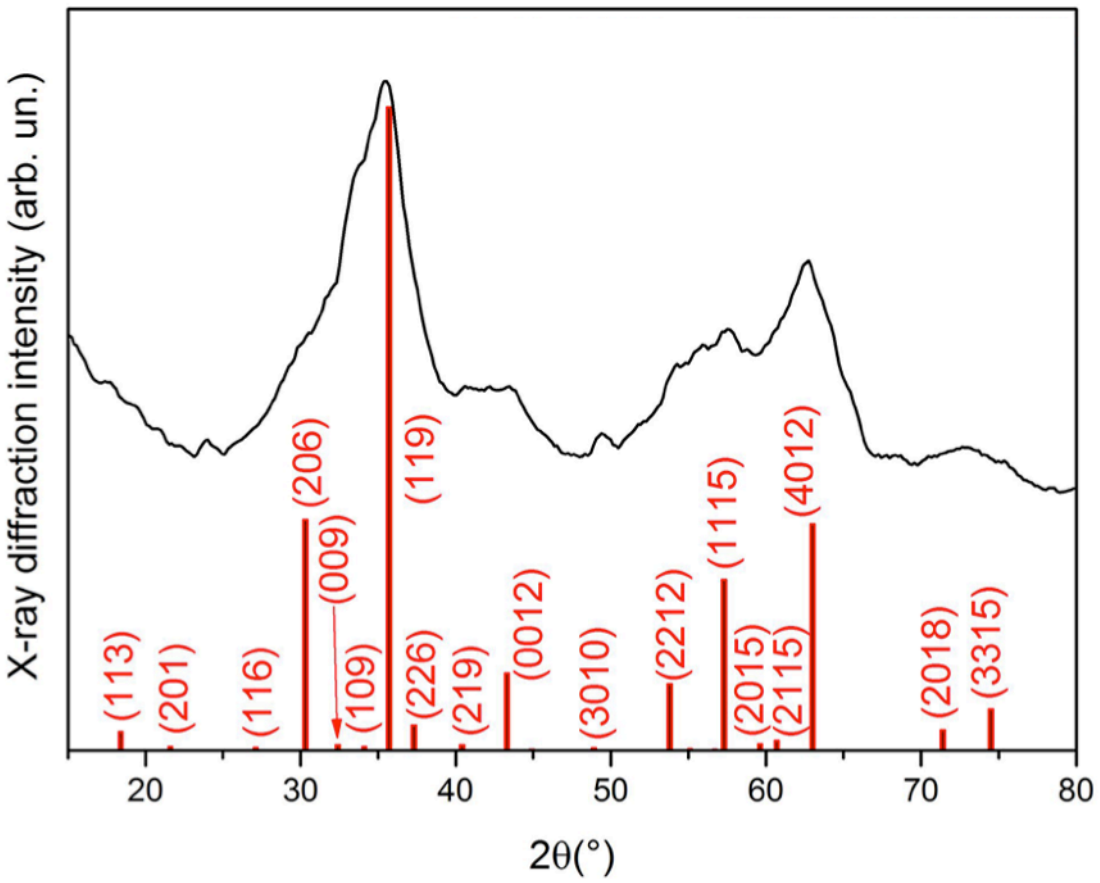

Figure 4 XRD pattern (black line) of sample B and reference card for maghemite (red columns)

The Auger Emission Spectroscopy (AES) evidences traces of impurities such as carbonate, sodium and chloride, probably introduced with reagents and not completely removed by washing (See Figure 5).

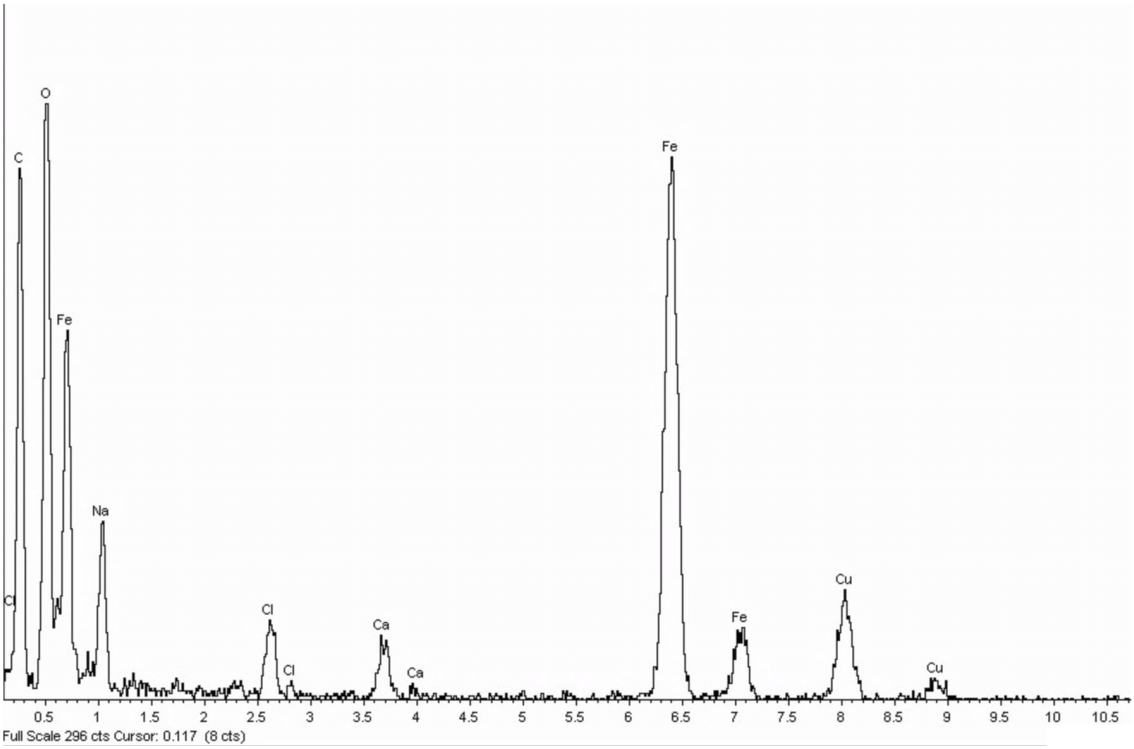

Figure 5 AES analysis of sample B, maghemite

The morphology and size distribution of maghemite nanoparticles was deeply investigated through AFM and TEM micrographs.

In Figure 6 the AFM micrographs of sample B are reported, which show good particle dispersion characterized by a huge number of small particles and few nanoclusters.

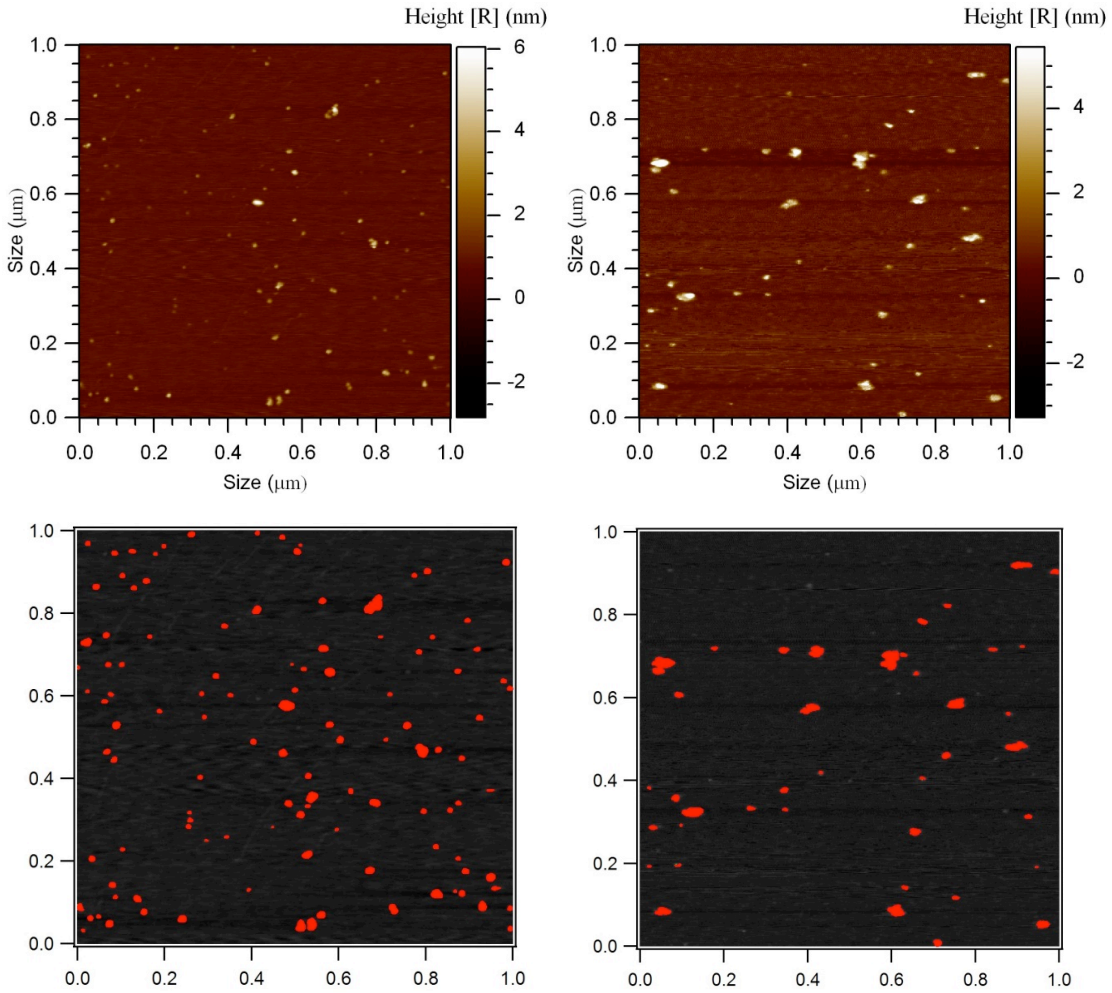

Figure 6 AFM micrograph of sample maghemite, Sample B

The TEM micrographs of sample B are reported in Figure 7 and better help us to analyse the particle distribution.

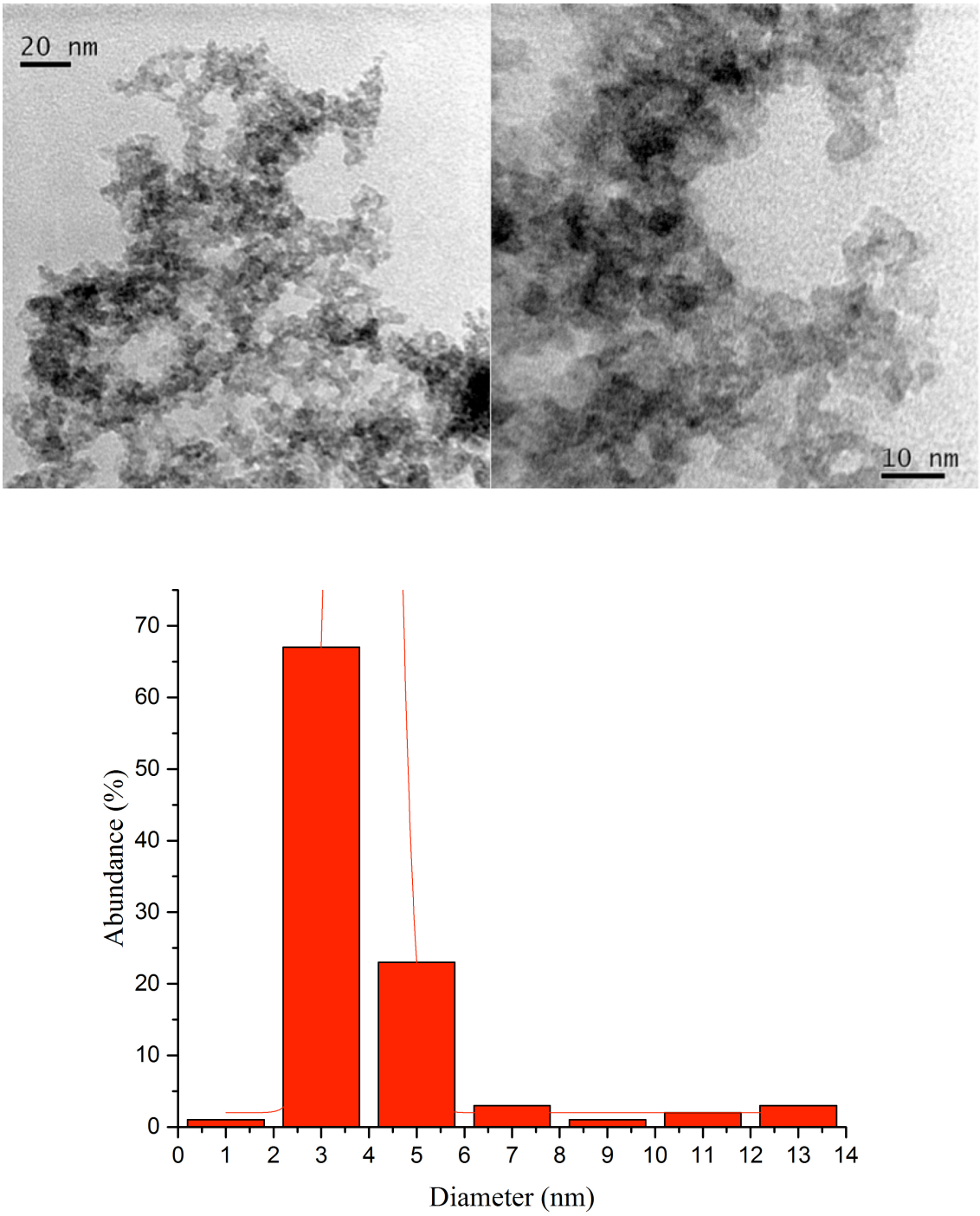

Figure 7 TEM micrograph and particle size distribution of sample B

From the TEM micrographs, in fact, it is possible to evidence narrow particle size distribution with an average diameter of 3-4 nm. The maghemite samples (B and B bis, Table 1) were also characterized by a surface area of about 62 m^2 /g relatively bigger than that commonly reported[12]. The magnetization curve of sample B is shown in Figure 7, where the magnetization values are reported per gram of sample. The

saturation magnetization M_0, taken as the maximum magnetization recorded at 90 KOe is 9.7 emu/g. The sample does not present any coercivity, as expected for paramagnetic or superparamagnetic materials. The shape of the curve shows a low initial susceptibility and is far from saturation even at 90 KOe, suggesting the presence of ultra small magnetic nanoparticles[13].

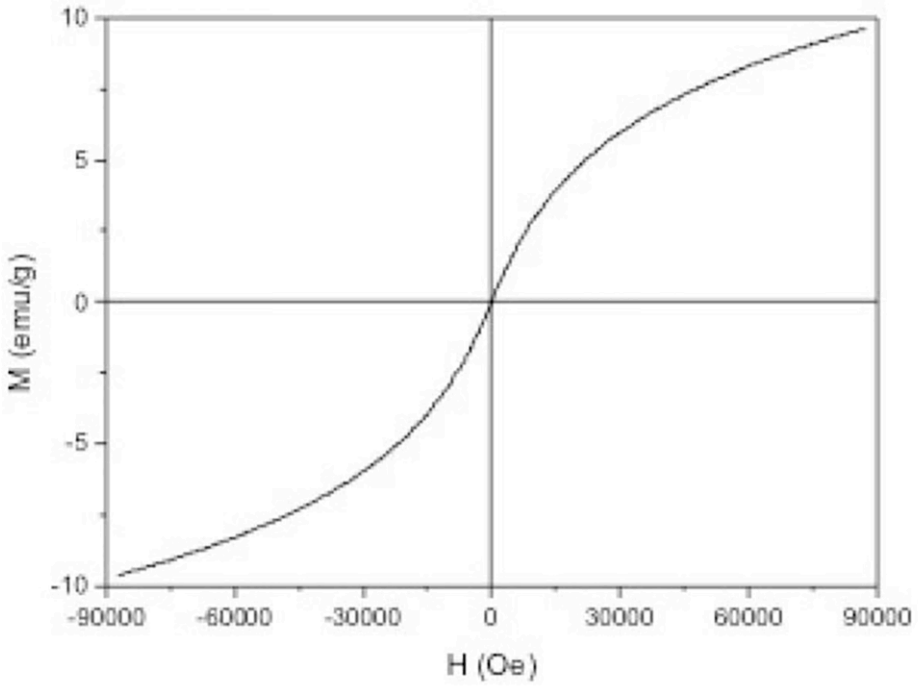

Figure 8 Magnetization curve of maghemite, sample B.

4.2 Synthesis of magnetite: Microwave assisted hydrothermal procedure

The second proposed approach for the green preparation of magnetic nanoparticles in absence of any stabilizing agents is a new hydrothermal method based on a one-pot strategy. This new hydrothermal approach leads to the formation of magnetite Fe_3O_4, another iron oxide diverse from the ones obtained with the precipitate approach.

The obtained magnetite nanoparticles exhibit interesting magnetic performances allowing their easy recovery from complex reaction media as shown in Figure 9.

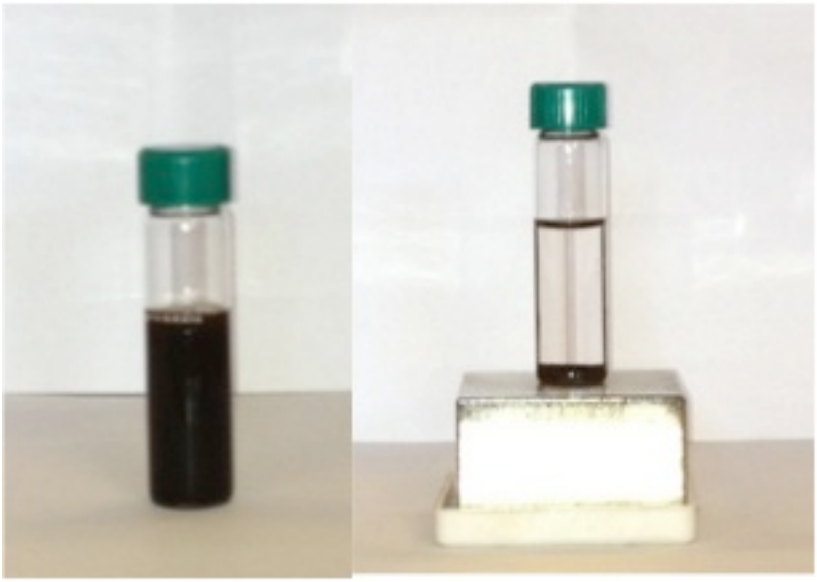

Figure 9 Photograph of sample 2, Magnetite

In a typical experiment the desired amount of $Fe(OAc)_2$ (see table 2) was dissolved in EtOH 96 wt% (44 mL). Then this solution was thermally treated by monomode microwave irradiation (CEM discovery S-class equipped with the 80 mL glass vessel) at 120°C for 15 minutes at 250W. At the end of this treatment, particles were magnetically collected using a neodymium magnet, washed and dried under vacuum for 12 h. This approach was also investigated using different heat sources, such as multimode microwave oven (MARS.6 equipped with 80 mL Teflon vessel) and 100 mL Parr autoclave electrically heated and the corresponding reaction conditions are reported in Table 2.

Table 2 Hydrothermal syntheses of MNPs using different heat sources and Fe precursor concentrations

Samples	$Fe(OAc)_2$ (g)	Heating source	Surface area (m^2/g)	Average diameter (nm)	σDm (nm)	Magnetic saturation (emu/g)
1[a]	0.25	MW Monomode	84.64	11.5	2.5	75.32
2[a]	0.5	MW Monomode	45.14	10.4	4.5	39.49
3[a]	1	MW Monomode	78.85	14	5.9	45.88
4[b]	1	MW Multimode	31.98	7	1.6	16.74
5[c]	1	Traditional	89.37	Few 7,6 nm particles together with many big cluster		N.D

[a] Reaction conditions: 44 mL EtOH at 96 wt%, microwave heating: 120 °C, 15 min, 250 W
[b] Reaction conditions: 44 mL EtOH at 96 wt%, microwave heating: 150 °C, 15 min, 450 W
[c] Reaction conditions: 44 mL EtOH at 96 wt%, traditional heating: 120 °C, 4.5 h.

It is well known that nanoparticle magnetic properties are strongly related to their morphology, size and crystalline degree, which in turn depend on the synthetic conditions. The control of these properties is still a great challenge for researchers and for this reason the effects of some synthetic parameters, such as kind of heat source and iron precursor concentration on the resulting Fe_3O_4 properties, were investigated. As can be observed in Table 2, the $Fe(OAc)_2$ concentration strongly influences nanoparticle size distribution and magnetic behaviour. In particular, using the lowest precursor amount of 0.25 g (sample 1), it is possible to obtain nanoparticles characterized by a remarkably narrow size distribution and with the highest magnetic saturation, 75.32 emu/g. By increasing the $Fe(OAc)_2$ amount to 1 g the average diameter and its standard deviation increase, whereas magnetic saturation decreases. In fact, sample 3 shows bimodal particle size distribution and lower magnetic saturation than that measured for sample 1. These results suggest that by regulating the $Fe(OAc)_2$ concentration it is possible to tune the size and magnetic saturation of nanoparticles[6b, 14]. Figure 10 shows TEM micrographs and particle size distributions for samples 1, 2, 3, 4 and 5. It is important to note the small average diameter and the narrow particle size dispersion of sample 1. Furthermore the role of different heating sources was investigated, repeating the reactions using the multimode microwave MARS 6 (sample 4) and the autoclave Parr (sample 5), ascertaining a marked effect on the characteristic of MNPs. In fact, samples 1, 2 and 3 obtained using monomode microwave show a magnetic saturation many times higher than that observed for sample 4 synthetized using multimode microwave. In this context, it is important to highlight that monomode and multimode microwave reactors are characterized by a different instrumentation design. In fact, monomode reactors have small compact cavities, in which not only the distribution of the electromagnetic field is well known and controllable but also microwave irradiation is directly focused on the reaction mixture, providing in this way high microwave field density and fast heating rates. On the other hand, multimode reactors have large cavities, in which the microwave field is distributed in a random manner. In fact, in this case, the waves are reflected from the cavity walls and the modes in which the electromagnetic waves interact with the cavity are multiple, leading to a reactor geometry not optimized for any specific compounds. The random distribution of microwaves in the multimode reactor causes the irregular growth of nanocrystals thus lower magnetic properties.

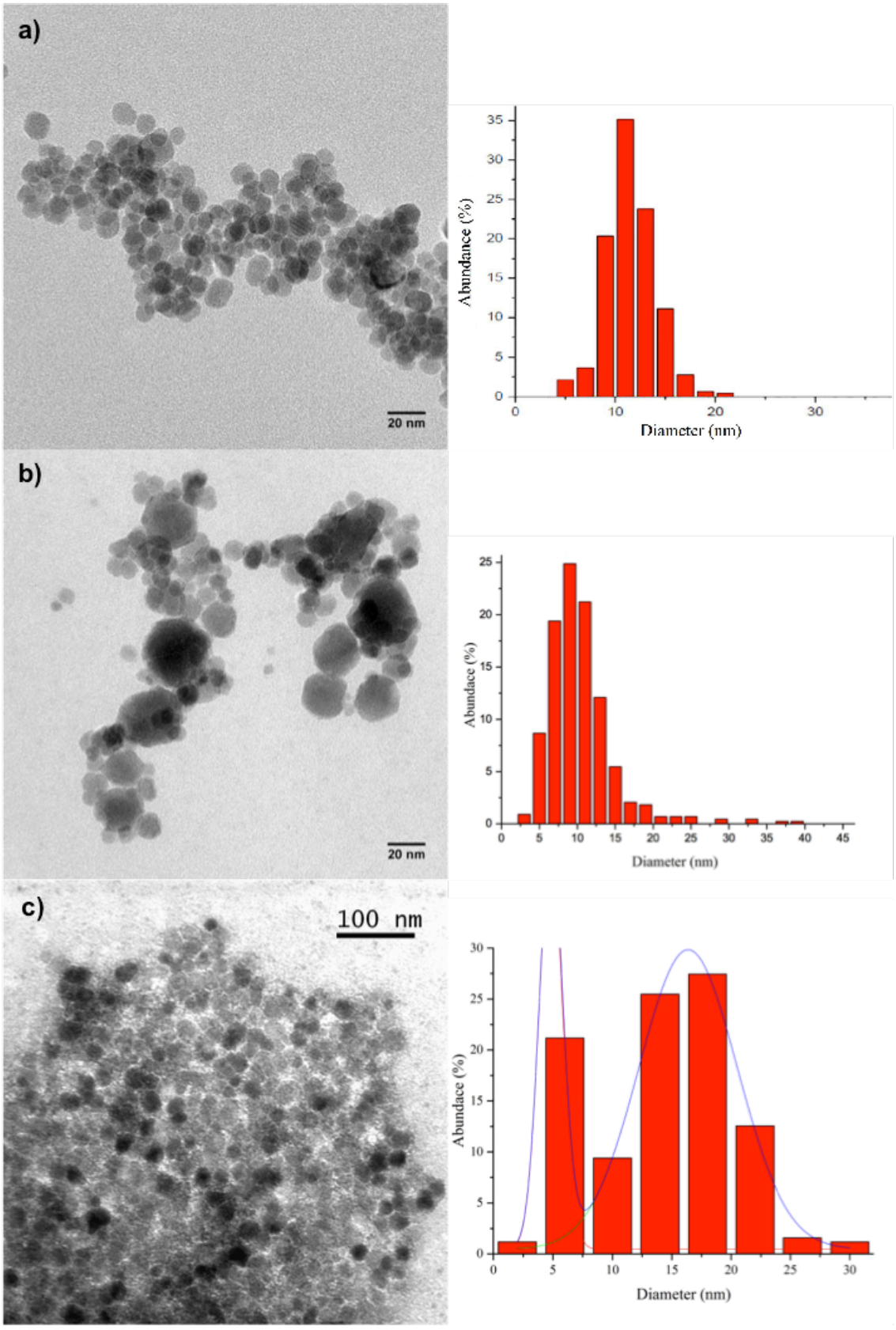
a)
20 nm
Abundance (%)
Diameter (nm)
b)
20 nm
Abundace (%)
Diameter (nm)
c)
100 nm
Abundace (%)
Diameter (nm)

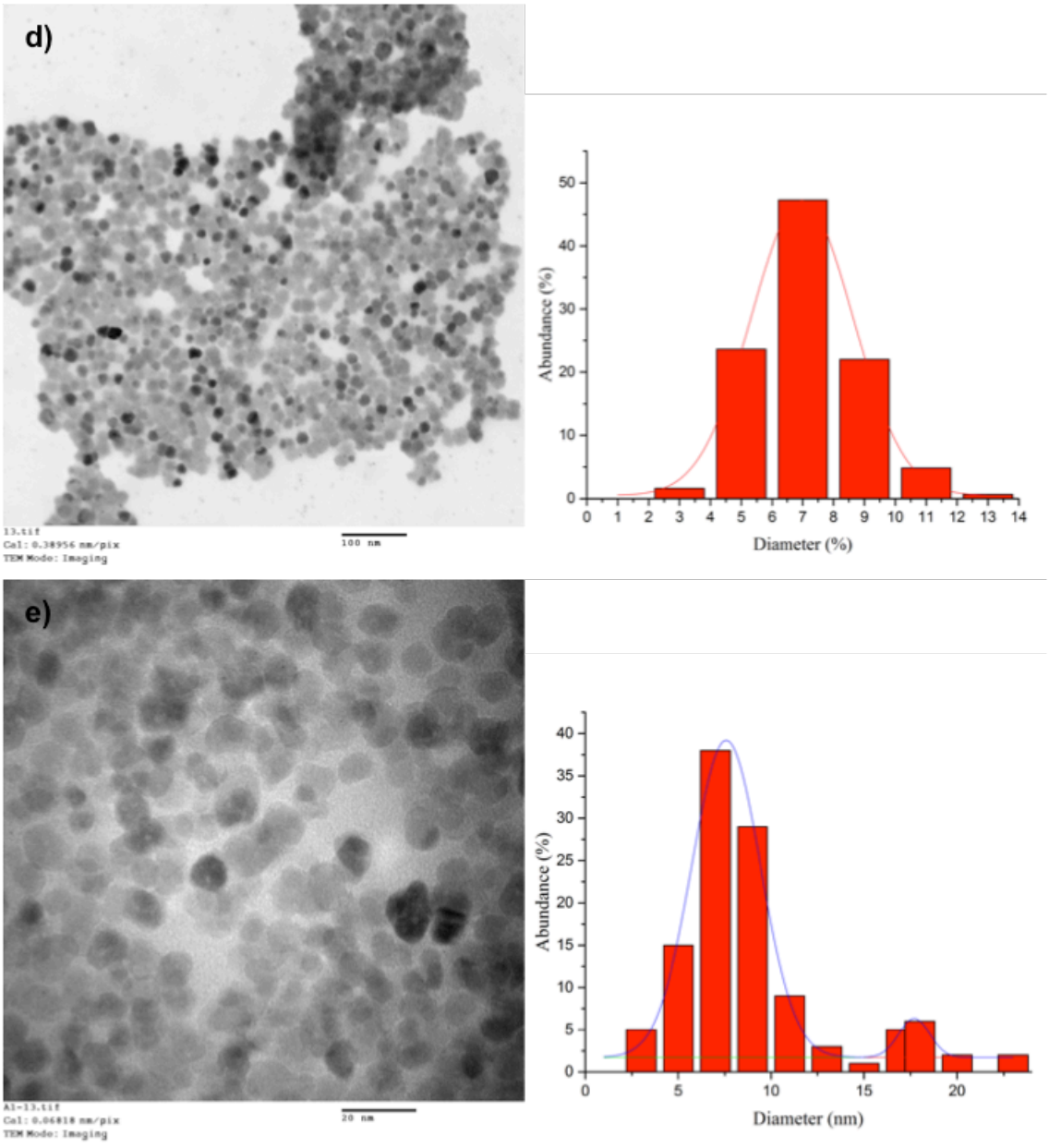

Figure 10 a) TEM Micrographs of sample 1 prepared using 0.25 g of iron precursor , b) TEM Micrograph of sample 2 prepared using 0,5g of iron precursor and c) TEM Micrograph of sample 3 prepared using 1g of iron precursor, d) TEM Micrograph of sample 4 prepared adopting multimode microwave and e) TEM Micrograph of sample 5 prepared adopting traditional thermal heating

The XRD analysis clearly shows that for samples synthetized using monomode microwave a higher crystallinity degree is observed than that achieved using multimode microwave, again suggesting that only monomode microwave is able to guarantee an ordered growth of magnetite crystals, thus improving their magnetic saturation. Finally, the MNPs prepared under traditional heating in autoclave (sample 5) show the largest and most heterogeneous particle size dispersion together with big particle aggregates.

This result can be related to the main drawbacks of the conventional batch autoclaves whose wall dimensions are designed for high-pressure applications: the heating and cooling of the steel body of the reactor involves time, leading to an irregular and non-uniform warming with marked temperature gradients and high thermal inertia. In addition, during the long transient heating/cooling intervals different and undesirable reactions could take place, making the reaction control difficult [15]. On the contrary, MW-irradiation represents a sustainable, efficient, cost effective and powerful tool for conducting processes, involving lower energy demanding conditions, rate enhancement, higher yields and greater selectivities compared to those achieved adopting traditional heating. In particular, MW-irradiation results in an almost instantaneous "in core" heating of materials in a homogeneous and selective manner allowing rapid transfer of the energy into the bulk of the reaction mixture, eliminating the wall effects[16]. All samples were prepared in duplicate and characterized by Raman, FT-IR, AES, XRD, TEM and VSM analyses. Raman spectrum of sample 1 (see Figure 11) clearly shows the strong band at 669 1/cm typical of magnetite. Moreover, a little peak at 945 1/cm was observed which could result from iron (II) acetate employed as precursor during the synthesis.

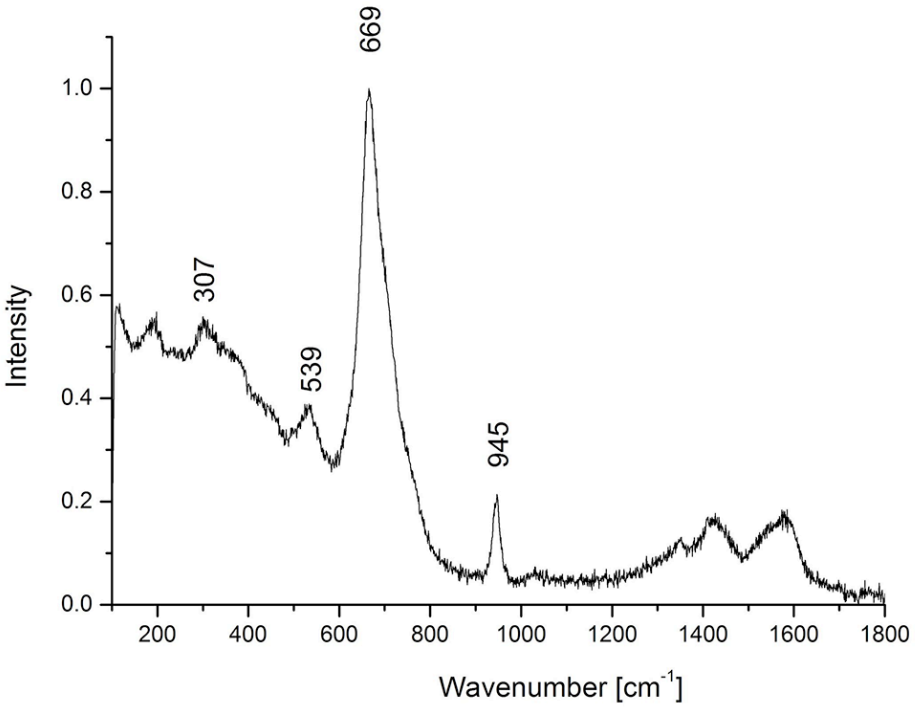

Figure 11 Raman spectrum of sample 1, magnetite.

The FT-IR spectra of all samples confirm the above results and the adsorption bands at 590 1/cm and 630 1/cm of the Fe-O bonds in the tetrahedral Fe_3O_4 sites are ascertained.[17] Moreover, two big peaks between 1400 1/cm and 1600 1/cm show the presence of acetate, underlining that the organic part of the iron precursor was not completely decomposed and removed (see Figure 12).

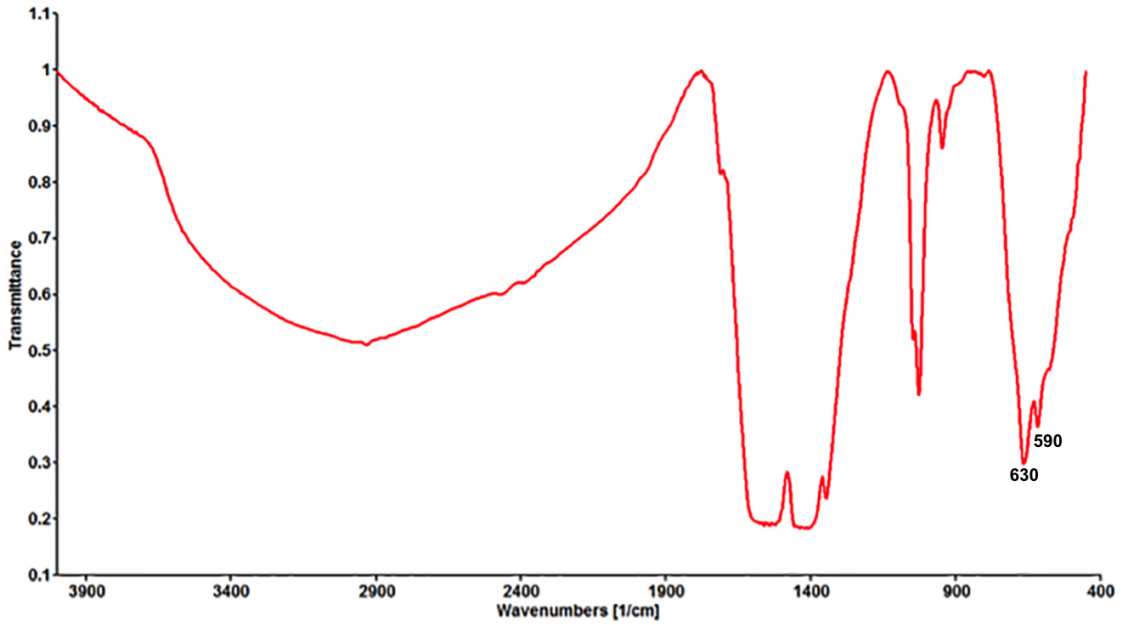

Figure 12 FTIR spectrum of sample 1, magnetite

All the X-ray diffraction peaks collected for sample 1 can be indexed by the Miller indexes of the cubic Fe_3O_4 magnetite-like structure (220), (311), (222), (400), (422) (511), (440), (620), (533) and (622) (Figure 13). For this reason, the sample under investigation can be considered a pure polycrystalline Fe_3O_4 compound with magnetite structure. The calculated lattice parameter (8.360(1) Å) is quite similar to the one reported in the literature for magnetite (8.3941(7) Å). The broadness of the diffraction peaks reveals the nanocrystalline nature of the powder, as confirmed by TEM reported in Figure 10.

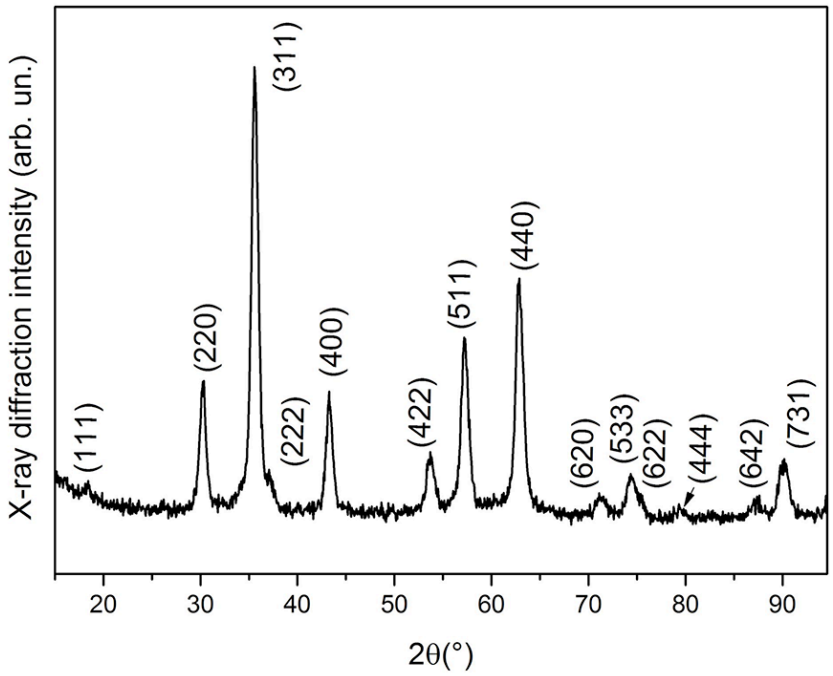

Figure 13 XRD patterns of magnetite, sample 1.

The purity of the obtained magnetite samples was ascertained by AES analysis, as shown in Figure 14.

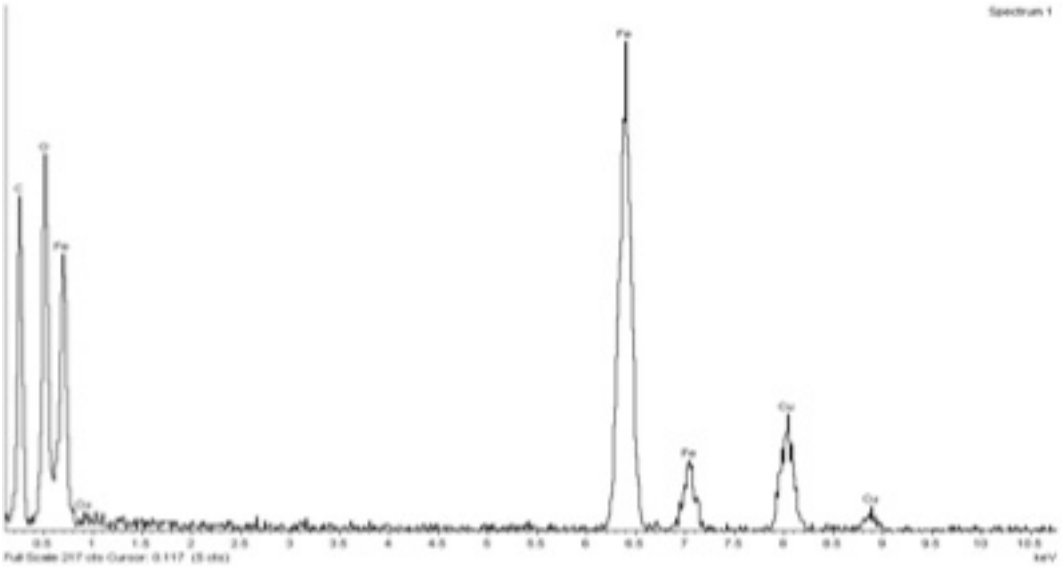

Figure 14 AES analysis of sample 1, magnetite

Promising magnetic behaviour was observed by placing a neodymium permanent magnet near the vessels containing MNPs and better determined with the vibrating sample magnetometer (VSM). The magnetization curves are shown in Figure 15 for

samples 1, 2 and 4, where the magnetization values are reported per gram of measured sample. The saturation magnetizations, M_0, taken as the maximum value measured at 90 KOe, are 75.3, 45.9 and 16.7 emu/g for samples 1, 2 and 4 respectively. This M_0 value ascertained for sample 1 is relatively higher than that which was commonly reported[1a, 18]. The samples do not present any coercivity, as expected for superparamagnetic materials. The comparison of the shape of the curve in Figure 9, however, presents significant differences. In particular, samples 1, 2 and 4 show large initial magnetic susceptibility reaching saturation at high fields, thus presenting typical superparamagnetic behaviour consistent with a set of iron oxide nanoparticles with an average size of about 10 nm.

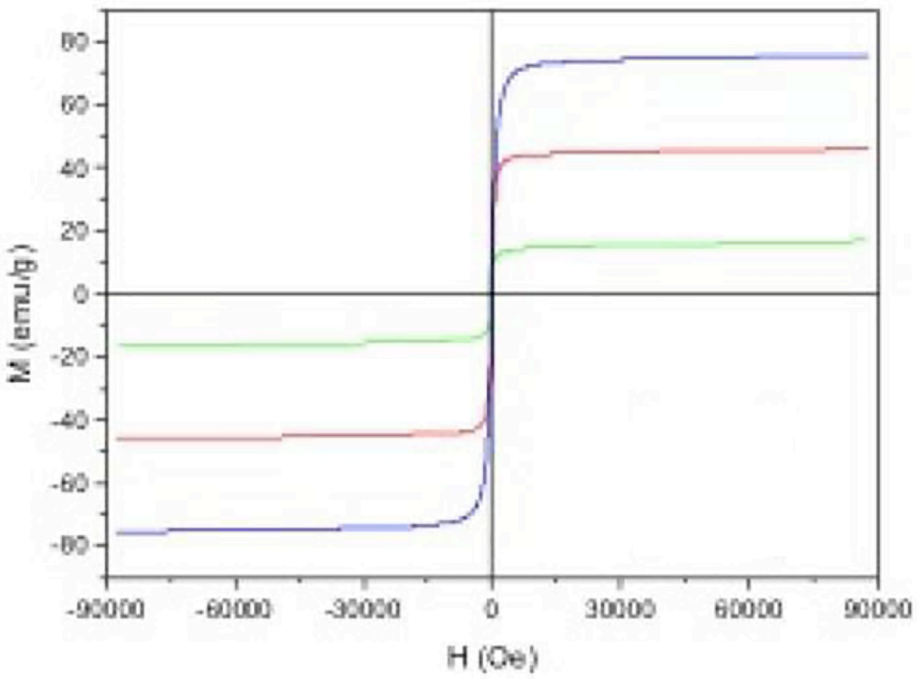

Figure 15 Magnetization curves of sample 1 (blue), sample 2 (red) and sample 4 (green).

4.3 References

[1] a) R. Y. Hong, J. H. Li, H. Z. Li, J. Ding, Y. Zheng and D. G. Wei, *Journal of Magnetism and Magnetic Materials* **2008**, *320*, 1605-1614; b) D. Maity, J. U. N. Ding and J.-M. Xue, *Functional Materials Letters* **2008**, *01*, 189-193; c) T. J. Daou, G. Pourroy, S. Bégin-Colin, J. M. Grenèche, C. Ulhaq-Bouillet, P. Legaré, P. Bernhardt, C. Leuvrey and G. Rogez, *Chemistry of Materials* **2006**, *18*, 4399-4404; d) D. Horák and N. Chekina, *Journal of Applied Polymer Science* **2006**, *102*, 4348-4357.

[2] a) F. Y. Jiang, C. M. Wang, Y. Fu and R. C. Liu, *Journal of Alloys and Compounds* **2010**, *503*, L31-L33; b) O. Pascu, E. Carenza, M. Gich, S. Estradé, F. Peiró, G. Herranz and A. Roig, *The Journal of Physical Chemistry C* **2012**, *116*, 15108-15116.
[3] a) B. Sarah, L. Sophie, V. Marjorie, E. Luce Vander, P.-M. David and N. M. Robert, *Nanotechnology* **2013**, *24*, 055705; b) P. Nicolás, M. Saleta, H. Troiani, R. Zysler, V. Lassalle and M. L. Ferreira, *Acta Biomaterialia* **2013**, *9*, 4754-4762; c) S. Sun, S. Anders, H. F. Hamann, J.-U. Thiele, J. E. E. Baglin, T. Thomson, E. E. Fullerton, C. B. Murray and B. D. Terris, *Journal of the American Chemical Society* **2002**, *124*, 2884-2885.
[4] a) D. Arndt, V. Zielasek, W. Dreher and M. Bäumer, *Journal of Colloid and Interface Science* **2014**, *417*, 188-198; b) H. Zhang, X. Zhong, J.-J. Xu and H.-Y. Chen, *Langmuir* **2008**, *24*, 13748-13752; c) Z. Li, Q. Sun and M. Gao, *Angewandte Chemie International Edition* **2005**, *44*, 123-126.
[5] K. A. Porter, Barnhardt, Keller E. in *Synthesis and use of intermetallic iron palladium nanoparticle composition*, *Vol.* United States, **2012**, pp. 1-13.
[6] a) P. Kucheryavy, J. He, V. T. John, P. Maharjan, L. Spinu, G. Z. Goloverda and V. L. Kolesnichenko, *Langmuir* **2012**, *29*, 710-716; b) W.-W. Wang, Y.-J. Zhu and M.-L. Ruan, *Journal of Nanoparticle Research* **2007**, *9*, 419-426.
[7] a) E. Rafiee and S. Eavani, *Green Chemistry* **2011**, *13*, 2116-2122; b) E. Hee Kim, H. Sook Lee, B. Kook Kwak and B.-K. Kim, *Journal of Magnetism and Magnetic Materials* **2005**, *289*, 328-330.
[8] a) J. R. Correa, D. Canetti, R. Castillo, J. C. Llópiz and J. Dufour, *Materials Research Bulletin* **2006**, *41*, 703-713; b) S. R. Dhage, Y. B. Khollam, H. S. Potdar, S. B. Deshpande, P. P. Bakare, S. R. Sainkar and S. K. Date, *Materials Letters* **2002**, *57*, 457-462; c) C. M. Flynn, *Chemical Reviews* **1984**, *84*, 31-41.
[9] a) M. F. Silva, L. A. S. de Oliveira, M. A. Ciciliati, L. T. Silva, B. S. Pereira, A. A. W. Hechenleitner, D. M. F. Oliveira, K. R. Pirota, F. F. Ivashita, A. Paesano, J. Martin Pastor, J. Iñaki Pérez-Landazábal and E. A. G. Pineda, *Journal of Applied Physics* **2013**, *114*, 104311; b) R. M. Cornell and U. Schwertmann in *Electronic, Electrical and Magnetic Properties and Colour*, *Vol.* Wiley-VCH Verlag GmbH & Co. KGaA, **2004**, pp. 111-137; c) D. L. A. de Faria, S. Venâncio Silva and M. T. de Oliveira, *Journal of Raman Spectroscopy* **1997**, *28*, 873-878.
[10] a) R. Zboril, M. Mashlan and D. Petridis, *Chemistry of Materials* **2002**, *14*, 969-982; b) U. Schwertmann and R. M. Cornell in *Methods of Characterization*, *Vol.* Wiley-VCH Verlag GmbH, **2007**, pp. 27-54.
[11] a) Y. Cudennec and A. Lecerf, *Journal of Solid State Chemistry* **2006**, *179*, 716-722; b) V. Sreeja and P. A. Joy, *Materials Research Bulletin* **2007**, *42*, 1570-1576; c) Y. Li, H. Li and R. Cao, *Journal of the American Ceramic Society* **2009**, *92*, 2188-2191.
[12] L. S. Zhong, J. S. Hu, H. P. Liang, A. M. Cao, W. G. Song and L. J. Wan, *Advanced Materials* **2006**, *18*, 2426-2431.
[13] A. Millan, A. Urtizberea, N. J. O. silva, F. Palacio, V. S. Amaral, E. Snoeck and V. Serin, *Journal of Magnetism and Magnetic Materials* **2007**, *312*.
[14] A. R. Galletti, E. Bertolucci, M. Marracci, B. Tellini and C. Visone, *Instrumentation and Measurement Technology Conference (I2MTC) Proceedings, 2014 IEEE International* **2014**, pp. 464-467.
[15] H. Werhan, N. Assmann and P. Rudolf von Rohr, *Chemical Engineering and Processing: Process Intensification* **2013**, *73*, 29-37.
[16] a) A. M. Raspolli Galletti, C. Antonetti, M. Marracci, F. Piccinelli and B. Tellini, *Applied Surface Science* **2013**, *280*, 610-618; b) I. Bilecka and M. Niederberger,

Nanoscale **2010**, *2*, 1358-1374; c) M. Baghbanzadeh, L. Carbone, P. D. Cozzoli and C. O. Kappe, *Angewandte Chemie International Edition* **2011**, *50*, 11312-11359.
[17] C. Lu, L. R. Bhatt, H. Y. Jun, S. H. Park and K. Y. Chai, *Journal of Materials Chemistry* **2012**, *22*, 19806-19811.
[18] a) A. M. Hirt, G. A. Sotiriou, P. R. Kidambi and A. Teleki, *Journal of Applied Physics* **2014**, *115*, 044314; b) C.-R. Lin, R.-K. Chiang, J.-S. Wang and T.-W. Sung, *Journal of Applied Physics* **2006**, *99*, 08N710.

5. SYNTHESIS OF MAGNETIC NANOCATALYSTS

Nowadays transition and noble metal nanoparticles attract huge interest in catalysis thanks to their promising properties.

Unfortunately, as deeply discussed in Chapter 2, these interesting nanomaterials due to their small size are difficult to separate from the reaction mixture leading to unsustainable separation and purification steps. In order to overcome these onerous steps, transition and noble metal nanoparticles can be supported or trapped inside magnetic nanostructures.

Traditionally these kind of magnetic bimetallic nanosystems are prepared following two diverse techniques: wet impregnation or co-precipitation[1].

It is important to underline that the chosen synthetic approach strongly influences the nanocatalytst structure and the arrangements of catalytic active sites, thus defining its final catalytic performances[2]. In particular, the wet impregnation method leads to the formation of hierarchical nanostructures, where the core is composed of magnetic iron oxide and is surrounded by metal particles. Instead, the co-precipitation technique allows us to obtain complex bimetallic structures where the metal nanoparticles are trapped inside the iron oxide nanocrystal. Both these particular structures present advantages and disadvantages from a catalytic point of view. In fact, hierarchical structures lead to a more direct contact between active metal sites and reagents resulting in a higher catalytic activity but due to this aspect, these kinds of systems can easily occur in deactivation by poisoning or leaching. The complex catalytic systems usually obtained by co-precipitation methods are more stable and more difficult to deactivate through poisoning or leaching than those with a hierarchical structure. Despite this positive aspect, the complex structure suffers limited transportation of reagents toward the active metal site resulting in low catalytic activity. In conclusion, the final structure of the catalytic systems is fundamental and must be carefully considered during the catalyst selection in order to design the best system for a certain reaction.

The traditional wet impregnation approach is based on two steps: firstly the magnetic nanosupport is impregnated with a metal salt solution, and then the metal salts adsorbed on the support surface are reduced under strong reducing media[3]. Several authors describe in more detail the preparation of the magnetic iron oxide support through

classical alkaline precipitate or solvothermal procedures, its subsequent wet impregnation with a metal chlorines or nitrate solution and the final reduction of the metals through strong reducing agents or heavy calcination processes.[4] For example Li et al.[5] describe the preparation of magnetite nanoparticles through the alkaline precipitation of iron salts. The obtained magnetic particles are then impregnated with a palladium salt solution and the palladium is then reduced using an excess of sodium borohydride.

Moreover, in literature metal wet impregnation on commercial magnetic nanostructures is reported.[6] Other authors describe the immobilization of metal nanoparticles over magnetic nanosupports, using organic ligands[7] or reducing the metal nanoparticles through ultrasound treatment[8].

On the other hand the co-precipitation technique is based on the contemporary precipitation of magnetic nanocystal and metal particles[9]. For example Wand et al.[10] show the co-precipitation of iron, platinum and ruthenium salts in the presence of diluted ammonia and hydrazine.

In literature, other interesting procedures for preparing magnetic bimetallic nanomaterials are reported. For example Liu and Zhang et al.[11] report a two-step approach based on the co-calcination of iron and palladium precursors and the subsequent reduction under hydrogen flow of the calcinated products. Basinska et al.[12] show another interesting calcination technique, where firstly the maghemite support is prepared through the calcination of the iron hydroxide and is subsequently impregnated with a ruthenium solution. Finally, the system is calcinated in air at 400°C to partially reduce the ruthenium salts.

The main drawback of all these methods is the use of different hazardous stabilizing and reducing agents. These process auxiliaries are not only unsustainable from an environmental point of view but influence also the final properties of nanomaterials.

In fact, the stabilizing agents can generate a protective layer around the particles, resulting in active catalytic site passivation. [13]

For all these reasons in this work the new greener precipitation and hydrothermal procedures were employed for the preparation of diverse magnetic bimetallic systems. In particular diverse transition and noble metal nanoparticles are supported or trapped inside magnetic iron oxide nanoobjects (M@Fe_3O_4 and M@γ-Fe_2O_3 (M: Pd, RuO_X, Pt, CuO)).

All the obtained nanocatalysts were characterized by X-Ray Diffraction (XRD), Fourier Transform Infrared Spectroscopy (FT-IR), Auger electron spectroscopy (AES), X-Ray Photoelectron Spectroscopy (XPS), Transmission Electron Microscopy (TEM), Atomic Force Microscopy (AFM), Raman spectroscopy, BET surface analysis (BET), Vibrating Sample Magnetometer (VSM), Temperature Programmed Reduction analysis (TPR) and Inductively coupled plasma-optical emission spectrometer (ICP-OES).

5.1 Synthesis of magnetic palladium nanocatalysts

Palladium nanocatalysts attract huge interest for their surprising activity in a wide range of important industrial reactions such as hydrogenation[14], oxidation[15] and C-C coupling[16].

In this context the immobilization of palladium nanoparticles over magnetic nanostructure become of great importance and could be a strategic choice able to guarantee an efficient and easy recovery[17]. Moreover magnetic separation avoids the use of auxiliary substances, making the process cleaner, safer and faster than the normal separation procedure[18].

In this PhD work, two different sustainable approaches to prepare palladium nanoparticles over magnetic nanostructure have been optimized.

The first approach is a two-step procedure for preparing a hierarchical magnetic palladium system characterized by palladium nanoparticles anchored on magnetite or maghemite nanostructures. The magnetite was prepared through the new hydrothermal procedure and the maghemite nanoparticles were obtained with the new precipitate procedure. The second approach is a one-pot synthesis developed from the new hydrothermal approach. This procedure deals with the contemporaneous precipitation of magnetite and palladium leading to the formation of a complex nanostructure where palladium particles are trapped inside the iron oxide nanocrystals.

5.1.1 Palladium nanoparticles anchored over iron oxide nanocrystal

Palladium nanoparticles anchored over iron oxide nanocrystal were prepared following a two-step procedure. Firstly, the magnetic nanostructures were prepared following the new hydrothermal or precipitate procedure described in Chapter 4.

Then the palladium salts were reduced over the surface of the iron oxide through MW-irradiation. In more detail, 0.5g of iron oxide nanopowder and 0.05g of palladium acetate ($Pd(OAc)_2$) were dispersed in 44 ml di aqueous ethanol. Then the obtained dispersion were MW-irradiated at 120°C for 15 min. At the end of this treatment the particles were magnetically collected and dried under vacuum.

Table 1 summarizes the characteristics of palladium nanoparticles anchored on three diverse supports such as maghemite which is prepared following the precipitate method, reference magnetite ($Fe_3O_{4\ ref.}$, magnetite Sigma Aldrich) and magnetite prepared following the hydrothermal procedure.

Table 1 Characteristics of palladium nanoparticles supported on the surface of diverse iron oxides

Samples	Magnetic support	AAS (Pd %wt)	BET (m^2/g)	Core diameter (nm)	Palladium diameter (nm)	VSM M0 (emu/g)
Pd1[a]	γ-Fe_2O_3	2.1	74.4	5.6	N.D	9.96
Pd2[b]	$Fe_3O_{4\ ref.}$	4.5	99	50	3.7	75
Pd3[c]	Fe_3O_4	4.3	112.1	14	2.8	55

[a] Palladium nanoparticles supported over maghemite which was prepared following the new precipitate method.
[b] Palladium nanoparticles supported over reference magnetite
[c] Palladium nanoparticles supported over magnetite which was prepared following the new hydrothermal method

From Table 1 it is possible to observe that Pd2 ($Pd@Fe_3O_{4\ ref.}$) and Pd3 ($Pd@Fe_3O_4$) samples show a bigger palladium amount than Pd1 sample ($Pd@\gamma$-Fe_2O_3). This can be explained by the diverse interaction between palladium and the two iron oxides. In particular, palladium shows more affinity with magnetite than maghemite probably due to the presence of diverse iron oxidation states.

Pd2 and Pd3 samples present diverse particle size distribution and surface area. In particular, sample Pd2 prepared using the reference magnetite is characterized by smaller palladium nanoparticles than the ones observed in sample Pd3.

It is noteworthy that Pd3 shows the biggest surface area underlining that the new hydrothermal method permits the production of small particles characterized by a high surface area. This last aspect is particularly important in catalysis because a high surface area can result in an easier and closer contact between reagents and catalysts, thus improving the reaction yield. The magnetization curves of samples Pd1, Pd2 and Pd3 do not permit any hysteresis as expected for superparamagnetic materials. Moreover the magnetic saturation values of Pd1 and Pd2 systems are the same as the iron oxide used

as supports, whereas the M_0 of sample Pd3 results higher than the magnetite ones. The M_0 improvement observed in sample Pd3 can be due to the strong interaction between magnetite and palladium atoms, which was highlighted also by XRD and BET analysis.[19] The comparison between the magnetization curves of magnetite support and sample Pd3 is shown in Figure 1.

In conclusion, sample Pd3 presents promising magnetic properties, the highest surface area and small particle size, characteristics that are very interesting for its catalytic applications.

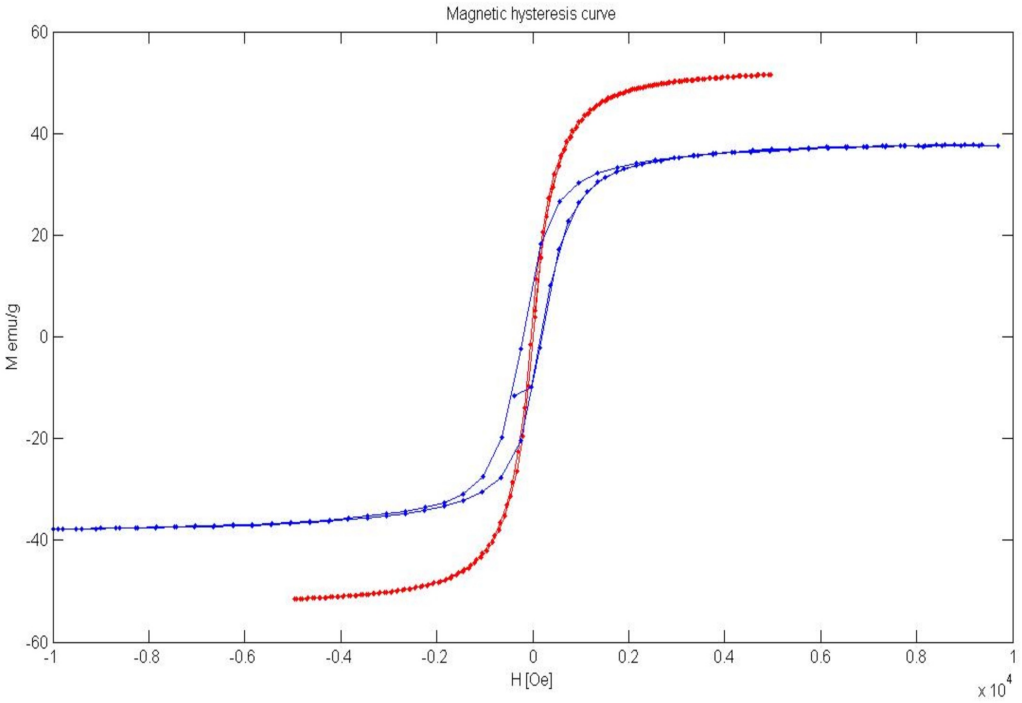

Figure 1 Comparison between the magnetization curves of sample Pd3 in red and the magnetite particles used as support in red

FT-IR spectra of samples Pd1, Pd2 and Pd3 are reported in Figure 2. In particular the FT-IR spectrum of sample Pd1 (black line) shows well defined peaks at 630 1/cm typical of maghemite, broad peaks at 1400 1/cm ascribable to impurities of carbonates and a band at 3300 1/cm due to the hydroxyl group of ethanol trapped inside the maghemite structure. Conversely, the FT-IR spectra of both samples Pd2 and Pd3 (green and red lines respectively) show a big peak at 590 1/cm typical of the Fe-O bonds in the tetrahedral Fe_3O_4 sites. Moreover, in the FTIR spectrum of sample Pd3 it is possible to observe two big peaks between 1400 1/cm and 1600 1/cm ascribable to acetate impurity derived from the iron precursor.

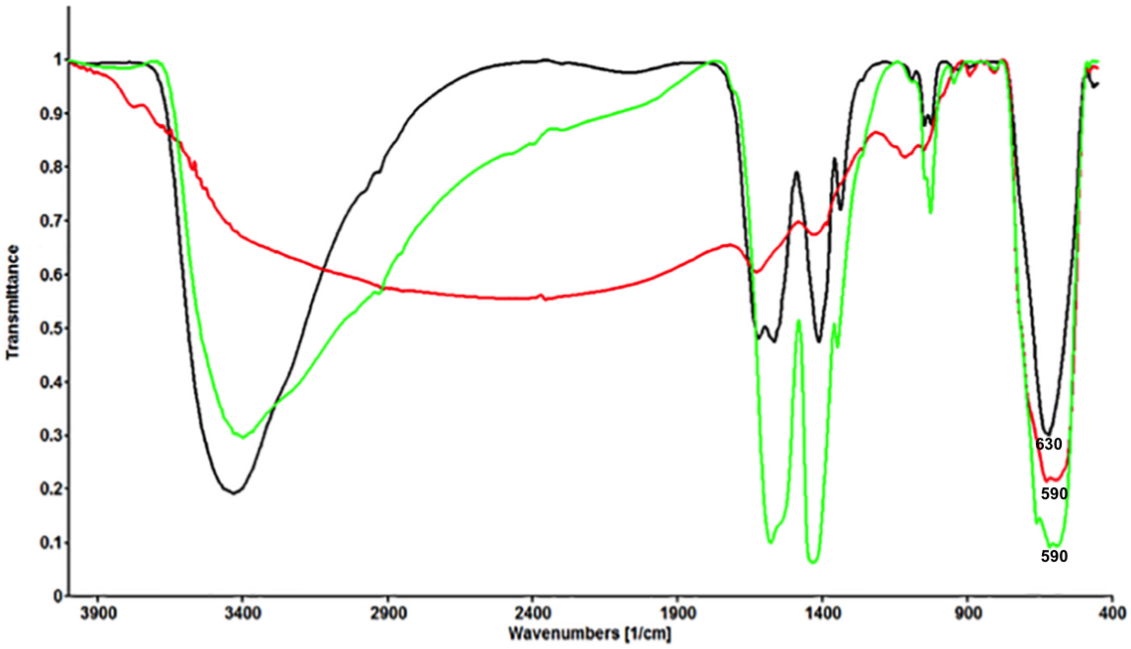

Figure 2 FT-IR spectra of samples: Pd1, palladium nanoparticles over maghemite nanocrystals (black), Pd2, palladium nanoparticles over reference magnetite nanoctrystals (green) and Pd3 palladium nanoparticles over hydrothermal magnetite nanoctrystals (red)

The identification of iron oxide phases further confirmed the Raman and XRD analysis. In particular, the Raman spectrum of Pd1 reports a main peak at 672 1/cm with a bump at 712 1/cm and a broad peak at 513, proper to the maghemite phase, whereas the Raman spectra of samples Pd2 and Pd3 clearly show the strong band at 669 1/cm typical of magnetite. The Raman spectrum of sample Pd3 shows also a little peak at 945 1/cm, which could be due to the iron (II) acetate employed as precursor in the hydrothermal synthesis.

The XRD patterns of samples Pd1, Pd2 and Pd3 are reported in Figure 3. The Pd1 XRD diffractogram presents broad reflection peaks, which can be indexed as Miller indexes of γ-Fe_2O_3 maghemite like structure (206), (119), (0012), (1115), (3315) as observed for the XRD of maghemite sample in Chapter 4.1 (sample B). It was not possible to reveal the presence of metallic palladium in sample Pd1, probably due to the smaller palladium particle size.

The XRD diffractograms of Pd2 and Pd3 samples clearly show the well-defined patterns of magnetite and the typical peaks of metallic palladium. In particular for both samples it was possible to index the reflection peaks by the Miller indexes of the cubic Fe_3O_4 magnetite like structure (220), (311), (222), (400), (422), (511), (400), (620),

(530), (622). Moreover in the Pd2 and Pd3 samples it was possible to identify the (111), (200), (220) (311) (222) reflection patterns due to metallic palladium.

All the reflection pattern attributions agree with the ones reported in literature for palladium/magnetite nanostructures.[11a]

The calculated cell parameters for Pd2 and Pd3 samples are respectively 8.355(1) and 8.357(1) quite similar to the ones reported for magnetite. Finally, it was observed that the XRD patterns of the Pd2 sample are more definite than the ones acquired for the Pd3 sample, probably due to the bigger particle size of reference magnetite used as support in its preparation.

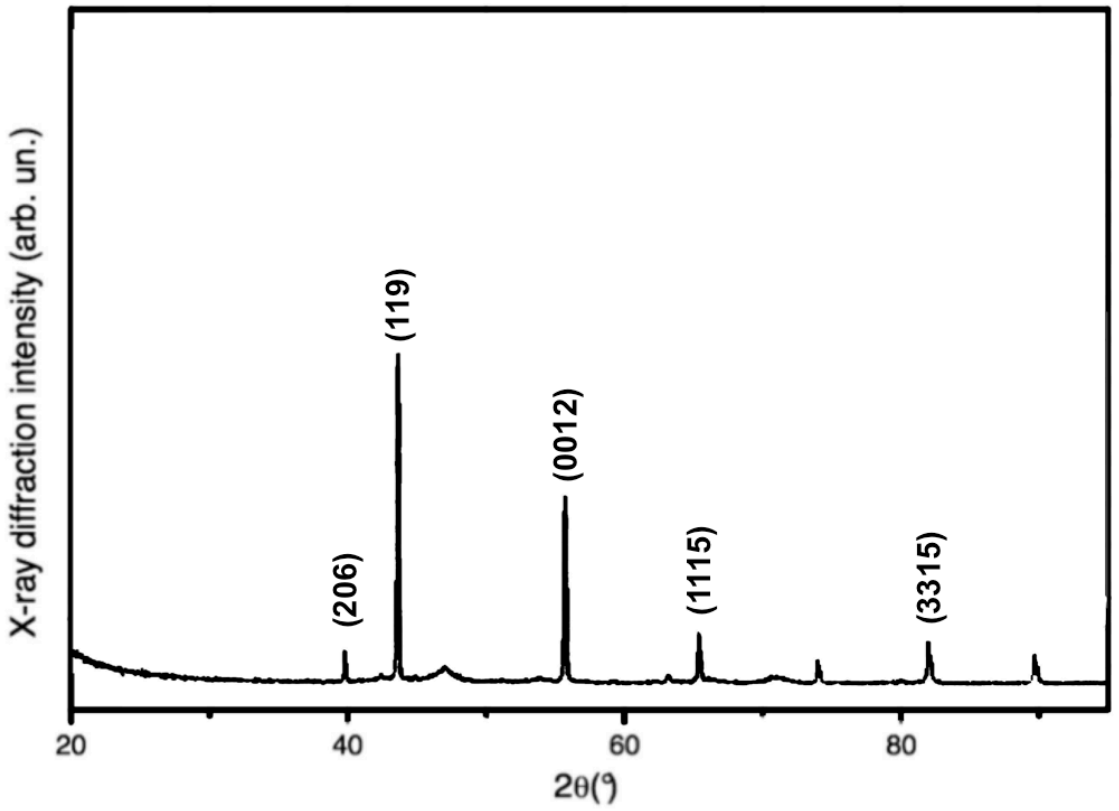

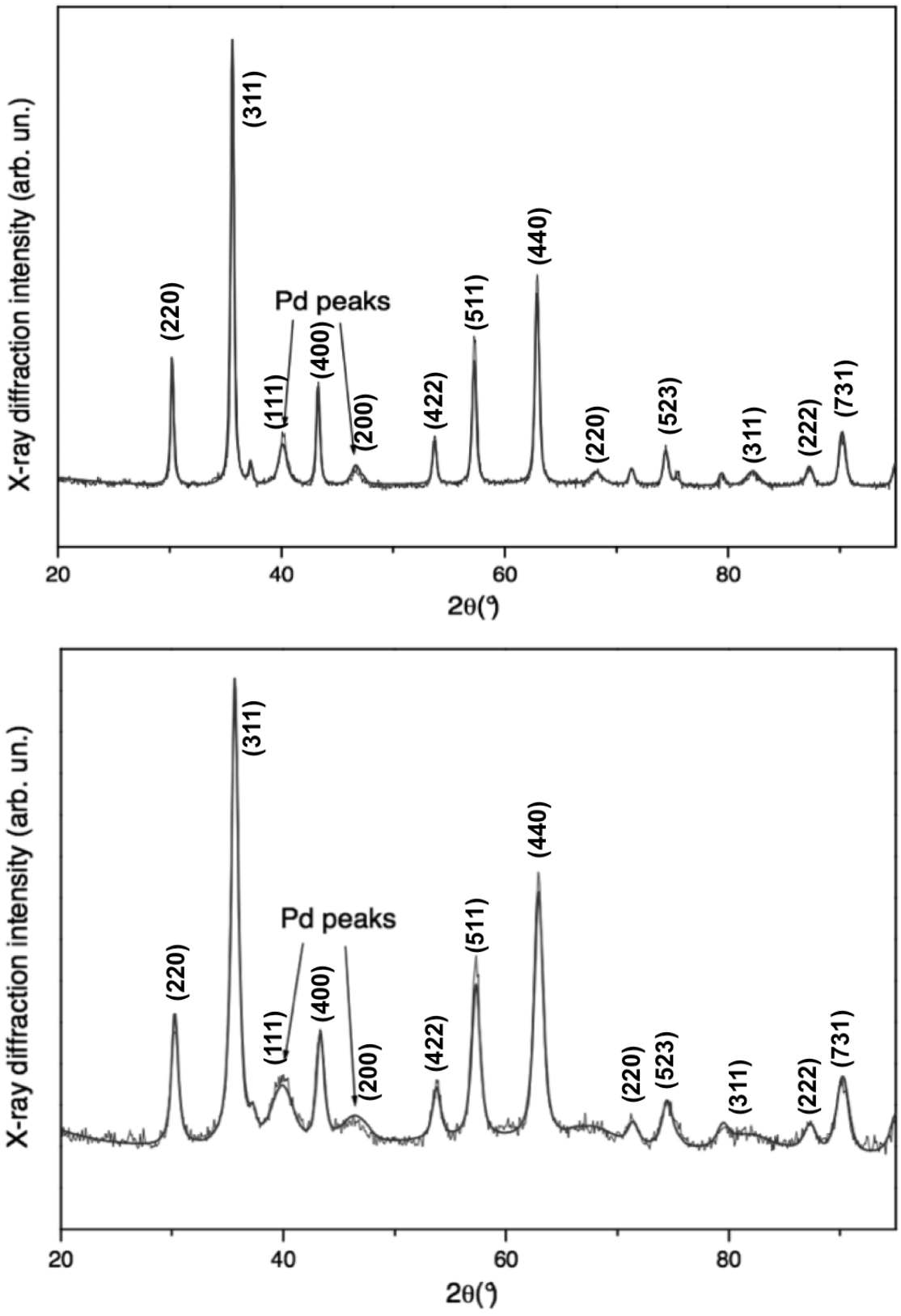

Figure 3 XRD diffractogram of samples Pd1, Pd2 and Pd3.

The presence of metallic palladium in each sample was also ascertained by AES analysis and quantified through ICP-OES analysis.

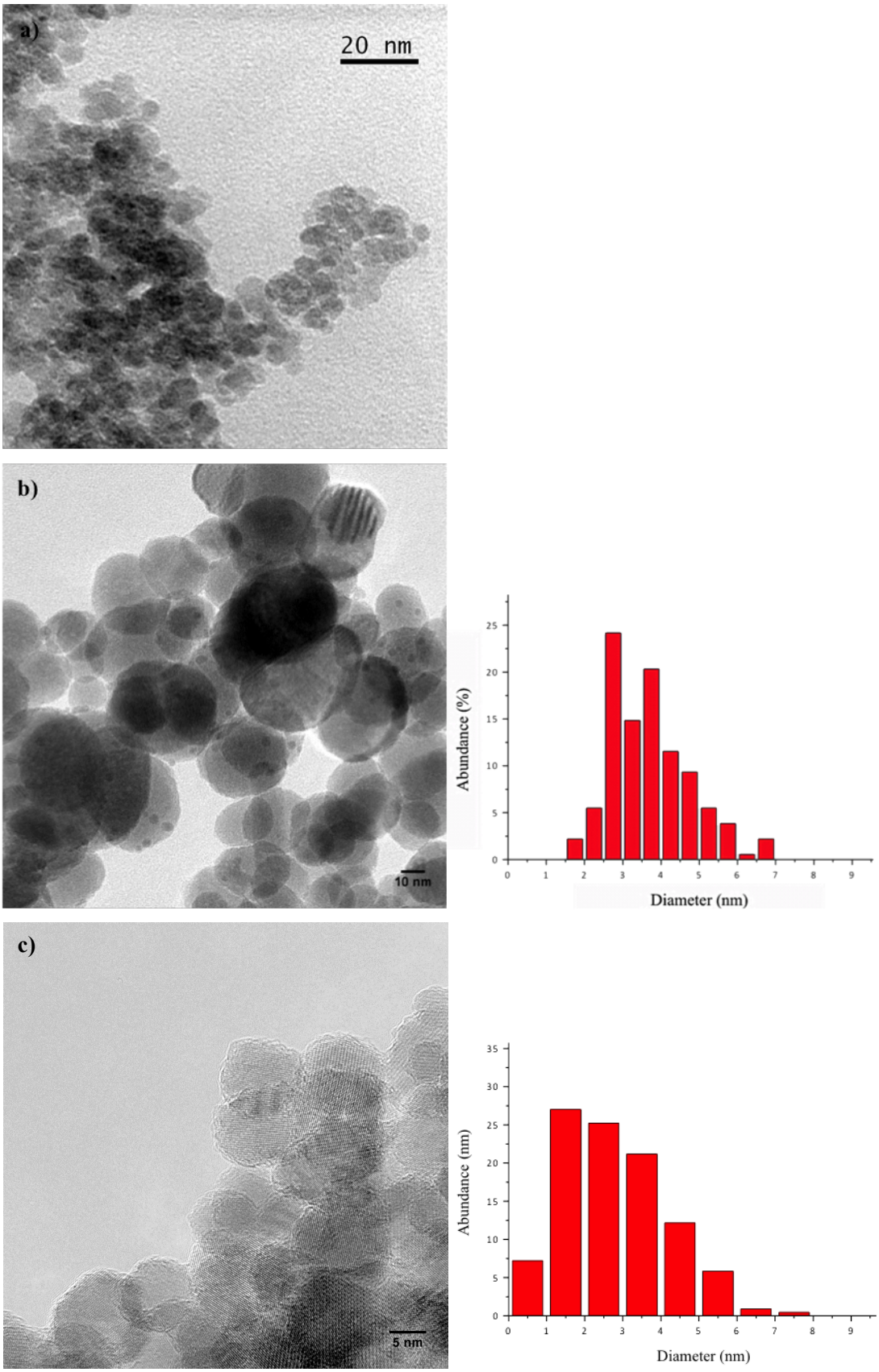

Figure 4 TEM micrographs and palladium particle size distribution of samples: a) Pd1 Pd@γ-Fe_2O_3, b) Pd2 Pd@Fe_3O_4 $_{ref}$ and c) Pd3 Pd@Fe_3O_4

As it is possible to observe in Figure 4, sample Pd1 is characterized by the smallest magnetic particles with an average diameter of 5.6 nm. Due to the small size of the

maghemite used as support and the smaller palladium particles it was not possible to determine the palladium particle distribution.

The Pd2 and Pd3 samples were prepared using magnetic support characterized by bigger particles than the ones used for the synthesis of sample Pd1. In more detail, the magnetic particle used as support for samples Pd2 and Pd3 show average diameters of 50 nm and 14 nm respectively. In these two samples, it is possible to observe palladium particles with average diameters of 3.7 nm and 2.8 nm (for samples Pd2 and Pd3 respectively).

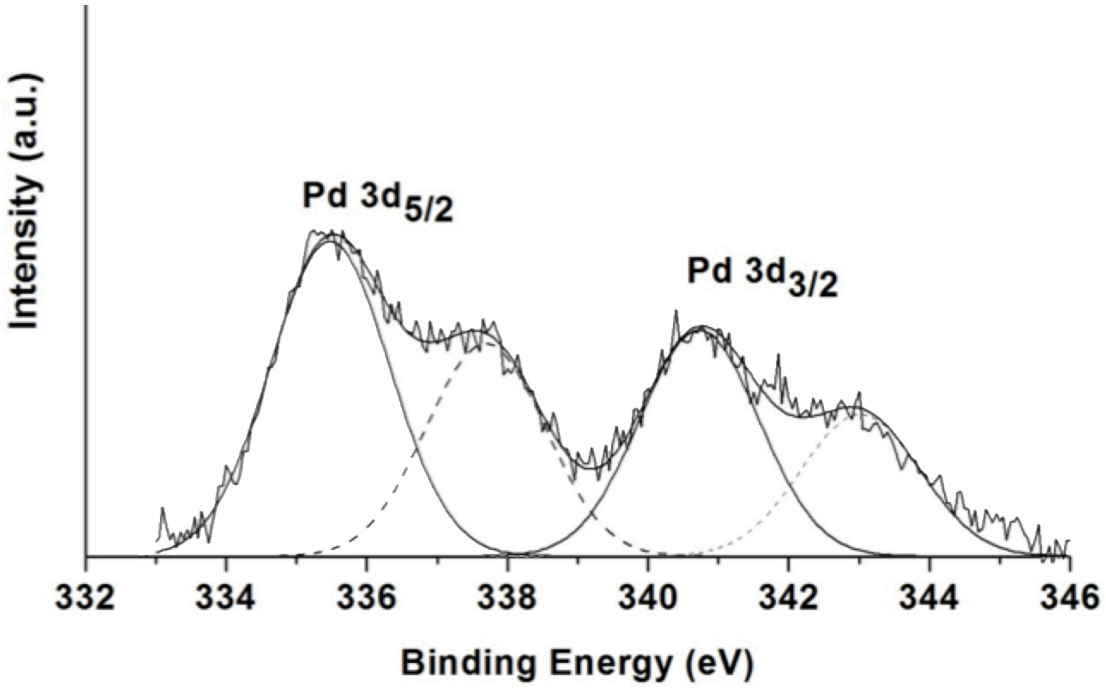

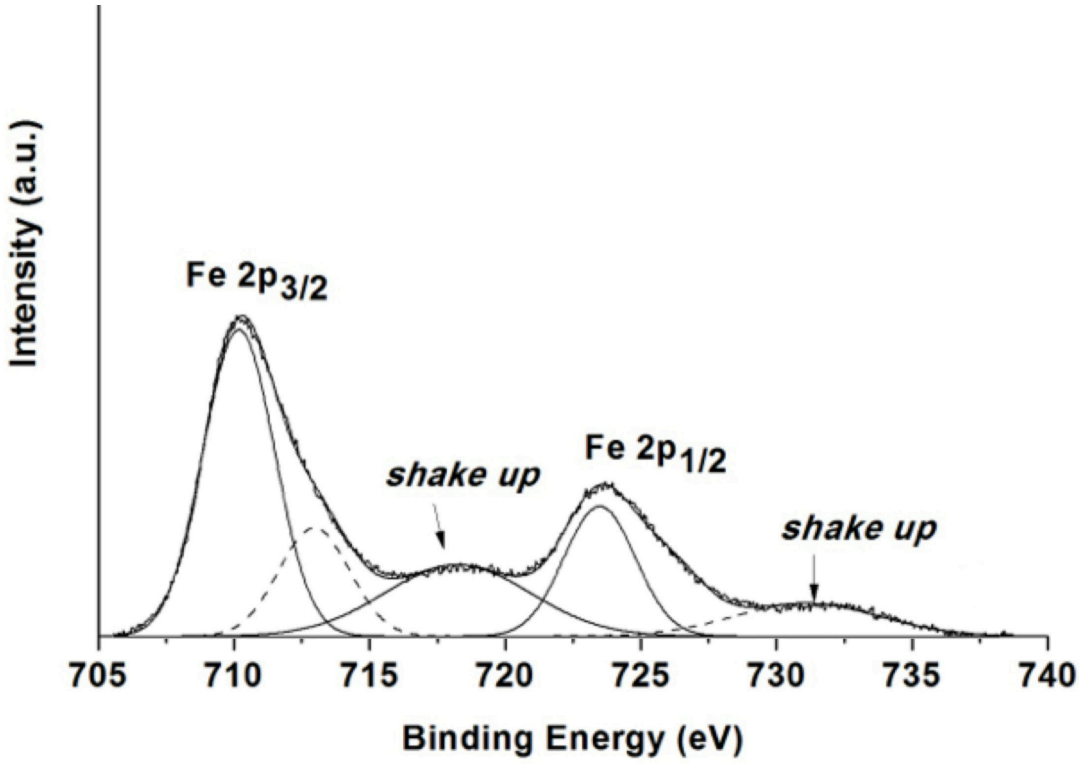

Figure 5 XPS analysis of sample Pd1

Figure 5 reports the XPS analysis of sample Pd1. From this analysis it is possible to observe the two components of palladium present in the sample, one at low binding energy (335,5 eV) and another at high binding energy (337,7 eV). The low binding energy peak can be attributed to metallic palladium slightly positively charged because of chemical interaction with the support.[3e, 11a]

The high energy peak is attributed to unreduced Pd(II). In particular 60% of the palladium present in Pd1 samples is metallic palladium and the remaining 40 % is Pd(II). The peaks at the binding energy of 200 eV are ascribable to Cl 2p underlining the presence of chlorine ions, which can be due to the iron precursor used. Furthermore iron shows two components at binding energy of 710.5 eV and 713,3 eV, both ascribable to Fe $2p_{3/2}$. The other peaks observed at high energy could be attributed to surface species or some iron chloride species.

5.1.2 Palladium trapped inside magnetite nanocrystal

Following a procedure based on the new hydrothermal method described in Chapter 4.2 it was possible to prepare palladium nanoparticles trapped inside magnetite nanocrystal, $Pd@Fe_3O_4$.

The $Pd@Fe_3O_4$ nanoparticle preparation deals with the contemporaneous decomposition of iron acetate ($Fe(OAc)_2$), and palladium acetate ($Pd(OAc)_2$) through MW-irradiation at 120°C for 15 minutes. At the end of this treatment, the particles were magnetically collected, washed and dried. This preparation was repeated adopting diverse palladium amounts as summarized in Table 2. Moreover, this hydrothermal approach was also investigated using diverse heating sources such as multimode microwave MARS 6 and traditional heating with 100 ml Parr autoclave.

Table 2 Characteristics of palladium nanoparticles intercalated in magnetite nanocrystal

Samples	Composition	AAS (Pd %wt)	BET (m^2/g)	VSM M0 (emu/g)
Pd4[a]	1% $Pd@Fe_3O_4$	0.89	93.8	56.79
Pd5[a]	2% $Pd@Fe_3O_4$	1.6	103.8	N.D
Pd6[a]	5% $Pd@Fe_3O_4$	4.7	106.5	63
Pd7[a]	10% $Pd@Fe_3O_4$	8.8	101.1	N.D
Pd8[b]	5% $Pd@Fe_3O_4$	4.3	85.8	47.86
Pd9[c]	5% $Pd@Fe_3O_4$	5.02	90.5	N.D

[a] Reaction conditions: 1g of $Fe(OAc)_2$, 0.05g $Pd(OAc)_2$, 44 mL EtOH at 96 wt%, microwave heating: 120 °C, 15 min, 250 W

[b] Reaction conditions: 0.25g $Fe(OAc)_2$ 0.0125g $Pd(OAc)_2$, 44 mL EtOH at 96 wt%, microwave heating: 120 °C, 15 min, 250W.

[c] Reaction conditions: 1g of $Fe(OAc)_2$, 0.05g $Pd(OAc)_2$, 44 mL EtOH at 96 wt%, traditional heating: 120 °C, 4.5 h.

As can be observed in Table 2, by increasing the amount of palladium the surface area of the samples changes. In particular, comparing samples Pd4, Pd5, Pd6 and Pd7, it is possible to observe an increase of the surface area with an increase of the sample palladium amount, until a maximum of palladium content of about 4.7 % is reached. Over this value, the surface area does not change any more (see Figure 6). This trend can be due to the strong influence of palladium atoms on the magnetite crystalline arrangement. In fact, the introduction of palladium atoms inside the crystalline cell of magnetite can result in the generation of defects, which lead to a modified surface area.

However, when the palladium amount is greater than 4,7 % not only no increase in the surface area of samples was ascertained but a little decrease of sample surface area was observed.

Furthermore, when samples Pd4 and Pd6 prepared adopting the same synthetic procedure were compared, it was observed that by increasing the quantity of palladium the magnetic saturation of the catalytic system increases. In fact, the metallic interaction between Fe and Pd inside the magnetite crystal can improve conductibility and magnetic saturation of the materials. This strong interaction was observed only in the hydrothermal samples, when palladium particles are trapped inside the Fe_3O_4 and not in the hierarchical samples described in Chapter 5.1.1.

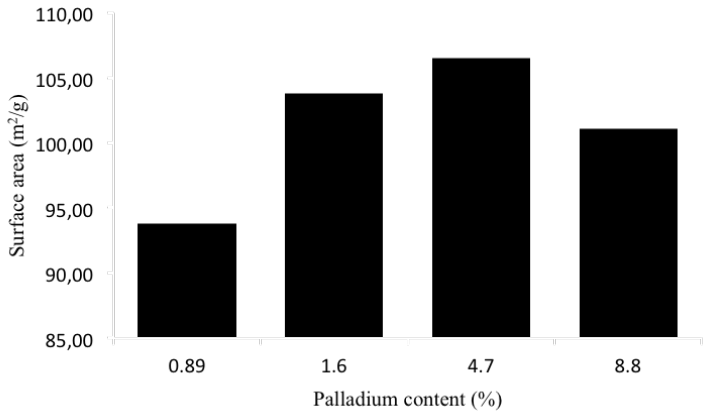

Figure 6 Influence of palladium content on surface area samples

The Raman spectra of all samples confirmed the identification of magnetite as the iron oxide phase, in fact each spectrum reports the typical magnetite strong band at 669 1/cm.

Figure 7 shows the FT-IR spectra of samples Pd4, Pd5, Pd6, Pd7 and Pd9, which present the typical strong band at 590 1/cm ascribable at Fe_3O_4, whilst the peculiar bands of maghemite phase in the spectral range of 740-620 1/cm are absent. These results show that the hydrothermal method allows the synthesis of pure magnetite crystal also in the presence of the noble metal. Moreover, all FT-IR spectra show the peak at 1240 1/cm ascribable to acetate, impurity due to the metal precursors adopted in the synthesis and a broad band at 3000-3500 1/cm, which is caused by the hydroxyl stretching vibrations of ethanol and water molecules trapped in iron oxide nanoparticles.

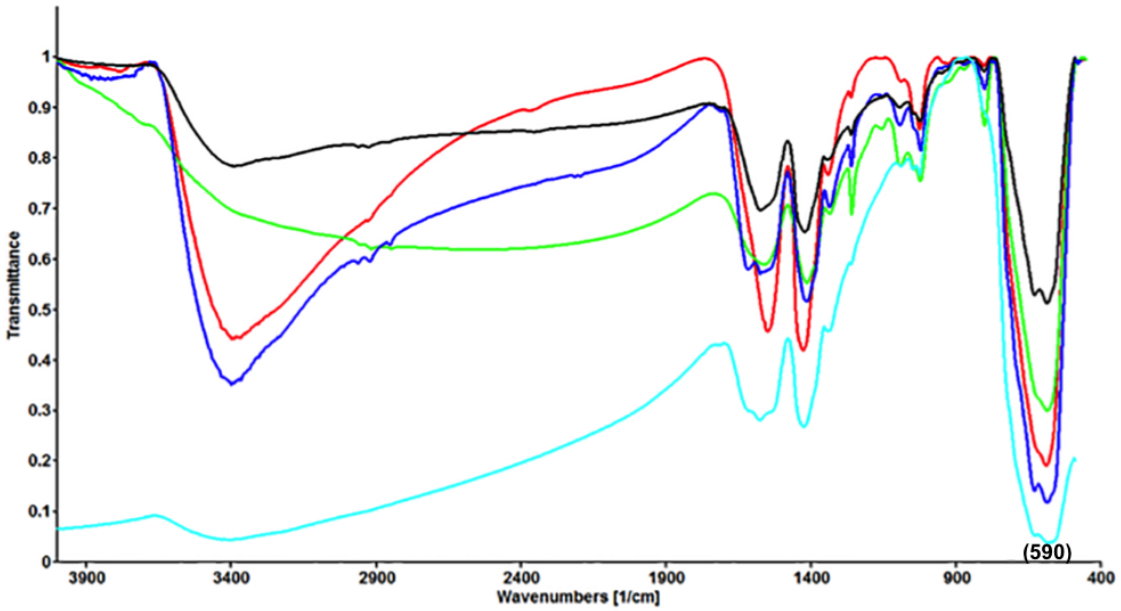

Figure 7 FTIR spectra of samples: Pd4, 1% Pd@Fe_3O_4 in red, Pd5 2% Pd@Fe_3O_4 in light blue, Pd6 5% Pd@Fe_3O_4 in blue, Pd7 10% Pd@Fe_3O_4 in black and Pd9 5% Pd@Fe_3O_4, obtained with traditional heating, in green

The X-ray diffraction patterns of samples Pd4, Pd6 and Pd9 are shown in Figure 8 and were compared with magnetite reference card 98-001-2141 from the ICSD database in red, matching for 93-98%. The diffraction peaks of these samples can be indexed by the Miller indexes of the cubic Fe_3O_4 magnetite-like structure (220), (311), (222), (400), (422), (511), (400), (620), (533) and (622). Furthermore, the broad diffraction peaks around $2\theta = 40$ are compatible with the presence of nanocrystalline metallic palladium.

The refined lattice parameters for Pd4, Pd6 and Pd9 are respectively 8.371(1) Å, 8.360(1) Å, (8.370 (1) Å and the observed microstrains are respectively 0.0018, 0.0024 and 0.0023. These microstrains are double than ones calculated for the pure magnetite thus underlining the presence of defects inside the crystalline magnetite structure, showing again the high interaction that occurs between palladium nanoparticles and iron oxide structure.

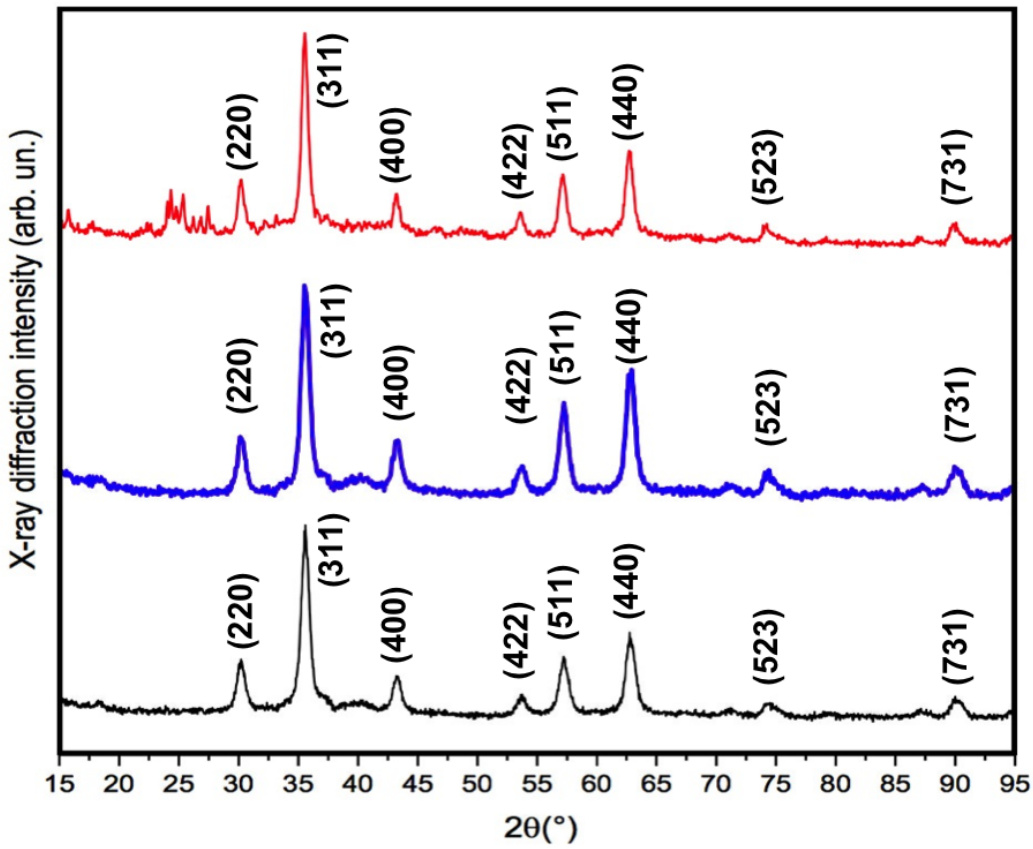

Figure 8 XRD diffractograms of sample: Pd4 in red, Pd6 in black and Pd9 in blue

The TEM images of samples Pd6 and Pd9 reported in Figure 9 evidence the effect of the adopted heating source on particle size distribution. In fact, the MNPs prepared under traditional heating in autoclave (sample Pd9) show the largest and most heterogeneous particle size dispersion characterized by an average diameter of 10 nm together with big particle aggregates. The particles obtained using monomode microwave (sample Pd6) show a narrow and homogeneous particle size distribution characterized by particles with an average diameter of about 8 nm.

This result can be related to the main drawbacks of the conventional batch autoclaves whose wall dimensions are designed for high-pressure applications: the heating and cooling of the steel body of the reactor involve time leading to an irregular and non-uniform warming with marked temperature gradients and high thermal inertia. On the contrary, MW-irradiation results in an almost instantaneous “in core” heating of materials in a homogeneous and selective manner allowing rapid transfer of the energy into the bulk of the reaction mixture, eliminating the wall effects. The effect of the

heating source on particle characteristics was observed also in the magnetite preparation described in Chapter 4.2, confirming that the best heating source for the preparation of well-defined nanoparticles is the monomode microwave irradiation.

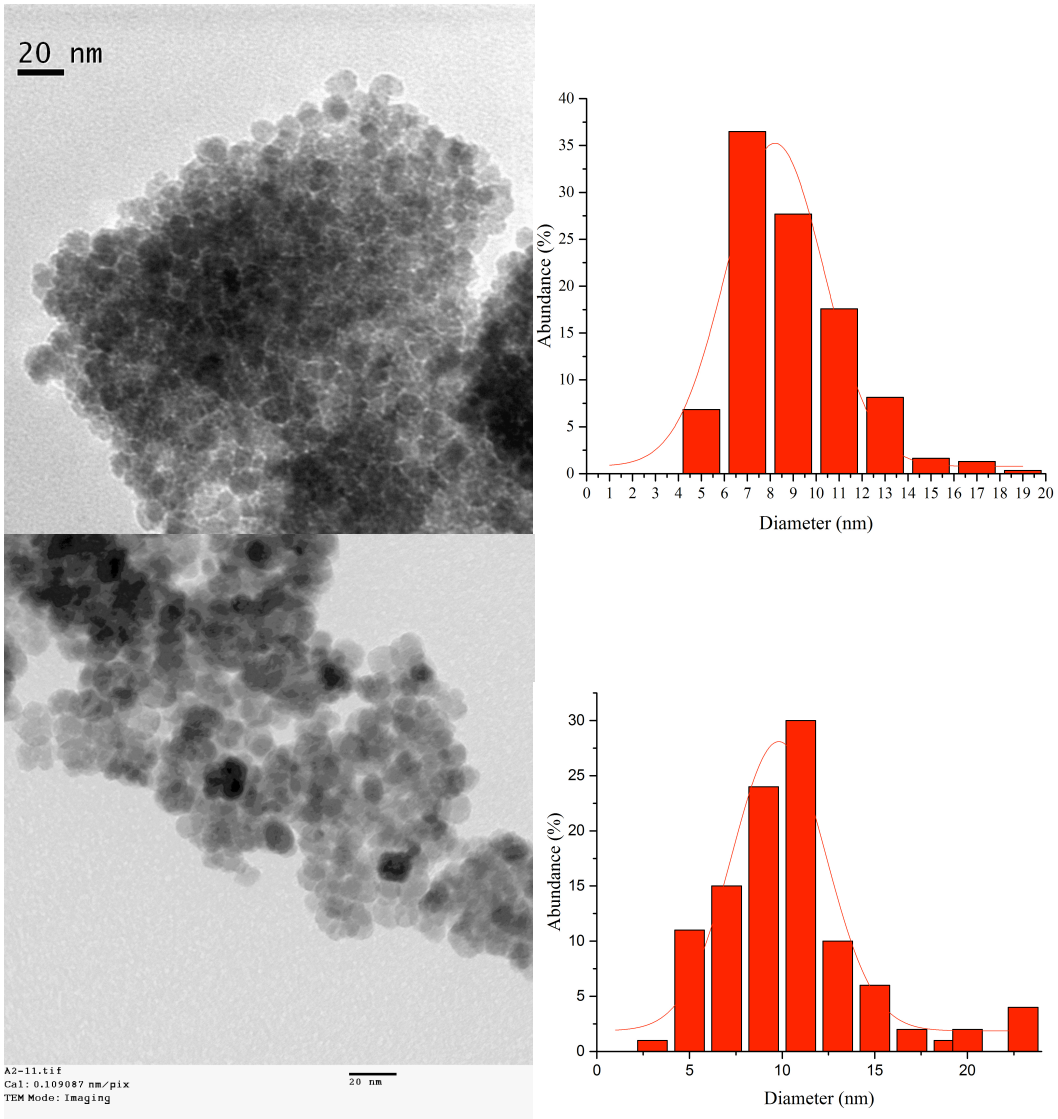

Figure 9 TEM micrograph and particle size distribution of sample Pd6 and Pd9

The oxidation state of the palladium species present in Pd6 sample was determined by XPS analysis. As it is possible to see in Figure 10 the palladium of sample Pd6 has two components, one at low binding energy (335,5 eV) and another at high binding energy (337,9 eV). The low binding energy peak can be attributed to metallic palladium, slightly positively charged because of chemical interaction with the support.[3e, 11a]

The high energy peak is attributed to highly charged Pd(II). In particular 90% of the palladium present in Pd6 sample is metallic palladium and the remaining 10 % is Pd(II).

Furthermore, iron shows two components at binding energy of 710.5 eV and 713,7 eV both ascribable to Fe $2p_{3/2}$.

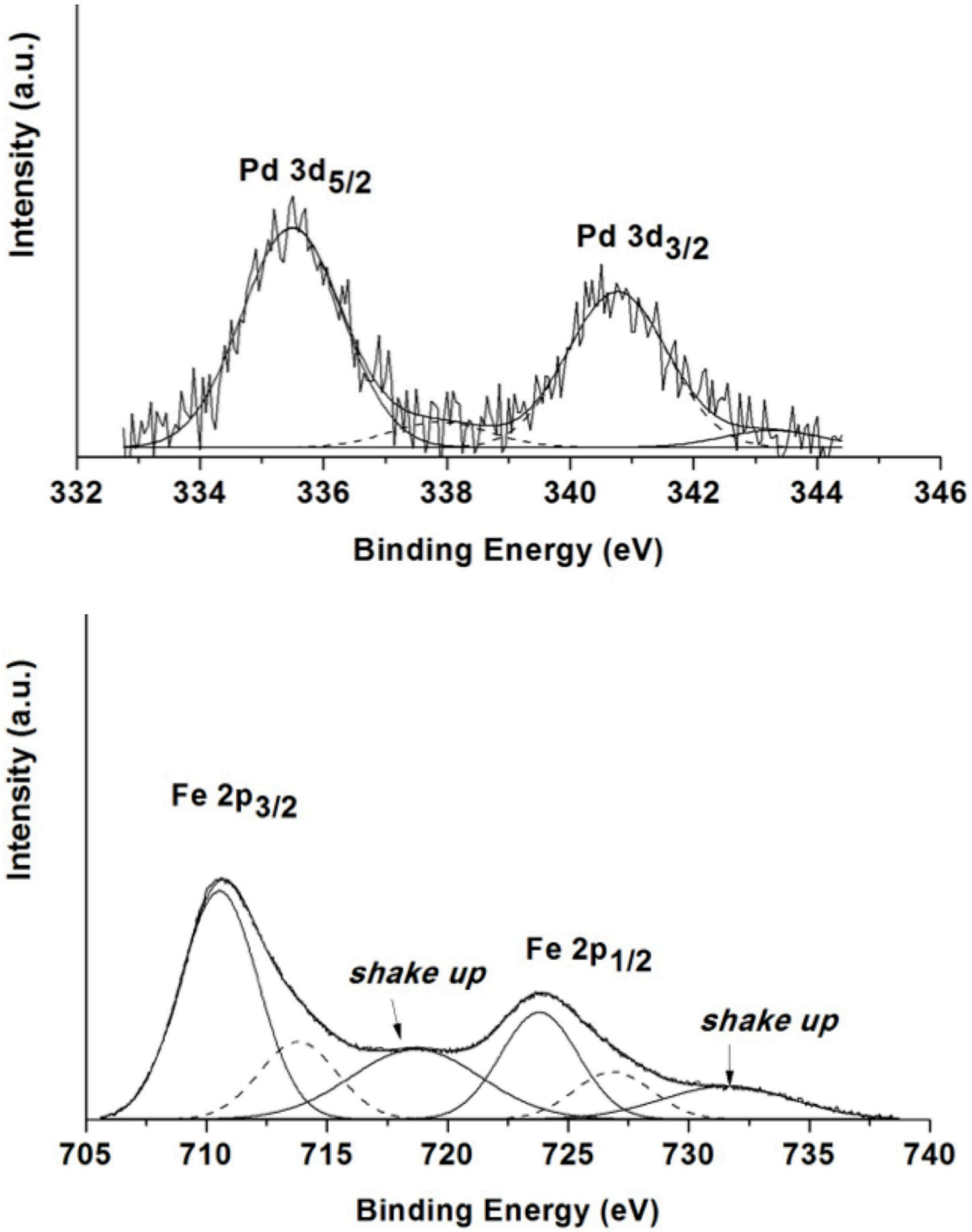

Figure 10 Photoemission spectrum of sample Pd6.

The temperature programmed reduction (TPR) profile of sample Pd6 is displayed in Figure 11 and can be separated into two zones: before and after 300°C. The big broad

band after 300°C, which corresponds to the last event, can be assigned to the bulk reduction of the magnetite to FeO and Fe, [20] whereas on the zone before 300°C, a small reduction peak might indicate that the Pd species content in the samples is not completely reduced to the metallic form as confirmed also by the XPS analysis.

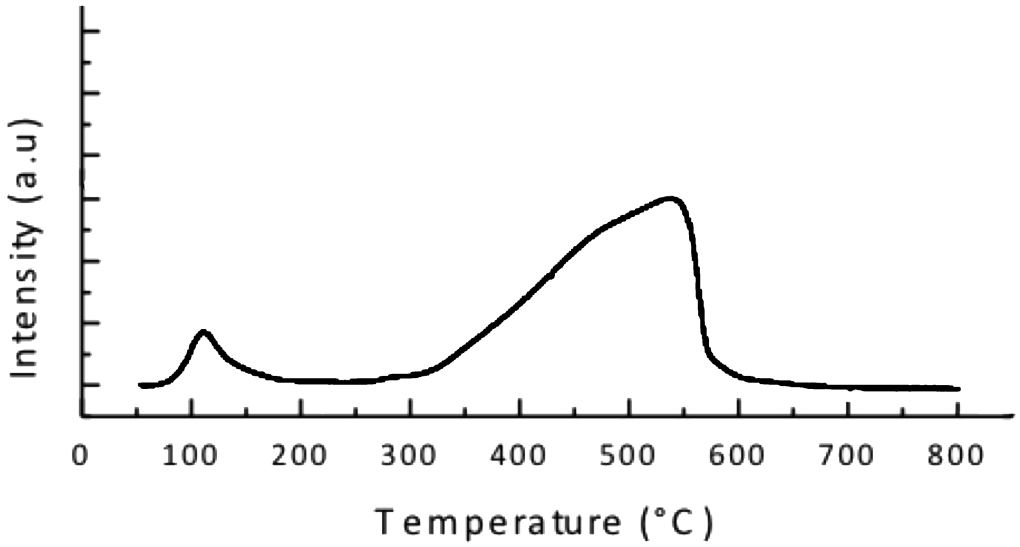

Figure 11 TPR analysis of sample Pd6

The magnetic behaviour of the synthetized systems was measured at room temperature with a vibrating sample magnetometer (VSM). The magnetization curves of samples Pd6, Pd8 and Pd9 are shown in Figures 12 and 13.

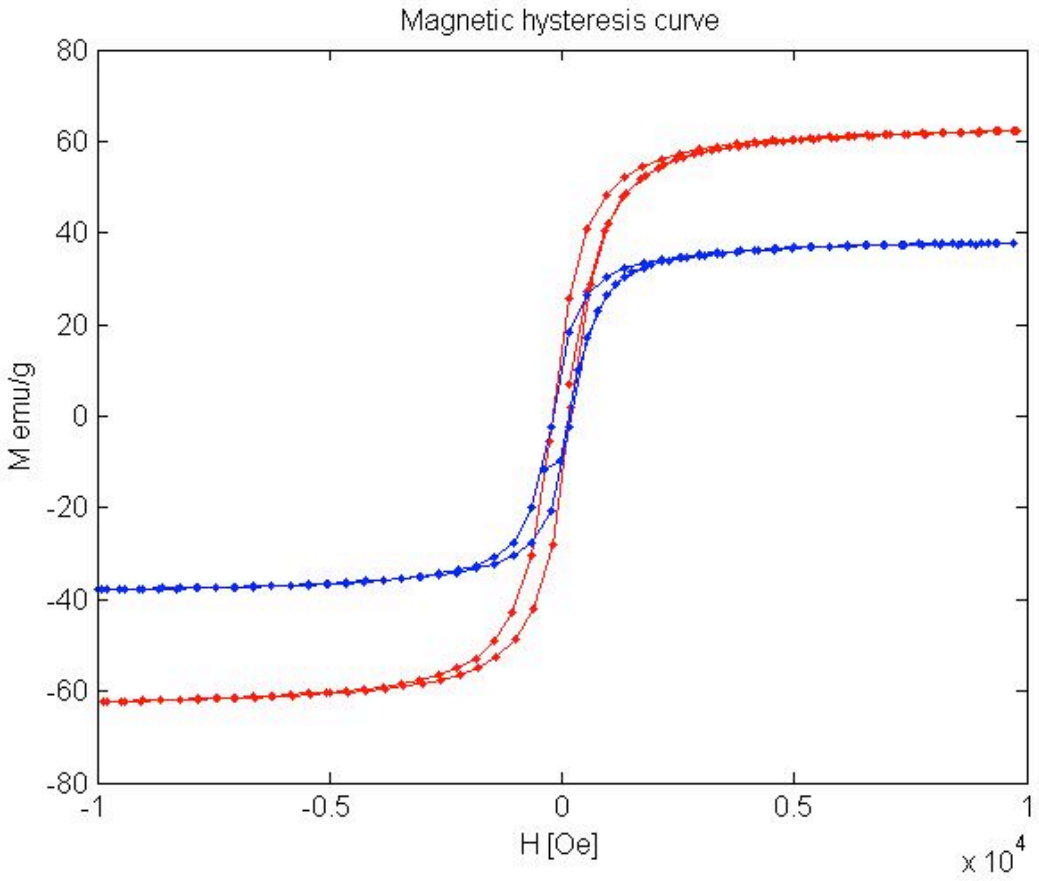

Figure 12 The comparison between the magnetization curves pure magnetite in blue and the sample Pd6 in red

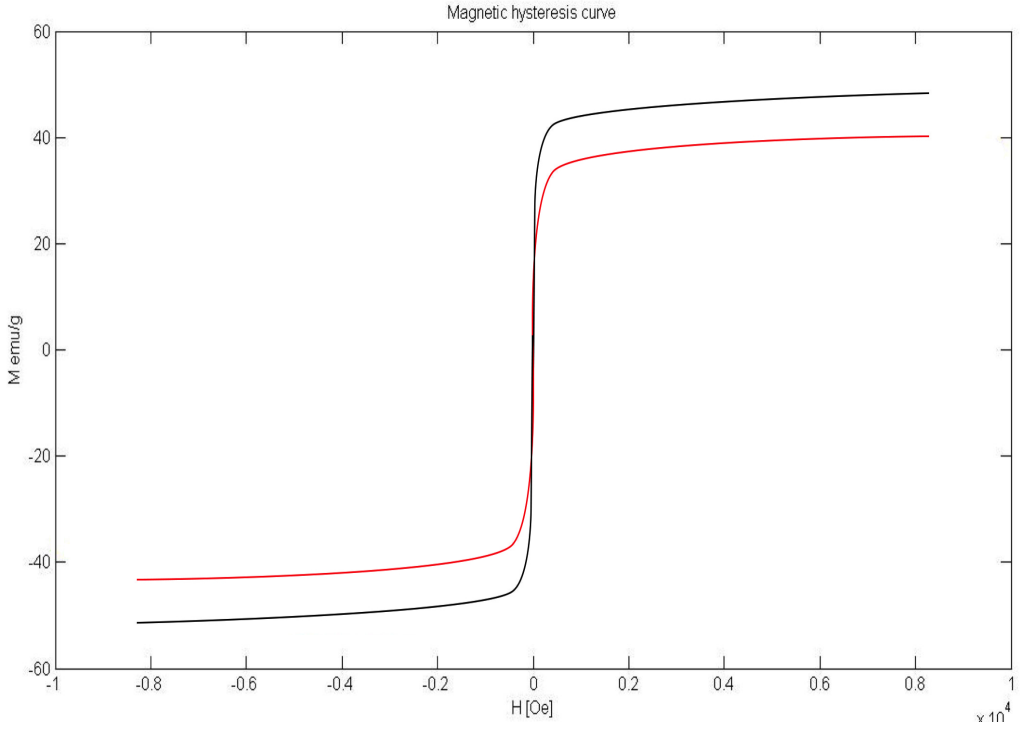

Figure 13 Magnetization curve of samples Pd4 in black and Pd8 in red

Pd4 and Pd8 samples show a superparamagnetic behaviour as confirmed by the absence of magnetic hysteresis (Figure 13), while this is visible for pure magnetite and sample Pd6 (Figure 12) in the adopted representation scale.

As known from literature, the magnetic behaviour of iron oxide nanoparticles is very sensitive to particle size and to crystallinity, as well as to the presence of other molecules or metals. In fact, from the magnetic analysis reported in Figures 12 and 13 it was possible to observe the effect of palladium content on sample magnetization saturation values. In particular, by comparing samples Pd4 and Pd6 with pure magnetite it is possible to see that by increasing the palladium content, the magnetization saturation values increase. In more detail, the measured M_0 for magnetite, Pd4 and Pd6 samples are respectively 45.88 emu/g, 56.79 emu/g, 63 emu/g.

Furthermore, a strong effect of particle crystallinity and particle size distribution on the magnetic behaviour was also observed. In fact, taking into account samples Pd6 and Pd8 characterized by the same palladium content but obtained using two diverse heating sources, two diverse M_0 values were measured, 63 emu/g and 47.86 emu/g respectively. This difference is due to the their diverse structure as observed with XRD diffractograms and TEM images. In fact sample Pd6 presents a higher crystalline degree and narrow size distribution (see Figures 8 and 9). In conclusion the introduction of palladium atoms in a high crystalline magnetite can improve its magnetic properties leading to higher magnetization saturation values.[21]

5.2 Synthesis of ruthenium magnetic nanocatalysts

Ruthenium oxide nanocatalysts attract huge interest for their surprising activity in a wide range of important industrial reactions such as hydrogenation[13c], oxidation[22] and water gas shift [12c].

In this context, as underlined for the palladium nanoparticles in Chapter 5.1, the introduction of magnetic nanosupports could be a strategic choice able to guarantee an efficient and easy separation[17]. Moreover, magnetic separation avoids the use of auxiliary substances, making the process cleaner, safer and faster than normal separation procedures[18].

The ruthenium oxide magnetic nanocatalysts, $RuO_x@Fe_3O_4$ are prepared following a procedure based on a new hydrothermal method similar to that described in Chapter 5.1.2 for the preparation of $Pd@Fe_3O_4$ samples.

The reactive process involved in the $RuO_x@Fe_3O_4$ sample preparation is shown in scheme 1.

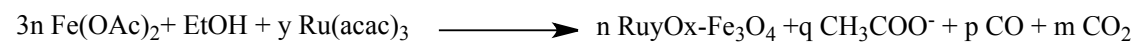

Scheme 1 General reaction scheme for the hydrothermal preparation of $RuO_x@Fe_3O_4$

In particular, the $RuO_x@Fe_3O_4$ nanoparticles were prepared through the contemporaneous decomposition of iron acetate ($Fe(OAc)_2$), and ruthenium acetylacetonate ($Ru(acac)_3$) under MW-irradiation. This approach was repeated adopting diverse ruthenium amounts and the results are summarized in Table 3.

Table 3 Characteristics of ruthenium oxide nanoparticles intercalated in magnetite nanocrystal

Samples	Composition	AAS (Pd %wt)	BET (m^2/g)	Diameter (nm)	VSM M0 (emu/g)
Ru1[a]	2% $RuO_x@Fe_3O_4$	0.85	62.0	ND	ND
Ru2[b]	5% $RuO_x@Fe_3O_4$	1.87	66.6	10.1	40

[a] Reaction conditions: 1g of $Fe(OAc)_2$, 0.088g $Ru(acac)_3$, 44 mL EtOH at 96 wt%, microwave heating: 120 °C, 15 min, 250 W

[b] Reaction conditions: 1g $Fe(OAc)_2$ 0.035g $Ru(acaca)_3$, 44 mL EtOH at 96 wt%, microwave heating: 120 °C, 15 min, 250.

The increase in ruthenium content results in an increase in the particle surface area as can be observed in Table 3. This positive effect of metal content on the particle surface area was observed also for the palladium samples described in Chapter 5.1.2.

Although the new hydrothermal procedure permits the production of samples characterized by a high surface area, it is less efficient in ruthenium reduction. In fact, the measured ruthenium loads for samples Ru1 and Ru2 are a third of the theoretical values calculated on the basis of the amount of ruthenium precursor adopted for the preparation. Probably the energy supplied by the adopted temperature was not enough to reach the complete redaction and deposition of the ruthenium species present in the solution. However it was not possible to increase the reaction temperature due to the microwave reactor safety pressure limits. In fact under the adopted condition (aqueous

ethanol as solvent and 120°C as reaction temperature) the instrumental pressure limit was reached.

The FT-IR spectra reported in Figure 14 shows the adsorption band at 590 1/cm typical of the Fe-O bonds in tetrahedral Fe_3O_4 sites. Furthermore, the Ru1 and Ru2 spectra show two low absorbance bands at 900 1/cm and 960 1/cm ascribable to ruthenium oxide species in agreement with what is reported by Key et al.[23] These two last peaks are more evident in sample Ru2 (red line, Figure 14) due to its higher ruthenium content.

Both Ru1 and Ru2 spectra also present strong peaks around 1400 1/cm ascribable to acetate traces introduced with the metal precursor, and a broad band at 3000-3500 1/cm, which corresponds to water and ethanol molecules trapped in the magnetite particles. The good overlapping of the FTIR spectra of samples Ru1 and Ru2 at low wavenumbers underline the stability and reproducibility of the adopted hydrothermal methods.

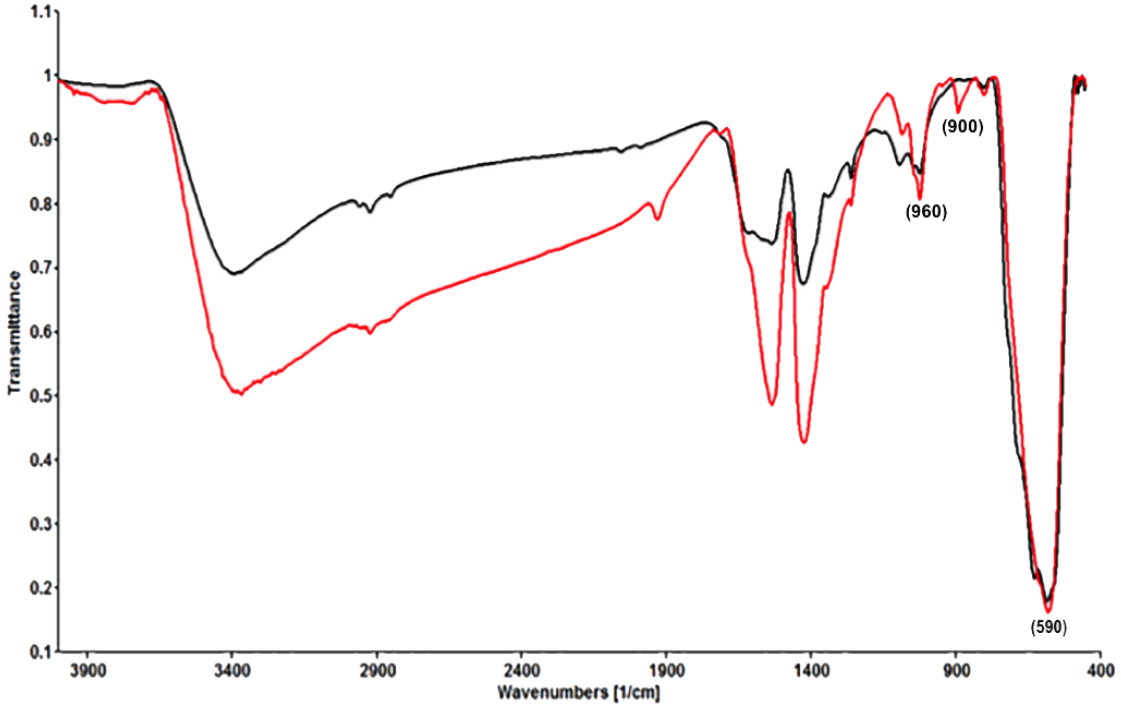

Figure 14 FTIR spectra of samples Ru1 2% RuO_x@Fe_3O_4 in black and Ru2 5% RuO_x@Fe_3O_4 in red

Ru1 and Ru2 sample compositions were also ascertained by AES and Raman analysis. The Raman spectra of both samples in fact report the typical magnetite strong band at 669 1/cm.

The XRD diffractogram of sample Ru2 is portrayed in Figure 15. The diffraction patterns can be indexed as the Miller indexes of the cubic magnetite-like structure (220), (311), (222), (400), (422), (511), (400), (620), (533) and (622). The calculated cell parameter is identical to the ones

reported for magnetite, 8.367(1) Å. Moreover the crystal plans of Ru2 samples show the presence of defects probably due to the presence of ruthenium atoms inside the crystalline cell of magnetite. The calculated microstrain of Ru2 samples is 0.0024(1) similar to the ones observed for palladium samples.

This last characteristic is an interesting aspect for the catalytic application of $RuO_x@Fe_3O_4$ samples; in fact if the active metal is trapped inside the support structure, the deactivation by poisoning and leaching could be reduced.

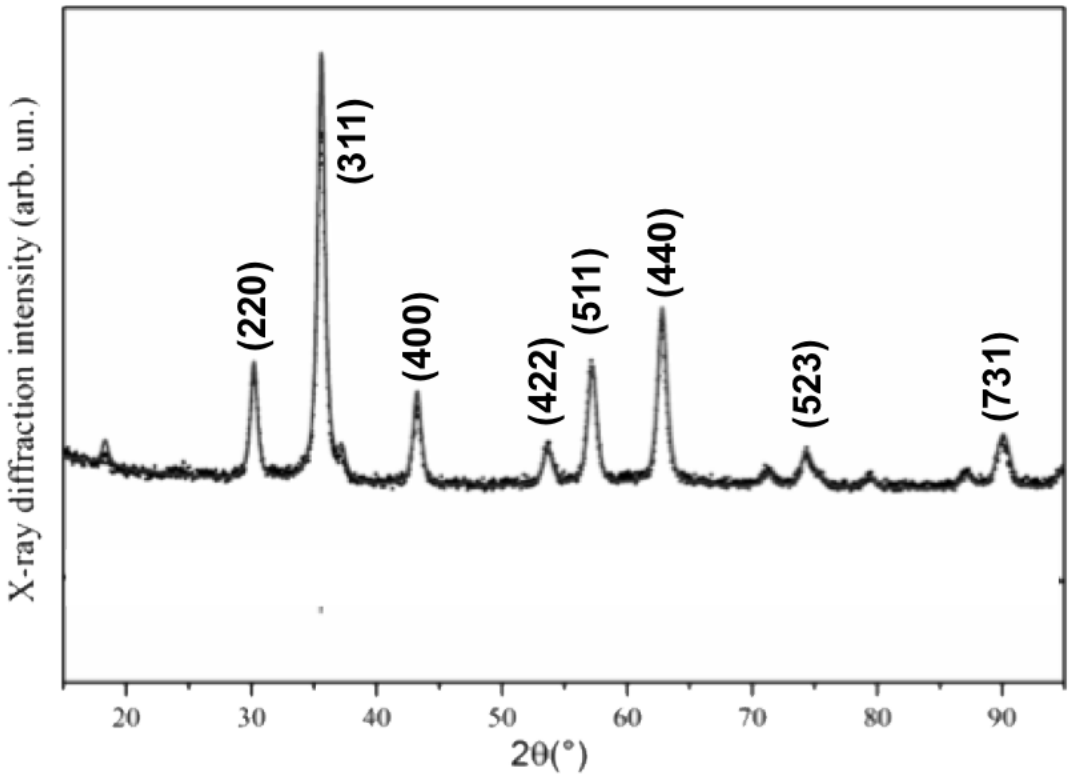

Figure 15 XRD diffractogram of Ru2 sample

TEM micrographs and particle size distribution reveal the morphology of these catalytic systems (see Figure 16). In particular, sample Ru2 presents good particle dispersion characterized by close size distribution of magnetite particles with an average diameter of 10.1 nm and a standard deviation of 0.1 nm. It was not possible to detect ruthenium nanoparticles due to their small size and their position inside the magnetite crystal.

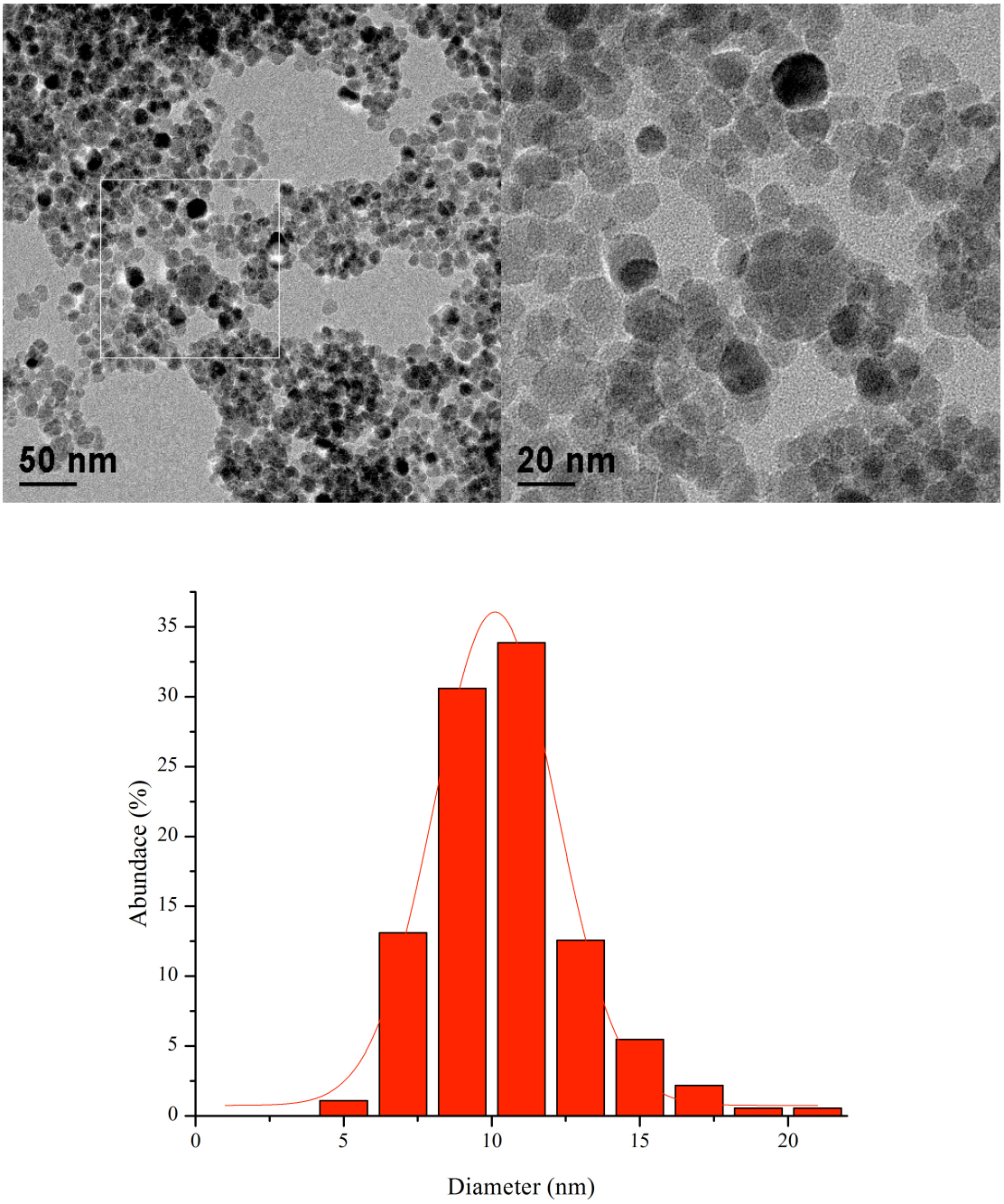

Figure 16 TEM micrographs and particle size distribution of sample Ru2, 5 %wt RuOx-Fe_3O_4

The surface composition of samples Ru1 and Ru2 was investigated with the X-Ray Photoelectron Spectroscopy. As it is possible to see in Figure 17, the ruthenium of samples Ru1 and Ru2 show the binding energy of component Ru $3d_{5/2}$ at low binding energy 282.4 eV and component Ru $3d_{3/2}$ at the binding energy of 286.4 eV. The Ru 3d components with the presence of the signals of C 1s is ascribable to ruthenium at high oxidation state, possibly as Ru(III) or Ru(IV) as reported also in literature.[13b, c] However, an unequivocal determination of the ruthenium oxidation state is not possible

because the binding energy of ruthenium species is strongly influenced by the presence of iron oxides. In fact, as reported in literature, the strong interaction between Fe_3O_4 and ruthenium can result in a positive shift of the ruthenium species binding energy.[10] Furthermore, iron shows two components at binding energy of 710.6 eV and 713,6 eV both ascribable to Fe $2p_{3/2}$.

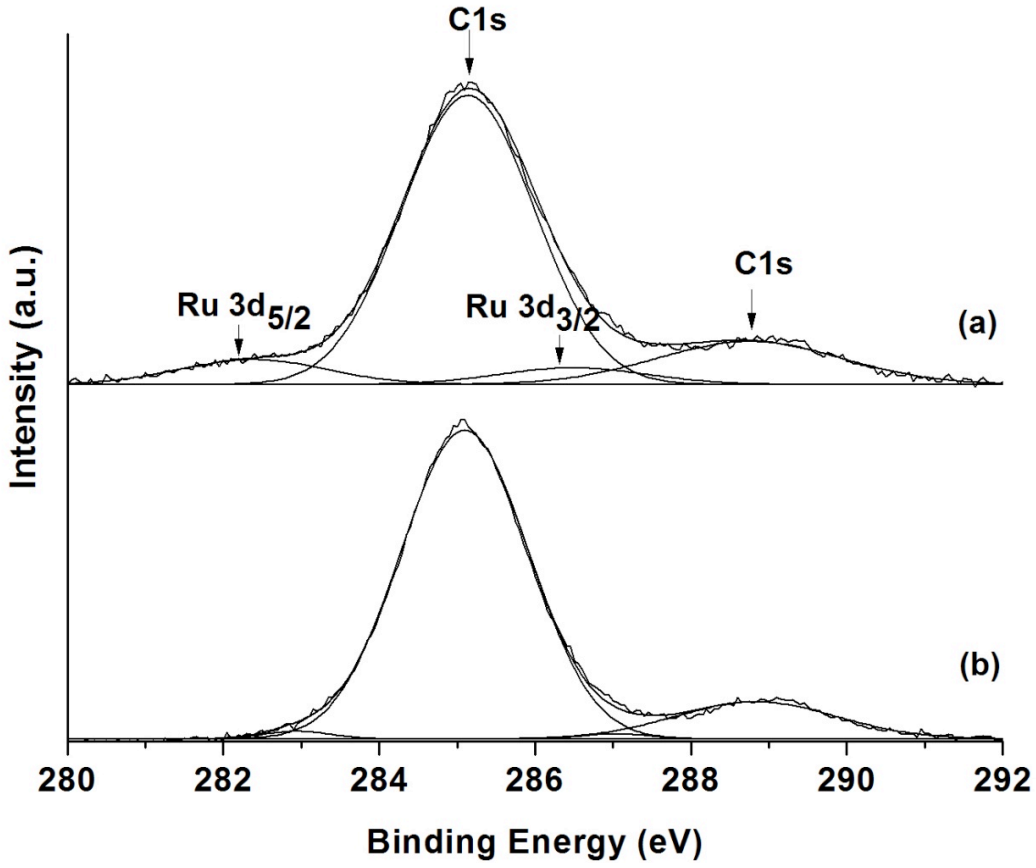

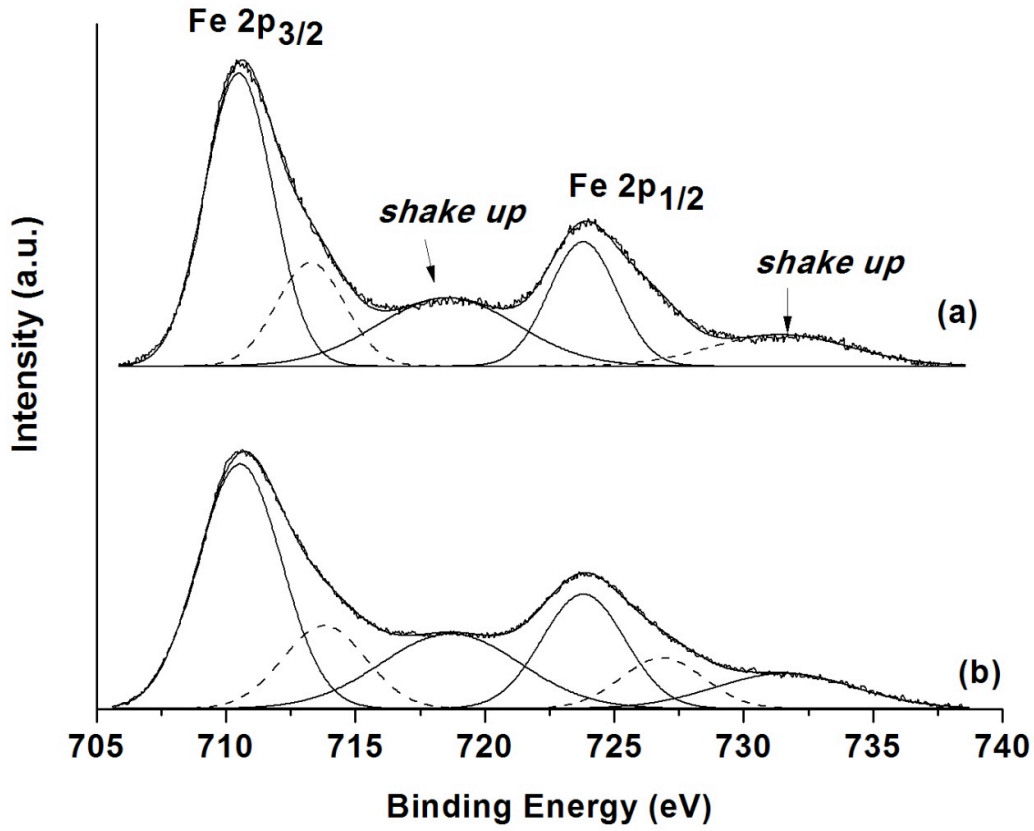

Figure 17 XPS analysis of :(a) sample Ru2, 5 %wt RuOx-Fe_3O_4 and (b) sample Ru1, 2%wt RuOx-Fe_3O_4

The temperature programmed reduction (TPR) profile for sample Ru2 is displayed in Figure 18 and can be separated into two zones: below and above 300°C. The big broad band above 300°C, which is the last event, can be attributed to the bulk reduction of the magnetite to FeO and Fe [12b, 20], whereas in the former zone below 300°C, it is possible to observe the peak ascribable to the reduction of RuOx species.

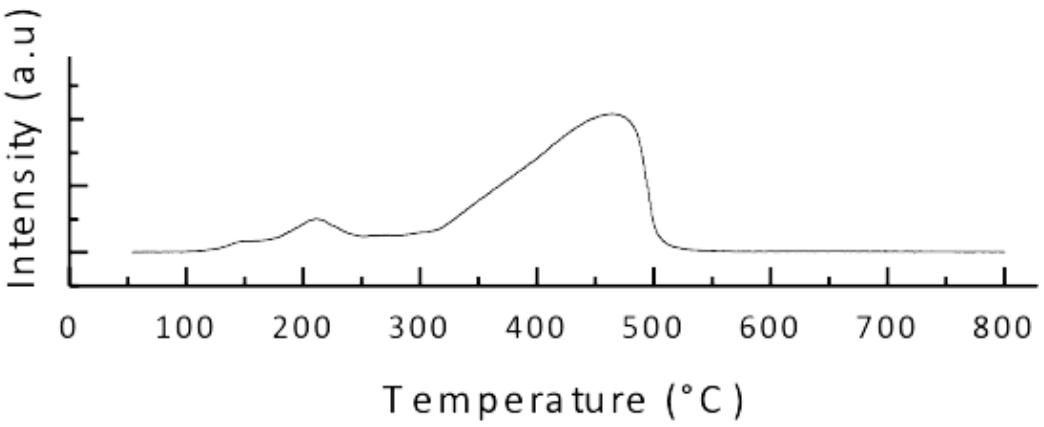

Figure 18 TPR analysis of sample Ru2

In the magnetization curve of sample Ru2 it is no possible to recognize the presence of magnetic hysteresis confirming the superparamagnetic behaviour of this sample (Figure 19). The magnetic saturation values measured for this sample are about 40 emu /g lower than the ones observed for magnetite samples. The introduction of ruthenium species inside the magnetite structure causes the reduction of the sample magnetic properties. However, this negative effect does not compromise the recoverability of the sample; in fact, Ru2 displays sufficient magnetic behaviour, which guarantees its separation from liquid media.

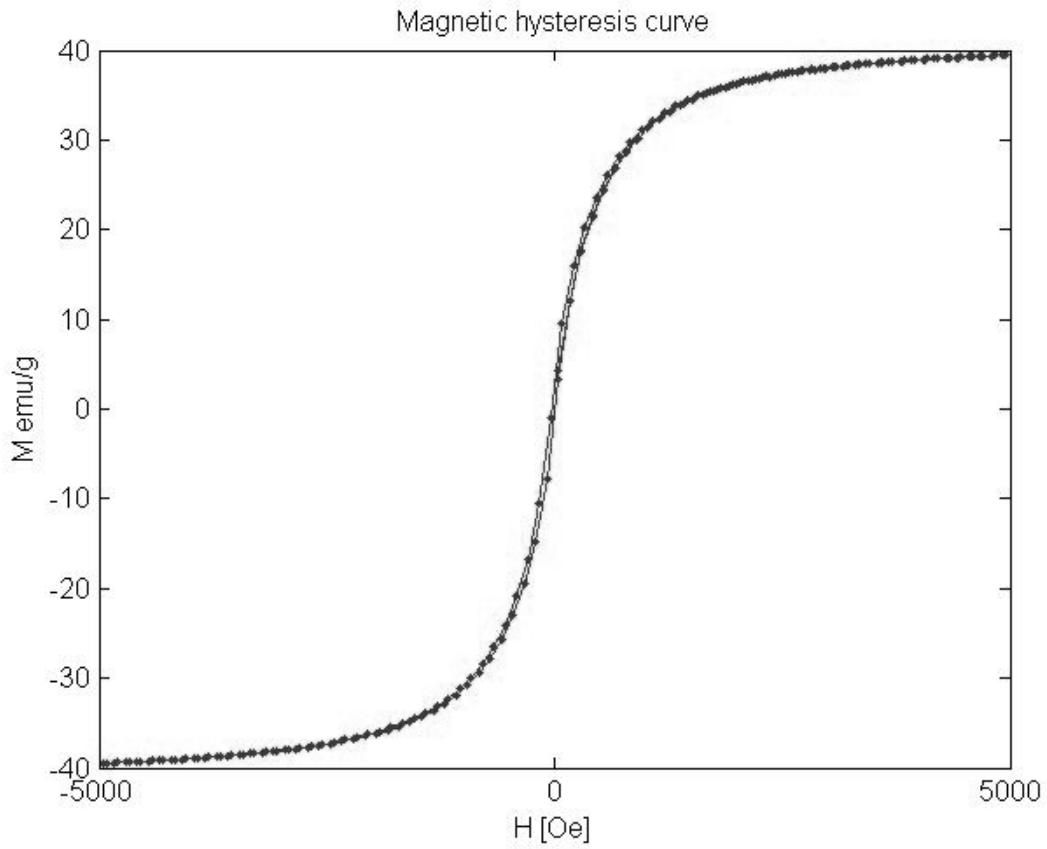

Figure 19 Magnetization curve of sample Ru2

5.3 Synthesis of magnetic platinum nanocatalysts

Platinum nanoparticles are a very interesting material used in diverse technological and industrial fields. In fact platinum nanoparticles are studied as catalysts in many industrial and organic reactions[24] and they are employed for the production of sensors[25], or biocompatible materials[26]. In catalysis, in particular, platinum nanoparticles are very promising but their extensive application is strongly limited not only by their high cost but also for the difficult separation and recycle steps.

In this context, the introduction of magnetic nanosupports could be again a strategic choice able to guarantee an efficient and easy separation.

The platinum magnetic nanoparticles $Pt@Fe_3O_4$ are prepared following a procedure similar to that adopted for the preparation of ruthenium samples. In fact the $Pt@Fe_3O_4$ nanoparticles were prepared through the contemporaneous decomposition of iron acetate ($Fe(OAc)_2$), and platinum acetate ($[Pt_4(OAc)_8] \cdot 2HOAc$) under MW-irradiation. This approach was investigated by adopting two different heating sources, the

monomodal microwave CEM discovery S Class and the multimode microwave MARS 6, and the results are summarized in table 4.

Table 4 Characteristics of platinum nanoparticles trapped inside magnetite nanocrystal

Samples	AAS (Pt wt%)	BET (m^2/g)	Core diameter (nm)	σDm (nm)	Pt diameter (nm)
Pt1[a]	6.7	101.9	9.1	0.3	2.2
Pt2[b]	4.8	N.D	10	0.2	2.1

[a] Reaction conditions: 1g of $Fe(OAc)_2$, 0.45g [Pt4(OAc)8]·2HOAc, 44 mL EtOH at 96 wt%, monomode microwave heating: 120 °C, 15 min, 250 W

[b] Reaction conditions: 1g $Fe(OAc)_2$ 0.45g [Pt4(OAc)8]·2HOAc, 44 mL EtOH at 96 wt%,multimode microwave heating: 120 °C, 15 min, 1800W.

As can be observed in table 4, the particles obtained using the monomode microwave irradiation contain a higher amount of platinum than the ones obtained using the multimode microwave. This difference can be explained by the ability of the monomode microwave to heat homogeneously the reactor thus permitting an efficient energy transfer between the reactor and the reagents, whereas the multimode microwave supplies microwave radiations randomly directed resulting in an inefficient and discontinuous energy transfer. The differences between monomode and multimode microwave reactors were also discussed for the synthesis of magnetite reported in Chapter 4.2.

Furthermore, Pt1 has a higher surface area than the ones measured for magnetite. Thus, the introduction of platinum species inside the magnetite structure results in an increase of sample surface area, as previously observed also for palladium and ruthenium samples (see Chapter 5.1.2 and 5.2).

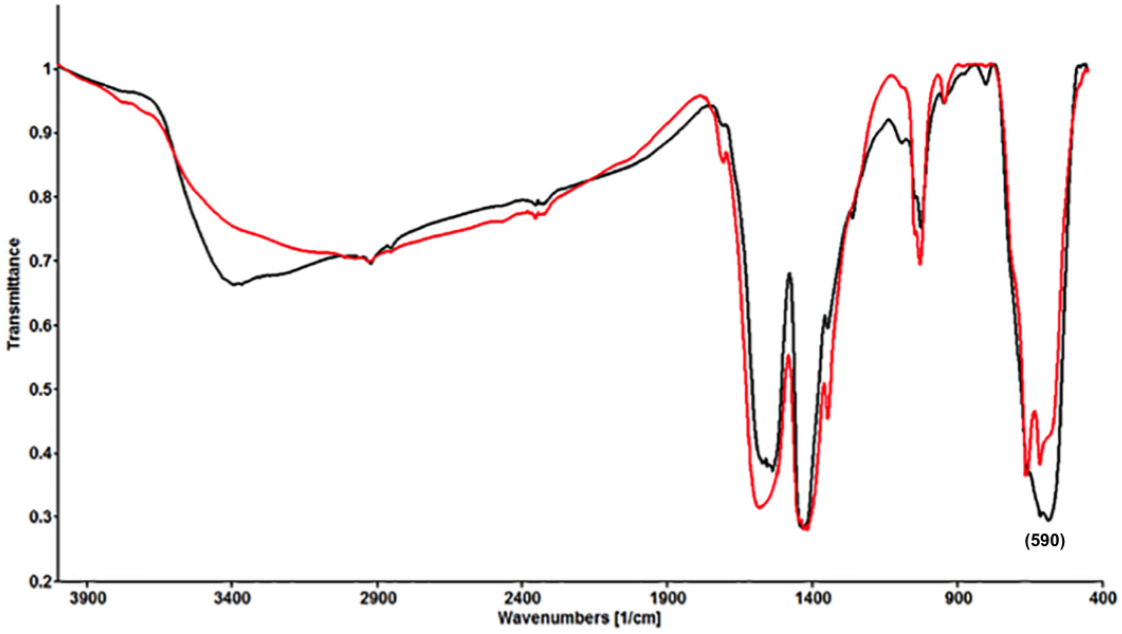

Figure 20 FTIR spectra of sample Pt1 in black and Pt2 in red

The FT-IR spectra of samples Pt1 and Pt2 show the adsorption band at 590 1/cm typical of the Fe-O bonds in tetrahedral Fe_3O_4 sites (see Figure 20). The two narrow peaks between 1400 1/cm and 1600 1/cm are due to acetate traces, introduced with the iron precursor. Finally, the broad band at 3000-3500 1/cm is ascribable to water and ethanol molecules trapped in magnetite particles.

The Raman spectra of both Pt1 and Pt2 samples report the typical magnetite strong band at 669 1/cm confirming the identification of the iron oxide phase.

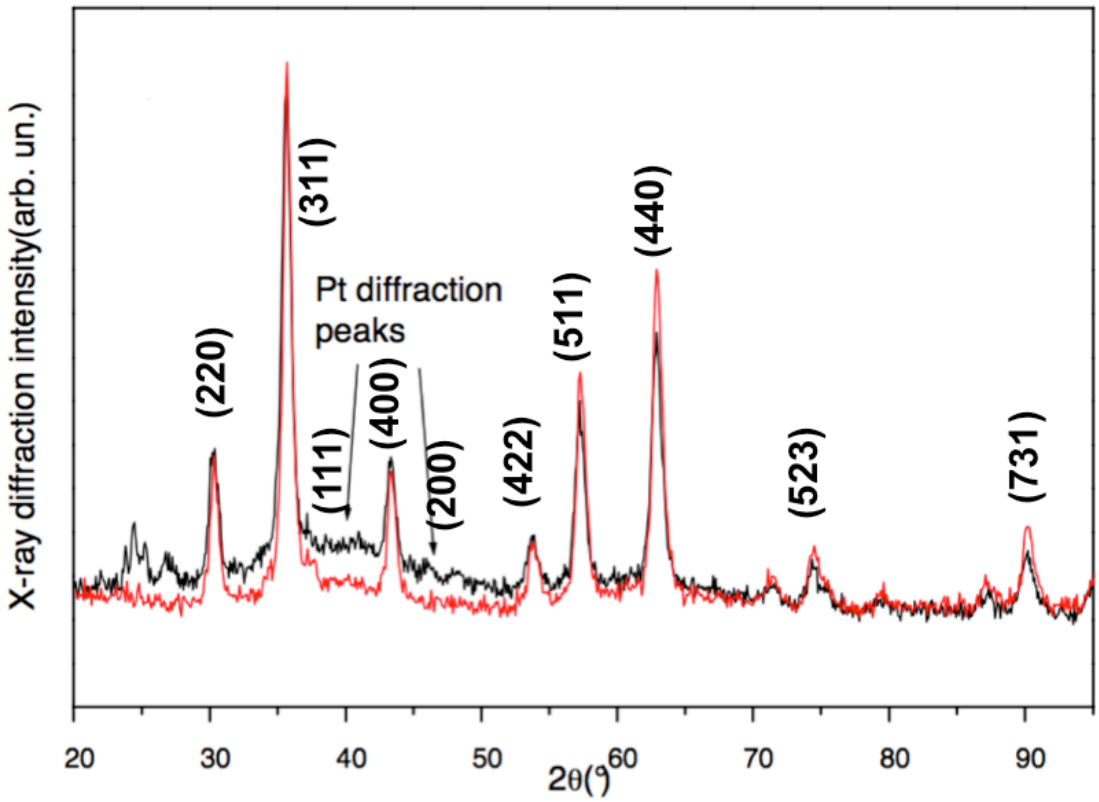

Figure 21 XRD diffractograms of: Pt1 in red and Pt2 in black

The XRD patterns of samples Pt1 and Pt2 are reported in Figure 21. Both the Pt1 and Pt2 XRD diffractograms present reflection peaks, which can be indexed as Miller indexes of the cubic Fe_3O_4 magnetite like structure (220), (311), (222), (400), (422), (511), (400), (620), (530), (622) and little bumps ascribable to metallic platinum. The platinum bumps can be indexed according to literature as Miller indexes (111) and (200). [27]

The calculated cell parameters for Pt1 and Pt2 samples are respectively 8.362(1) and 8.357(1) and quite similar to the ones reported for magnetite. Finally, the crystalline structure of samples Pt1 and Pt2 present a microstrain of respectively 0.0017 and 0.0019 underlining the presence of structural defects in magnetite nanocrystal.

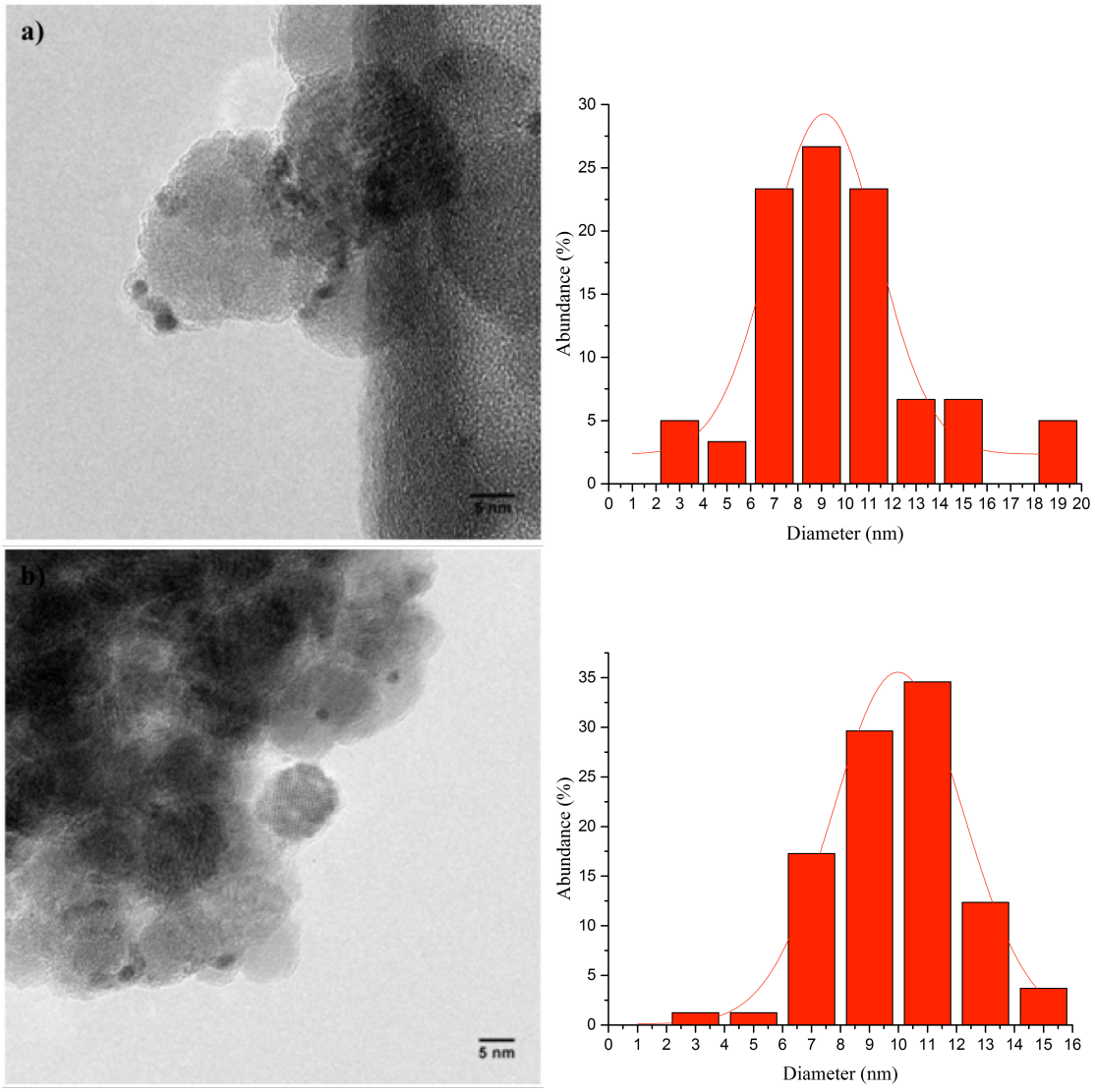

Figure 22 TEM micrographs and particle size distributions of samples a) Pt1, Pt@Fe_3O_4 obtained using monomode microwave and b) Pt2, Pt@Fe_3O_4 obtained using multimode microwave

The Pt1 and Pt2 samples are characterized by narrow magnetite size distribution with an average diameter of about 9.1 nm and 10 nm respectively (see Figure 22). Furthermore, in both samples palladium nanoparticles are well-dispersed and extremely small, about 2 nm in diameter. No marked effects of the kind of heating source adopted on particle size distribution was observed in contrast with what was appreciated in magnetite preparation (see Chapter 4.2).

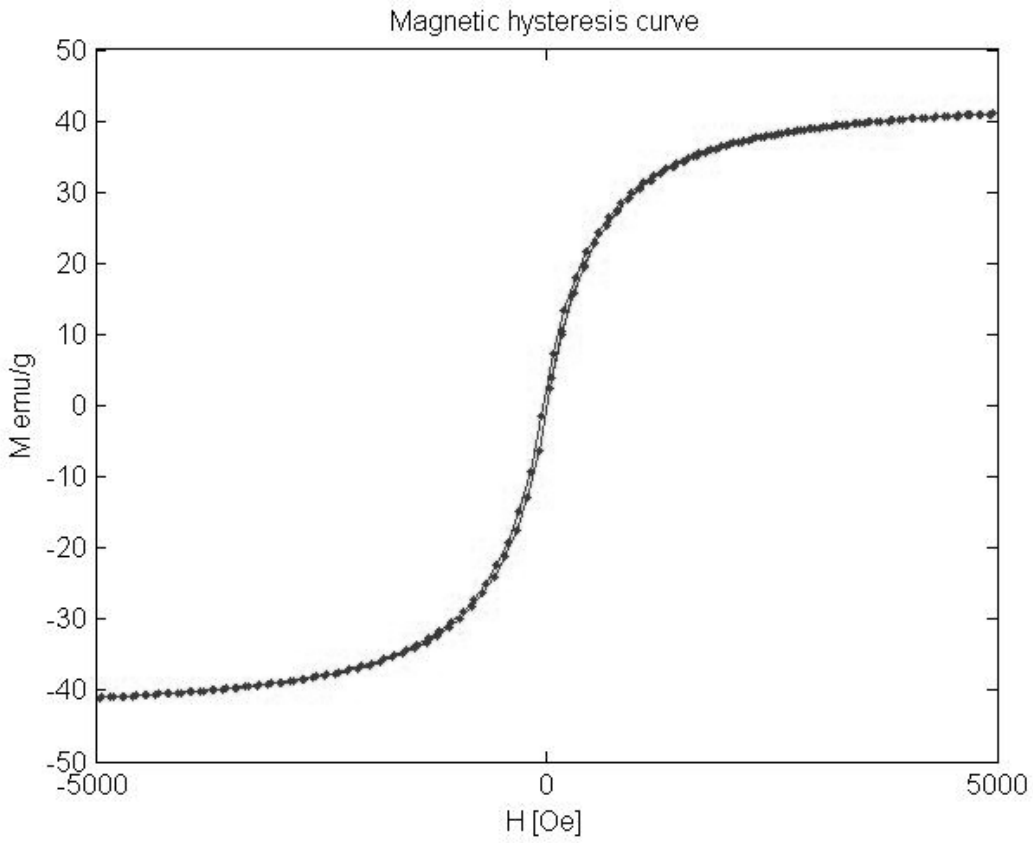

Figure 23 Magnetization curve of sample Pt1, 6,7Pt@Fe_3O_4

The Pt1 sample shows a superparamagnetic behaviour as confirmed by the absence of magnetic hysteresis (Figure 23). The magnetic saturation values measured for this sample are about 35 emu/g lower than those observed for magnetite and ruthenium samples. The introduction of platinum species inside the magnetite structure causes the reduction of the magnetic properties as was observed for the ruthenium samples in Chapter 5.2. However, this negative effect does not compromise the recoverability of these systems; in fact Pt1 displays sufficient magnetic behaviour which guarantees its separation from the liquid media.

5.4 Synthesis of magnetic copper oxides nanocatalysts

Particular transition metals gain huge success in catalysis due to their low price and good availability. Nowadays an ever-increasing number of industrial and organic reactions are studied using transition metals such as copper, iron, vanadium, etc. Among

them copper and copper oxides find interesting application in oxidation and coupling reactions.

For this reason, in this PhD work a new magnetic copper oxide catalyst was developed. The copper oxide magnetic nanoparticles, $Cu_2O@Fe_3O_4$, are prepared following the hydrothermal procedure similar to the ones used to prepare Pd, Ru and Pt based systems described in the previous chapters. In particular, the $Cu_2O@Fe_3O_4$ nanoparticles are prepared adopting the contemporaneous decomposition of iron acetate ($Fe(OAc)_2$) and a copper precursor. For the preparation of magnetic copper nanostructures two kinds of copper precursors were studied, the commercial copper acetate ($Cu(OAc)_2$) and the copper carbamato complex ($Cu_2(O_2CNEt_2)_4 \cdot 2NHEt_2$) which was prepared in collaboration with the Prof. Pampaloni laboratory, following the procedure reported by Agostinelli et al.[28] In a typical preparation $Fe(OAc)_2$ and the chosen copper precursor are dissolved in aqueous ethanol, then the solution is MW-irradiated at 120°C for 15 minutes and at the end of this treatment the particles are magnetically collected, washed and dried. In order to better understand the role of the support on nanoparticle growth and on the final catalytic performances, copper oxide nanoparticles were supported also on γ-alumina. In more detail, 1g of γ-Al_2O_3 and the right amount of copper precursor were dispersed in 44 ml of aqueous ethanol and MW-treated at 120°C for 15 minutes.

The results are summarized in table 5.

Table 5 Characteristics of copper oxide nanoparticles trapped inside magnetite nanocrystal

Samples	Support	Theoretic Cu load (%wt)	BET (m^2/g)	Core diameter (nm)	σDm (nm)
Cu1[a]	Fe_3O_4	5	60	6.1	0.1
Cu2[b]	Fe_3O_4	5	56.8	5.5	0.2
Cu3[a]	γ-Al_2O_3	5	154.6	51.5	1.8
Cu4[b]	γ-Al_2O_3	5	152.1	17.1	0.5

[a] Obtained using a synthetic copper precursor ($Cu_2(O_2CNEt_2)_4 \cdot 2NHEt_2$) provided from the Prof. Pampaloni laboratory

[b] Obtained using a commercial copper precursor $Cu(OAc)_2$

As can be observed in Table 5 and in the TEM images displayed in Figure 24, samples Cu1 and Cu2 present a similar magnetite particle distribution characterized by an average diameter of 6.1 nm and 5.5 nm respectively. Furthermore from TEM images of samples Cu1 and Cu2 it is no possible to appreciate the copper oxide size distribution.

On the other hand sample Cu3 supported on alumina is characterized by alumina acicular particles with an average length of 51.1 nm and small spherical and cubic copper oxide particles with an average diameter of 5.2 nm (see Figure 25a). Sample Cu2 shows spherical alumina particle with an average diameter of 17.1 nm and small copper oxide particle with a diameter of 4.1 nm. The different final alumina shape can be due to the interaction with the two diverse copper precursors used during the sample preparations.

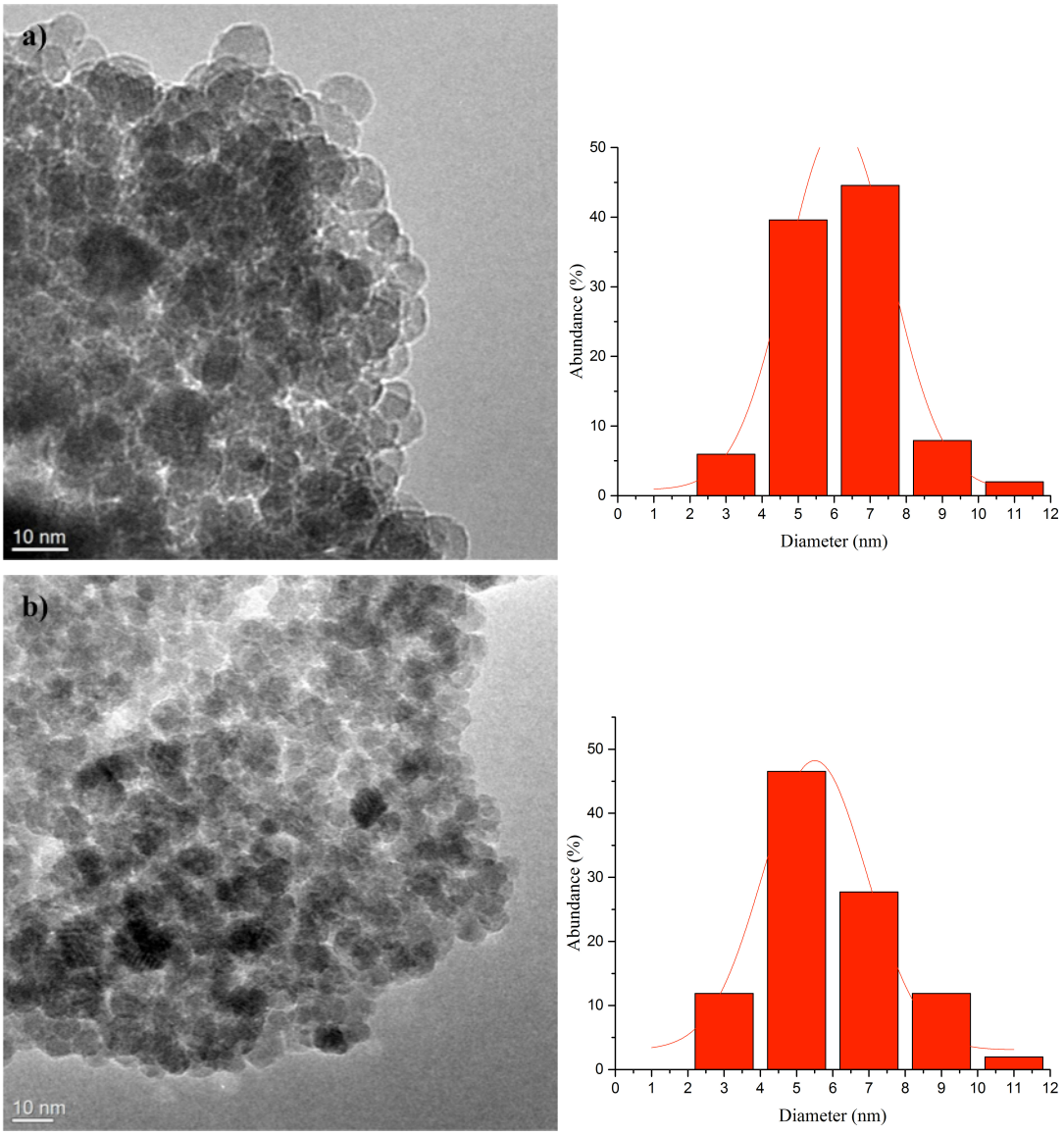

Figure 24 TEM micrographs and particle size distributions of samples a) Cu1, $Cu_2O@Fe_3O_4$ obtained using the copper carbamato complex as copper precursor and b) Cu2, $Cu_2O@Fe_3O_4$ obtained using the copper acetate as copper precursor.

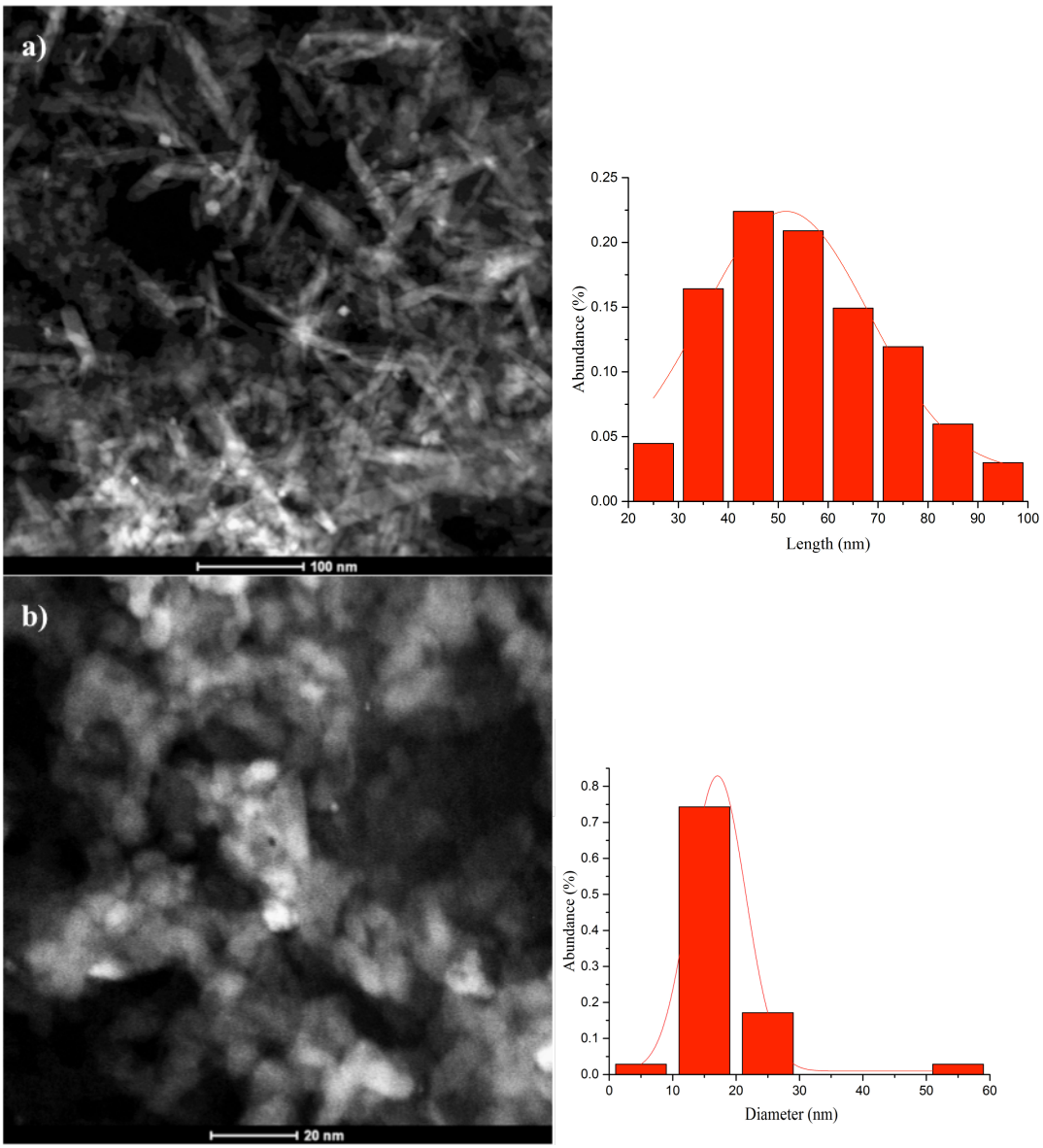

Figure 25 SEM immages and size distribution of samples a) Cu3, $Cu_2O@Al_2O_3$ obtained using the copper carbamato complex as copper precursor and b) Cu4, $Cu_2O@Al_2O_3$ obtained using the copper acetate as copper precursor.

The FT-IR spectra of samples Cu1 and Cu2 (see Figure 26) show a large peak around 590 1/cm which can be associated with the Fe-O vibrations of tetrahedral Fe_3O_4. Moreover both samples present a big bump near the mean magnetite peak (around 592 1/cm) that can be related to the Cu-O vibrations of Cu_2O and the peaks at 1121 1/cm and 1360 1/cm ascribable to the Cu-OH vibrations of $Cu(OH)_2$ species.[29]

As was observed in the palladium, ruthenium and platinum samples, the two narrow peaks between 1400 cm^{-1} and 1600 cm^{-1} can be related to acetate traces, introduced with the iron precursor, and the broad band at 3000-3500 cm^{-1} to water and ethanol molecules trapped in the magnetite particles.

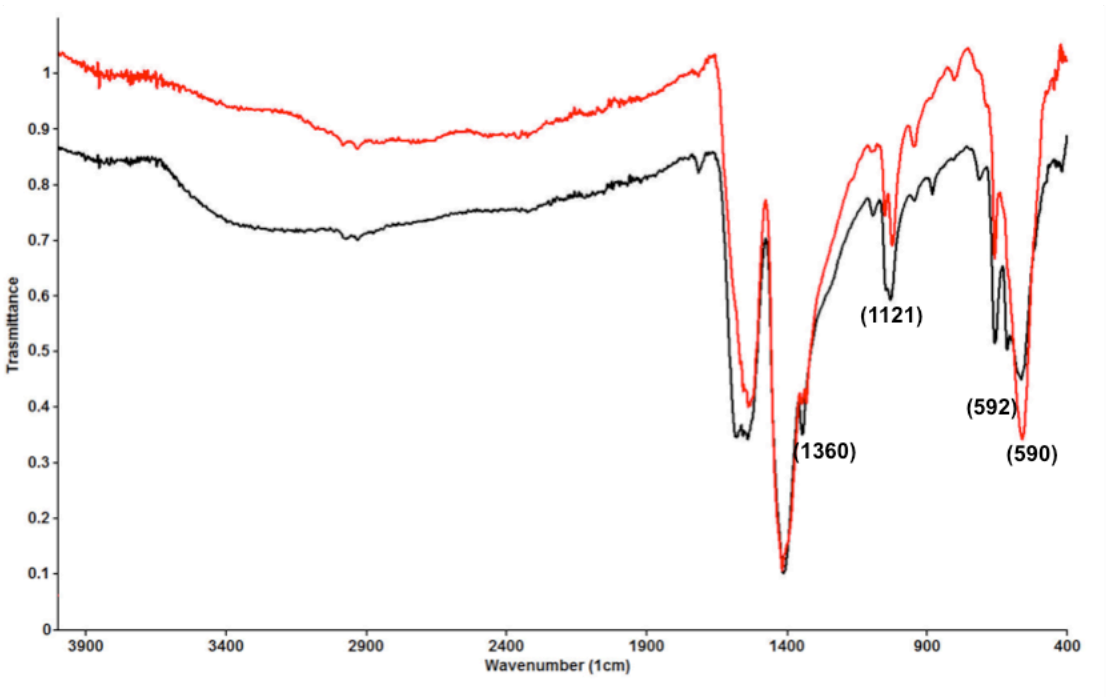

Figure 26 FTIR spectra of samples: Cu1 in black and Cu2 in red

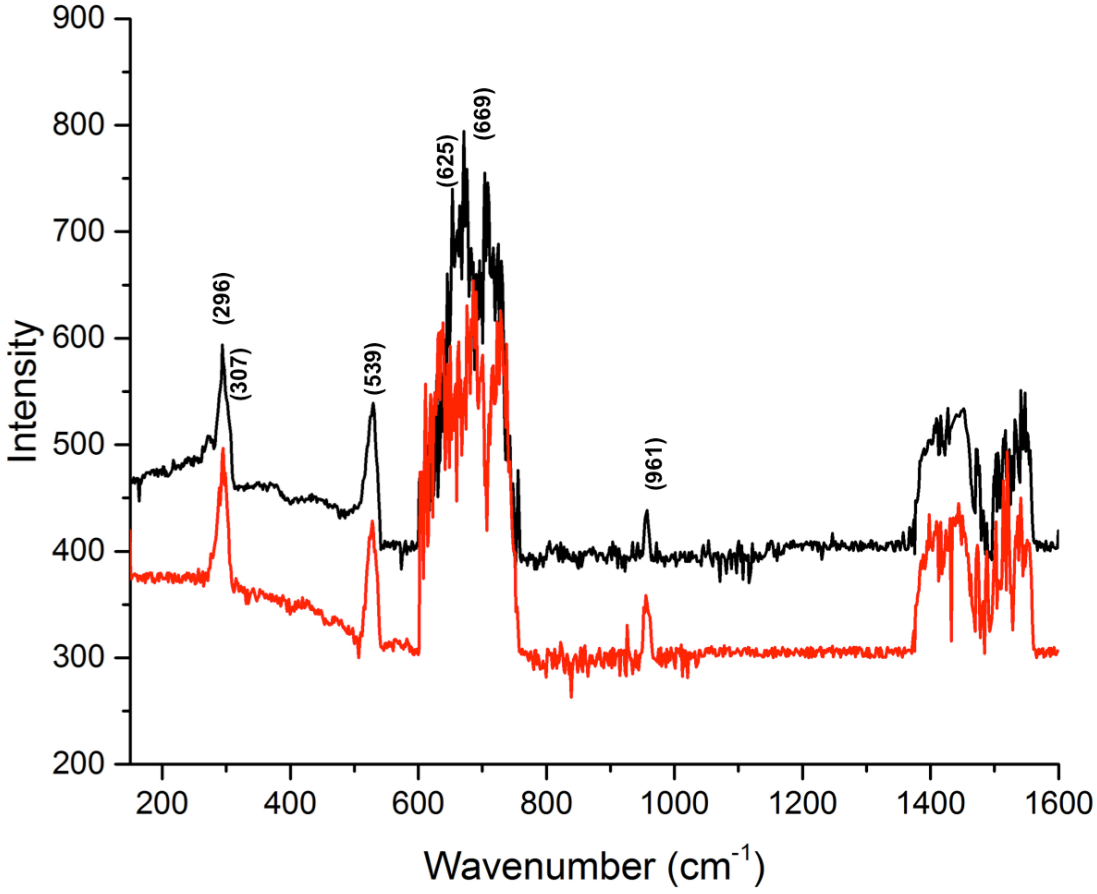

Figure 27 Raman spectra of samples: Cu1 in bleck and Cu2 in red

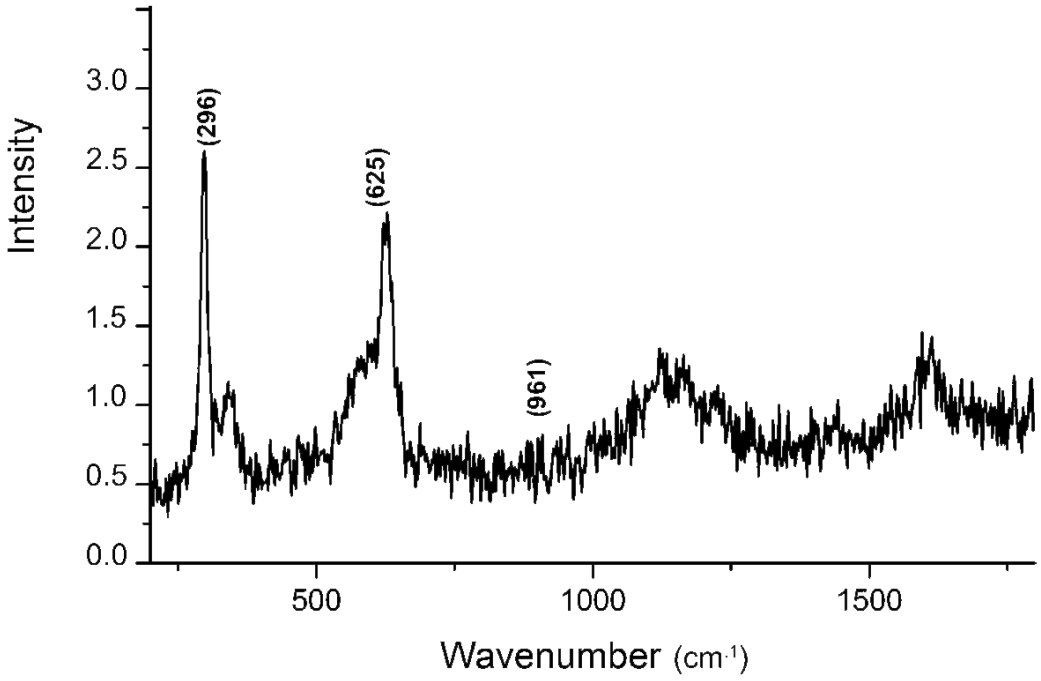

Figure 28 Raman spectrum of sample Cu3, $Cu_2O@Al_2O_3$

In Figure 27 the Raman spectra of samples Cu1 (red line) and Cu2 (black line), show peaks at 296 1/cm 625 1/cm and 961/cm ascribable to copper monoxide[30]. Moreover, an overlapping of the peaks at 625 1/cm, which correspond to the Cu_2O species, and a big peak at 699 1/cm typical of magnetite was observed, due to the broadness of the observed peaks.

The Raman spectrum of sample Cu3 shows the peaks at 296 1/cm 625 1/cm and 961/cm ascribable to copper monoxide but it is not possible to detect any signal ascribable to γ-alumina (see Figure 28). As is well known in literature, γ-Al_2O_3 does not show any Raman signal from 100 1/cm to 1100 1/cm.[31]

The structure of the magnetite and alumina support used in the preparation of samples Cu1, Cu2, Cu3 and Cu4 were further investigated through XRD analysis (see Figures 29 and 30).

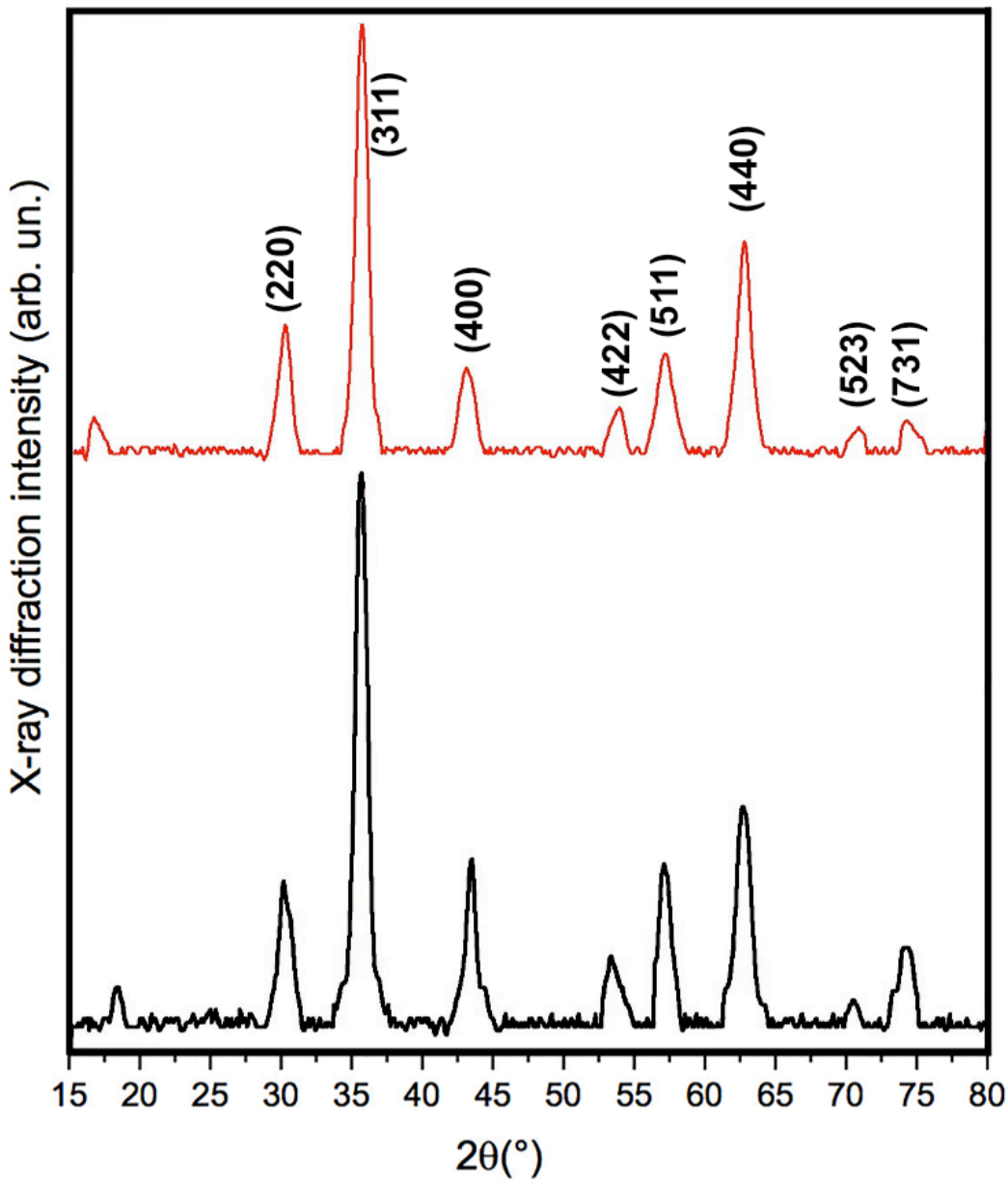

Figure 29 XRD diffractograms of Cu1 (red line) and Cu2 (black line)

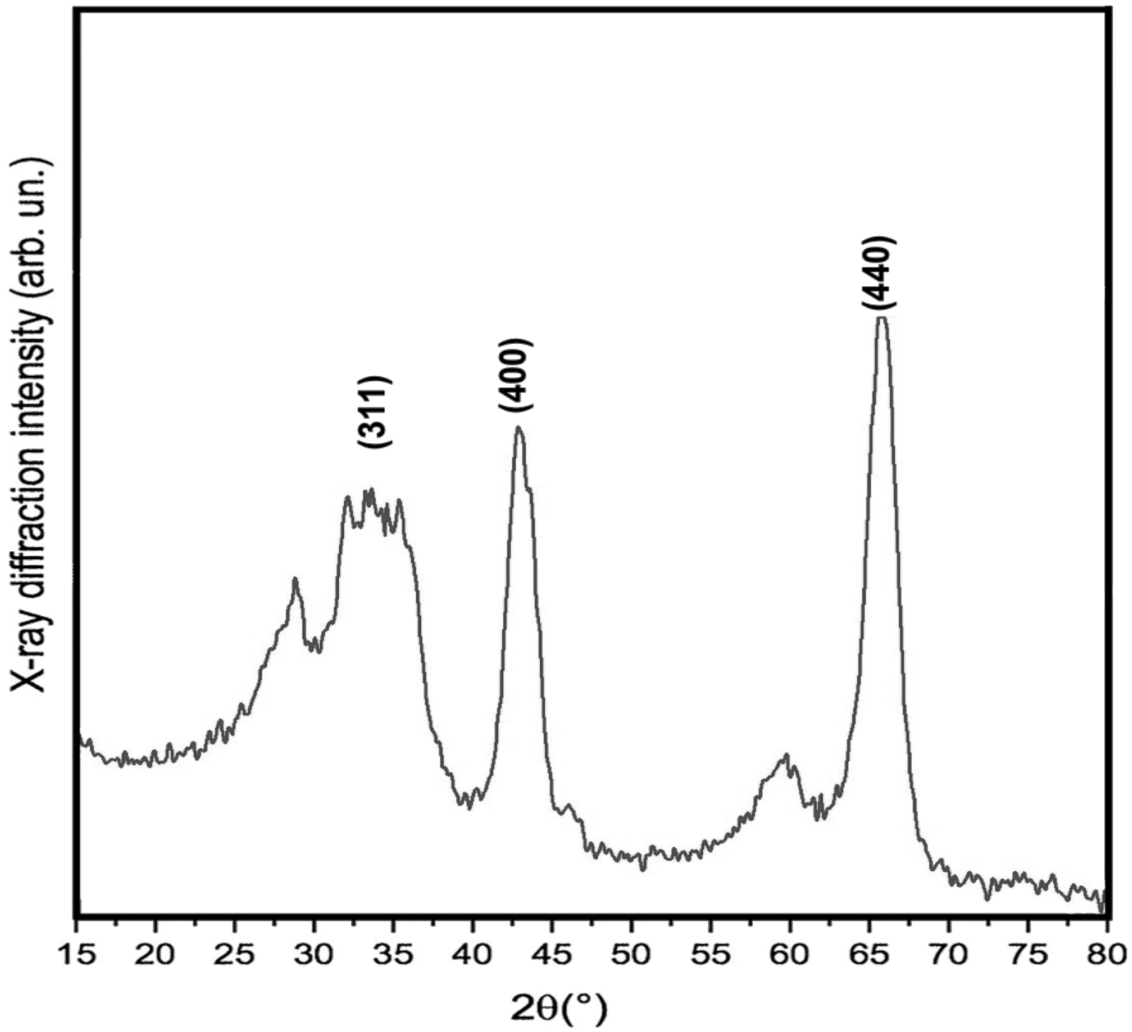

Figure 30 XRD patterns of samples Cu3, $CuO@Al_2O_3$

The XRD diffractograms of samples Cu1 and Cu2 ($Cu_2O@Fe_3O_4$) present the reflection peaks, which can be indexed as Miller indexes of the cubic Fe_3O_4 magnetite like structure (220), (311), (222), (400), (422), (511), (400), (620), (530), (622) (see Figure 28), whereas the patterns displayed in the XRD diffractograms of samples Cu3 can be indexed as Miller indexes of γ-Al_2O_3 alumina structure (311), (400), (440) (see Figure 30)[32].

In all samples, it was not possible to observe the copper oxide reflection peaks due to the small size of the copper oxide nanoparticles.

5.5 References

[1] F.-h. Lin, W. Chen, Y.-H. Liao, R.-a. Doong and Y. Li, *Nano Research* **2011**, *4*, 1223-1232.

[2] A. Basińska, A. Nowacki and F. Domka, *Reaction Kinetics and Catalysis Letters* **1999**, *66*, 3-11.

[3] a) V. Polshettiwar and R. S. Varma, *Chemistry-A European Journal* **2009**, *15*, 1582-1586; b) B. Baruwati, V. Polshettiwar and R. S. Varma, *Tetrahedron Letters* **2009**, *50*, 1215-1218; c) A. Venugopal, J. Aluha, D. Mogano and M. S. Scurrell, *Applied Catalysis A: General* **2003**, *245*, 149-158; d) K. Yamaguchi and N. Mizuno, *Angewandte Chemie International Edition* **2002**, *41*, 4538-4542; e) H. A. Hui-Feng Wang, Rhys Dowler, Martin Sterrer, Hans-Joachim Freund, *Journal of Catalysis* **2012**, *286*, 1-5; f) D. J. R. n. Rafael Cano, Miguel Yus, *Tetrahedron* **2011**, *67*, 5432-5436; g) H. Hildebrand, K. Mackenzie and F.-D. Kopinke, *Applied Catalysis B: Environmental* **2009**, *91*, 389-396.

[4] a) J. K. Edwards, B. E. Solsona, P. Landon, A. F. Carley, A. Herzing, C. J. Kiely and G. J. Hutchings, *Journal of Catalysis* **2005**, *236*, 69-79; b) K. Mori, S. Kanai, T. Hara, T. Mizugaki, K. Ebitani, K. Jitsukawa and K. Kaneda, *Chemistry of Materials* **2007**, *19*, 1249-1256.

[5] J. L. J. R. G. Y. P. W. H. L. X. S. L. C. J.-T. M. R. Li, *Materials Science and Engineering B* **2010**, *172*,
207-212.

[6] a) R. Cano, D. J. Ramón and M. Yus, *The Journal of Organic Chemistry* **2011**, *76*, 5547-5557; b) M. Kotani, T. Koike, K. Yamaguchi and N. Mizuno, *Green Chemistry* **2006**, *8*, 735-741.

[7] a) J.-B. K. Ji-Young Jung, Abu Taher, and Myung-Jong Jin, *Bull. Korean Chem. Soc.* **2009**, *30*, 3082-3084; b) Q. Z. Mingliang Ma, Dezhong Yin, Jinbo Dou, Hepeng Zhang, Hailong Xu, *Catalysis Communications* **2012**, *17*, 168-172; c) P. X. Zhifei Wang, Bin Shen, Nongyue He, *Colloids and Surfaces A: Physicochem. Eng. Aspects* **2006**, *276*, 116-121; d) S. C. P. Zhu Yinghuai, A. Emi, Su Zhenshun, Monalisa, Richard A. Kemp, *Adv. Synth. Catal.* **2007**, *349*, 1917-1922.

[8] a) M. Y. Hiroaki Nitani, Takahiro Ono, Takashi Nakagawa, Satoshi Seino, Kenji Okitsu, Yoshiteru Mizukoshi, Shuichi Emura, Takao A. Yamamoto, *Journal of Nanoparticle Research* **2006**, *8*, 951-958; b) M.-J. K. Yunwoong Kim, *Bull. Korean Chem. Soc.* **2010**, *31*, 1368-1370; c) Y. Mizukoshi, K. Sato, T. J. Konno, N. Masahashi and S. Tanabe, *Chemistry Letters* **2008**, *37*, 922-923.

[9] a) E. K. B. Keith A. Porter in *Synthesis and use of intermetallic iron palladium nanoparticle compositions*
, *Vol.* **2011**; b) Y. Jang, J. Chung, S. Kim, S. W. Jun, B. H. Kim, D. W. Lee, B. M. Kim and T. Hyeon, *Physical Chemistry Chemical Physics* **2011**, *13*, 2512-2516; c) K. A. Porter and E. K. Barnhardt in *Synthesis and Use of Intermetallic Iron Palladium Nanoparticle Compositions*, *Vol.* Google Patents, **2011**.

[10] Y. Wang, Y. Yang, Y. Li, J. Lai and K. Sun, *Catalysis Communications* **2012**, *19*, 110-114.

[11] a) B. S. Jun Liu, Jiye Hu, Yan Pei, Hexing Li, Minghua Qiao, *Journal of Catalysis* **2010**, *274*, 287-295; b) J. N. Fengwei Zhang, Haibo Wang, Honglei Yang, Jun Jin, Na Liu, Yubin Zhang, Rong Li , Jiantai Ma, *Materials Research Bulletin* **2012**, *47*, 504-507.

[12] a) A. Basińska and K. Pawełczyk, *Reaction Kinetics and Catalysis Letters* **2006**, *89*, 325-331; b) A. Basińska, W. K. Jóźwiak, J. Góralski and F. Domka, *Applied Catalysis A: General* **2000**, *190*, 107-115; c) A. Basińska and F. Domka, *Reaction Kinetics and Catalysis Letters* **1999**, *67*, 111-116; d) A. Basińska, R. Klimkiewicz and F. Domka, *Applied Catalysis A: General* **2001**, *207*, 287-294; e) A. Basińska, *Reaction Kinetics and Catalysis Letters* **1997**, *60*, 49-56.
[13] a) A. Baykal, E. Karaoglu, H. Sözeri, E. Uysal and M. Toprak, *Journal of Superconductivity and Novel Magnetism* **2013**, *26*, 165-171; b) V. V. Costa, M. J. Jacinto, L. M. Rossi, R. Landers and E. V. Gusevskaya, *Journal of Catalysis* **2011**, *282*, 209-214; c) M. J. Jacinto, O. H. C. F. Santos, R. F. Jardim, R. Landers and L. M. Rossi, *Applied Catalysis A: General* **2009**, *360*, 177-182.
[14] a) F. A. Harraz, S. E. El-Hout, H. M. Killa and I. A. Ibrahim, *Journal of Catalysis* **2012**, *286*, 184-192; b) C. P. Ruas, D. K. Fischer and M. A. Gelesky, *Journal of Nanotechnology* **2013**, *2013*, 6; c) Y. Wang, J. Yao, H. Li, D. Su and M. Antonietti, *Journal of the American Chemical Society* **2011**, *133*, 2362-2365; d) H. K. Afef Mehri, Stéphane Daniele, Violaine Mendez, Abdelhamid Ghorbel, Gilles Berhault, *Journal of Colloid and Interface Science* **2012**, *369*, 309-316.
[15] a) M. Mifsud, K. V. Parkhomenko, I. W. C. E. Arends and R. A. Sheldon, *Tetrahedron* **2010**, *66*, 1040-1044; b) J. Yang, C. Tian, L. Wang and H. Fu, *Journal of Materials Chemistry* **2011**, *21*, 3384-3390.
[16] a) A. Balanta, C. Godard and C. Claver, *Chemical Society Reviews* **2011**, *40*, 4973-4985; b) Yin and J. Liebscher, *Chemical Reviews* **2007**, *107*, 133-173; c) D. Astruc, *Inorganic Chemistry* **2007**, *46*, 1884-1894; d) A. R. Siamaki, A. E. R. S. Khder, V. Abdelsayed, M. S. El-Shall and B. F. Gupton, *Journal of Catalysis* **2011**, *279*, 1-11.
[17] D. Wang and D. Astruc, *Chemical Reviews* **2014**, *114*, 6949-6985.
[18] V. Polshettiwar, R. Luque, A. Fihri, H. Zhu, M. Bouhrara and J.-M. Basset, *Chemical reviews* **2011**, *111*, 3036-3075.
[19] J. Liu, B. Sun, J. Hu, Y. Pei, H. Li and M. Qiao, *Journal of Catalysis* **2010**, *274*, 287-295.
[20] a) A. Khan and P. G. Smirniotis, *Journal of Molecular Catalysis A: Chemical* **2008**, *280*, 43-51; b) J. Zieliński, I. Zglinicka, L. Znak and Z. Kaszkur, *Applied Catalysis A: General* **2010**, *381*, 191-196.
[21] C. A. Elisa Bertolucci; Anna Maria Raspolli Galletti, Mirko Marracci, Bernardo Tellini, Fabio Piccinelli, Ciro Visone in *Chemical and Magnetic Properties Characterization of Magnetic Nanoparticles*, *Vol.* IEEE, Pisa, **2015**.
[22] a) M. Pagliaro, S. Campestrini and R. Ciriminna, *Chemical Society Reviews* **2005**, *34*, 837-845; b) T. Mallat and A. Baiker, *Chemical Reviews* **2004**, *104*, 3037-3058; c) Y. Gorbanev, S. Kegnæs and A. Riisager, *Catalysis Letters* **2011**, *141*, 1752-1760.
[23] J. G. Kay, D. W. Green, K. Duca and G. L. Zimmerman, *Journal of Molecular Spectroscopy* **1989**, *138*, 49-61.
[24] a) J. R. Applegate, D. McNally, H. Pearlman and S. D. Bakrania, *Energy & Fuels* **2013**, *27*, 4014-4020; b) A. K. Shil and P. Das, *Green Chemistry* **2013**, *15*, 3421-3428; c) R. Narayanan and M. A. El-Sayed, *Nano Letters* **2004**, *4*, 1343-1348; d) C. Wang, H. Daimon, T. Onodera, T. Koda and S. Sun, *Angewandte Chemie International Edition* **2008**, *47*, 3588-3591.
[25] a) M. Yang, Y. Yang, Y. Liu, G. Shen and R. Yu, *Biosensors and Bioelectronics* **2006**, *21*, 1125-1131; b) S. Hrapovic, Y. Liu, K. B. Male and J. H. T. Luong, *Analytical Chemistry* **2004**, *76*, 1083-1088.

[26] a) P. Erika, L. Samuel, R. Hynd, U. Noriko, K. Katsumi, F. Yoshiya, S. Claude Le and L. Sandrine, *Nanotechnology* **2010**, *21*, 085103; b) P. V. Asharani, Y. lianwu, Z. Gong and S. Valiyaveettil, *Nanotoxicology* **2010**, *5*, 43-54.
[27] M. R. Buck, J. F. Bondi and R. E. Schaak, *Nat Chem* **2012**, *4*, 37-44.
[28] Elisabetta Agostinelli, Daniela Belli Dell'amico, Fausto Calderazzo, Dino Fiorani and G. Pellizzi, *Gazzetta Chimica Italiana* **1988**, *118*, 729-740.
[29] S. K. Shinde, D. P. Dubal, G. S. Ghodake, P. Gomez-Romero, S. Kim and V. J. Fulari, *RSC Advances* **2015**, *5*, 30478-30484.
[30] S. Wang, Q. Huang, X. Wen, X.-y. Li and S. Yang, *Physical Chemistry Chemical Physics* **2002**, *4*, 3425-3429.
[31] I. E. Wachs, *Catalysis Today* **1996**, *27*, 437-455.
[32] S. Lu, H. Chunfeng, S. Yoshio and H. Qing, *Journal of Physics D: Applied Physics* **2012**, *45*, 215302.

6. ELECTRICAL AND MAGNETIC PROPERTIES OF MAGNETITE NANOPOWDERS

Metal oxide nanoparticles gain huge interest for their catalytic, electrical, and magnetic properties, which are strongly different from those of their bulk counterparts[1]. In particular, magnetite Fe_3O_4 is the most common mineral on Earth with a cubic inverse spinel structure with fcc close packed oxygen and Fe cations occupying interstitial tetrahedral and octahedral sites. Thanks to its properties and biocompatibility, this material has a wide range of applications in different fields, such as energy storage devices, sensors, drug delivery systems, magnetic resonance imaging and nanocatalysis.[2] In particular in catalysis, magnetite nanoparticles modified with noble metals show promising results. The electrical and magnetic properties of these nanostructures are not completely understood, thus the characterization and the study of the influence of the final textural particle characteristics on electrical and magnetic properties has become fundamental[2].

In this work the magnetic and electrical behaviour of reference and synthetized nanopowders were deeply studied. In particular, the influence of noble metals and nanoparticle size distribution on magnetization curves and dielectric permittivity were analysed.

6.1 Magnetic characterization of magnetite nanopowders

The magnetic properties of materials can be analysed through diverse kinds of magnetic field sensors. Magnetic field sensors can be divided into vector sensors, which detect the vector components of a magnetic field and scalar sensors that measure the magnitude of the vector magnetic fields. The vector types can be further divided into sensors able to measure low fields (commonly called magnetometers) and high fields (named gaussmeters).

Among them the most common instruments used to study the magnetization of materials are the Vibrating Sample Magnetometer (VSM), the Superconducting Quantum Interference Device (SQUID) and the voltamperometric device.

VSM systems are used to measure the magnetic properties of materials as a function of magnetic field, temperature and time. Powders, solids, liquids, single crystals, and thin films are all readily accommodated in a VSM. The operating principle is based on the exhibition of a magnetic moment by a magnetic sample placed within a uniform magnetic field. By mechanically vibrating the sample within suitably placed sensing coils, a voltage is induced along the sensing coils. The measurement of the induced voltage can be related to the magnetic moment of the sample. The magnetic field may be generated by an electromagnet, or a superconducting magnet while variable temperatures may be achieved using either cryostats or furnace assemblies.
Figure 1 shows the Lake Shore© vibrating sample magnetometer used to analyse the nanopowder prepared in this PhD work.

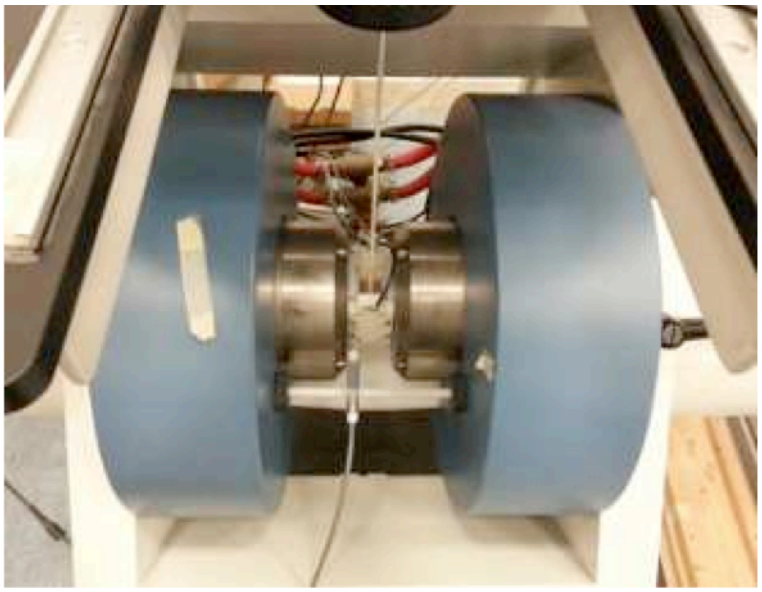

Figure 1 Lake Shore vibrating sample magnetometer

The nanopowders were embedded in a suitable plastic cylindrical holder, as shown in Figure 2. The centring of the sample was performed through the so-called "saddling procedure" aimed to seek the saddle point of the field around the centre of the pole caps that guarantees the perfect centring of the sample in the gap.
It should be stressed that as the samples are made of powder, the shape of the sample, i.e. its geometry, is not well defined inside the holder. This does not allow us to "extract" the demagnetizing field component from the measurement. An accurate estimation of the demagnetizing field appears to be a critical task in these measurements. At a first analysis, if we are interested in coercing field and saturation

magnetization (not affected by the demagnetizing field), the measurements are however not critical and data can be considered relatively accurate.



Figure 2 VSM cylindrical sample holder

Superconducting Quantum Interference Devices are the most sensitive of all magnetometers. The operating principles of a SQUID magnetometer is based on the "dc Josephson effect" that reveals low magnetic field strength or slight changes in the magnetic field; the schematic representation of the SQUID is reported in Figure 3.

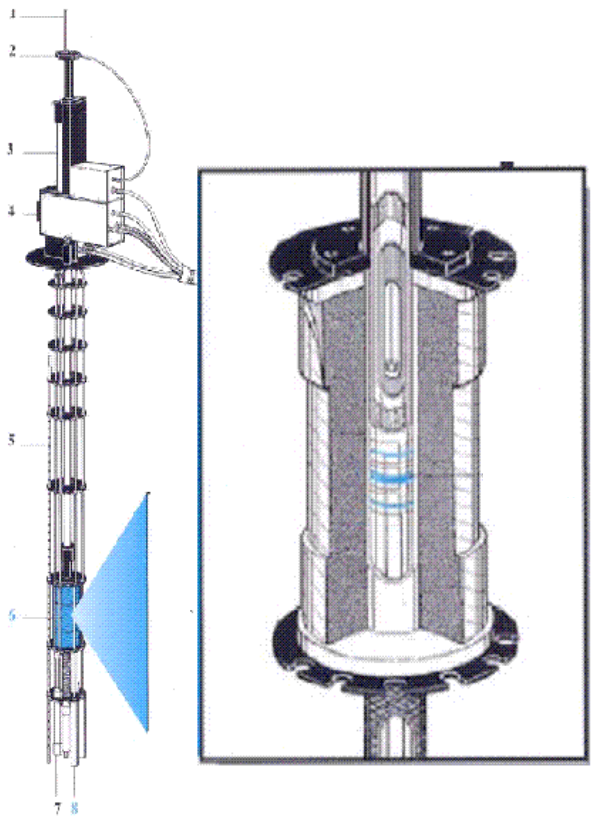

Figure 3 SQUID apparatus

These sensors operate at a near to absolute zero temperature and require cooling with liquid helium or nitrogen. For these reasons, the SQUID is more expensive, less rugged and less reliable than the VSM magnetometer. Like the VSM instrument the SQUID can also analyse powders, solids, liquids, single crystals and show the same problems connected with the geometry of the sample inside the sample holder.

Finally, volt-amperometric devices are based on the volt-amperometric theory, which shows that the magnetic flux density and magnetic field values can be reconstructed via the Ampère and Faraday-Neumann laws obtained by the measurement of the primary current and secondary voltage of a two-coil winding system wound on a magnetically closed sample. The volt-amperometric method is generally applied in order to characterize symmetric cycles of soft materials[3], even if it has been shown how to extend such a technique to the measurement of asymmetric cycles as well as to more complex behaviours[4]. In general, the demagnetizing field does not represent a critical task for such a method, while its main limitations are the tight window of work frequency and the practical inability to reach high field values. A combined use of magnetometers and the volt-amperometric method appears to be a reasonable approach to meet the requirements for a magnetic analysis of nanopowders.

In this PhD work both VSM magnetometer and volt-amperometric devices were used to analyze the macroscopic magnetic behavior of MNPs. Indeed, the aim is to characterize magnetic nanoparticles under equivalent macroscopic conditions that is not clearly discussed in literature. [5]

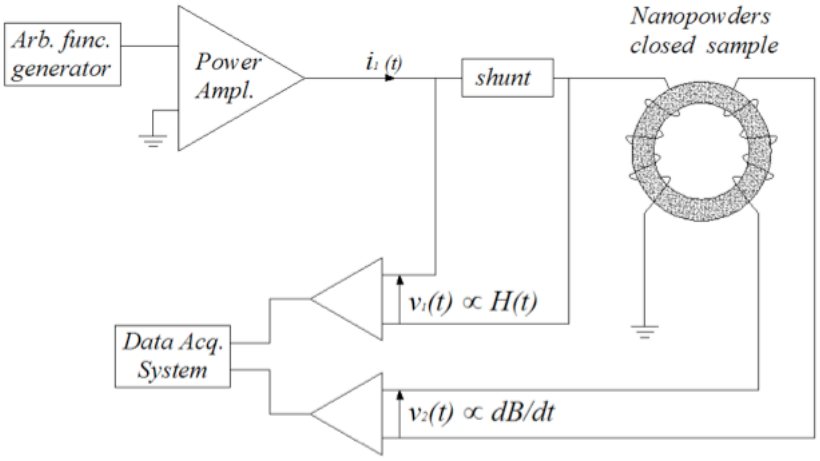

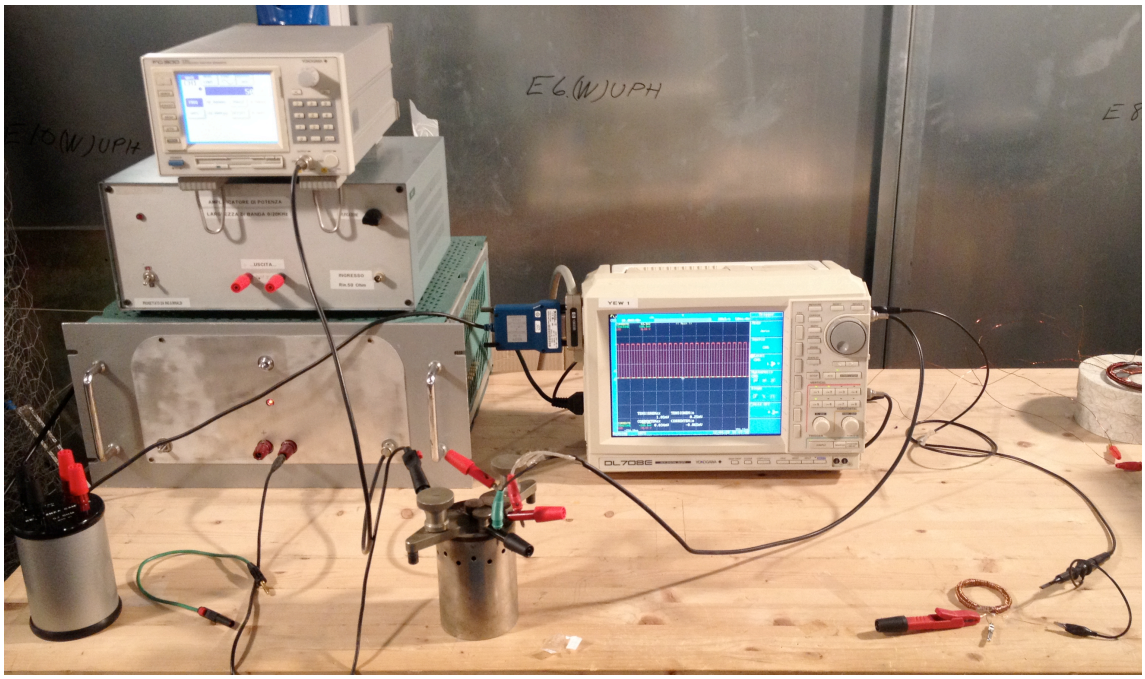

Figure 4 Representation of voltamperometric setup

The volt-amperometric system adopted in this work is displayed in Figure 4. In particular, a signal generator drives a power amplifier connected in a transconductive configuration, thus working as a current generator and imposing the current in the primary coil.

The primary current i_1 is measured through a shunt with a frequency range from DC to 10 kHz. The declared shunt accuracy is ±0.1 % while the phase error is below 1° at 100 kHz. The voltage drop across the shunt and the secondary voltage v_2 are measured through two 16-bit analog to digital converters (ADCs).

The magnetic field H and flux density B are reconstructed using the Ampère and

Faraday–Neumann laws through the primary current i_1 and the open-circuit voltage induced in secondary coil v_2, as reported in (1) and (2).

$$H = \frac{N_1 i_1}{L} \quad (1)$$

$$v_2 = N_2 S \frac{dB}{dt} \quad (2)$$

Where N_1 and N_2 represent the turn numbers of the primary and secondary windings and S is the effective cross-section area. As the ratio between the external and internal diameter of the sample is greater than 1.1, L was chosen according to the expression thus representing the mean field line.

$$L = \frac{\pi\left(D_{ext} - D_{\text{int}}\right)}{\ln\left(\frac{D_{ext}}{D_{\text{int}}}\right)} \quad (3)$$

Commercial and synthesized powders were inserted into a hollow glass torus to prepare a magnetically closed sample over which the secondary (inner) and primary (outer) windings are wound.

A secondary winding of 98 turns is wound directly on the glass support, while the primary winding of 124 turns is distributed along three sheets of about 40 turns each one. Such sheets are separated one from each other by an insulating tape and the turns are arranged to obtain a uniform winding distribution, as shown in Figure 5. The insulation tape among the sheets and the larger separation among the turns avoid a possible short circuit among the turns as a consequence of the relatively high current values in the primary winding.

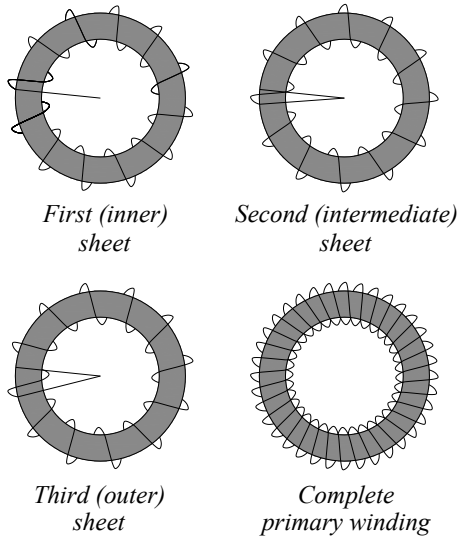

Figure 5 Schematic representation of primary and secondary windings arrangement.

The control of the local temperature of the copper wire along the primary winding is in general a complex task and care must be taken to avoid damage to the circuit. The current density adopted for our experiments varied from about 10 A/mm^2 to 400 A/mm^2. For higher current density values, we could reach 70 kA/m magnetic field values close to the beginning of the saturation region for the materials investigated. It is clear how such current density values are critical from a thermal point of view for our apparatus and how this is an intrinsic limit of the adopted measurement method. On the other hand, we could find a compromise solution between the obtainable magnetic field values and the thermal stress of the copper wire. The thermal inertia of the magnetic sample positioned in a climatic chamber during the test was evaluated high with respect to the constraints relevant to the primary copper wire.

Particular care was taken during sample preparation to guarantee an approximately homogeneous distribution of the powder within the glass torus holder. The packing of the powders appears to be a critical task that can affect measurement accuracy, thus the repeatability of the filling up of the chosen glass torus by an easy vibration technique was verified first.

The uncertainty of the filling up method was evaluated so as not to exceed 1% in weight for each sample, thus ensuring the same geometry for each tested nanopowder. This in particular defined the measurand well, and it seems to respond in part to a lack of discussion in literature, i.e. in the field of nanoparticle magnetic characterization from a

macroscopic point of view. The simplicity of the packing method and the geometry of the glass holder make the method easy to use in different laboratories, thus enabling the reproducibility of our approach.

In more detail, commercial and synthesized powders were inserted into the glass torus using a vibrating device and sonication to obtain the complete packing of the internal volume. This ensured the powder would form a macro-continuous system inside the sample holder. The packing procedure reproducibility was assured by repeating the packing procedure five times for each powder and the relative standard deviation of the measured weight was less than 1%. Of course, different commercial and synthesized nanoparticles show different final sample weights, because of different micro-arrangements inside the sample holder. Indeed, materials characterized by different textural, chemical and physical properties (such as density, porosity, nanoparticle size and shape) show different packing fraction. On the other hand, it was ensured that the macroscopic sample geometry was repeatable for each powder as well as for different powders in agreement with our purpose and discussion.

A photograph of the glass torus sample with commercial nanopowder without (left plot) and with (right plot) the secondary and primary windings is shown in Figure 6.



Figure 6 Glass toroid sample without (left plot) and with (right plot) the secondary and primary windings.

This voltamperometric setup allows us to obtain repeatable and reproducible measures to characterize the magnetic behaviour of nanoparticles from a macroscopic point of view, contrary to the VSM and SQUID analysis.

To better analyze the differences between the VSM magnetometer and the adopted voltamperometric technique, these two analyses were employed in the characterization of the reference nanopowder. This reference nanopowder is Sigma Aldrich commercial magnetite characterized by an average particle diameter of 50 nm.

The VSM magnetometer permits the analysis of the variations of sample magnetization

by varying the applied magnetic field from 10 Oe to10^4 Oe, leading to material magnetic saturation and to the building of the typical magnetic hysteresis curves.
Figure 7 reports the hysteresis curves of the reference nanopowder.

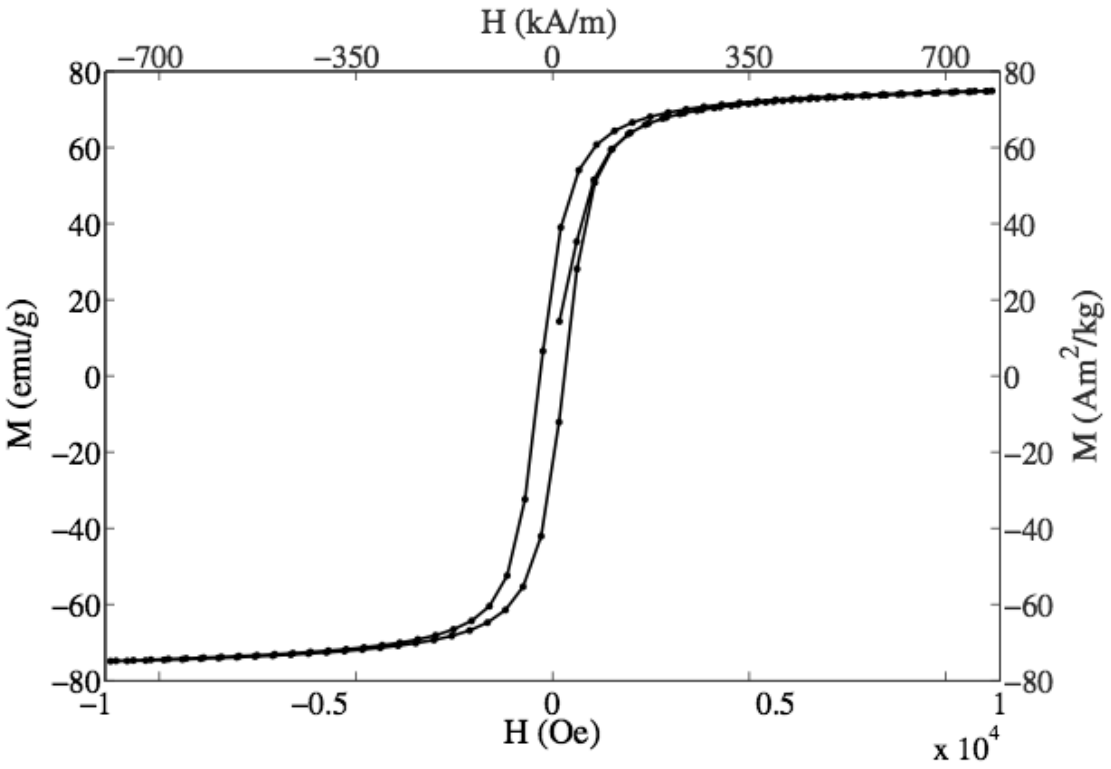

Figure 7 Hysteresis curves of Sigma Aldrich magnetite nanopowder obtained with VSM magnetometer

The same nanopowder was analysed adopting the voltamperometric setup, which permits a more accurate scan of material magnetization variations in a short range of magnetic fields (0-300 Oe). Thanks to this deep analysis, it is possible to observe minor hysteresis loops of the material as shown in Figure 8.

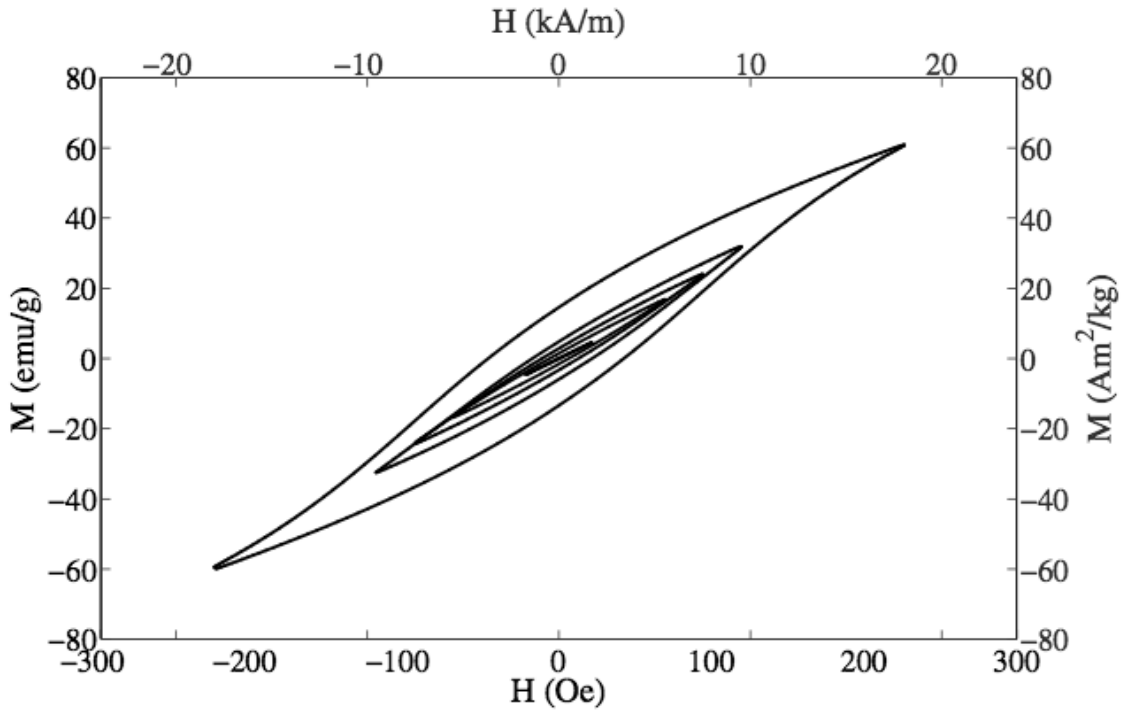

Figure 8 Minor hysteresis loop of magnetite nanopowder obtained with the voltamperometric technique.

In conclusion, the VSM analysis allows us to obtain a complete description of the magnetic hysteresis curve and to quantify the material magnetization saturation value M_0. Instead, the voltamperometric technique permits an extremely accurate evaluation of material magnetic behaviour in a short range of magnetic fields. This short range of magnetic fields is particularly important because they correspond to ones commonly used in industrial application.

Therefore, by combining the information obtained using VSM and voltamperometric instruments it is possible to obtain a satisfactory magnetic description of a nanopowder.

By adopting these two techniques, it was possible to deeply investigate the correlation between magnetic properties and chemical and morphological characteristics of nanoparticles. In particular, in order to better understand the relationship between particle characteristics and properties the synthesized Fe_3O_4 and $M@Fe_3O_4$ (M: Ru, Pd or Pt) nanopowders described in Chapter 4 and 5 and the reference magnetite nanopowder ($Fe_3O_{4\ ref\ 5um}$ and $Fe_3O_{4\ ref\ 50\text{-}100\ nm}$) were further analysed.

The main characteristics of the synthesized Fe_3O_4 samples and the different bimetallic systems $M@Fe_3O_4$ (M: RuO_x, Pd or Pt), are summarized in Table 1, together with those of reference Fe_3O_4 nanopowders.

Table 1 Main morphological and chemical characteristics of reference and synthetized nanopowders

Sample	Noble metal (wt%)	Surface area (m^2/g)	Mean diameter (nm)	s.d (nm)	M_{sat} (emu/g)
Fe_3O_4 ref 5um	-	-	132.0	18,4	-
Fe_3O_4 ref 50-100 nm	-	> 60	26.1	0.5	50
Fe_3O_4	-	78.8	4.8 (16.3)	0.6 (0.2)	37
Pd@Fe_3O_4	4.70	106.8	8.2	0.3	47
Ru@Fe_3O_4	1.87	62.0	10.1	0.1	40
Pt@Fe_3O_4	6.01	101.9	9.1	0.3	35

As can be observed in Table 1, the synthesized Fe_3O_4 and M@Fe_3O_4 samples show higher surface area than the commercial samples; this peculiar aspect can be explained by the different synthetic approach employed for the preparation of Fe_3O_4 and M@Fe_3O_4 nanoparticles. In fact, the final textural, magnetic and electrical characteristics of nanoparticles are strongly influenced by the adopted synthetic procedures[6]. The bimetallic systems (Pd@Fe_3O_4, RuO_x@Fe_3O_4 and Pt@Fe_3O_4) synthetized following the same procedures show a marked difference in noble metal content that can be explained by the different affinity of these noble metals with the magnetite structure and the different reduction potential of the noble metal precursors.

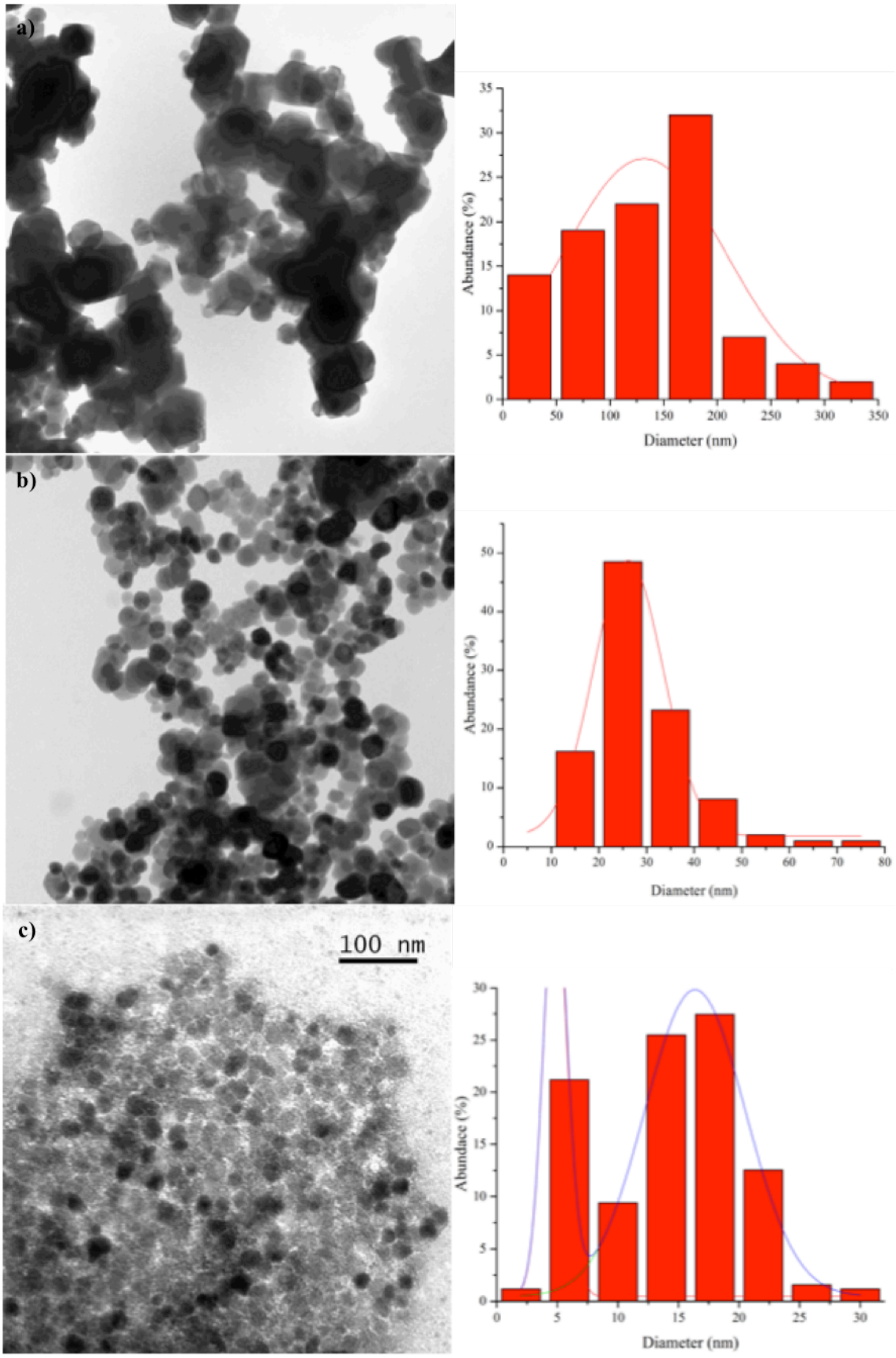
a)
Abundance (%)
Diameter (nm)
b)
Abundance (%)
Diameter (nm)
c)
100 nm
Abundace (%)
Diameter (nm)

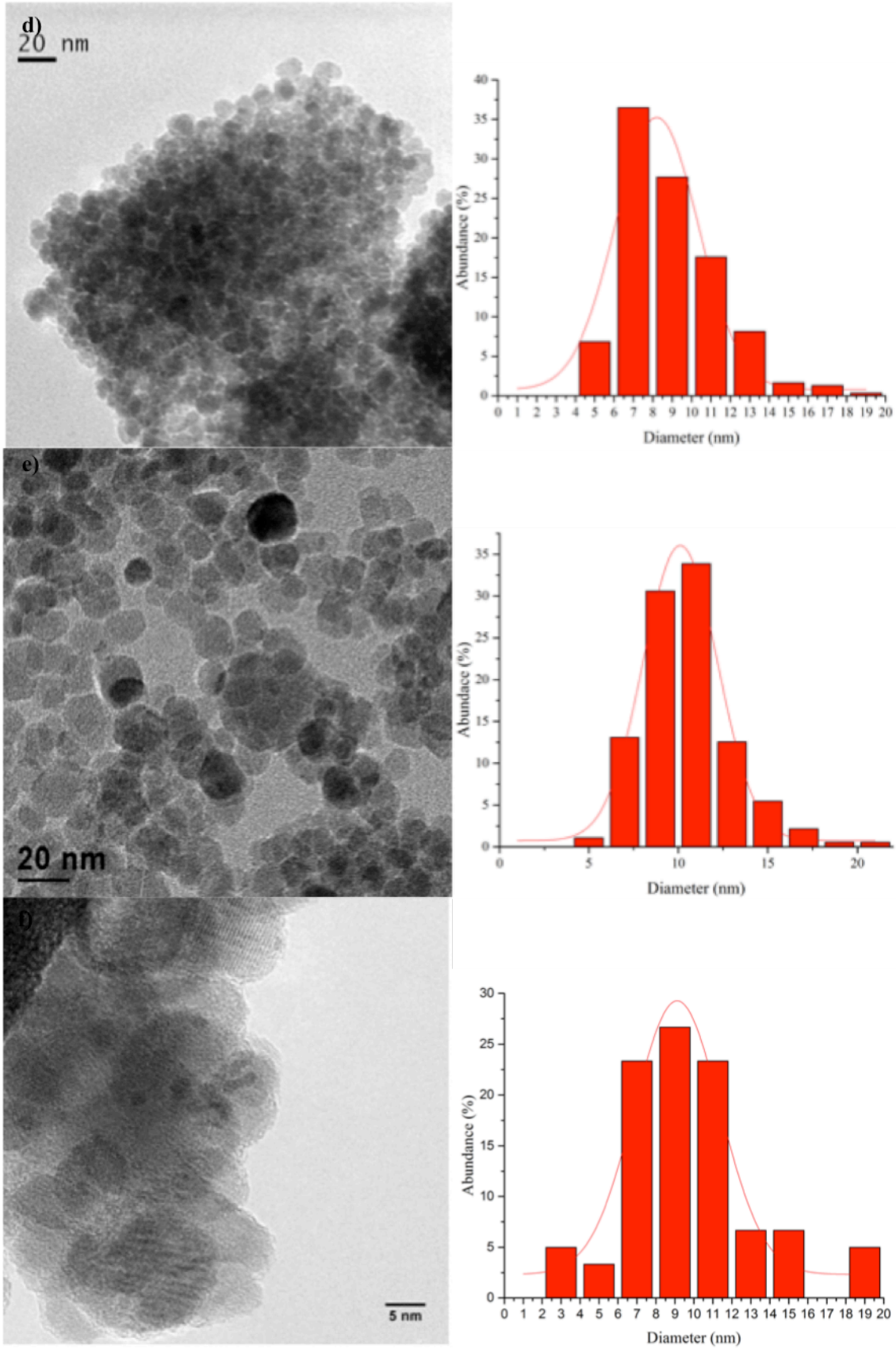

Figure 9 TEM micrographs and particles size distribution of commercial and synthetic samples: a) Fe_3O_4 ref 5 um, b) Fe_3O_4 ref 50-100, c) Fe_3O_4, d) Pd@ Fe_3O_4, e) RuO_x@ Fe_3O_4 and f) Pt@ Fe_3O_4

Commercial and synthetic samples show a marked difference in shape and particle size distribution (see Figure 9). In particular $Fe_3O_{4\ ref\ 5um}$ shows cubic morphology while $Fe_3O_{4\ ref\ 50\text{-}100}$, Fe_3O_4, $Pd@Fe_3O_4$ and $Ru@Fe_3O_4$ samples show spherical morphology; this difference could be explained by the shape evolution that occurs during long particle growth[7]. Moreover, the reference nanoparticles show broad particle size distribution characterized by high standard deviation compared with the synthetic counterpart. The synthetic Fe_3O_4 has a bimodal size distribution characterized by a bigger particle population with an average diameter of 16.3 nm and a smaller one with an average diameter of 4.8 nm. Finally, the synthetic $Pd@Fe_3O_4$, $RuO_x@Fe_3O_4$ and $Pt@Fe_3O_4$ samples show remarkably narrow particle size distribution characterized by an extremely low standard deviation. These results ultimately confirm that the synthetic approach drastically affects the textural and morphological particle characteristics and confirms the good size control reached during synthesis.

The magnetic behaviors of the synthesized and commercial samples were analyzed at room temperature with the voltaperometric system and their magnetization curves are reported in Figures 10 and 11.

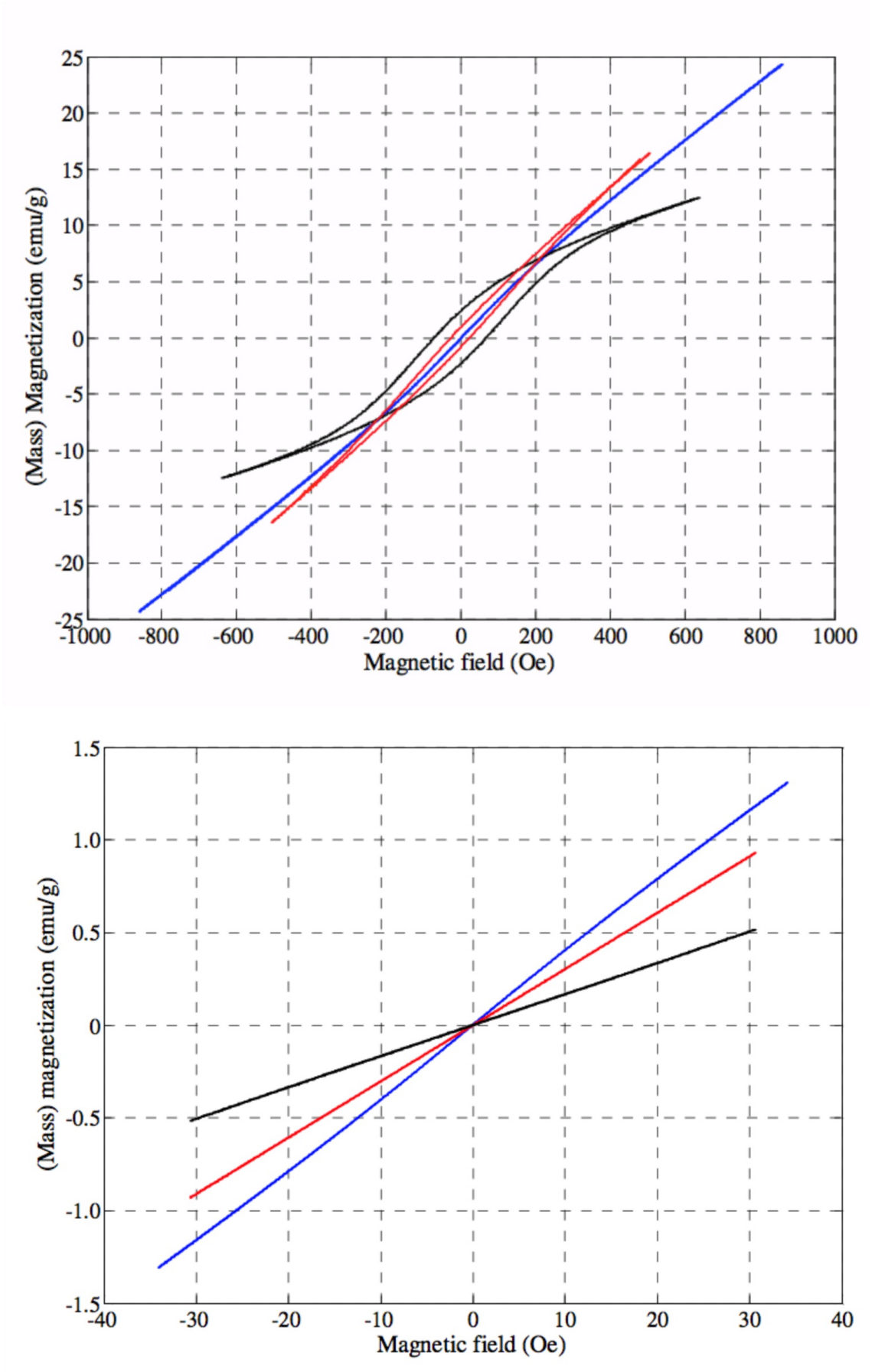

Figure 10 Magnetic behaviour of reference magnetite 5 µm (red curve), reference magnetite 50-100 nm (black curve) and synthesized magnetite (blue curve)

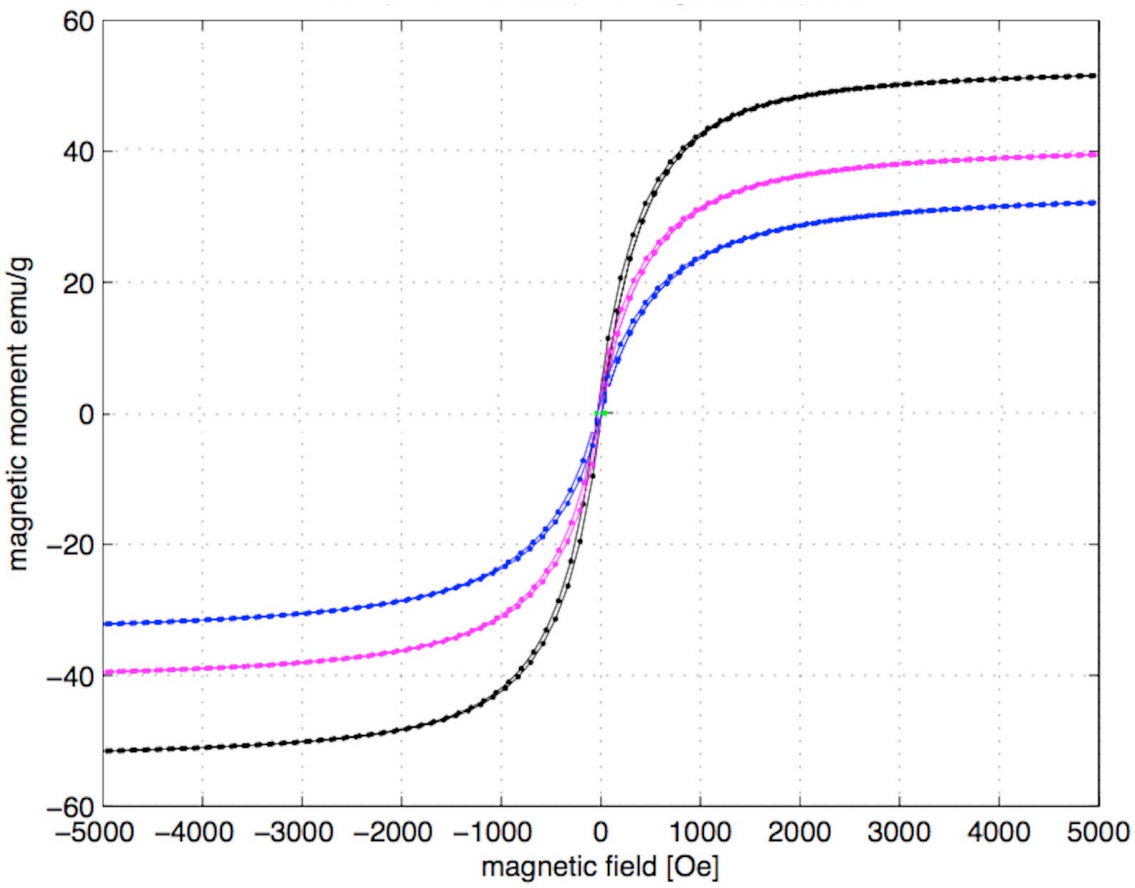

Figure 11 Magnetization curves of $Pd@Fe_3O_4$ (black), $Pt@Fe_3O_4$ (blue), $RuO_x@Fe_3O_4$ (pink), nanoparticles.

The saturation magnetization value of the synthesized reference nanostructured Fe_3O_4 was 37 emu/g, a smaller value than the 90 emu/g of bulk magnetite. In particular, when comparing samples ($Fe_3O_{4\ ref\ 5um}$, $Fe_3O_{4\ ref\ 50\text{-}100}$ and Fe_3O_4) it is possible to observe that by increasing the diameter of the particles the M_0 increases. However, it is remarkable that when passing from a diameter of 132 nm ($Fe_3O_{4\ ref\ 5um}$ sample) to a diameter of 26.1 nm ($Fe_3O_{4\ ref\ 50\text{-}100}$ sample) the decrement of the M_0 is less marked because particles characterized by a dimension below the Weiss domain dimension (100 nm) show a superparamgnetic behaviour that can compensate the loss of magnetic moment due to the decrease in crystal size.

As known from literature, the magnetic behaviour of iron oxide nanoparticles is very sensitive not only to particle size and to crystallinity, but also to the presence of other molecules on the surface of nanoparticles. The introduction of palladium changes the magnetic behaviour of the magnetic nanopowders with respect to that made by pure

magnetite. In fact, the Pd@Fe_3O_4 sample show a significant reduction of hysteresis and an evident increment of the saturation magnetization value that reaches in this case the 47 emu/g value. RuO_x@Fe_3O_4 and Pt@Fe_3O_4 samples instead show an evident reduction of hysteresis and slight variations of the saturation magnetization value limited to a few percentage points. The ruthenium and platinum effect on magnetic saturation agrees with the study reported by Andreev at al.[8] The correlation between textural particle characteristics and electrical and magnetic properties has been published[9].

6.2 Electrical characterization of magnetite nanopowders

The dielectric permeability of synthesized Fe_3O_4 and M@Fe_3O_4 (M: RuO_x or Pd) nanopowders described in Chapters 4 and 5 and the reference magnetite nanopowder ($Fe_3O_{4\ ref\ 5um}$ and $Fe_3O_{4\ ref\ 50\text{-}100\ nm}$) were tested via spectroscopic analysis of the equivalent electrical properties of the samples. A capacitor was made by inserting each nanopowder or pellet between two copper plates and connected to an E4980A Agilent LCR meter (see Figure 12). The equivalent parallel conductance (Gp) and capacitance (Cp) values were estimated via an impedance spectroscopy technique.

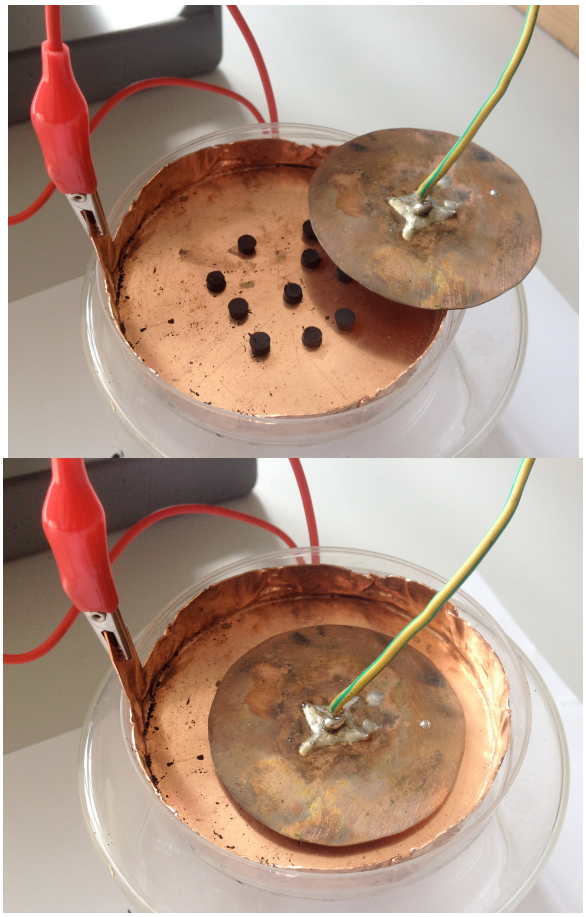

Figure 12 Examples of setup for spectroscopic analysis IES on nanopowders and pellets

The capacitance C_p of all nanostructured samples was measured at room temperature using an impedance spectroscopy, equipped with a specific handmade probe (see Figure 12), from the frequency of 10^2 to 10^6 Hz. In particular, in this work we studied the effect of nanoparticle size and noble metal presence on magnetite relative dielectric permittivity ξ_r. Sample dielectric permittivities ξ were obtained following the standard equation 4.

$$\xi = (C_p * d)/ S \qquad (4)$$

Where C_p is the measured capacitance of the material, d is thickness of the sample and S is the surface of the sample involved in the measurement. The relative permittivity ξ_r was calculated as:

$$\xi_r = \xi / \xi_0 \qquad (5)$$

Where ξ_0 is vacuum permittivity (ξ_0 = 8.852 pF/m).

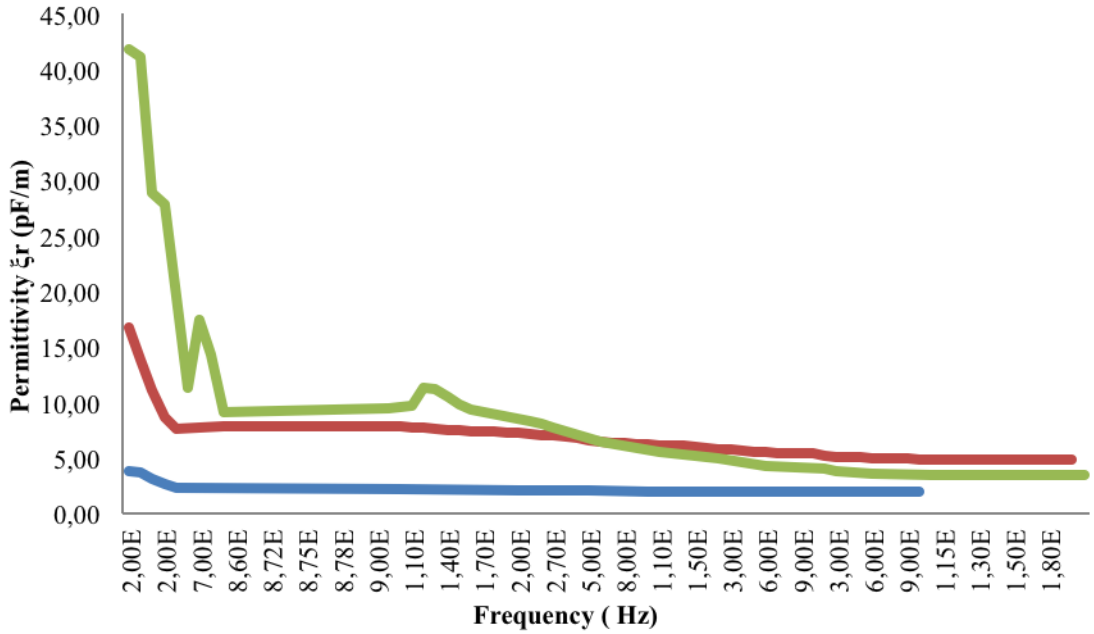

Figure 13 Curves of relative dielectric permettivity as a function of the applied frequency for commercial and synthetic magnetite nanopowder: Fe_3O_4 com 5um (in green), Fe_3O_4 com 50-100 (in red), Fe_3O_4 (in blue)

Figure 13 shows the variation of relative dielectric permittivity (ξ_r) with frequency at room temperature for reference magnetite nanopowders (Fe_3O_4 ref 5um (green line), Fe_3O_4 ref 50-100 (red line)) and synthetic Fe_3O_4 nanopowder (blue line). The relative dielectric permittivity decreases, thus decreasing magnetite nanoparticle size. A strong dependence between size of nanoparticles and electrical properties was observed also for other nanostructured metals as reported by M. Anwar et al.[10]

Moreover, the commercial samples (Fe_3O_4 ref 5um, Fe_3O_4 ref 50-100) show a resonance effect of dielectric permittivity, underlining the ionic polarization that occurs at the interface between the nanoparticles. Ionic polarization or interfacial polarization in fact, is caused by the accumulation of free ions at the interfaces between materials having different conductivities and dielectric constants[11]. In particular, reference magnetite nanoparticles characterized by a bigger size (Fe_3O_4 ref 5um) show a more marked resonance effect than magnetite of a smaller size (Fe_3O_4 ref 50-100), while for the synthetic magnetite samples no resonance effect was appreciated probably due to their extremely small size. The dielectric permittivity values obtained are comparable with the ones reported in literature for the same materials[12].

In order to better understand the size and morphology effects on the dielectric permittivity of the samples both the commercial magnetite and the synthetic one were pressed in pellets using a manual press. The pellets were prepared using 100 mg of nanopowder per pellet, ten pellets for each sample were placed between the copper plates as shown in Figure 12 and analysed. In this last case, dielectric permittivity ξ was calculated taking into account the amount of air between the pellets, $\xi = (C_p - C_{aria}) * d)/S$ where C_p is the measured capacitance of the material, C_{aria} is the capacitance of the air between the pellets (calculated as $C_{aria} = \xi_0 * (S_p - S)/d$), d is thickness of the pellets, S is the sum of the surface of ten pellets and S_p is the surface of the copper plate. Relative dielectric permittivity was calculated as previously reported using the vacuum permittivity ξ_0 of 8.852 pF/m.

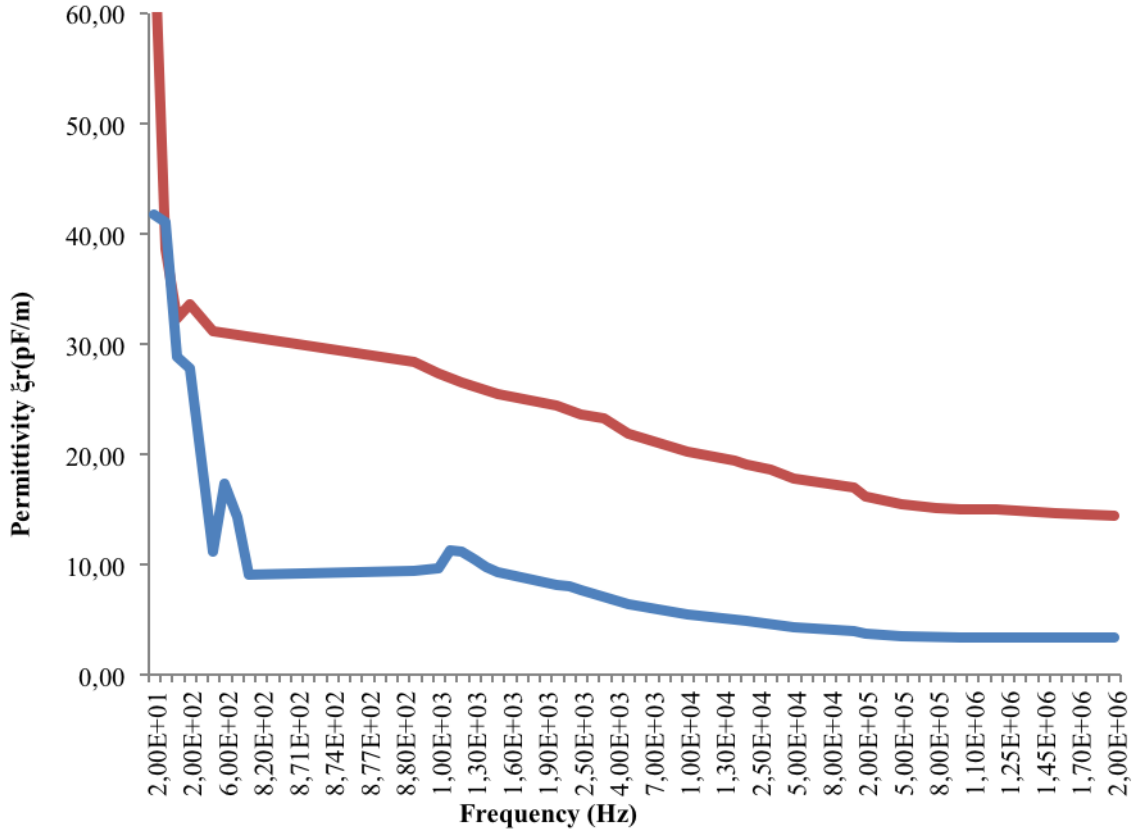

Figure 14 Comparison between the curves of relative dielectric permettivity as a function of the applied frequency for the Fe_3O_4 ref 5um nanopowder in blue and pellets in red.

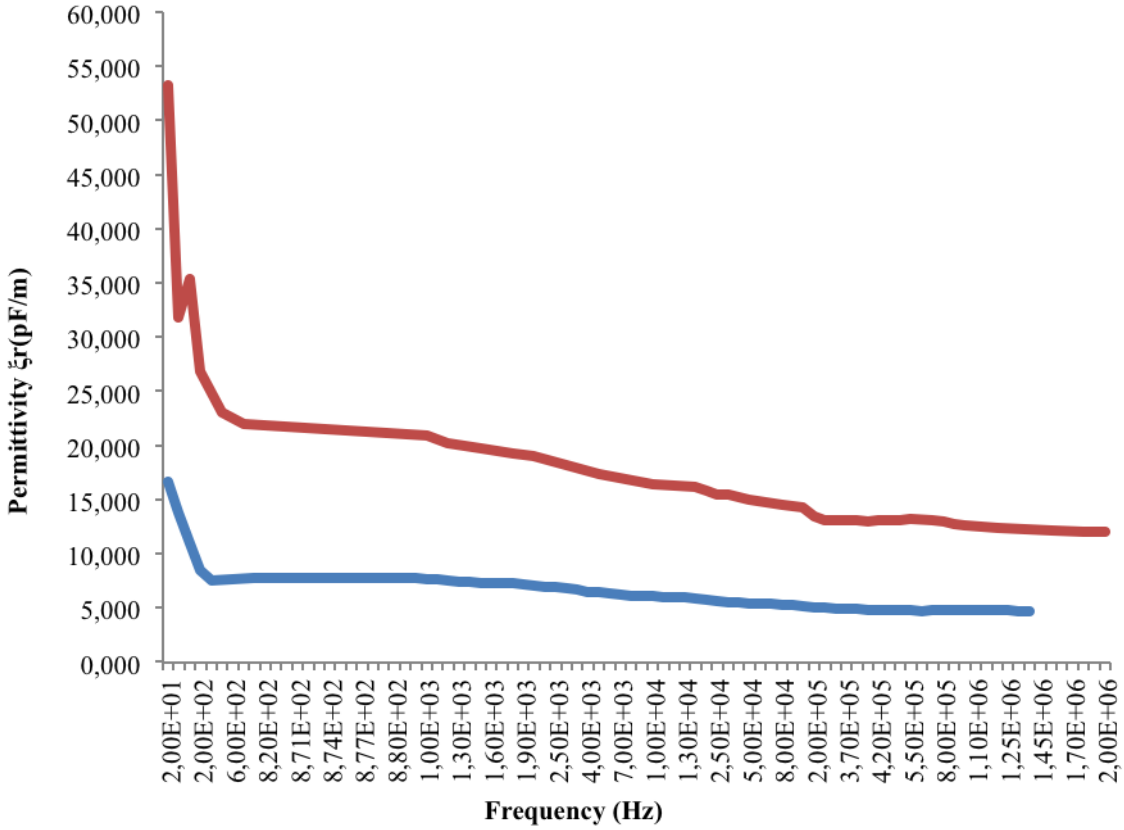

Figure 15 Comparison between the curves of relative dielectric permettivity as a function of the applied frequency for the Fe_3O_4 ref 50-100 nanopowder in blue and pellets in red.

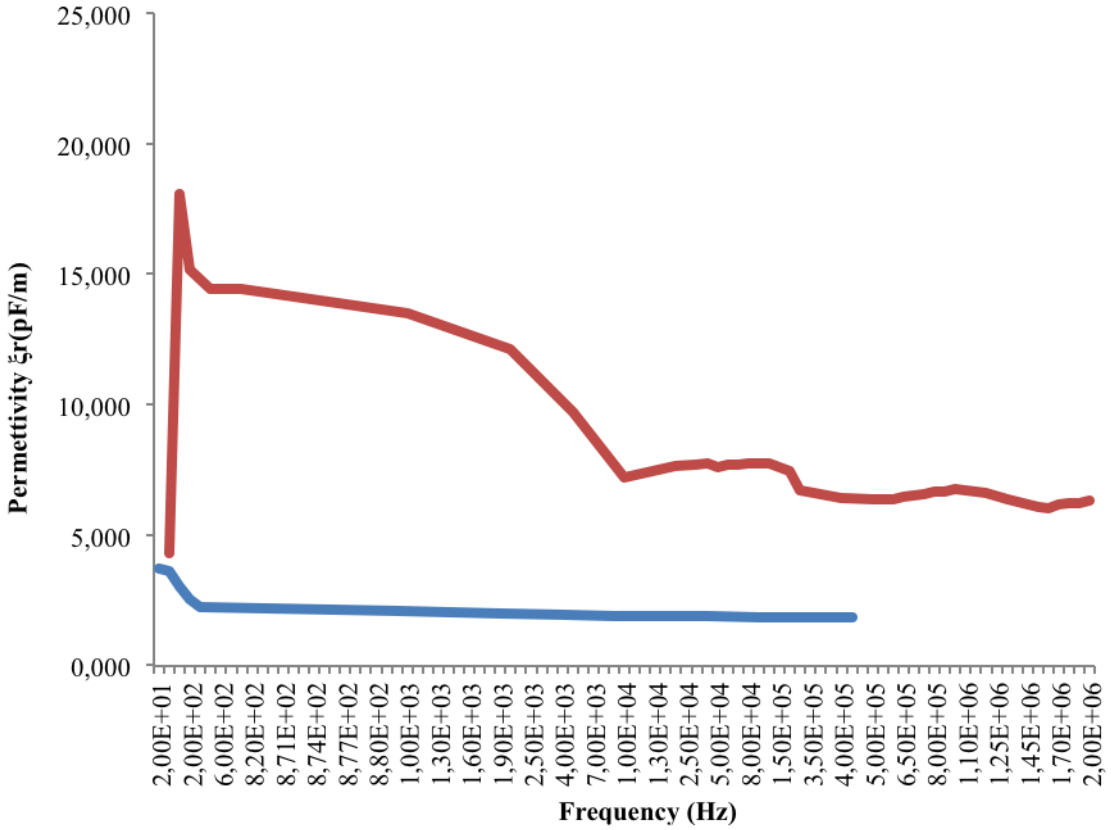

Figure 16 Comparison between the curves of relative dielectric permettivity as a function of the applied frequency for the Fe_3O_4 nanopowder in blue and pellets in red.

As can be seen in Figures 14, 15 and 16, by pressing the nanopowders in pellets their dielectric permittivity increases due to the improvement in the interfacial polarization and the reduction of air between the nanoparticles. In particular, in synthetized Fe_3O_4 pellets the resonance effect became appreciable while in the same materials as nanopowders it was not observed. Futhermore, the resonance effect of Fe_3O_4 $_{ref\ 50\text{-}100}$ pellets results shifted to a higher frequency compared to the one observed in Fe_3O_4 $_{ref\ 50\text{-}100}$ nanopowders.

Finally, in the Fe_3O_4 $_{ref\ 5um}$ pellets the resonance effect was not appreciated, probably because it had shifted to a higher frequency which our instrument could not reach.

Taking into account the differences between powder and pellets observed for the same materials, it became extremely important to characterize these kinds of nanostructures under the final application conditions.

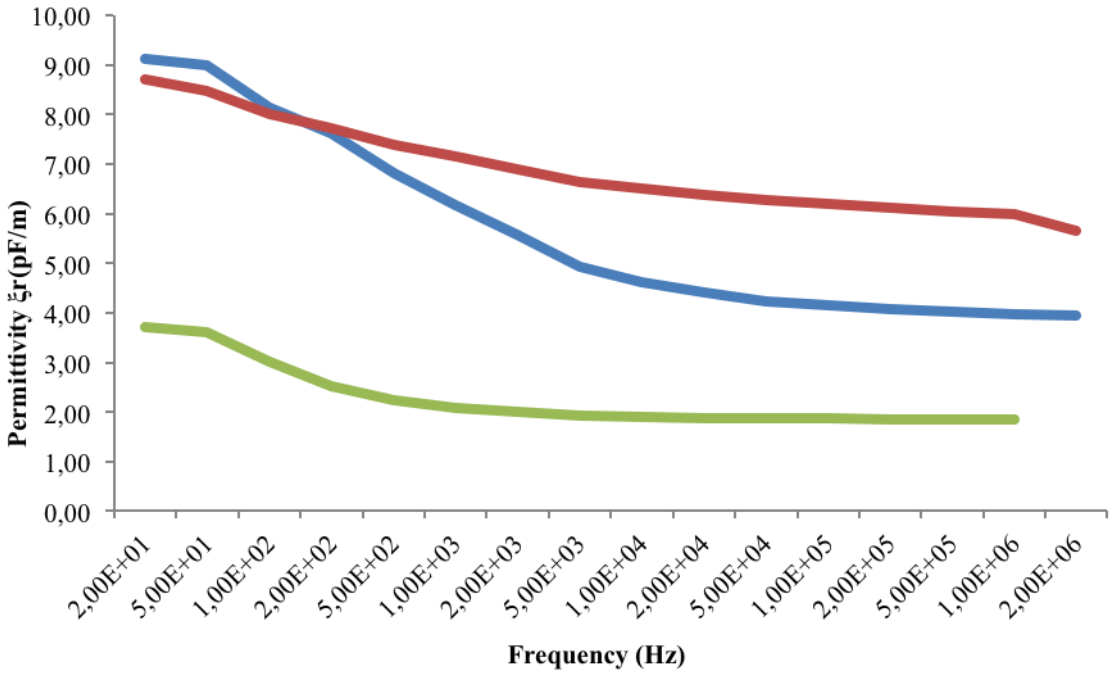

Figure 17 Comparison between relative permittivity as function of frequency for synthetic Fe_3O_4 and $M@Fe_3O_4$ nanopowders :a) dielectric permettivity curves of $Pd@Fe_3O_4$ nanopowders (red) b) dielectric permettivity curves of $Ru@Fe_3O_4$ nanopowders (blue) c) dielectric permettivity curves of Fe_3O_4 nanopowders (green).

Finally, the introduction of ruthenium or palladium in the magnetite structure seems to promote the mobility of charge increasing interface polarization, in fact $Pd@Fe_3O_4$ and $Ru@Fe_3O_4$ have a higher dielectric permittivity than pure synthetic magnetite Fe_3O_4. Furthermore, for all these samples no resonance effect was appreciated due to their small size.

6.3 References

[1] S. Laurent, D. Forge, M. Port, A. Roch, C. Robic, L. Vander Elst and R. N. Muller, *Chemical reviews* **2008**, *108*, 2064-2110.

[2] a) N. J. S. C. L. M. Rossi, F. P. Silva, R. V. Goncalves, *Nanotechnology Reviews* **2013**, *2*, 597-614; b) S. Shylesh, V. Schünemann and W. R. Thiel, *Angewandte Chemie International Edition* **2010**, *49*, 3428-3459; c) J. S. Weinstein, C. G. Varallyay, E. Dosa, S. Gahramanov, B. Hamilton, W. D. Rooney, L. L. Muldoon and E. A. Neuwelt, *J Cereb Blood Flow Metab* **2009**, *30*, 15-35; d) A. K. Gupta and M. Gupta, *Biomaterials* **2005**, *26*, 3995-4021.

[3] a) T. Ozkaya, M. S. Toprak, A. Baykal, H. Kavas, Y. Köseoğlu and B. Aktaş, *Journal of Alloys and Compounds* **2009**, *472*, 18-23; b) G. Y. Yurkov, A. S. Fionov, Y. A. Koksharov, V. V. Koleso and S. P. Gubin, *Inorganic Materials* **2007**, *43*, 834-844.

[4] a) D. Grimaldi, L. Michaeli and A. Palumbo, *Instrumentation and Measurement, IEEE Transactions on* **2000**, *49*, 154-160; b) L. D'Alessandro and A. Ferrero, *Instrumentation and Measurement, IEEE Transactions on* **1994**, *43*, 599-605.

[5] B. Tellini, R. Giannetti, S. Lizon-Martinez and M. Marracci, *Instrumentation and Measurement, IEEE Transactions on* **2009**, *58*, 2807-2814.

[6] F. Adamo, F. Attivissimo, M. Marracci and B. Tellini, *Measurement Science and Technology* **2012**, *23*, 085602.

[7] a) R. Y. Hong, J. H. Li, H. Z. Li, J. Ding, Y. Zheng and D. G. Wei, *Journal of Magnetism and Magnetic Materials* **2008**, *320*, 1605-1614; b) D. Maity, J. U. N. Ding and J.-M. Xue, *Functional Materials Letters* **2008**, *01*, 189-193; c) T. J. Daou, G. Pourroy, S. Bégin-Colin, J. M. Grenèche, C. Ulhaq-Bouillet, P. Legaré, P. Bernhardt, C. Leuvrey and G. Rogez, *Chemistry of Materials* **2006**, *18*, 4399-4404; d) D. Horák and N. Chekina, *Journal of Applied Polymer Science* **2006**, *102*, 4348-4357.

[8] J. Cheon, N.-J. Kang, S.-M. Lee, J.-H. Lee, J.-H. Yoon and S. J. Oh, *Journal of the American Chemical Society* **2004**, *126*, 1950-1951.

[9] A. V. Andreev, E. A. Tereshina, D. I. Gorbunov, E. Šantavá, J. Šebek, M. Žáček, S. Daniš, J. Pospíšil and L. Havela, *Journal of Alloys and Compounds* **2015**, *621*, 415-422.

[10] M. A. K. Abdelhalim;, M. M. Mady; and M. M. Ghannam, *International Journal of Physical Sciences* **2011**, *6*, 5487-5491.

[11] a) A. M. R. Galletti;, E. Bertolucci;, Mirko Marracci, B. Tellini; and C. Visone, *Instrumentation and Measurement Technology Conference (I2MTC)* **2014**, pp. 464-467; b) C. A. Elisa Bertolucci; Anna Maria Raspolli Galletti, Mirko Marracci, Bernardo Tellini, Fabio Piccinelli, Ciro Visone in *Chemical and Magnetic Properties Characterization of Magnetic Nanoparticles*, *Vol.* IEEE, Pisa, **2015**.

[12] B. Unal, Z. Durmus, H. Kavas, A. Baykal and M. S. Toprak, *Materials Chemistry and Physics* **2010**, *123*, 184-190.

7. SYNTHESIS OF MAGNETIC NANOCOMPOSITES

Magnetic nanocomposites (MNCs) find smart and increasing applications in diverse technological and medical fields. In particular, these materials are attractive in biomedicine and biotechnology for the production of magnetic imaging agents[1], cancer treatments[2], and targeted drug delivery[3]. In industry, MNCs are applied to information storage devices[4], printing inks[5], fuel cell membranes[6], catalysts[7] and sensors[8].

Typically, magnetic nanocomposites show a core-shell structure characterized by a magnetic core and a polymeric shell. This hierarchical multilayer structure is very versatile because by selecting the opportune polymeric shell it is possible to obtain MNCs with diverse properties. The polymeric shell in fact can be functionalized with the desired groups able to drive the MNC properties such as acidic or alkaline strength, electrical behaviour, stability and chemical compatibility to a selected medium.[9] These aspects are extremely important for the design of new MNC based materials.

Despite these positive aspects, the presence of the polymeric shell around magnetic particles causes the passivation of their surface, decreasing their magnetic behaviour.

Generally, the magnetic core is composed of iron oxides, which are cheap, biocompatible and involve the most abundant mineral on Earth. Instead, for the preparation of the polymeric shell a wide range of polymers can be used, in particular the selected polymer must be able to arrange itself in polar and apolar regions that can be filled by the metal precursors. In this class of polymeric compounds, there are resins, dendrimers and copolymers. Moreover, it is possible to use a polymer characterized by a high coordinative group such as nitrogen and oxygen based functional groups.

It is well known that the magnetic, electrical and catalytic properties of MNCs are strongly connected to their size, shape, composition and stability, thus to their synthetic procedure. There are numerous procedures reported in literature for the preparation of MNCs using a wide range of polymeric shells.

For example Ma et Al.[10] described the preparation of MNCs using sodium alginate as a biocompatible polymeric shell. In more detail, they describe the alkaline co-

precipitation of iron oxides and subsequently the addition of sodium alginate as a polymeric shell. Conversely, Ngomsik and Idris et Al.[11] developed a two-step procedure to produce a smaller maghemite/alginate system based on the alkaline precipitation of magnetite particles, their oxidation to maghemite in acid media and the final treatment with alginate and organic extractants.

Keshavars et Al.[12] showed the preparation of MNCs using polyacrylic acid as a sustainable polymeric shell. Finally Zhang et Al.[13] developed a microwave assisted one-pot procedure to prepare a magnetite/polypyrrole nanocomposite.

Other interesting synthetic procedures report the use of diverse polymers as a polymeric shell, such as alginate[14], polyvinylpyrrolidone[15], polyvinyl alcohol[16], polycaprolactone[17], polystyrene[18] and other copolymers[19].

Furthermore, it is possible to prepare MNCs characterized by acidic behaviour suitable as recoverable heterogeneous acid catalysts. Several important industrial reactions such as hydrolysis[20], transesterification[21] etc. are acid catalysed and generally involve the use of traditional homogenous acids. Nowadays the use of homogeneous acids is strongly discouraged due to their hazardous and corrosive nature, thus leading to environmental and health risks.

In fact, homogeneous acids are difficult to recover and separate from the reaction medium resulting in the production of huge amounts of hazardous waste. Moreover, the corrosive nature of these compounds causes the rapid deterioration of industrial plants, increasing process costs. [22]

Taking into account all these problems, the development of new acid magnetic nanocomposite catalysts became extremely important. In fact, these new materials show an extremely small size able to guarantee a closer contact between reagents and catalytic active sites, thus mimicking the homogenous catalyst. Moreover, the magnetic nature of MNCs assures an easy and efficient recovery and recycle.

Several procedures are reported in literature for the preparation of acid MNCs, involving diverse acid polymeric or organic compounds such as sulfamic acid[23], oleic acid[24], Nafion resin[25], poly lactic acid[26], humic acid[27] etc.

The acidity of these catalysts, thus their catalytic activity, strongly depend on their chemical composition and final structure as underlined by Fujii et Al.[28]

In this context, diverse biocompatible and sustainable magnetic nanocomposites were prepared following the new greener precipitate and hydrothermal procedures described in Chapters 4.1 and 4.2.

In particular, two acidic MNCs were prepared following the new precipitate procedure and four biocompatible MNCs were prepared through the new hydrothermal procedure. The acidic MNCs are composed of a maghemite (γ-Fe_2O_3) core, which is surrounded by Nafion 177 (Perfluorinated resin) or Nafion SAC-13 (Nafion/Silica composites).
Instead, the biocompatible MNCs are composed of a magnetite core (Fe_3O_4), which is surrounded by diverse biocompatible polymers such as alginate, polyvinylpyrrolidone and polyvinyl alcohol at high (85000-146000 Mw) and low (31000-50000 Mw) molecular weight.

7.1 Synthesis of acid magnetic nanocomposites: the microwave assisted precipitate approach

The acid MNCs were prepared following a procedure based on the new precipitate method described in Chapter 4.1. In particular $FeCl_3 \cdot 1.5H_2O$ (1g) and NaOH (1.5g) were dissolved in EtOH 96 wt% (44 mL) under stirring. The proper amount of Nafion alcohol suspension was neutralized by adding NaOH and added at iron basic solution.
The resulting mixture was treated by monomode microwave (CEM discovery S-class equipped with an 80 mL glass vessel) at 160°C for 15 minutes at 250W under inert atmosphere. At the end of the treatment, particles were collected using centrifuge at 1500 rpm for 5 minutes, washed three times with EtOH at 96 wt% (40 mL) and dried under vacuum for 12 h. They were stored under argon.
This preparation was repeated using two kinds of Nafion resins, Nafion 117 and Nafion SAC-13, characterized by diverse acidity. In particular Nafion 117 presents an acidity of 0.91 meq H^+/g, whereas Nafion SAC-13 of 0.12 meq H^+/g.[29] The final characteristics of the obtained MNCs are summarized in Table 1.

Table 1 Magnetic acid nanocomposites

Samples	Composition	BET (m^2/g)	Diameter (nm)	σDm (nm)
MNC1	50%Nafion 117@γ-Fe_2O_3	36.7	6.1	0.6
MNC2	50%Nafion SAC13@γ-Fe_2O_3	47.7	3.3	0.3

The MNC1 and MNC2 samples show lower surface areas than those observed for maghemite γ-Fe_2O_3 (62 m^2/g) due to the presence of Nafion chains, which influence the growth of maghemite particles filling the surface irregularity of maghemite nanoparticles. Moreover, the MNC2 sample obtained using Nafion SAC-13 shows a smaller particle diameter than the MNC1 sample prepared using Nafion117.

This size difference could be explained by the peculiar characteristic of Nafion SAC-13, which is a nanocomposite of Nafion with 20-30% wt. of porous silica. Nafion SAC-13 is characterized by pores with a diameter of about 10 nm and a volume of 0.6 mL/g. These nano-pores can influence particle growth leading to a smaller size.

It is remarkable that both MNC1 and MNC2 nanocomposites have a narrow size distribution characterized by an average diameter of 6.1 nm and 3.3 nm, respectively (see Figure1).

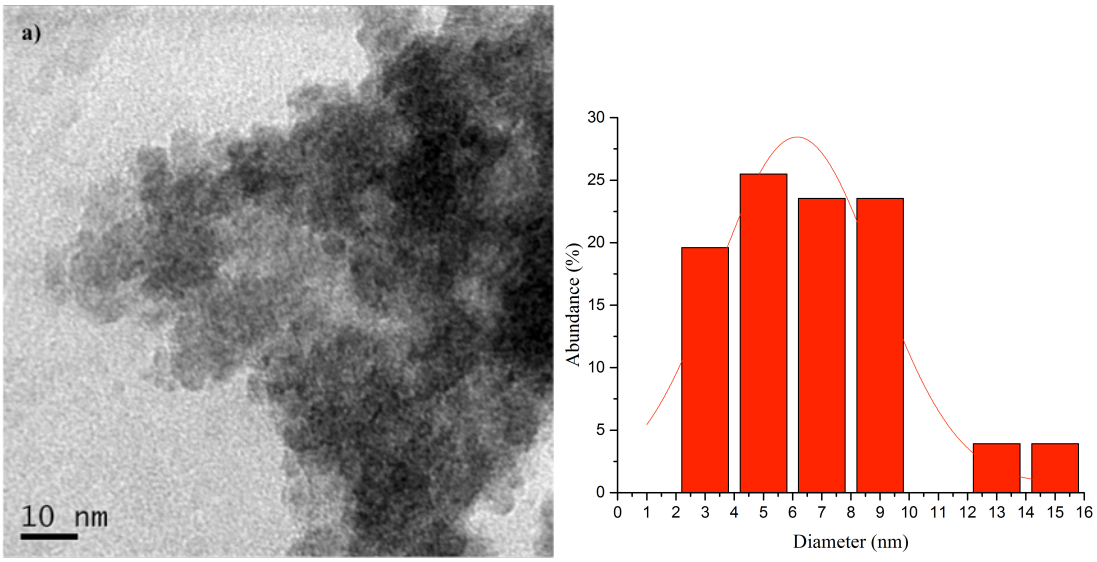

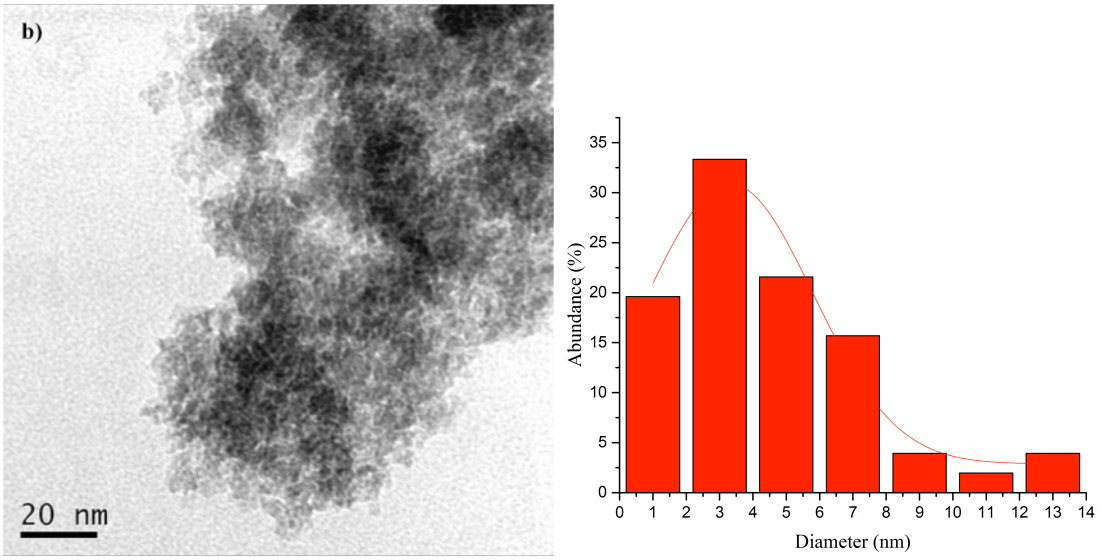

Figure 1 TEM micrographs and size distribution of samples: a) MNC1 obtained using Nafion117 and b) MNC2 prepared using Nafion SAC-13

The structural nature of the iron oxide phase was investigated by FT-IR and XRD analysis.

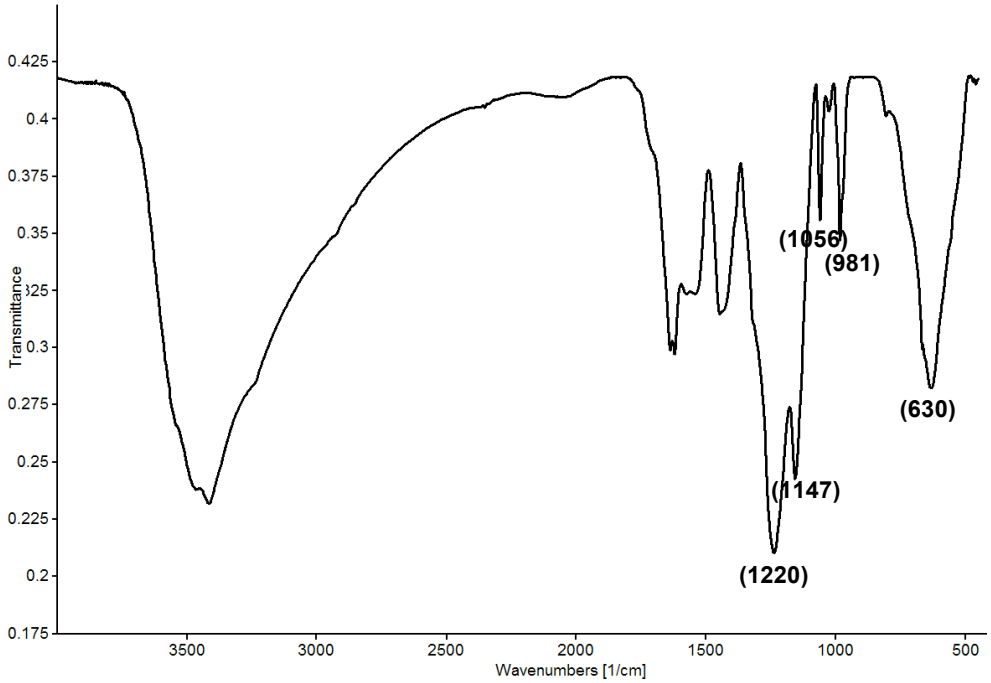

Figure 2 FT-IR spectrum of sample MC1, magnetite/Nafio117 nanocomposite

The FT-IR spectrum of sample MNC1 reported in Figure 2 shows strong peaks at 1220 1/cm and 1147 1/cm ascribable to C-F stretching of CF_2 groups, a strong peak at 1056 1/cm due to S-O stretching of the SO_3 group and the band around 981 1/cm which corresponds to C-O-C stretching. All these peaks are ascribable to the diverse functional

groups present in Nafion 117 chains, in agreement with literature[30]. Moreover sample MNC1 displays the typical band of the maghemite phase at 630 1/cm, the peaks around 1400 1/cm ascribable to acetate trace and the broad band around 3300 1/cm due to the O-H stretching of water and ethanol trapped in the nanoparticle structure.

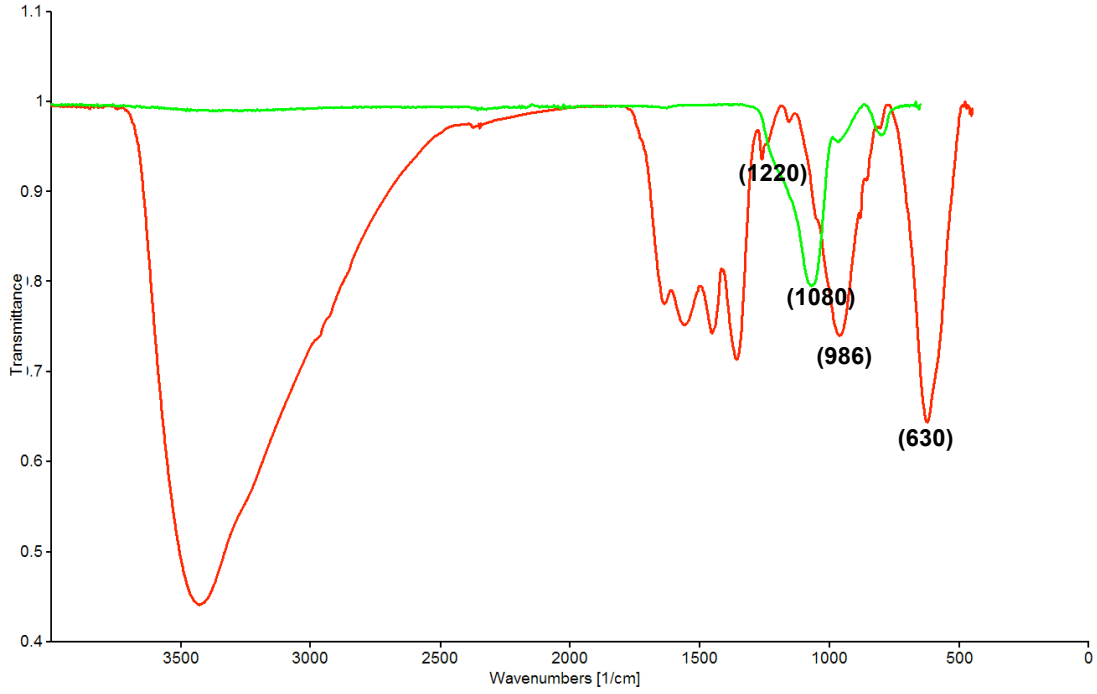

Figure 3 Comparison between the FT-IR spectra of Nafion SAC-13 and MNC2 sample

The comparison between the FT-IR spectra of Nafion SAC-13 (green line) and sample MNC2 (red line) is reported in Figure 3.

The big multiple peaks between 1200 1/cm and 945 1/cm of Si-O-Si stretching ascribable to the silica present in Nafion SAC-13 is clearly visible in both Nafion SAC-13 (green line) and MNC2 (red line) spectra.[31] In the MNC2 spectrum, the peak due to the silica has shifted slightly compared to the ones observed for pure Nafion SAC-13 highlighting the strong interactions between maghemite and Nafion SAC-13. Moreover, in both these spectra it was not possible to appreciate the C-F peaks due to the presence of the strong silica peak. The spectrum of the MNC2 sample shows the strong band at 630 1/cm typical of the Fe-O stretching of maghemite, the peaks around 1400 due to the presence of acetate trace and the broad band at 3300 1/cm due to the water and ethanol trapped in the sample structure.

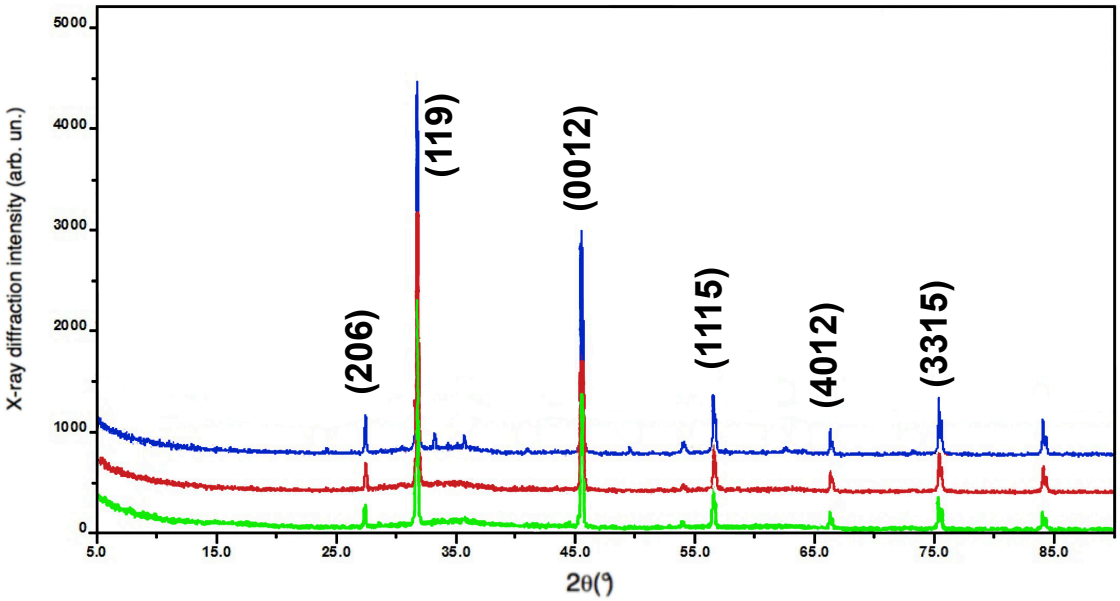

Figure 4 XRD diffractograms of MNC1 sample, magnemite/Nafiion 117 nanocomposite in red, MNC2 sample , maghemite/Nafion SAC-13 in blue and maghemite in green

Figure 4 reports the collected X-ray powder diffraction patterns of MNC1 (red line), MNC2 (blue line) and maghemite (green line) samples. These diffractograms present broad peaks due to the polycrystalline nature of these samples as confirmed also by the TEM analysis displayed in Figure 1.

The patterns observed for all these samples can be indexed as Miller indexes of γ-Fe_2O_3 maghemite like structure (206), (009), (119), (0012), (1115), (4012), (3315) confirming the identification of the maghemite as a magnetic iron oxide phase.

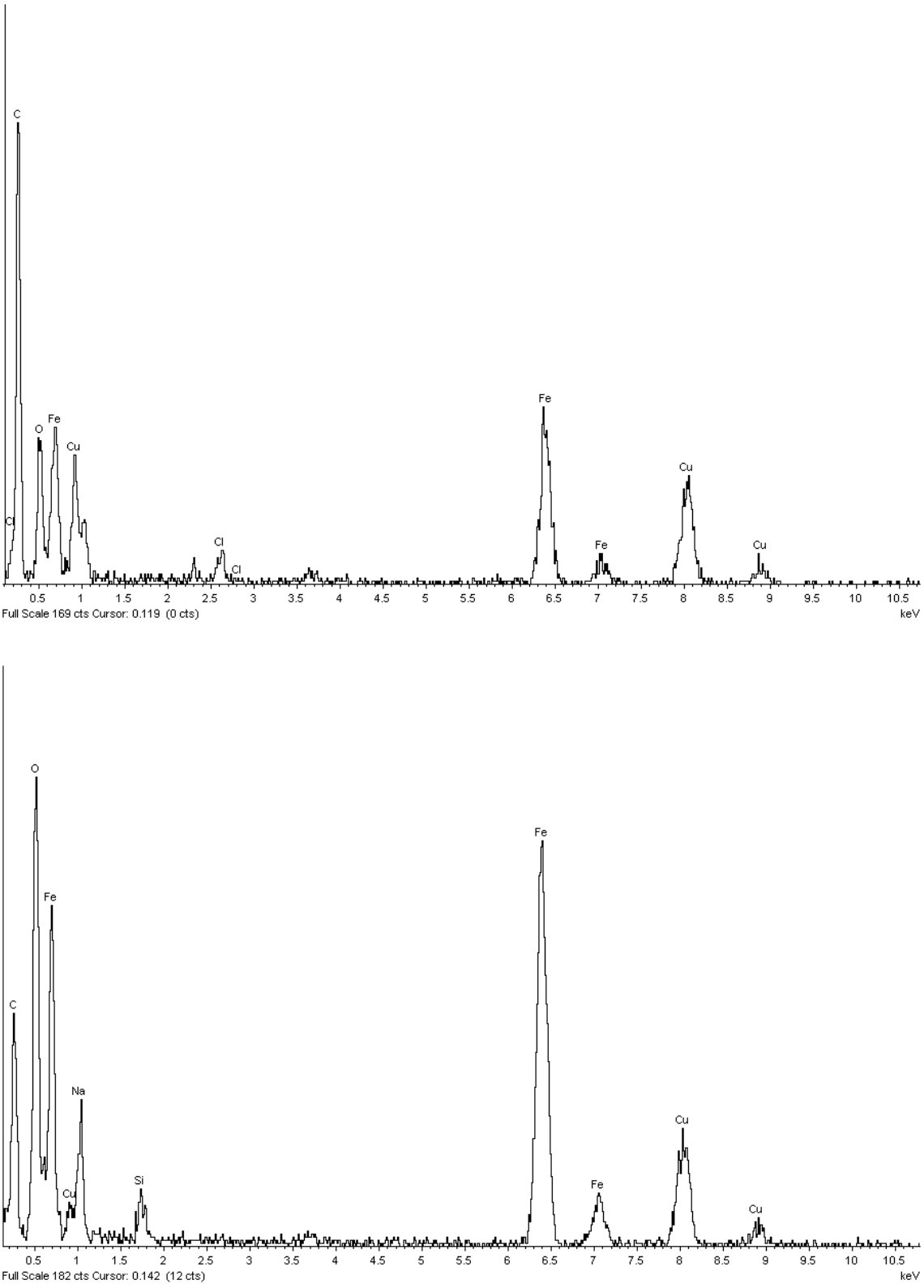

Figure 5 AES analysis of samples: a) MNC1 obtained using Nafion117 and b) MNC2 prepared using Nafion SAC-13

The presence of Nafion chains in MNC1 and MNC2 samples was confirmed also by elemental analysis, which shows a strong carbon signal (see Figure 5). Sample MNC1

also presents the signals of chlorine, an impurity introduced with the iron precursor and not completely removed.

Conversely, the MNC2 sample shows the characteristic signal of silica due to the presence of Nafion SAC-13.

In conclusion, the precipitate procedure permits the preparation of magnetic nanocomposite materials characterized by strong acidic functional groups and by the presence of maghemite as unique iron oxide.

7.2 Synthesis of magnetic nanocomposites: the microwave assisted hydrothermal approach

Diverse biocompatible magnetic nanocomposites were prepared following the new hydrothermal procedure described in Chapter 4.2. These nanocomposites are characterized by a core-shell structure and they can be applied in the biomedical field or the technological industry for polymeric smart materials.

The MNCs show a magnetic core composed of a magnetite nanocrystals and a polymeric biocompatible shell. The polymer shells were selected for their sustainability and biocompatibility (polyvinyl alcohol, polyvinylpirrolidone and alginate).

In a typical preparation, iron acetate $Fe(OAc)_2$ (1g) and the selected polymer were dispersed in ethanol 96% wt. (44ml) and treated by multimode microwave (MARS6 equipped with 6 Teflon vessels) at 150°C for 15 minutes. Finally, nanoparticles were collected using an external magnet, dried and characterized.

This method was employed to prepare different types of nanocomposites, which are summarized in table 2.

Table 2 Magnetic nanocomposite characteristics

Samples	Composition	Diameter (nm)	σDm (nm)	VSM M_0 (emu/cm^3)
MNC3	10%Alg-Fe_3O_4	5.2	0.1	20.84
MNC4	10%PVP-Fe_3O_4	13.2	0.2	51.76
MNC5[a]	10%PVA^+-Fe_3O_4	12.7	0.1	34.35
MNC6[b]	10%PVA^--Fe_3O_4	10.6 (16.2)	0.2 (0.3)	17.44

[a] Magnetite nanoparticles functionalized with poly vinyl alcohol characterized by low molecular weight (MW 31000-50000)

[b] Magnetite nanoparticles functionalized with poly vinyl alcohol characterized by high molecular weight (MW 85000-146000)

Sample MNC3 shows a narrow particle size distribution characterized by the smallest diameter (5.2 nm). This result could be due to the complex and bulky structure of alginate, which arranges its chains in microdomain able to control particle growth.

As can be observed in Figure 6, MNC3, MNC4 and MNC5 present a narrow monomodal particle size distribution characterized by an average diameter of 5.2 nm, 13.2 nm and 12.7 nm respectively. Instead, sample MNC6 obtained using polyvinyl alcohol at low molecular weight presents bimodal size distribution characterized by a main particle population with a diameter of 10.6 nm and a small particle population with a diameter of 16.2 nm. This bimodal distribution is similar to the ones observed for pure magnetite; the polyvinyl alcohol at lower molecular weight (MW 31000-50000) probably has shorter chains not able to arrange themselves in a domain enough big to control the particle growth.

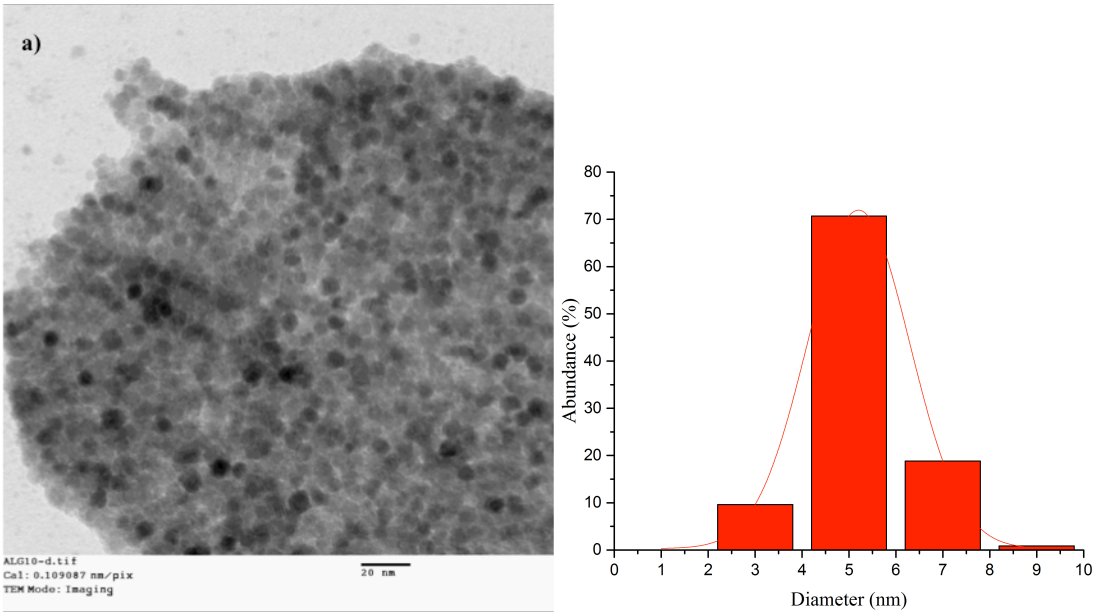

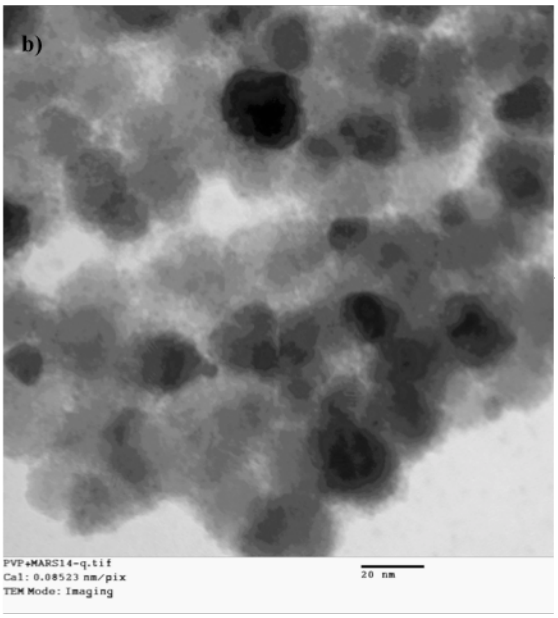
b)
PVP+MARS14-q.tif
Cal: 0.08523 nm/pix
TEM Mode: Imaging
20 nm

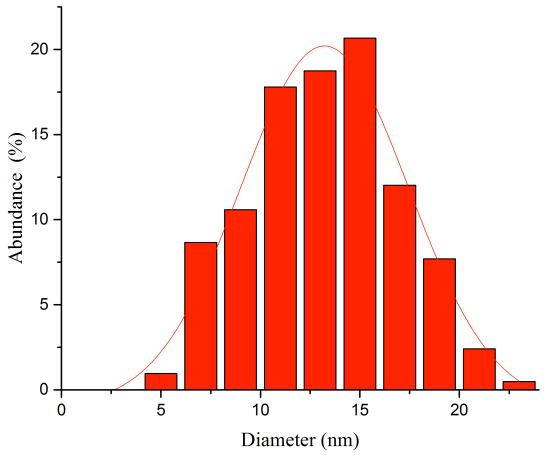
Abundance (%)
Diameter (nm)
0
5
10
15
20

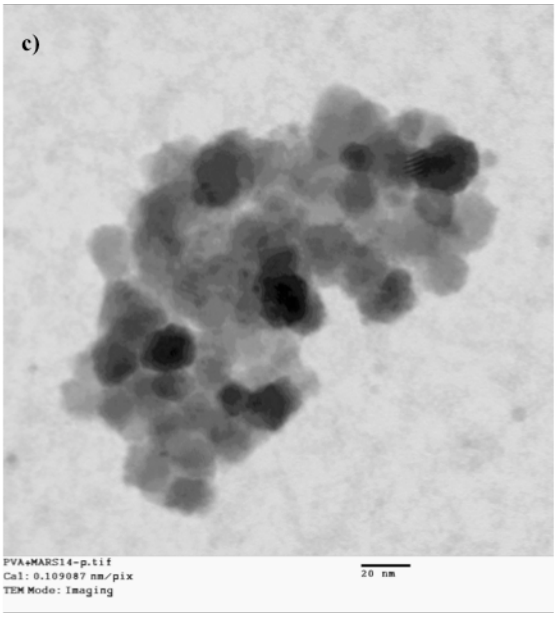
c)
PVA+MARS14-p.tif
Cal: 0.109087 nm/pix
TEM Mode: Imaging
20 nm

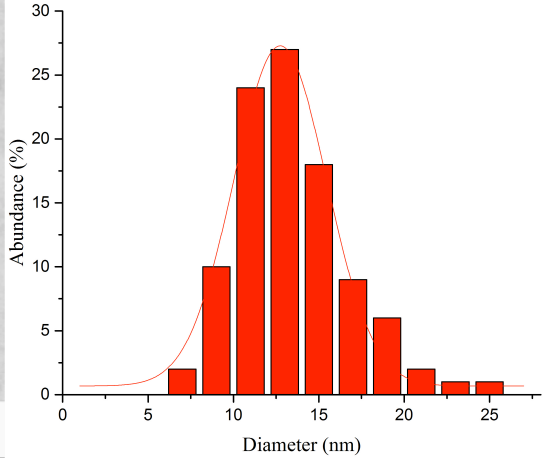
Abundance (%)
Diameter (nm)
0
5
10
15
20
25
30

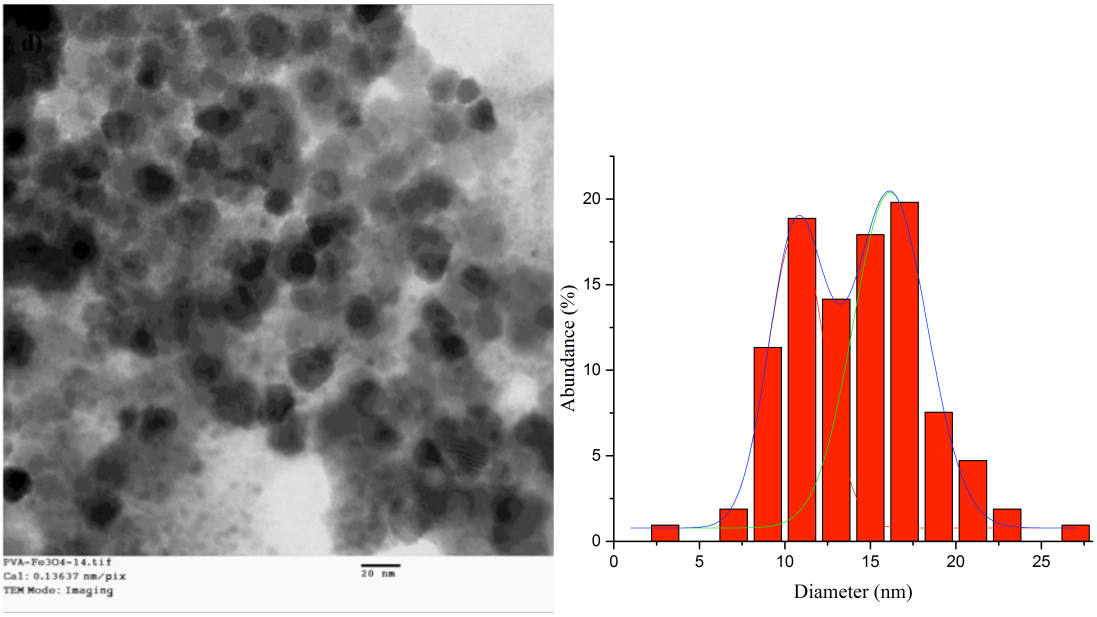

Figure 6 TEM micrographs and particle size distributions of samples: a) alginate magnetic nanocomposites MNC3, b) polyvinylpyrrolidone magnetic nanocomposite MNC4, c) polyvinyl alcohol at higher molecular weight nanocomposite MNC5 and d) polyvinyl alcohol at lower molecular weight nanocompoiste MNC6.

The SEM images of sample MNC3 confirm again the presence of an alginate shell on magnetite surface (see Figure 7).

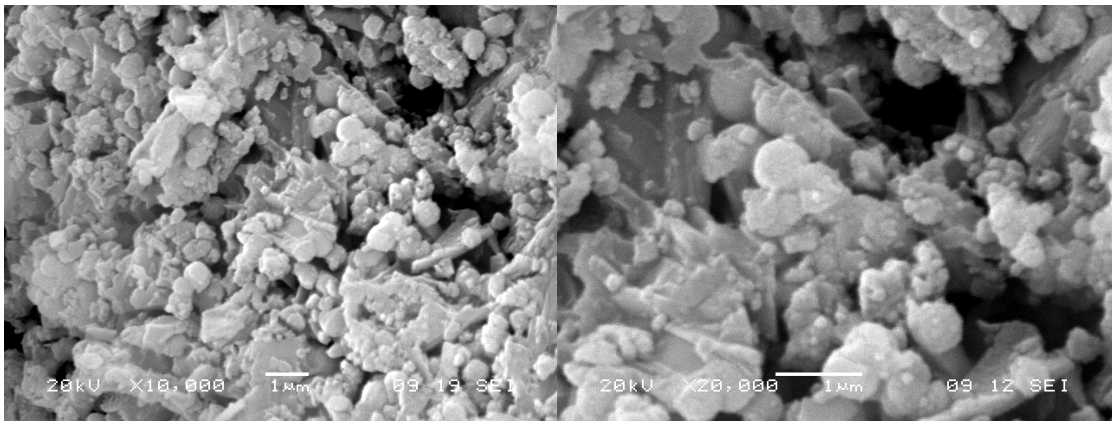

Figure 7 SEM micrographs of alginate magnetic nanocomposite , MNC3.

The Selected Area Electron Diffraction (SAED) rings of samples MNC3, MNC4, MNC5 and MNC6 evidence the high polycrystalline nature of the nanocomposites (see Figure 8).

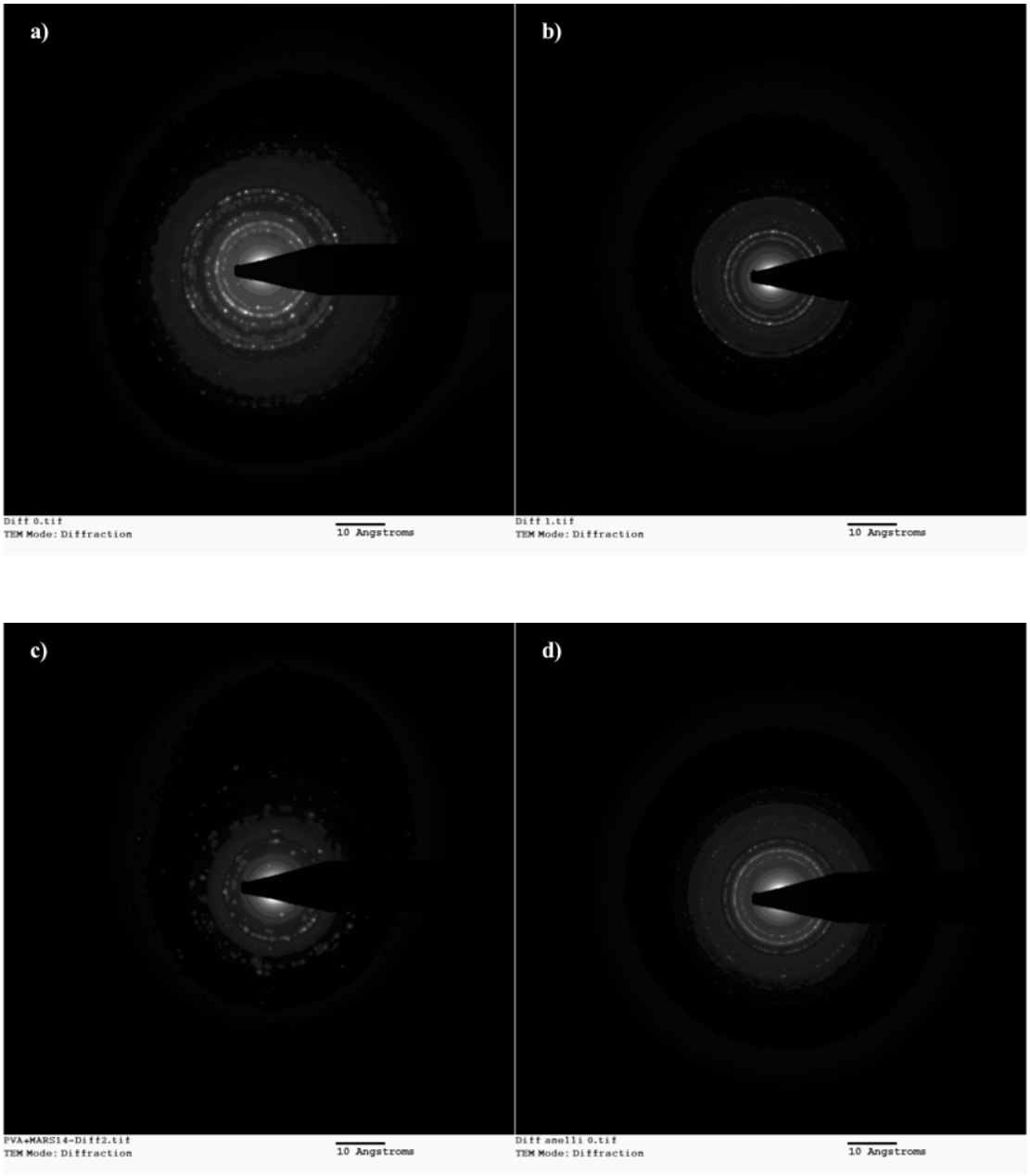

Figure 8 SAED diffraction rings respectively of samples a) alginate magnetic nanocomposites MNC3 b) polyvinylpyrrolidone magnetic nanocomposite MNC4 c) polyvinyl alcohol at higher molecular weight nanocomposite MNC5 and d) polyvinyl alcohol at lower molecular weight nanocompoiste MNC6.

The MNC3, MNC4, MNC5 and MNC6 diffraction patterns can be indexed as Miller indexes of cubic magnetite like structure as confirmed by XRD analysis reported in Figure 12.

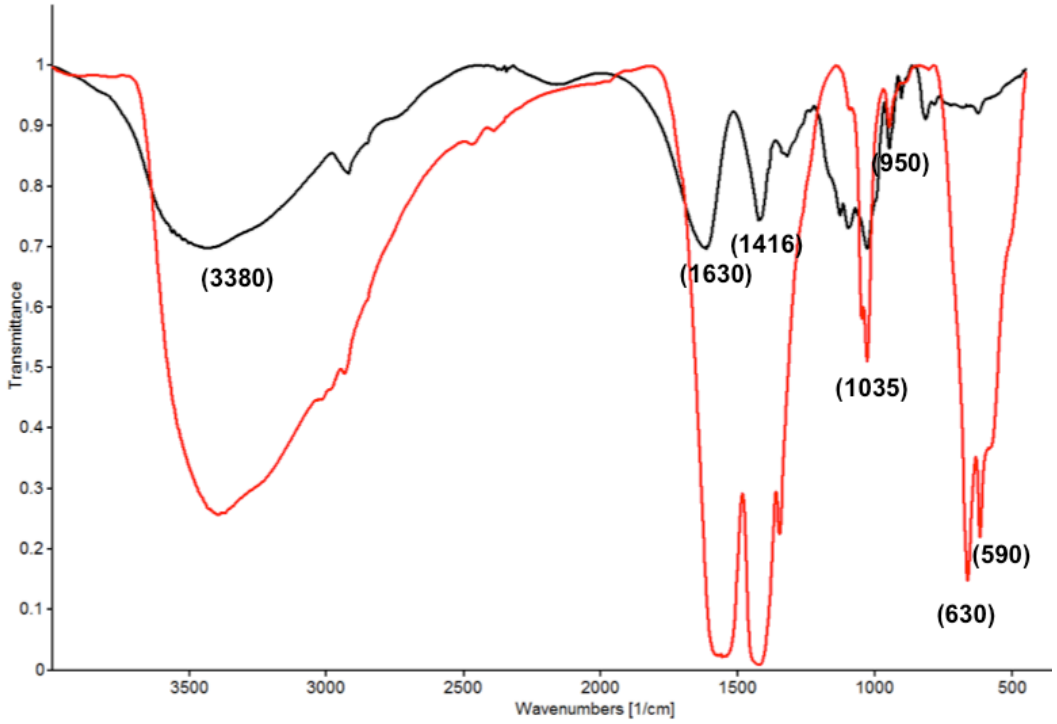

Figure 9 Comparison between FT-IR spectra of alginate in black and alginate magnetic nanocomposites MNC3 sample in red.

The FT-IR spectrum of sodium alginate shows peaks at 950 1/cm and 1035 1/cm due to C-O-C bond stretching. Peaks 1416 1/cm and 1630 1/cm are ascribable to carboxylic groups and 3380 1/cm is caused by the presence of OH groups that are present in alginate chains.[32]As can be observed in Figure 9 the peaks observed in the sodium alginate FT-IR spectrum (black line) are clearly visible also in the alginate magnetic nanocomposite MNC3 sample (red line).

Moreover, MNC3 shows typical magnetite peaks at 590 1/cm and 630 1/cm and big peaks around 1580 1/cm due to acetate trace introduced with an iron precursor.

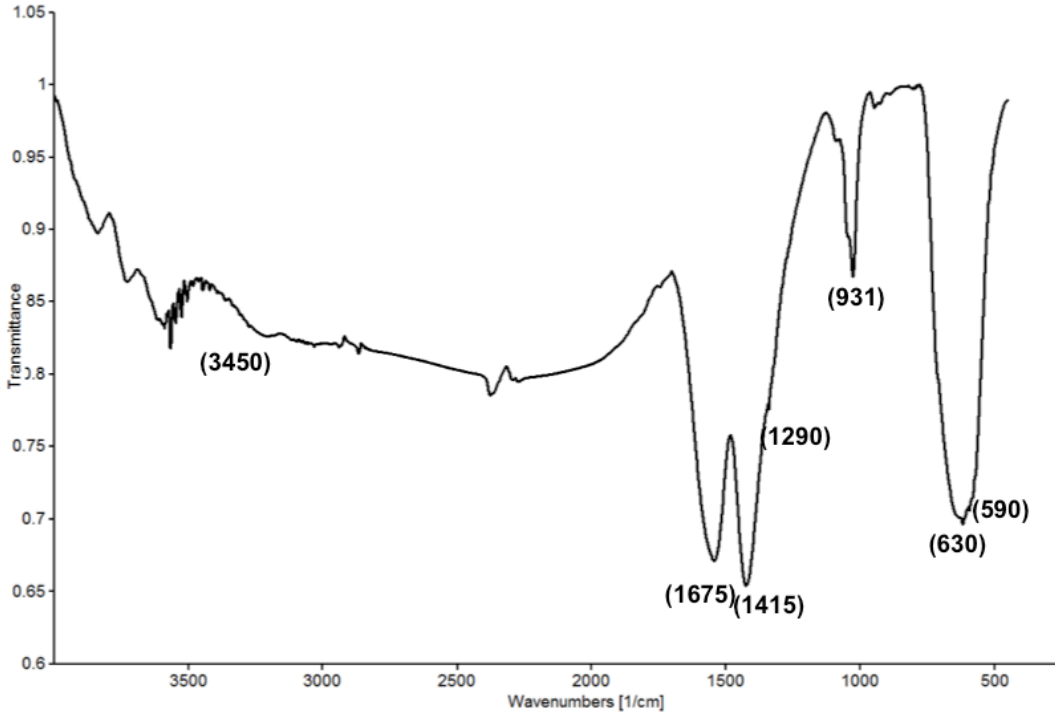

Figure 10 FT-IR spectrum of polyvinylpyrrolidone magnetic nanocomposite MNC4

The MNC4 FT-IR spectrum displayed in Figure 10 shows a narrow peak at 931 1/cm due to C-C bond breathing, a bump at 1290 1/cm due to C-H bending, a big peak at 1415 1/cm ascribable to C-N stretching, the peak at 1675 1/cm due to the C=O and C-N amide stretch and a broad band around 3450 due to O-H vibration. All these peaks can be attributed to polyvinylpyrrolidone chains in agreement with literature. [33]

Moreover, in the MNC3 spectrum big double peaks at 590 1/cm and 630 1/cm due to Fe-O bond of magnetite are clearly visible.

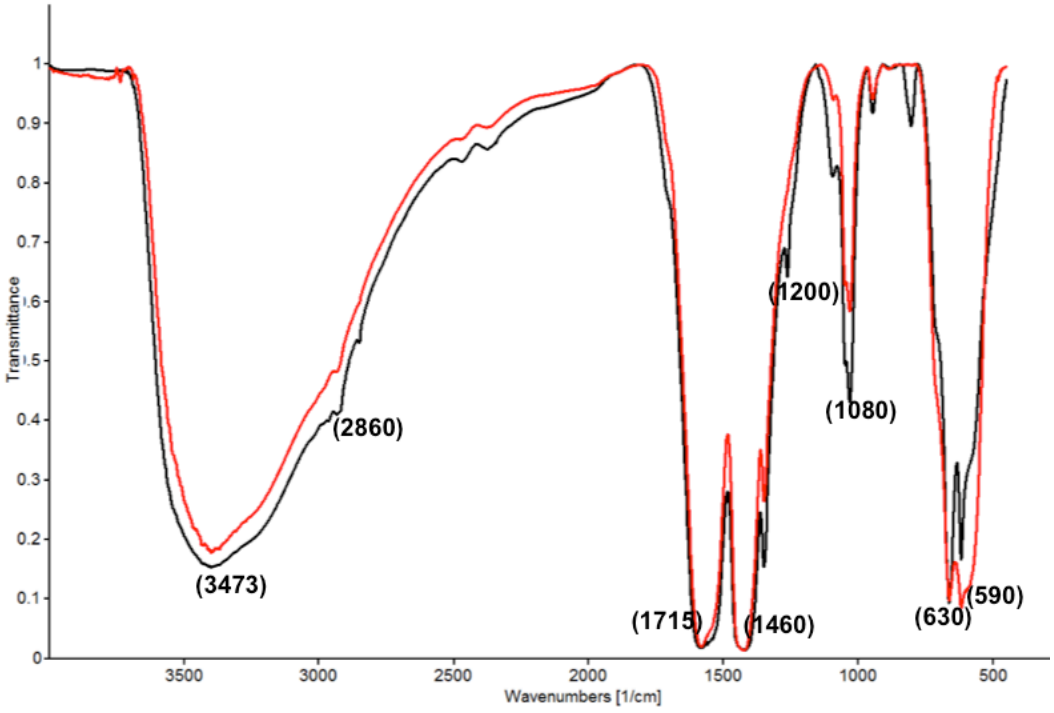

Figure 11 FT-IR spectra of polyvinyl alcohol magnetic nanocomposites samples MNC5 (red line) and MNC6 (black line)

The spectra of MNC5 and MNC6 samples are reported in figure 11, which show the typical signals of polyvinyl alcohol such as the peak of C-O bond vibration at 1080 1/cm, C-O-C stretching at 1200 1/cm, the peak at 1460 due to CH_2 groups , the peak at 1715 typical of C=O stretching, peaks at 2860 1/cm and 2910 1/cm ascribable to C-H and the broad band around 3473 due to O-H stretching .[34]

Furthermore, both MNC5 and MNC6 spectra have peaks at 590 1/cm and 630 1/cm due to Fe-O bond of magnetite.

The magnetite structure of all these nanocomposites was further investigated through XRD analysis.

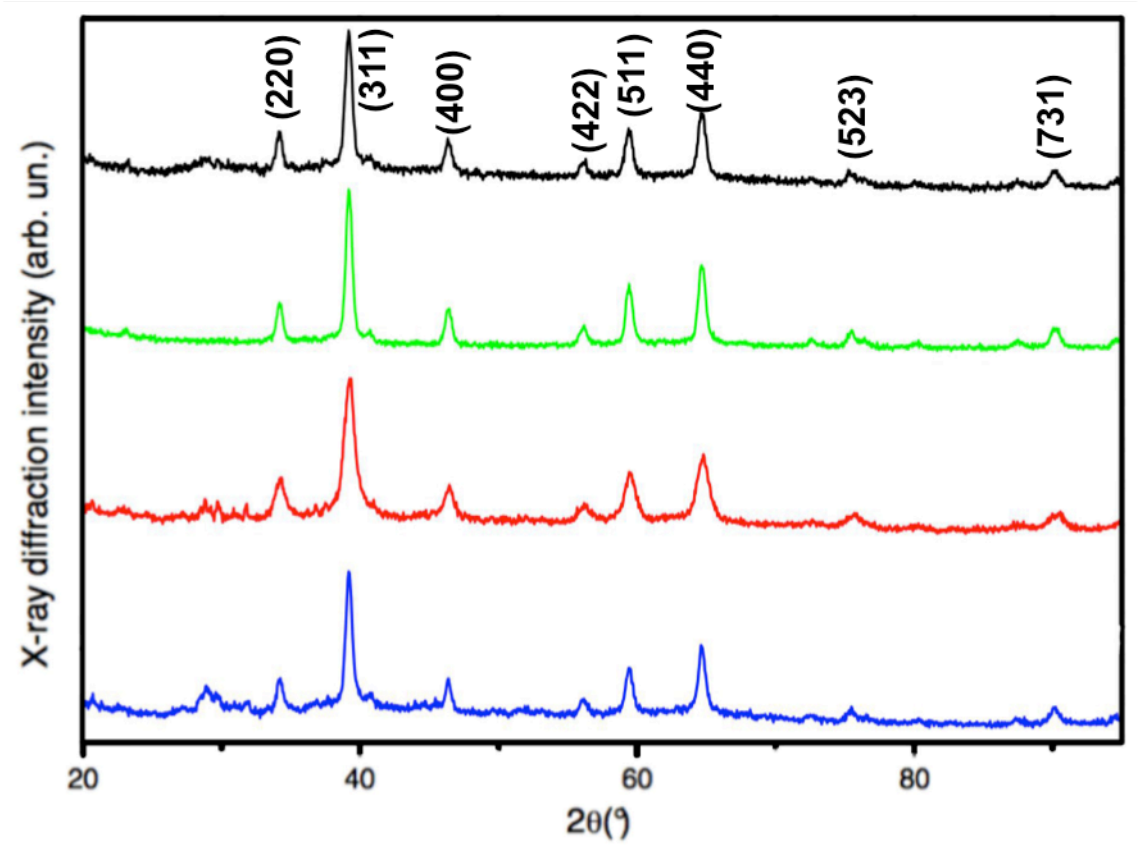

Figure 12 X-Ray Diffractograms of samples: a) alginate magnetic nanocomposites MNC3 (black line) b) polyvinylpyrrolidone magnetic nanocomposite MNC4 (green line) c) polyvinyl alcohol at higher molecular weight nanocomposite MNC5 (red line) and d) polyvinyl alcohol at lower molecular weight nanocompoiste MNC6 (blue line).

The X-ray diffraction peaks collected for sample MNC3 (black line), MNC4 (green line), MNC5 (red line) and MNC6 (blue line) can be indexed by the Miller indexes of the cubic Fe_3O_4 magnetite-like structure (220), (311), (222), (400), (422) (511), (440), (620), (533) and (622) (see Figure 12). For this reason, the samples under investigation can be considered pure polycrystalline materials with magnetite structure as observed from the SAED analysis (see Figure 8). The calculated lattice parameters are (8.381(1) Å), (8.378(1) Å), (8.370(1) Å) and (8.379(1) Å) respectively and microstrain of (0.00179), (0.000201), (0.00234) and (0.00084) respectively. It is remarkable that sample MNC4 obtained using polyvinylpyrrolidone is composed of magnetite particles characterized by a smaller size and higher crystallinity degree as confirmed by its lower microstrain.

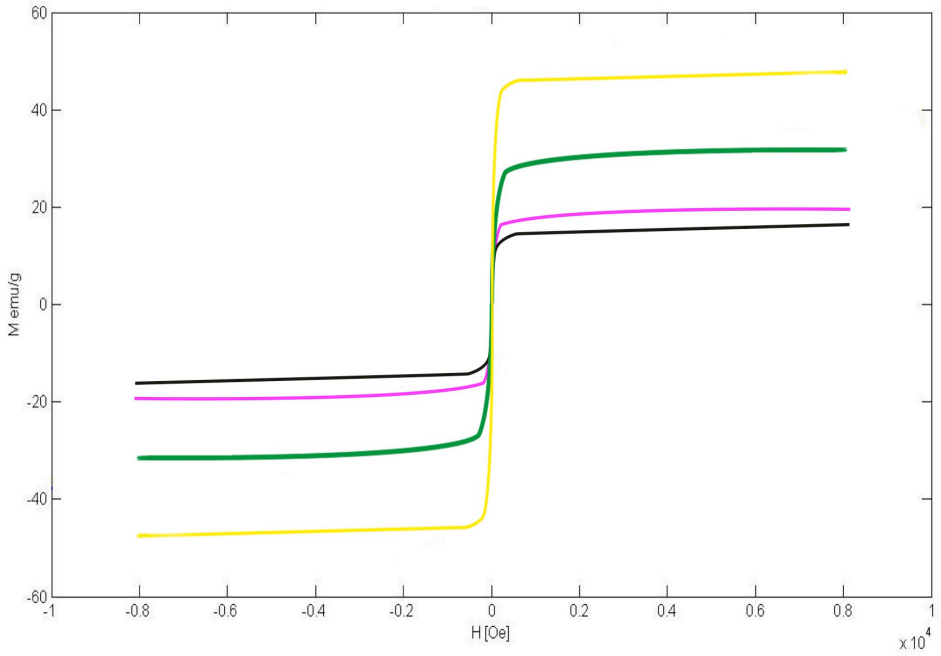

Figure 13 Magnetic curves of samples: a) Alginate magnetic nanocomposites MNC3 (pink line), b) polyvinylpyrrolidone magnetic nanocomposites MNC4 (yellow line), c) polyvinyl alcohol at higher molecular weight (green line) and d) polyvinyl alcohol at lower molecular weight (black line).

The magnetic curves of samples MNC3, MNC4, MNC5 and MNC6 shown in Figure 13 do not present any hysteresis, which indicated that the nanoparticles are superparamagnetic according to literature.[10]

It is noteworthy that MNC3, MNC4, MNC5 and MNC6 samples have bigger magnetic saturation than those observed for pure magnetite prepared at the same conditions (16.74 emu/g), in fact the introduction of a polymeric shell around magnetite particles generally decreases their magnetic behaviour (see Table 2). This surprising result could be due to more controlled crystal growth reached in the presence of the polymeric chains. Moreover the polyvinylpyrrolidone magnetic nanocomposite (sample MNC4) has higher magnetic saturation due to its higher crystallinity as observed by XRD and SAED analysis reported in Figures 8 and 12.

7.2 References

[1] a) A. Joshi, S. Solanki, R. Chaudhari, D. Bahadur, M. Aslam and R. Srivastava, *Acta Biomaterialia* **2011**, *7*, 3955-3963; b) C.-R. Lin, R.-K. Chiang, J.-S. Wang and T.-W. Sung, *Journal of Applied Physics* **2006**, *99*, 08N710.

[2] C. Wang, H. Xu, C. Liang, Y. Liu, Z. Li, G. Yang, L. Cheng, Y. Li and Z. Liu, *ACS Nano* **2013**, *7*, 6782-6795.
[3] N. Işıklan and G. Küçükbalcı, *European Journal of Pharmaceutics and Biopharmaceutics* **2012**, *82*, 316-331.
[4] P. Tartaj, M. P. Morales, T. Gonzalez-Carreño, S. Veintemillas-Verdaguer and C. J. Serna, *Advanced Materials* **2011**, *23*, 5243-5249.
[5] M. Singh, H. M. Haverinen, P. Dhagat and G. E. Jabbour, *Advanced Materials* **2010**, *22*, 673-685.
[6] H. Wang and J. A. Turner, *Journal of Power Sources* **2004**, *128*, 193-200.
[7] C. S. Gill, B. A. Price and C. W. Jones, *Journal of Catalysis* **2007**, *251*, 145-152.
[8] K. Suri, S. Annapoorni, A. K. Sarkar and R. P. Tandon, *Sensors and Actuators B: Chemical* **2002**, *81*, 277-282.
[9] T. Phenrat, N. Saleh, K. Sirk, R. D. Tilton and G. V. Lowry, *Environmental Science & Technology* **2007**, *41*, 284-290.
[10] H.-l. Ma, X.-r. Qi, Y. Maitani and T. Nagai, *International Journal of Pharmaceutics* **2007**, *333*, 177-186.
[11] a) A.-F. Ngomsik, A. Bee, J.-M. Siaugue, V. Cabuil and G. Cote, *Water Research* **2006**, *40*, 1848-1856; b) A. Idris, N. S. M. Ismail, N. Hassan, E. Misran and A.-F. Ngomsik, *Journal of Industrial and Engineering Chemistry* **2012**, *18*, 1582-1589.
[12] S. Keshavarz, Y. Xu, S. Hrdy, C. Lemley, T. Mewes and Y. Bao, *Magnetics, IEEE Transactions on* **2010**, *46*, 1541-1543.
[13] H. Zhang, X. Zhong, J.-J. Xu and H.-Y. Chen, *Langmuir* **2008**, *24*, 13748-13752.
[14] a) S. Gao, Y. Shi, S. Zhang, K. Jiang, S. Yang, Z. Li and E. Takayama-Muromachi, *The Journal of Physical Chemistry C* **2008**, *112*, 10398-10401; b) K. L. Chen, S. E. Mylon and M. Elimelech, *Langmuir* **2007**, *23*, 5920-5928.
[15] A. Millan, F. Palacio, A. Falqui, E. Snoeck, V. Serin, A. Bhattacharjee, V. Ksenofontov, P. Gütlich and I. Gilbert, *Acta Materialia* **2007**, *55*, 2201-2209.
[16] A. A. Novakova, E. V. Smirnov and T. S. Gendler, *Journal of Magnetism and Magnetic Materials* **2006**, *300*, e354-e358.
[17] R. Turcu, A. Nan, I. Craciunescu, O. Pana, C. Leostean and S. Macavei, *Journal of Physics: Conference Series* **2009**, *182*, 012081.
[18] Z. Qian, Z. Zhang and Y. Chen, *Journal of Colloid and Interface Science* **2008**, *327*, 354-361.
[19] N. A. D. Burke, H. D. H. Stöver and F. P. Dawson, *Chemistry of Materials* **2002**, *14*, 4752-4761.
[20] a) I. S. Goldstein, H. Pereira, J. L. Pittman, B. A. Strouse and F. P. Scaringelli, *Hydrolysis of cellulose with superconcentrated hydrochloric acid*, **1983**, p. Medium: X; Size: Pages: 17-25; b) R. Rinaldi and F. Schüth, *ChemSusChem* **2009**, *2*, 1096-1107.
[21] a) N. U. Soriano Jr, R. Venditti and D. S. Argyropoulos, *Fuel* **2009**, *88*, 560-565; b) D. Y. C. Leung, X. Wu and M. K. H. Leung, *Applied Energy* **2010**, *87*, 1083-1095.
[22] A. Corma and H. García, *Chemical Reviews* **2003**, *103*, 4307-4366.
[23] M. A. Nasseri, B. Zakerinasab and M. M. Samieadel, *RSC Advances* **2014**, *4*, 41753-41762.
[24] N. V. Jadhav, A. I. Prasad, A. Kumar, R. Mishra, S. Dhara, K. R. Babu, C. L. Prajapat, N. L. Misra, R. S. Ningthoujam, B. N. Pandey and R. K. Vatsa, *Colloids and Surfaces B: Biointerfaces* **2013**, *108*, 158-168.
[25] D.-J. Kim, Y.-K. Lyu, H. N. Choi, I.-H. Min and W.-Y. Lee, *Chemical Communications* **2005**, 2966-2968.
[26] C. Grüttner, S. Rudershausen and J. Teller, *Journal of Magnetism and Magnetic Materials* **2001**, *225*, 1-7.

[27] J.-f. Liu, Z.-s. Zhao and G.-b. Jiang, *Environmental Science & Technology* **2008**, *42*, 6949-6954.
[28] S. Fujii, Y. Cai, J. V. M. Weaver and S. P. Armes, *Journal of the American Chemical Society* **2005**, *127*, 7304-7305.
[29] E. Lam, E. Majid, A. C. W. Leung, J. H. Chong, K. A. Mahmoud and J. H. T. Luong, *ChemSusChem* **2011**, *4*, 535-541.
[30] a) K. Kunimatsu, T. Yoda, D. A. Tryk, H. Uchida and M. Watanabe, *Physical Chemistry Chemical Physics* **2010**, *12*, 621-629; b) J. Liu, H. Wang, S. Cheng and K.-Y. Chan, *Chemical Communications* **2004**, 728-729; c) D. G. Abebe and T. R. Farhat, *Soft Matter* **2010**, *6*, 1325-1335.
[31] H. L. Tang and M. Pan, *The Journal of Physical Chemistry C* **2008**, *112*, 11556-11568.
[32] a) S. A. Pablo, D. Lorena, S. N. Alba, I. A. Javier and N. M. Miriam, *Journal of Encapsulation and Adsorption Sciences* **2011**, *Vol.01No.04*, 8; b) S. Koburger, A. Bannerman, L. M. Grover, F. A. Muller, J. Bowen and J. Z. Paxton, *Biomaterials Science* **2014**, *2*, 41-51; c) X. Q. Xu, H. Shen, J. R. Xu, M. Q. Xie and X. J. Li, *Applied Surface Science* **2006**, *253*, 2158-2164.
[33] a) M. A.-F. Basha, *Polym J* **2010**, *42*, 728-734; b) J. Zhao, Y. Cheng, X. Yan, D. Sun, F. Zhu and Q. Xue, *CrystEngComm* **2012**, *14*, 5879-5885.
[34] A. Singhal, M. Kaur, K. A. Dubey, Y. K. Bhardwaj, D. Jain, C. G. S. Pillai and A. K. Tyagi, *RSC Advances* **2012**, *2*, 7180-7189.

8. SYNTHESIS OF MAGNETIC CARBON NANONOCATALYSTS

Carbon nanostructures find a wide range of applications in different industrial and technological fields thanks to their often unique electrical, chemical and physical properties[1] . These materials are deeply investigated for their application as sensor[2], photovoltaic[3], fuel cell[4], supercapacitor[5], composite [6], gas storage[7] and catalytic materials [8].

Carbon nanomaterials see an increasing interest especially in catalysis due to the fact that metal nanoparticles anchored over nanostructured carbon surfaces exhibit an improved catalytic activity compared with their colloidal dispersion.[9] Despite this positive effect, for liquid-phase reactions, nanostructured catalytic systems are difficult to recover and recycle from the reaction mixture, which affects the sustainability and the cost of the entire catalytic processes. To overcome these limitations, the introduction of magnetic nanoparticles anchored on the surface of carbon nanomaterials is an interesting alternative to solve the recovery and recycling issues connected with the extremely small size of these nanocatalysts.[10] Moreover, magnetic separation is a green process that permits energy, time and solvents to be saved, which paves the way to the industrial application of these nanostructured catalysts.[11]

The synthesis of magnetic carbon nanostructures has been poorly investigated and generally involves two steps, long reaction times, and hazardous reducing agents. The carbon nanostructures are usually impregnated with an iron salt solution and then the adsorbed Fe ions are reduced in the presence of stabilizing agents.[12] For example, Zafour-Hadj-Ziane et Al.[13] described the alkaline precipitation of iron oxide particles over a carbon nanotube surface. Another interesting procedure to obtain a magnetic carbon nanosupport is described by Korneva et Al.[14] in which the carbon nanotube was filled with commercial ferrofluids, obtaining a material characterized by high magnetic saturation.

There are several protocols to support metal nanoparticles over carbon nanostructures: deposition from solutions; self-assembly methods; electro- and electrophoretic deposition and deposition from the gas phase. The final properties and morphology of nanoparticles attached on the surface of carbon nanostructures are strongly influenced by the adopted procedure.

The deposition from solutions is the most common technique and involves the impregnation of the carbon nanostructure surface with a solution of the metal precursor, followed by a reduction step. This reduction step is the crucial point of this preparation and generally involves non eco-friendly, hazardous compounds and long reaction times.
Several methodologies have been reported for the preparation of noble-metal nanoparticles over carbon nanostructures.[15] For example, Deng et al. described the impregnation of carbon nanotubes (CNTs) with a solution of $RuCl_3$ and their subsequent reduction under an H_2 flow.[16] Antonetti et al. reported a wet-impregnation method that involves the use of microwaves an alcohol solution for the reduction of Ru nanoparticles on carbon nanostructures.[17] Yoon and Wai proposed an alternative technique based on the microemulsion template deposition of Ru nanoparticles on the CNT surface.[18]
In this context, and due to the fact that the decoration of carbon nanostructures with magnetic nanoparticles has been poorly investigated, a new greener synthetic procedure to prepare magnetic carbon nanocatalysts was developed. In particular ruthenium and/or magnetite nanoparticles were anchored on diverse carbon nanostructures to investigate their catalytic properties.[19]

8.1 Carbon nanostructures

Carbon is the most abundant element on Earth and it is naturally present under diverse allotropic forms. [20]
At atmospheric pressure, carbon is organized in a graphite structure, which is characterized by a hexagonal arrangement of carbon atoms, hybridized sp^2. At high pressure, instead, carbon can organize itself in diamond tetrahedral structures, where carbon atoms are hybridized sp^3.
Moreover, there are several interesting carbon nanostructured materials characterized by peculiar atom arrangement such as fullerene, black carbon, active carbon, graphene, carbon onion, single-walled carbon nanohorns, nanofibers, nanotube, nanodiamonds etc. Thanks to their unique atomic structures, these allotropes of carbon show surprising mechanical, electrical, optoelectronic, and thermal properties diverse from their bulk counterpart and are extensively investigated for a wide range of industrial and technological applications.

In particular, fullerenes C_{60} was discovered in 1985 by Kroto, Curl and Smalley during the laser vaporization of graphite. Fullerenes, named also buckyballs, have a truncated icosahedron structure characterized by 20 hexagons and 12 pentagons.[21] More recently other interesting fullerene-like structures characterized by a higher carbon atom number organized in hallow spheres or ellipsoids were discovered, such as C_{70}, C_{76}, C_{78}, C_{84} C_{540} etc. (see Figure 1). Fullerene family nanostructures show good conductibility and are classified as semiconductors. These carbon materials find their application in drug delivery and superconductors.[22]

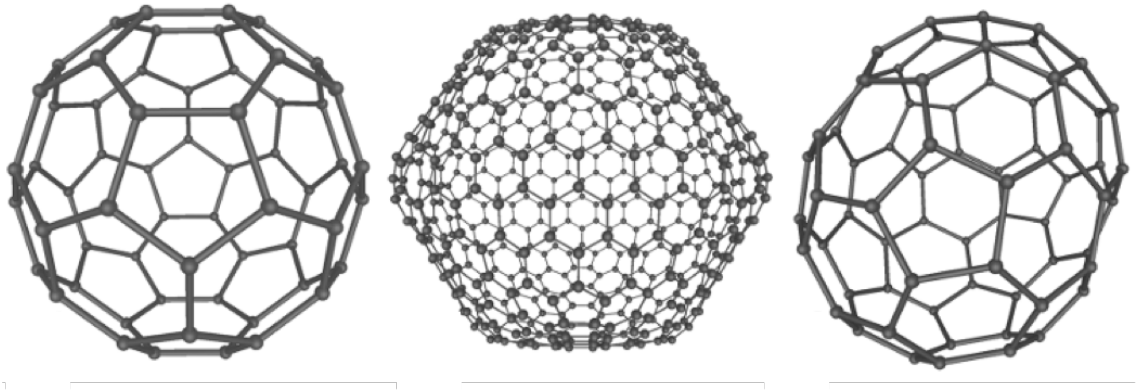

Figure 1 Fullerene structures: C60, C540 and C70 respectively.

Black carbon is a polycrystalline carbon material characterized by a high surface area to volume ratio. It presents atomic structures similar to graphite.[23] Black carbon is generally obtained through partial oxidation of hydrocarbons and thanks to its mechanical properties is commonly employed as a pigment or reinforcing filler for a wide range of polymeric materials.[24]

The activated carbon has an amorphous structure characterized by graphitic domains randomly oriented (see Figure 2). This peculiar arrangement results in high porosity and leads to extraordinary adsorption properties.[25] Activated carbon can be obtained through the pyrolysis of diverse natural carbonaceous materials and the kind of carbonaceous precursor adopted strongly influences the porous structure of activated carbon.[26]

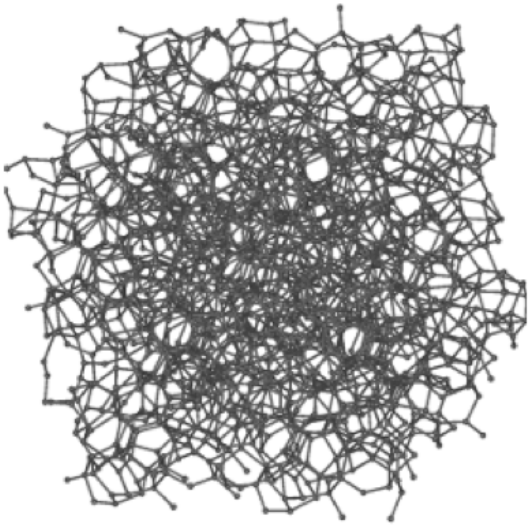

Figure 2 Schematic representation of amorphous activated carbon

Graphene is an interesting 2D carbon nanomaterial discovered in 2010 by Geim and Novoselov. It is composed of a flat monolayer of carbon atoms hybridized sp^2 organized in a regular hexagon (see Figure 3).

Thanks to its structure, graphene presents extraordinary mechanical and electrical properties, if fact it is stronger than steel and can efficiently conduct electricity and heat.[27] Moreover, graphene has a theoretical surface area bigger than nanodiamonds, fullerenes and nanotubes. Graphene is considered the building block for the formation of nanotubes and fullerenes.[28] It is generally prepared by exfoliation, chemical vapour deposition, nanotube slicing and carbon dioxide reduction.

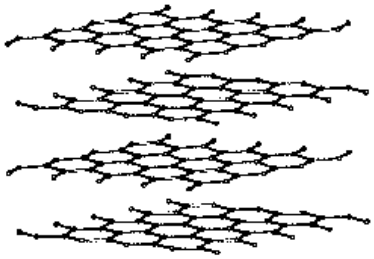

Figure 3 Schematic representation of graphene structure

Carbon onions have a complex hierarchical 0D structure where fullerenes are encapsulated one inside the other like onion shells (see Figure 4). It is generally prepared through laser pyrolysis, chemical vapour deposition or electrochemical methods.[29]

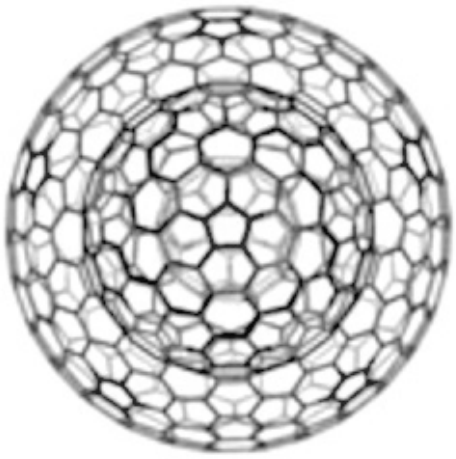

Figure 4 Schematic structure of carbon onion

The single walled nanohorns (SWNHs) are 1D nanomaterials with an irregular and unique graphene form characterized by a diameter between 2-5 nm, a length of about 30-50 nm and a conic tip as shown in Figure 5. This peculiar carbon nanostructure can be synthetized by arc discharge or laser pyrolysis of graphite. Single walled nanohorns are employed in diverse technological and biotechnological fields such as drug delivery, hydrogen and methane storage and sensors.[30]



Figure 5 Schematic structures of single walled nanohorns

Carbon nanofibers are 1D nanomaterial with a regular structure composed of diverse graphene planes equally oriented. On the basis of the graphene plane orientation it is possible to divide the nanofibers into three classes, such as fishbone type, platelet type and ribbon type (see Figure 6).[31] It is remarkable that all these structures show diverse mechanical and electrical properties. Carbon nanofibers are commonly employed as reinforcing filler for automotive materials.[32]

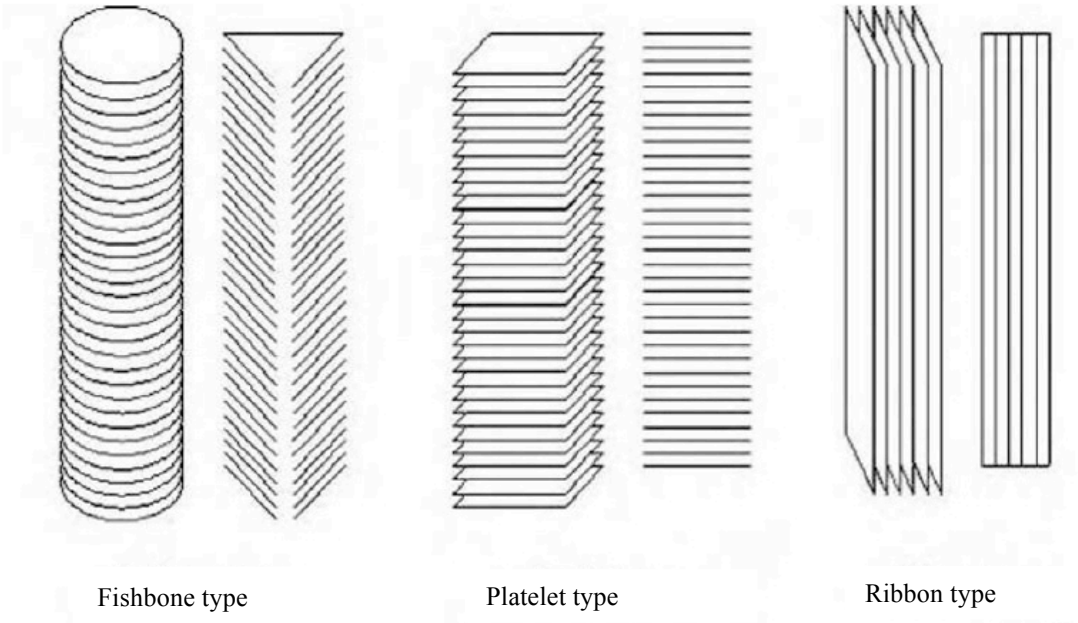

Figure 6 Classification of the diverse fibre structures

Carbon nanotubes are 1D cylindrical carbon structures formed by one or more rolled graphene planes. Carbon nanotubes can be classified in a single-walled nanotube (SWCNT) if composed of a single rolled graphene layer or a multi-walled nanotube (MWCNT), if composed of numerous graphene layers (see Figure 7).

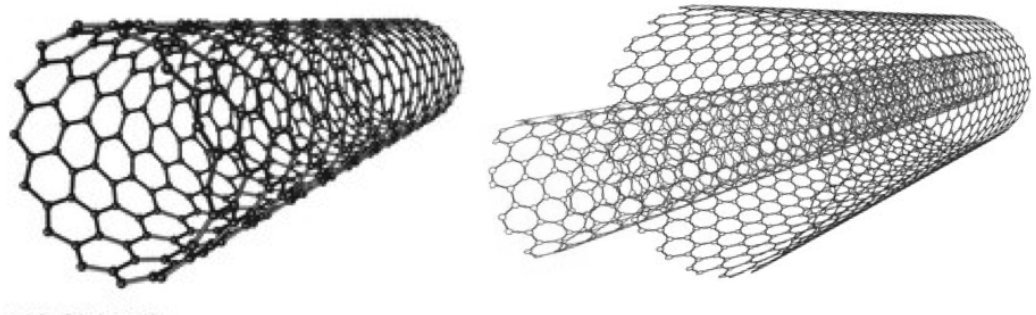

Figure 7 Schematic structures of single wall nanotube and multi wall nanotube

The carbon nanotubes present a hybrid structure between the graphite and the diamante ones. It is possible to distinguish three diverse nanotube types on the basis of carbon

atom arrangements. In particular when the angle of the graphene sheet enrolment θ is 30°, nanotubes are classified as armchair, whereas when θ is 0° as zigzag and finally, when the θ angle is between 0° and 30° as chiral (see Figure 8). The final atom arrangements strongly influence the electrical mechanical and thermal nanotube properties. In fact the armchair type nanotube presents a metallic behaviour whereas the zigzag and chiral type nanotubes present a semiconductor behaviour.[33] These carbon nanostructures are generally prepared through arc discharge of graphite electrodes, the laser-furnace method or chemical vapour deposition.

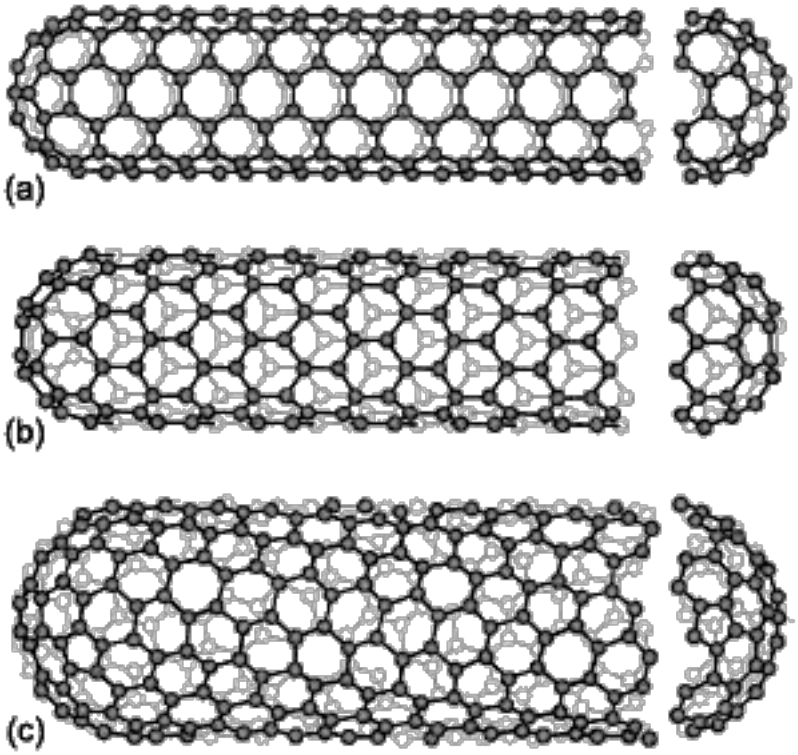

Figure 8 Carbon nanotube types a) armchair b) zigzag and c) chiral

Finally, nanodiamonds are small carbon nanostructures whose dimension is about 4-5 nm (see Figure 9); they are formed by carbon atoms hybridized sp^3 and are classified as 0D nanostructures.

In particular, nanodiamonds are characterized by a high surface area and promising mechanical and optical properties. They present high hardness, elevated Young's modulus, good biocompatibility, high thermal conductivity and electrical resistivity.[34]

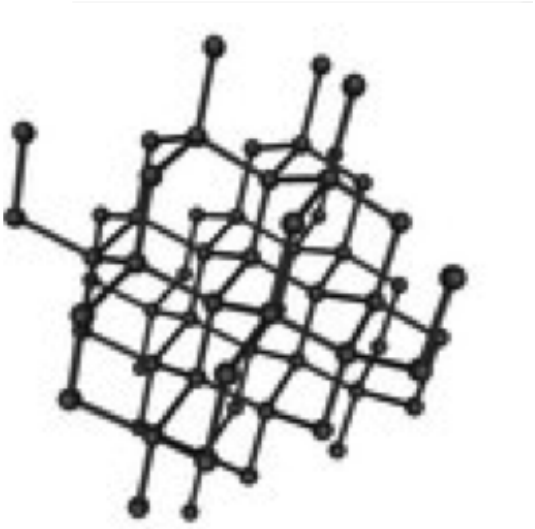

Figure 9 Schematic structures of nanodiamod

Moreover, it is possible to functionalize carbon surface with other heteroatoms to improve and modulate the catalyst dispersion and loading and thus catalytic activity, selectivity and stability. The most common functionalization is the oxidation of the carbon surface, which generates diverse oxygen-containing moieties such as carboxylic acids, phenols, carboxylic anhydrides, ethers, quinones, aldehydes, lactones, pyrones, carbonyls, and lactols. This kind of carbon surface modification generally involves nitric acid and results in the creation of various oxygen-containing surface groups (phenol, carboxylic acid, carbonyl, quinone, anhydride, and lactone), in which carboxylic acid, carboxylic anhydride, and lactone groups play an important role for metal grafting, especially for Ru.[35] Moreover these functional groups are fundamental for the dispersion and stability of carbon nanostructures in polar solvents.[36]

Furthermore, it is possible to modify the carbon surface with other dopant heteroatoms such as B, N, S, F, and P. Among them, N possesses advantages in several aspects, such as a facile doping process and effective modulation of graphitic structure and properties to maintain high electrical conductivity. [37]

For all these aspects and thanks to their outstanding thermal[38], electrical[39], optical[40], and mechanical properties[41], as well as higher specific surface areas, shown in Table 1, carbon nanostructures can be considered suitable candidates to support metal nanocatalysts.

Table 1 Mechanical electrical and thermal characteristics of the main carbon nanostructures

Materials	D. (g/cm^3)	S. area (m^2/g)	Porosity (cm^3/g)	Young module (TPa)	E.R. (Ωcm)	E.C. (S/cm)	T.C. (W//mK)
BC	<2	20-2500	0.001-0.003	***	0.0001	***	***
AC	<2	500-3000	1	***	0.001-1	***	***
G	0.03-0.15	***	***	1	10^{-6}	2000	5000
C_{60}	1.72	1-170	***	0.014	***	2	0.4
FC	0.3-1.4	10-250	0.2-2 (meso)	0.3-0.7	1.5-3	300	1500-2500
SWCNT	0.5-1	400-900	0.15-0.3 (micro)	1.05-1.3	0.0061	550	300-3000
MCWCNT	0.02-0.3	150-450	0.5-2 (meso)	0.5-1.2	0,0006-0,002	80-1000	1000-6000

BC black carbon, AC activated carbon, G graphene, FC carbon fibre, SWCNT single wall carbon nanotube, MWCNT multi wall carbon nanotube, D density, S. area Surface area, E. R. electrical resistance, E.C. electrical conductibility, T.C. thermal conductibility.

8.2 Synthesis of mono and bimetallic carbon nanocatalyts by Microwave assisted procedure

The mono and bimetallic carbon nanocatalysts were prepared following a green hydrothermal procedure, developed on the basis of the ones reported in Chapter 4.2.
Adopting these procedures, diverse monometallic and bimetallic carbon nanocatalysts were prepared, in particular ruthenium and/or magnetite nanoparticles were anchored on different carbon nanostructures such as multi walled carbon nanotubes (CNT), graphene oxides (GO), nanodiamonds (Nd) and N doped multi walled carbon nanotubes (N-CNT). Monometallic nanocatalysts were obtained by the decomposition of 0.0785 g of ruthenium acetylacetonate [$Ru(acac)_3$] or 1g of iron acetate [$Fe(OAc)_2$] in 40 mL of isopropanol in the presence of 1 g of the corresponding carbon support (GO, CNT, or

NCNT, Nd) using MW irradiation. The [$Fe(OAc)_2$] precursor can be easily oxidized to give Fe^{III} species by a weak oxidant or traces of oxygen. The partial oxidation of [$Fe(OAc)_2$] to the sole magnetite phase under sonochemical irradiation in the presence of water has been reported.[42] In the presence of commercial isopropanol, which contains water, under MW irradiation, Fe^{II} is oxidized to the sole spinel iron phase magnetite. The presence of the alcohol medium under MW irradiation allows also the partial reduction of [$Ru(acac)_3$] to Ru^0 as described previously.[17]

Bimetallic nanocatalysts (Ru-Fe_3O_4/GO, Ru-Fe_3O_4/CNT, Ru-Fe_3O_4/NCNT and Ru-Fe_3O_4/Nd) were prepared with a two-step procedure: first Fe_3O_4 nanoparticles were prepared by the decomposition of 1 g of [$Fe(OAc)_2$] by MW irradiation in 40 mL of isopropanol in the presence of the respective 1 g pf carbon support. Then the 0.1184 g of [$Ru(acac)_3$] compound was added to the dispersion, which was treated again with MW irradiation to reduce the Ru precursor to ruthenium nanoparticles . The resulting nanocatalysts are summarized in Table1.

Table 2 Metal content, mean size and magnetic saturation vales of mono and bimetallic nanocatalysts

Samples	Diameter Ru (nm)	σD (nm)	Diameter Fe_3O_4 (nm)	σD (nm)	Ms (emu/g)
Ru-GO[a]	2.59	0.07	***	***	***
Ru-CNT[a]	1.56	0.03	***	***	***
Ru-NCNT[a]	2.29	0.09	***	***	***
Ru-Nd[a]	***	***	***	***	***
Fe_3O_4/GO[b]	***	***	3.20 (7.45)	0.32(1.02)	14.02
Fe_3O_4/CNT[b]	***	***	6.09	0.13	34.21
Fe_3O_4/NCNT[b]	***	***	1.76 (3.25)	0.03 (0.07)	53.66
Fe_3O_4/Nd[b]	***	***	***	***	1.34
Ru-Fe_3O_4/GO[c]	1.5	0.1	5.01	0.06	7.32
Ru-Fe_3O_4/CNT[c]	***	***	5.40	0.12	36.45
Ru-Fe_3O_4/NCNT[c]	***	***	2.86	0.05	43.20
Ru-Fe_3O_4/Nd[c]	***	***	***	***	2.68

[a] Reaction conditions: Temperature 180°C, Pressure limit 200 PSI, Power 250W and Time 12 minutes
[b] Reaction conditions: Temperature 120°C, Pressure limit 200 PSI, Power 250W and Time 15 minutes
[c] Reaction conditions: First step :Temperature 120°C, Pressure limit 200 PSI, Power 250W, time 15 minutes and second step: Temperature 180°C, Pressure limit 200 PSI, Power 250W, time 12 minutes

The nature of the support plays an important role on the final characteristics of the catalysts (see Table 2).

Moreover the carbon nanosupports influenced also the final ruthenium and/or iron nanocatalyst loadings, in fact as it is possible to see in Table 3 the carbon nanosystems show different ruthenium and/or iron loadings although they were prepared using the same theoretical amount of metal.

In particular low surface-area graphene oxide stabilizes Ru nanoparticles poorly compared to CNTs and NCNT, as the Ru nanoparticles are bigger (2.58 nm) while the Ru loading is the lowest (0.77% Ru). CNTs better stabilize Ru nanoparticles and provide small nanoparticles on the surface (1.56 nm). The high affinity of Ru for the CNT surface is mainly because of the presence of carboxylic groups created by the oxidation treatment of the CNT surface. [35] These results indicate indirectly that the functional groups able to anchor well Ru nanoparticles are less accessible and/or less abundant on the GO support. The good dispersion obtained on NCNT can be related to the presence of N-containing groups.[43] The diverse functionality degree was also confirmed by the potentiometric titrations of carbon nanostructure, after the acid treatment. [44]

Table 3 ICP analysis of mono and bimetallic carbon nanostructured catalysts

Samples	Ru (%)	Fe(%)	C(%)	H(%)	N(%)
Ru-GO	0.77	***	94.46	0	***
Ru-CNT	1.5	***	91.61	00.1	***
Ru-NCNT	0.91	***	82.16	***	5.68
Ru-Nd	0.33	***	86.99	0.66	***
Fe_3O_4-GO	***	16.36	62.26	1.32	***
Fe_3O_4-CNT	***	15.8	62.97	0.88	***
Fe_3O_4-NCNT	***	10.18	66.32	0.84	4.11
Fe_3O_4-Nd	***	20.91	61.16	1.07	***
Ru-Fe_3O_4/GO	0.58	18.09	79.96	0.12	***
Ru-Fe_3O_4/CNT	1.13	13.54	70.34	0.60	***
Ru-Fe_3O_4/NCNT	1.03	13.6	66.51	0.51	4.15
Ru-Fe_3O_4/Nd	0.55	30.34	59.88	1.31	***

Interestingly, size distribution and Fe loading of the magnetic carbon nanocomposites show that GO stabilizes Fe_3O_4 nanoparticles better than CNTs (see Table 2 and 3). Indeed, the nanoparticles are significantly smaller in Fe_3O_4/GO (3.20 nm) than in Fe_3O_4/CNT (6.09 nm), and the Fe content is the highest on GO (16.36%). These results suggest the existence of different anchoring sites for Fe_3O_4 and Ru. However, NCNT can stabilize very small Fe_3O_4 (1.76 nm) particles. Therefore, the different behaviour of NCNTs compared to CNTs is probably because of the presence of N-containing groups on the CNT surface.[43]

In conclusion, due to the diverse functional groups on the CNT and NCNT surfaces, they show diverse affinity for Ru and Fe_3O_4. In particular, the carboxylic groups present on CNT samples (Ru-CNT, Fe_3O_4/CNT, Ru- Fe_3O_4/CNT) determine higher Ru and Fe_3O_4 loadings than pyridinic, pyrrolitic quaternary and pyrridinic-oxyde groups present in N-doped CNT (samples Ru-NCNT , Fe_3O_4/NCNT, Ru- Fe_3O_4NCNT).

Finally, nanodiamonds show the highest Fe_3O_4 load and the lowest Ru load probably due to the surface functional groups (typically lactones and carboxylic anhydrides). [45]

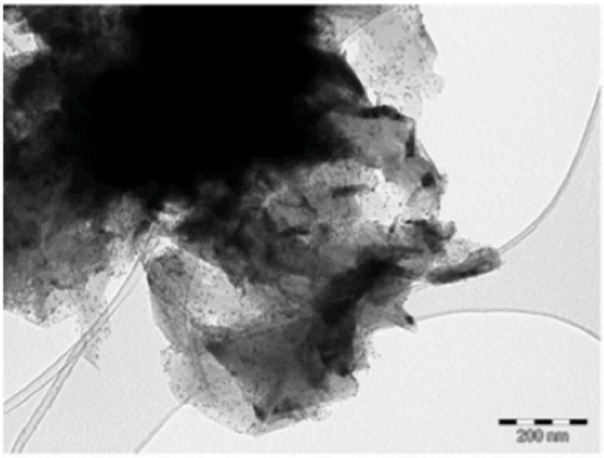
200 nm

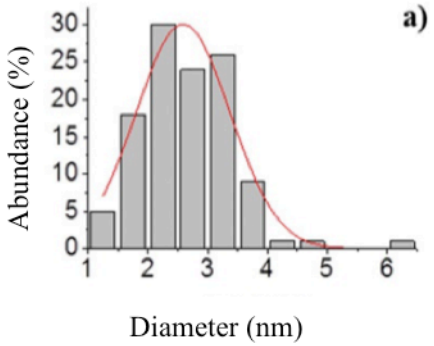
a)
Abundance (%)
Diameter (nm)

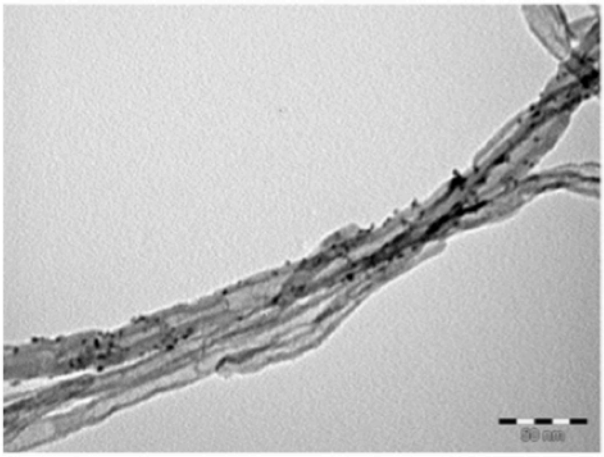

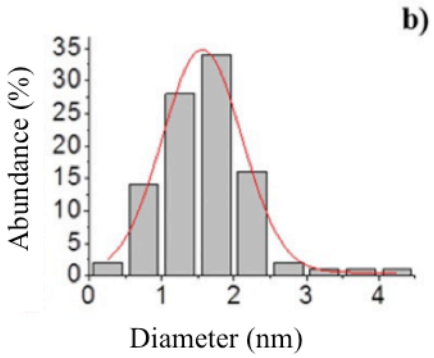
b)
Abundance (%)
Diameter (nm)

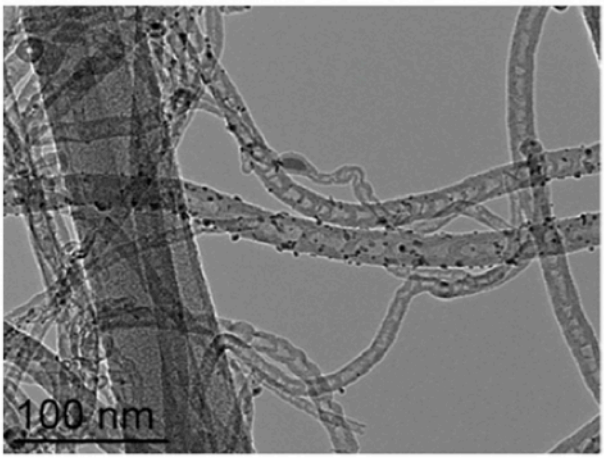
100 nm

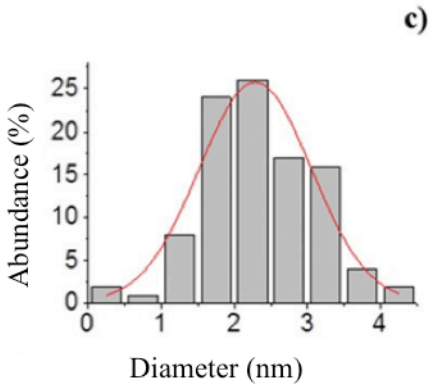
c)
Abundance (%)
Diameter (nm)

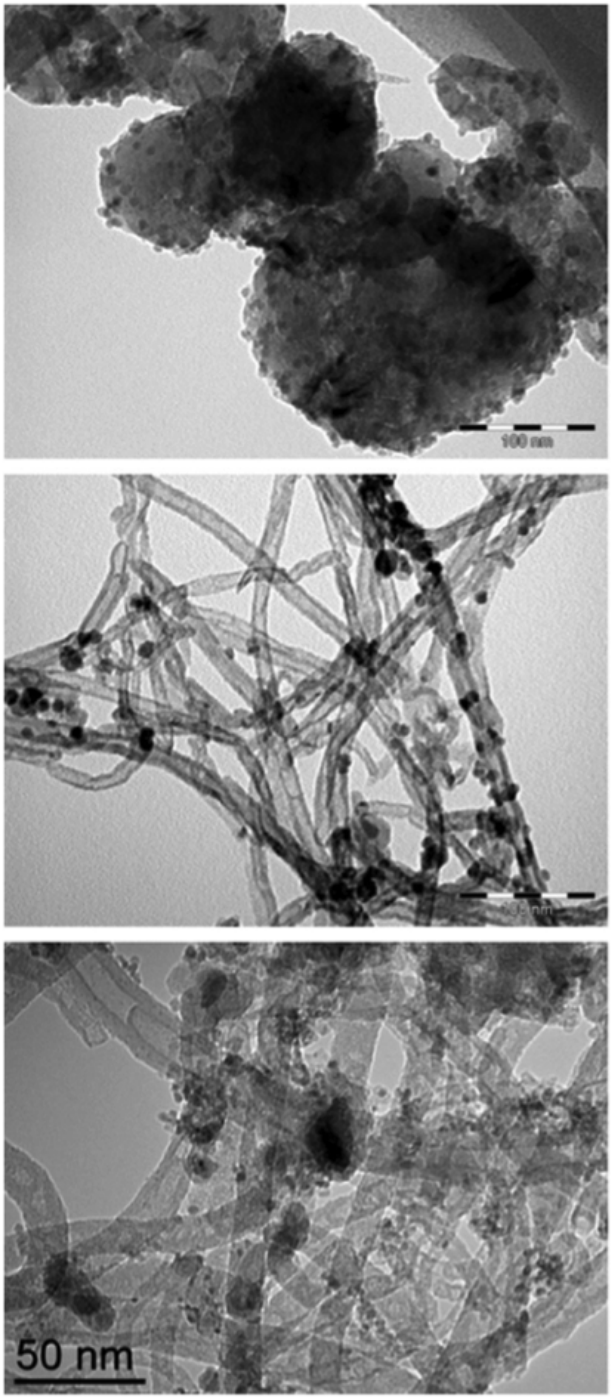
50 nm

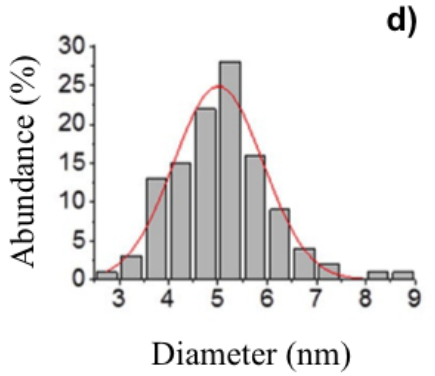
d)
Abundance (%)
Diameter (nm)

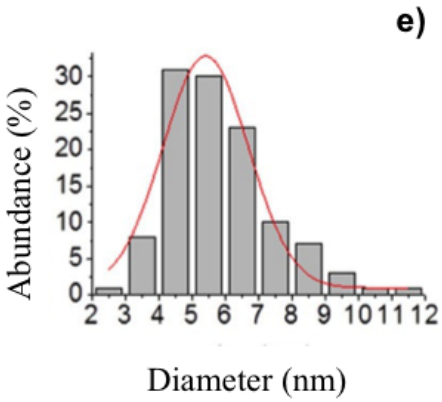
e)
Abundance (%)
Diameter (nm)

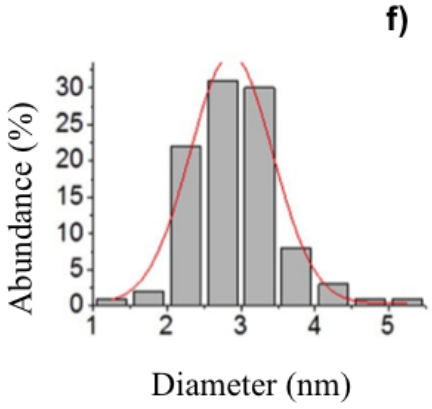
f)
Abundance (%)
Diameter (nm)

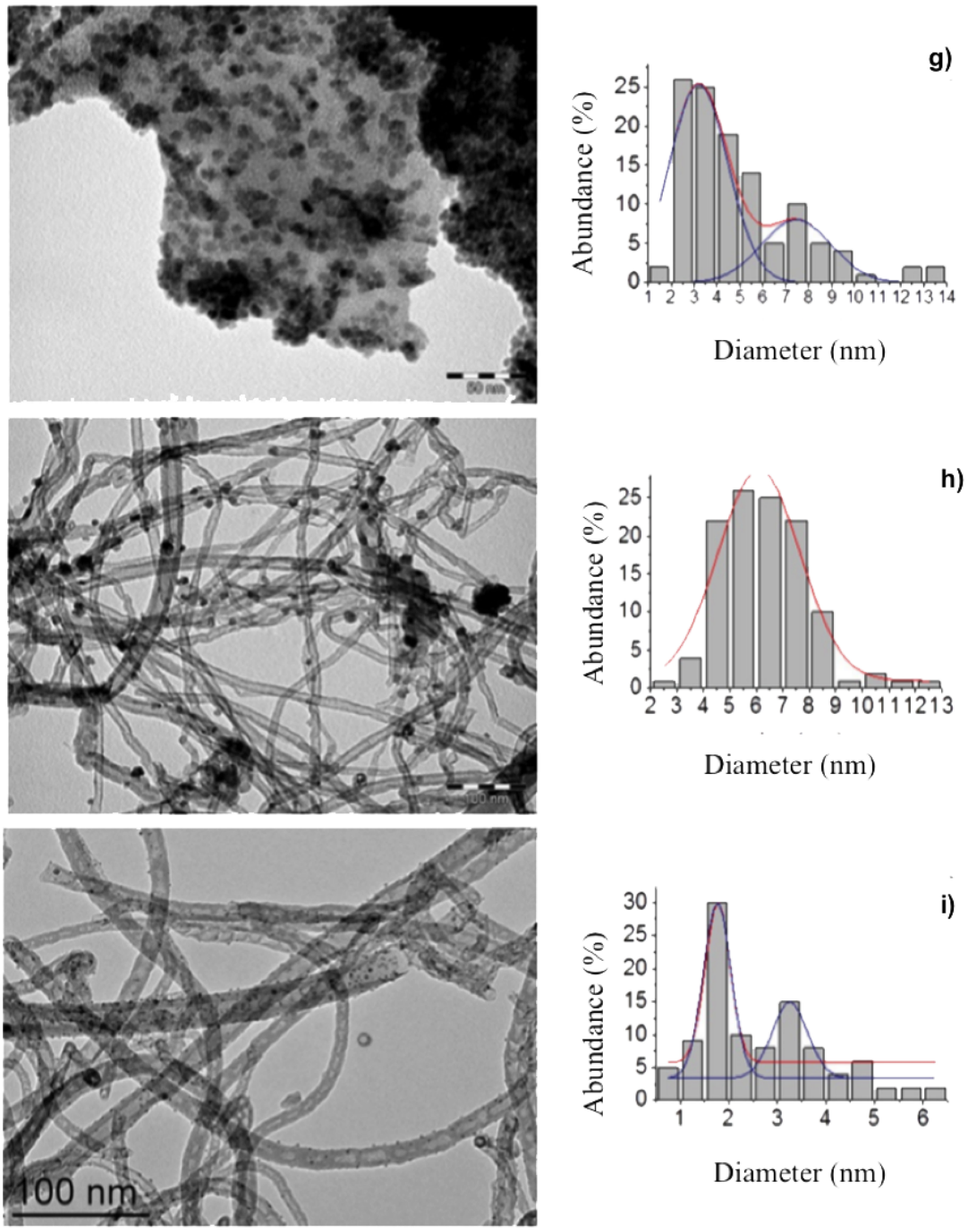

Figure 10 TEM micrographs and particle size distributions a) Graphene oxide supported catalysts, Ru-GO, b) Carbon nanotube supported catalysts, Ru-CNT, c) N doped carbon nanotube supported catalysts, Ru-NCNT, d) Graphene oxide supported catalysts, Ru-Fe_3O_4/GO, e) Carbon nanotube supported catalysts, Fe_3O_4/CNT, f) N doped carbon nanotube supported catalysts, Fe_3O_4/NCNT g) Graphene oxide supported catalysts Ru-Fe_3O_4/GO, h) Carbon nanotube supported catalysts, Ru-Fe_3O_4/CNT and i) N-doped carbon nanotube supported catalysts, Ru-Fe_3O_4/NCNT.

TEM images reported in Figure 10a, b and c show Ru nanoparticles anchored on the surface of the diverse carbon supports. The mean diameters of the Ru nanoparticles are as follows: Ru/FLG 2.59 nm, Ru/CNT 1.56 nm, and Ru/NCNT 2.29 nm, whereas the

TEM images of magnetic monometallic systems show small nanoparticles homogeneously dispersed on the carbon surfaces (Figure 10d, e and f). In particular, on CNT, the particle size distribution is monomodal, centered at 6.09 nm. The nanoparticle size distributions of Fe_3O_4/GO and Fe_3O_4/NCNT are bimodal: Fe_3O_4/GO shows two populations centred at 3.20 and 7.45 nm and Fe_3O_4/NCNT presents two populations centred at 1.76 and 3.25 nm. The different nanoparticle size distributions obtained on NCNT and GO might be due to the presence of two different kinds of sites for adsorption on these supports: more reactive N-doped and less reactive undoped sites for NCNT, which leads to small and large particle sizes, respectively, and poorly reactive basal and more reactive edge sites for GO.

The TEM images of bimetallic samples (Figure 10g, h and i) show that in all samples the nanoparticles were well dispersed on the support with a mean diameter of 5.01 nm for Ru- Fe_3O_4/GO, 5.40 nm for Ru- Fe_3O_4/CNT, and 2.86 nm for Ru- Fe_3O_4/NCNT (Figure 3). It was not possible to distinguish Ru and Fe_3O_4 nanoparticles due to their small size; these mean diameters correspond to both Ru and Fe_3O_4 nanoparticles. Moreover, it was not possible to appreciate the ruthenium or magnetite particle size in nanodiamond supported catalysts (Ru-Nd, Fe_3O_4/Nd,Ru-Fe_3O_4/Nd) due to the small nanodiamond size and the smaller metal particle size.

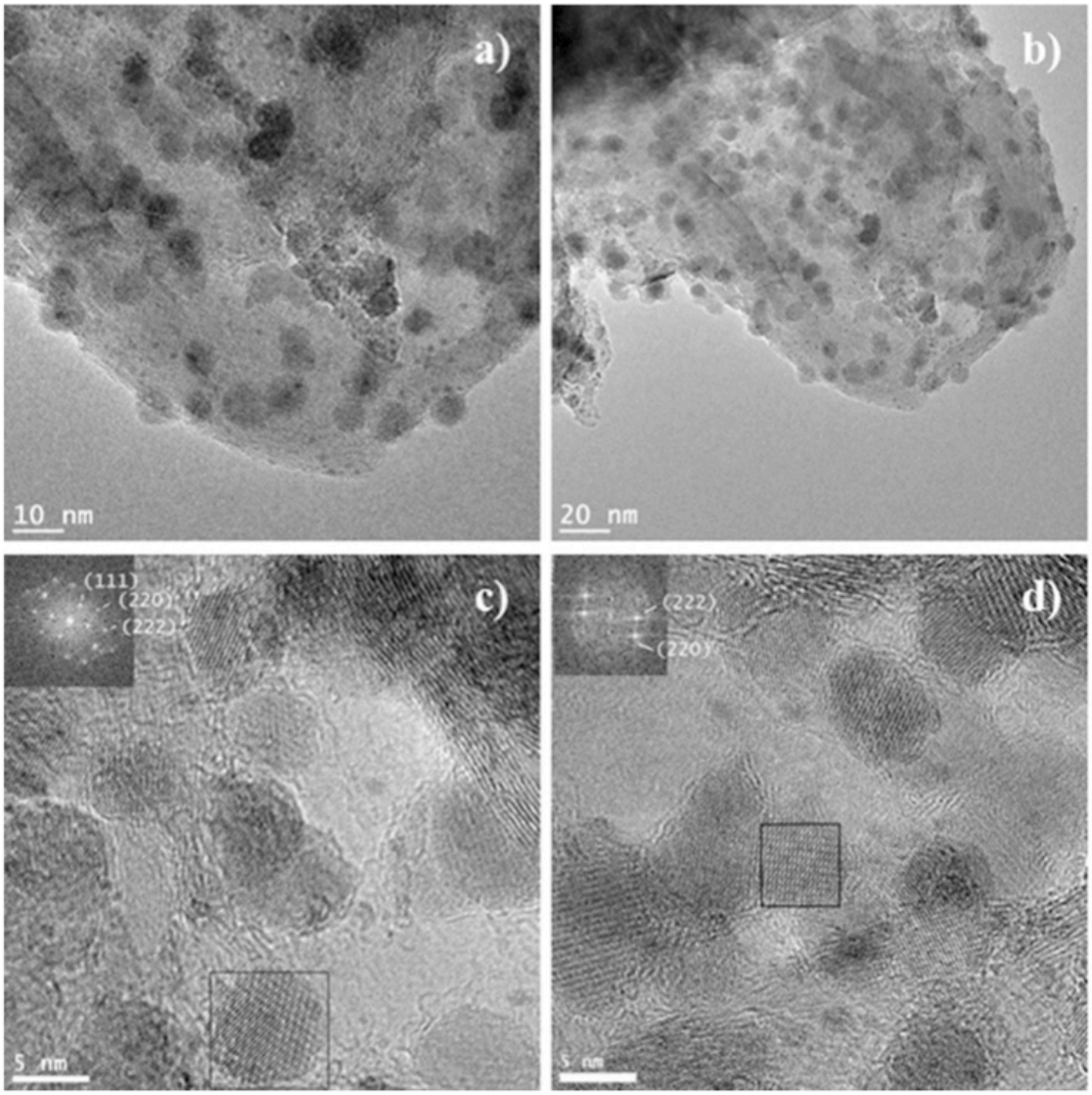

Figure 11 HRTEM images of: a) Ru-Fe3O4/GO and b) show the Ru and Fe3O4 nanoparticles on the GO surface; c and d) show 5 nm of Fe3O4 nanoparticles that display crystalline structure.

The high-resolution transmission electron microscopy (HRTEM) images of Ru-Fe_3O_4/GO confirmed the presence of two kinds of metal nanoparticles, small Ru nanoparticles (mean diameter of 1.5 nm) and larger Fe_3O_4 nanoparticles (mean diameter of 5 nm; Figures 11a and 11b). The HRTEM images of Fe_3O_4 nanoparticles highlight the crystalline nature of Fe_3O_4, and the insets show the corresponding fast Fourier transform (FFT) images (see Figures 11c and d). All the spots of the FFT patterns obtained from the HRTEM images can be indexed to face-centred cubic Fe_3O_4. Unfortunately, the Ru nanoparticles were too small to obtain a well-resolved image of

the crystal structure. The crystalline nature of Fe_3O_4 was further investigated through XRD analysis.

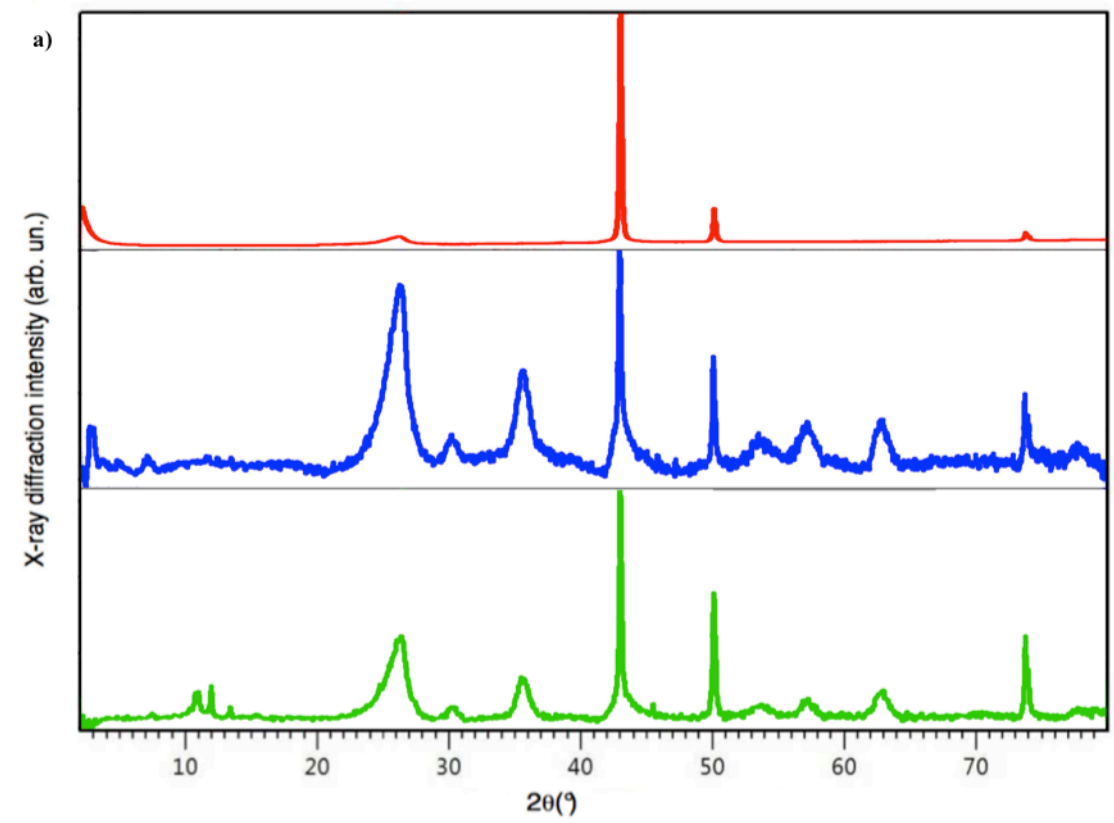

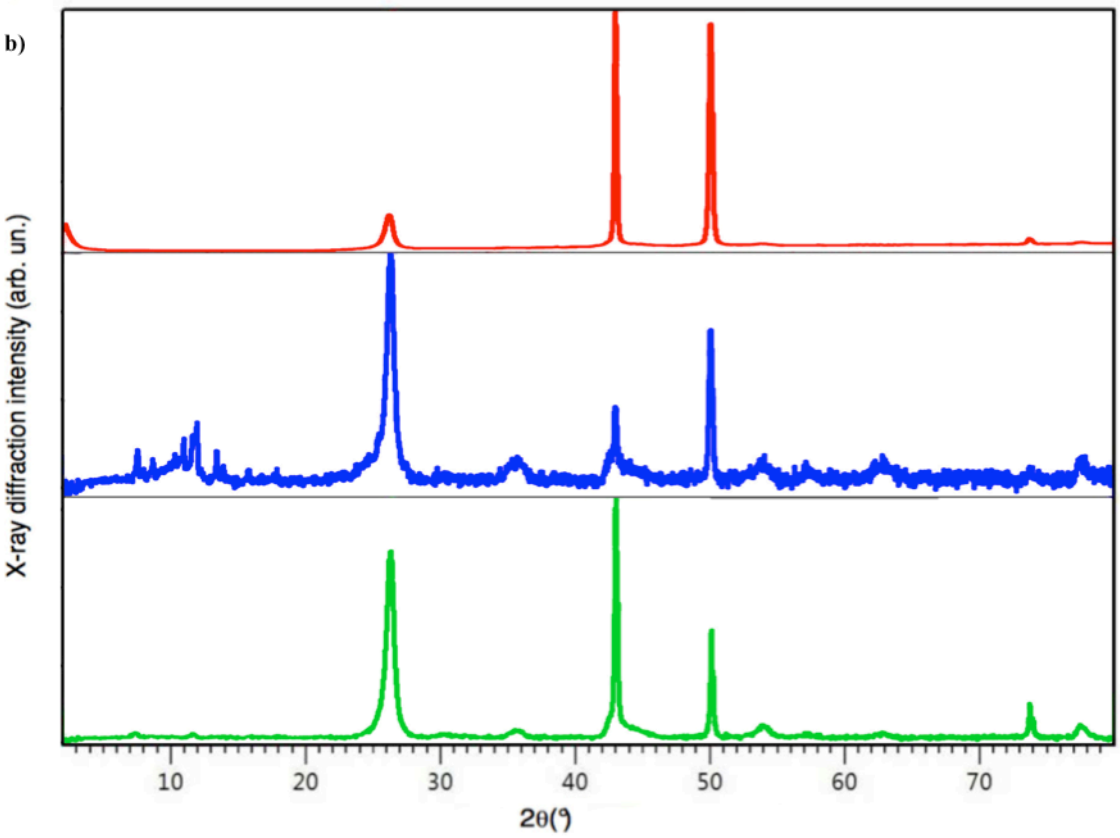

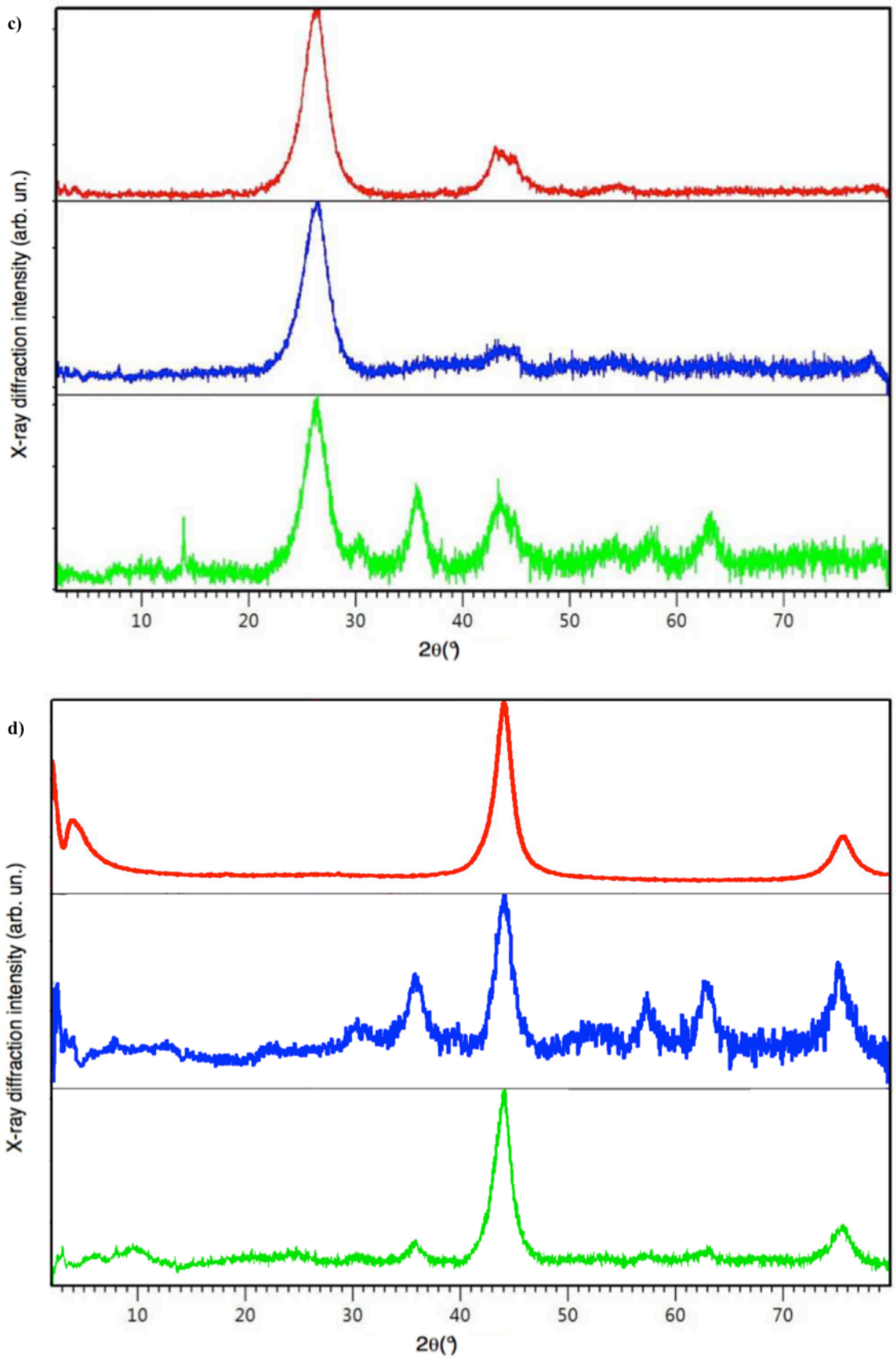

Figure 12 XRD diffractograms of carbon nanostructures supported catalysts a) Graphene oxide supported catalysts, Ru-GO in red, Fe_3O_4/GO in blue and Ru-Fe_3O_4/GO in green, b) Carbon nanotube supported catalysts, Ru-CNT in red, Fe_3O_4/CNT in blue and Ru-Fe_3O_4/CNT in green, c) N doped carbon nanotube supported catalysts, Ru-NCNT in red, Fe_3O_4/NCNT in blue and Ru-Fe_3O_4/NCNT in green, and d) Nanodiamond supported catalysts, Ru-Nd in red, Fe_3O_4/Nd in blue and Ru-Fe_3O_4/Nd in green.

The XRD patterns of samples Ru-GO, Ru-CNT, Ru-NCNT reported in Figures 12a, b, c (red line) show only diffraction peaks at 2θ = 26.2 and 42.98, which are assigned to the hexagonal graphite structures (002) and (100) respectively, in agreement with literature.[46] The diffractogram of sample Ru-Nd shown in Figure 12d (red line) reports only one peak at 2θ = 42.98 ascribable to the carbon nanodiamond structure.[47] Furthermore, in all these ruthenium nanocatalysts no diffraction peaks characteristic of metallic ruthenium were ascertained due to the small Ru particle size.

The diffractograms of magnetic nanocatalysts Fe_3O_4/GO Fe_3O_4 /CNT , Fe_3O_4 /NCNT and Fe_3O_4 /Nd are displayed in Figures 12a, b, c, d (blue lines) and show broad reflections at 2θ = 30.1, 35.5, 43.1, 53.4, 56.9, and 62.48, which can be assigned to the (222), (311), (400), (422), (511), and (440) crystal planes of cubic magnetite, respectively. The broad peaks confirm the smaller size of the Fe_3O_4 crystal as observed by TEM analysis (see Figure 11).

The XRD pattern of Fe_3O_4/NCNT, instead, only shows peaks of the support at 2θ = 26.2 and 42.98 as observed also in the Ru/NCNT sample (Figure 12c red line), and the peaks of Fe_3O_4 were not observed due to the smaller size of the Fe_3O_4 nanoparticles (< 3 nm). Finally, the XRD diffractograms of the bimetallic nanocatalysts Ru- Fe_3O_4/GO, Ru- Fe_3O_4/CNT, Ru- Fe_3O_4/NCNT and Ru-Fe_3O_4/Nd reported in Figures 12a, b, c and d (green lines) were similar to those of the monometallic Fe_3O_4 nanocatalysts and displayed broad reflections at 2θ= 30.1, 35.5, 43.1, 53.4, 56.9, and 62.48, which correspond to the crystal planes of cubic magnetite and carbon supports. In this case, the Ru-Fe_3O_4/NCNT sample also shows a broad reflection caused by the Fe_3O_4 nanoparticles, which were not observed for Fe_3O_4/NCNT, confirming the increased nanoparticle size revealed by TEM (see Figures 10f and i). In the bimetallic samples, no reflection of the Ru nanoparticles was observed, because of the small Ru particle size.

The high crystalline structure of magnetite nanoparticles in monometallic and bimetallic samples was also confirmed by the magnetic behaviour of these samples. The samples in fact react very well to an external neodymium magnet, as can be observed in Figure 13.

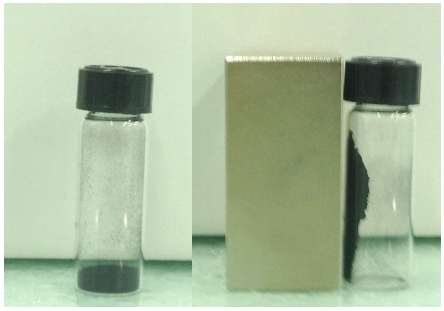

Figure 13 Example of the magnetic behaviour of Fe_3O_4/GO sample

The magnetic curves of Fe_3O_4 and Ru-Fe_3O_4 nanocatalysts measured at 273 K are shown in Figure 14. Generally, CNT and NCNT present low intrinsic magnetic saturation values (M_0) caused by the metal impurities trapped inside their structure during preparation (the intrinsic M_0 observed were 0.37 and 1.50 emu/g for CNT and NCNT, respectively), whereas GO and Nd did not present any magnetic behaviour (see Table 2). The M_0 values of these diverse carbon supports increased significantly if magnetite nanoparticles were anchored on their surfaces (Table 2). The M_0 values of Ru- Fe_3O_4 samples are slightly lower than those of Fe_3O_4 ones on GO and NCNT supports. This behaviour could be related to the increase of defects in the Fe_3O_4 crystalline structures caused by the introduction of Ru nanoparticles, which decreases the magnetic properties of the sample. An analogous effect of the introduction of Ru on the magnetic properties of different magnetite samples has been recently reported.[48] This decrease was not observed for the CNT and Nd supported samples in which the magnetic properties were essentially the same for Fe_3O_4 monometallic and Ru- Fe_3O_4 bimetallic systems, which suggests that Ru nanoparticles do not interact with Fe_3O_4 nanoparticles, probably because of the high affinity of Ru to CNT and Nd surfaces. In spite of the lower magnetization compared with the bare magnetite particles (62 emu/g at T=300 K and H=2 kOe),[49] which can be attributed to a significant contribution of the small superparamagnetic Fe_3O_4 nanoparticles at room temperature,[50] the solid can be separated readily from the liquid medium by using a small permanent neodymium magnet. In conclusion, the magnetic carbon nanostructures show promising magnetic properties with magnetic saturation values higher than those reported in literature.[51]

a)

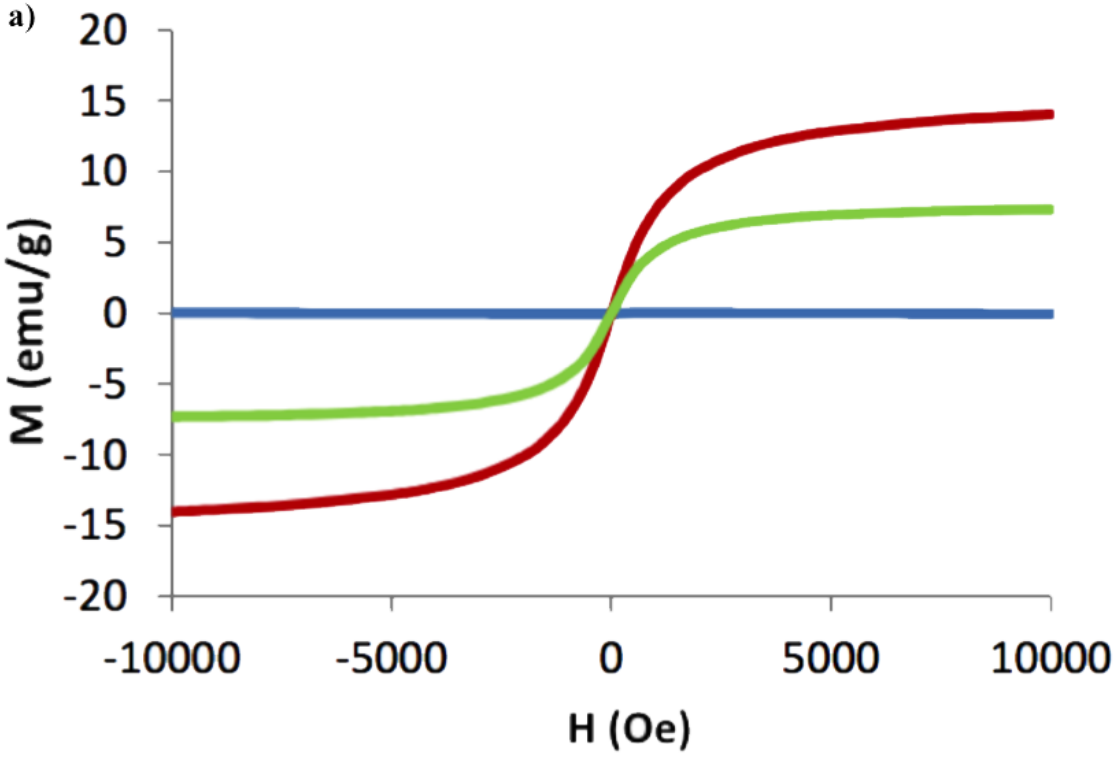
20
15
10
5
0
-5
-10
-15
-20
M (emu/g)
-10000
-5000
0
5000
10000
H (Oe)

b)

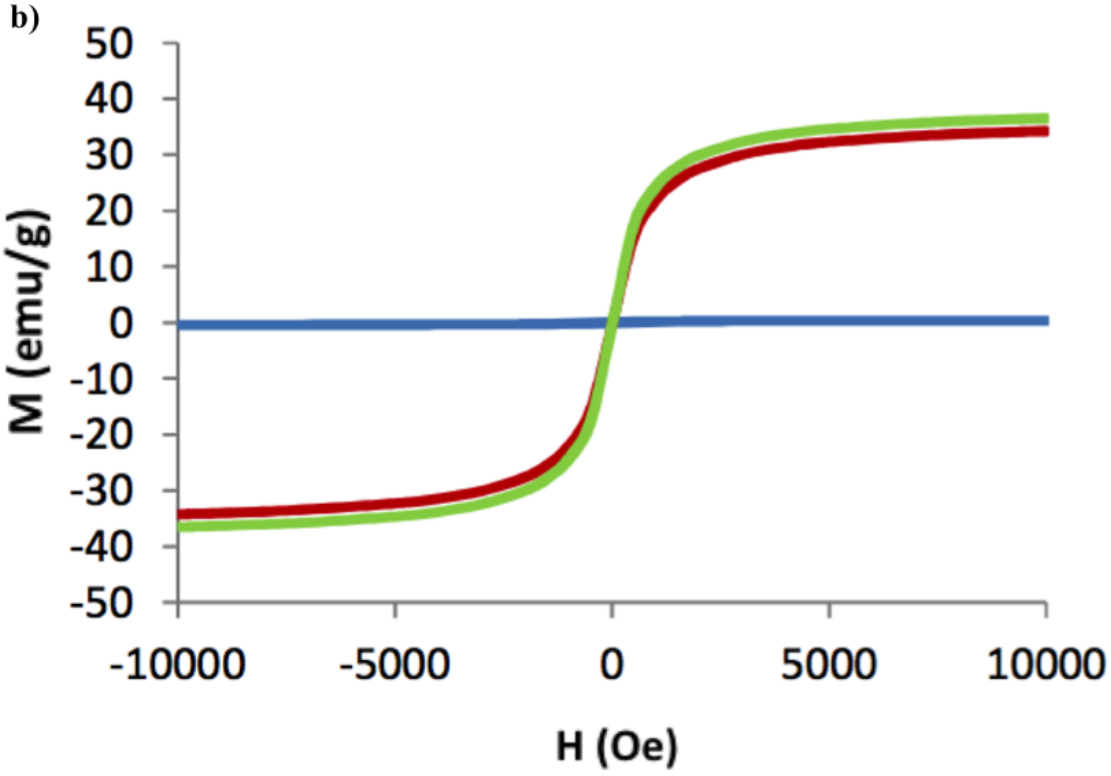
50
40
30
20
10
0
-10
-20
-30
-40
-50
M (emu/g)
-10000
-5000
0
5000
10000
H (Oe)

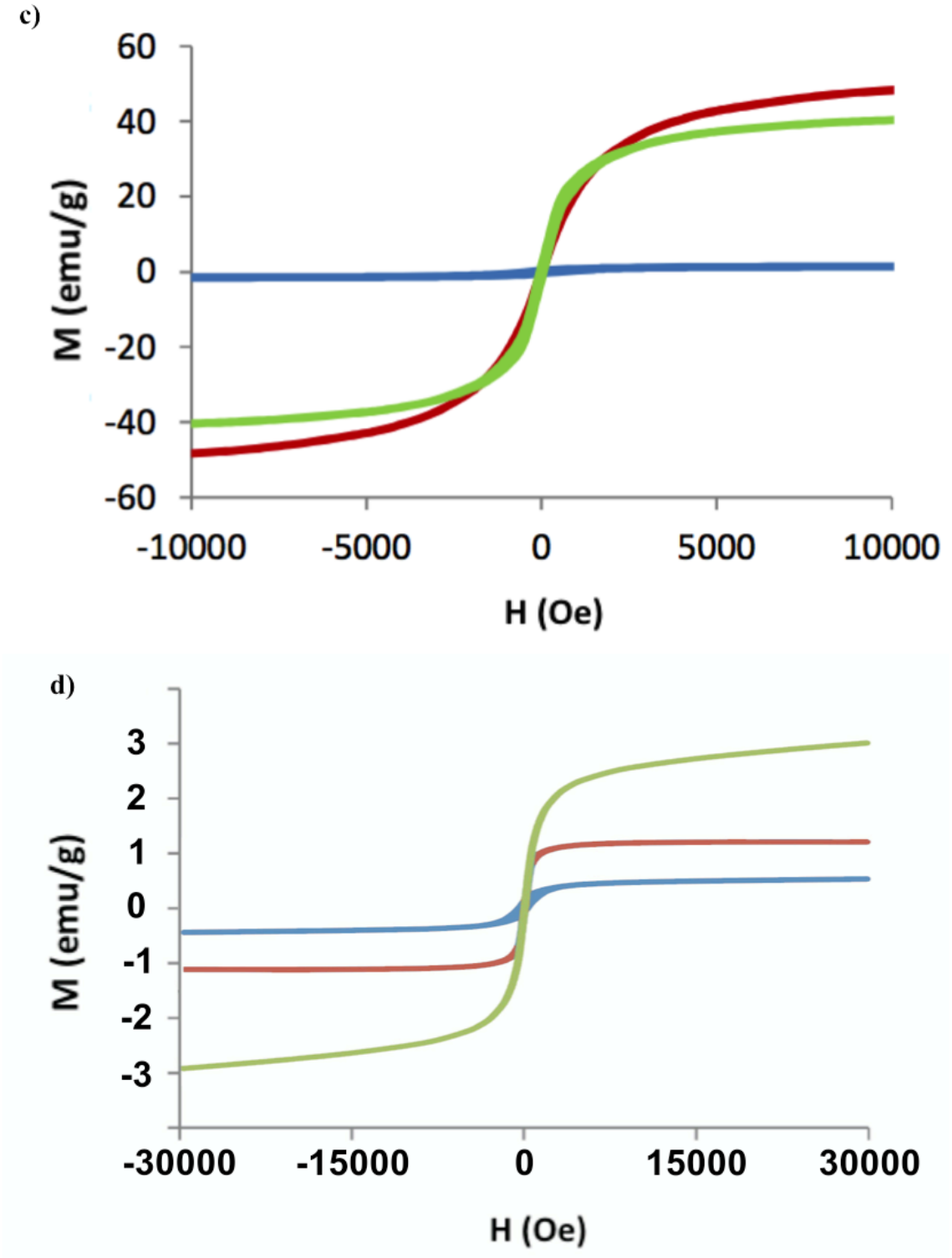

Figure 14 Magnetic curves of a) Graphene oxide supported catalysts, GO in blue, Fe_3O_4/GO in red and Ru-Fe_3O_4/GO in green, b) Carbon nanotube supported catalysts, CNT in blue, Fe_3O_4/CNT in red and Ru-Fe_3O_4/CNT in green, c) N doped carbon nanotube supported catalysts, NCNT in blue, Fe_3O_4/NCNT in red and Ru-Fe_3O_4/NCNT in green, and d) Nanodiamond supported catalysts, Nd in red, Fe_3O_4/Nd in blue and Ru-Fe_3O_4/Nd in green.

8.3 References

[1] S. Petr, H. Tomáš, K. Zdeňka, T. Simona, K. Nikola Slepičková, B. Lucie and Š. Václav, *The Properties and Application of Carbon Nanostructures*, **2013**, p.
[2] a) D. J. Lipomi, M. Vosgueritchian, B. C. K. Tee, S. L. Hellstrom, J. A. Lee, C. H. Fox and Z. Bao, *Nat Nano* **2011**, *6*, 788-792; b) E. K. Wujcik, H. Wei, X. Zhang, J. Guo, X. Yan, N. Sutrave, S. Wei and Z. Guo, *RSC Advances* **2014**, *4*, 43725-43745.
[3] C. X. Guo, H. B. Yang, Z. M. Sheng, Z. S. Lu, Q. L. Song and C. M. Li, *Angewandte Chemie International Edition* **2010**, *49*, 3014-3017.
[4] a) W. Li, C. Liang, W. Zhou, J. Qiu, Zhou, G. Sun and Q. Xin, *The Journal of Physical Chemistry B* **2003**, *107*, 6292-6299; b) B. Seger and P. V. Kamat, *The Journal of Physical Chemistry C* **2009**, *113*, 7990-7995.
[5] a) X. Wang, Y. Ouyang, X. Li, H. Wang, J. Guo and H. Dai, *Physical Review Letters* **2008**, *100*, 206803; b) M. D. Stoller, S. Park, Y. Zhu, J. An and R. S. Ruoff, *Nano letters* **2008**, *8*, 3498-3502; c) C. Liu, Z. Yu, D. Neff, A. Zhamu and B. Z. Jang, *Nano letters* **2010**, *10*, 4863-4868.
[6] a) J. Zhu, M. Chen, H. Qu, Z. Luo, S. Wu, H. A. Colorado, S. Wei and Z. Guo, *Energy & Environmental Science* **2013**, *6*, 194-204; b) P. M. Ajayan, O. Stephan, C. Colliex and D. Trauth, *Science* **1994**, *265*, 1212-1214; c) *Dalton Trans.* **2014**, *43*, 2948.
[7] a) G. E. Froudakis, *Materials Today* **2011**, *14*, 324-328; b) A. Züttel, P. Sudan, P. Mauron, T. Kiyobayashi, C. Emmenegger and L. Schlapbach, *International Journal of Hydrogen Energy* **2002**, *27*, 203-212.
[8] Philippe Serp and B. Machado in *CHAPTER 1 Carbon (Nano)materials for Catalysis*, *Vol.* The Royal Society of Chemistry, **2015**, pp. 1-45.
[9] P. Serp, M. Corrias and P. Kalck, *Applied Catalysis A: General* **2003**, *253*, 337-358.
[10] a) N. J. S. C. L. M. Rossi, F. P. Silva, R. V. Goncalves, *Nanotechnology Reviews* **2013**, *2*, 597-614; b) V. Polshettiwar, R. Luque, A. Fihri, H. Zhu, M. Bouhrara and J.-M. Basset, *Chemical reviews* **2011**, *111*, 3036-3075.
[11] S. B. Kalidindi and B. R. Jagirdar, *ChemSusChem* **2012**, *5*, 65-75.
[12] a) J. P. Cheng, J. Yu, D. Shi, D. S. Wang, Y. F. Liu, F. Liu, X. B. Zhang and J. G. Li, *Applied Physics A* **2012**, *106*, 837-842; b) S. Shen, J. Ren, X. Zhu, Z. Pang, X. Lu, C. Deng, R. Zhang and X. Jiang, *Journal of Materials Chemistry B* **2013**, *1*, 1939-1946; c) J. Li, R. Yuan, Y. Chai and X. Che, *Journal of Molecular Catalysis B: Enzymatic* **2010**, *66*, 8-14; d) Y. Zhan, R. Zhao, Y. Lei, F. Meng, J. Zhong and X. Liu, *Applied Surface Science* **2011**, *257*, 4524-4528; e) X. Zuo, C. Peng, Q. Huang, S. Song, L. Wang, D. Li and C. Fan, *Nano Research* **2009**, *2*, 617-623; f) L. Ren, S. Huang, W. Fan and T. Liu, *Applied Surface Science* **2011**, *258*, 1132-1138.
[13] A. Zafour-Hadj-Ziane, M. Djiab and E. Flahaut, *MATEC Web of Conferences* **2013**, *5*, 04024.
[14] G. Korneva, H. Ye, Y. Gogotsi, D. Halverson, G. Friedman, J.-C. Bradley and K. G. Kornev, *Nano Letters* **2005**, *5*, 879-884.
[15] G. G. Wildgoose, C. E. Banks and R. G. Compton, *Small* **2006**, *2*, 182-193.
[16] W. Deng, X. Tan, W. Fang, Q. Zhang and Y. Wang, *Catalysis letters* **2009**, *133*, 167-174.
[17] C. Antonetti, M. Oubenali, A. M. Raspolli Galletti, P. Serp and G. Vannucci, *Applied Catalysis A: General* **2012**, *421–422*, 99-107.
[18] B. Yoon and C. M. Wai, *Journal of the American Chemical Society* **2005**, *127*, 17174-17175.

[19] E. Bertolucci, R. Bacsa, A. Benyounes, A. M. Raspolli-Galletti, M. R. Axet and P. Serp, *ChemCatChem* **2015**, *7*, 2971-2978.
[20] A. Hirsch, *Nat Mater* **2010**, *9*, 868-871.
[21] B. C. Yadav and R. Kumar, *International Journal of Nanotechnology and Applications* **2008**, *2*, 15-24.
[22] Y. Iwasa, *Nature* **2010**, *466*, 191-192.
[23] R. J. Hopkins, A. V. Tivanski, B. D. Marten and M. K. Gilles, *Journal of Aerosol Science* **2007**, *38*, 573-591.
[24] F. S. Rostler, R. M. White and E. M. Dannenberg, *Association of Asphalt Paving Technologists Proc* **1977**.
[25] L. Monser and N. Adhoum, *Separation and Purification Technology* **2002**, *26*, 137-146.
[26] M. Shimada, T. Iida, K. Kawarada, Y. Chiba, T. Mamoto and T. Okayama, *Journal of Material Cycles and Waste Management* **2004**, *6*, 111-118.
[27] Y. H. Wu, T. Yu and Z. X. Shen, *Journal of Applied Physics* **2010**, *108*, 071301.
[28] R. Tenne, *Angewandte Chemie International Edition* **2003**, *42*, 5124-5132.
[29] a) J. Bartelmess and S. Giordani, *Beilstein Journal of Nanotechnology* **2014**, *5*, 1980-1998; b) S. Tomita, T. Sakurai, H. Ohta, M. Fujii and S. Hayashi, *The Journal of Chemical Physics* **2001**, *114*, 7477-7482.
[30] S. Zhu and G. Xu, *Nanoscale* **2010**, *2*, 2538-2549.
[31] J.-P. Tessonnier, D. Rosenthal, T. W. Hansen, C. Hess, M. E. Schuster, R. Blume, F. Girgsdies, N. Pfänder, O. Timpe, D. S. Su and R. Schlögl, *Carbon* **2009**, *47*, 1779-1798.
[32] Y. Zhou, F. Pervin, S. Jeelani and P. K. Mallick, *Journal of Materials Processing Technology* **2008**, *198*, 445-453.
[33] A. F. Ávila and G. S. R. Lacerda, *Materials Research* **2008**, *11*, 325-333.
[34] V. N. Mochalin, O. Shenderova, D. Ho and Y. Gogotsi, *Nat Nano* **2012**, *7*, 11-23.
[35] B. F. Machado, M. Oubenali, M. Rosa Axet, T. Trang Nguyen, M. Tunckol, M. Girleanu, O. Ersen, I. C. Gerber and P. Serp, *Journal of Catalysis* **2014**, *309*, 185-198.
[36] M. N. Tchoul, W. T. Ford, G. Lolli, D. E. Resasco and S. Arepalli, *Chemistry of Materials* **2007**, *19*, 5765-5772.
[37] L. Mabena, S. Sinha Ray, S. Mhlanga and N. Coville, *Applied Nanoscience* **2011**, *1*, 67-77.
[38] a) J. Hone, M. Whitney, C. Piskoti and A. Zettl, *Physical Review B* **1999**, *59*, R2514-R2516; b) S. Berber, Y.-K. Kwon and D. Tománek, *Physical Review Letters* **2000**, *84*, 4613-4616.
[39] a) R. A. Jishi, M. S. Dresselhaus and G. Dresselhaus, *Physical Review B* **1993**, *48*, 11385-11389; b) T. W. Ebbesen, H. J. Lezec, H. Hiura, J. W. Bennett, H. F. Ghaemi and T. Thio, *Nature* **1996**, *382*, 54-56; c) Z. Yao, C. L. Kane and C. Dekker, *Physical Review Letters* **2000**, *84*, 2941-2944; d) A. H. Castro Neto, F. Guinea, N. M. R. Peres, K. S. Novoselov and A. K. Geim, *Mod. Phys* **2009**, *81*, 109.
[40] a) H. Kataura, Y. Maniwa, M. Abe, A. Fujiwara, T. Kodama, K. Kikuchi, H. Imahori, Y. Misaki, S. Suzuki and Y. Achiba, *Applied Physics A* **2002**, *74*, 349-354; b) S. M. Bachilo, M. S. Strano, C. Kittrell, R. H. Hauge, R. E. Smalley and R. B. Weisman, *Science* **2002**, *298*, 2361-2366.
[41] C. Lee, X. Wei, J. W. Kysar and J. Hone, *Science* **2008**, *321*, 385-388.
[42] N. Perkas, G. Amirian, C. Rottman, F. de la Vega and A. Gedanken, *Ultrasonics Sonochemistry* **2009**, *16*, 132-135.

[43] A. D. Purceno, B. F. Machado, A. P. C. Teixeira, T. V. Medeiros, A. Benyounes, J. Beausoleil, H. C. Menezes, Z. L. Cardeal, R. M. Lago and P. Serp, *Nanoscale* **2015**, *7*, 294-300.
[44] B. F. M. A. Solhy, J. Beausoleil, Y. Kihn, F. Goncalves, M.F.R Pereira, J.J.M. Orfao, J.L. Figueiredo, J.L. Faria, P. Serp, *Carbon* **2008**, *46*, 1194-1207.
[45] I. P. Chang, K. C. Hwang, J.-a. A. Ho, C.-C. Lin, R. J. R. Hwu and J.-C. Horng, *Langmuir* **2009**, *26*, 3685-3689.
[46] a) C. Huiqun, Z. Meifang and L. Yaogang, *Journal of Magnetism and Magnetic Materials* **2006**, *305*, 321-324; b) X. Hu and C. Wang, *Microchimica Acta* **2012**, *179*, 329-335.
[47] G. S. Yur'ev and V. Y. Dolmatov, *Journal of Superhard Materials* **2010**, *32*, 311-328.
[48] a) A. M. R. Galletti;, E. Bertolucci;, Mirko Marracci, B. Tellini; and C. Visone, *Instrumentation and Measurement Technology Conference (I2MTC)* **2014**, pp. 464-467; b) C. A. Elisa Bertolucci; Anna Maria Raspolli Galletti, Mirko Marracci, Bernardo Tellini, Fabio Piccinelli, Ciro Visone in *Chemical and Magnetic Properties Characterization of Magnetic Nanoparticles*, *Vol.* IEEE, Pisa, **2015**.
[49] M. J. Jacinto, P. K. Kiyohara, S. H. Masunaga, R. F. Jardim and L. M. Rossi, *Applied Catalysis A: General* **2008**, *338*, 52-57.
[50] L.-h. Shen, J.-f. Bao, D. Wang, Y.-x. Wang, Z.-w. Chen, L. Ren, X. Zhou, X.-b. Ke, M. Chen and A.-q. Yang, *Nanoscale* **2013**, *5*, 2133-2141.
[51] L. Jiang and L. Gao, *Journal of Electroceramics* **2006**, *17*, 87-90.

9. SYNTHESIS OF COPPER NANOOBJECTS

9.1 Introduction

Copper and copper oxide nanoobjects are very important materials due to their high electrical and thermal conductivities. These nanomaterials in fact are widely investigated for their application in photothermal, photoconductive, superconductor[1], sensor[2], piezoelectric[3], catalytic[4] and antibacterial materials[5].

Several procedures are reported in literature for copper and copper oxide nanoparticle preparation such as thermal decomposition, metal salt reduction, micro emulsion techniques, laser ablation, the polyol method, the solvothermal method, sonochemical reduction and seed mediated growth techniques.

For example, Salavati-Niasari et Al.[6] described the preparation of copper oxide nanoparticles through [bis(salicylaldiminato)copper(II)] decomposition in the presence of oleylamine. Chandra et Al.[7] obtained narrow particle size distribution by reducing nitric copper salt in the presence of ligands.

Furthermore, it is possible to prepare nanoobjects characterized by diverse complex shapes, such as one-dimensional, prism, core-shell, interior hollow structures, nanorods, nanowire and two-dimensional sheets, which show peculiar optical, magnetic, and catalytic properties. These complex structures are generally obtained with an accurate size and shape control, involving inorganic or organic template or surfactants such as porous alumina[8], peptides[9], cellulose[10], gluconate[11], viruses[12], lysozyme[13] etc.

For example, Panigrahi et Al.[14] studied glucose seed mediated growth techniques showing the influence of glucose concentration on the final copper shape. Wei et Al.[5] reported a controlled thermal decomposition method to produce copper nanoparticles or nanorods, whereas Patra et At.[4] investigated the influence of ethylenediamine on the formation of copper nanorods or nanospheres.

However, by adopting also templates and stabilizing agents, which are generally unsustainable from an environmental and economic point of view, a mixture of shapes is generally obtained. In fact, Zhang et Al.[15] showed the preparation of copper nanorods with rectangular cross sections through the controlled reduction of nitric

copper salt, underlining the by-production of spherical nanoparticles. Other authors report the co-production of spherical and cylindrical copper nanoobjects through salt reduction techniques under controlled conditions. [16] The co-presence of diverse nanostructured shapes could be a serious limitation for certain optical and electrical applications.

Furthermore, most of these methods are complicated and require long reaction steps, expensive equipment and unfriendly compounds.

Taking into account all these aspects, the development of greener reproducible methods for the production of well-defined copper and copper oxide nanostructures is a key issue of significant importance in fundamental studies. For this reason the effect of diverse reducing/templating agents, reaction times and heating source on copper nanoobject shapes were deeply investigated, with the aim of their successive catalytic application.

9.2 Synthesis of copper nanoparticles

In a typical experiment, $Cu(NO_3)_2 \cdot 3H_2O$ (80mg), Polyvinyl alcohol (0.1g) and ascorbic acid (1.3 g) were dissolved in ethylene glycol (40 ml) under stirring, and MW-irradiated at 140°C and 150W for 25 minutes. After the MW treatment the copper nanoparticles were formed as confirmed by the suspension colour, which turned from light blue for the presence of free Cu^{2+} ions to reddish (see Figure 1).

This preparation was repeated at diverse reaction times and the results are summarized in Table 1.

Table 1 Reaction time effect of copper nanoparticles formation

Run	$Cu(NO_3)_2 \cdot 3H_2O$ (g)	Ethylene glycol (ml)	PVA (g)	Ascorbic acid (g)	Reaction time (min)
CuNP4	0.0812	40	0.1	1.3	10
CuNP6	0.0856	40	0.1	1.3	20
CuNP8	0.0817	40	0.1	1.3	25

The UV-Vis spectrum of sample CuNP4 obtained with the lowest reaction time does not show the adsorption peak at 540 nm, typical of metallic copper nanoparticles. Only by increasing the reaction time up to 20 (sample CuNP6) is possible to observe copper reduction underlining that the moderate temperature and the adopted weak reducing media require a longer reaction time to guarantee an efficient reduction of copper salt. The UV-Vis spectrum of sample CuNP8 obtained with a reaction time of 25 minutes reported in Figure 1, in fact, shows a big peak at 450 nm ascribable to copper nanoparticles.

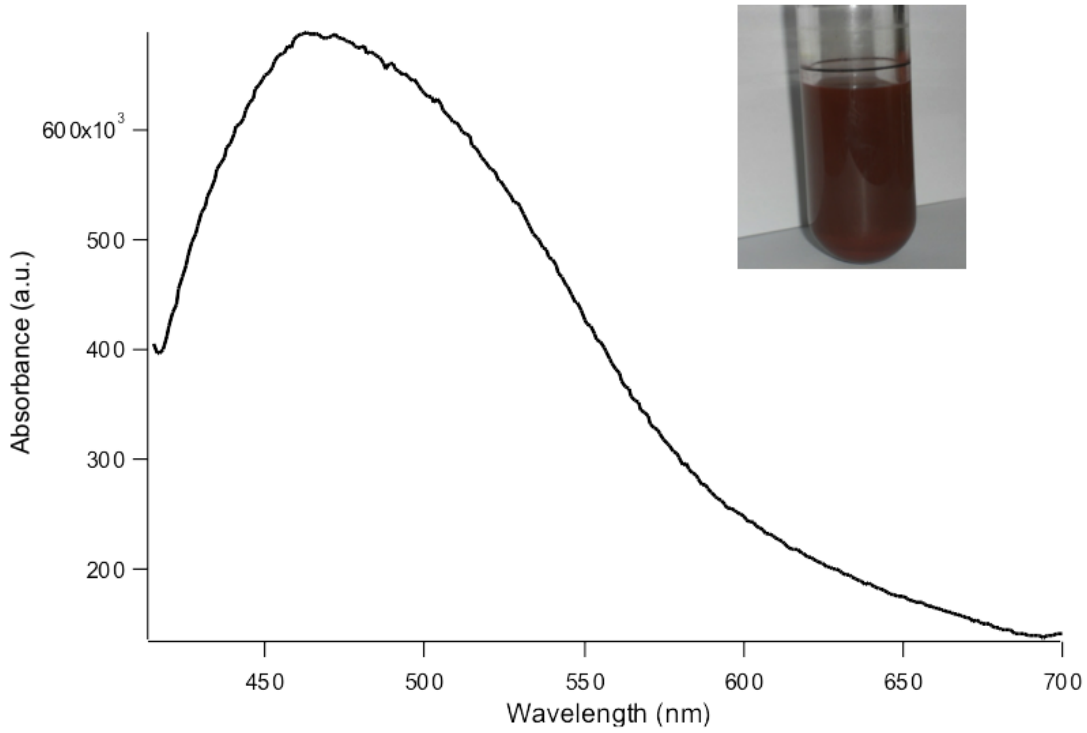

Figure 1 UV-Vis spectrum of sample CuPN8 obtained with a reaction time of 25 minutes.

The reduction of copper was confirmed also by X-Ray diffractograms as reported in Figure 2, which shows peaks at 2θ = 45°, 52°, 72° and 86° indexed as Miller indexes of face-centred cubic copper crystals (111), (200), (220) and (311) respectively.[4, 16a]

The broad peaks at low 2θ can be ascribable to polyvinyl alcohol used as a stabilizer during sample preparation.

Moreover, the XRD analysis underlines the polycrystalline nature of the CuNP8 sample, which is composed of particles with an average diameter of 150 nm.

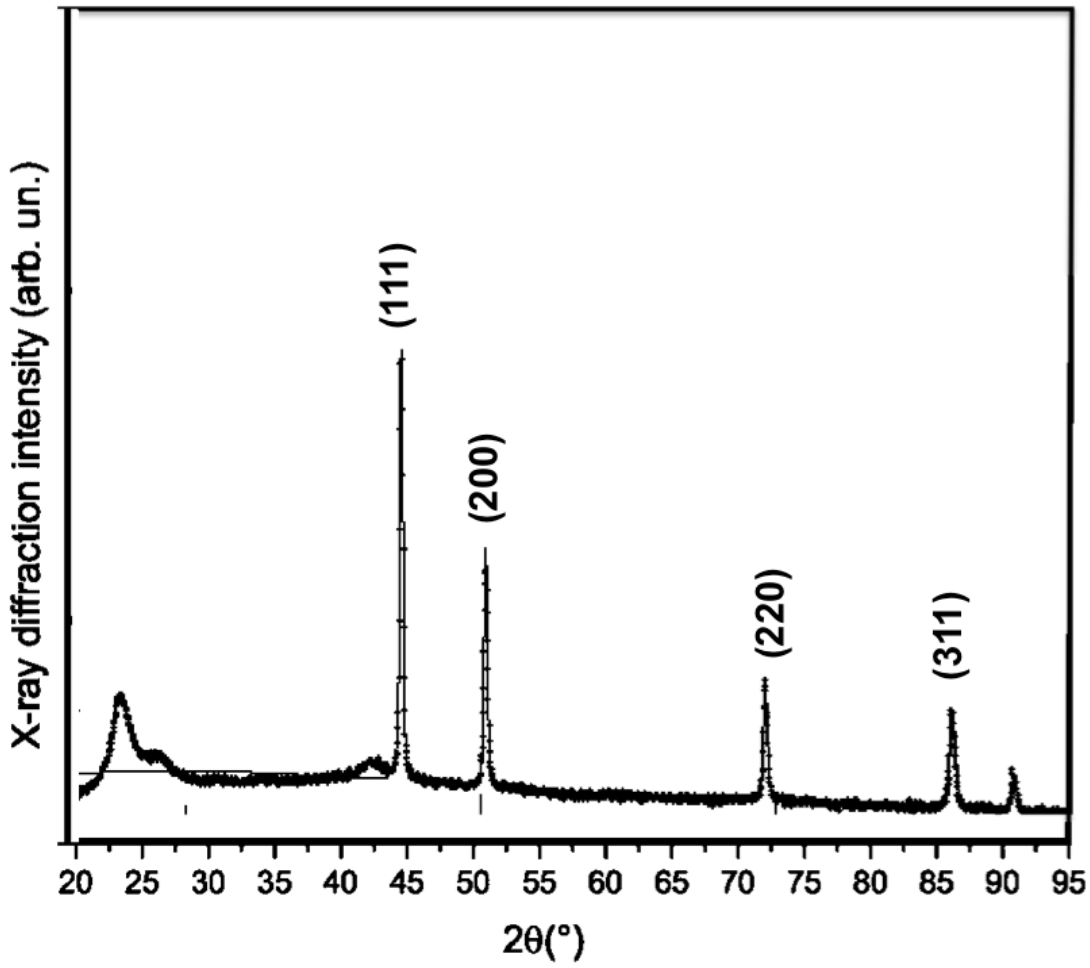

Figure 2 XRD diffractograms of sample CuNP8 obtained after a reaction time of 25 minutes

In order to develop a greener synthetic procedure the ethylene glycol was replaced with water and the temperature was decreased to 120 °C. In a general preparation, $Cu(NO_3)_2 \cdot 3H_2O$ (0.24g), Polyvinyl alcohol (0.2g) and ascorbic acid (1.3g) were dissolved in distilled water (40ml) under stirring, and MW-irradiated at 120°C and 150W.

The syntheses were performed using diverse heating sources to better understand their effect on copper reduction. In particular, monomode microwave (CEM discover S.class equipped with an 80 ml glass vessel), 300ml and 150 ml Parr autoclave electrically heated were employed and the corresponding reaction conditions are reported in Table 2.

Table 2 Heating sources effect on copper reduction

Run	$Cu(NO_3)_2 \cdot 3H_2O$ (g)	PVA (g)	Ascorbic acid (g)	Heating source
CuNP9[a]	0.24	0.2	0.5	300 ml Autoclave
CuNP10[a]	0.24	0.2	0.5	150 ml Autoclave
CuNP11[b]	0.24	0.2	0.5	MW

[a] Reaction conditions: Temperature 120° , 4h

[b] Reaction conditions: Temperature 120°, 20 minutes

Unfortunately, the reaction conditions adopted did not permit an efficient reduction of copper as confirmed by UV-Vis spectra of samples CuNP9, CuNP10, CuNP11, which showed no peak around 450 nm contrary to what was observed for the CuNP8 sample obtained in ethylene glycol.

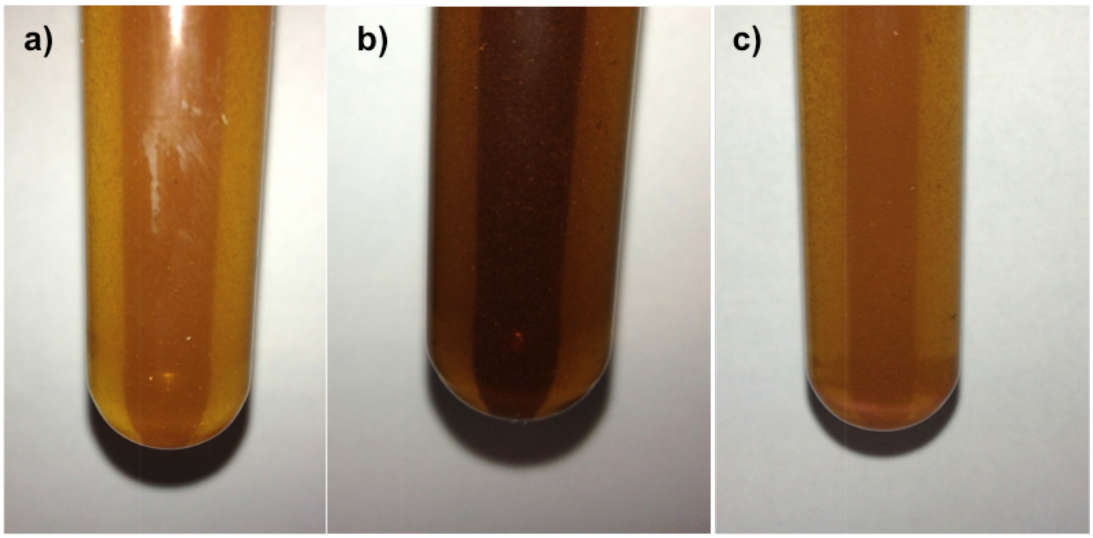

Figure 3 Images of samples: a) CuPN9 obtained using a 300 ml Parr Autoclave as heating source, b) CuPN10 obtained using a 150 ml Parr Autoclave as heating source and c) CuPN11 obtained using a monomode microwave

In conclusion, the ascorbic acid/water system resulted in an inefficient reducing medium for copper salt, thus glucose was employed to replace ascorbic acid.

In a typical preparation, 0.1 ml of NaOH 1M and glucose (3g) were dissolved in distilled water (40ml) under stirring at 60°C. Then 2 ml of $CuSO_4$ 2M were added to the hot solution and the final mixture was heated up to 80°C for 3 minutes.

The obtained sample has a yellow colour, as can be seen in Figure 4. This diverse coloration can be due to the diverse particle size or to a diverse oxidation state of the obtained copper particles.

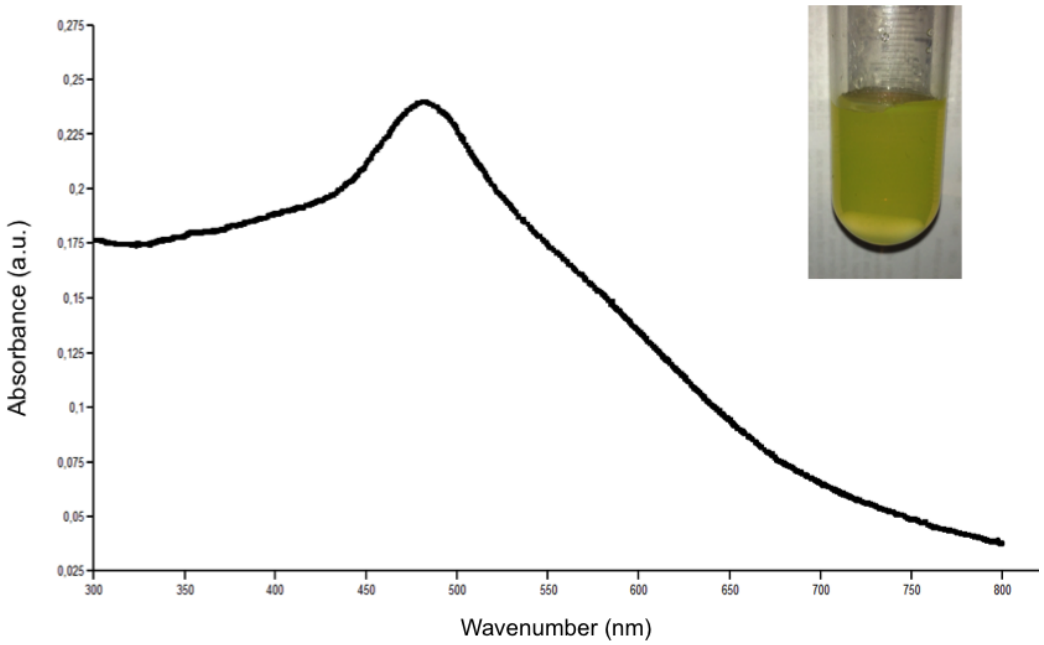

Figure 4 UV-Vis spectra of copper nanoparticles obtained using glucose/water systems

The UV-Vis spectrum of the samples obtained with glucose/water systems shows a broad peak around 450 nm ascribable to metallic copper. The main drawback of the proposed procedure is the employment of NaOH, an extremely corrosive and hazardous compound.

The role of NaOH is fundamental for the reduction of copper as confirmed by some experiments run without NaOH, which did not lead to metallic copper nanoparticle formation. In more detail, the alkaline media transform α-glucose to β-glucose through the open chain structure, which has the aldehyde group available. This aldehyde functionality under alkaline condition permits the reduction of Cu(II) to Cu(0) as reported also by Panigrahi et al.[14] Furthermore the reduction of copper ions result in the oxidation of aldehyde group to carboxylic acid group which is a good stabilizing agent for copper nanoparticles.

However, NaOH was employed in extremely low concentration thus limiting health and environmental risks. In conclusion, this procedure can be considered as greener method to produce metallic copper nanoparticles.

9.3 Synthesis of copper nanowires by sugar assisted growth

A new greener seed mediated growth method for the preparation of copper nanorods was developed based on the classical seed mediated growth techniques reported by Panigrahi et al.[14] The seed mediated growth technique is a two-step procedure which generally involves a first step for the preparation of the nanoparticles seed and a second step of unidirectional growth. Taking into account the results showed in Chapter 9.2 and focusing our attention on green chemistry principles, diverse sugar and sugar derivates were investigated as reducing and templating agents for the growth of copper nanorods using the microwave irradiation as efficient and time saving heating source.

In the first experiment (CuPN13) glucose (4g) and 0.1 ml of NaOH 1 M were dissolved in water (50 ml), under stirring at 60°C, then 2 ml of $CuSO_4$ 10^{-2} M were added and the temperature of the mixture was increased up to 80°C. After 3 minutes, the nanoparticle seeds were formed as confirmed by the suspension colour, which turned from light blue to yellow. Meanwhile 0.1 ml of NaOH 1 M and 3g of glucose were dissolved in water (50ml) under stirring at 60°C, then this hot solution and 2 ml of $CuSO_4$ 10^{-2} M were added to the seed suspension and the final mixture was heated up to 80°C for 15 minutes.

The apparatus used in this first experiment is reported in Figure 5.



Figure 5 Apparatus for the synthesis of copper nanorods

The reaction suspension was sampled during the growth of the nanorods and analysed at UV-Vis. After five minutes of growth, sample CuPN13 shows two broad peaks at 500 nm and 630 nm, which could be due to the two dimensions (diameter and length) of anisotropic copper nanorods (see Figure 6, black line). The anisotropic growth of nanostructures, in fact, results in peculiar UV-Vis absorbance characteristics of each nanostructure dimension.[17]

The UV-Vis spectrum of the CuPN13 sample taken after 15 minutes of growth presents more marked peaks at 500 nm and 650 nm (see Figure 6, red line). The second peak resulted slightly shifted compared to the one observed after 5 minutes of growth, confirming the possible increment of nanorod length.

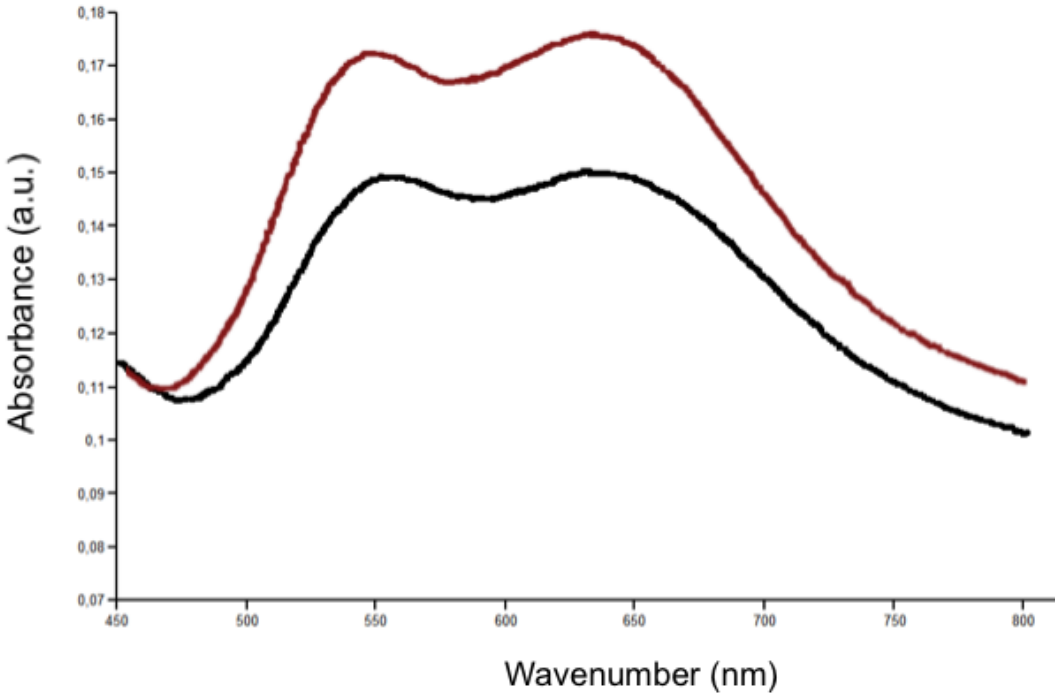

Figure 6 UV-Vis spectra of sample CuPN13 obtained through glucose seed mediated growth a) after 5 minutes of growth (black line) b) after 15 minutes of growth (red line)

Based on these promising results, the sugar seed mediated growth was developed studying the effect of different sugar and sugar derivates as reducing and templating agents, the kind of heating source and the growth time on copper nanorod final characteristics.

9.3.1 Effect of diverse reducing/templating agents on copper nanorod shape

Diverse sugar and sugar derivates were employed as reducing and templating agents for the copper nanorod preparations. In particular, glucose, sorbitol, and sodium gluconate were investigated.

In a typical experiment the seed solution was prepared dissolving sodium gluconate (2.5g) in 30 ml of water and adding 0.12 ml of NaOH 1M and 1.2 ml of $CuSO_4$ 10^{-2} M, then the mixture was treated with microwave at 80°C, 250W for 5 min. Meanwhile the growth solution was prepared dissolving sodium gluconate (1.9) in 6 ml of water and adding 1.2 ml of $CuSO_4$ 10^{-2} M. Finally, the growth solution was added to the seed solution and treated with microwave at 80°C, 250W for 10 minutes. The procedure was repeated using diverse sugars and the obtained results are summarized in Table 3.

Table 3 Copper nanorods synthesis with diverse reducing/templantig agents

Sample	Steps	H_2O (ml)	Riducing/templanting agent	V NaOH 1M (ml)	Color	Shape
CuPN21	1	30	Glucose	0.12	yellow	spherical
	2	6	Sodium Gluconate	***		
CuPN22	1	30	Sorbitol	0.12	Light red	cylindrical
	2	6	Sodium Gluconate	***		
CuPN23	1	30	Sodium Gluconate	0.12	Light yellow	Spherical, acicular and cylindrical
	2	6	Sodium Gluconate	***		

Samples CuPN21, CuPN22 and CuPN23 show different colours, which underline the formation of different copper nanostructures. The UV-VIS spectrums of CuPN21, CuPN22 and CuPN23 show a big absorption before 300 nm caused by sugar decomposition products. Besides, samples CuPN21 and CuPN23 show a large peak at 500 nm typical of copper nanoparticles (see Figure 6, red and green lines), whereas sample CuPN22 has two large peaks, at 450 nm and 700 nm, characteristics of copper nanorods (see Figure 6, black line). However, whereas glucose/sodium gluconate and sodium gluconate/sodium gluconate systems permit the formation of spherical nanoparticles, sorbitol/sodium gluconate systems allow the preparation of cylindrical nanorods.

Moreover, the same experiments were performed adopting the same reaction conditions and reducing/templating systems in the absence of NaOH. These last runs did not allow us to obtain copper nanoparticles or nanorods, in fact, the obtained solutions were colourless and their UV-VIS spectra did not have any peak around 450 nm, underlining again the fundamental role of NaOH.

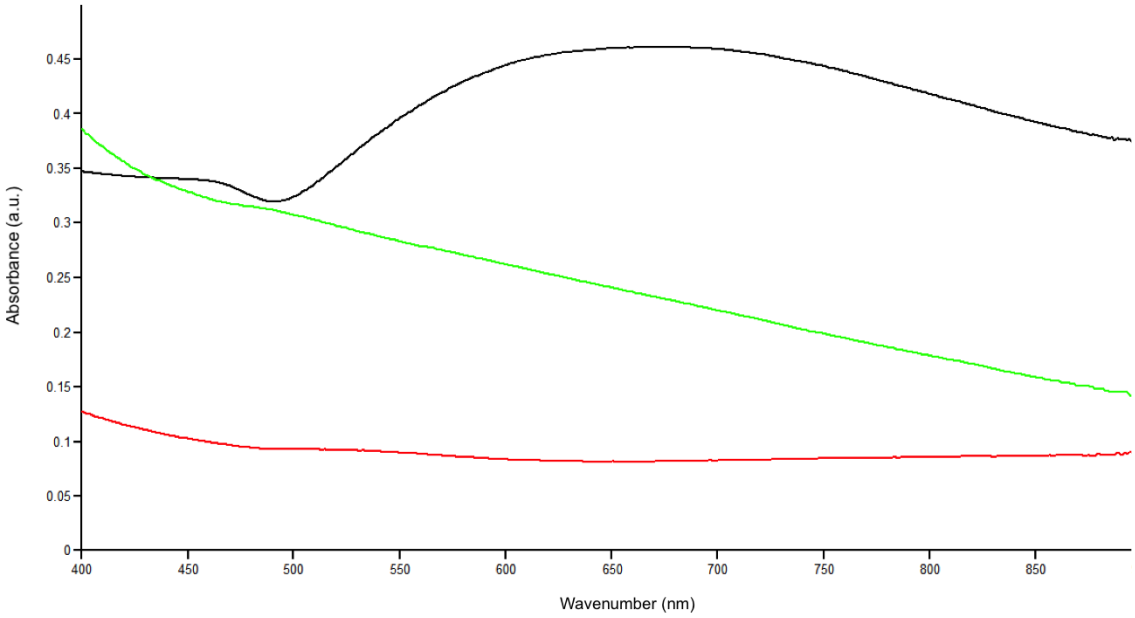

Figure 7 UV-Vis spectra of samples: a) CuPN21 obtained using glucose/sodium gluconate systems(red line), b) CuPN22 obtained using sorbitol/sodium gluconate system (black line) and d) CuPN23 sodium gluconate/sodium gluconate system (green line)

TEM micrographs of samples CuPN22 and CuPN23, confirm the diverse morphology observed through UV-Vis analysis (see Figure 7). In particular, sample CuPN22 is characterized by well-defined cylindrical nanorods, whereas sample CuPN23 is composed of spherical, acicular and cylindrical nanostructures (see Figure 8).

In conclusion, the sorbitol/sodium gluconate system shows the best reducing and templating power leading to the formation of well-defined copper nanorods with an average diameter of 15 nm and length of about 100-150 nm (sample CuPN22 Figure 7a). Conversely, glucose/sodium gluconate and sodium gluconate/sodium gluconate systems were not efficient enough to drive the growth of nanorods as shown by the UV-Vis and TEM analysis reported in Figures 7 and 8.

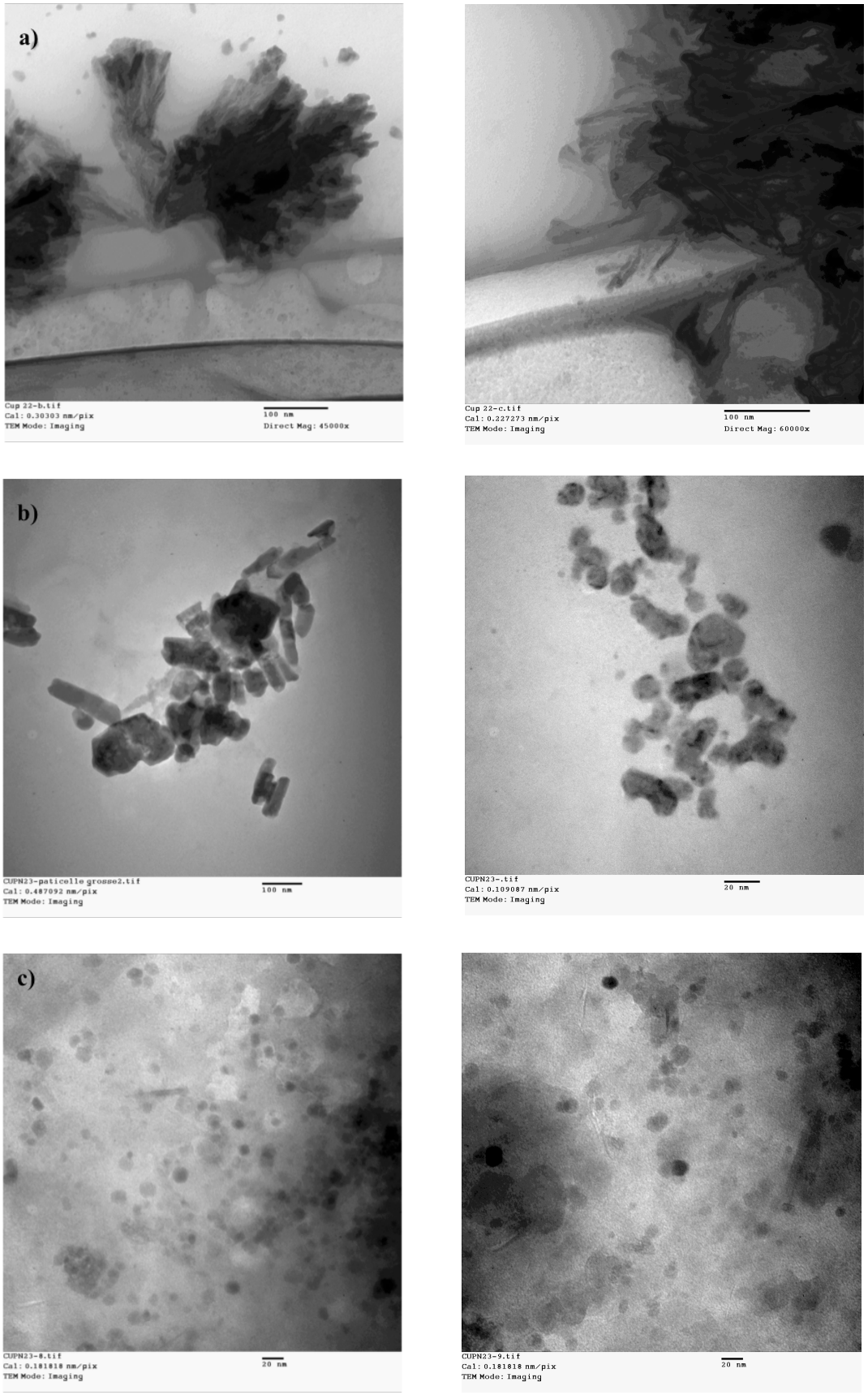

Figure 8 TEM micrographs of samples: a) CuPN22 sample obtained using sorbitol/ sodium gluconate system and b) CuPN23 sample obtained using sodium gluconate/ sodium gluconate system, c) CuPN21 sample obtained using glucose/ sodium gluconate system.

9.3.2 Effect of diverse heating sources on copper nanorod shape

In order to increase the growth of nanowire and minimize the decomposition of sorbitol and sodium gluconate observed from the UV-Vis analysis in Chapter 9.3.1, the effect of diverse heating source was investigated.

In a typical experiment, the seed solution was prepared dissolving sorbitol (2.5g) in 30 ml of water and adding 0.12 ml of NaOH 1M and 1.2 ml of $CuSO_4$ 10^{-2} M, then the resulting solution was irradiated with microwave at 80°C for 5 min. Meanwhile the growth solution was prepared dissolving sodium gluconate (1.9g) in 6 ml of water and adding .2 ml of $CuSO_4$ 10^{-2} M. Finally, the growth solution was added to the seed solution and treated with microwave at 80°C for 10 minutes. In particular, the runs were performed using a monomode microwave (CEM Discovery S-Class equipped with 80 ml glass vessels) and 150 ml Parr autoclave electrically heated and the results are summarized in Table 4.

Table 4 Effect of heating sources on nanorod shape

Sample	Step	Heating source	Observations	Nanorod length (nm)
CuPN24[a]	1	MW power 50W	Cylindrical well-defined nanorods	200
	2	MW power 50W		
CuPN27[a]	1	MW power 250W	Cylindrical and spherical nanostructures	149
	2	MW power 250W		
CuPN28[b]	1	Traditional heating	Cylindrical well-defined nanorods	83 (222)
	2	Traditional heating		

[a] First step last 5 minutes, second step last 10 minutes
[b] First step last 10 minutes, second step last 15 minutes

As can be observed in Table 4, the final properties of copper nanorods is straightly dependent on the heating power, in particular by decreasing the microwave power the undesired decomposition of sorbitol and sodium gluconate was partially avoided.

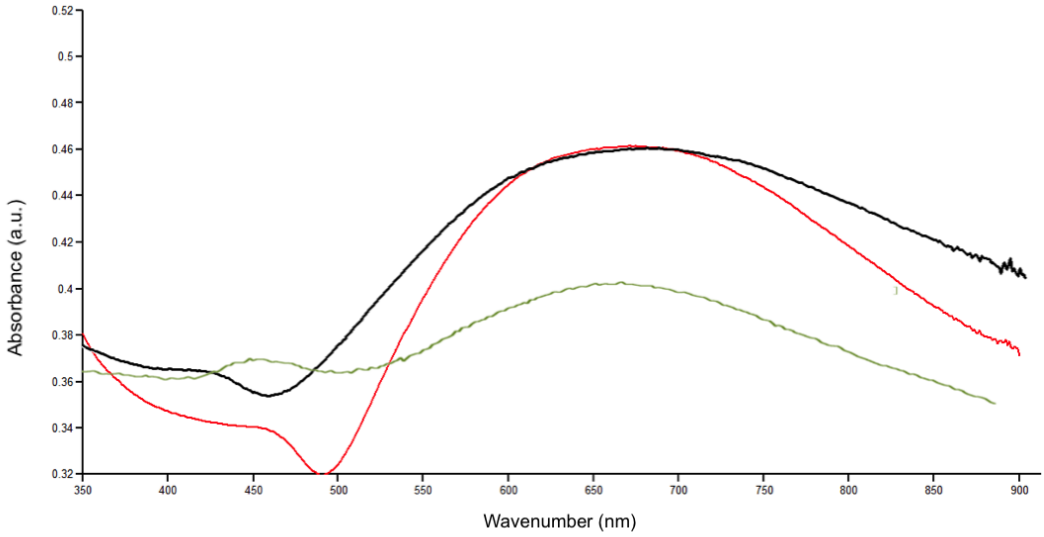

Figure 9 UV-Vis spectrums of a) Sample CuPN24, obtained using 50W of microwave power (red line), b) Sample CuPN27 obtained using 250W of microwave power (black line) and c) Sample CuPN28 obtained with the traditional heating source (green line).

As shown in Figure 9a, sample CuPN24 (red line) obtained under the lower microwave power has two marked peaks at 450 nm and 700 nm, characteristic of copper nanorods. Sample CuPN27 (black line) obtained with the highest microwave power shows more broad peaks at the same wavenumber compared to those observed for sample CuPN24, underlining a lower nanorod growth. The lower nanorod growth could be due to the decomposition of sorbitol and sodium gluconate that occurs at high MW power, leading to worse control of particle growth (sample CuPN27).

However, sample CuPN28 obtained using the traditional heating source shows a light yellow colour and has small absorbance at 450 nm and 700 nm, which underlines the formation of few copper nanorods. Traditional heating did not supply enough energy to the reactive mixture to guarantee efficient copper reduction, contrary to what was observed using microwave as a heating source.

These effects were confirmed also by TEM analysis as reported in Figure 10. Sample CuPN24 shows well defined nanorods characterized by an average diameter of 15 nm and a length of about 200 nm, whereas sample CuPN27 is composed of diverse cylindrical nanostructures similar to the ones observed in sample CuPN24 characterized by an average length of 149 nm. Finally, sample CuPN28 shows smaller cylindrical nanostructures characterized by a bimodal size distribution, with a main nanorod population of a length of 83 nm and another nanorod population of a length of 222 nm.

In conclusion, the microwave at lower power irradiation (50W) allows us to obtain longer nanorods characterized by narrow size distribution.

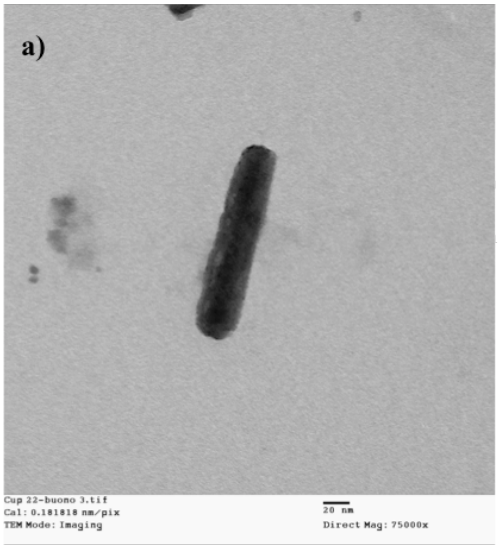

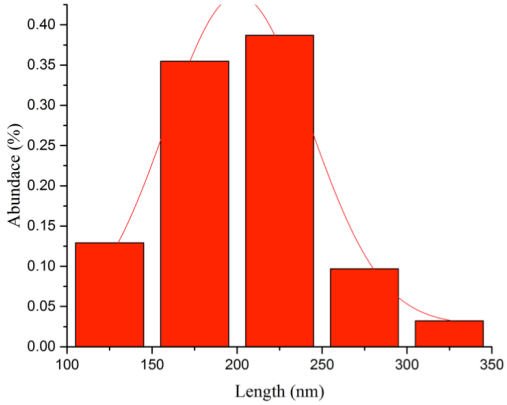

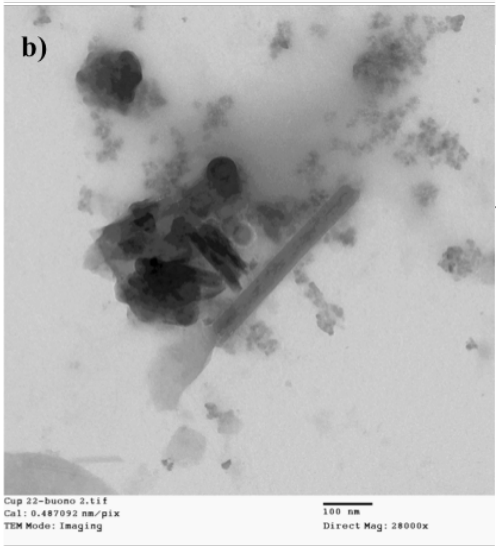

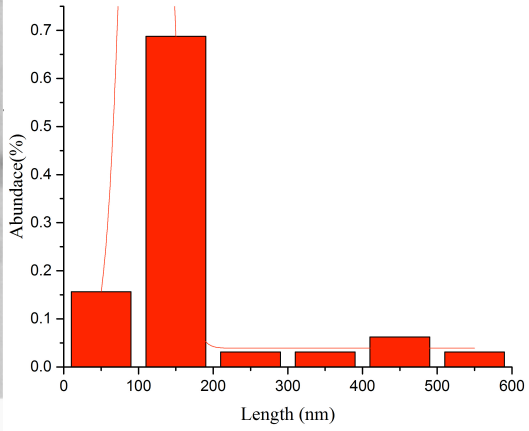

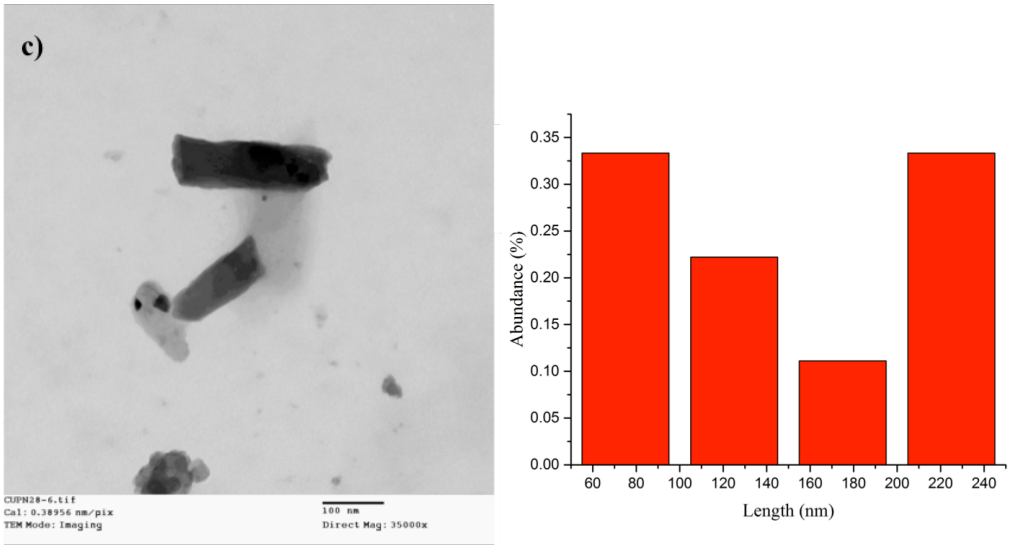

Figure 10 TEM micrographs and nanorods length distributions of samples: a) Sample CuPN24, obtained using 50W of microwave power, b) Sample CuPN27 obtained using 250W of microwave power and c) Sample CuPN28 obtained with the traditional heating source.

9.3.3 Effect of growth times on copper nanorod shape

The effect of diverse growth times on nanorod shapes was investigated by adopting selected sorbitol/sodium gluconate systems and the microwave as a heating source. In a typical experiment the seed solution was prepared dissolving sorbitol (2.5g) in 30 ml of water and adding 0.12 ml of NaOH 1M and 1.2 ml of $CuSO_4$ 10^{-2} M, then the mixture was treated with microwave at 80°C and 50W. Meanwhile the growth solution was prepared dissolving sodium gluconate (1.9) in 6 ml of water and adding .2 ml of $CuSO_4$ 10^{-2} M. Finally, the growth solution was added to the seed solution and treated with microwave at 80°C at 50W. The results are summarized in Table 5.

Table 5 Effect of growth times on nanorod morphologies

Sample	Step	Time (min)	Nanorod lengh (nm)
CuPN24	1	5	200
	2	10	
CuPN29	1	5	269
	2	20	

By increasing growth time and taking well separated seed and growth stages it is possible to obtain better defined and longer nanorods.

The UV-Vis spectra of CuPN24 and CuPN29 samples show peaks at 450 nm and 700 nm ascribable again to the two dimensions of nanorods, diameter and length.

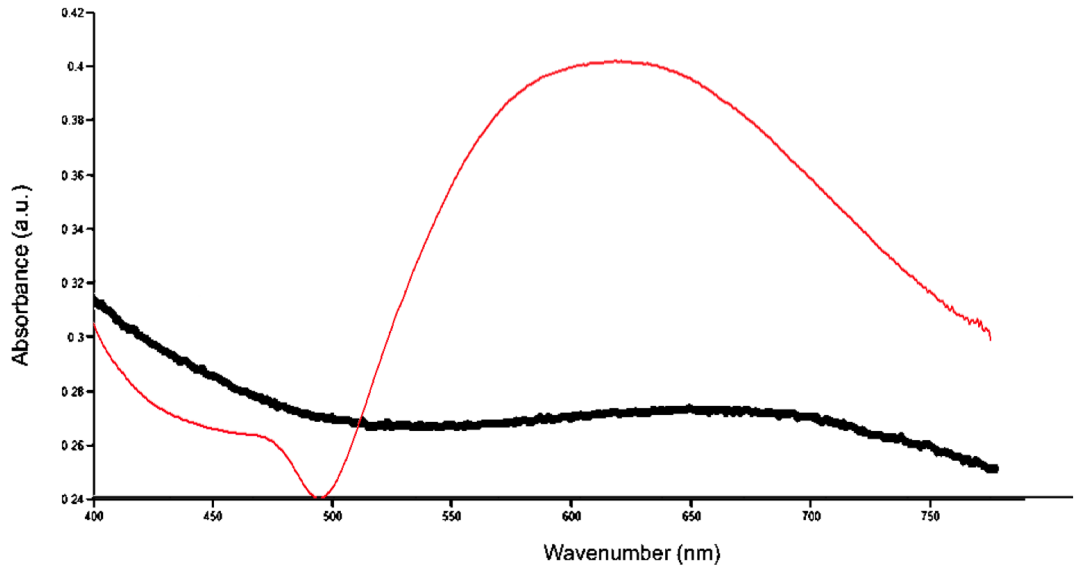

Figure 11 a) Sample CuPN24, obtained with 10 minutes of growth (red curve), b) Sample CuPN29 obtained with 20 minutes of growth (black curve).

TEM images of sample CuPN29 reported in Figure 12b show nanorods longer than those observed for sample CuPN24 (see Figure 12a). In particular, the nanorods obtained with a growth time of 10 minutes show a length of around 200 nm (sample CuPn24) whereas the ones obtained with a growth time of 20 minutes (sample CuPn29) show a length of about 269 nm. Therefore, by adopting a longer growth time (sample CuPN29) it is possible to increase the length of nanorods.

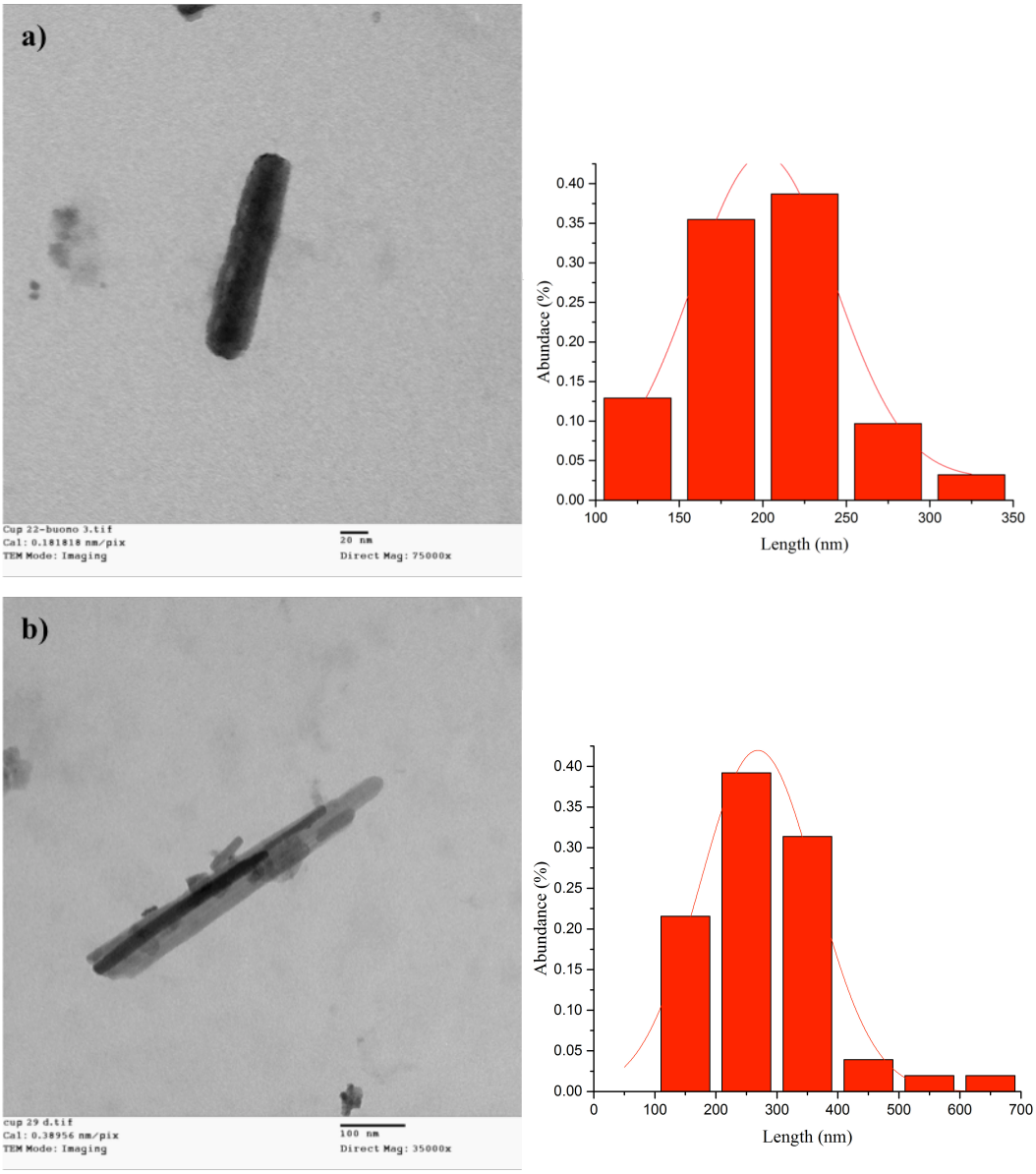

Figure 12 TEM micrographs of and nanorod length distribution samples a) Sample CuPN24, obtained with 10 minutes of growth, b) Sample CuPN29 obtained with 20 minutes of growth.

9.3.4 Effect of cupper sulphate concentration on nanorod morphology

The effect of diverse copper precursor concentrations on final nanorod morphology was investigated on the sorbitol/sodium gluconate systems under microwave irradiation.

In a typical experiment the seed solution was prepared dissolving sorbitol (2.5g) in 30 ml of water and adding 0.12 ml of NaOH 1M and the selected amount of $CuSO_4$ then the mixture was treated with microwave at 80°C and 50W. Meanwhile the growth solution was prepared dissolving sodium gluconate (1.9) in 6 ml of water and adding .2

ml of $CuSO_4$ 10^{-2} M. Finally, the growth solution was added to the seed solution and treated with microwave at 80°C at 50W. The results are summarized in Table 6.

Table 6 Effect of cupper sulphate concentration on nannorods final morphologies

Sample	Step	V CuSO4 10^{-2} M (ml)	Nanorods Leghnt (nm)
CuPN29	1	1,2	268
	2	1,2	
CuPN30	1	0,8	256
	2	1,2	

By decreasing the initial copper concentration it is possible to obtain cylindrical nanorods characterized by a smaller length than those obtained with a higher concentration as confirmed by the UV-Vis analysis of samples CuPN29 and CuPN30.
In particular, sample CuPN29 shows a bigger intense peak at 700 nm than sample CuPN30; this particular peak is correlated to the nanorod length, thus confirming that the nanorods of sample CuPn29 are longer than the ones observed in sample CuPN30 (see Figure 13).

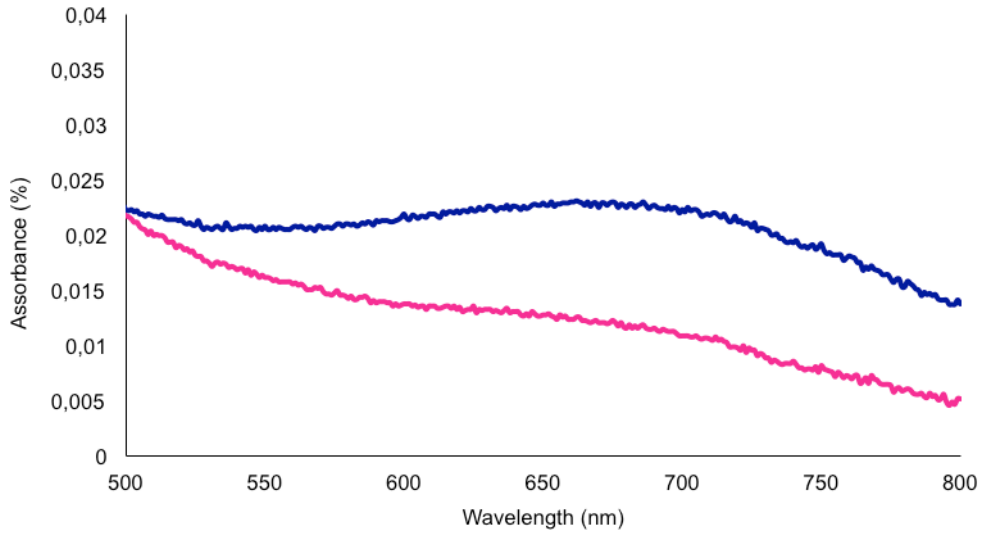

Figure 13 UV-VIs spectra of samples a) sample CuPN29 obtained with the higher copper precursor concentration (blue line) and b) sample CuPN30 obtained with the lower copper precursor concentration (pink line).

TEM micrographs reported in Figure 14 confirm that sample CuPN29 is composed of slightly longer nanorods characterized by irregular surfaces, whereas sample CuPN30 shows well defined cylindrical nanorods, probably due to a more regular geometrical evolution of their surface that occurs at a low metal precursor concentration (see Figure 14b). The geometrical evolution of asymmetric nanostructures was observed by Elechiguerra and Yan et Al.[18]

In conclusion, based on the final application of these nanomaterials it is necessary to find a compromise between the control of nanorod shape and length.

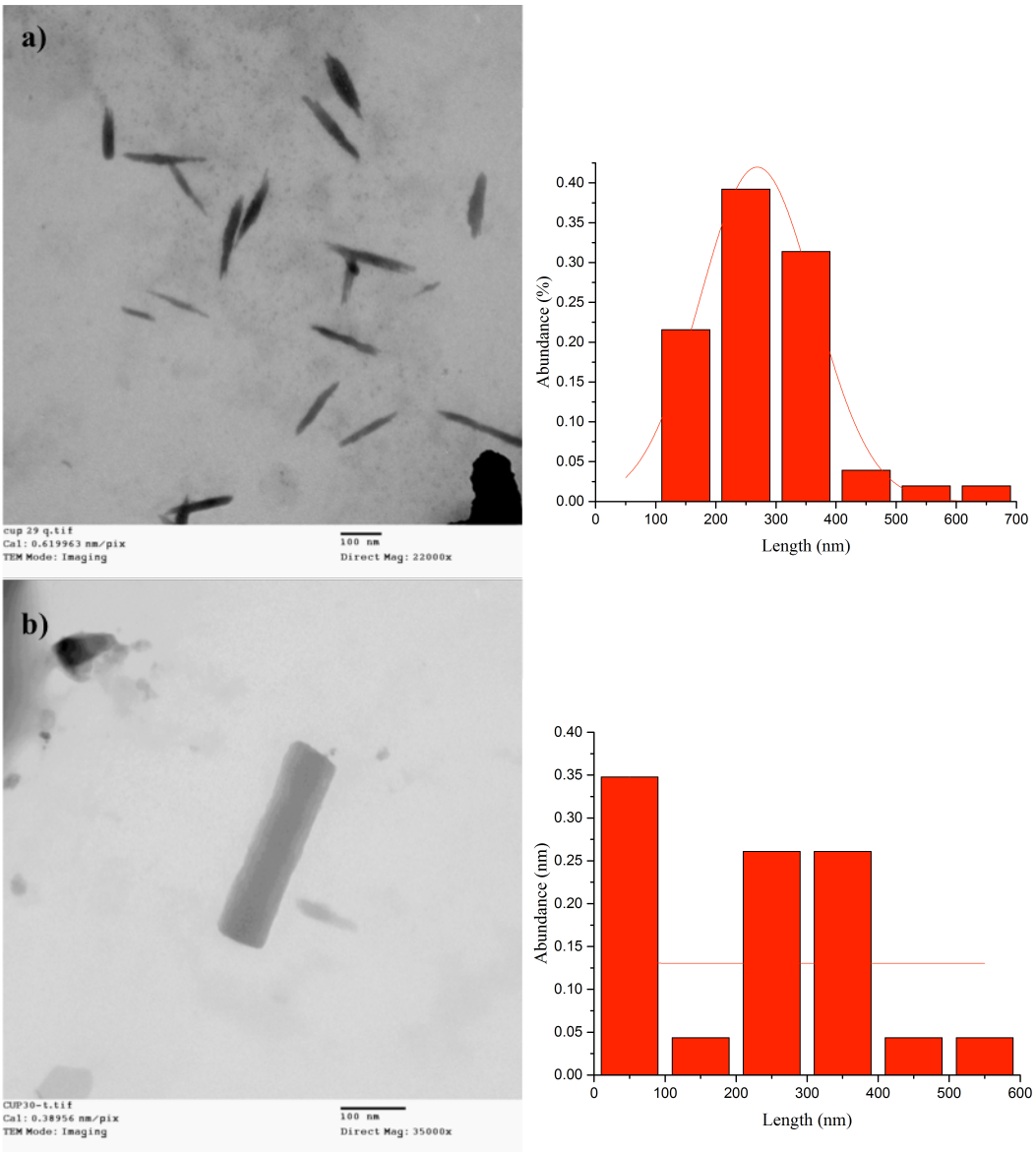

Figure 14 TEM micrographs of samples a) sample CuPN29 obtained with the higher copper precursor concentration and b) sample CuPN30 obtained with the lower copper precursor concentration.

9.4 References

[1] B. Lin, G. A. Gelves, J. A. Haber and U. Sundararaj, *Industrial & Engineering Chemistry Research* **2007**, *46*, 2481-2487.
[2] a) C. Wang, X. Q. Fu, X. Y. Xue, Y. G. Wang and T. H. Wang, *Nanotechnology* **2007**, *18*, 145506; b) E. K. Athanassiou, R. N. Grass and W. J. Stark, *Nanotechnology* **2006**, *17*, 1668.
[3] a) G. Jiao, H. Fan, L. Liu and W. Wang, *Materials Letters* **2007**, *61*, 4185-4187; b) J. Feenstra and H. A. Sodano, *Journal of Applied Physics* **2008**, *103*, 124108.
[4] A. K. Patra, A. Dutta and A. Bhaumik, *Catalysis Communications* **2010**, *11*, 651-655.
[5] Y. Wei, S. Chen, B. Kowalczyk, S. Huda, T. P. Gray and B. A. Grzybowski, *The Journal of Physical Chemistry C* **2010**, *114*, 15612-15616.
[6] M. Salavati-Niasari and F. Davar, *Materials Letters* **2009**, *63*, 441-443.
[7] S. Chandra, A. Kumar and P. K. Tomar, *Journal of Saudi Chemical Society* **2014**, *18*, 149-153.
[8] a) G.-q. Zheng, S.-y. Ni, H.-j. Zheng, X.-h. Gan and J.-y. Zhang, *Journal of Central South University of Technology* **2004**, *11*, 371-374; b) M. Lai and D. J. Riley, *Journal of Colloid and Interface Science* **2008**, *323*, 203-212.
[9] H. Acar, R. Genc, M. Urel, T. S. Erkal, A. Dana and M. O. Guler, *Langmuir* **2012**, *28*, 16347-16354.
[10] Q. Lu, F. Gao and S. Komarneni, *Chemistry of Materials* **2006**, *18*, 159-163.
[11] F. Gao, Q. Lu and S. Komarneni, *Journal of Materials Research* **2006**, *21*, 343-348.
[12] J. Zhou, C. Soto, M.-S. Chen, M. Bruckman, M. Moore, E. Barry, B. Ratna, P. Pehrsson, B. Spies and T. Confer, *Journal of Nanobiotechnology* **2012**, *10*, 18.
[13] F. Gao, Q. Lu, X. Meng and S. Komarneni, *Journal of Materials Science* **2008**, *43*, 2377-2386.
[14] S. Panigrahi, S. Kundu, S. K. Ghosh, S. Nath, S. Praharaj, S. Basu and T. Pal, *Polyhedron* **2006**, *25*, 1263-1269.
[15] X. Zhang, D. Zhang, X. Ni and H. Zheng, *Solid State Communications* **2006**, *139*, 412-414.
[16] a) M. Biçer and İ. Şişman, *Powder Technology* **2010**, *198*, 279-284; b) Z. Liu and Y. Bando, *Advanced Materials* **2003**, *15*, 303-305.
[17] P. R. Sajanlal, T. S. Sreeprasad, A. K. Samal and T. Pradeep, *2011* **2011**.
[18] a) J. L. Elechiguerra, J. Reyes-Gasga and M. J. Yacaman, *Journal of Materials Chemistry* **2006**, *16*, 3906-3919; b) W. Yan, J. Peng, J. Ming, W. Tie-Wei, G. Chuan-Fei, X. Si-Shen and W. Zhong-Lin, *Nanotechnology* **2009**, *20*, 305602.

10. STUDY OF THE SELECTIVE HYDROGENATION OF CYNNAMALDEHYDE TO HYDROCINNAMALDEHYDE IN THE PRESENCE OF THE MAGNETIC PALLADIUM CATALYSTS

10.1 Introduction

Cinnamaldehyde (CAL) is an organic compound that can be found naturally in cinnamon plants. It is an α,β-unsaturated molecule that can be selectively hydrogenated on the aldehyde group to obtain cinnamyl alcohol (COL), on the C=C bond to give hydrocinnamaldehyde (HCAL) or on both the aldehyde and the C=C bond to give hydrocinnamic alcohol (HCOL), as described in Scheme 1.

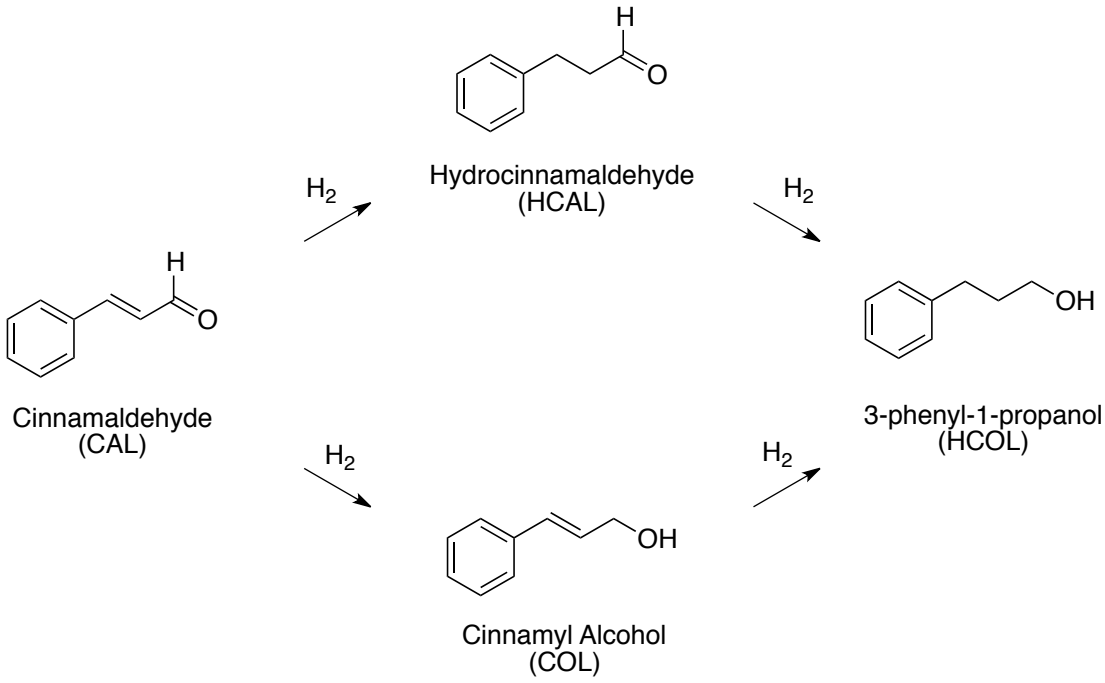

Scheme 1 Reaction scheme of the hydrogenation of cinnamaldehyde

Among cinnamaldehyde-hydrogenated products, hydrocinnamaldehyde is the most important from an industrial point of view. In fact, HCAL is a building block for a wide range of fine chemicals such as perfumes[1] and pharmaceutics[2].

For these reasons, hydrogenation conditions such as temperature, pressure, solvent and catalyst have been deeply studied to improve the selectivity toward hydrocinnamaldehyde production.

As underlined by Zhang et al. polar and apolar solvents strongly influence hydrogenation yield and selectivity. For example, apolar solvents such as toluene, decalin, decane and also ethyl ether resulted the best solvents whereas alcohols the worst. [3]

Furthermore, other fundamental aspects able to influence selectivity and yield of this reaction are the kind of metal catalyst, metal loading and catalytic support.[4]

Several catalysts were employed in the selective hydrogenation of cinnamaldehyde, among them palladium or ruthenium based catalysts showed the best selectivity in hydrocinnamaldehyde, whereas platinum and iridium resulted active towards cinnamyl alchol.

For example, Mehri et al. reported the hydrogenation of cinnamaldehyde over palladium on titanium oxide at 50°C under 10 bar of H_2 obtaining low conversion (20%) and HCAL selectivity of 76%.[5] Yang et al.[6] employed palladium trapped inside titanate nanotubes at 30°C under 5 bar of H_2 obtaining almost complete conversion and 80% hydrocinnamaldehyde selectivity.

Cabiac et al.[7] employed palladium over carbon at 60°C obtaining high cinnamaldehyde conversion (90%) and high hydrocinnamaldehyde yield (90%), whereas Lashdaf et al. described the use of palladium on alumina or silica in propanol obtaining higher conversion (100%) but lower selectivity in hydrocinnamaldehyde (50%).[8] Jabou et al. described the use of palladium over titanium oxide nanofibers obtaining Cal conversion of 20% and HCAL selectivity of 70% at room temperature under 10 bar of H_2.[9]

Zhao et al.[10] described the hydrogenation of cinnamaldehyde over palladium supported on zeolitic imidazolate framework (ZIFs) under 40°C and 20 bar of hydrogen for 6 h obtaining the complete cinnamadehyde conversion with a hydrocinnamadehyde yield of 90%.

The literature shows that the catalytic activity of palladium is strongly connected to catalyst morphology and to the kind of support.[11]

Moreover, other metals and bimetallic compounds were employed in the hydrogenation of cinnamaldehyde with very diverse results such as Cu[12], Pt[13], Co[14], Ni[15], Au[16], Ir[17], Co-Pt,[18] Cu-Pt[19], Pd-Au[20], Cu-Au[21], Sn-Pt[22], Pt-GO[23], Ni-TiO_2[24] and Ni-Cu[25]. Up to now magnetic core shell nanostructures were poorly investigated in the hydrogenation of cynnamadehyde to hydrocinnamadehyde, for example very recently Yu et al.[26] reported the use of palladium supported on a core-shell Fe_3O_4@C as catalyst, obtained by Fe_3O_4 coated with glucose-derivated carbon and successive Pd loadind via hydrothermal reduction in ethyl glycol, obtaining high cinnmaldehyde conversion but relatively low selectivity toward the hydrocinnamadehyde (<70%). Song et al.[27] described the employ of platinum supported on magnetite flake (Pt@Fe_3O_4) reaching low cinnamaldehyde conversion (50%) and high hydrocinnamadehyde selectivity (96%) whereas, Liu et al. [28] reported the employ of platinum

supported over magnetic carbon nanotube (Pt-Fe_3O_4@CNT) obtaining higher cinnamadehyde conversion and a slightly lower hydrocinnamaldehyde yield (93%).

Taking into account the promising results of magnetic nanocatalysts and their easy an efficient recovery, the new magnetic palladium systems described in Chapter 5.1 were employed in the selective hydrogenation of cinnamaldehyde to hydrocinnamaldeyhde as a model reaction for the hydrogenation of unsaturated aldehydes. In particular, the effect of palladium loading, catalyst structure, catalyst recyclability and temperature on the hydrogenation rate and selectivity were evaluated.

10.2 The effect of the palladium loading on hydrogenation rate

The effect of palladium loading on the hydrogenation rate was evaluated using the magnetic palladium catalyst synthetized and characterised as reported in chapter 5.1. The obtained results were compared with those reported in the literature[29]. The main characteristics of the adopted palladium catalyst are reported in Table 1.

Table 1 Main characteristics of the selected magnetic palladium nanocatalysts

Catalysts	Pd load (%)	Surface area (m^2/g)	Diameter of the support (nm)	Diameter of palladium (nm)
Pd1 (Pd@γFe_2O_3)	2.1	74.4	5.6	N.D
Pd@Al_2O_3[a]	1.9	130	N.D	8

[a] Reference catalyst from literature[29]

A typical hydrogenation experiment was carried out at 100°C under 20 bar of hydrogen using 3.8 ml of cinnamaldehyde, the desired amount of palladium catalyst and 100 ml of decaline. The reaction was followed by a gas chromatograph (Hewlett-Packard 5890, equipped with FID detector and a PONA column (cross-linked methyl silicon gum)) and the results are summarized in Table 2.

Table 2 Selective hydrogenation of cinnamaldehyde to hydrocinnamaldehyde

Run	Pd (mg)	CAL Conversion[a] (%)	HCAL Selectivity[a] (%)	HCAL Yield[a] (%)	A[a] (mol/g h)	TOF[a] (h^{-1})
CIN1[b]	1.1	68	87	60	0.0031	0.20
CIN2[b]	2.5	73.7	96.3	71	0.0015	0.16
CINR[c]	2.5	74.7	93.3	69.6	0.0015	0.16

[a] values obtained after 6h of reaction

[b] catalyst Pd1, Pd@γ-Fe_2O_3 characterized by a Pd loading of 2.1% wt.

[c] reference results from the literature[29]

As can be observed from Table 2, the run CIN2 carried out using the higher palladium loading (2.5 mg) showed a slightly higher CAL conversion (73.7%) and higher HCAL selectivity (96.3%), whereas the run CIN1 carried out using lower palladium loading (1.1 mg), showed a slightly lower conversion and selectivity, 68% and 87%, respectively. Increasing the palladium content from 1.1 mg to 2.5 mg it was possible to limit the side reactions. In particular as it is possible to see in Figure 1 after 4 h of reaction, run CIN1, carried out with lower palladium, showed an increase in CAL conversion but not in HCAL yield underlining that using 1.1 mg of palladium a by products formation was observed.

Furthermore, the catalytic activity of magnetic palladium catalyst (Pd1) resulted similar to those reported in literature for palladium supported on alumina (Pd@Al_2O_3) (see Table 2, run CINR).

Taking into account the high hydrocinnamaldehyde selectivity reached in both runs (CIN1 and CIN2), the well-known selectivity problem connected with this hydrogenation as reported in literature[8-9] and the easy and efficient recovery of the new magnetic catalyst, the magnetic palladium systems can be considered a strategic tool for industrial hydrogenation processes.

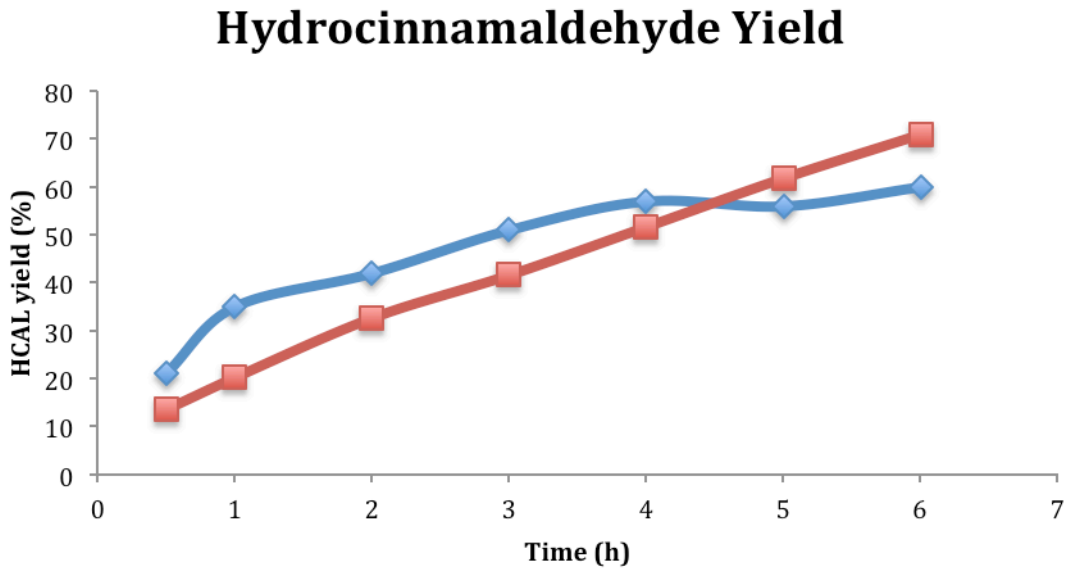

Figure 1 Hydrocinnamaldehyde yield vs. time using two diverse Pd load: a) Pd load of 1.1 mg, CIN1 (blue line) and b) Pd load of 2.5 mg CIN2 (red line)

Figure 1 shows the hydrocinnamaldehyde yield trends for CIN1 and CIN2 runs (blue and red lines, respectively). In particular, CIN2 showed a linear crescent yield, whereas the CIN1 run yield reaches a maximum after 4 hours of reaction.

It is important to underline that all the catalytic systems maintained their magnetic properties and were easily magnetically recovered from the reaction mixture.

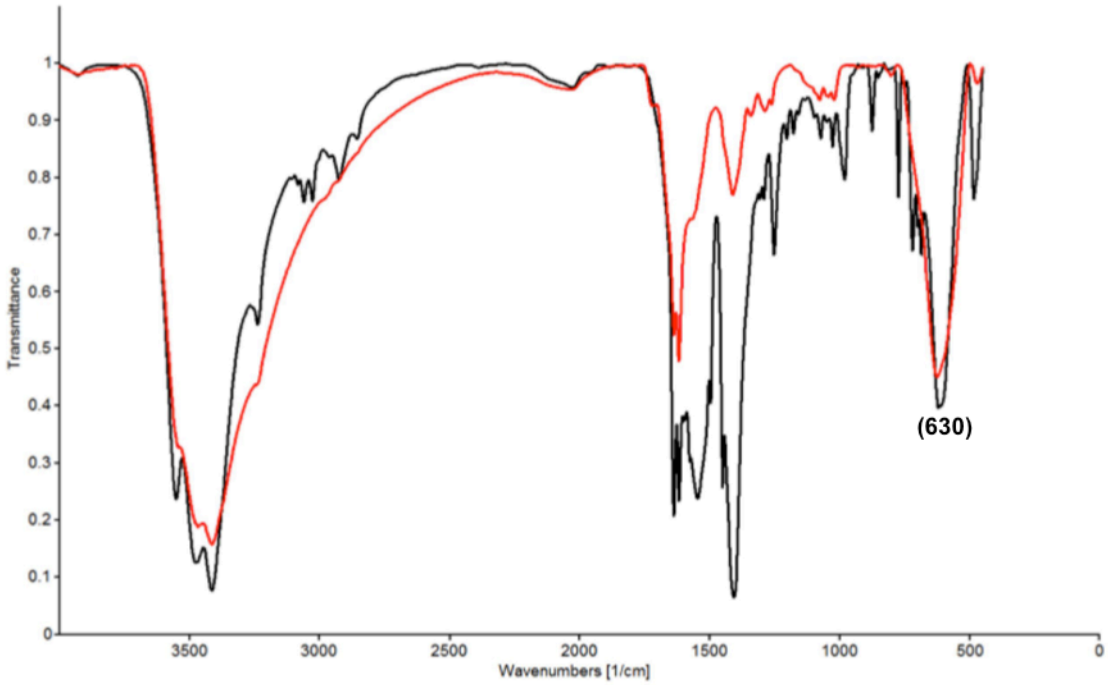

Figure 2 FT-IR spectra of Pd1 catalysts a) before reaction (red line) b) after reaction (black line)

The FT-IR spectra of the Pd1 catalyst before (red line) and after (black line) hydrogenation are reported in Figure 2. Both the FT-IR spectra show a typical maghemite peak at 630 1/cm, peaks around 1400 1/cm due to carbonate trace introduced during catalyst preparation and a broad peak between 3000 1/cm and 3500 1/cm ascribable to hydroxyl stretching vibration of ethanol and water molecules trapped in the iron oxide structure.

The good overlapping of the maghemite peaks at 630 1/cm confirmed the stability of this catalyst.

Furthermore, the FT-IR spectrum of the catalyst after reaction (black line) presents numerous other peaks due to the aromatic and unsaturated bond of cinnamaldehyde and hydrocinnamdehyde adsorbed on the catalyst surface. For example, the peaks between 1500 1/cm and 1600 1/cm are ascribable to C=O of the aldehyde group present in cinnamadehyde and hydrocinnamaldehyde molecules and the narrow peaks between 900 1/cm and 1300 1/cm are ascribable to the aromatic ring present in reagent and products.

Furthermore, the Pd1 catalyst showed a significant reduction of surface area after the reaction, from 74.42 m^2/g to 47.3 m^2/g.

10.3 The effect of the Pd catalyst characteristics on the hydrogenation rate

The effect of the Pd catalyst characteristics on the hydrogenation rate was investigated adopting the reaction conditions showed above and three diverse magnetic palladium systems were studied: They were Pd supported on maghemite Pd1 (Pd@γ-Fe_2O_3), palladium nanoparticles impregnated on magnetite Pd3 (Pd@Fe_3O_4) and palladium nanoparticles trapped inside magnetite structure Pd6 (Pd@Fe_3O_4). All these catalysts were synthetized and characterized as reported in Chapter 5.1 and their main characteristics are summarized in Table 3.

Table 3 Main characteristics of the adopted palladium magnetic nanocatalysts

Samples	Composition	AAS (Pd %wt)	BET (m^2/g)	Support diameter (nm)	Palladium diameter (nm)
Pd1[a]	5% Pd@γ-Fe_2O_3	2.1	74.4	5.6	N.D
Pd3[b]	5% Pd@Fe_3O_4	4.3	112.0	14	3.7
Pd6[c]	5% Pd@Fe_3O_4	4.7	106.5	8	N.D

[a] Palladium nanoparticles impregnated on maghemite nanostructure, Synthesis: 0.5g of γ-Fe_2O_3, 0.05g $Pd(OAc)_2$, 44 mL EtOH at 96 wt%, microwave heating: 120 °C, 15 min, 250 W

[b] Palladium nanoparticles impregnated on magnetite nanostructure, Synthesis: 0.5g Fe_3O_4, 0.05g $Pd(OAc)_2$, 44 mL EtOH at 96 wt%, microwave heating: 120 °C, 15 min, 250W.

[c] Palladium nanoparticles intercalated into magnetite nanostructure, Synthesis: 1g of $Fe(OAc)_2$, 0.05g $Pd(OAc)_2$, 44 mL EtOH at 96 wt%, microwave heating: 120 °C, 15 min, 250 W

The hydrogenation results obtained with all the above catalysts are summarized in Table 4.

Table 4 Effect of catalyst support and morphology on hydrogenation rate[a]

Run	Catalyst	CAL Conversion (%)	HCAL selectivity (%)	HCAL Yield (%)	A (mol/g h)	TOF (h^{-1})
CIN2	Pd1	73.7	96.3	71	0.0015	0.16
CIN3	Pd3	35.4	92.4	33	0.0007	0.08
CIN4	Pd6	58.2	93	54	0.0012	0.12

[a] reaction conditions: Temperature 100°C, H_2 Pressure 20 bar, 3,8 ml of cinnamaldehyde, 100 ml of decaline, 2.5 mg of Pd and reaction time 6 h

As it is possible to see in Table 4, Pd1 catalyst, characterized by palladium supported on maghemite, showed the highest conversion and selectivity (run CIN2), higher than those reported in literature for analogues magnetic palladium catalysts[26]. The result could be due to a positive synergic effect between the maghemite and the palladium nanoparticles. A similar maghemite positive effect was evidenced also by Milone et al.[30] who studied the effect of different iron oxides on the hydrogenation rate of α,β unsaturated aldehydes and ketones.

Furthermore, Pd6 catalyst permits to reach higher conversion than the Pd3 catalyst, (run CIN3). The marked difference ascertained in the catalytic performances of these two magnetite-based catalysts (Pd3 and Pd6) can be explained by their different nanostructure. In fact the Pd3 catalyst shows a hierarchical structure where palladium nanoparticles are anchored on magnetite surface whereas Pd6 catalyst shows a complex structure where palladium nanoparticles are intercalated into magnetite nanostructure. These structural differences confirmed also by XRD analysis lead to different Fe-Pd interactions, which strongly influence the reaction rate.

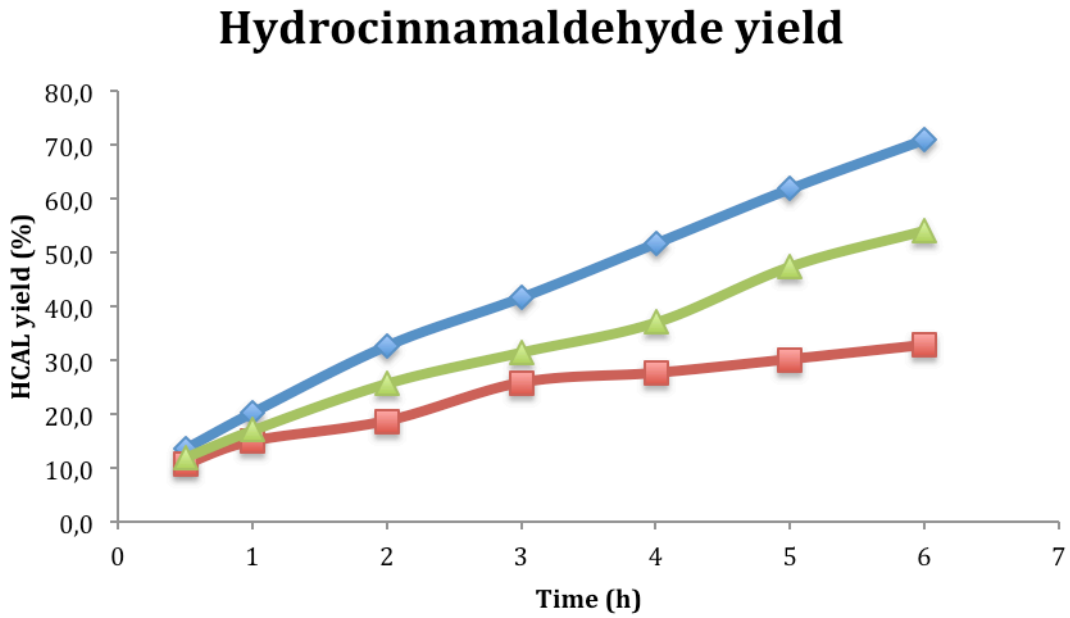

Figure 3 Hydrocinnamaldehyde yield vs. time using diverse catalysts: a) palladium nanoparticle over maghemite, Pd1 (blue line), b) palladium nanoparticles over magnetite, Pd3 (red line) and c) palladium nanoparticles trapped inside magnetite, Pd6 (green line)

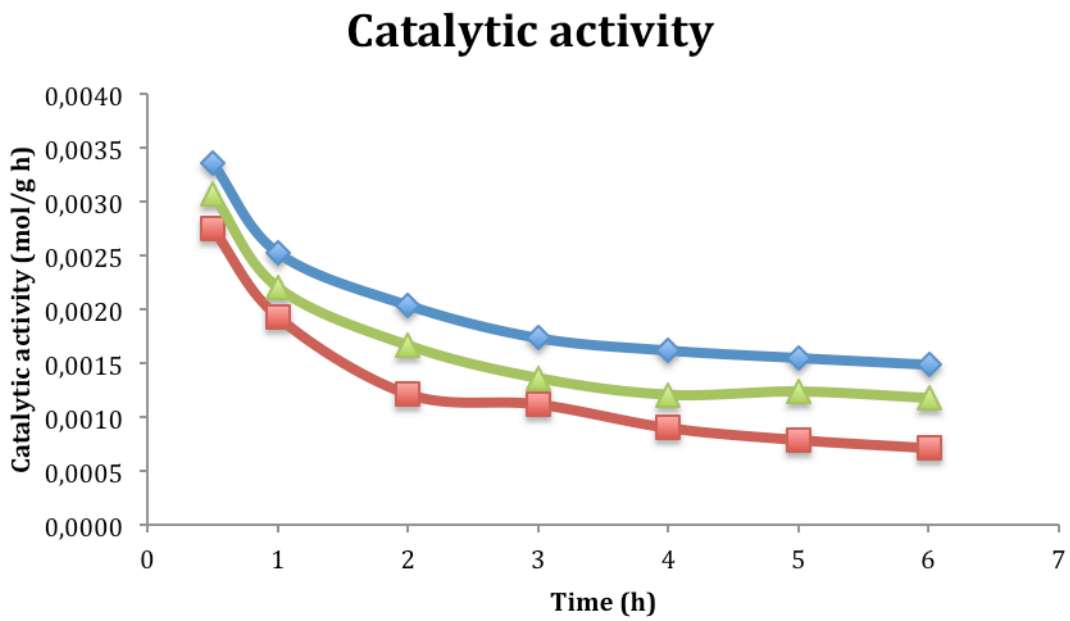

Figure 4 Catalytic activity vs. time using diverse catalysts: a) palladium nanoparticle over maghemite, Pd1 (blue line), b) palladium nanoparticles over magnetite, Pd3 (red line) and c) palladium nanoparticles trapped inside magnetite, Pd6 (green line)

The hydrocinnamaldehyde yield and catalytic activity trends of the three different catalysts are shown in Figures 3 and 4.

The catalysts characterised by more exposed active metal sites, generally show better catalytic activity than the catalysts characterized by a complex structure where the active metal is

confined inside the support. However, in this study the opposite behaviour was observed. This result is particularly important because when the active metal is exposed on the catalyst surface, deactivation of the catalytic system could easily occur because of poisoning or leaching, contrary to what is commonly observed for a catalyst strongly interacting with the support. Furthermore, these magnetic systems maintained good magnetic properties after the reaction.

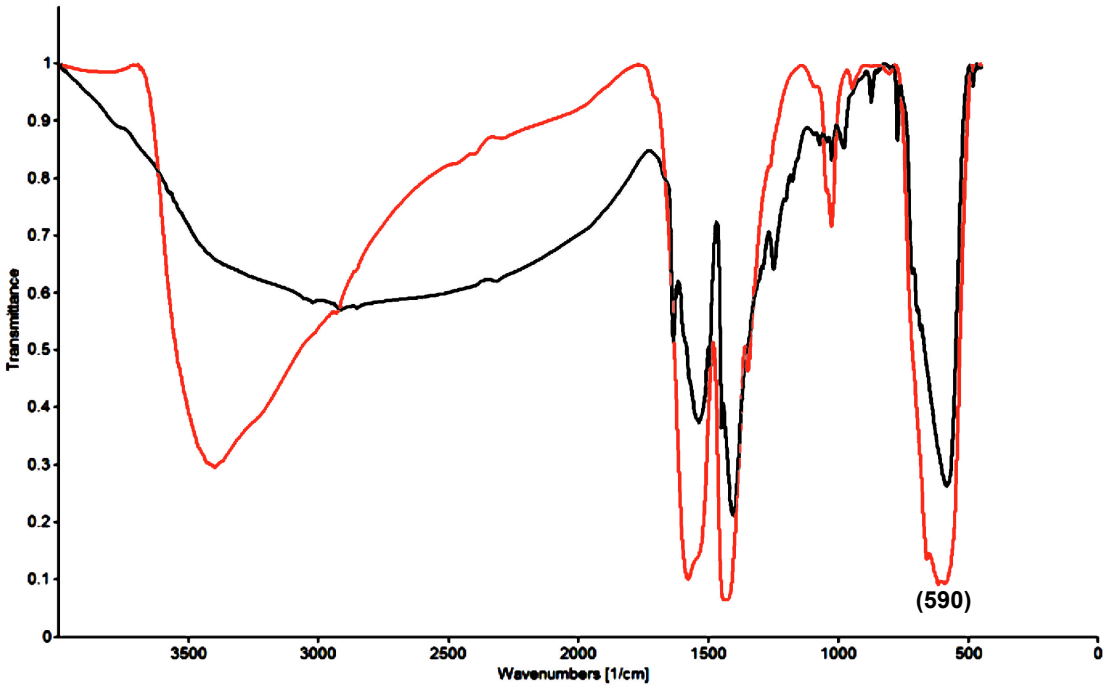

Figure 5 FT-IR spectra of Pd3 catalysts a) before reaction (red line) b) after reaction (black line)

The FT-IR spectra of the Pd3 catalyst before (red line) and after (black line) hydrogenation are reported in Figure 5. Both FT-IR spectra show a typical magnetite peak at 590 1/cm, peaks around 1400 1/cm due to acetate trace introduced during the catalyst preparation and a broad peak between 3000 1/cm and 3500 1/cm ascribable to hydroxyl stretching vibration of ethanol and water molecules trapped in the iron oxide structure.

The presence of the magnetite peak at 590 1/cm confirms the stability of this catalyst.

Furthermore, the FT-IR spectrum of the catalyst after reaction (black line) presents numerous other peaks, for example peaks between 1500 1/cm and 1600 1/cm which are ascribable to C=O of aldehyde groups present in cinnamadehyde and hydrocinnamaldehyde molecules, and narrow peaks between 900 1/cm and 1300 1/cm due to the aromatic rings present in reagent and products.

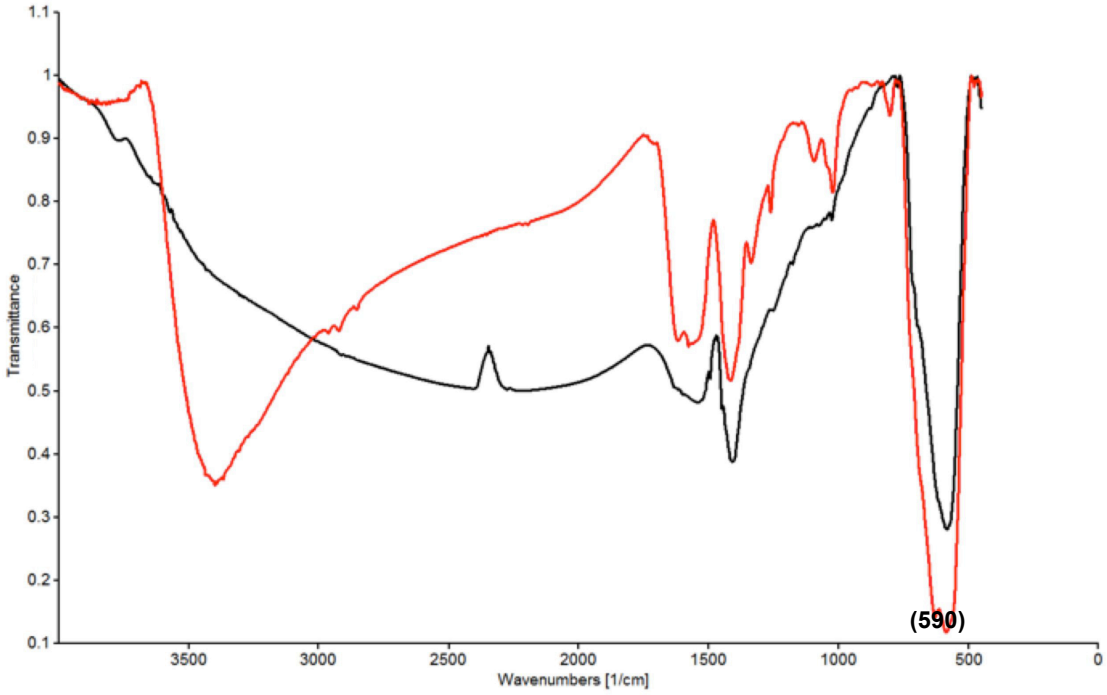

Figure 6 FT-IR spectra of Pd6 catalysts a) before reaction (red line) b) after reaction (black line)

The FT-IR spectra of the Pd6 catalyst before (red line) and after (black line) hydrogenation are reported in Figure 6. Both FT-IR spectra show a typical magnetite peak at 590 1/cm, confirming the stability of this catalyst.

Once again, the FT-IR spectrum of the catalyst after reaction (black line) presents numerous other peaks due to the aromatic and unsaturated bond of cinnamaldehyde and hydrocinnamdehyde adsorbed on the catalyst surface.

The Pd6 catalyst showed a certain reduction of the surface area after the hydrogenation reaction, from 106.5 m^2/g to 84.4 m^2/g, lower than that ascertained for the Pd1 catalyst.

10.4 The effect of temperature on the hydrogenation rate

The effect of temperature on the hydrogenation rate was studied using two diverse magnetite based catalytic systems and the results are summarized in Table 5.

Table 5 Effect of temperature effect on the hydrogenation rate

Run	Catalyst	T (°C)	CAL Conversion (%)	HCAL selectivity (%)	HCAL Yield (%)	A (mol/ g h)	TOF (h^{-1})
CIN3[a]	Pd3	100	35,4	92,4	33	0,0007	0,08
CIN5[a]	Pd3	130	58,2	89,1	52	0,0012	0,12
CIN4[a]	Pd6	100	58,2	93	54	0,0012	0,12
CIN6[a]	Pd6	130	83,4	81,7	68	0,0017	0,18

[a] reaction conditions: H_2 Pressure 20 bar, 3.8 ml of cinnamaldehyde, 100 ml of decaline, 2.5 mg of Pd and reaction time 6 .

By increasing the reaction temperature from 100°C up to 130°C the conversion of cinnamadehyde increased and the selectivity in hydrocinnamadehyde decreased. In particular, at 130°C the Pd3 catalyst reached the same conversion obtained at the lower temperature using the Pd6 catalyst, with diverse products distribution as displayed in Figure 7.

Therefore, a compromise between conversion and selectivity must be reached, considering that in the case of low selectivity a heavy purification step is necessary whereas in the case of low conversion the unreacted reagent must be recycled.

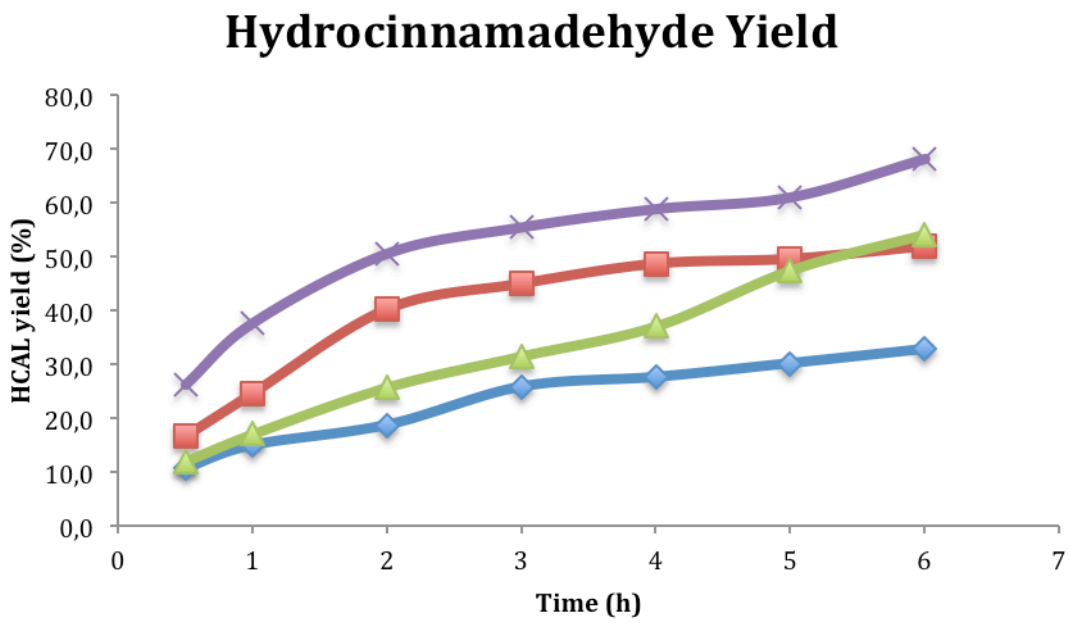

Figure 7 Hydrocinnamaldehyde yield vs. time at diverse temperature: a) palladium nanoparticle over magnetite, Pd3 at 100°C CIN3 (blue line), b) palladium nanoparticles over magnetite, at 130°C Pd3 CIN5 (red line), c) palladium nanoparticles trapped inside magnetite, Pd6 at 100°C CIN4 (green line) and d) palladium nanoparticles trapped inside magnetite, Pd6 at 130°C CIN6 (purple line)

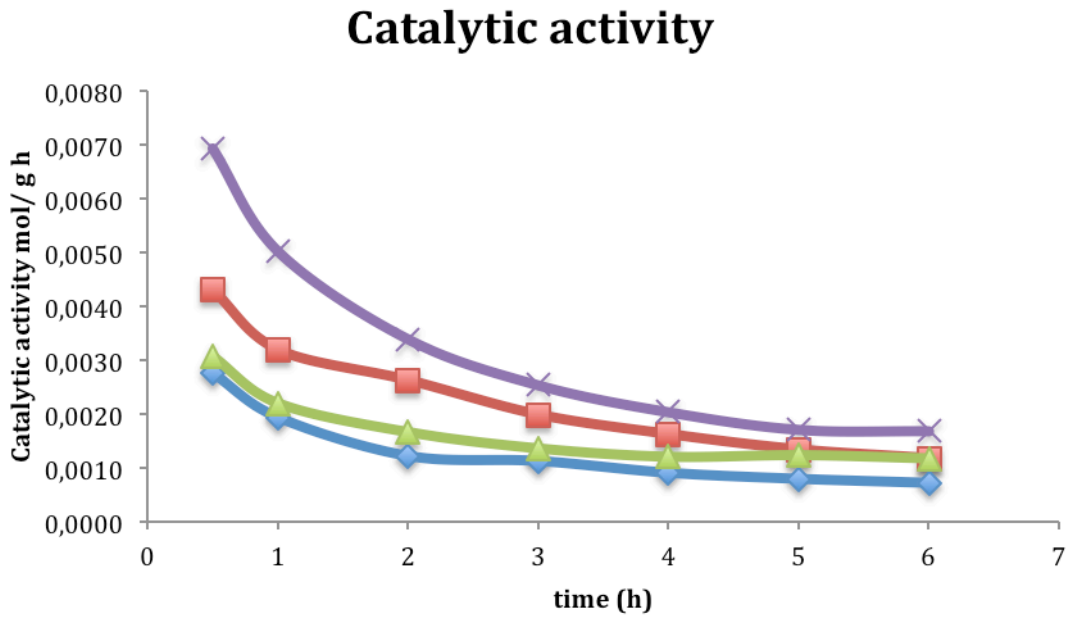

Figure 8 Catalytic activity vs. time at diverse temperature: a) palladium nanoparticle over magnetite, Pd3 at 100°C CIN3 (blue line), b) palladium nanoparticles over magnetite, at 130°C Pd3 CIN5 (red line), c) palladium nanoparticles trapped inside magnetite, Pd6 at 100°C CIN4 (green line) and d) palladium nanoparticles trapped inside magnetite, Pd6 at 130°C CIN6 (purple line)

The catalytic activity trends of reactions CIN3 and CIN4 carried out at 100°C are very similar and almost overlap (see Figure 8) but CIN4 where Pd6 catalyst was employed led to a higher HCAL yield. The Pd6 catalyst characterized by a more complex structure where palladium nanoparticles were trapped inside the magnetite structure, exhibited the highest catalytic activity, especially at the beginning of the reaction.

10.5 Recyclability tests

The catalytic activities of the most promising catalysts (Pd1 and Pd6) were further investigated through recycle tests. The recycle runs were carried out under the same reaction conditions reported above. After each reaction cycle the reaction mixture was removed keeping the catalyst inside with a permanent neodymium magnet. Then the catalyst was washed with fresh solvent and the reactor was charged again with the fresh reagent. The catalytic results are summarized in Table 6.

Table 6 Recycle tests on two diverse catalysts Pd1 and Pd6 catalysts

Run	Catalyst	CAL Conversion (%)	HCAL selectivity (%)	HCAL Yield (%)	A (mol/g h)	TOF (h^{-1})
CIN2[a]	Pd1	73,7	96,3	71	0,0015	0,16
CIN2 ricycle[a]	Pd1	29	95,8	28	0,0006	0,06
CIN4[a]	Pd6	58,2	93	54	0,0012	0,12
CIN4 ricycle[a]	Pd6	41,3	92,1	38	0,0008	0,09

[a] Reaction conditions: Temperature 100°C, H_2 Pressure 20 bar, 3.8 ml of cinnamaldehyde, 100 ml of decaline, 2.5 mg of Pd and reaction time 6h.

The recycled runs (CIN2 recycle and CIN4 recycle) showed lower catalytic activity than the fresh runs (CIN2 and CIN4), see Figure 9. However, the loss in activity was more evident in the CIN2 run where Pd1 was used. This result can be due to the diverse catalyst structure, in fact Pd1 is characterized by a hierarchical structure where palladium is exposed on the maghemite surface, thus deactivation could easily occur because of poisoning or leaching, whereas the Pd6 catalyst is characterized by a more complex structure where palladium nanoparticles are protected inside the magnetite structure. In particular after the first reaction cycle, the recycled Pd6 catalyst (CIN4 recycled) showed a lower lost in catalytic activity than Pd1, confirming its better recyclability (see Figure 9).

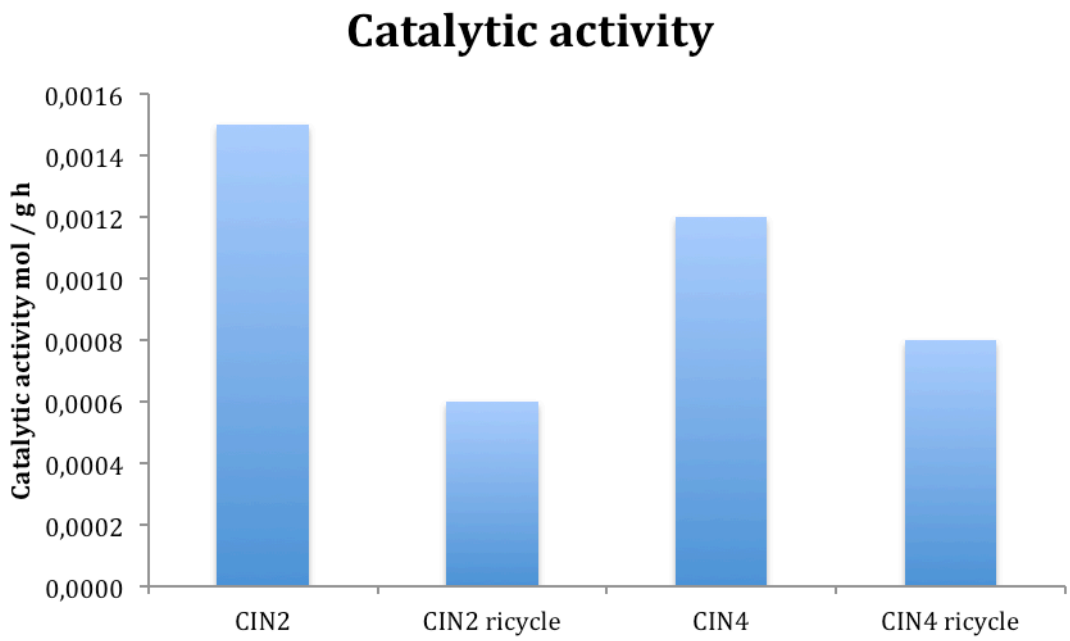

Figure 9 Catalytic activity after 6h of reaction for fresh and recycled catalysts

10.6 Conclusion

Diverse magnetic palladium systems were employed in the selective hydrogenation of CAL to HCAL.

The Pd1 catalyst characterized by palladium nanoparticles supported over maghemite showed the best cinnamaldehyde conversion and the highest hydrocinnamadehyde selectivity, higher than those reported in literature for analogues magnetic palladium catalysts.[26] Unfortunately Pd1 nanocatalyst lost the 60% of its catalytic activity after the first reactive cycle.

On the other hand Pd6 catalyst, characterized by palladium nanoparticles trapped inside magnetite structure, led to lower cinnamaldehyde conversion but to a minor catalyst deactivation during the recycle tests.

Furthermore, it is noteworthy that all the catalysts maintained their magnetic properties and structure after each reactive cycle. These investigation is currently in progress in order to better understand the reasons of the deactivation and improve the performances.

10.7 References

[1] a) H. Wang, Y. Shu, M. Zheng and T. Zhang, *Catalysis Letters* **2008**, *124*, 219-225; b) I. Scriabine in *Aldehydes useful in perfumery*, *Vol.* Google Patents, **1970**.

[2] A. J. Muller, J. S. Bowers, J. R. I. Eubanks, C. C. Geiger and J. G. Santobianco in *Processes for preparing hydrocinnamic acid*, *Vol.* Google Patents, **1999**.

[3] L. Zhang, J. M. Winterbottom, A. P. Boyes and S. Raymahasay, *Journal of Chemical Technology & Biotechnology* **1998**, *72*, 264-272.

[4] a) A. Giroir-Fendler, D. Richard and P. Gallezot, *Catalysis Letters* **1990**, *5*, 175-181; b) N. M. Callis, E. Thiery, J. Le Bras and J. Muzart, *Tetrahedron Letters* **2007**, *48*, 8128-8131; c) L. T. Anna Maria Raspolli Galletti, Claudia Antonetti, Claudio Evangelisti, Claudia Forte, *Applied Catalysis A: General* **2012**, *447*, 49-59.

[5] A. Mehri, H. Kochkar, S. Daniele, V. Mendez, A. Ghorbel and G. Berhault, *Journal of Colloid and Interface Science* **2012**, *369*, 309-316.

[6] X. Yang, L. Wu, L. Ma, X. Li, T. Wang and S. Liao, *Catalysis Communications* **2015**, *59*, 184-188.

[7] A. Cabiac, T. Cacciaguerra, P. Trens, R. Durand, G. Delahay, A. Medevielle, D. Plée and B. Coq, *Applied Catalysis A: General* **2008**, *340*, 229-235.

[8] M. Lashdaf, A. O. I. Krause, M. Lindblad, M. Tiitta and T. Venäläinen, *Applied Catalysis A: General* **2003**, *241*, 65-75.

[9] K. Jabou, H. Kochkar, G. Berhault and A. Ghorbel, *Journal of Materials Science* **2009**, *44*, 6677-6682.

[10] Y. Zhao, M. Liu, B. Fan, Y. Chen, W. Lv, N. Lu and R. Li, *Catalysis Communications* **2014**, *57*, 119-123.
[11] a) Z.-C. Zhang, X. Zhang, Q.-Y. Yu, Z.-C. Liu, C.-M. Xu, J.-S. Gao, J. Zhuang and X. Wang, *Chemistry – A European Journal* **2012**, *18*, 2639-2645; b) G. R. Cairns, R. J. Cross and D. Stirling, *Journal of Catalysis* **1997**, *166*, 89-97; c) D. Divakar, D. Manikandan, V. Rupa, E. L. Preethi, R. Chandrasekar and T. Sivakumar, *Journal of Chemical Technology & Biotechnology* **2007**, *82*, 253-258; d) K.-C. Tin, N.-B. Wong, R.-X. Li, Y.-Z. Li, J.-Y. Hu and X.-J. Li, *Journal of Molecular Catalysis A: Chemical* **1999**, *137*, 121-125; e) K. Wasikowska, P. Dmowska, N. Baczek, K. Strzelec, J. Pernak and B. Markiewicz, *Pol. J. Chem. Technol.* **2013**, *15*, 28-32.
[12] V. Gutierrez, M. Alvarez and M. A. Volpe, *Applied Catalysis A: General* **2012**, *413–414*, 358-365.
[13] Y. Zhu and F. Zaera, *Catal. Sci. Technol.* **2014**, *4*, 955-962.
[14] K. Joseph Antony Raj, M. G. Prakash, T. Elangovan and B. Viswanathan, *Catalysis Letters* **2012**, *142*, 87-94.
[15] S.-Y. Chin, F.-J. Lin and A.-N. Ko, *Catalysis Letters* **2009**, *132*, 389-394.
[16] J. Lenz, B. C. Campo, M. Alvarez and M. A. Volpe, *Journal of Catalysis* **2009**, *267*, 50-56.
[17] a) H. Rojas, G. Díaz, J. J. Martínez, C. Castañeda, A. Gómez-Cortés and J. Arenas-Alatorre, *Journal of Molecular Catalysis A: Chemical* **2012**, *363–364*, 122-128; b) A. Giroir-Fendler, D. Richard and P. Gallezot in *Selectivity in Cinnamaldehyde Hydrogenation of Group-VIII Metals Supported on Graphite and Carbon*, *Vol. Volume 41* Eds.: J. B. C. B. D. D. C. M. M. Guisnet and G. Pérot), Elsevier, **1988**, pp. 171-178.
[18] F. Li, R. Han, G. Fan and L. Yang in *Preparation and application of high-dispersity supported PtCo nano alloy catalyst for selective hydrogenation of cinnamaldehyde*, *Vol.* Beijing University of Chemical Technology, Peop. Rep. China . **2015**, p. 8pp.
[19] R. Zheng, M. D. Porosoff, J. L. Weiner, S. Lu, Y. Zhu and J. G. Chen, *Applied Catalysis A: General* **2012**, *419–420*, 126-132.
[20] X. Yang, D. Chen, S. Liao, H. Song, Y. Li, Z. Fu and Y. Su, *Journal of Catalysis* **2012**, *291*, 36-43.
[21] X. Yuan, J. Zheng, Q. Zhang, S. Li, Y. Yang and J. Gong, *AIChE J.* **2014**, *60*, 3300-3311.
[22] K. Taniya, T. Hara, T. Imai, Y. Ichihashi and S. Nishiyama, *J. Chem. Eng. Jpn.* **2014**, *47*, 130-135.
[23] Y. Sun, G. Zhao, X. Mo, G. Wang and L. Chen, *Zhongguo Keji Lunwen* **2014**, *9*, 1344-1350.
[24] M. G. Prakash, R. Mahalakshmy, K. R. Krishnamurthy and B. Viswanathan, *Catal. Sci. Technol.* **2015**, *5*, 3313-3321.
[25] M. G. Prakash, R. Mahalakshmy, K. R. Krishnamurthy and B. Viswanathan, *Catal. Today* **2015**, Ahead of Print.
[26] J. Yu, L. Yan, G. Tu, C. Xu, X. Ye, Y. Zhong, W. Zhu and Q. Xiao, *Catalysis Letters* **2014**, *144*, 2065-2070.
[27] Y. Liu, J. Chung, Y. Jang, S. Mao, B. M. Kim, Y. Wang and X. Guo, *ACS Applied Materials & Interfaces* **2014**, *6*, 1887-1892.
[28] S. Song, J. Yu, Q. Xiao, X. Ye, Y. Zhong and W. Zhu, *Nanoscale Research Letters* **2014**, *9*, 1-7.
[29] A. M. R. Galletti, C. Antonetti, A. M. Venezia and G. Giambastiani, *Applied Catalysis A: General* **2010**, *386*, 124-131.

[30] C. Milone, C. Crisafulli, R. Ingoglia, L. Schipilliti and S. Galvagno, *Catalysis Today* **2007**, *122*, 341-351.

11. STUDY OF THE SELECTIVE OXIDATION OF 1-PHENYLETHANOL TO ACETOPHENONE IN THE PRESENCE OF THE MAGNETIC RUTHENIUM CATALYSTS

11.1 Introduction

Acetophenone is an aromatic ketone, which naturally occurs in numerous fruits. It finds application in resin, perfume and pharmaceutical industries. [1]

Acetophenone can be obtained through the selective oxidation of 1-phenylethanol as described in Scheme 1.

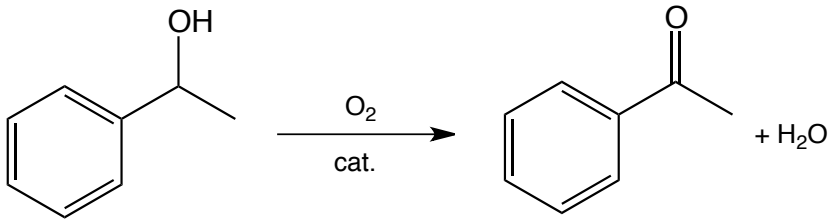

Scheme 1 Oxidation of 1-phenylethanol to acetophenone

The oxidation of 1-phenylethanol to acetophenone is a highly selective and quantitative process characterized by absence of by-products under mild reaction conditions. Thanks to these peculiar aspects, the selective oxidation of 1-phenylethanol to acetophenone can be considered a model for the oxidation of secondary alcohols to ketones.

Generally, this oxidation is carried out in organic solvents using heterogeneous ruthenium catalysts. For example, Zhan et al.[2] studied the selective oxidation of 1-phenylethanol and other alcohols in toluene using ruthenium oxide nanoparticles confined in zeolite as catalytic systems. Yamaguchi et al. [3] reported the catalytic oxidation of 1-phenylethanol in trifluorotoluene obtaining a mixture of benzaldehyde and acetophenone, whereas Mori et al. utilized toluene as solvent and ruthenium supported on hydroxyapatite as catalysts with encouraging results.[4] Mizuno et al. studied diverse ruthenium catalysts in the selective oxidation of 1-phenylethanol underlining that ruthenium hydroxide gives the highest conversion under mild reaction

conditions.[5] Kotani et al. studied the selective oxidation of 1-phenylethanol to acetophenone in toluene using magnetic ruthenium hydroxide catalyst [6].

Moreover, in literature the employment of other interesting heterogeneous catalysts is reported such as $MnFe_{1.5}Ru_{0.35}Cu_{0.15}O_4$[7], Mn compound[8], Ru-Mg-Al-hydrotalcite[9], Ru-Co-Al-hydrotalcite[10], $Pr_4N^+RuO_4^-$/ormosil(SiO_2) [11], Pt[12], Au-Ag/PVP[13], PdAu-TiO_2[14], Co-Fe_3O_4[15], Cu(II)-TEMPO[16], and $Na_5PMo_{10}V_2O_{40}$/C[17].

More interesting from an environmental and a safety point of view are the reactions carried out in an aqueous medium. In fact, water not only replaces unfriendly and toxic organic solvents but also reduces the risk of explosion, reducing the window of compositions, which could lead to the explosion event.

Despite these positive aspects connected with the use of water as a solvent, this route has been poorly investigated due to the solubility problems connected with the use of organic reagents. In fact, the immiscibility and the limited solubility of organic compounds generate complex multiphasic systems, which limit the transportation of reagents toward the catalytic active sites, thus reducing conversion and reaction rates.

In particular, Bliff et al. described the use of a Pd nanocluster as an efficient catalyst for alcohol oxidation in an aqueous medium.[18] Mallat et al. reported the oxidation of 1-phenylethanol in aqueous media involving platinum on alumina as a catalyst and a bismuth promoter. [19] Brink et al. studied the employment of a homogeneous palladim acetate catalyst for the oxidation of diverse alcohols in water with encouraging results. [20]

Finally Antonetti et al. reported the oxidation of 1-phenylethanol in water using palladium nanoparticles supported on an organic-inorganic hybrid material as catalyst. [21]

Taking into account all these aspects, this work verified the catalytic activity of ruthenium magnetic catalysts described in Chapter 5.2 towards the oxidation of 1-phenylethanol to acetophenone in aqueous medium.

11.2 Results and discussion

The preliminary oxidation reactions were carried out in a glass reactor equipped with a reflux apparatus and an entry for oxygen.

In particular, 1-phenylethanol (0.9 mmol) and magnetic ruthenium catalyst (Ru2, 1.87%RuO_x@Fe_3O_4) (0.07g) were dispersed in the solvent (5 ml) and introduced into the reactor. Then the system was heated up to 100°C under a continuous oxygen flow and maintained for 3 h. At the end of the reaction, the catalyst was magnetically recovered and the reaction mixture was submitted to work-up and analysed. The work-up consisted in the extraction of the unreacted reagent and product with 5 ml of ethyl ether three times and the subsequent dehydration on sodium sulphate. The organic mixture was analysed using a gas chromatograph Perkin Elmer Auto System 8700, equipped with a FID and a DB1701 column (methyl silicone and 5% diphenilsilicone) and the catalytic results are summarized in Table 1.

Table 1 Oxidation of 1-phenylethanol to acetophenone in toluene or water medium

Run	Solvent	Conversion (%)	Selectivity (%)	Yield (%)	Activity (mol/g h)	TOF (h^{-1})
ACE1	toluene	4	100	4	0.0032	0.32
ACE2	water	trace	100	trace	***	***

Reaction conditions: 0.9 mmol of 1-phenylethanol, 0.07 g of Ru2 catalyst (1.87%RuO_x@Fe_3O_4), 5ml of solvent, under continue oxygen flow at100°C for 3h.

Under the adopted mild reaction conditions the oxidation of 1-phenylethanol did not proceed. In particular, using water as the solvent (run ACE2) 1-phanylethanol conversion was lower than that observed using toluene (run ACE1). In fact, when water was used as the solvent, a complex multiphase system was generated which decreased the availability of the reactive species, thus decreasing the conversion and reaction rate. The multiphase system was composed of an organic phase (1-phenylethanol and acetophenone), an aqueous phase where oxygen was partially dissolved, a gaseous phase (oxygen) and a solid insoluble one (ruthenium catalyst). In this complex system, the transportation of organic and gaseous reagents toward the catalyst surface is the real limiting step. However, by improving oxygen pressure it is possible to improve oxygen solubility, partially overcoming transportation problems. The improvement of oxygen pressure was possible thanks to the aqueous medium, which increased the pressure work window reducing the risk of explosion. The effect of oxygen pressure on the selective oxidation rate is summarized in Table 2.

Table 2 Effect of oxygen pressure on the selective oxidation rate

Run	P O_2 (bar)	Conversion (%)	Selectivity (%)	Yield (%)	Activity (mol/g h)	TOF (h^{-1})
ACE2[a]	1	trace	100	trace	***	***
ACE3[a]	3	trace	100	trace	***	***
ACE4[a]	10	8	100	8	0.01	0.63

[a] The oxidation was carried out in 15 ml Parr autoclave electrically heated, using 0,9 mmol of 1-phenylethanol, 0,07g of magnetic ruthenium catalyst , 10 ml of water at 100°C for 3h

As expected, by increasing oxygen pressure, 1-phenylethanol conversion increased and reached a yield of 8% after 3 h (run ACE4, see Table 2). Furthermore, Ru2 catalytic activity was further investigated to verify the recoverability and recyclability of these new catalytic systems. The recycle test was carried out under the same reaction conditions. In particular, after each cycle the catalyst was kept on the bottom of the autoclave with a permanent neodymium magnet and the reaction mixture was collected from the reactor pipeline. Then the catalyst was washed and the reactor was charged with the fresh reagent. The recycle test results are summarized in Table 3.

Table 3 Recycle test of oxidation of 1-phenylethanol to acetophenone

Run	P O2	Conversion (%)	Selectivity (%)	Yield (%)	Activity (mol/g h)	TOF (h^{-1})
ACE4[a]	10	8	100	8	0.006	0.63
ACE4 recycle[a]	10	6	100	6	0.004	0.42

[a] The oxidation was carried out in 15 ml Parr autoclave electrically heated, using 0,9 mmol of 1-phenylethanol, 0,07g of magnetic ruthenium catalyst , 10 ml of water at 100°C for 3h

The recycled catalyst (ACE recycle) led to similar conversion as the fresh one, (ACE4 run), underlining that the catalytic activity of the recycled catalyst was only slightly lower than that of the fresh catalyst (see Figure 1). These results confirmed the recyclability of the Ru2 magnetic catalyst.

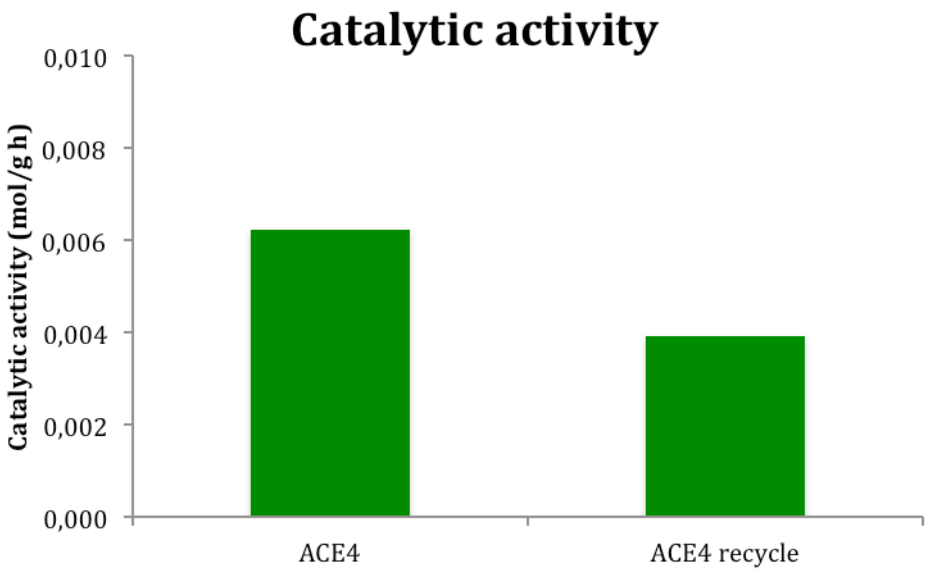

Figure 1 Catalytic activity of fresh and recycled catalyst

The oxidation of 1-phenylethanol was repeated (run ACE6) using the optimized reaction condition, (100°C and 10 bar of oxygen) and followed for 6 h to study yield and activity trends (see Figures 2 and 3).

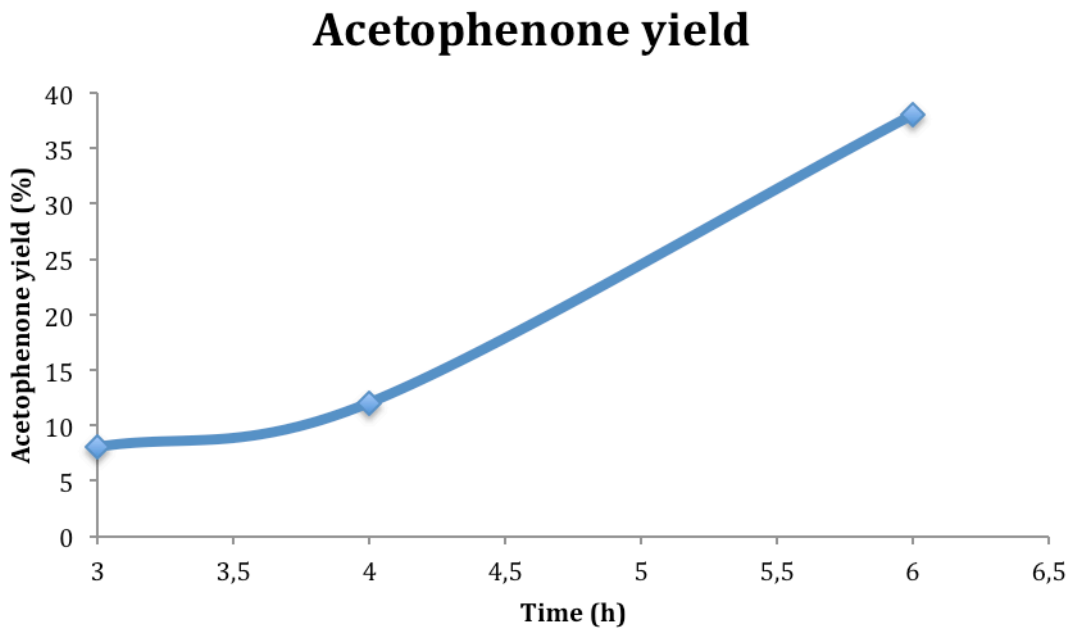

Figure 2 Acetophenone yield vs. time of run ACE6

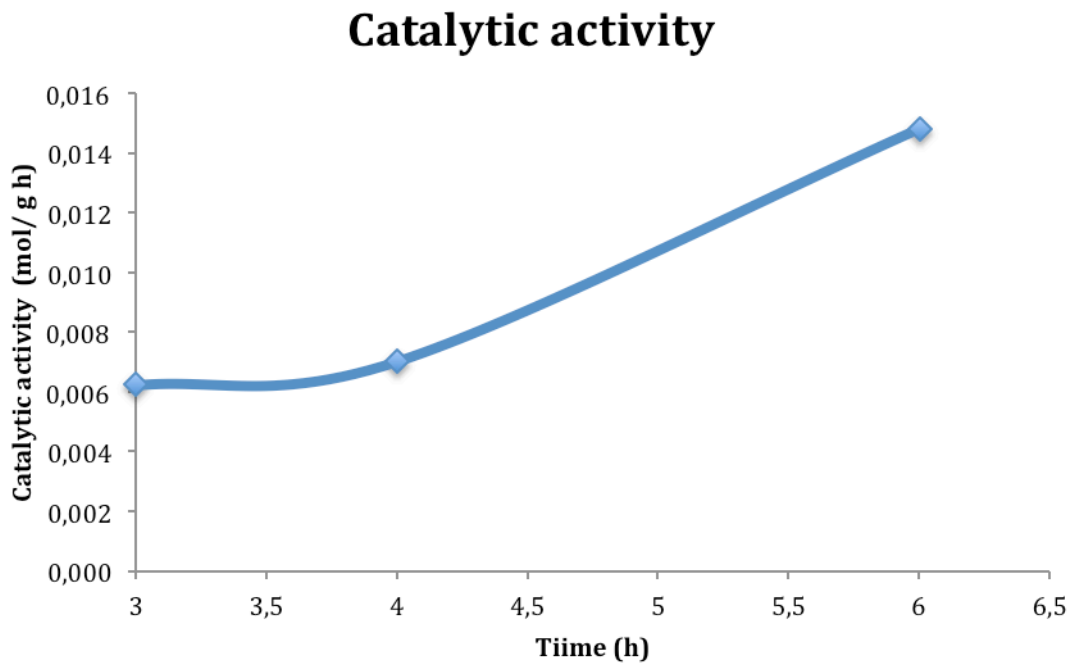

Figure 3 Catalytic activity vs. time trend of run ACE6

As it is possible to see in Figure 2 the acetophenone yield and catalytic activity (Figure 3) drastically increased after the first 4 h of reaction, this peculiar trend can be due to the complex multiphasic reactive system, which needed a lot of time and energy to overcome the problem of transportation.

Finally, the catalytic activity of the Ru2 catalyst was compared with that displayed by commercial catalysts and the results are reported in Table 4.

Table 4 Comparison between commercial and magnetic ruthenium catalysts

Run	Catalyst	Ru load (%)	Conversion (%)	Selectivity (%)	Yield (%)	Activity (mol/g h)	TOF (h^{-1})
ACE5[a]	Fe_3O_4	0	0	0	0	0	0
ACE6[a]	Ru2	1.87	38	100	38	0.01	1.51
ACE7[a]	Ru/C	2	100	100	100	0.04	3.96
ACE8	Ru/Al_2O_3	2	100	100	100	0.04	3.96

[a] The oxidation was carried out in 15 ml Parr autoclave electrically heated, using 0.9 mmol of 1-phenylethanol, 0.21 mg of ruthenium, 10 ml of water at 100°C for 6h

The blank experiment carried out with the magnetic support confirmed that magnetite did not catalyse the reaction (ACE5).

The commercial ruthenium on carbon (2%Ru/C) and ruthenium on alumina (2%Ru/Al_2O_3) showed the complete conversion of 1-phenylethanol (ACE 7 and ACE8) exhibiting a catalytic activity higher than the Ru2 system ones.

This last result can be due to the higher surface area of the commercial systems, 900 m^2/g for Ru/C and 100 m^2/g for Ru/Al_2O_3 respect to 62 m^2/g of the Ru2. The huge surface area of the commercial Ru/C in fact helped the contact between the active ruthenium site and reagents thus overcoming the problem of transportation due to the multiphasic reaction medium. Moreover, these results underline that ruthenium characterized by oxidation state 0 contained in the commercial catalysts was more active than ruthenium characterized by oxidation state 3^+ present in the Ru2 nanocatalyst. However both ruthenium oxidation states resulted active for the oxidation of alcohols as confirmed by the literature.[11, 22]

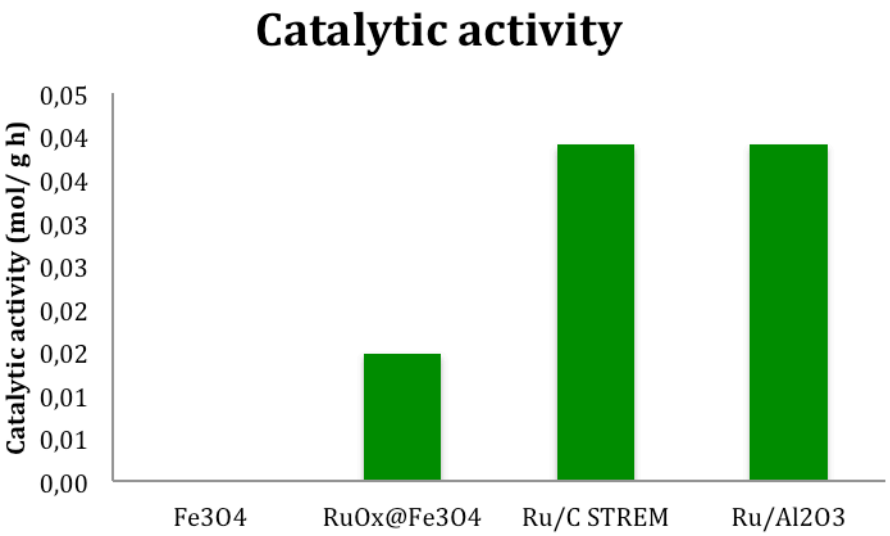

Figure 4 catalytic activities of diverse catalytic systems

Fresh and used magnetic ruthenium catalysts were analysed through FT-IR spectroscopy and the results are illustrated in Figure 5.

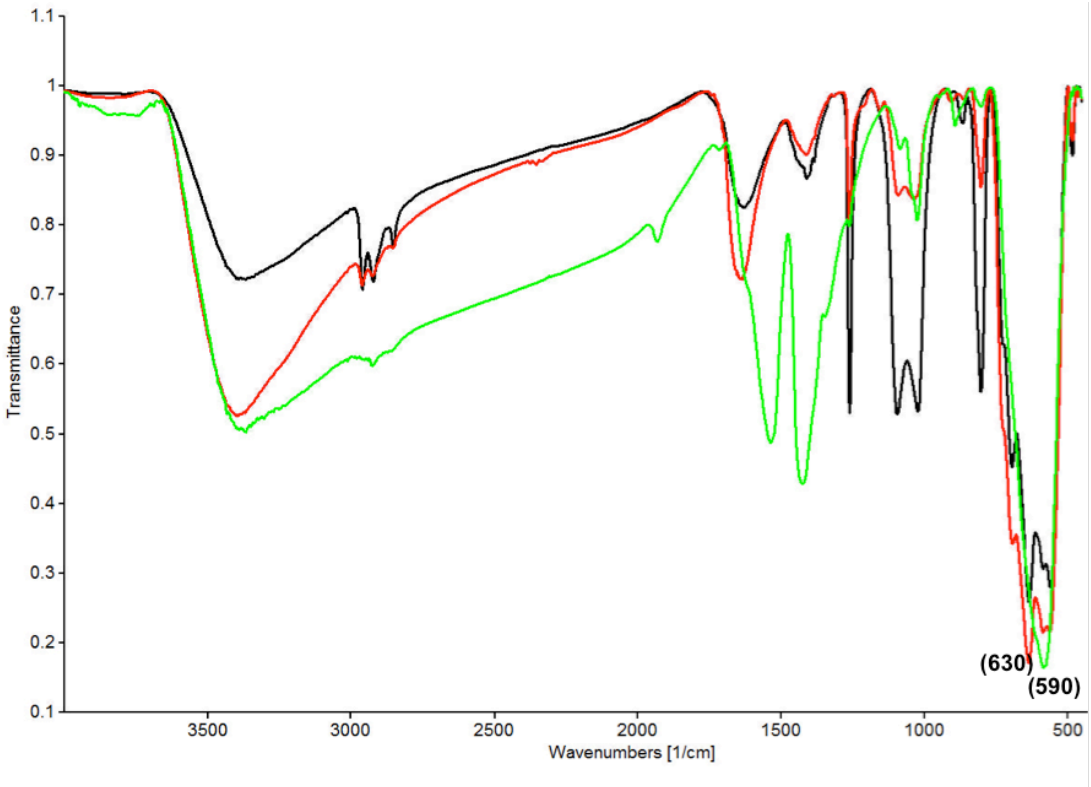

Figure 5 FT-IR spectra of fresh Ru2 catalysts (green line) b) recycled catalysts, ACE 4 recycle (red line) and c) catalysts recovered after 6 h of reaction ACE6 (black line)

The FT-IR spectrum of the Ru2 fresh catalyst (see Figure 5 green line) shows the adsorption band at 590 1/cm typical of the Fe-O bonds in tetrahedral Fe_3O_4 sites,

whereas the peak at 630 1/cm ascribable to maghemite is absent. Instead, this last peak was visible in the used catalyst spectrum (black and red lines).

Furthermore, the Ru2 fresh catalyst spectrum shows two absorbance bands at 900 1/cm and 960 1/cm ascribable to ruthenium oxide species in agreement with what is reported by Key et al.[23] The strong peaks around 1400 1/cm are ascribable to acetate traces introduced with the metal precursor, and a broad band at 3000-3500 1/cm, which is due to water and ethanol molecules trapped in the magnetite particles.

In the recycled catalyst (red line) and in the used catalyst (black line) spectra it was not possible to ascertain the ruthenium oxide and acetate peaks because in the same area there are numerous strong peaks due to aromatic species such as 1-phenylethanol and acetophenone, adsorbed on the catalyst surface.

For example, the peak around 1700 1/cm due to C=O stretching, the strong narrow peak at 1300 1/cm ascribable to ketone bending, the small peaks between 2900 1/cm and 3000 1/cm due to C-H stretching of the adsorbed organic species and the broad peak at 3400 1/cm due to the OH groups.

The presence of organic species adsorbed on the catalyst surface underlines a strong interaction that occurs between the catalyst and acetophenone or 1-phenylethanol, which can inhibit the adsorption and desorption of the reactive species and decrease the reaction rate.

11.3 Conclusion

In conclusion, the magnetic ruthenium catalyst was employed in the oxidation of 1-phenylethanol to acetophenone in aqueous media.

The commercial ruthenium catalysts (2%Ru/C and 2%Ru/Al_2O_3) allowed the complete conversion of 1-phenylethanol whereas the Ru2 catalyst exhibited lower catalytic activity leading to a 38% yield. Despite the lower catalytic activity of Ru2, ascribable to the huge difference in surface area between commercial and magnetic systems, the easier and more efficient magnetic recover and recycle is remarkable. Taking into account the interesting results of the Ru2, the magnetic ruthenium catalyst can be considered a promising catalytic system, which deserves further investigation.

11.4 References

[1] a) H. Siegel and M. Eggersdorfer in *Ketones*, *Vol.* Wiley-VCH Verlag GmbH & Co. KGaA, **2000**; b) M. J. Climent, A. Corma, S. Iborra and A. Velty, *Journal of Catalysis* **2004**, *221*, 474-482; c) J. A. R. Rodrigues, P. J. S. Moran, G. J. A. Conceição and L. C. Fardelone, *Food Technol. Biotechnol* **2004**, *42*, 295-303.
[2] B.-Z. Zhan, M. A. White, T.-K. Sham, J. A. Pincock, R. J. Doucet, K. V. R. Rao, K. N. Robertson and T. S. Cameron, *Journal of the American Chemical Society* **2003**, *125*, 2195-2199.
[3] K. Yamaguchi and N. Mizuno, *Angewandte Chemie International Edition* **2002**, *41*, 4538-4542.
[4] K. Mori, S. Kanai, T. Hara, T. Mizugaki, K. Ebitani, K. Jitsukawa and K. Kaneda, *Chemistry of Materials* **2007**, *19*, 1249-1256.
[5] N. Mizuno and K. Yamaguchi, *Catalysis Today* **2008**, *132*, 18-26.
[6] M. Pagliaro and R. Ciriminna, *Tetrahedron Letters* **2001**, *42*, 4511-4514.
[7] H.-B. Ji, K. Ebitani, T. Mizugaki and K. Kaneda, *Catalysis Communications* **2002**, *3*, 511-517.
[8] Y.-C. Son, V. D. Makwana, A. R. Howell and S. L. Suib, *Angewandte Chemie International Edition* **2001**, *40*, 4280-4283.
[9] K. Kaneda, T. Yamashita, T. Matsushita and K. Ebitani, *The Journal of Organic Chemistry* **1998**, *63*, 1750-1751.
[10] T. Matsushita, K. Ebitani and K. Kaneda, *Chemical Communications* **1999**, 265-266.
[11] M. Kotani, T. Koike, K. Yamaguchi and N. Mizuno, *Green Chemistry* **2006**, *8*, 735-741.
[12] P. Maity, C. S. Gopinath, S. Bhaduri and G. K. Lahiri, *Green Chemistry* **2009**, *11*, 554-561.
[13] S. Nishimura, T. Takahashi, Y. Yakita and K. Ebitani, *MRS Online Proceedings Library Archive* **2015**, *1758*, null-null.
[14] J.-B. Chang, C.-H. Liu, J. Liu, Y.-Y. Zhou, X. Gao and S.-D. Wang, *Nano-Micro Letters* **2015**, *7*, 307-315.
[15] M. B. Gawande, A. Rathi, I. D. Nogueira, C. A. A. Ghumman, N. Bundaleski, O. M. N. D. Teodoro and P. S. Branco, *ChemPlusChem* **2012**, *77*, 865-871.
[16] A. Sabbatini, L. M. D. R. S. Martins, K. T. Mahmudov, M. N. Kopylovich, M. G. B. Drew, C. Pettinari and A. J. L. Pombeiro, *Catal. Commun.* **2014**, *48*, 69-72.
[17] R. Neumann and M. Levin, *The Journal of Organic Chemistry* **1991**, *56*, 5707-5710.
[18] A. Biffis and L. Minati, *Journal of Catalysis* **2005**, *236*, 405-409.
[19] T. Mallat, Z. Bodnar and A. Baiker, *Studies in Surface Science and Catalysis* **1993**, *78*, 377-384.
[20] G.-J. t. Brink, I. W. C. E. Arends and R. A. Sheldon, *Science* **2000**, *287*, 1636-1639.
[21] C. Antonetti, L. Toniolo, G. Cavinato, C. Forte, C. Ghignoli, R. Ishak, F. Cavani and A. M. Raspolli Galletti, *Applied Catalysis A: General* **2015**, *496*, 40-50.
[22] M. J. Jacinto, O. H. C. F. Santos, R. F. Jardim, R. Landers and L. M. Rossi, *Applied Catalysis A: General* **2009**, *360*, 177-182.

[23] J. G. Kay, D. W. Green, K. Duca and G. L. Zimmerman, *Journal of Molecular Spectroscopy* **1989**, *138*, 49-61.

12. THE USE OF RUTHENIUM, PLATINUM AND PALLADIUM MAGNETIC NANOCATALYSTS IN THE SELECTIVE OXIDATION OF HMF TO FDCA

12.1 Introduction

Furan compounds are the most promising materials for fuel and fine chemical production starting from biomass. Recently, the US department of energy introduced hydroxymethylfurfural (HMF), furfural (FA) and 2,5 furan dicarboxylic acid (FDCA) in the top 10 most important biomass derivate compounds.[1] In particular, HMF and its derivatives have attracted huge interest as confirmed by the ever-increasing number of publications registered on Web of Science[2]. Hydroxymethylfurfural can be obtained by acid hydrolysis and successive dehydration of biomass, but unfortunately both these reactions result in a high by-product formation. Moreover, biomass is a highly variable substrate, which is still difficult to manage on industrial scale. HMF is considered an interesting building block for a wide range of fine chemicals due to its multifunctional nature; in fact, it finds application in fungicides, anticorrosion agents and perfume.[3]
Moreover, the multifunctional nature of hydroxymethylfurfural results in a wide range of possible reactions, thus forming diverse interesting derivatives (see Figure 1).
In particular, the HMF hydroxyl group reacts like primary alcohol leading to the formation of esters or halogenated products, whereas the aldehyde group can easily condensate leading to heavy compound formations and the furan ring can be decomposed to humines. Moreover, HMF can be easily polymerized, oxidised, decarboxylated etc. as summarized in Figure 1.

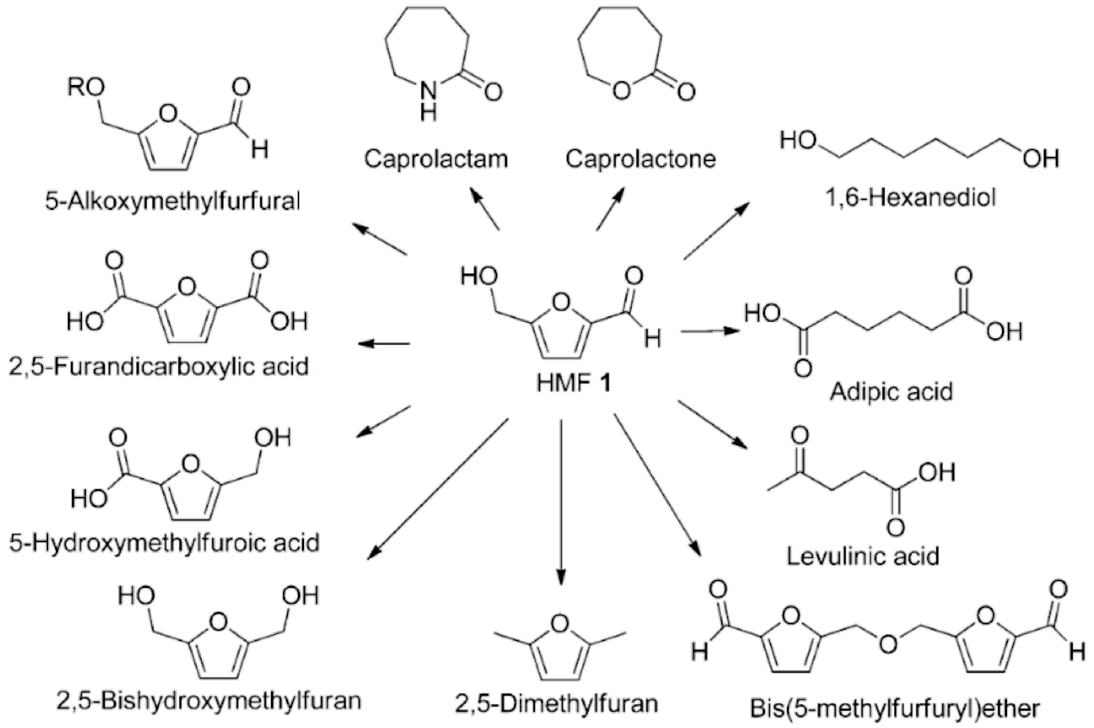

Figure 1 HMF possible derivates

Among these possible reactions, the oxidation of HMF is the most studied and can involve the hydroxyl group and/or the aldehyde group leading to four diverse products, 2,5-furandicarbaldehyde (DFF), 2,5-furan dicarboxylic acid (FDCA), 5-idroxymethyl-2-furan carboxylic acid (HFCA) and 5-formil-2-furancarboxylic acid (FFCA) (see Scheme 1).

Among them, FDCA is one of the most interesting and it is used in diverse biotechnological and technological industries for the production of pharmaceutics, antibacterial materials, implantable devices and polymers.[4] Especially in polymer science, FDCA is considered a sustainable alternative to terephthalic acid, and an eco-friendly monomer for polyesters and polyamides.[5]

However, the industrial use of FDCA is still limited due to the difficulties connected with the production of HMF from biomass.

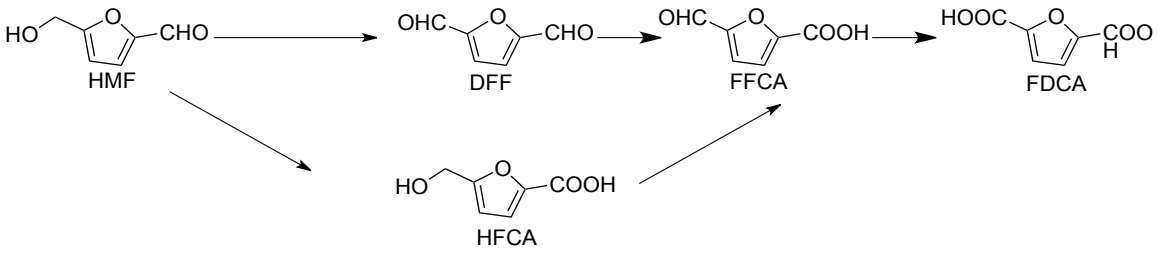

Scheme 1 Oxidation of HMF

The oxidation of hydroxymethylfurfural has been extensively studied, underlining the effect of diverse catalysts and solvents on the product distribution.

In particular, when an organic solvent is used, the formation of 2,5-furandicarbaldehyde is observed, which cannot be hydrated to geminal diols, thus avoiding the formation of carboxylic acids. It is well known, in fact, that only in aqueous media aldehydes can be hydrated to geminal diols, which for β-elimination leads to the formation of carboxylic acid. [6]

For example, Taarning et al. described the oxidation of HMF using methanol as the solvent and gold on titania as the catalyst, obtaining the direct formation of methyl furan carboxylic ester[7].

Moreau et al. utilized vanadium oxide on titania as the catalyst and toluene as the solvent reaching a DFF yield of 85%[8], whereas Corma et al. reported the use of trifluorotoluene as the solvent and vanadium-pyridine complex as the catalyst obtaining a DFF yield of 99% and an HMF conversion of 82%[9]. Carlini et al. also employed a vanadium-based catalyst in an organic medium obtaining high selectivity in DFF (97%) and good conversion (84%)[10]. Takagaki et al. showed the employment of ruthenium hydroxide supported on hydrotalcite as the catalyst in an organic medium reaching the highest HMF conversion (95%) and a DFF selectivity of 97%.[11]

Oxidation of HMF in an organic medium was also studied using other interesting metallic catalysts such as Ru/C, Pt/C, Pd/C, Rh/C and Au/C. Among them Ru/C showed the highest stability and DFF selectivity (96%)[12].

On the other hand, in an aqueous medium the oxidation of HMF proceeded through the formation of a mono or dialdehyde intermediate leading to FDCA production. This oxidation mechanism was further investigated by Davis et al.[13] who underlined the effect of gaseous oxygen and water in oxidized product formation. In particular they showed that the oxygen atoms contained in the oxidized species came from water molecules and not from gaseous oxygen, which instead helped the regeneration of the active catalytic system.[14]

Furthermore, the selective oxidation of hydroxymethylfurfural to 2,5-furandicarboxylic acid in water resulted favoured by the high pH, because the FDCA obtained is rapidly removed as carboxylic salt thus avoiding its degradation to levulinic acid, formic acid or humines. Under this condition, a by-production of HFCA is observed underlining that the oxidation of hydroxyl group to aldehyde is the limiting reaction step.[15]

Several authors reported the oxidation of HMF to FDCA in alkaline aqueous media under mild reaction conditions using diverse supported systems based on Pt[15b, 16], Pd[17], Au[15a, 18], Au-Cu[19], Mo[20], Ru[21] and $Ru(OH)_x$.

For example, Siyo et al.[22] studied the influence of different catalytic supports on the HMF oxidation rate underlining that palladium supported on ZrO_2/La_2O_3 led to higher FDCA yield.

Moreover, kind and concentration of alkaline compounds are two key issues, which strongly influence the reaction rate as confirmed also by Verdeguer et al.[15b] and Pasini et al.[19].

The use of an alkaline compound is strongly discouraged due to the connected environmental, corrosion and health risks. Futhermore, under neutral conditions FDCA is insoluble in water, helping its separation and recovery from the reaction medium. [23]

Gupta et al. reported the oxidation of HMF under neutral conditions using gold supported on hydrotalcite as a catalyst with high conversion and selectivity to FDCA but underlined the consumption of hydrotalcide during the reaction.[24] Other authors described the consumption of the basic catalytic support when neutral conditions are used to oxidize HMF, underlining the fundamental role of alakaline compound in this reaction.[25]

Taking into account the ever-increasing interest in the oxidation of HMF and that noble metals, are expensive and must be efficiently recovered, the use of magnetic noble metal nanocatalysts can be a strategic choice. In particular, the ruthenium, platinum and palladium magnetic nanocatalysts described in Chapter 5 were employed in the selective oxidation of HMF to FDCA studying this reaction with the collaboration of Prof. Funaioli of our Department.

12.2 Oxidation of HMF catalysed by magnetic ruthenium nanocatalysts

Hydroxymethylfurfural oxidation was carried out using the magnetic ruthenium catalysts Ru1 and Ru2 described in Chapter 5.2, working under neutral conditions as reported by Gorbanev et al.[25b] The main characteristics of the used magnetic ruthenium catalysts are summarized in Table 1.

Table 1 The main characteristics of magnetic ruthenium catalysts

Catalyst	Ruthenium loading (%)	BET (m^2/g)	Diameter (nm)
Ru1	0.85	62.04	N.D
Ru2	1.87	66.62	10.1

Magnetic ruthenium catalyst, Synthesis: 1g $Fe(OAc)_2$, 0.08g $Ru(acac)_3$, 44 mL EtOH at 96 wt%, microwave heating: 120 °C, 15 min, 250 W

A typical oxidation reaction was carried out in a 40 ml Parr autoclave electrically heated and was followed using HPLC Perkin Elmer Flexer Series 200 equipped with a MPLC Polypore CA column. HMF (0.23 mmol) and the ruthenium (0.047 mg) were dispersed in 5 mL of H_2O and heated up to 140°C under 3 bar of oxygen. The catalytic results are summarized in Table 2.

Table 2 The oxidation of HMF catalysed by magnetic ruthenium nanocatalysts Ru2 (1.87%Ru/Fe_3O_4) and Ru1 (0.85Ru/Fe_3O_4)

Run	Catalyst	Ru load (wt. %)	t (h)	Conv. (%)	FDCA Yield (%)	HFCA Yield (%)	FFCA Yield (%)	DFF Yield (%)	AF Yield (%)	CO Yield (%)
OX45[a]	***	0	6	98.8	0.0	0.0	0.0	0.0	17.7	27.8
OX13	Ru2	1.87	2	30.3	1.3	0.0	6.0	16.3	1.3	N.D
OX14	Ru2	1.87	4	84.3	0.4	0.0	0.7	1.0	18.7	47.8
OX26	Ru2	1.87	6	91.4	0.4	0.0	0.0	0.0	20.2	37.7
OX25[b]	Ru2	1.87	6	99.0	0.0	0.0	0.3	0.3	24.3	56.6
OX33[c]	Ru2	1.87	2	10.5	0.0	0.0	0.4	2.1	N.D	N.D
OX34[c]	Ru2	1.87	4	68.0	0.0	0.9	0.8	2.1	18.1	30.4
OX36	Ru1	0.85	2	40.8	0.0	0.0	4.7	10.0	13.6	26.7
OX35	Ru1	0.85	4	92.6	0.1	0.5	1.0	1.2	19.6	35.3
OX37[c]	Ru1	0.85	4	44.0	0.0	0.3	1.3	5.2	15.1	27.3

[a] Blank experiment, reaction carried out with magnetite support.

[b] Reaction carried out under 8 bar of oxygen.

[c] Pre-activated catalyst, the catalyst was dispersed in 10 ml of water, and heated up to 140°C under 3 bar of O_2 for 2h.

After 2 h of reaction (run OX13) the HMF conversion reached 30.3% leading to the formation of DFF and FFCA with a yield of 16.1% and 6%, respectively. Improving the reaction time, HMF conversion increased but no FDCA production was ascertained due to the high degradation of HMF (see Figure 2).

After 6 h of oxidation under neutral conditions (run OX26), the HMF was almost completely degraded to formic acid (AF), carbon dioxide and humines. HMF oxidation in fact leads to the formation of acidic species, which are able to decrease the pH of the solution. Under these acidic conditions, the furan rings can condense or degrade resulting in the formation of formic acid, levulinic acid, carbon dioxide and heavy compounds (humines). These results are comparable WITH those reported in THE literature for ruthenium hydroxide supported on magnesium oxide.[25b]

HMF degradation was observed also in the blank experiment (run OX45) where only magnetite support was used.

As extensively explained in Paragraph 12.1, under alkaline conditions the obtained carboxylic species are removed from the reactive mixture, in fact at high pH value FDCA is easily deprotonated increasing its stability against degradation.

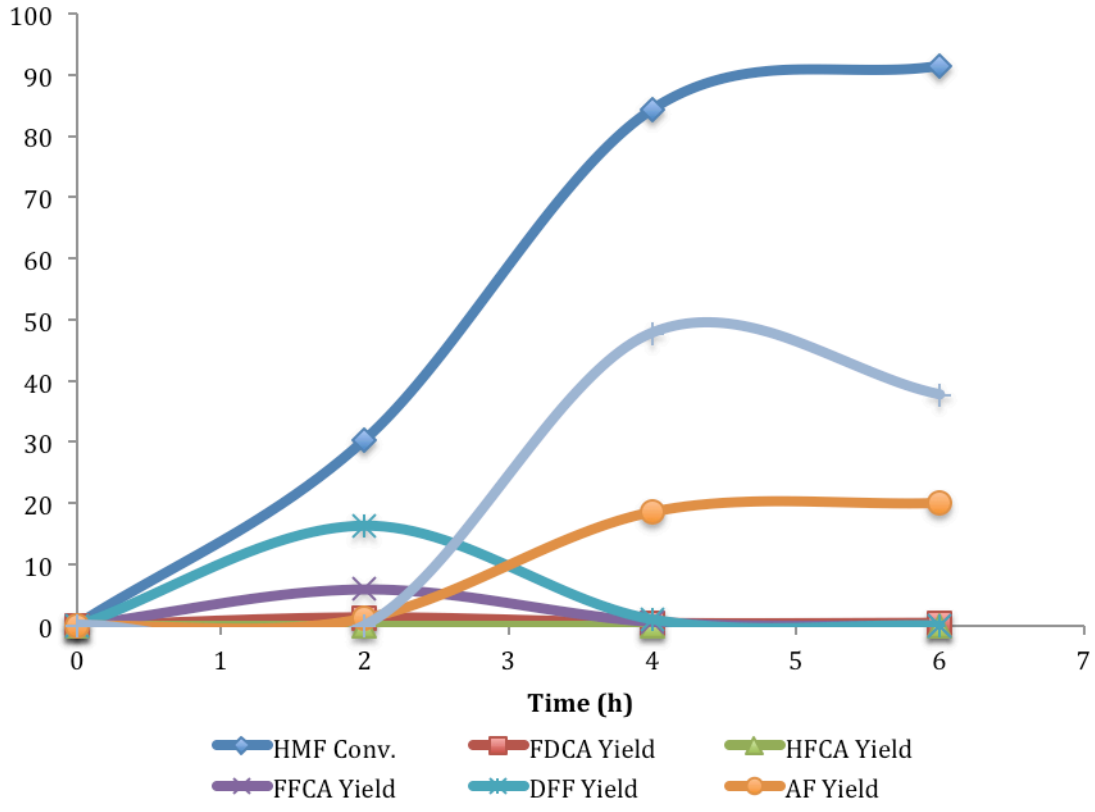

Figure 2 The oxydation of HMF at 140°C under 3 bar of oxygen using Ru2 catalyst

Increasing the oxygen pressure from 3 bar (run OX26) up to 8 bar (run OX25) an improvement in HMF conversion was observed but also in this case no FDCA was obtained (see Figure 2).

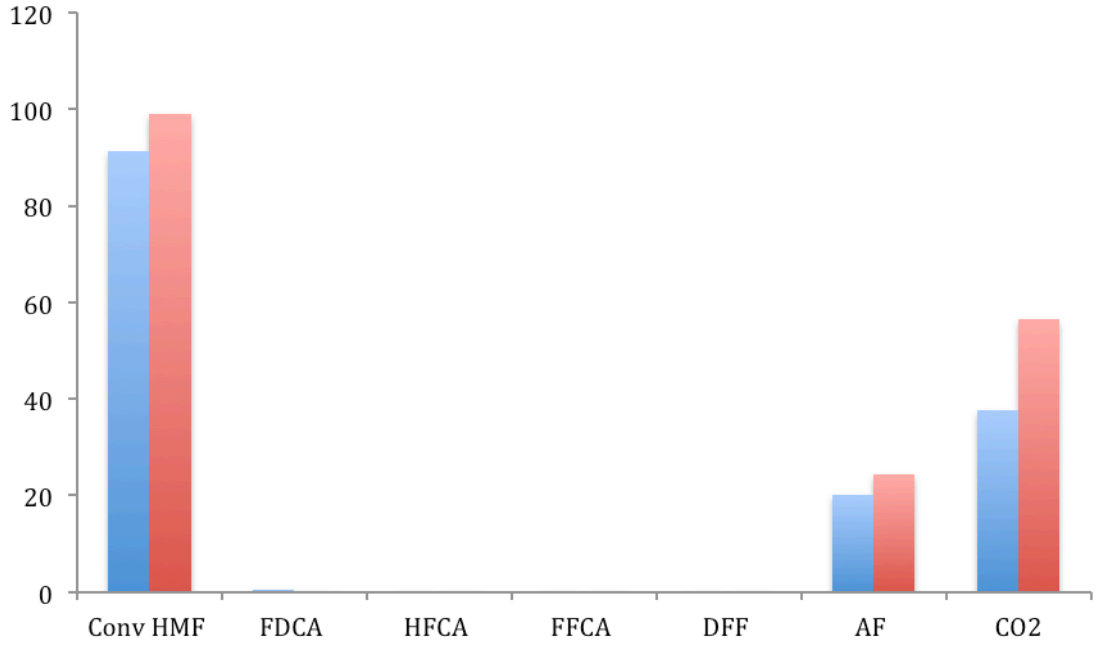

Figure 3 The HMF oxidation under 3 bar of oxygen (run 26 in blue) and under 8 bar of oxygen (run 25 in red)

When the ruthenium loading decreased from 1.87%wt. of Ru2 catalyst (run OX14) to 0.85%wt. of Ru1 catalyst (run OX35) a change in the oxidised product distribution was observed. In particular, both these experiments led to the degradation of HMF but by using the catalyst characterized by lower ruthenium load Ru1 (run OX35), slightly higher HFCA, FFCA and DFF yields were observed.

Furthermore, pre-treated Ru1 and Ru2 catalysts showed lower conversion with a higher yield in HFCA, FFCA and DFF. In particular, the pre-treated Ru1 catalyst (run OX37) exhibited higher catalytic activity than the pre-treated Ru2.

These last results underline that under neutral conditions a pre-activation of the catalysts can slightly limit the degradation of HMF. Moreover, the high temperature adopted (140°C) favoured HMF degradation.

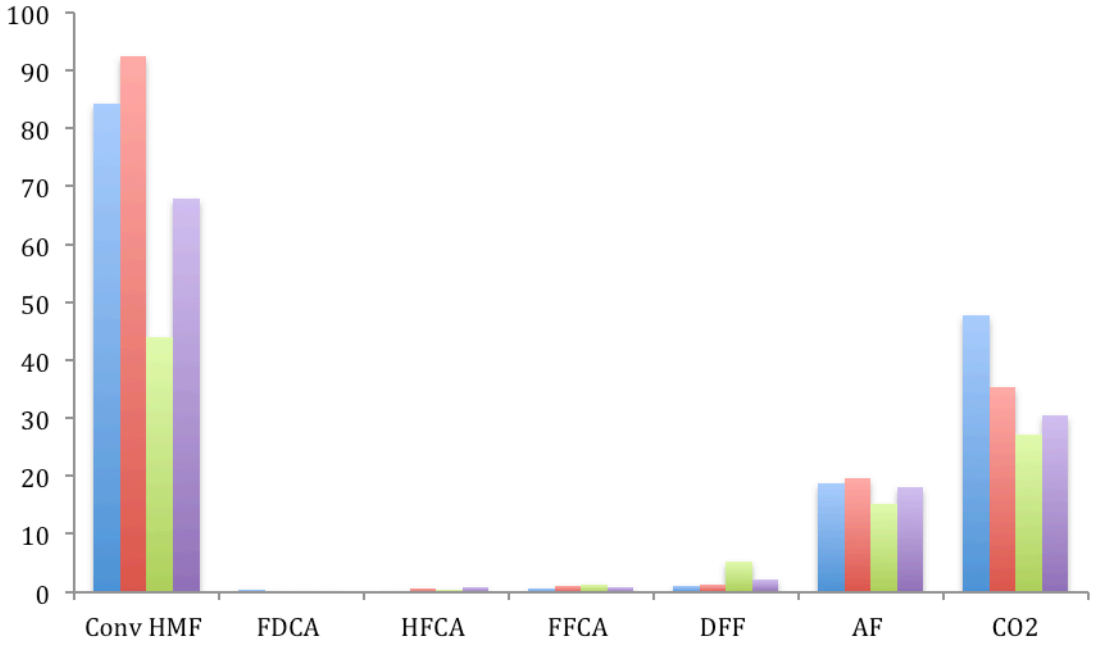

Figure 4 Coparison between reactivity of: a) Ru2, OX14 in blue, b) Ru1 OX35 in red, c) pre-activated Ru2 OX34 in violet and d) pre-activated Ru1 OX37 in green.

Taking into account these preliminary results, the oxidation of HMF was further investigated by decreasing the temperature and the results are reported in Table 2.

Table 2 The oxidation of HMF to FDCA[c]

Run	P O_2 (bar)	Time (h)	Conv. (%)	FDCA Yield (%)	HFCA Yield (%)	FFCA Yield (%)	DFF Yield (%)	AF Yield (%)	CO Yield (%)
OX16[a]	3	4	8.4	0	0	2.5	8.5	0.3	9
OX19[a]	3.5	24	35.1	0	0	6.7	13.7	2.4	11.4
OX20[a]	3.5	48	91.7	0	0	3	2.5	11	75
OX50[b]	3	4	16.4	0	0	2.5	10.5	0	0
OX48[b]	12	4	22.6	0	0	3.4	15.3	0	0.1
OX51[b]	12	8	27.5	0	0	4.8	18.8	0	6
OX49[b]	25	4	27	0.1	0	4.3	18.2	N.D	0

[a] Using Ru2 1.87$Ru(OH)_x$@Fe_3O_4

[b] Using Ru1 0.85$Ru(OH)_x$@Fe_3O_4

[c] Reaction condition: Temperature 100°C, 0.047 mg of Ruthenium, 0.23 mmol of HMF, 5 mL of H_2O

As it is possible to see from runs OX16, OX50, OX48 and OX49, by decreasing the temperature from 140°C to 100°C degradation of HMF was reduced, HMF conversion decreased and the reaction became more selective toward DFF.

By increasing the reaction time (run OX19 and OX20) the conversion of HMF increased again but DFF selectivity drastically decreased, confirming that in neutral aqueous media the degradation of furanic rings (starting from HMF and produces DFF) is favoured.

Furthermore, oxygen pressure showed a positive effect on HMF oxidation leading to higher selectivity in DFF. Among the HMF oxidation products the DFF resulted the favoured one when ruthenium was employed as catalyst as reported also in literature.[26]

As it is possible to see in Figure 5, under 25 bar of oxygen the Ru1 ($0.85Ru(OH)_x@Fe_3O_4$) catalyst showed a conversion of 27% characterized by a DFF yield of 18.4% and an FFCA yield of 4.3%.

In conclusion, the best conditions for the oxidation of HMF in neutral acqueous medium are: moderate temperature (100°C), intermediate pressure (25 bar of oxygen) using the lower ruthenium content catalyst Ru1 (run OX50).

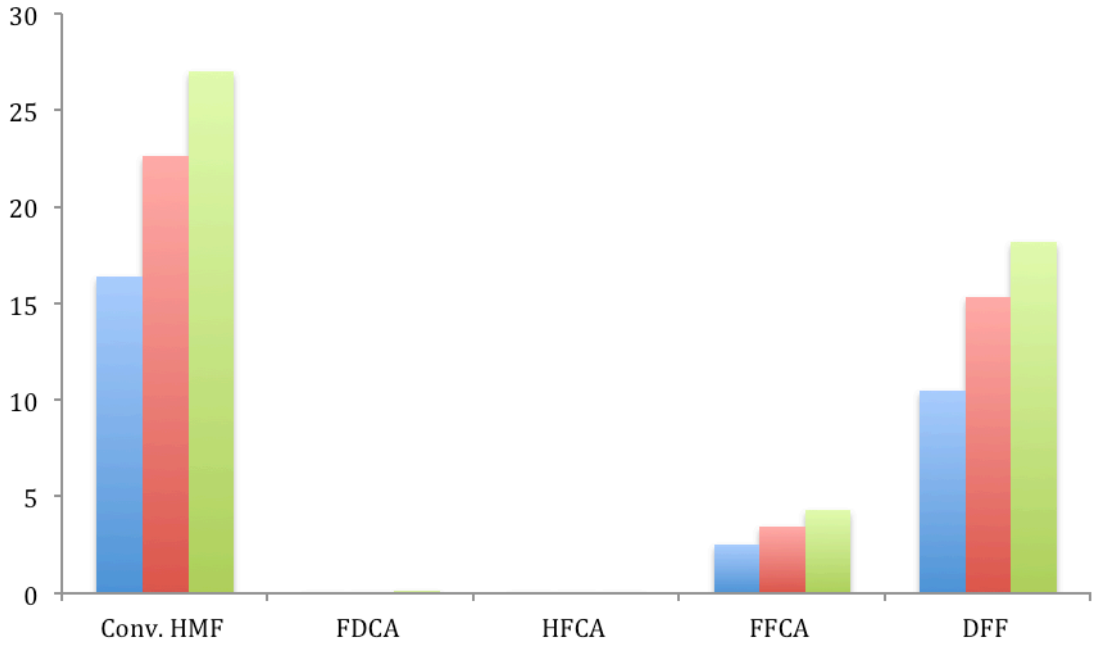

Figure 5 Effec of oxygen pressure on HMF oxidation, in blue the OX50 reaction carried out at 3 bar, in red the OX48 reaction carried out at 12 bar and in green the OX49 reaction carried out at 25 bar.

In the presence of these Ru systems a diverse oxidation mechanism was achieve compared to those reported in literature for Au and Pt[13], which involve the formation of DFF as an oxidized intermediate for FDCA formation (see Scheme 1).

In order to improve FDCA selectivity the introduction of diverse base components was evaluated and the results are summarized in Table 4.

Table 4 Effect of diverse basic compounds on HMF oxidation

Run	Base	Conv. (%)	FDCA Yield (%)	HFCA Yield (%)	FFCA Yield (%)	DFF Yield (%)	AF Yield (%)	CO Yield (%)
OX 232[a]	NaOH	90.2	0	9.3	0	0	9.7	N.D
OX50	***	16.4	0	0	2.5	10.5	0	0
OX68	Na_2CO_3	59.3	0	8.3	11.1	1.4	3.9	11.5
OX18	NaOH	96.8	4.1	13.2	0	0	16	N.D
OX87	KOH	96.7	4.3	13.6	0.0	0.0	16	65.9
OX233	$CaCO_3$	52.1	4.3	4.4	16.2	7.1	0	N.D

Reaction condition: Temperature 100°C, Oxygen pressure 3 bar, reaction time 4h and Ru1 catalysts.

[a] Blank experiment, carried out without catalyst.

The blank experiment (run OX 232) carried out at 100°C under 3 bar of oxygen without the ruthenium catalyst, led to the formation of heavy compound such as humines.

Moreover as it is possible to see in Table 4 the introduction of a base component showed a positive effect on the reaction rate, in fact the HMF conversion toward the desired oxidised products increase (see run OX50 and Run OX68).

The run OX50 carried out under neutral condition led to 16.4% of HMF conversion characterized by a DFF yield of 10.5%, whereas runs OX68 and OX233 carried out with a weak basic compound, (Na_2CO_3 and $CaCO_3$ respectively) permitted to reach an higher conversion, 59.3 % and 52.1% respectively and higher FFCA and HFCA yields, (See Table 4).

Furthermore depending on the reached alkaline strength a diverse product distribution was ascertained. In particular, run OX233 where $CaCO_3$ was employed, had higher DFF and HFCA yields than run OX68, where Na_2CO_3 was employed.

On the other hand, the use of strong alkaline compounds such as NaOH or KOH (run OX18 and run OX87) led to high HMF degradation with similar oxidized product distributions (see Figure 6).

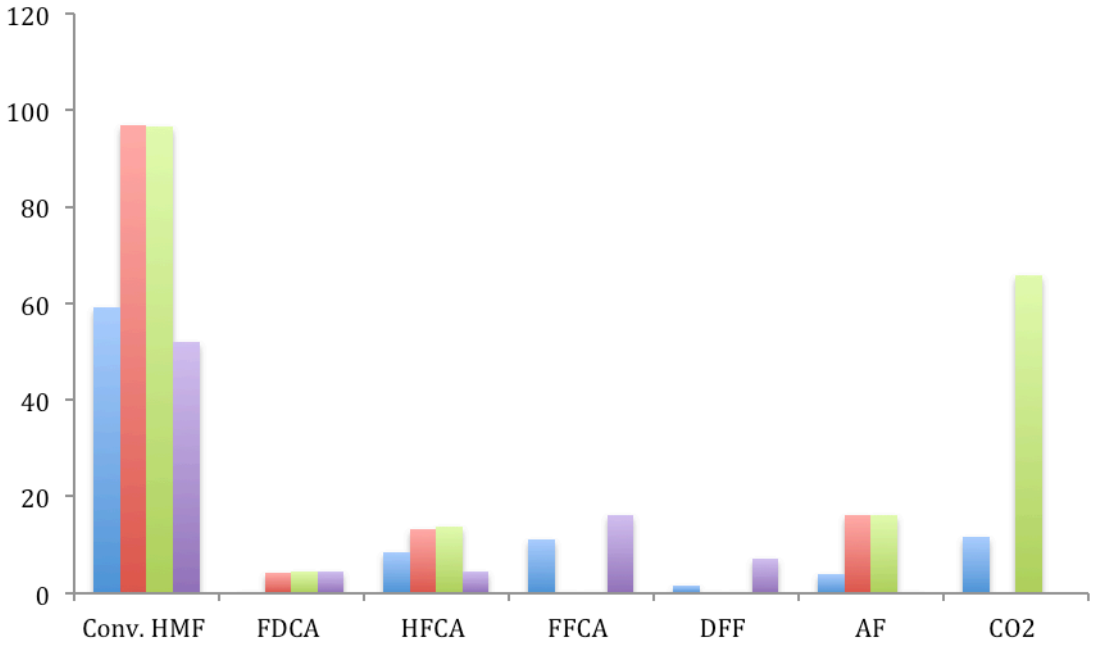

Figure 6 Effect of alkaline compounds on oxidation of HMF, in blue the reaction OX68 carried out with Na_2CO_3, in violet the reaction OX233 carried out with $CaCO_3$, in red the reaction OX18 carried out with NaOH and in green the reaction OX87 carried out with KOH.

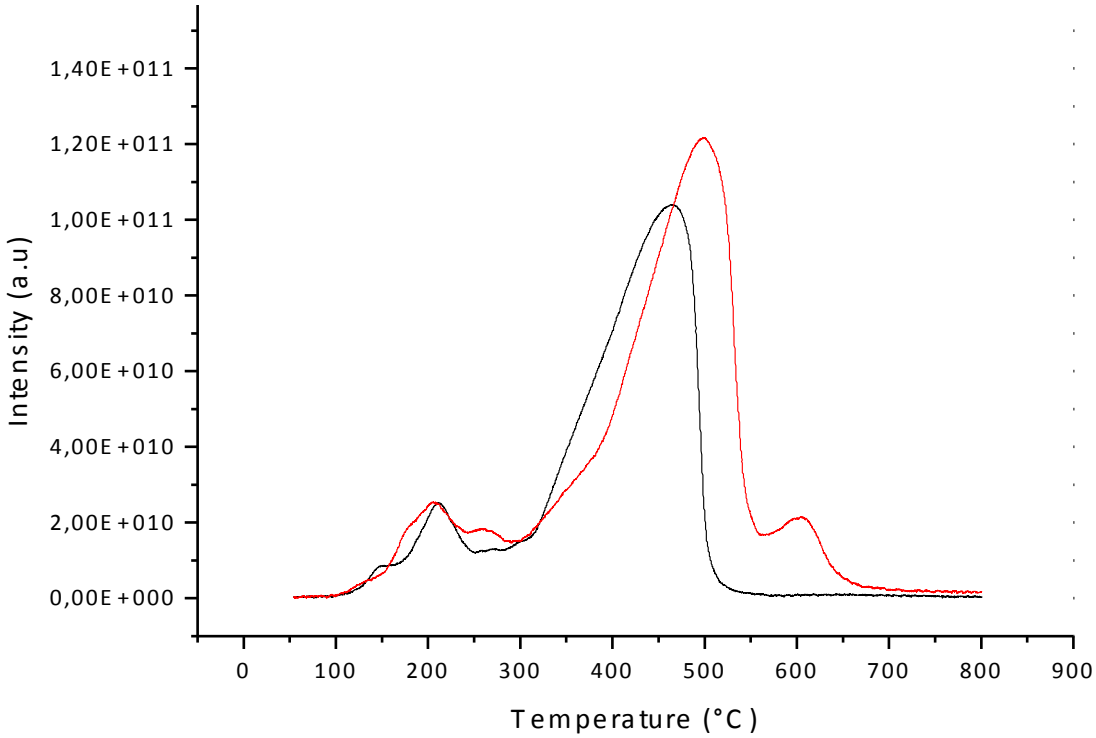

Figure 7 H_2-TPR of Ru2 catalyst before (black line) and after run OX18 (red line)

The TPR profiles of Ru2 catalyst before and after OX18 run can be separated in two zones: before and after 300°C. The big broad band present after 300°C can be assigned to the bulk reduction of the magnetite to FeO and Fe (at least partially) [27]. On the former zone, i.e. before 300°C, the more easily reducible species as Ru [28] show a different trend depending on the synthesis procedure and that at the end also affects the temperature of reduction for the bulk [29].

Making a comparison of the sample Ru2 1.87% RuO_x@Fe_3O_4 before and after an aqueous oxidation reaction (Figure 7) it can be observed that the maximum temperature in the first zone of reduction is still around 200°C and thus the main change is in the support which is more oxidized in the sample after reaction. The appearance of a high temperature reduction peak (around 600°C) in Ru2 after reaction is difficult to explain; however as the sample was used repeatedly for and oxidation reaction, it might be due either to the release of some adsorbed compound or to the reduction of some other species (for example, the formation of methane by reduction of some carbonaceous compound).

12.3 Oxidation of HMF catalysed by magnetic platinum nanocatalyst

Several authors have described the catalytic oxidation of HMF in aqueous medium using heterogeneous platinum catalysts, for example, Lilga et al. obtained almost complete HMF conversion and high FDCA selectivity using elevated reaction rates in a continuous flow reactor. [16] Vuyyuru et al. reached complete conversion after 4 h and high FDCA selectivity (72%) using platinum on carbon as a catalyst under mild reaction conditions (temperature 50°C and 10 bar of oxygen).[30] Similar results were obtained by Davis at al. who used higher HMF concentration and elevated oxygen pressure.[17a]

In this work, hydroxymethylfurfural oxidation was catalysed using the new magnetic platinum catalyst described in Chapter 5.3. The main characteristics of Pt1 catalyst are summarized in Table 5.

Table 5 Main characteristics of magnetic platinum catalyst Pt1

Catalyst	Platinum load (%)	BET (m^2/g)	Core diameter (nm)
Pt1	6.7	101.94	9.1

Synthesis condition: 1g of $Fe(OAc)_2$, 0.45g of $[Pt_4(OAc)_8]$ • 2HOAc, 44mL EtOH at 96 wt%, monomode microwave heating: 120°C, 15 min, 250 W.

A typical oxidation experiment was carried out in a 40 ml Parr autoclave electrically heated and was followed using an HPLC Perkin Elmer Flexer Series 200 equipped with an MPLC Polypore CA column. In particular, HMF (0.29 mmol), the platinum magnetic catalyst (Pt1, 6.7%Pt@Fe_3O_4) (22 mg) and NaOH (0.02 mol) were dispersed in 5 mL of H_2O and heated up to 40°C under 10 bar oxygen, the results of which are reported in Table 6.

Table 6 Oxidation of HMF catalysed by magnetic platinum under diverse condition

Run	T (°C)	Time (h)	Conv. (%)	FDCA Yield (%)	HFCA Yield (%)	FFCA Yield (%)	DFF Yield (%)	Others Yield (%)
OX86[a]	40	6	58.5	1.5	34.4	0	0	***
OX73[b]	40	6	100	55	32.3	10	0	2.7
OX85	40	6	93.8	40	46.1	10.3	0	0
OX91	40	3	95.7	39.2	49.6	10.4	0	1
OX89	60	3	97.6	48.4	38	10.4	0	0.8
OX88	80	3	95.9	39.7	19.3	33.4	0	5.9

Reaction condition: HMF 0.29 mmol, NaOH 0.02 mol, H_2O 5 ml, catalyst 22 mg (1.47 mg of Pt) and P O_2 10 bar
[a] Blank experiment carried out without the catalyst
[b] Reaction carried out using commercial Pt/C catalyst

As it is possible to see in Table 6, run OX73 carried out using commercial platinum on carbon reached complete conversion with FDCA and HFCA yields of 55% and 32.2% respectively, whereas the magnetic platinum catalyst Pt1 (run OX85) led to lower HMF conversion (93.8%) with FDCA and HFCA yields of 40% and 46.1%, respectively.
Pt1 activity was slightly lower than that of Pt/C, but it must be taken into consideration that Pt/C has a surface area of about 900 m^2/g, nine times higher than Pt1 (101.94 m^2/g).

Furthermore, the Pt@Fe_3O_4 catalyst was magnetically removed from the reaction mixture with a mass recovery extent of 95%. The ICP-OES analysis on the recovered catalyst ascertained that catalyst leaching had been avoided, revealing a platinum load of 6.7 %wt. equal to that of the fresh catalyst.

Taking into account the good FDCA and HFCA yields obtained using the magnetic platinum catalyst and its easy and efficient recovery, the oxidation of HMF was further investigated optimizing the main conditions, temperature and pH.

In particular, by increasing the reaction temperature from 40°C (run OX91) to 60°C (run OX89) and 80°C (run OX88), a change in oxidized product distribution was observed, whereas HMF conversion was almost complete in all runs (see Figure 8). Run OX88 carried out at the highest temperature showed a higher FFCA yield underlining that also in this case oxidation of the aldehyde group to carboxylic acid is the slow reaction step as was observed with the ruthenium magnetic catalyst.

Conversely, oxidation carried out at an intermediate temperature (60°C) run OX89 led to higher FDCA selectivity.

It is noteworthy that in each case the adopted reaction conditions avoided HMF degradation favouring selective oxidation toward the desired furanic products as FFCA, HFCA and FDCA.

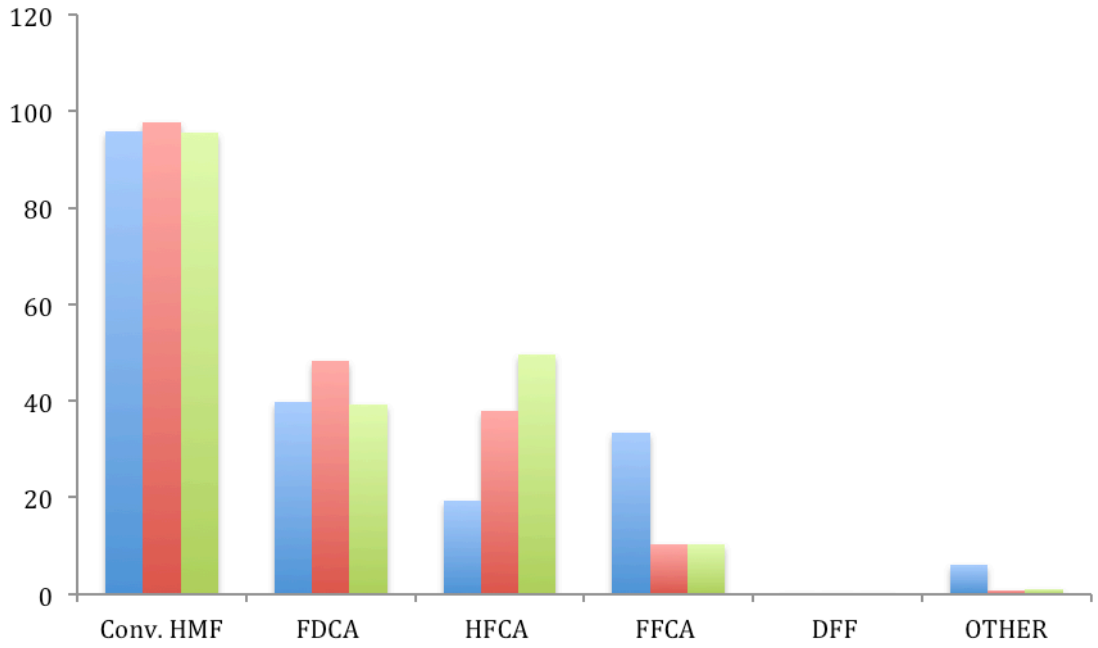

Figure 8 The oxidised product distribution carried out at diverse temperatures: a) in green at 40°C, b) in red at 60°C and d) in blue at 80°C.

The effect of alkaline pH on the HMF oxidation rate was further investigated, and the results are summarized in Table 7.

Table 7 Effect of pH on HMF oxidation rate

Run	Base	pH	Conv. (%)	FDCA Yield (%)	HFCA Yield (%)	FFCA Yield (%)	DFF Yield (%)	Others Yield (%)
OX98	***	7	22.1	2.1	1.1	8.6	4.3	6
OX100	$CaCO_3$	7	35.4	3.5	2.8	23.6	5.4	<1
OX103	$H_3BO_3/H_2BO_3^-$	10	49.6	3.9	12.2	43.4	1.7	<1
OX91	NaOH	13	95.7	39.2	49.6	10.4	0	0

Reaction condition: 0.29 mmol of HMF, 5ml H_2O, 22mg of Catalyst at 40°C under 10 bar of oxygen for 3h

Run OX98 carried out in a neutral aqueous medium showed the lowest HMF conversion with high amount of degradation products and low yields in non-completely oxidized products such as FFCA and DFF. It is well known that in an aqueous neutral medium aldehydes are not converted to geminal diols and thus to carboxylic acid, however when the pH is increased the formation of geminal diols is favoured.

$CaCO_3$ allowed to reach higher HMF conversion toward FFCA, HFCA and FDCA (run OX100) respect to what was observed when neutral conditions were adopted (run OX98).

Furthermore, as it is possible to see in Figure 9, conversion toward the desired products increased by increasing alkaline strength. In fact, by using NaOH and thus reaching pH 13, the highest HMF conversion and FDCA yield were obtained (see run OX91).

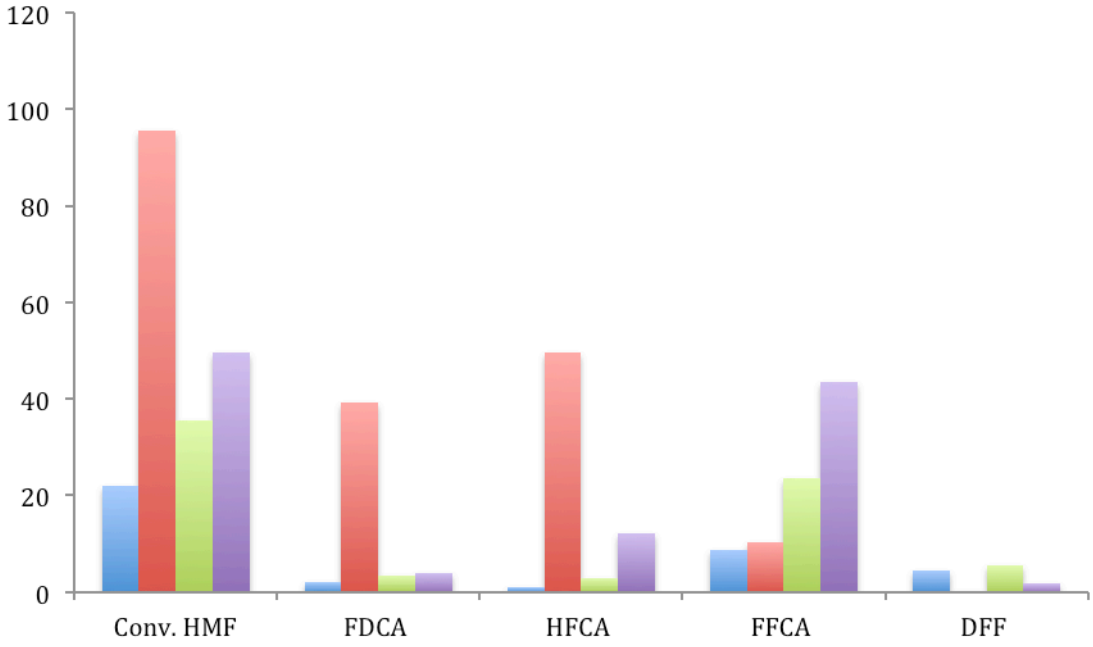

Figure 9 Effect of alkaline strength on HMF oxidation products, a) run OX98 carried out under neutral condition, blue graph, b) run OX100 carried out using $CaCO_3$ as insoluble basic compound, green graph, c) run OX103 carried out using the $H_3BO_3/H_2BO_3^-$ buffer, violet graph and d) run OX91 carried out using NaOH, red graph.

Taking into account that the use of NaOH gives the best results, a run with higher NaOH concentration and lower oxygen pressure was carried out (see run 150, Table 8).

Table 8 Distribution of HMF oxidized products at diverse reaction time

Run	Time (h)	HMF Conv. (%)	FDCA Yield (%)	HFCA Yield (%)	FFCA Yield (%)	DFF Yield (%)
OX150-1	0.5	51.4	2.8	14.9	14.4	0.3
OX150-2	1.5	80.3	15.6	31.4	12.2	0.1
OX150-3	3	95.6	28.9	42.3	0.0	0.0
OX150-4	6	99.1	38.1	39.1	0.0	0.0
OX150-5	8	99.8	61.2	25.1	0.0	0.0

Reaction condition: temperature 40°C , pressure of O_2 1 bar, 0.029 mmol HMF, 0.04 mol of NaOH, 5 ml of H_2O, Pt@Fe_3O_4 catalyst 22mg

After 8 h, the reaction was almost complete with an FDCA yield of 61.2% and HFCA yield of 25.1% (see run OX150-5). The reached FDCA yield is higher than those reported in literature for platinum nanoparticles, under the same reaction conditions.[31]

Furthermore as it is possible to observe from the kinetic trend displayed in Figure 10, the HFCA yield increased until the fourth hour and then decreased while the FDCA yield increased. This trend underlined once again that oxidation of the aldehyde group is the slowest reaction step that occurs at the end of the reaction.

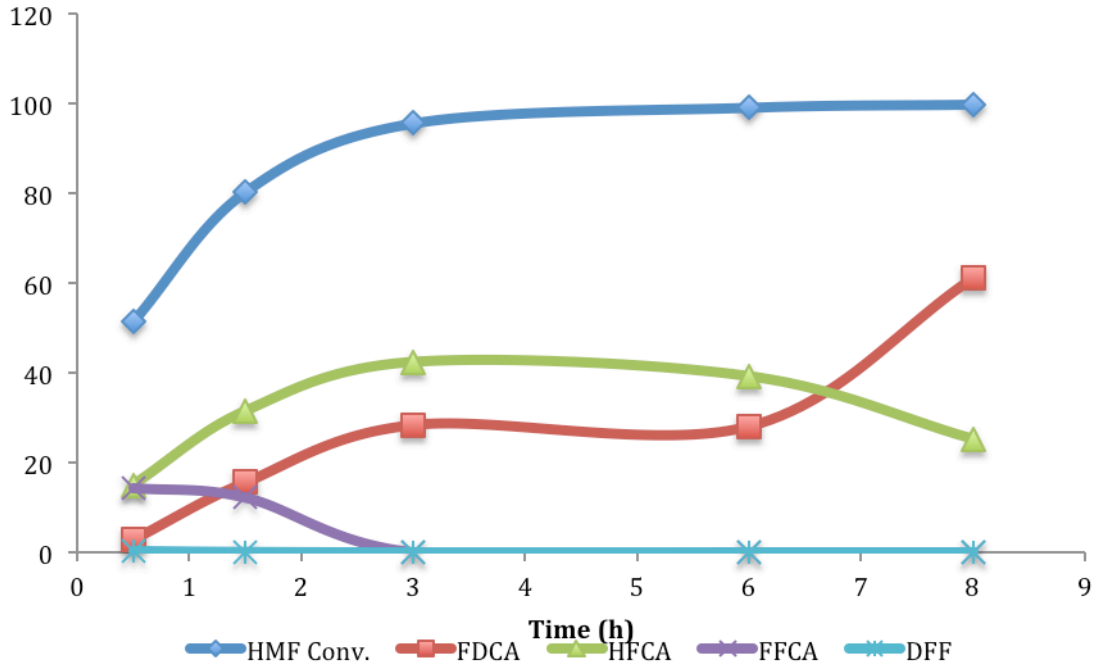

Figure 10 Kinetic behaviour of HMF oxidation carried out using Pt1 catalyst, 40 °C, 1 bar of O_2

In conclusion, the Pt1 catalyst showed good catalytic activity similar to that of commercial Pt/C. Furthermore, the use of Fe_3O_4 support guaranteed an efficient magnetic recovery from the reaction media without influencing the reaction rate and did not show any leaching effect. The best FDCA yield was obtained using NaOH under mild reaction conditions, at atmospheric pressure of oxygen.

12.4 Oxidation of HMF catalysed by magnetic palladium nanocatalyst

The oxidation of hydroxymethylfurfural to furandicarboxylic acid on a palladium-based catalyst has been poorly investigated. In this work, the magnetic palladium catalyst described in chapter 5.1.2 was employed in the selective oxidation of HMF to FDCA using different alkaline compounds and temperatures.

The main characteristics of magnetic palladium catalyst Pd6 are summarized in Table 9.

Table 9 Main characteristic of magnetic palladium catalyst

Catalyst	Palladium loading (%)	BET (m^2/g)	Diamter (nm)
Pd6	4.7	106.48	8

Synthesis condition: 1g of $Fe(OAc)_2$, 0.05g of $Pd(OAc)_2$, 44mL EtOH at 96 wt%, monomode microwave heating: 120°C, 15 min, 250 W.

A typical oxidation experiment was carried out in a 40 ml Parr autoclave electrically heated and was followed using an HPLC Perkin Elmer Flexer Series 200 equipped with an MPLC Polypore CA column. In particular, HMF (0.28 mmol), the palladium magnetic catalyst (Pd6, $Pd@Fe_3O_4$) (22 mg) and the selected alkaline compound were dispersed in 5 mL of H_2O and heated up to 40°C under 10 bar of oxygen. The catalytic results are reported in Table 10.

Table 10 Effect of diverse base and temperature on the catalytic oxidation of HMF to FDCA

Run	Base	pH	T (°C)	t (h)	HMF Conv. (%)	FDCA Yield (%)	HFCA Yield (%)	FFCA Yield (%)	DFF Yield (%)
OX97	***	7	40	3	9.2	0	6	0	0
OX101	$CaCO_3$	7	40	3	0	0	0	0	0
OX104	$H_3BO_3/H_2BO_3^-$	10	40	3	28.5	0	20.9	5	0
OX110	$H_3BO_3/H_2BO_3^-$	10	60	3	54.4	2.4	35.6	14.4	0
OX115	$H_3BO_3/H_2BO_3^-$	10	60	6	68.7	3.5	46.1	17.4	0
OX93	NaOH	13	40	3	92.1	12.8	75.3	3.9	0
OX123	NaOH	13	60	3	92.7	7.3	78.2	0	0
OX119	NaOH	13	80	3	97.3	11.8	77.6	0	0
OX133[a]	NaOH	13	60	3	77.7	3.7	28.9	34.9	0

[a] Reaction carried our with commercial 5%Pd/C BASF

These results confirmed that also using a magnetic palladium catalyst, strong alkaline conditions are required to obtain a good oxidation rate (see run OX93).

In fact, oxidation OX93 carried out at 40°C and pH 13 led to high HMF conversion (90%) and a high HFCA yield (75%). Under these conditions, the catalytic activity of palladium is very similar to that observed for the platinum catalyst ($Pt@Fe_3O_4$). However, oxidized product distribution was very different; in fact, palladium allows a high HFCA yield whereas platinum a high FFCA yield.

The effect of temperature on the oxidation of HMF was investigated using two diverse alkaline compounds, the $H_3BO_3/H_2BO_3^-$ system, at a pH 10, and NaOH at pH 13.

At pH 10 ($H_3BO_3/H_2BO_3^-$ basic system) and with an increase in temperature to 60°C, HMF conversion increased reaching a high HFCA yield (run OX110). When the reaction time (run OX115) was increased, only very little improvement in the conversion was ascertained, highlighting that pH 10 ($H_3BO_3/H_2BO_3^-$) was not adequate for alcohol oxidation even when temperature and time were increased.

On the other hand, at pH 13 (NaOH 0.1 M) by increasing the temperature up to 60°C HMF conversion reached 100% but no difference was observed in oxidized product distribution (see Figure 11).

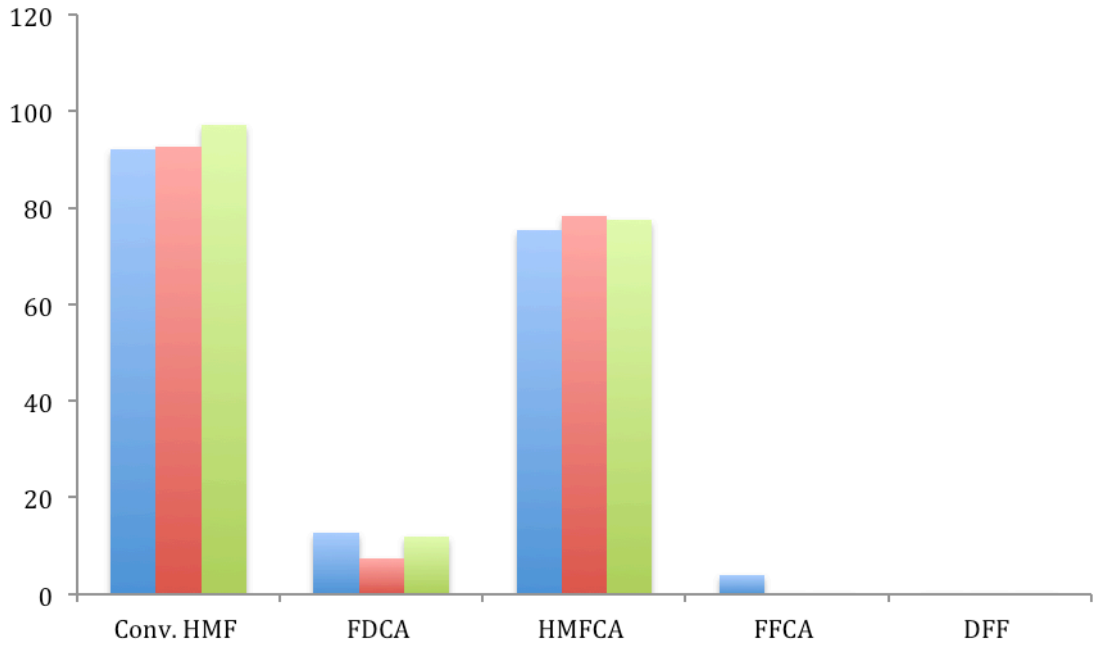

Figure 11 Effect of temperature on the oxidation of HMF at pH 13, a) reaction OX93 carried out at 40°C, blue graph, b) reaction OX123 carried out at 60°C, red graph and c) reaction carried out at 80°C, green graph.

Furthermore, the effect of low oxygen pressure at three diverse temperatures such as 40°C, 60°C and 80°C on the oxidation rate was investigated and the results are reported in Table 11.

Table 11 Effect of low pressure on oxidation of HMF

Run	T (°C)	PO_2 (bar)	HMF Conv. (%)	FDCA Yield (%)	HFCA Yield (%)	FFCA Yield (%)	DFF Yield (%)
OX127	40	1	97.4	19.7	77.9	0	0
OX130	60	1	98.6	43.2	35.7	8.5	0
OX131	80	1	99	18.8	27.9	10.8	0

At low oxygen pressure (1 bar), the temperature increase caused the degradation of HMF and FDCA production reached its maximum value at 60°C.

Comparing these results with the ones reported by Davis et al.[17a] it was observed that the different catalytic activity can be due to the diverse palladium oxidation states. In fact, the Pd/C catalyst described in the literature was previously reduced before its use to guarantee the complete reduction of palladium. Instead, the magnetic palladium catalyst did not contain completely reduced palladium as confirmed by the TPR analysis reported in Chapter 5.1.2, Figure 26.

Taking into account all these aspects, commercial palladium on carbon and magnetic palladium catalysts were pre-treated to reduce the palladium species present before their use in HMF oxidation and the results are summarized in Table 12.

Table 12 The oxidation of HMF carried out at 40°C, 1 bar for 3 h using different pre-treated Pd@Fe_3O_4 catalysts

Run	Catalyst	NaOH	Conv. HMF	FDCA Yield (%)	HFCA Yield (%)	FFCA Yield (%)	DFF Yield (%)	Other Yield (%)
OX139	Pd/ C Aldrich[a]	0.2	100	40,2	23,2	41,4	0	1
OX148	Pd/ C Aldrich[b]	0.2	96,5	16,2	47,6	13	0	13.2
OX143	Pd6	0.2	39,1	1	18,5	0	0,1	10.7
OX144	Pd6 [b]	0.2	98,8	42,6	45,8	1,8	0	1.4

OX176	Pd6 [c]	0.2	100	44	50	4.3	0	<1
OX146	Pd6 [d]	0.2	98,5	31,4	59,8	0	0	0
OX154	Pd6 [e]	0.2	96.5	17.8	69.9	0.0	0.0	0
OX218	Pd6 [b]	0.3	100	59.6	37.4	0	0	3
OX221	Pd6 [b,g]	0.2	100	71	21.3	0	0	7.7

[a]Pre-treated at 300°C under H_2 flow for 6h

[b]Pre-treated at room temperature under H_2 atmosphere for 12h

[c]Pre-treated at room temperature under H_2 atmosphere for 60h

[d]Pre-treated at 50°C under 20 bar of H_2 for 4h

[e]Pre-treated at 100°C in methanol under 20 bar of H_2 for 4h

[g]HMF/Pd molar ratio decreased up to 10

Oxidation OX139 carried out with pre-treated commercial palladium on carbon confirmed the high activity of reduced palladium. In fact, after 3 h 100 % of the HMF was converted with a high FDCA yield (40.2%) and after 9 h the FDCA yield increased up to 69.1% (see Figure 12). Among the oxidation carried out using magnetic palladium catalyst Pd6, runs OX218 and OX221 showed the higher FDCA yield. In particular run OX221 carried out using a higher palladium load led high HMF conversion with a FDCA yield of 71%, and also the run OX218 carried out with the lower palladium amount showed a good FDCA yield (59.6%). These results are better than those reported in literature for magnetic palladium thanks to the mild reaction condition and the higher FDCA yield.[32]

Moreover, from Figure 11 it is possible to see that after 1.5 hours the concentration of HFCA remained constant, underlining that when HFCA was formed it was no longer oxidised.

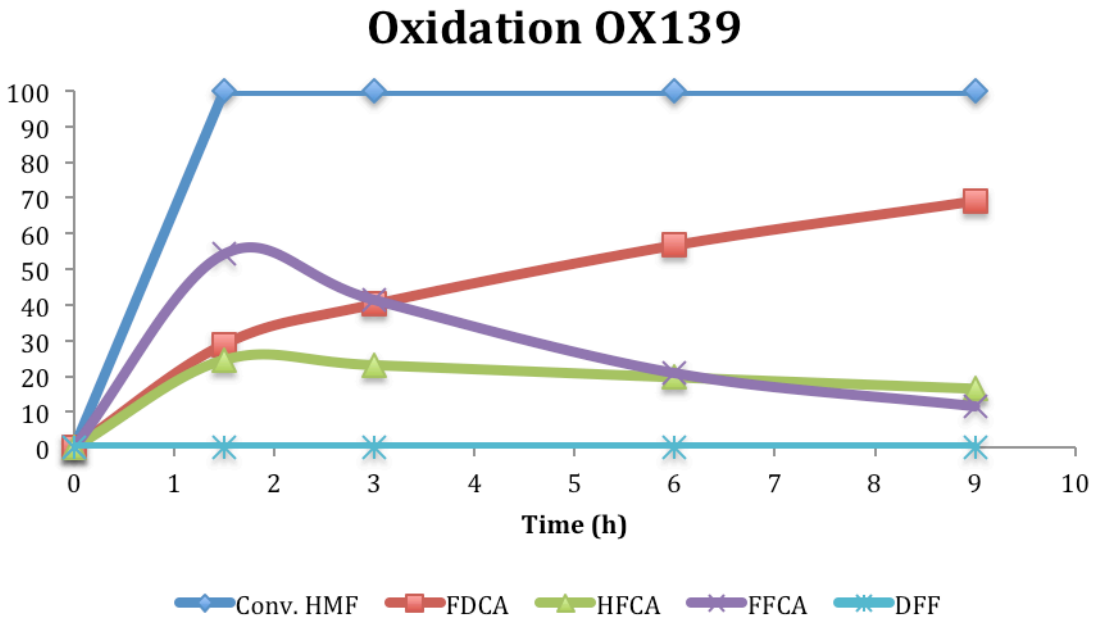

Figure 12 The oxidation of HMF using pre-treated palladium on carbon run OX139

Furthermore, by comparing oxidation OX127 (see Table 8) carried out with a lower NaOH amount and run OX143 (see Table 9) carried out with a higher NaOH amount, it was possible to observe that by increasing NaOH the degradation of HMF was favoured whereas at low NaOH concentration, HMF was oxidized to HFCA and FDCA.

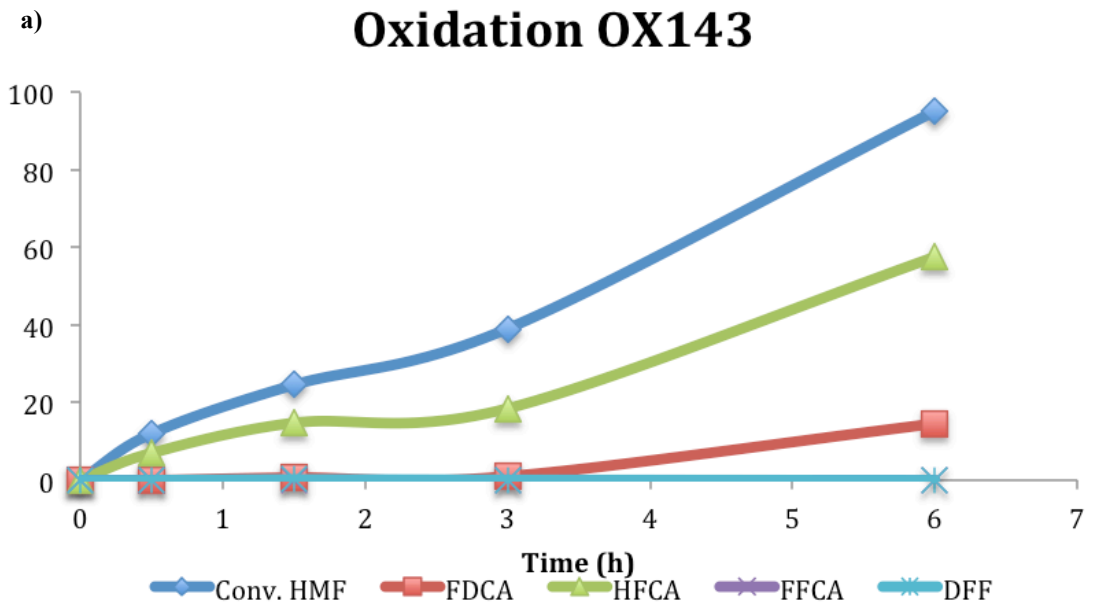

b)

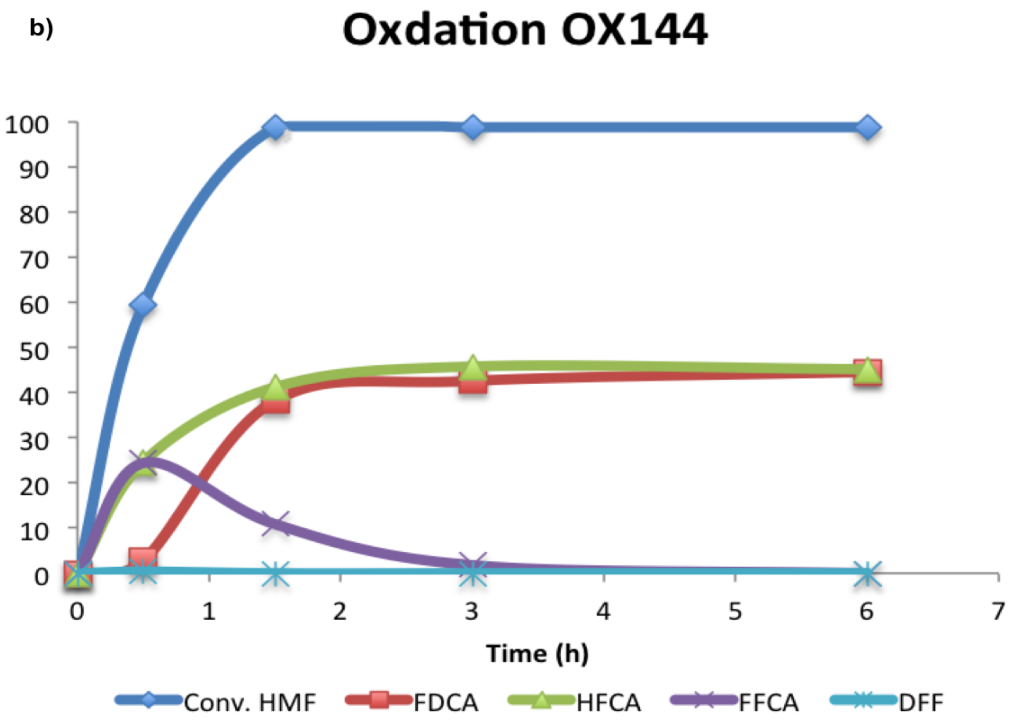
Oxdation OX144
100
90
80
70
60
50
40
30
20
10
0
0
1
2
3
4
5
6
7
Time (h)
Conv. HMF
FDCA
HFCA
FFCA
DFF

c)

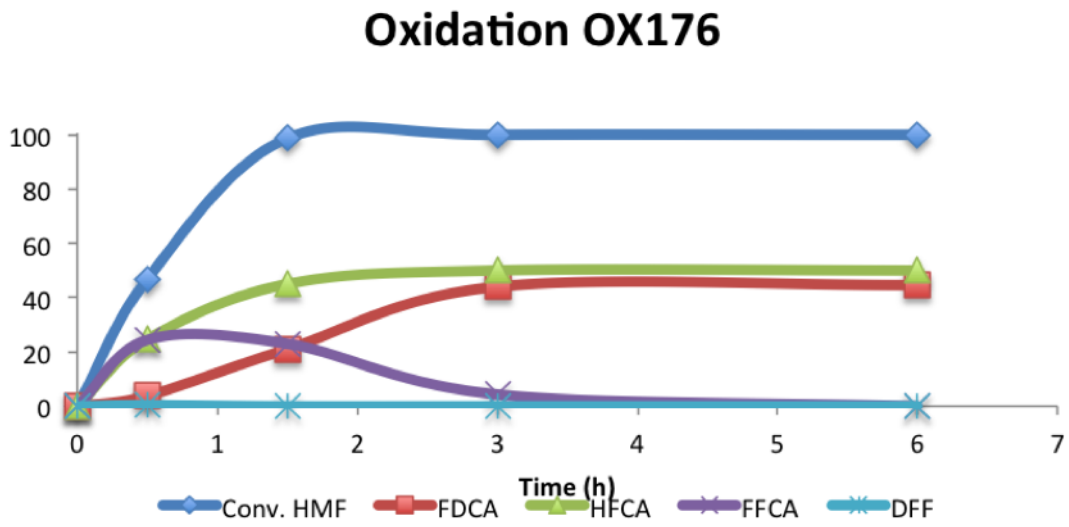
Oxidation OX176
100
80
60
40
20
0
0
1
2
3
4
5
6
7
Time (h)
Conv. HMF
FDCA
HFCA
FFCA
DFF

d)

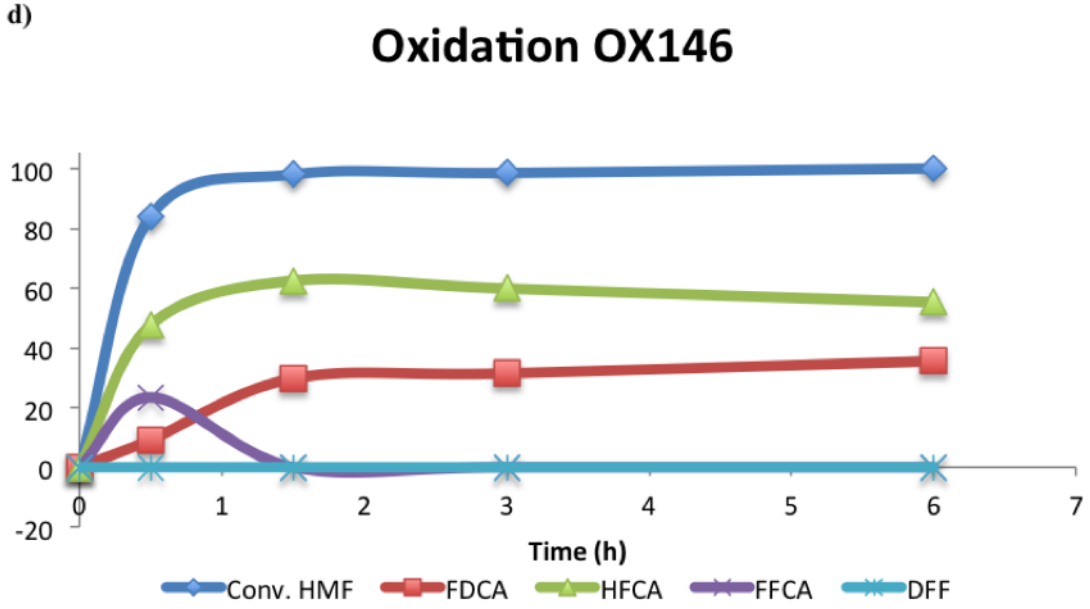

e)

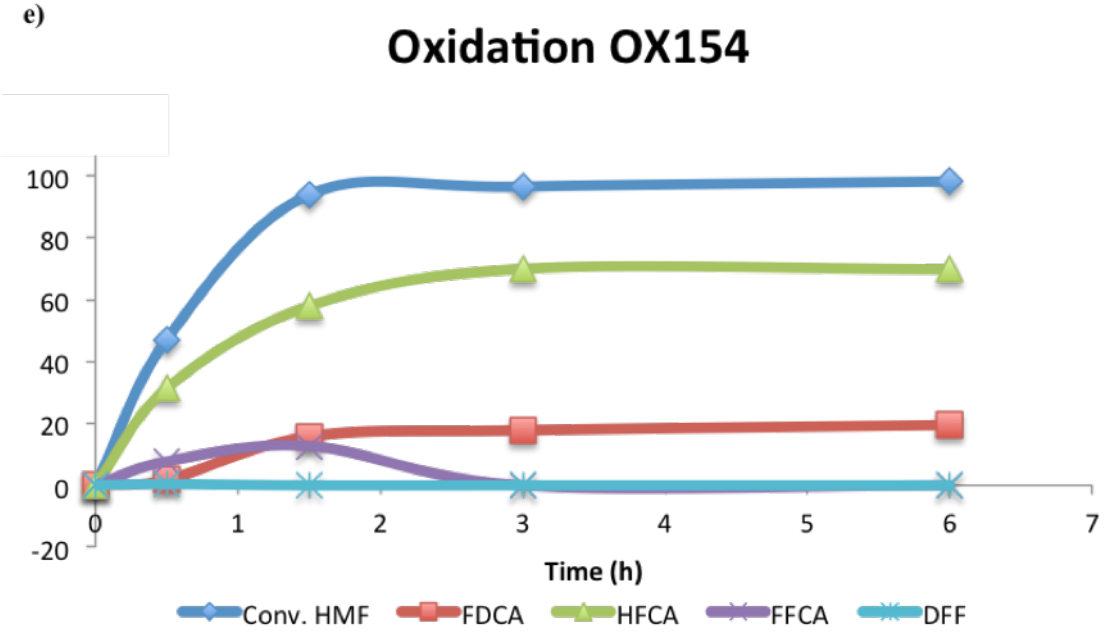

Figure 13 The oxidation runs : a) carried out with Pd6 catalyst, OX143, b) carried out with Pd6 catalyst pre-treated at room temperature under 1 bar of H_2 for 12h, OX144, c) carried out with Pd6 catalyst pre- treated at room temperature under 1 bar of H_2 for 60h, OX176, d) carried out with Pd6 catalyst pre- treated at 50°C under 20 bar of H_2 for 4h, OX146 and e) carried out with Pd6 catalyst pre- treated at 100°C in methanol under 20 bar of H_2 for 4h, OX154

As it is possible to see in Figure 13, the pre-treated catalysts (runs OX 144, OX176, OX146 and OX154) were more active in the selective oxidation of HMF leading to an almost complete conversion after 1.5 hours. The HFCA concentrations reached a maximum after 1.5 hour and remained constant during the reaction, as was observed in run OX139 with the commercial Pd/C.

On the other hand, in all runs, the DFF concentration did not reach 1% because it was quickly converted to FFCA as confirmed by a DFF oxidation experiment. DFF oxidation experiment was carried out under the same reaction conditions and showed complete DFF conversion after 30 minutes with high FFCA and FDCA yields.

Moreover, the pre-treated catalysts used in runs OX144 and OX176 showed the highest FDCA selectivity. These results are particularly interesting due to the mild pre-treatment conditions used, which are not enough to activate the commercial palladium on carbon. In fact, the commercial palladium on carbon activated under these mild conditions (run OX148) showed lower FDCA yields than ones observed in OX144 and OX176 (see Table 9).

Using the optimized pre-treatment conditions (OX176), a recycle test was performed, the catalyst was pre-activated at room temperature under hydrogen flow for 12 h, then HMF (0.28 mmol), NaOH (0.5 mmol) and H_2O (5 mL) were added and the reactor was heated up to 40°C. After 1 hour of reaction, the reaction mixture was removed while the catalyst was magnetically kept on the bottom of the reactor using a neodymium magnet. Then fresh reagents were added and the reaction was restarted. Table 13 illustrates the results of the oxidation recycles.

Table 13 Recycle test of pre-treated catalyst

Run	Conv. HMF	FDCA Yield (%)	HFCA Yield (%)	FFCA Yield (%)	DFF Yield (%)
OX151-1	76.9	6.6	24.7	39.4	0.5
OX151-2	85.8	9.2	32.6	40.5	0.3
OX151-3	86.0	6.3	29.1	36.3	0.2
OX151-4	92.0	10.9	33.9	46.6	0.3
OX151-5	84.6	9.1	29.9	40.6	0.4
OX151-6	89.5	11.1	35.0	42.0	0.2
OX151-7	87.0	9.7	33.3	41.0	0.2
OX151-8	91.5	12.9	31.4	46.5	0.2

After each cycle, conversion and oxidized product distribution were very similar thus confirming the easy recovery and recycling of the magnetic palladium catalyst, see Figure 14.

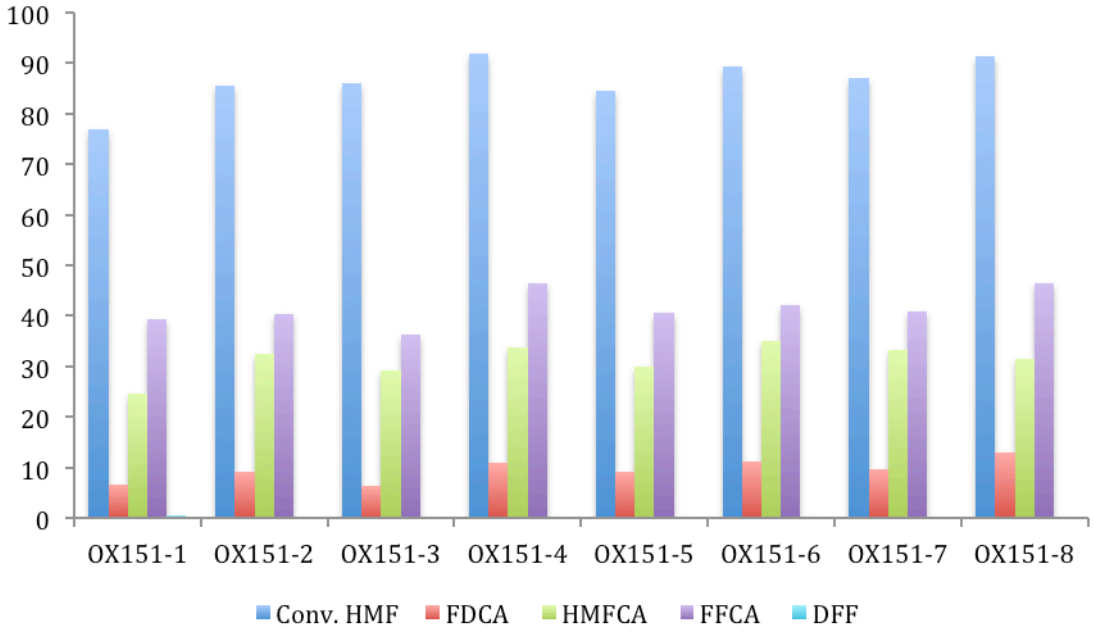

Figure 14 product distribution in the oxidation of HMF recycle tests

In conclusion, the pre-treated Pd6 catalyst at room temperature under hydrogen flow for 12 h showed the best catalytic activity and thanks to its magnetic support was easily and efficiently recovered and recycled. It is noteworthy that also after 8 recycle runs the conversion and yields were very close to the ones obtained with the fresh catalyst.

Furthermore, using the same pre-treatment commercial palladium on carbon showed lower activity.

As explained in the introduction (Chapter 12.1), the use of HMF as a platform for fine chemical production is still limited due to the high separation and production costs. The use of renewable resources for HMF production is still a great challenge for the researcher and for this reason an oxidation experiment was carried out using a raw HMF solution obtained from acid hydrolysis of cellulose.

In particular, an aqueous suspension of cellulose 5 % wt. was treated with $NbOPO_4$ at high temperature (160-180°C). The final mixture obtained containing HMF 0.027 M, furfural 0.013 M and unreacted glucose was oxidised using NaOH, and the pre-treated Pd6 catalyst at 40°C under1 bar of oxygen for 3 h.

Finally, HMF was almost completely converted (96%) with yields in HFCA and FDCA of 81% and 4% respectively, whereas the furfural was oxidized to furoic acid with a yield of 80%.

These preliminary experiments carried out using raw hydrolysed cellulose showed that the magnetic palladium catalyst can be used directly on a raw reaction mixture with high HMF and furfural conversion.

12.5 Conclusion

The ruthenium, platinum and palladium magnetic systems were employed in the selective oxidation of hydroxymethyl furfural leading to diverse oxidized product distributions. The three metals in fact showed diverse activity leading to the formation of different partially oxidized products (DFF, FFCA or HFCA) (see Scheme 2).

The effect of temperature and pH on the catalytic activity of these three diverse magnetic catalysts was investigated. In each case, as the temperature increased, the degradation of HMF increased resulting in a non-industrially sustainable process, whereas when the alkaline strength increased, the conversion of HMF increased thus avoiding degradation.

In particular, under optimized alkaline aqueous conditions, Ru2 showed good activity toward the oxidation of the alcoholic group but it was not able to oxidize the aldehyde group to carboxilic acid leading to a high production of DFF.

Pt1 allows the high formation of HFCA underlining that platinum is able to oxidize the aldehyde group but it is not efficient in hydroxyl group oxidation.

Finally, Pd6 reached better results with the highest FDCA yield, especially if pre-treated at room temperature under hydrogen flow for 12 h. In conclusion, under the adopted aqueous alkaline conditions, Ru2 and Pd6 easily oxidized the hydroxylic group leading to the production of aldehyde furan derivates but they were not able to oxidize the aldehyde group to carboxylic acid efficiently. On the other hand, Pt1 easily oxidized the aldehyde group allowing the accumulation of HFCA.

Moreover, the Pd6 catalyst showed good efficiency also when employed on raw HMF solution, obtained from the hydrolysis of cellulose.

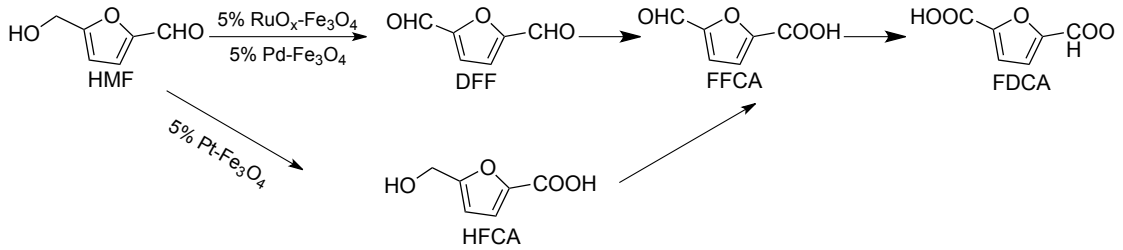

Scheme 2 Schematic mechanisms of oxidation of HMF using the three different metals catalysts.

12.6 References

[1] J. J. Bozell and G. R. Petersen, *Green Chemistry* **2010**, *12*, 539-554.
[2] R.-J. van Putten, J. C. van der Waal, E. de Jong, C. B. Rasrendra, H. J. Heeres and J. G. de Vries, *Chemical Reviews* **2013**, *113*, 1499-1597.
[3] a) Z. Zhang and Z. Zhao, *Bioresource Technology* **2011**, *102*, 3970-3972; b) C. Shi, Y. Zhao, J. Xin, J. Wang, X. Lu, X. Zhang and S. Zhang, *Chemical Communications* **2012**, *48*, 4103-4105.
[4] J. Lewkowski, **2001**.
[5] a) A. Gandini, A. J. D. Silvestre, C. P. Neto, A. F. Sousa and M. Gomes, *Journal of Polymer Science Part A: Polymer Chemistry* **2009**, *47*, 295-298; b) C. H. R. M. Wilsens, B. A. J. Noordover and S. Rastogi, *Polymer* **2014**, *55*, 2432-2439.
[6] G. An, H. Ahn, K. A. De Castro and H. Rhee, *Synthesis* **2010**, *2010*, 477-485.
[7] E. Taarning, I. S. Nielsen, K. Egeblad, R. Madsen and C. H. Christensen, *ChemSusChem* **2008**, *1*, 75-78.
[8] C. Moreau, R. Durand, C. Pourcheron and D. Tichit in *Selective oxidation of 5-hydroxymethylfurfural to 2,5-furan-dicarboxaldehyde in the presence of titania supported vanadia catalysts*, *Vol. Volume 108* Eds.: A. B. H.U. Blaser and R. Prins), Elsevier, **1997**, pp. 399-406.
[9] O. Navarro, A. Canós and S. Chornet, *Topics in Catalysis* **2009**, *52*, 304-314.
[10] C. Carlini, P. Patrono, A. M. R. Galletti, G. Sbrana and V. Zima, *Applied Catalysis A: General* **2005**, *289*, 197-204.
[11] A. Takagaki, M. Takahashi, S. Nishimura and K. Ebitani, *ACS Catalysis* **2011**, *1*, 1562-1565.
[12] J. Nie, J. Xie and H. Liu, *Journal of Catalysis* **2013**, *301*, 83-91.
[13] S. E. Davis, B. N. Zope and R. J. Davis, *Green Chemistry* **2012**, *14*, 143-147.
[14] B. N. Zope, D. D. Hibbitts, M. Neurock and R. J. Davis, *Science* **2010**, *330*, 74-78.
[15] a) O. Casanova, S. Iborra and A. Corma, *ChemSusChem* **2009**, *2*, 1138-1144; b) P. Verdeguer, N. Merat and A. Gaset, *Journal of Molecular Catalysis* **1993**, *85*, 327-344.
[16] M. Lilga, R. Hallen and M. Gray, *Topics in Catalysis* **2010**, *53*, 1264-1269.
[17] a) S. E. Davis, L. R. Houk, E. C. Tamargo, A. K. Datye and R. J. Davis, *Catalysis Today* **2011**, *160*, 55-60; b) N. Mei, B. Liu, J. Zheng, K. Lv, D. Tang and Z. Zhang, *Catalysis Science & Technology* **2015**, *5*, 3194-3202.
[18] a) Y. Y. Gorbanev, S. K. Klitgaard, J. M. Woodley, C. H. Christensen and A. Riisager, *ChemSusChem* **2009**, *2*, 672-675; b) B. Saha, S. Dutta and M. M. Abu-Omar, *Catalysis Science & Technology* **2012**, *2*, 79-81.
[19] T. Pasini, M. Piccinini, M. Blosi, R. Bonelli, S. Albonetti, N. Dimitratos, J. A. Lopez-Sanchez, M. Sankar, Q. He, C. J. Kiely, G. J. Hutchings and F. Cavani, *Green Chemistry* **2011**, *13*, 2091-2099.

[20] S. Wang, B. Liu, Z. Yuan and Z. Zhang, *Journal of the Taiwan Institute of Chemical Engineers* **2016**, *58*, 92-96.
[21] a) C. A. Antonyraj, J. Jeong, B. Kim, S. Shin, S. Kim, K.-Y. Lee and J. K. Cho, *Journal of Industrial and Engineering Chemistry* **2013**, *19*, 1056-1059; b) F. Kerdi, H. Ait Rass, C. Pinel, M. Besson, G. Peru, B. Leger, S. Rio, E. Monflier and A. Ponchel, *Applied Catalysis A: General* **2015**, *506*, 206-219.
[22] B. Siyo, M. Schneider, J. Radnik, M.-M. Pohl, P. Langer and N. Steinfeldt, *Applied Catalysis A: General* **2014**, *478*, 107-116.
[23] S. M. Payne and F. M. Kerton, *Green Chemistry* **2010**, *12*, 1648-1653.
[24] N. K. Gupta, S. Nishimura, A. Takagaki and K. Ebitani, *Green Chemistry* **2011**, *13*, 824-827.
[25] a) B. Zope, S. Davis and R. Davis, *Topics in Catalysis* **2012**, *55*, 24-32; b) Y. Gorbanev, S. Kegnæs and A. Riisager, *Catalysis Letters* **2011**, *141*, 1752-1760; c) Y. Gorbanev, S. Kegnæs and A. Riisager, *Topics in Catalysis* **2011**, *54*, 1318-1324.
[26] a) S. Wang, Z. Zhang, B. Liu and J. Li, *Industrial & Engineering Chemistry Research* **2014**, *53*, 5820-5827; b) L. Hu, X. Tang, J. Xu, Z. Wu, L. Lin and S. Liu, *Industrial & Engineering Chemistry Research* **2014**, *53*, 3056-3064.
[27] a) A. Khan and P. G. Smirniotis, *Journal of Molecular Catalysis A: Chemical* **2008**, *280*, 43-51; b) J. Zieliński, I. Zglinicka, L. Znak and Z. Kaszkur, *Applied Catalysis A: General* **2010**, *381*, 191-196.
[28] S. Hosokawa, H. Kanai, K. Utani, Y.-i. Taniguchi, Y. Saito and S. Imamura, *Applied Catalysis B: Environmental* **2003**, *45*, 181-187.
[29] a) H. Imanishi, A. Maeda, T. Maegawa, S. Matsuno and T. Aida, *Chemical Engineering Science* **2008**, *63*, 4974-4980; b) J.-C. Ryu, D.-H. Lee, K.-S. Kang, C.-S. Park, J.-W. Kim and Y.-H. Kim, *Journal of Industrial and Engineering Chemistry* **2008**, *14*, 252-260.
[30] K. R. Vuyyuru and P. Strasser, *Catalysis Today* **2012**, *195*, 144-154.
[31] S. Siankevich, G. Savoglidis, Z. Fei, G. Laurenczy, D. T. L. Alexander, N. Yan and P. J. Dyson, *Journal of Catalysis* **2014**, *315*, 67-74.
[32] Z. Zhang, J. Zhen, B. Liu, K. Lv and K. Deng, *Green Chemistry* **2015**, *17*, 1308-1317.

13. STUDY OF THE CROSS-COUPLIG REACTIONS USING MAGNETIC PALLADIUM NANOCATALYSTS

13.1 Introduction

Cross-coupling reactions are important industrial reactions fundamental for the production of a wide range of fine chemicals. Generally, cross-coupling leads to the formation of a C-C bond between nucleophile and electrophilic organic compounds mediated by a transition metal catalyst (see Scheme 1).

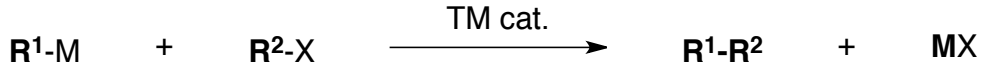

Scheme 1 Cross-coupling reaction scheme

Several transition metals are employed as catalysts in cross-coupling reactions such as palladium, platinum[1], copper[2], nickel[3] and iron[4], among which palladium is the most extensively studied thanks to its high activity[5].

Tsuji et al.[6] were the first to introduce palladium as a catalyst for cross-coupling reactions, in particular they synthetized allylmalonate through allylpalladium chlorine and malonate. Heck et al.[7] and Mizoroki et al.[8] described the employment of homogeneous palladium catalysts in the cross-coupling reaction between aryl halides and alkenes.

Negishi et al.[9] and Suzuki et al.[10] showed how palladium catalysts were able to efficiently catalyse cross-coupling between halides and organometallic compounds.

Furthermore, in literature other efficient palladium catalysed cross-coupling reactions were reported, for example Sonogashira et al.[11] described palladium catalysed cross-coupling between terminal alkines and aryl halides.

Nowadays, palladium catalysed cross-couplings are used not only for the formation of C-C bonds but also for the formation of C-N, C-O and C-S bonds thus paving the way for the production of a wide range of important fine chemicals especially for pharmaceutical [12] and electronic industries[4b, 13].

For pharmaceutical use in particular, cross-coupling products require an extremely high grade of purity, thus expensive and difficult purification stages are required to guarantee the complete elimination of impurities and trace of metal catalysts.

Taking into account that cross coupling is generally carried out in a liquid phase using a homogeneous metal catalyst, the separation of metal species from the reaction mixture is particularly hard. In this context, the use of magnetic heterogeneous nanocatalysts is gaining ever increasing success also in cross-coupling reactions because it is a strategic choice to facilitate the catalyst recovery still maintaining the typical high activity of homogeneous systems, as reported by Karimi et al.[14]. For example, Deraedt et al. studied the employment of palladium nanoparticles supported on a magnetic support in diverse cross-coupling reactions underlining the easy recoverability and the encouraging results.[15]

In this work, palladium magnetic catalysts characterized by hierarchical or complex structures, previously described in Chapter 5.1, were employed in some cross-coupling reactions such as the Suzuki-Miyaura reaction (see Scheme 2a), the Heck-Mizoroki reaction (see Scheme 2b), the Cassar-Heck reaction (see Scheme 2c) and C2 arylation of N-methyl-1-H-imidazole (see Scheme 2d).

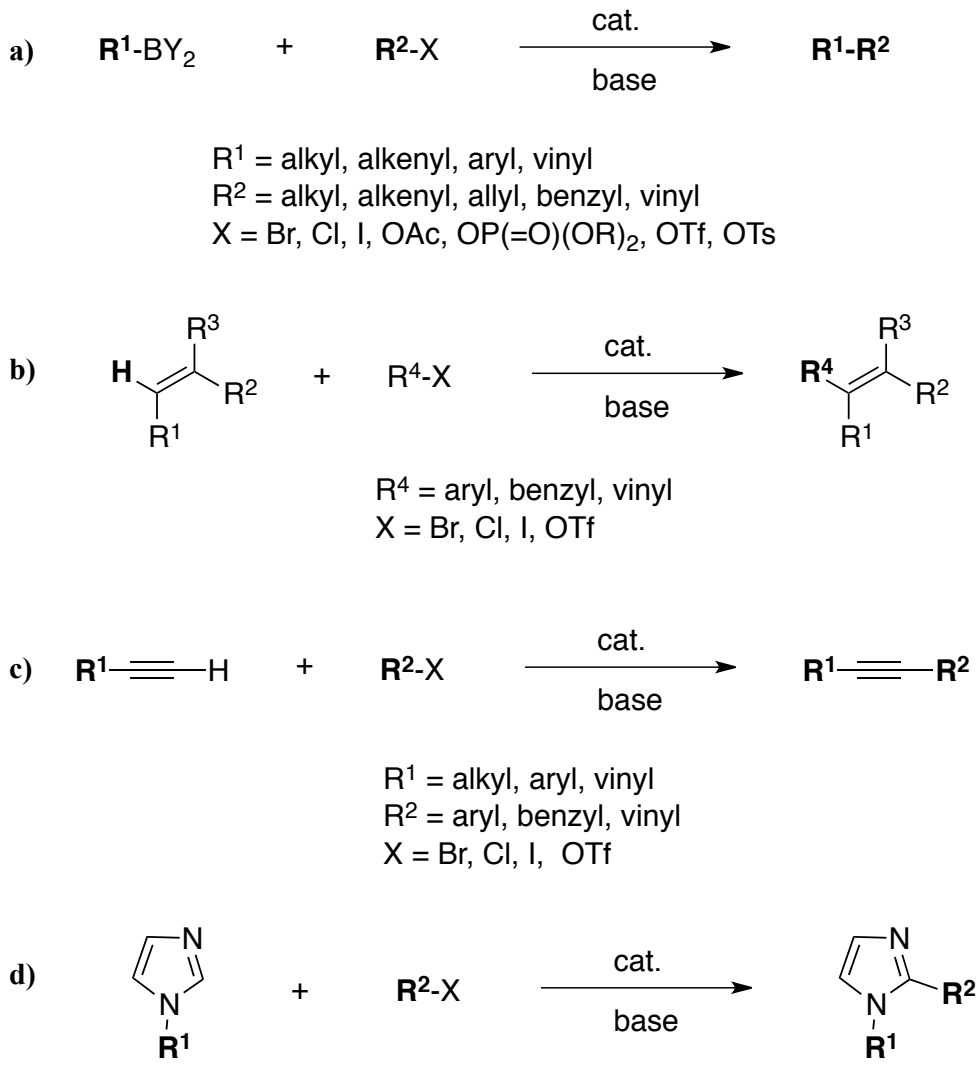

Scheme 2 Cross-coupling reaction: a) Suzuki- Miyaura, b) Heck-Mizoroki, c) Cassar-Heck and d) C2 arylation of N-methyl-1-*H*-imidazole

These catalytic tests were performed in collaboration with the research group of Prof. Bellina of University of Pisa.

13.2 The Suzuki-Miyaura reaction catalysed by magnetic palladium catalyst

The Suzuki-Miyaura reaction is the most versatile cross-coupling which leads to a wide range of complex organic compounds such as biaryl compounds.

Biaryl products are important building blocks of numerous pharmaceutical[16], herbicide, polymeric and natural products.[17]

Suzuki-Miyaura cross-coupling is generally carried out in an alkaline aqueous medium between an organic halide and an organoborane compound in the presence of a palladium catalyst as described in Scheme 3.

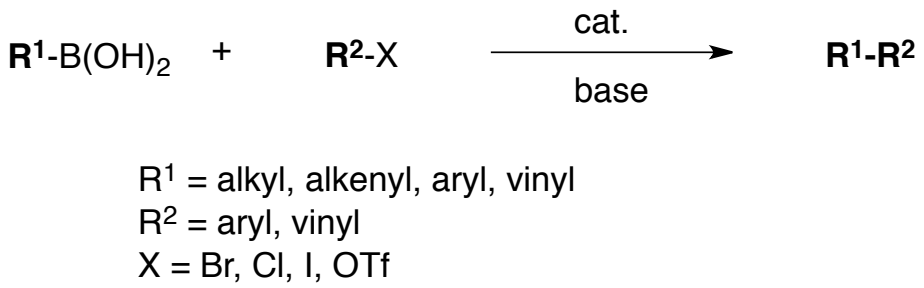

Scheme 3 Suzuki-Miyaura cross-coupling reaction scheme

The use of water as the solvent is particularly important from an environmental and economic point of view, in fact water is cheap, safe and eco-friendly. Moreover, another remarkable advantage of water is that organic products are usually insoluble in water, thus easily recoverable and separable from the reaction medium.

The Suzuki-Miyaura cross-coupling catalytic cycle reported in Figure 1 is based on three key steps: (i) the oxidative addition of organic halide to the palladium(0) catalyst, (ii) the transmetallation between the oxidative addition product and the organoborane compound and finally (iii) the reductive elimination of the coupling product to regenerate the palladium catalytic site.[10]

The transmetallation step is considered the reaction-limiting step because it is generally the slowest one.

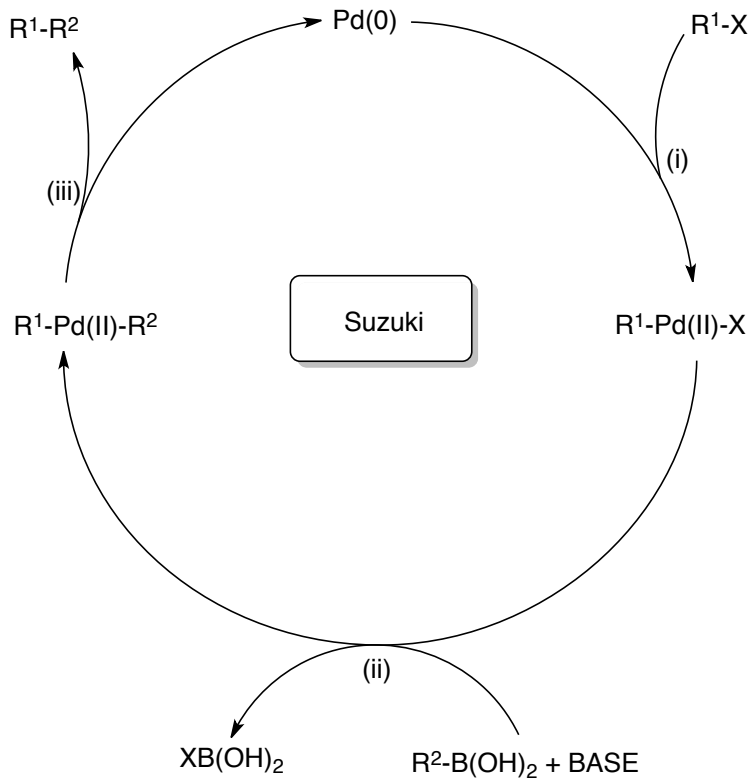

Figure 1 Suzuki-Miyaura cross-coupling catalytic cycle

Several authors describe the use of palladium supported catalysts in Suzuki-Miyaura cross-coupling reactions, underlining that especially with electron rich halide compounds carbon, alumina supported palladium shows higher catalytic activity than homogeneous ones.[18] For example, Marck et al.[19] employed palladium on carbon to catalyse the cross-coupling of diverse phenylboronic acidS and aryl halides with a high yield. Heidenreich et al.[20] reported promising results in the cross-coupling of aryl halides using an extremely low palladium loading and short reaction time, whereas Zhang et al.[21] utilized a high palladium loading, but greener conditions such as room temperature and an aqueous solvent for the cross-coupling of diverse aryl boranes.

Usually bromide, iodide and trifluoromethanesulfonate compounds are very reactive in cross-coupling reactions, whereas chlorine compounds show high inertia toward the oxidative addition step of the cross-coupling catalytic cycle. However, Leblonde et al. [22] were able to optimize aryl chlorine cross-coupling using palladium on carbon as the catalyst and an aqueous dimethylamide solution as the solvent.

Suzuki-Miyaura cross-coupling has also been investigated with the adoption of a magnetic supported catalyst. Stevens et al.[23], for example, described the use of palladium anchored on a maghemite/oleate core shell system, underlining the high activity and recoverability of this magnetic catalyst. Rehm et al. developed a new interesting system in which magnetic palladium catalysts were immobilized in a continuous flow reactor for the Suzuki cross-

coupling of phenylboronic acid and 4-bromoanisole, obtaining low conversion and high selectivity. [24] Hajipour et al. employed palladium(II) acetylacetonate supported on magnetic mesoporoue silica core-shell in the Suzuki cross-coupling reaction of acyl halides with boronic acids underlinig the fast and easy recovery of the catalyst from the reaction mixture.[25]

Yinghuai et al.[26] showed the use of palladium anchored on a starch/magnetic nanoparticle core shell system in the cross-coupling of bromobenzene and phenylboronic acid obtaining a yield of 83%. Gholinejad et al. reported the employment of palladium supported on magnetite to catalyse the cross-coupliing of aryl halides and phenylboronic acid under mild reaction conditions obtaining good yields.[27]

In the literature, other interesting magnetic catalysts for Suzuki-Miyaura cross-coupling are reported such as Pd-$CoFe_3O_4$[28],Pd@Fe_xO_y/Fe[29],Pd-αFe_2O_3[30] Pd@Fe_3O_4[31], Pd$(OAc)_2$@Fe_3O_4[32].

Now the diverse magnetic palladium catalysts described in Chapter 5.1 were employed in the Suzuki-Miyaura cross-coupling of phenylboronic acid with *p*-bromoanisole (see Scheme 4).

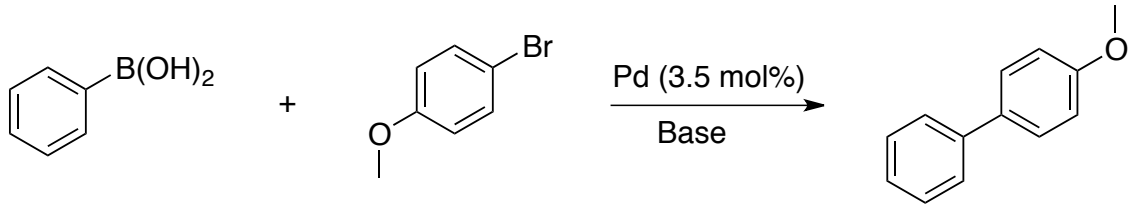

Scheme 4 Suzuki-Miyaura cross-coupling of phenylboronic acid and *p*-bromoanisole

In order to select the best reaction parameters, magnetic palladium catalyst 4.7%Pd@Fe_3O_4 (Pd6), was employed in the cross-coupling of phenylboronic acid and *p*-bromoanisole testing four diverse reaction conditions reported in literature[21, 33], and the results are summarized in Table 1.

Table 1 Suzuki-Miyaura cross-coupling reactions carried out under diverse conditions using the magnetic palladium Pd6

Run	solvent	Base	T (°C)	time (h)	Isolated yield (%)[a]
1	EtOH:H_2O 1:1	Na_2CO_3	RT	24	Trace
2	EtOH:H_2O 1:1	Na_2CO_3	80	24	68
3	EtOH:H_2O 1:1	Na_2CO_3	80	1	60
4	DMF	K_3PO_4	80	24	26
5	PhMe	Na_2CO_3	110	72	5
6	MeOH	K_3PO_4	60	24	14

Reaction condition: 3.5 mol% of Pd6 catalyst, 1mmol of phenylboronic acid, 1.2 mmol of *p*-bromoanisole, 3 mmol of base and 5 ml of solvent.

[a] Yield after the purification of the product

The used palladium catalysts Pd6 is characterized and described in Chapter 5.1 and shows a palladium loading of 4.7%, a surface area of about 106.48 m^2 and a narrow size distribution centred at 8 nm.

It is noteworthy that for each reaction no by products formation was evidenced thus the obtained isolated yields were close to the conversions.

As it is possible to see in Table 1, the best results were obtained using aqueous ethanol as the solvent and sodium carbonate as the alkaline compound. However, it was not possible to work at room temperature as reported by Zhang et al.[21] due to the low catalytic activity shown in run 1, thus the temperature was increased up to 80°C. After 1 h of reaction at this condition, good activity was observed with a 60% yield.

The low yields obtained in runs 4, 5 and 6 carried out in organic media confirmed that water plays a fundamental role in the cross-coupling reaction.

The best conditions (3.5 mol% of catalyst, 1 mmol of phenylboronic acid, 1.2 mmol of p-bromoanisole, 3 mmol of Na_2CO_3 and 5 ml of EtOH:H_2O 1:1) were then employed to verify the catalytic activity of diverse commercial or synthetic palladium catalysts, such as palladium on carbon (Pd/C 5% Engelhard), palladium on allumina (5%Pd@Al_2O_3 Aldrich), palladium trapped inside magnetite (4.7%Pd@Fe_3O_4 $_{int.}$, Pd6), palladium impregnated on commercial magnetite (4.5%Pd@Fe_3O_4, Pd2) and palladium impregnated on synthetic magnetite (4.3%Pd@Fe_3O_4, Pd3). The main characteristics of the employed magnetic palladium catalysts are summarized in Table 2 and the obtained results are reported in Table 3.

Table 2 The main characteristics of magnetic palladium catalyst

Catalysts	AAS (Pd wt.%)	BET (m^2/g)	Core diameter (nm)	Pd diameter (nm)
Pd2[a]	4.5	99	50	3.7
Pd3[b]	4.3	112.07	14	2.8
Pd6[c]	4.7	106.48	8	N.D

[a] Palladium nanoparticles supported over reference magnetite

[b] Palladium nanoparticles supported over synthetic magnetite

[c] Synthesis condition: 1g of $Fe(OAc)_2$ 0.05 $Pd(OAc)_2$, 44 mL EtOH 96 wt%, microwave heating: 120°C, 15 min 250W

Table 3 Comparison between commercial and synthetic palladium catalysts in the Suzuki-Miyaura cross-coupling

Run	Catalyst	Pd loading (mol%)	T (°C)	Time (h)	Isolated yield (%)[b]
7	Pd/C	3.5	RT	24	65

1	Pd6	3.5	RT	24	trace
8[a]	Fe_3O_4	***	80	24	0
14	Pd6	3.5	80	24	68
9	Pd/C	3.5	80	1	58
10	Pd6	3.5	80	1	60
11	Pd/Al_2O_3	3.5	80	1	76
12	Pd3	3.5	80	1	17
13	Pd2	3.5	80	1	0

Reaction condition: 3.5 mol% of catalyst, 1mmol of phenylboronic acid, 1.2 mmol of p-bromoanisole, 3mmol of Na_2CO_3 and 5 ml of EtOH:H_2O 1:1 for 24h.

[a] blank experiment carried out with 70 mg of magnetite

b Yield after the purification of the product

At room temperature, the commercial palladium on carbon showed higher activity than the magnetic Pd6 catalyst, whereas at 80°C and shorter reaction time (1h instead of 24h) Pd6 gave a higher coupling yield than commercial Pd/C. The Pd6 catalyst guarantees high selectivity, avoiding the formation of homocoupling and dehalogenation by-products.

The blank experiment, run 8, carried with bare magnetite confirmed that this support was not active in the cross-coupling reaction.

However, at 80°C the best catalytic system resulted commercial palladium on alumina, followed by the synthetic magnetic palladium catalyst Pd6 and commercial palladium on carbon. Alumina, magnetite and carbon show different acidity, which could explain their different catalytic activity. In fact, it is well known that the right acidity of the catalyst can help the adsorption of reagents and the product release thus improving the reaction rate.

Under the adopted conditions, the palladium impregnated on commercial and synthetic magnetite catalysts (Pd3 and Pd2) showed the lowest yield, 17% and 0 %, respectively. The lower catalytic activity of Pd3 and Pd2 respect to Pd6 catalyst could be due to a lower interaction between Fe and Pd atoms in the catalytic structure. In fact Pd6 has a complex structure where palladium nanoparticles are trapped inside magnetite structure favouring a strong Fe-Pd interaction. Whereas Pd3 and Pd2 catalyst are characterized by a hierarchical structure where palladium nanoparticles are impregnated on the surface of magnetite resulting in a minor Fe-Pd interaction.

In conclusion, the Pd6 catalyst showed promising results, which can be improved with further optimization of the reaction parameters, such as catalyst loading, time and temperature.

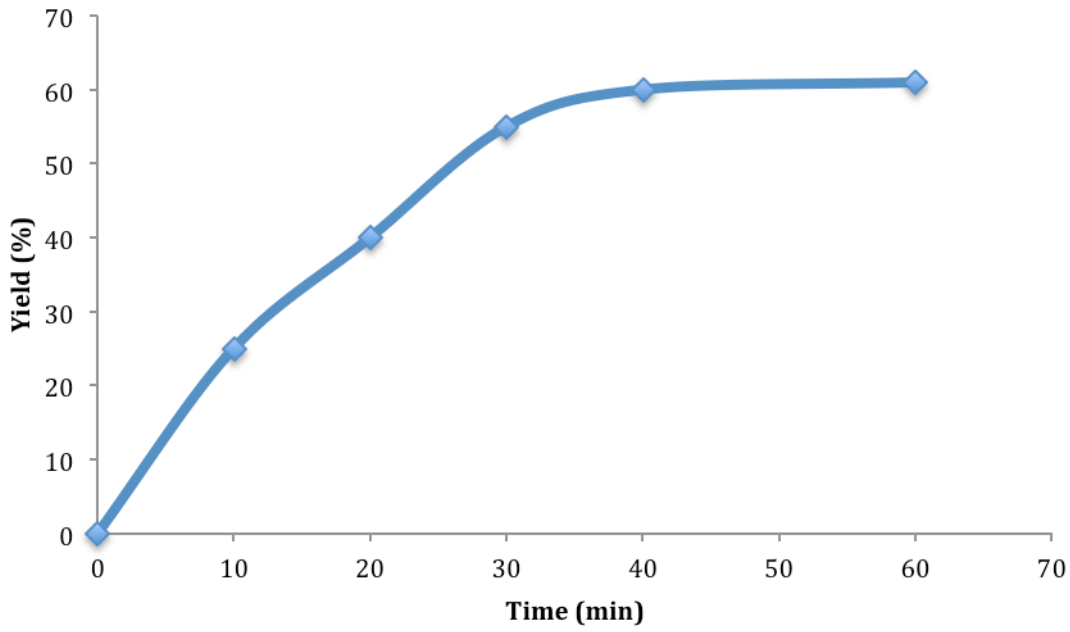

Figure 2 Suzuki-Miyaura cross-coupling at 80°C catalyzed by Pd6 catalyst

Figure 2 illustrates the kinetic trend of the cross-coupling catalysed by the Pd6 catalyst. The reaction induction time is very short, almost absent, as reported in literature for Suzuki-Miyaura cross-coupling. [34] In fact, the reaction started very quickly and reached a plateau around a yield of 60% after 40 minutes. This deactivation can be due to the passivation of the surface and/or Pd leaching. This aspect will be better investigated in further experiment.

13.3 The Heck-Mizoroki reaction catalysed by magnetic palladium catalyst

Generally, Heck-Mizoroki cross-coupling occurs between aryl halides and vinyl compounds and is catalysed by palladium catalysts in the presence of an alkaline compound. Heck-Mizoroki cross-coupling follows a different catalytic mechanism from other cross-coupling reactions. The reaction starts with an oxidative addition between the catalyst and the organic halide, and this activated complex is able to coordinate the double bond of the vinyl compound leading to C-C bond formation. This last step determines the regio and stereo selectivity of the coupling product. Then the coupling product is released by β-elimination together with the palladium hydride. Finally, the alkaline compound reacts with the palladium hydride to regenerate the catalyst.[35]

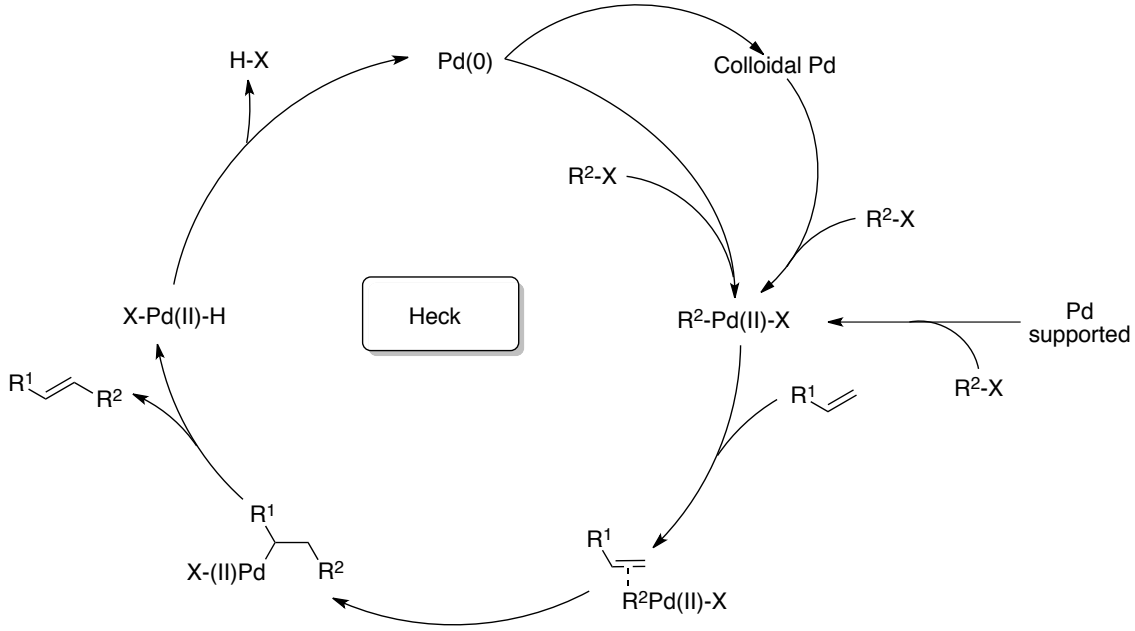

Figure 3 Heck-Mizoroki cross-coupling catalytic mechanism

Several authors reported the use of heterogeneous palladium catalysts in the Heck-Mizoroki cross-coupling reaction, for example Wall et al. developed the synthesis of 4-octyl methoxycinnamate, an important industrial product, by cross-coupling 4-bromoanisole and octyl acrilate.[36] Heindenreich et al. studied the Heck cross-coupling of aryl bromides and olefins catalysed by palladium supported on activated carbon underlining good control of palladium leaching.[37] Köhler et al. also underlined the importance of heterogeneous palladium on carbon for Heck-Mizoroki cross-coupling reactions, studying the correlation between catalyst structure and catalytic activity[38].

Bliff et al. summarized the diverse heterogeneous cross-coupling catalysts underlining their diverse structures and the effects on palladium leaching.[39]

The leaching effect is particularly important in this kind of reaction because the real active catalyst phase resulted the free metal released in the reaction mixture as confirmed by Zhao et al. studies.[40]

The work of Wang et al. is particularly interesting for our study as reports the employment of palladium supported on magnetite in the cross-coupling of iodobenzene and acrylic acid with a yield of 81%.[41] Furthermore, Du et al. showed the high performances of palladium immobilized on a magnetite/silica core shell structure, underlining good stability and recyclability of the magnetic system.[42] Other authors have compared the activity of the magnetic palladium systems in Suzuki and Heck

cross-coupling underlining that these systems lead to a higher yield in the Heck reaction.[32, 43]

In this context, the diverse magnetic palladium catalysts described in chapter 5.1 and summarized in Table 2 were employed in the Heck-Mizoroki cross-coupling of bromoacetophenone and styrene adopting the reaction conditions reported by Köhler et al, (see Scheme 5).[38]

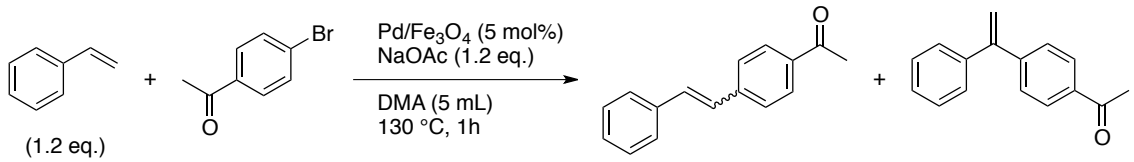

Scheme 5 Heck-Mizoroki cross-coupling of bromoacetophenone and styrene

The catalytic activity of synthetic palladium catalysts such as palladium trapped inside magnetite (4.7%Pd@Fe_3O_4 $_{int.}$, Pd6), palladium impregnated on commercial magnetite (4.5%Pd@Fe_3O_4, Pd2) and palladium impregnated on synthetic magnetite (4.3%Pd@Fe_3O_4, Pd3) were compared with commercial catalysts such as palladium on carbon (5%Pd/C Engelhard) and palladium on alumina (Pd@Al_2O_3 Aldrich), and the results are reported in Table 4.

Table 4 Comparison between commercial and synthetic palladium catalysts

Run	Catalyst	Pd load (mol%)	T (°C)	Time (h)	Isolated yield (%)[c]
1	Pd/C	0.1	100	20	66
2	Pd6	0.1	100	20	17
3	Pd/C	5	130	1	66
4	Pd6	5	130	1	55
5[a]	Pd6	5	130	21	52
6[b]	Fe_3O_4	***	130	1	trace
7	Pd/Al_2O_3	5	130	1	26
8	Pd2	5	130	1	3
9	Pd3	5	130	1	5
10	Pd3	5	130	24	40

Reaction condition: 1mmol of *p*-bromoacetophenone, 1.5 mmol styrene, 1.2 mmol of NaOAc and 5 ml of Dimethylacetamide (DMA).

[a] This reaction is carried out using NMP as solvent and K_2CO_3 as alkaline compound.

[b] The blank experiment is carried out using 100 mg of magnetite.

[c] Yield after the purification of the product

As it is possible to see in Table 4, at 100°C commercial palladium on the carbon catalyst showed higher yield than magnetic palladium Pd6. In particular, in each

reaction the formation of trace diphenylethylene as only by-product was observed thus the reached conversions were similar to the isolated yield.

By increasing the catalyst amount up to 5 mol% and the temperature up to 130 °C, the catalytic activity of Pd6 improved reaching that of commercial palladium on carbon, (run 3). Adopting the same reaction conditions, commercial palladium on alumina, Pd3 and Pd2 catalysts led to lower yields, 26%, 5% and 3% respectively.

The blank experiment (run 6) again confirms that bare magnetite is inert toward cross-coupling.

Furthermore, the Pd6 catalyst was employed testing diverse reaction conditions such as 1-methyl-1-1pyrrolidone (NMP) as the solvent and K_2CO_3 as the alkaline agent obtaining almost the same yield, (see run 4 and run 5).

Finally, in Figure 4 the kinetic trend of the cross-coupling catalysed by the Pd6 catalyst is reported where it is possible to observe a short induction time in agreement with what is reported in literature[44]. A deactivation of the catalytic system is ascertained when abut 60% of yield is reached probably due to catalytic surface changes. This aspect need further investigation to better understand the catalytic deactivation process.

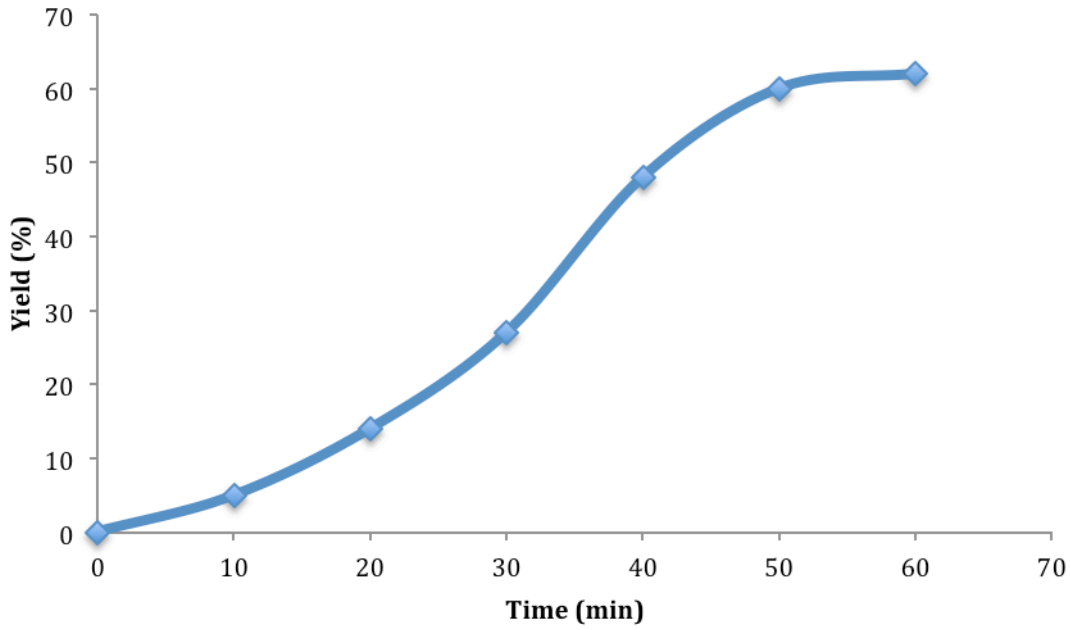

Figure 4 Heck-Mizoroki cross-coupling at 130°C using Pd6

13.4 Cassar-Heck reaction catalysed by magnetic palladium catalyst

Cassar-Heck cross-coupling is commonly named “copper free” Sonogashira and involves aryl halides and terminal alkyne. This reaction is an important industrial tool for the synthesis of alkyl-aryl and diaryl substituted acetylene derivatives. Alkyl-aryl and diaryl substituted acetylene are important building blocks for the synthesis of biological active molecules and natural compounds.[45]

Cassar and Heck were the first to report the synthesis of aryl and vinyl substituted acetylene derivatives using palladium complexes avoiding the presence of copper salts.[46]

Despite the importance of this cross-coupling, the use of heterogeneous catalysis has been poorly investigated: Heidenreich et al. reported the cross-coupling of iodobenzene and phenyl acetylene catalysed by Pd/C in a polar solvent, reaching a conversion of 70% in 30 minutes[20]. Hussain et al. studied the catalytic performance of Nickel nanoparticles supported on graphene for the cross-coupling of diverse aryl halides and phenylacetylenes underlining the good catalytic activity of these systems and their easy and efficient magnetic recovery.[47]

Mori et al.[48] studied the cross-coupling of iodoaromatic compounds and aliphatic alkynes catalysed by Pd/C in a *n*-propanol aqueous solution. Wang et al. showed the cross-coupling of acrylic acid with iodobenzene catalysed by magnetic palladium nanoparticles (Pd@Fe_3O_4) obtaining high yields, about 70% after 6 hours[41]. Navidi et al. showed the cross-coupling of iodobenzene and phenylacetylene catalysed by palladium nanoparticles supported on carbon nanotubes under mild reaction conditions.[49]

Firouzabadi et al.[50] utilized a magnetic palladium catalyst in cross-coupling reactions with yields of 75% .

Given the promising results of the magnetic palladium catalyst, diverse synthetic magnetic palladium systems, (described in chapter 5.1), such as palladium trapped inside magnetite (4.7%Pd@Fe_3O_4 $_{int.}$, Pd6 and 8.8%Pd@Fe_3O_4 $_{int.}$, Pd7), palladium impregnated on commercial magnetite (4.5%Pd@Fe_3O_4, Pd2) and palladium

impregnated on synthetic magnetite (4.3%Pd@Fe_3O_4, Pd3), were employed in the Cassar-Heck cross-coupling of *p*-iodoanisole and phenylacetate adopting the reaction conditions reported in the literature[48] (see Scheme 6).

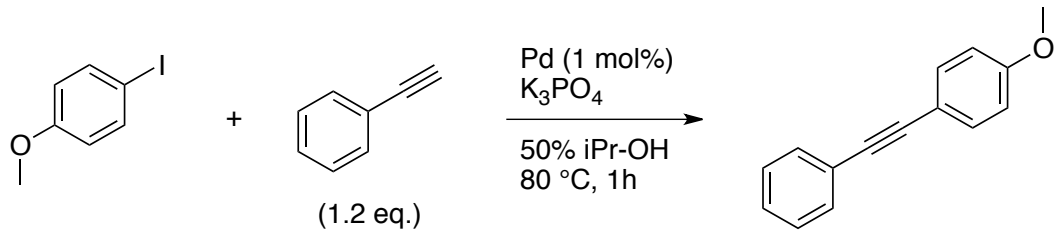

Scheme 6 Cassar-Heck cross-coupling of *p*-iodoanisole and phenylacetate

Their catalytic results together with those obtained employing commercial palladium catalysts, (palladium on carbon (Pd/C 5% Engelhard), palladium on alumina (5%Pd@Al_2O_3 Aldrich)) are summarized in Table 5.

Table 5 Comparison of synthetized magnetic palladium catalysts and commercial ones in the Cassar-Heck cross-coupling of *p*-iodoanisole and phenylacetate

Run	Catalyst	Catalyst load (mol%)	Isolated yield[d]
1	Pd6	0.4	33
2	Pd7	0.4	23
3	Pd6	1	41
4	Pd6	5	40
5[a]	Pd6	1	45
6[b]	Fe_3O_4	***	trace
7	Pd/C	0.4	17
8	Pd/C	1	26
9	Pd@Al_2O_3	1	11
10	Pd2	1	8
11	Pd3	1	***
12	Pd6[c]	1	33

Reaction condition: 1 mol% of palladium catalyst, 1mmol of *p*-iodoanisole, 1.2 mmol of phenylacetylene, 2 mmol of K_3PO_4, 5ml of i-PrOH:H_2O 1:1, 80°C, 1h.

[a] Reaction carried out in DMF using K_2CO_3 as alkaline compound, 100°C, 6h.

[b] Blank reaction carried out with 20 mg of Fe_3O_4.

[c] Catalyst pre-treated under 20 bar of hydrogen at 50°C for 6h.

[d] Yield after the purification of the product

In each reaction the presence of by-products was ascertained but it was no possible to isolate, quantify and identify them.

As it is possible to see in Table 5, by increasing the Pd6 catalyst amount from 0.4 mol % up to 1 mol % the coupling yield increased from 33% to 41%, (run 1 and run 3,

respectively). However, when using more catalyst, 5 mol %, (run 4) yield improvement was not ascertained, confirming that under these reaction conditions 1 % mol of catalyst led to the highest yield.

Run 2 underlines that the palladium magnetic catalyst characterized by a higher palladium loading (8.8 wt.% of Palladium, Pd7) showed lower activity than the catalyst with a lower palladium load Pd6 (run 1), probably due to the worst palladium dispersion on the catalyst surface.

The blank experiment carried out using only magnetite confirmed again that magnetite support is not active toward the cross-coupling reaction.

Under the optimized reaction conditions, 1 % mol of the catalyst, the commercial catalysts (Pd/C and Pd@Al_2O_3) showed lower catalytic activity than the synthetized magnetic palladium Pd6 system (see run 8 and 9). Furthermore, among the diverse synthetic magnetic catalysts (Pd6, Pd2 and Pd3), Pd6, which is characterized by palladium particles trapped inside the magnetite structure, displayed the highest activity leading to a yield of 41%, whereas the Pd2 and Pd3 catalysts (runs 10 and 11), which are characterized by palladium impregnated on commercial magnetite and synthetized magnetite, gave lower yields. The lower catalytic activity of Pd2 and Pd3 catalysts again could be due to their structure, which leads to a lower Fe-Pd interaction. Furthermore it is well known that the particle dimension strongly influences the reaction rate due to a diverse surface energy as reported also by Li et al which studied the effect of palladium nanoparticles diameter on Suzuki reaction rate.[51]

For these reasons the lower catalytic activity of Pd2 and Pd3 catalyst can due to the bigger size of their particles, in fact magnetite particles of Pd2 and Pd3 catalyst show a diameter of 50 nm and 14 nm respectively, and palladium nanoparticles a diameter of 3.7 nm and 2.8 nm, respectively. Instead the Pd6 catalyst, which has a better catalytic performance, is characterized by smaller magnetic particles with diameter of 8 nm.

The best catalytic system, Pd6, was pre-treated under 20 bar of hydrogen at 50°C for 6 h to guarantee the complete reduction of palladium. The pre-reduced catalyst revealed lower catalytic activity than non pre-treated ones, thus underlining that catalytic activity is reduced starting from Pd(0).

Furthermore, the magnetic palladium catalyst Pd6 exhibited a slightly higher conversion using diverse reaction conditions such as dimethylformamide (DMF) as solvent potassium carbonate as an alkaline compound at 100°C for 6 h, (run 5).

Figure 5 illustrates the kinetic trend of the cross-coupling catalysed by the Pd6 catalyst. The reaction induction time is almost absent as observed for the Suzuki-Miyaura cross-coupling. [34]

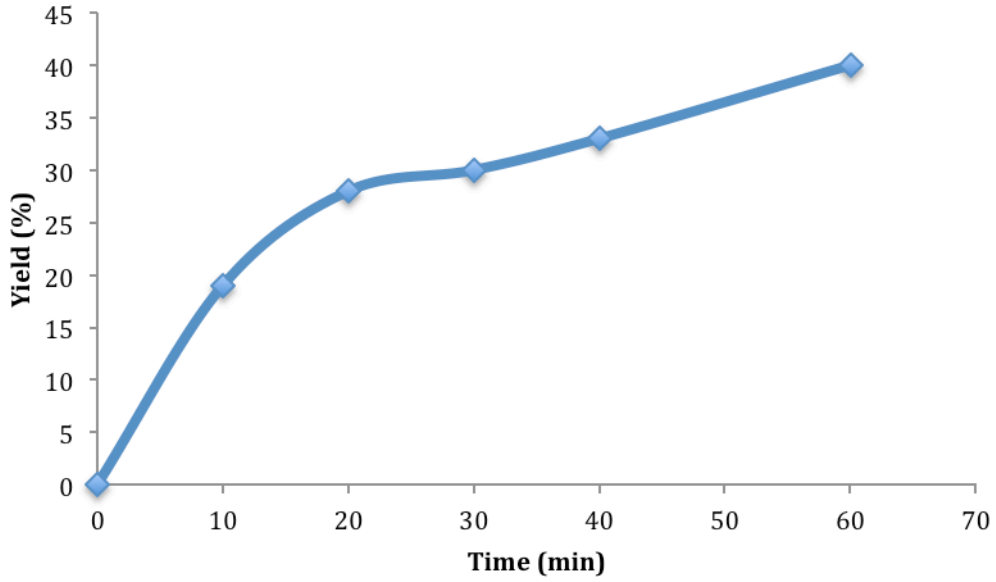

Figure 5 Cassar-Heck cross-coupling of p-iodoanisole and phenylacetate using Pd6 magnetic palladium catalyst

The activity of the Pd6 catalyst was further investigated in recycle tests and the results are reported in Table 6.

Table 6 Recycle tests of Pd6 palladium amgnetic catalyst.

Run	Yield
14	34
1° recycle	28
2° recycle	trace

Reaction condition: 1 mol% of palladium catalyst, 1mmol of p-iodoanisole, 1.2 mmol of phenylacetylene, 2 mmol of K_3PO_4, 5ml of i-PrOH:H_2O 1:1, 80°C, 1h

In the first recycle run, the yield was slightly lower than that observed in the fresh run but after the second recycle the catalyst exhibited no catalytic activity. These results could be due to changes of the catalyst surface or a passivation effects, because not enough leaching was ascertained in order to explain the observed decrease of the activity. In fact, only 2 ppm of free palladium was detected in the reaction mixture by ICP-MS analysis.

13.5 Arylation of N-Methyl-1-*H*-imidazole catalysed by magnetic palladium catalyst

The arylation of imidazole has gained huge industrial interest due to the application of imidazole derivatives in pharmaceutical industries.[52]

Traditionally, this cross-coupling was catalysed by a metal complex and involves numerous reactive steps in which the diverse functional groups of imidazole are protected to drive the arylation on the selected carbon atoms. Recently, direct arylation approaches have been developed using aerobic conditions[53] in presence of copper or organic oxidants[54]. The adopted conditions strongly influence the stereo- and region-selectivity of the arylation, as confirmed by Pvisa-Art et al.[55] who underlined that using copper salt C2 arylation can be preferred instead of C5.

Another interesting approach is reported by Bellina et al. [56] who developed direct C2 arylation of azoles avoiding the presence of ligands and alkaline compounds.

Arylation catalysed by heterogeneous supported catalysts has been poorly investigated. Parisien et al.[57] reported the use of palladium hydroxide supported on carbon as a catalyst for the selective arylation of imidazo-1,2-pyrimidine and thiazole. Lee et al.[58] showed the arylation of the imidazo-1,2-pyrimidine and aryl halogenated compound catalysed by palladium on magnetite obtaining a yield of 85%.

In this context, the magnetic palladium catalysts described in chapter 5.1 were employed in the arylation of N-Me-1*H*-imidazole and *p*-iodoanisole under the reaction conditions reported in the literature (see Scheme 7).[56]

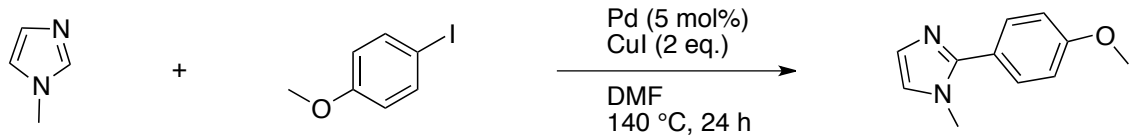

Scheme 7 The arylation of N-Me-1*H*-imidazole and *p*-iodoanisole

The catalytic activity of synthetic palladium catalysts such as palladium trapped inside magnetite (Pd6, 4.7%Pd@Fe_3O_4, and Pd7 8.8%Pd@Fe_3O_4), palladium impregnated on commercial magnetite (4.5%Pd@Fe_3O_4, Pd2), palladium impregnated on synthetic magnetite (4.3%Pd@Fe_3O_4, Pd3) and palladium impregnated on maghemite (2.1%Pd@γFe_2O_3, Pd1) were compared with that of commercial catalysts such as palladium on carbon (5%Pd/C Engelhard) and palladium on alumina (5%Pd@Al_2O_3

Aldrich) The main characteristic of the adopted synthetic palladium catalysts are summarized in Table 7 and their catalytic results are reported in Table 8.

Table 7 Main characteristic of the adopted synthetic catalysts

Catalyst	AAS Pd loading (%)	Surface area (m^2/g)	Core diameter (nm)
Pd1[a] **(Pd@γFe_2O_3)**	2.1	74.42	5.6
Pd2[b] **(Pd@Fe_3O_4)**	4.5	99	50
Pd3[c] **(Pd@Fe_3O_4)**	4.3	112.07	14
Pd6[d] **(Pd@Fe_3O_4)**	4.7	106.48	8
Pd7[e] **(Pd@Fe_3O_4)**	8.8	101.05	N.D

[a] Palladium nanoparticles supported over synthetized maghemite

[b] Palladium nanoparticles supported over reference magnetite

[c] Palladium nanoparticles supported over synthetized magnetite

[d] Synthesis condition: 1g of $Fe(OAc)_2$ 0.05 $Pd(OAc)_2$, 44 mL EtOH 96 wt%, microwave heating: 120°C, 15 min 250W

e Synthesis condition: 1g of $Fe(OAc)_2$ 0.1 $Pd(OAc)_2$, 44 mL EtOH 96 wt%, microwave heating: 120°C, 15 min 250W

Table 8 Comparison of the catalytic performances of synthetized magnetic palladium catalyst and commercial ones

Run	Catalyst	Yield (%)
1	Pd/C	47
2	Pd6	100
3	Pd6[a]	90
4	Pd@Al_2O_3	0
5[b]	Fe_3O_4	0
6	Pd7	22
7	Pd1	69
8	Pd2	0
9	Pd3	51
10	Pd6	100

Reaction condition: 5 mol% of palladium catalyst, 1mmol of N-Me-1*H*-imidazole, 2 mmol of *p*-iodoanisole, 5 ml of DMF, 140°C, 24h

[a] The catalyst was pre-treated under 20 bar of hydrogen at 50°C for 6 h.

[b] Blanck reaction carried out with 100 mg of Fe_3O_4.

Except for run 7 no by-product formation was observed, thus the reaction conversions were very similar to the yields.

The Pd6 catalyst showed surprising catalytic activity leading to a yield of 100%, a value usually reached only with the traditional homogeneous palladium acetate system.[59]

The Pd7 catalyst characterized by a higher palladium loading than Pd6 showed an extremely lower yield due to the worst dispersion of palladium sites on the magnetite surface.

As it is possible to see in Table 8, commercial catalysts (run 1 and run 4) exhibited lower catalytic activity than the synthetized magnetic palladium catalysts. In particular, the commercial palladium on alumina did not show activity in C2 arylation.

The impregnated catalyst Pd1 showed a slightly lower yield compared to the ones obtained using Pd6, and a by-production of chlorine derivate. Unfortunately, the Pd1 catalyst contained traces of chlorine due to the iron precursor used in its preparation, this chlorine was easily released in the reactive mixture leading to the formation of a transhalogenated product observed in run 7. Furthermore, the other impregnated magnetic catalysts Pd2 and Pd3 showed lower activity, probably due to the diverse dispersion of palladium sites on the catalyst surface.

Figure 6 illustrates the kinetic profile of C2 arylation catalysed by the Pd6 catalyst, which shows a longer induction time than that observed in Heck cross-coupling. However, the reaction reached a yield of 100% after 24 h.

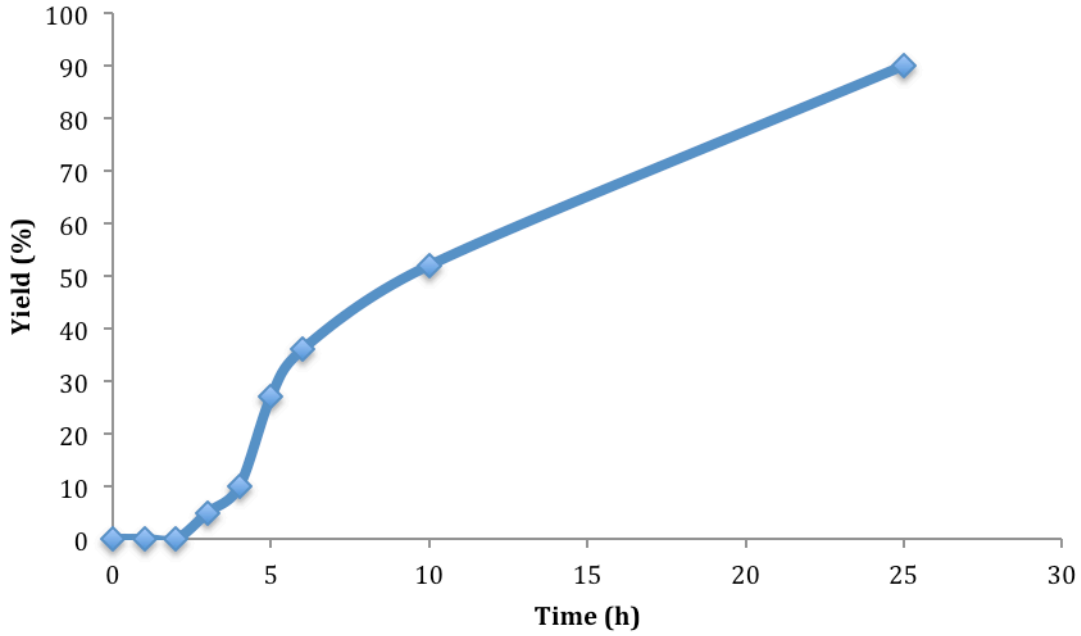

Figure 6 The arylation of N-Me-1*H*-imidazole and *p*-iodoanisole at 140°C using Pd6 catalyst

Due to the above promising results, the Pd6 catalyst was further investigated to verify its recyclability and the results are summarized in Table 9.

Table 9 Recycle tests of Pd6 palladium magnetic catalyst

Run	Catalyst	Yield (%)
11	Pd6	100
1° recycle		2
12	Pd6[a]	91
1° recycle		73
2° recycle		50
3° recycle		0

Reaction condition: 5 mol% of palladium catalyst, 1mmol of N-Me-1H-imidazole, 2 mmol of *p*-iodoanisole, 5 ml of DMF, 140°C, 24h

[a] The catalyst was pre-treated under 20 bar of hydrogen at 50°C for 6 h.

As it is possible to see in Table 9, after the first reaction cycle the yield was drastically reduced, this decrease cannot be explained by the leaching of palladium because no leaching was ascertained by ICP-OES. In fact, after the first reaction cycle only 0.1 ppm of free palladium was detected in the solution. To overcome this deactivation problem the Pd6 catalyst was pre-treated under 20 bar of hydrogen at 50°C for 6 h and employed in the recyclability tests.

The pre-treated catalyst exhibited slightly lower activity and lower deactivation during the recycling test (see run 11 and run 12), but in the 3rd recycle was deactivated. Once again passivation of the surface can be claimed for explaining this behaviour.

13.6 Conclusion

In conclusion, magnetic palladium catalysts can be considered a strategic tool for cross-coupling reactions. In particular, for the Suzuki-Miyaura reaction under the adopted conditions, the magnetic Pd6 catalyst showed high catalytic activity compared to that of commercial palladium on carbon, whereas the impregnated magnetic Pd3 and Pd2 catalysts exhibited extremely low activity. Instead, the Heck-Mizoroki and Cassar-Heck cross-coupling reactions require a larger amount of Pd6 to reach the same yield of commercial palladium on carbon, underlining that the magnetic palladium was less active for this cross-coupling.

Finally, the Pd6 catalyst showed surprisingly higher activity in C2 N-Me-1H imidazole arylation similar to that demonstrated by traditional homogeneous systems. The deactivation of the catalyst is now under investigation.

13.7 References

[1] a) T. Wang and J. A. Love, *Organometallics* **2008**, *27*, 3290-3296; b) T. Wang, B. J. Alfonso and J. A. Love, *Organic Letters* **2007**, *9*, 5629-5631.
[2] a) H. Plenio, *Angewandte Chemie International Edition* **2008**, *47*, 6954-6956; b) F. Monnier and M. Taillefer, *Angewandte Chemie International Edition* **2008**, *47*, 3096-3099.
[3] B. M. Rosen, K. W. Quasdorf, D. A. Wilson, N. Zhang, A.-M. Resmerita, N. K. Garg and V. Percec, *Chemical Reviews* **2011**, *111*, 1346-1416.
[4] a) A. Correa, O. Garcia Mancheno and C. Bolm, *Chemical Society Reviews* **2008**, *37*, 1108-1117; b) R. Jana, T. P. Pathak and M. S. Sigman, *Chemical Reviews* **2011**, *111*, 1417-1492.
[5] a) V. Farina, *Advanced Synthesis & Catalysis* **2004**, *346*, 1553-1582; b) S. Wan, S. R. Wang and W. Lu, *The Journal of Organic Chemistry* **2006**, *71*, 4349-4352; c) M. R. Biscoe, B. P. Fors and S. L. Buchwald, *Journal of the American Chemical Society* **2008**, *130*, 6686-6687; d) T. Ogata and J. F. Hartwig, *Journal of the American Chemical Society* **2008**, *130*, 13848-13849.
[6] J. Tsuji, H. Takahashi and M. Morikawa, *Tetrahedron Letters* **1965**, *6*, 4387-4388.
[7] R. F. Heck, *Journal of the American Chemical Society* **1969**, *91*, 6707-6714.
[8] T. Mizoroki, K. Mori and A. Ozaki, *Bulletin of the Chemical Society of Japan* **1971**, *44*, 581-581.
[9] A. O. King, N. Okukado and E.-i. Negishi, *Journal of the Chemical Society, Chemical Communications* **1977**, 683-684.
[10] N. Miyaura, K. Yamada and A. Suzuki, *Tetrahedron Letters* **1979**, *20*, 3437-3440.
[11] K. Sonogashira, Y. Tohda and N. Hagihara, *Tetrahedron Letters* **1975**, *16*, 4467-4470.
[12] a) P. K. Chakravarty, W. J. Greenlee, N. B. Mantlo, A. A. Patchett and T. F. Walsh in *Substituted imidazo-fused 6-membered heterocycles as angiotensin II antagonists*, *Vol.* Google Patents, **1994**; b) M. L. Belley, S. Leger, M. Labelle, P. Roy, Y. B. Xiang and D. Guay in *Unsaturated hydroxyalkylquinoline acids as leukotriene antagonists*, *Vol.* Google Patents, **1996**.
[13] C. Torborg and M. Beller, *Advanced Synthesis & Catalysis* **2009**, *351*, 3027-3043.
[14] B. Karimi, F. Mansouri and H. M. Mirzaei, *ChemCatChem* **2015**, *7*, 1736-1789.
[15] C. Deraedt, D. Wang, L. Salmon, L. Etienne, C. Labrugère, J. Ruiz and D. Astruc, *ChemCatChem* **2015**, *7*, 303-308.
[16] a) H. Gu, T. Guo, D. W. Hobbs and R. C. Hunter in *Aryl and biaryl compounds having mch modulatory activity*, *Vol.* Google Patents, **2002**; b) P. Diaz and E. Thoreau in *Heterocyclic biaryl compounds and pharmaceutical/cosmetic compositions comprised thereof*, *Vol.* Google Patents, **1999**.
[17] S. Kotha, K. Lahiri and D. Kashinath, *Tetrahedron* **2002**, *58*, 9633-9695.
[18] K.-i. Shimizu, T. Kan-no, T. Kodama, H. Hagiwara and Y. Kitayama, *Tetrahedron Letters* **2002**, *43*, 5653-5655.
[19] G. Marck, A. Villiger and R. Buchecker, *Tetrahedron Letters* **1994**, *35*, 3277-3280.
[20] R. G. Heidenreich, K. Köhler, J. G. E. Krauter and J. Pietsch, *Synlett* **2002**, *2002*, 1118-1122.

[21] G. Zhang, *Synthesis* **2005**, *2005*, 537-542.
[22] C. R. LeBlond, A. T. Andrews, Y. Sun and J. R. Sowa, *Organic Letters* **2001**, *3*, 1555-1557.
[23] P. D. Stevens, J. Fan, H. M. R. Gardimalla, M. Yen and Y. Gao, *Organic Letters* **2005**, *7*, 2085-2088.
[24] T. H. Rehm, A. Bogdan, C. Hofmann, P. Löb, Z. B. Shifrina, D. G. Morgan and L. M. Bronstein, *ACS Applied Materials & Interfaces* **2015**, *7*, 27254-27261.
[25] A. Hajipour and G. Azizi, *Appl. Organomet. Chem.* **2015**, *29*, 247-253.
[26] Z. Yinghuai, S. C. Peng, A. Emi, S. Zhenshun, Monalisa and R. A. Kemp, *Advanced Synthesis & Catalysis* **2007**, *349*, 1917-1922.
[27] M. Gholinejad, M. Seyedhamzeh, M. Razeghi, C. Najera and M. Kompany-Zareh, *ChemCatChem* **2015**, n/a-n/a.
[28] K. K. Senapati, S. Roy, C. Borgohain and P. Phukan, *Journal of Molecular Catalysis A: Chemical* **2012**, *352*, 128-134.
[29] S. Zhou, M. Johnson and J. G. C. Veinot, *Chemical Communications* **2010**, *46*, 2411-2413.
[30] V. Polshettiwar, M. N. Nadagouda and R. S. Varma, *Chemical Communications* **2008**, 6318-6320.
[31] B. Abbas Khakiani, K. Pourshamsian and H. Veisi, *Appl. Organomet. Chem.* **2015**, *29*, 259-265.
[32] U. Laska, C. G. Frost, G. J. Price and P. K. Plucinski, *Journal of Catalysis* **2009**, *268*, 318-328.
[33] a) T. B. D. H. V. L. E. N. T. S. P. Nghia T. Bui, *Chinese Journal of Catalysis* **2011**, *32*, 1667-1676; b) R. Cano, D. J. Ramón and M. Yus, *Tetrahedron* **2011**, *67*, 5432-5436; c) P. Li, L. Wang, L. Zhang and G.-W. Wang, *Advanced Synthesis & Catalysis* **2012**, *354*, 1307-1318.
[34] A. F. Schmidt, A. A. Kurokhtina, A. N. Svechkarev, V. V. Smirnov and A. Al-Halaiqa, *Kinetics and Catalysis* **2010**, *51*, 113-118.
[35] C. C. C. Johansson Seechurn, A. DeAngelis and T. J. Colacot in *CHAPTER 1 Introduction to New Trends in Cross-Coupling*, *Vol.* The Royal Society of Chemistry, **2015**, pp. 1-19.
[36] V. M. Wall, A. Eisenstadt, D. J. Ager and S. A. Laneman, *Platinum Metals Review* **1999**, *43*, 138-144.
[37] R. G. Heidenreich, J. G. E. Krauter, J. Pietsch and K. Köhler, *Journal of Molecular Catalysis A: Chemical* **2002**, *182–183*, 499-509.
[38] K. Köhler, R. G. Heidenreich, J. G. E. Krauter and J. Pietsch, *Chemistry – A European Journal* **2002**, *8*, 622-631.
[39] A. Biffis, M. Zecca and M. Basato, *Journal of Molecular Catalysis A: Chemical* **2001**, *173*, 249-274.
[40] F. Zhao, M. Shirai and M. Arai, *Journal of Molecular Catalysis A: Chemical* **2000**, *154*, 39-44.
[41] Z. Wang, B. Shen, Z. Aihua and N. He, *Chemical Engineering Journal* **2005**, *113*, 27-34.
[42] Q. Du, W. Zhang, H. Ma, J. Zheng, B. Zhou and Y. Li, *Tetrahedron* **2012**, *68*, 3577-3584.
[43] B. Baruwati, D. Guin and S. V. Manorama, *Organic Letters* **2007**, *9*, 5377-5380.
[44] K. Köhler, W. Kleist and S. S. Pröckl, *Inorganic Chemistry* **2007**, *46*, 1876-1883.
[45] a) D. Bonne, M. Dekhane and J. Zhu, *Angewandte Chemie International Edition* **2007**, *46*, 2485-2488; b) J. H. Moon, W. McDaniel, P. MacLean and L. F. Hancock, *Angewandte Chemie International Edition* **2007**, *46*, 8223-8225; c) T. Dutta, K. B.

Woody and M. D. Watson, *Journal of the American Chemical Society* **2008**, *130*, 452-453.
[46] a) L. Cassar, *Journal of Organometallic Chemistry* **1975**, *93*, 253-257; b) H. A. Dieck and F. R. Heck, *Journal of Organometallic Chemistry* **1975**, *93*, 259-263.
[47] N. Hussain, P. Gogoi, P. Khare and M. R. Das, *RSC Advances* **2015**, *5*, 103105-103115.
[48] S. Mori, T. Yanase, S. Aoyagi, Y. Monguchi, T. Maegawa and H. Sajiki, *Chemistry – A European Journal* **2008**, *14*, 6994-6999.
[49] M. Navidi, N. Rezaei and B. Movassagh, **2013**, pp. a008/001-a008/016.
[50] H. Firouzabadi, N. Iranpoor, M. Gholinejad and J. Hoseini, *Advanced Synthesis & Catalysis* **2011**, *353*, 125-132.
[51] Y. Li, E. Boone and M. A. El-Sayed, *Langmuir* **2002**, *18*, 4921-4925.
[52] a) D. J. Sheehan, C. A. Hitchcock and C. M. Sibley, *Clinical Microbiology Reviews* **1999**, *12*, 40-79; b) A. Mital, *Sci Pharm* **2009**, *77*, 497-520; c) A. Walser in *1,2,5-Oxadiazino[5,4-a][1,4]benzodiazepine derivatives*, *Vol.* Google Patents, **1980**.
[53] T. A. Dwight, N. R. Rue, D. Charyk, R. Josselyn and B. DeBoef, *Organic Letters* **2007**, *9*, 3137-3139.
[54] a) D. R. Stuart and K. Fagnou, *Science* **2007**, *316*, 1172-1175; b) K. L. Hull and M. S. Sanford, *Journal of the American Chemical Society* **2007**, *129*, 11904-11905; c) J.-B. Xia and S.-L. You, *Organometallics* **2007**, *26*, 4869-4871.
[55] S. Pivsa-Art, T. Satoh, Y. Kawamura, M. Miura and M. Nomura, *Bulletin of the Chemical Society of Japan* **1998**, *71*, 467-473.
[56] F. Bellina, S. Cauteruccio and R. Rossi, *European Journal of Organic Chemistry* **2006**, *2006*, 1379-1382.
[57] M. Parisien, D. Valette and K. Fagnou, *The Journal of Organic Chemistry* **2005**, *70*, 7578-7584.
[58] J. Lee, J. Chung, S. M. Byun, B. M. Kim and C. Lee, *Tetrahedron* **2013**, *69*, 5660-5664.
[59] B. Liégault, D. Lapointe, L. Caron, A. Vlassova and K. Fagnou, *The Journal of Organic Chemistry* **2009**, *74*, 1826-1834.

14. THE OXIDATION/CONDENSATION OF ETHANOL

14.1 Introduction

Ethanol "chemistry" gained success thanks to the increasing interest in renewable resources and sustainable green processes which permitted the development of bio-ethanol.[1]

Ethanol or bio-ethanol can be considered a versatile platform chemical for diverse valuable compounds such as ethylene, propylene, butadiene or oxygenated products such as acetaldehyde, acetic acid, ethyl acetate, butanol and butyraldehyde. Figure 1 summarizes the most important ethanol derivatives.[2]

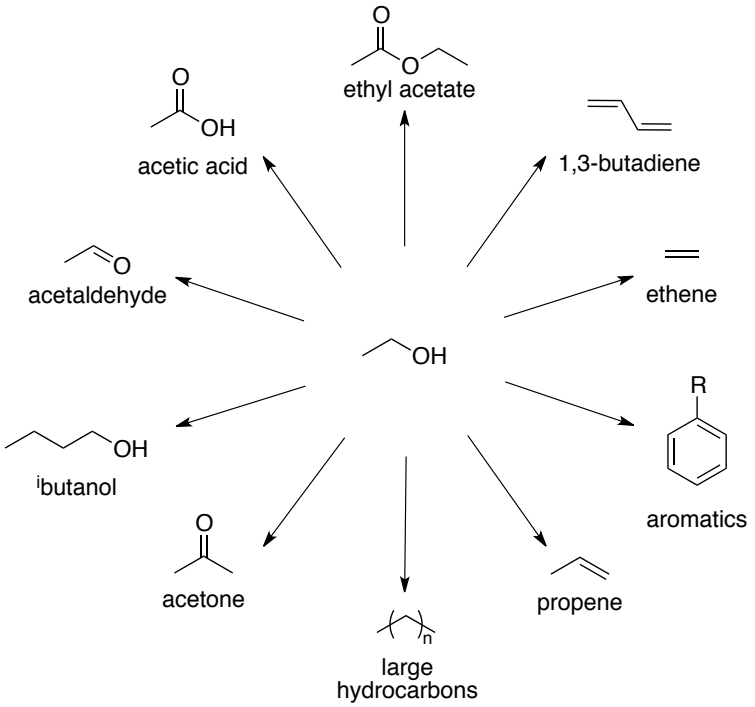

Figure 1 Ethanol derivatives

In particular, the controlled oxidation of ethanol to acetaldehyde, acid acetic and other oxygenated C4 products has huge industrial importance.

Under aerobic conditions, in the presence of a catalyst, ethanol can be oxidized to acetaldehyde, which can be further oxidized to acetic acid or condense with another acetaldehyde molecule leading to the formation of butanol (Guerbet-type reaction), butyradehyde and butadiene (Lebedev process).

Several authors report the catalytic oxidation of ethanol using diverse noble and transition metal catalysts such as Au[3], Cu[4], Pt[5], Pd[6], VO_x[7], Co[8] etc.

For example, Volanti et al.[9] employed copper supported on silica in the gas phase dehydrogenation of ethanol at 225°C-275°C , obtaining 41% of ethanol conversion with 87% of selectivity in acetaldehyde, 5.3% of selectivity in ethyl acetate and other by-products such as methyl ethyl ketone, butanol, crotonaldehyde and ethyl ether. Sato et al.[10] reported the use of copper supported on zirconia in the gas phase dehydrogenation of ethanol at 200°C-275°C leading to high ethyl acetate selectivity. These works underline that catalytic support strongly influences the selectivity of the reaction, in fact when copper was supported on silica the oxidation led to high acetaldehyde production, whereas when copper was supported on zirconia a higher ethyl acetate yield was obtained. The fundamental role of the catalyst support, which determines the selectivity of the oxidation was also confirmed by Takei et al.[11] and Earley et al.[12].

Furthermore the metal load is another key aspect in the ethanol chemistry as reported by Freitas et al. which studied the effect of copper load on the gas phase dehydrogenation of ethanol under diverse temperatures, underling that the highest ethyl acetate yield was obtained with the catalyst with the intermediate copper loading, 20%Cu/ZrO_2.[13]

Other interesting catalytic systems were employed in the oxidation/condensation of ethanol, in particular Gaspar et al.[14] employed palladium on zirconia and alumina as catalysts reaching low ethanol conversion and high selectivity toward acetaldehyde. Zheng et al.[15] described the importance of gold loading on oxidation selectivity underlining that at higher gold loading ethyl acetate selectivity increased.

Furthermore, Idriss et al. observed that different metal oxides such as Fe_3O_4 and Fe_2O_3, permitted to oxidise ethanol to acetaldehyde and ethyl acetate. More in details ethanol oxidation was carried out in a continuous flow reactor with temperature between 130°C and 270°C, underlining a marked difference in the oxidised product distribution between the two adopted iron oxides. In particular magnetite led to the highest acetaldehyde yield (89.3%) whereas maghemite permitted to obtain an acetaldehyde yield of 56.5% and an ethyl acetate yield of 43.5%. [16]

On the other hand, the butanol formation is generally catalysed by alkaline oxides such as MgO[17], CaO, BaO, SiO_2[18], hydroxyapatite[19] and γ-Al_2O_3[20].

Depending on the catalyst and the reaction conditions, ethanol can be activated through different reaction mechanisms. In particular it can be directly converted to butanol through the Guerbet reaction, which is a one pot process where two molecules of ethanol can be directly condensed to 1-butanol, as recently proposed [22].

In an alternative mechanism for the Guerbet reaction, ethanol is oxidized to acetaldehyde, which then condenses with another acetaldehyde molecule finally leading to 1-butanol formation.[21]

Moreover Cavani et al.[22] described an alternative mechanism for the formation of 1-butanol using magnesium oxide as the catalyst in a continuous-flow reactor, at 400°C. More in details, the experimental results were completed by theoretical modelling, which confirmed the formation of an ethanol carbanion, that can react with another ethanol molecule to give 1-butanol, via water elimination.

These studies present the complex context of the possible mechanisms, which are involved in the gas phase ethanol oxidation/condensation.

In this work, the magnetic copper oxide nanocatalysts described in Chapter 5.4 were employed for the gas phase partial oxidation/condensation of ethanol working in the laboratory of Prof. Cavani at the University of Bologna. In particular, the effect of diverse fundamental reaction parameters such as the catalytic support, contact time and temperature were studied.

14.2 Effect of the catalytic support on reaction pathways

The effect of the catalytic support on the reaction pathway was investigated using the copper oxide nanocatalysts synthetized and characterized as described in Chapter 5.4. In particular, the main characteristic of copper oxide nanoparticles supported on magnetite (Cu1 and Cu2) and copper oxide nanoparticles supported on alumina (Cu3) are reported in Table1.

Table 1 Main characteristic of magnetic copper nanocatalysts Cu1, Cu2 and Cu3

Catalysts	Theoretical composition	BET (m^2/g)	Diameter (nm)
Cu1[a]	5%Cu_2O@Fe_3O_4	60.0	6.1
Cu2[b]	5%Cu_2O@Fe_3O_4	56.8	5.5
Cu3[a]	5%Cu_2O@Al_2O_3	154.6	51.5

[a] Obtained using a synthetic copper precursor ($Cu_2(O_2CNEt_2)_4$ • $2NHEt_2$) provided from the Prof. Pampaloni laboratory

[b] Obtained using a commercial copper precursor $Cu(OAc)_2$

All the nanocatalysts above listed were employed in the gas phase oxidation/condensation of ethanol and the results are summarized in Table 2.

A typical oxidation was carried out in a continuous-flow reactor that operated under atmospheric pressure at 180°C. Typically, 0,02-0,2 g of catalyst were loaded as powder form, the residence time [calculated as the ratio between catalyst mass (g) and total gas flow (mL/s)] was 0.1 g s/ml. The inlet feed composition was constant and set at 5% ethanol, 23,8% air and 71,2% nitrogen. Downstream products were fed to an automatic sampling system for GC analysis. This was performed by using an Agilent-7890A instrument equipped with a thermal conductivity detector (TCD).

Table 2 The effect of catalytic support on reaction pathway

Catalyst	Blank	Fe_3O_4	Cu1	Cu2	γ-Al_2O_3	Cu3
EtOH Conv.	3.4	17.0	15.9	11.6	1.9	19.8
Acetaldehyde Yield	1.3	6.8	2.3	3.1	1.1	1.6
Acetone Yield	0.0	0.1	0.0	0.0	0.0	0.0
Ethyl ether Yield	0.0	0.0	0.0	0.0	0.0	0.0
Butyraldehyde Yield	0.0	7.4	10.3	5.2	0.0	0.0
Ethyl acetate Yield	0.0	0.0	0.0	0.0	0.0	0.0
Acetic acid Yield	1.0	0.0	0.2	0.0	0.0	0.0
Ethene Yield	0.0	0.0	0.0	0.0	0.0	0.0
CO Yield	0.0	0.0	0.0	0.0	0.0	0.0
CO2 Yield	0.3	0.9	1.1	0.7	0.2	0.5
Butanol yield	0.0	0.0	trace	0.0	0.0	16.8
unsaturated Yield	***	***	trace	***	***	***

Reaction conditions: Residence time 0.1, Time: 1.5 h, Temperature: 180°C

The blank experiment underlined that without the catalyst, at 180°C, in the presence of air, ethanol was quite stable, as well as in the presence of sole alumina it was not converted to oxidized products.

On the other hand, when using bare magnetite and the copper-based systems, Cu1, Cu2 and Cu3 catalysts under the same reaction conditions, a certain conversion was ascertained. In particular, catalyst Cu1 led to ethanol conversion (15.9%) but high selectivity toward butyraldehyde. The Cu2 catalyst showed a similar catalytic performance, (Ethanol conversion of 11.6%) thus confirming the catalytic behaviour of copper oxide supported on magnetite, (see Figure 2).

Instead, the catalytic support (magnetite) exhibited lower selectivity toward butyraldehyde than the Cu1 and Cu2 catalysts leading to higher acetaldehyde production. These results evidenced that magnetite has a catalytic role in the oxidation/condensation of ethanol but in the absence of copper it is more active in the simple oxidation to acetaldehyde.

This result is in agreement with the literature, in fact at 175°C it was observed that magnetite can selectively oxidize ethanol toward acetaldehyde .[16]

On the other hand, the Cu3 catalyst, characterized by copper oxide supported on alumina, led to a high butanol yield.

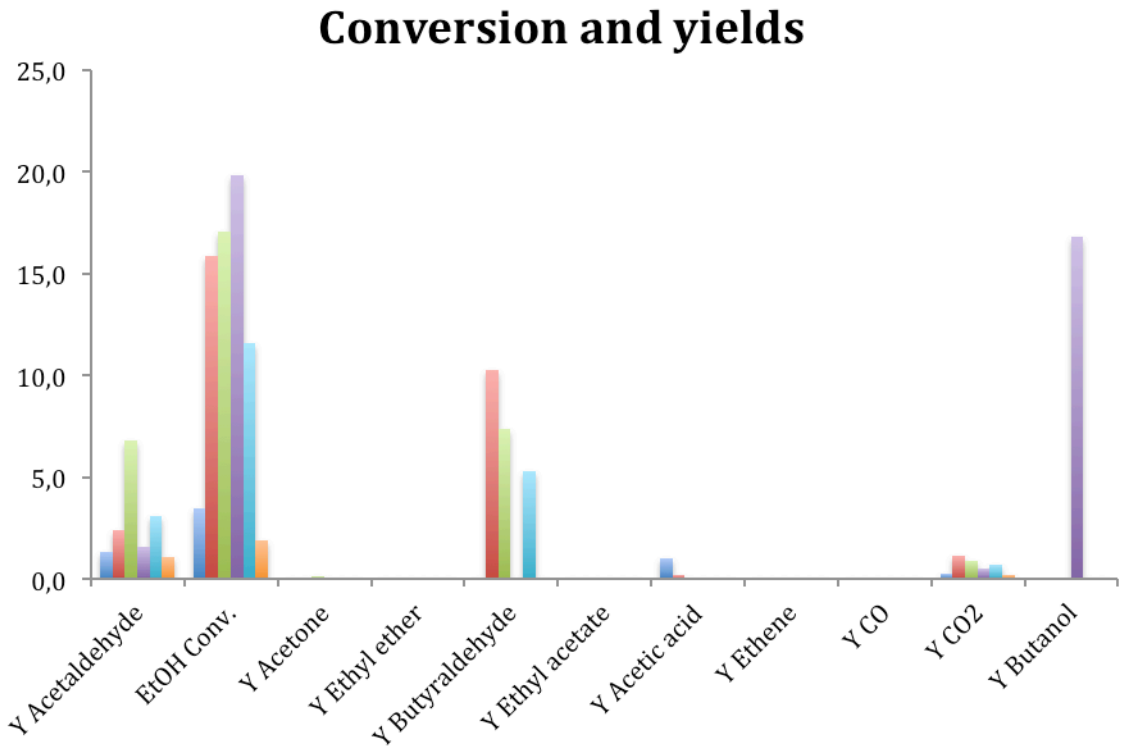

Figure 2 The oxidation of ethanol carried out at 180°C using: a) no catalyst, (blue), b) Cu1 catalyst (red), c) magnetite (green), d) Cu3 catalyst (violet), e) Cu2 catalyst (light blue) and f) alumina (orange).

Alumina and magnetite-supported Cu catalysts seem to drive the oxidation of ethanol with two different mechanisms. In particular, the oxidized product distribution obtained with alumina-supported catalyst Cu3 agrees with the Guerbet mechanism, whereas magnetite-supported catalysts Cu1 and Cu2, seemed to follow another mechanism. More in details, ethanol might be firstly oxidised to acetaldehyde, which can condense with an ethanol molecule to give crotyl alcohol (as in the mechanism leading to butadiene formation), which can be further dehydrated to butadiene or can isomerize to

butyraldehyde, or even dehydrogeate to crotonaldehyde, which might then undergo a MPV reduction to butyraldehyde. The supposed reaction pathway for magnetite-supported catalysts is reported in Scheme 1.

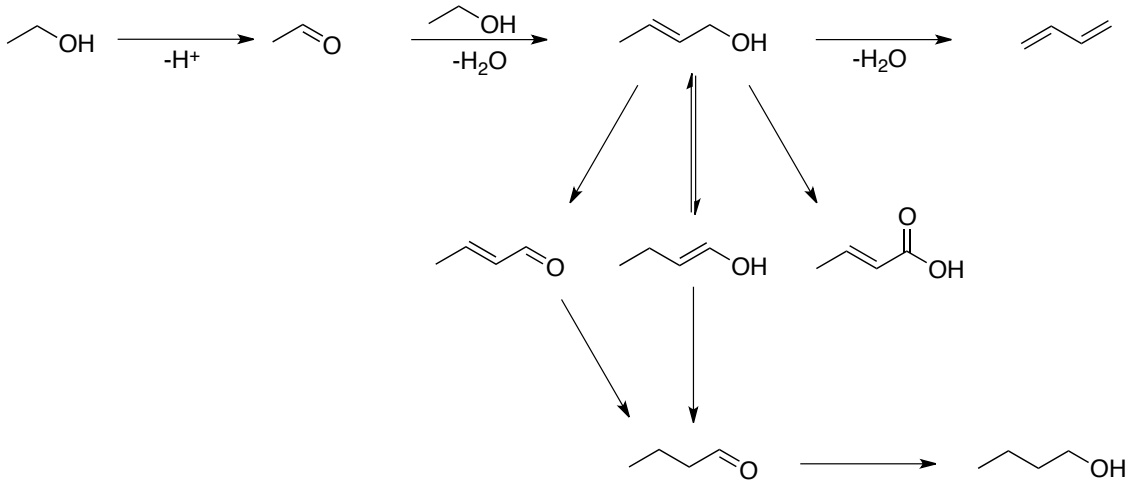

Scheme 1 Possible mechanism for the partial oxidation and condensation of ethanol

In order to confirm the mechanism reported in Scheme 1, oxidation reaction was carried out under the same reaction conditions but feeding as substrate the hypothetical reaction intermediate, crotyl alcohol, instead of ethanol. Under these conditions, crotyl alcohol was converted to 1-butanol, acetic acid and crotonaldehyde, and no formation of butyraldehyde was observed The formation of 1-butanol might occur as shown in Scheme 1, where however crotyl alcohol itself might act as an H-transfer reactant. This result showed that crotyl alcohol cannot be the intermediate of this reaction, thus the magnetite-supported catalyst did not follow the reaction mechanism proposed Scheme 1. For this reason a more direct mechanism was hypothesized. More in detail, an ethanol molecule can be oxidized to acetaldeyde, which forms a carbanion and reacts with another ethanol molecule to give directly butyraldehyde; therefore, this compound would not form from intermediate crotyl alcohol. As reported by Cavani et al. the formation of the acetaldehyde carbanion catalysed by metal oxides has lower energy barrier than that reported for the formation of ethanol carbanion, supporting last direct mechanism (see Scheme 2). [22]

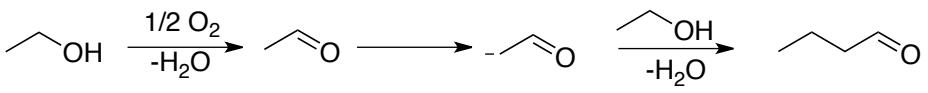

Scheme 2 possible direct mechanism for the oxidation and condesation of ethanol to butyraldehyde

The proposed mechanism is still under investigation in order to understand the catalytic behaviour of magnetic copper nanocatalysts. A new catalytic run, carried out adding acetaldehyde to the feed, will be necessary to confirm this proposed mechanism.

14.3 The effect of the residence time on reaction pathway

The effect of residence time on reaction pathways was studied employing two different catalysts, copper oxide supported on magnetite, Cu1, and copper oxide supported on alumina, Cu3.

Table 2 summarizes the catalytic results obtained with Cu1 catalyst working at diverse residence times.

Table 2 Effect of residence time on reaction pathway, using copper oxide supported on magnetite Cu1

τ (g s/ml)	EtOH Conv.	Acetaldehyde Yield	Acetone Yield	Ethyl ether Yield	Butyraldehyde Yield	Ethyl acetate Yield	Acetic acid Yield	Ethene Yield	CO Yield	CO_2 Yield	Butanol yield
0	3,4	1,3	0,0	0,0	0,0	0,0	0,0	0,0	0,0	0,3	0,0
0,02	5,0	1,6	0,0	0,0	1,8	0,0	0,0	0,0	0,0	0,2	0,0
0,05	8,9	1,5	0,0	0,0	3,4	0,0	0,0	0,0	0,0	0,2	0,0
0,1	15,9	2,3	0,0	0,0	10,3	0,0	0,2	0,0	0,0	0,4	0,0
0,2	20,6	0,7	0,0	0,0	11,8	0,0	1,4	0,0	0,0	0,2	2,7

Reaction conditions: Residence time 0.1, Time: 1.5 h, Temperature: 180°C

When the residence time was increased, ethanol conversion and the butyraldehyde yield increased whereas the acetaldehyde yield decreased. This behaviour confirms that ethanol was first oxidized to acetaldehyde, which then reacted with ethanol to give butyraldehyde (see Figure 3). The consecutive transformation of butyraldehyde to butanol occurs via the H-transfer from ethanol (MPV reaction). It is also interesting to see that these tests clearly showed that the formation of 1-butanol is consecutive to butyraldehyde, which is the opposite of what is generally proposed in the conventional Guerbet mechanism.

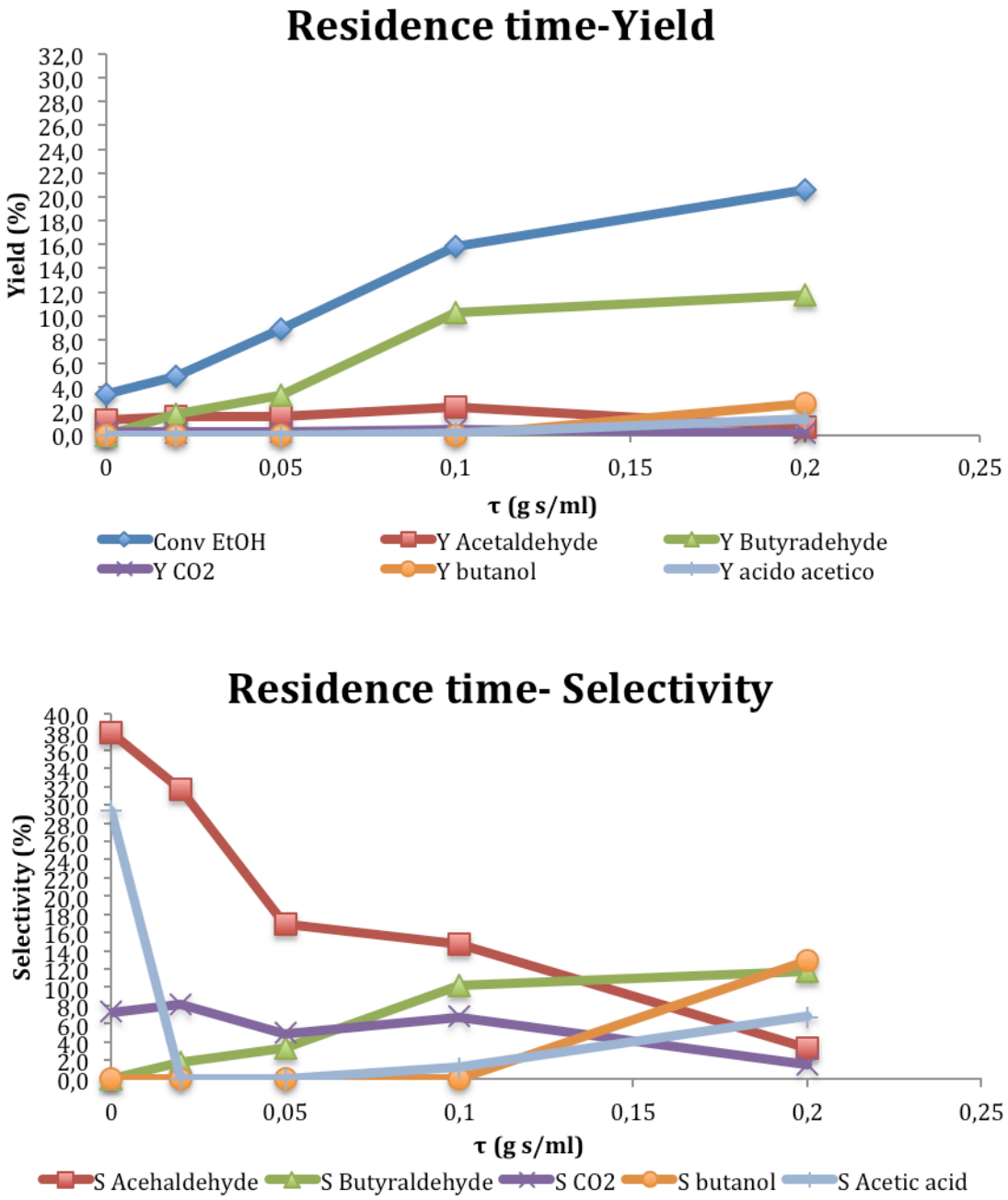

Figure 3 Yield and selectivity trend of the diverse oxidized product with contact time

Table 3 reports the catalytic results of the Cu3 catalyst at diverse residence times.

Table 3 Effect of residence time on reaction pathway, using copper oxide supported on alumina Cu3

τ	EtOH Conv.	Acetaldehyde Yield	Acetone Yield	Ethyl ether Yield	Butyraldehyde Yield	Ethyl acetate Yield	Acetic acid Yield	Ethene Yield	CO Yield	CO_2 Yield	Butanol yield
0	3,4	1,3	0,0	0,0	0,0	0,0	0,0	0,0	0,0	0,3	0,0
0,02	12,3	0,5	0,0	0,0	0,0	0,0	0,0	0,0	0,0	1,1	7,8
0,05	19,4	0,6	0,0	0,0	0,0	0,0	0,0	0,0	0,0	1,1	16,3

0,1	19,8	1,6	0,0	0,0	0,0	0,0	0,0	0,0	0,0	0,5	16,8
0,2	21,5	2,0	0,0	0,0	0,0	0,1	0,0	0,0	0,0	0,4	18,3

Reaction conditions: Residence time 0.1, Time: 1.5 h, Temperature: 180°C

When the residence time was increased, ethanol conversion and butanol yield increased, in agreement with the results reported in the literature for analogous catalytic systems.[23] However, it is also important to notice that the catalyst used is very selective to 1-butanol, which is not so common for the gas-phase Guerbet reaction. This means that according to the mechanism recently proposed [22], ethanol immediately reacts with another molecule of ethanol yielding 1-butanol, with water elimination; this reaction is faster than ethanol dehydrogenation to acetaldehyde. An alternative explanation is that acetaldehyde (the primary product according to results shown in Figure 4) reacts with either ethanol (to yield crotyl alcohol, which is then rapidly reduced to butanol via MPV reaction) or acetaldehyde, via a classical Guerbet mechanism.

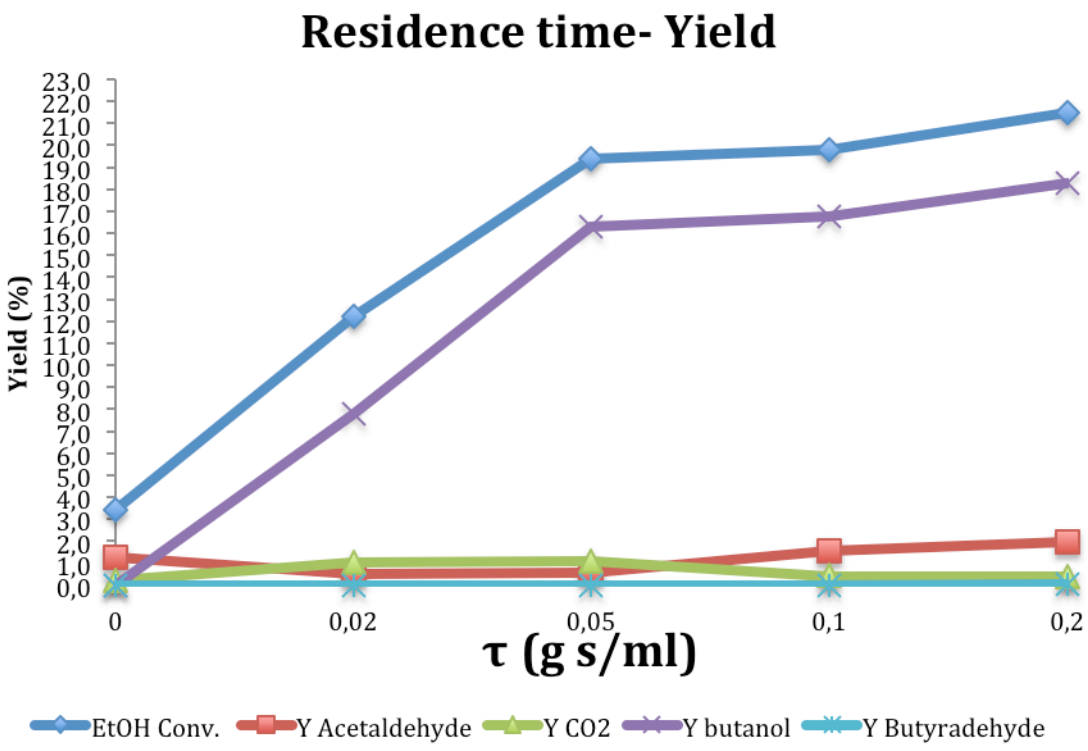

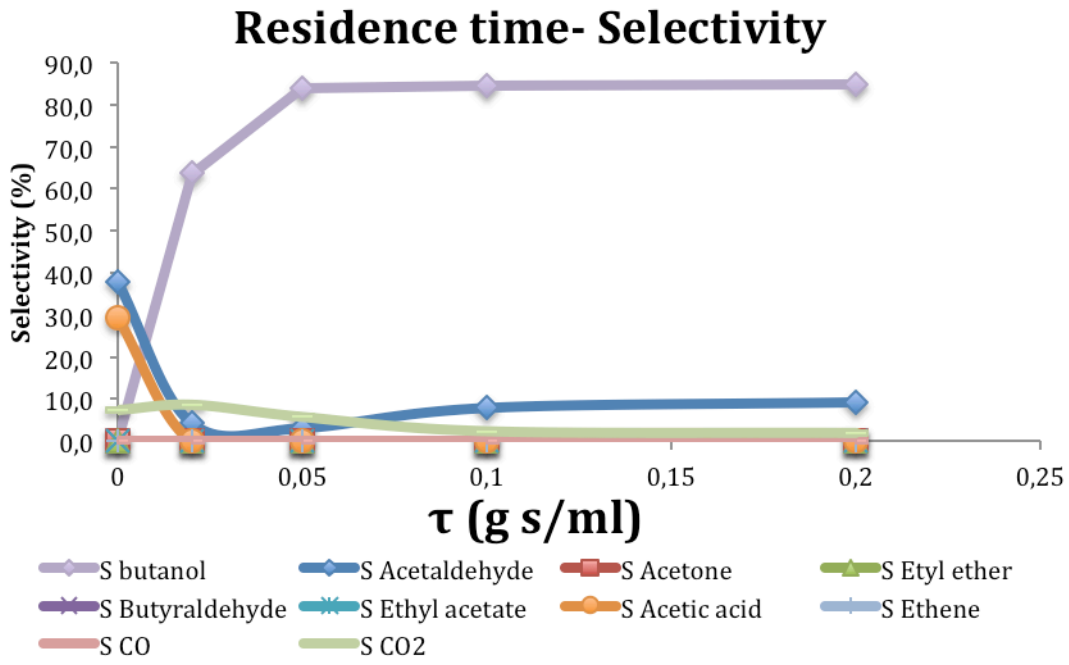

Figure 4 Yield and selectivity trend of the diverse oxidized products at different contact times

Both Cu1 and Cu3 catalysts were deactivated after 1.5 h of reaction. Deactivation can be due to the leaching of copper oxide or to the complete reduction of copper species as confirmed by the Raman spectra, which showed no copper oxide peaks. Furthermore, in order to regenerate the used catalyst, the Cu1 catalyst was treated under oxygen flow for 1 h at 180°C. Unfortunately, this regeneration procedure resulted inefficient because the treated Cu1 did not show any catalytic activity.

14.4 The effect of the temperature on the reaction products

The effect of temperature on reaction products was studied by using the most promising catalyst, copper oxide supported on magnetite (Cu1) and the results are reported in Table 4.

Table 4 Effect of temperature on oxydation product using Cu1 catalyst

T (°C)	EtOH Conv.	Acetaldehyde Yield	Acetone Yield	Ethyl ether Yield	Butyraldehyde Yield	Ethyl acetate Yield	Acetic acid Yield	Ethene Yield	CO Yield	CO_2 Yield	Butanol yield
180	15,9	2,3	0,0	0,0	10,3	0,0	0,2	0,0	0,0	0,4	0,0
220	74,9	26,1	0,3	0,0	5,7	0,0	0,8	0,5	3,6	38,3	0,0

When the temperature was increased from 180°C to 220°C, complete oxidation of ethanol resulted to be preferred as evidenced by the higher CO_2 yield.

As can be seen in Figure 5, at higher temperatures the butyraldehyde yield decreased due to the preferred combustion reaction.

Generally, gas phase reactions are carried out at higher temperatures but due to the degradation and combustion problems observed it is important to work at a low temperature (180°C).

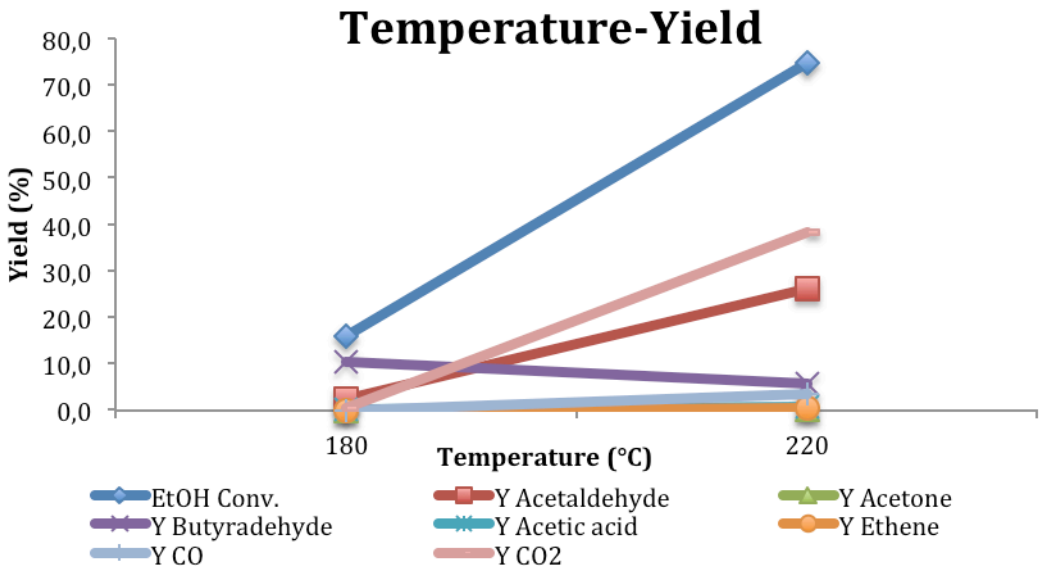

Figure 5 Effect of temperature on product yields

14.5 Conclusion

The gas phase oxidation/condensation of ethanol carried out with copper oxide supported on alumina (Cu3) led to a high butanol yield in agreement with the Guerbet mechanism. On the other hand, copper oxide supported on magnetite (Cu1 and Cu2) exhibited a peculiar catalytic activity leading to the selective formation of butyraldehyde.

Magnetite-supported catalysts seemed to follow an original reaction pathway, in which an ethanol molecule is first oxidized to acetaldehyde, and then condensed with another ethanol molecule to give butyraldehyde. This last mechanism will be further investigated to better understand the interesting catalytic behaviour of these novel magnetic copper nanocatalysts.

14.6 References

[1] J. V. Ochoa and F. Cavani in *CHAPTER 8 Gas-Phase Oxidation of Alcohols: Innovation in Industrial Technologies and Recent Developments*, *Vol.* The Royal Society of Chemistry, **2015**, pp. 203-230.
[2] J. M. R. Gallo, J. M. C. Bueno and U. Schuchardt, *Journal of the Brazilian Chemical Society* **2014**, *25*, 2229-2243.
[3] C. H. Christensen, B. Jørgensen, J. Rass-Hansen, K. Egeblad, R. Madsen, S. K. Klitgaard, S. M. Hansen, M. R. Hansen, H. C. Andersen and A. Riisager, *Angewandte Chemie International Edition* **2006**, *45*, 4648-4651.
[4] S.-i. Fujita, N. Iwasa, H. Tani, W. Nomura, M. Arai and N. Takezawa, *Reaction Kinetics and Catalysis Letters* **2001**, *73*, 367-372.
[5] L. V. Mattos and F. B. Noronha, *Journal of Power Sources* **2005**, *145*, 10-15.
[6] M. C. Greca, C. Moraes and A. M. Segadães, *Applied Catalysis A: General* **2001**, *216*, 267-276.
[7] a) Y.-C. Lin, C.-H. Chang, C.-C. Chen, J.-M. Jehng and S.-G. Shyu, *Catalysis Communications* **2008**, *9*, 675-679; b) E. Santacesaria, A. Sorrentino, R. Tesser, M. Di Serio and A. Ruggiero, *Journal of Molecular Catalysis A: Chemical* **2003**, *204–205*, 617-627.
[8] L. V. Mattos and F. B. Noronha, *Journal of Power Sources* **2005**, *152*, 50-59.
[9] D. P. Volanti, A. G. Sato, M. O. Orlandi, J. M. C. Bueno, E. Longo and J. Andrés, *ChemCatChem* **2011**, *3*, 839-843.
[10] A. G. Sato, D. P. Volanti, I. C. de Freitas, E. Longo and J. M. C. Bueno, *Catalysis Communications* **2012**, *26*, 122-126.
[11] T. Takei, N. Iguchi and M. Haruta, *New Journal of Chemistry* **2011**, *35*, 2227-2233.
[12] J. H. Earley, R. A. Bourne, M. J. Watson and M. Poliakoff, *Green Chemistry* **2015**, *17*, 3018-3025.
[13] I. C. Freitas, S. Damyanova, D. C. Oliveira, C. M. P. Marques and J. M. C. Bueno, *Journal of Molecular Catalysis A: Chemical* **2014**, *381*, 26-37.
[14] A. B. Gaspar, F. G. Barbosa, S. Letichevsky and L. G. Appel, *Applied Catalysis A: General* **2010**, *380*, 113-117.
[15] N. Zheng and G. D. Stucky, *Journal of the American Chemical Society* **2006**, *128*, 14278-14280.
[16] H. Idriss and E. G. Seebauer, *Journal of Molecular Catalysis A: Chemical* **2000**, *152*, 201-212.
[17] C. Yang and Z. Y. Meng, *Journal of Catalysis* **1993**, *142*, 37-44.
[18] V. I. Sobolev, O. A. Simakova and K. Y. Koltunov, *ChemCatChem* **2011**, *3*, 1422-1425.
[19] S. Ogo, A. Onda, Y. Iwasa, K. Hara, A. Fukuoka and K. Yanagisawa, *Journal of Catalysis* **2012**, *296*, 24-30.
[20] D. L. Carvalho, R. R. de Avillez, M. T. Rodrigues, L. E. P. Borges and L. G. Appel, *Applied Catalysis A: General* **2012**, *415–416*, 96-100.
[21] a) Z. Wang in *Guerbet Condensation*, *Vol.* John Wiley & Sons, Inc., **2010**; b) C. Angelici, B. M. Weckhuysen and P. C. A. Bruijnincx, *ChemSusChem* **2013**, *6*, 1595-1614.
[22] A. Chieregato, J. Velasquez Ochoa, C. Bandinelli, G. Fornasari, F. Cavani and M. Mella, *ChemSusChem* **2015**, *8*, 377-388.

[23] A.-M. Hilmen, M. Xu, M. J. L. Gines and E. Iglesia, *Applied Catalysis A: General* **1998**, *169*, 355-372.

15. THE SELECTIVE HYDROGENATION OF 1-CHLORONITROBENZENE TO 1-CHLOROANILINE

15.1 Introduction

Hydrogenation of nitrohaloaromatics to aromatic haloamines is an important industrial reaction for the synthesis of many fine chemicals such as pharmaceuticals, herbicides[1], pesticides[2] and polymers[3]. In particular, the selective hydrogenation of *p*-chloronitrobenzene (pCNB) to *p*-chloroaniline (pCAN) has been studied over a variety of supported catalysts but carbon nanostructures have not received much attention.

The hydrogenation of pCNB to pCAN follows a multistep reaction pathway (see Scheme 1). The main side reaction is hydrodechlorination, which leads to aniline (AN) as the ultimate product. Undesired dehalogenation can also happen with pCNB leading to nitrobenzene (NB) followed by the subsequent hydrogenation to AN or by hydrodechlorination of pCAN to AN.

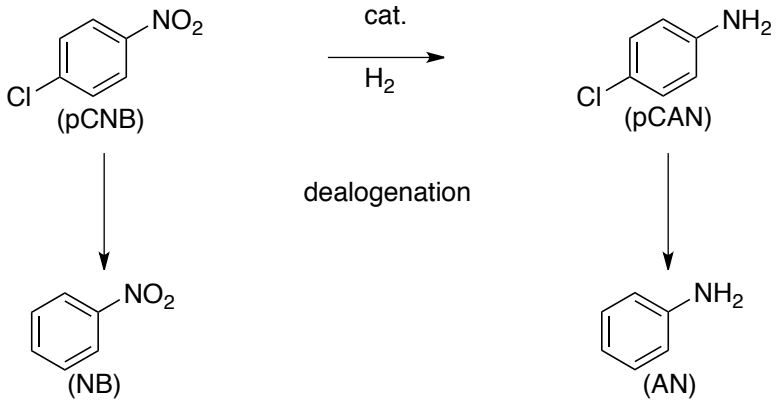

Scheme 1 p-chloronitrobenzene hydrogenation scheme

In this work, the ruthenium carbon nanocatalysts described in Chapter 8 were employed for the selective hydrogenation of pCNB to pCAN. In particular, the influence of different parameters such as the nature of the carbon supports, catalyst pre-treatment and the choice of the solvents on the yield and the selectivity of the hydrogenation were studied.

15.2 The effect of temperature on the hydrogenation of pCNB

The effect of temperature on the reaction yield was studied using diverse ruthenium carbon catalysts.

In particular, ruthenium and/or magnetite nanoparticles supported on a multi-walled carbon nanotube (CNT) and graphene oxide (GO) were employed in the selective hydrogenation of pCNB to pCAN.

All the catalysts were pre-activated before the hydrogenation experiments, and they were treated in an autoclave equipped with mechanical stirring at 110°C under 30 bar of H_2 for 1h. A typical hydrogenation run was carried out under 30 bar of hydrogen, using 0,4 g of pCNB, 36 mg of catalyst and 50 ml of Methanol. The reactions were followed using a gas chromatography (Perkin-Elmer Clarus 500 equipped with a stabilwax DA capillary column and a FID detector) using the program: 80°C for 3 minutes followed by a ramp of 35°C/min until 225 and a hold time of 10 minutes.

Table 1 Selective hydrogenation of pCNB to pCAN, Hydrogen pressure 30 bar, V MeOH 50 ml, M pCNB 0,4 g, M catalysts 36 mg, reaction time 6h.

Run	T (°C)	Catalyst	Ru load (wt.%)	Conversion (%)	pCAN Yield (%)	A (mol /g h)	TOF (h-1)
5	60	Ru@CNT	1,5	20	20	0,12	12,2
6	60	Ru@GO	0,77	18	18	0,10	10,6
7	60	Ru@(Fe_3O_4-CNT)	1,13	24	24	0,14	14,1
8	60	Ru@(Fe_3O_4-GO)	0,58	67	30	0,18	18,1
9	80	Ru@CNT	1,5	88	88	0,51	51,3
10	80	Ru@GO	0,77	86	86	0,50	50,5
11	80	Ru@(Fe_3O_4-CNT)	1,13	84	84	0,49	49,7
12	80	Ru@(Fe_3O_4-GO)	0,58	79	79	0,46	46,8

When the temperature increased from 60°C to 80°C, it was possible to improve the activity of the catalysts as illustrated in Table 5. However, in order to optimize the reaction conditions while focusing our attention on security and sustainability of the entire process, we decided to change other parameters maintaining a low temperature.

A TEM analysis of the catalysts after the hydrogenation experiments showed an increase of the metal particles size, for example, the ruthenium nanoparticles of spent Ru@GO had an average diameter of 3.07 nm and the ones of fresh Ru@GO had an average diameter of 2.59 nm.

15.3 The effect of solvent on hydrogenation of pCNB

The effect of solvents in the hydrogenation of pCNB to pCAN over three different catalytic systems was studied. For this purpose ethanol (EtOH), methanol (MeOH), tetrahydrofuran (THF), water (H_2O) and an ethanol/water solution were considered as possible reaction media. The experiments were carried out using the condition and the equipment described above.

The three different catalytic systems selected for this study were Ru@(Fe_3O_4-GO) HT, Ru-(Fe_3O_4/CNT) HT described in Chapter 8 and ruthenium supported on fullerene Ru/C_{60} (CFL68). Figure 1 shows the TOF trends of these three catalysts in the diverse solvents at 60°C.

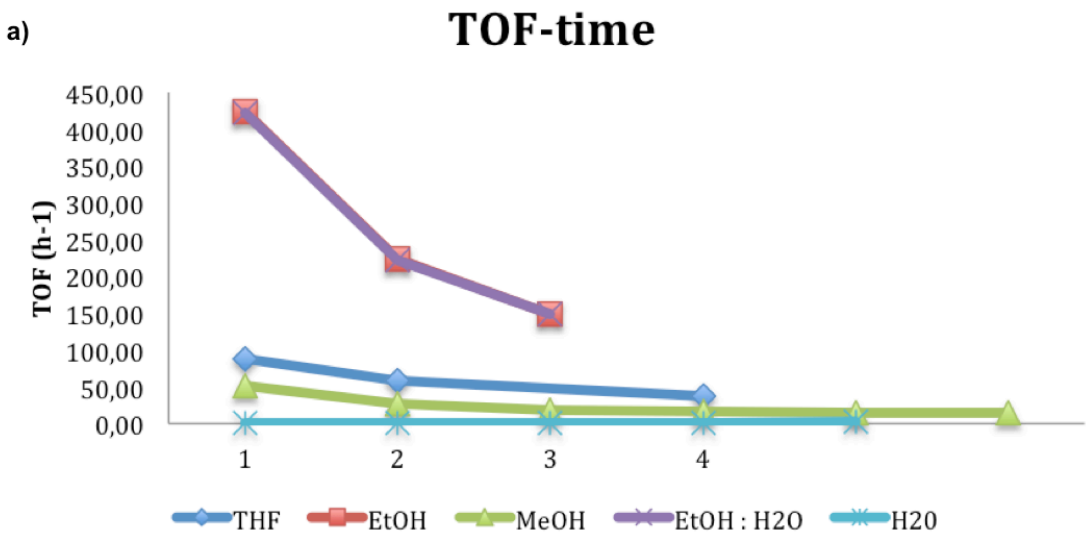

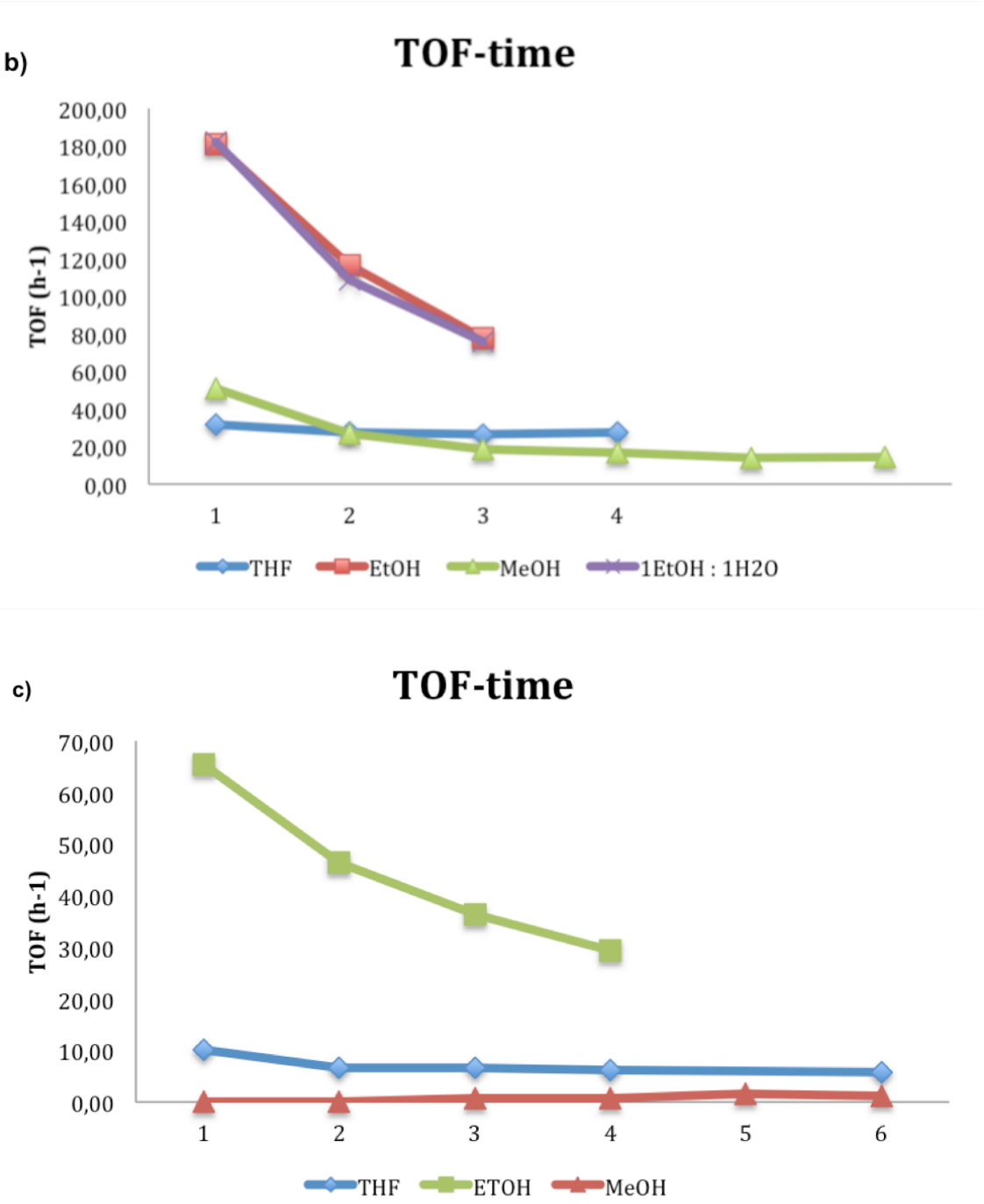

Figure 1 Turnover frequency curve for the hydrogenation of pCNB to pCAN in different solvents using the catalysts: a) 2%Ru-(30%Fe_3O_4-GO) HT, b) 2%Ru-(30%Fe_3O_4-CNT) HT and c) CFL68

As it is possible to observe from the TOF curve reported in Figure 1, ethanol gave the best results and THF the worst ones with each catalytic systems. This trend could be explained by the different solubility of reagent and product and the diverse dispersion degree of these catalysts in the selected solvents. Good dispersion of the catalyst is fundamental in the heterogeneous process because it can partially solve the

transportation, adsorption, desorption problems connected with heterogeneous catalysis, thus increasing the reaction rate. Furthermore, the fact that pCNB and pCAN are soluble in ethanol, methanol and THF but not in water must be taken into consideration. It is important to underline that the pre-treated Ru@(Fe_3O_4-GO) and Ru@(30%Fe_3O_4-CNT) were also used in a water/ethanol 50:50 mixture leading to the same yield obtained in pure ethanol. These last results are particularly interesting because they underline the possibility of employing a safer and cheaper aqueous bio-ethanol, avoiding the expensive distillation of industrial ethanol.

15.4 The effect of catalytic support on hydrogenation of pCNB

The effect of different catalytic supports on the hydrogenation rate was studied using the optimized condition (60°C and ethanol as solvent). All the catalysts were pre-activated before the hydrogenation experiment, and the hydrogenation run was carried out in a steel autoclave equipped with mechanical stirring at 60°C and 30 bar of hydrogen, using 0,4 g of pCNB, 100 mg of catalyst and 50 ml of ethanol.
Table 2 summarizes the catalytic results of the diverse ruthenium catalytic systems.

Table 2 Selective hydrogenation of pCNB to pCAN at 60°C, Hydrogen pressure 30 bar, V (ml) EtOH, M (g) pCNB 0,4, M(mg) catalysts 100.

Run	Catalyst	Ru load (wt.%)	t (h)	pCNB Conv. (%)	pCAN Yield (%)	pCAN Sel. (%)	A (mol/ g h) at 1h	TOF (h^{-1}) at 1h
17	Ru@CNT	1,5	5	100	100	100	1	73
18	Ru@GO	0,77	3	100	96	97	2,8	286
19	Ru@(Fe_3O_4-CNT)	1,13	4	100	98	98	1,2	124
20	Ru@(Fe_3O_4-GO)	0,58	3	100	94	94	3,2	328
26	Fe_3O_4@GO	0	6	38	38	100	***	***
27	Fe_3O_4@CNT	0	6	49	49	100	***	***
30	CFL66	0,99	6	67	67	100	0,6	62,2
31	CFL67	1,60	6	99	99	100	0,7	67,8
32	CFL68	2,19	4	100	100	100	0,6	65,5
33	CFL 72	0,45	6	45	45	100	1,2	117,1
40	Ru@Nd	0.33	5	41	41	100	1.8	185.1
41	Ru@NCNT	0.91	3	100	100	100	1.9	190.2
42	Ru@CNT	1.4	6	100	100	100	0.8	76.4

43	Ru@(Fe_3O_4-Nd)	0.55	6	52	52	100	0.8	83.7
44	Ru@(Fe_3O_4-NCNT)	1.03	6	88	88	100	0.8	84.8
45	Fe3O4@Nd	0	6	48	48	100	***	***
46	Fe3O4@NCNT	0	6	45	45	100	***	***

As a general trend we observe that GO supported catalysts are more active than others, maybe because the shape and the electrochemical properties of the carbon nanostructured support plays an important role during the reaction. In particular, the Ru@GO catalyst which displayed a lower ruthenium loading and larger nanoparticles than Ru@CNT, Ru@NCNT and Ru@Nd, provided the highest turnover frequency, 286 h^{-1}.

Generally, smaller metal nanoparticles show higher catalytic activity because of the increase in exposed metal surface, in contrast to this case where Ru@GO, which is characterized by larger nanoparticles, exhibits higher catalytic activity, 2.8 mol/g h.

This result highlights that the role of the support is more important than the size of the nanoparticles in the catalytic performance of nanocatalysts, which confirms that the environment of ruthenium nanoparticles on graphene oxide is different to that of CNT, NCNT or Nd as described in Chapter 8.

Ru-NCNT showed a bigger conversion than Ru-CNT, probably due to the N functional group on its surface that helped a better anchoring of the ruthenium nanoparticles.

The importance of the support on the catalytic hydrogenation of pCNB to pCAN has already been underlined by Blaser et al[4].

Furthermore, the influence of the diverse catalytic supports on this hydrogenation has been reported in the literature, for example Oubenali et al.[5] studied the effect of carbon nanofiber and carbon nanotube on the catalytic performance of ruthenium nanoparticles. Tijani et al.[6], instead, described the effect of alumina support on ruthenium catalytic activity.

Particle size effect, particle proximity and spatial distribution, which are crucial parameters that may influence catalytic activity[7] and stability[8], cannot be undervalued in the case of GO supported catalysts; that have a lower surface area (about 60 m^2/g) than the CNT supported ones (about 280 m^2/g). The lower surface area of GO leads to an higher nanoparticle density.

Other important effects of the supports are the charge transfers from the metal and the carbon support as reported by Gao et al.[9] and the different polarity of the support due to the functional groups.[10]

The magnetic bimetallic supported systems, characterized by magnetite and ruthenium nanoparticles anchored on the surface of the diverse carbon nanosupports showed the same tendency in the monomometallic ruthenium catalysts, except Ru@Fe_3O_4-NCNT which showed a lower turnover frequency than Ru@NCNT.

The introduction of magnetite not only helped the recovery and recyclability of the ruthenium catalyst but also showed a positive effect of the catalytic performance as observed by the results reported in Table 2.

The blank experiment carried out using only magnetite confirmed that magnetite presents some activity, thus the increased activity observed for bimetallic ruthenium/magnetite systems compared to the results of ruthenium-supported catalysts could be due to the magnetite contribution.

15.5 The Effect of catalyst pre-treatment the hydrogenation of pCNB

The effect of pre-treatment on ruthenium carbon nanocatalysts was investigated, in particular GO and CNT systems were pre-treated in a horizontal oven at 600°C for 2 h under an argon flow of 10 ml/min. The heat treatment enabled us to decompose the excess of functional groups and gave a closer contact between active catalytic sites and reagents leading to more active catalysts. As it is possible to see in Table 5, the activity and TOF of pre-treated catalysts are higher than the non-pre-treated ones.

Table 3 Selective hydrogenation of pCNB to pCAN at 60°C, Hydrogen pressure 30 bar, V (ml) EtOH, M (g) pCNB 0,4, M(mg) catalysts 100 over catalysts pre-treated and not pre-treated

Run	Catalyst	Ru load (%)	t (h)	Conv. (%)	Yield pCAN (%)	Sel. pCAN (%)	A (mol/g h) at 1h	TOF (h-1) at 1h
17	Ru@CNT	1,5	5	100	100	100	1	73
18	Ru@GO	0,77	3	100	96	97	2,8	286
19	Ru@(Fe_3O_4-CNT)	1,13	4	100	98	98	1,2	124
20	Ru@(Fe_3O_4-GO)	0,58	3	100	94	94	3,2	328
21	Ru@CNT ^{HT}	1,5	2	100	98	98	1,5	152

22	Ru@GO ^{HT}	0,77	1	100	100	100	3,3	334
23	Ru@(Fe_3O_4-CNT) ^{HT}	1,13	2	100	97	97	1,8	181
24	Ru@(Fe_3O_4-GO) ^{HT}	0,58	2	100	96	96	4,2	423,2
26	Fe_3O_4@GO	0	6	38	38	100	***	***
27	Fe_3O_4@CNT	0	6	49	49	100	***	***
28	Fe_3O_4@CNT ^{HT}	0	6	26	26	100	***	***
29	Fe_3O_4@GO ^{HT}	0	6	27	27	100	***	***

^{HT} pre-treated catalysts

Heat pre-treatment removes excess functional groups improving the contact between reagents and catalytic sites. The positive effect of thermal treatment was reported in the literature in the hydrogenation of diverse aromatic substrates.[10-11]

Moreover, the literature reports a model in which hydrogenation is assisted by the adsorption of the reagent on the carbon support after the removal of excess functional groups.[11c]

This increase was more evident for CNT supported catalysts than for GO nanocatalysts, in particular, pre-treated Ru-CNT was twice as active as non-pre-treated ones. This difference could be due to the higher surface area of CNT, which allows more reagents to be adsorbed than GO after the pre-treatment.

The best catalytic results were obtained with pre-treated Ru-(Fe_3O_4/GO) which shows a turnover frequency of 423 h^{-1}.

In Figure 2, the TOF of non-pre-treated catalysts are compared with pre-treated ones. During the first hour of reaction, we can clearly see two groups of catalysts: the pre-treated catalysts (in red, orange, pink and purple) characterized by the higher TOF and the non-pre-treated catalysts (in blue, green, light blue and blue green).

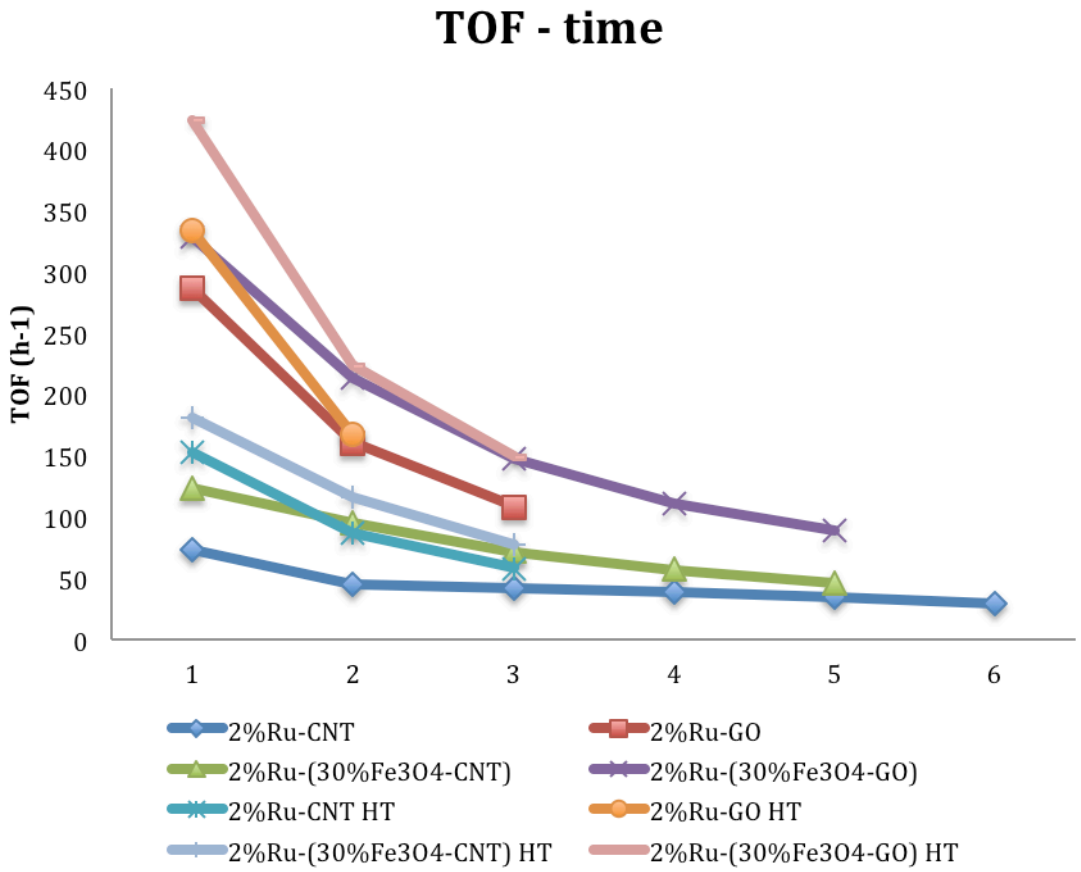

Figure 2 TOF-time graph of hydrogenation of pCNB to pCAN over different catalytic systems

Furthermore, after thermal pre-treatment an increase in ruthenium and/or magnetite particle size was observed (see Figure 3 and Table 4).

Table 3 Particle size distribution of catalysts before and after the thermal pre-treatment

Nanocatalyst	Diameter of fresh catalyst (nm)	σD (nm)	Diameter of pre-treated catalyst (nm)	σD (nm)
Ru@GO	2.59	0.07	4.54	0.23
Ru@CNT	1.56	0.03	4.48	0.11
Ru@Fe3O4-GO	5.01	0.06	2.10 (8.85)	0.23 (0.28)
Ru-Fe3O4/CNT	5.40	0.12	3.49 (16.14)	0.08 (0.77)
Fe3O4/GO	3.20 (7.45)	0.32 (1.02)	10.71	0.30
Fe3O4/CNT	6.09	0.13	10.73	0.29

The diameter of ruthenium nanoparticles in Ru@GO and Ru@CNT after pre-treatment was double that of non-pre-treated catalysts, as can be seen in Table 4. The diameters of

the magnetite particles of the pre-treated Fe_3O_4@GO and Fe_3O_4@CNT increased to about 10 nm. Moreover, after pre-treatment Ru-Fe3O4/GO and Ru-Fe_3O_4/CNT showed a bimodal size distribution.

Figure 3 illustrates the TEM micrographs of pre-treated catalysts and their size distribution.

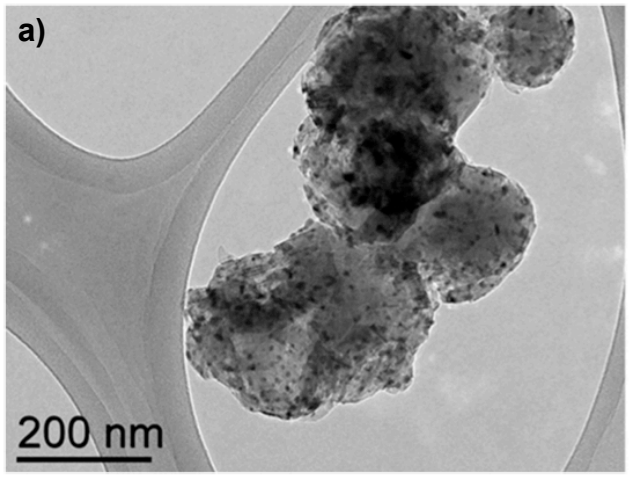

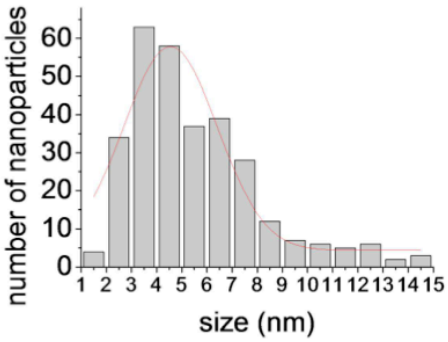

4.54 ± 0.23 nm

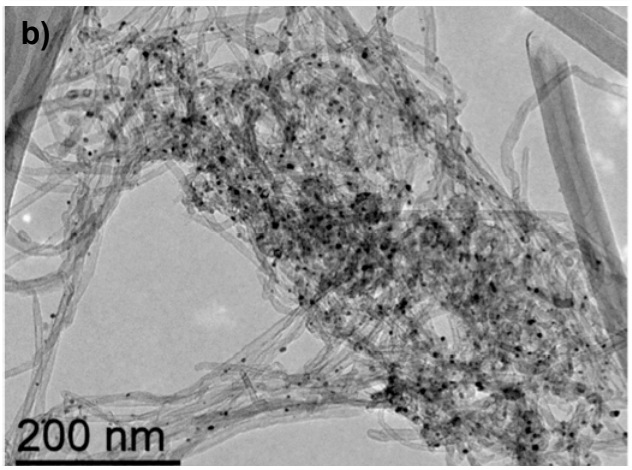

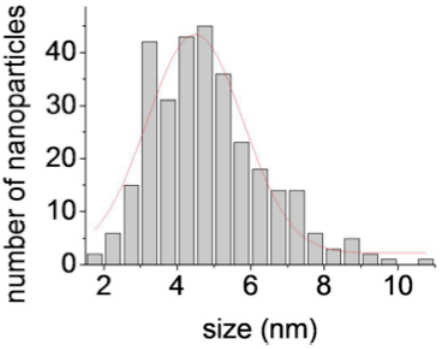

4.48 ± 0.11 nm

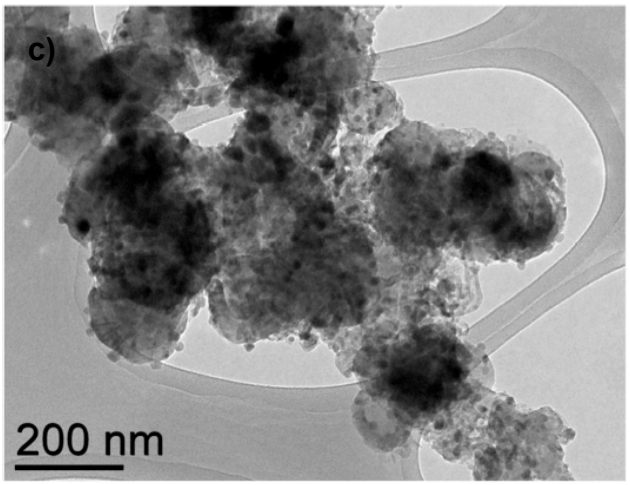

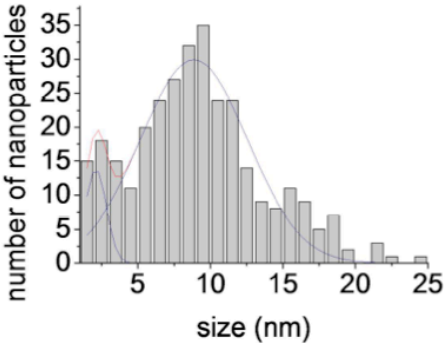

2.10 ± 0.23 nm | 8.85 ± 0.28 nm

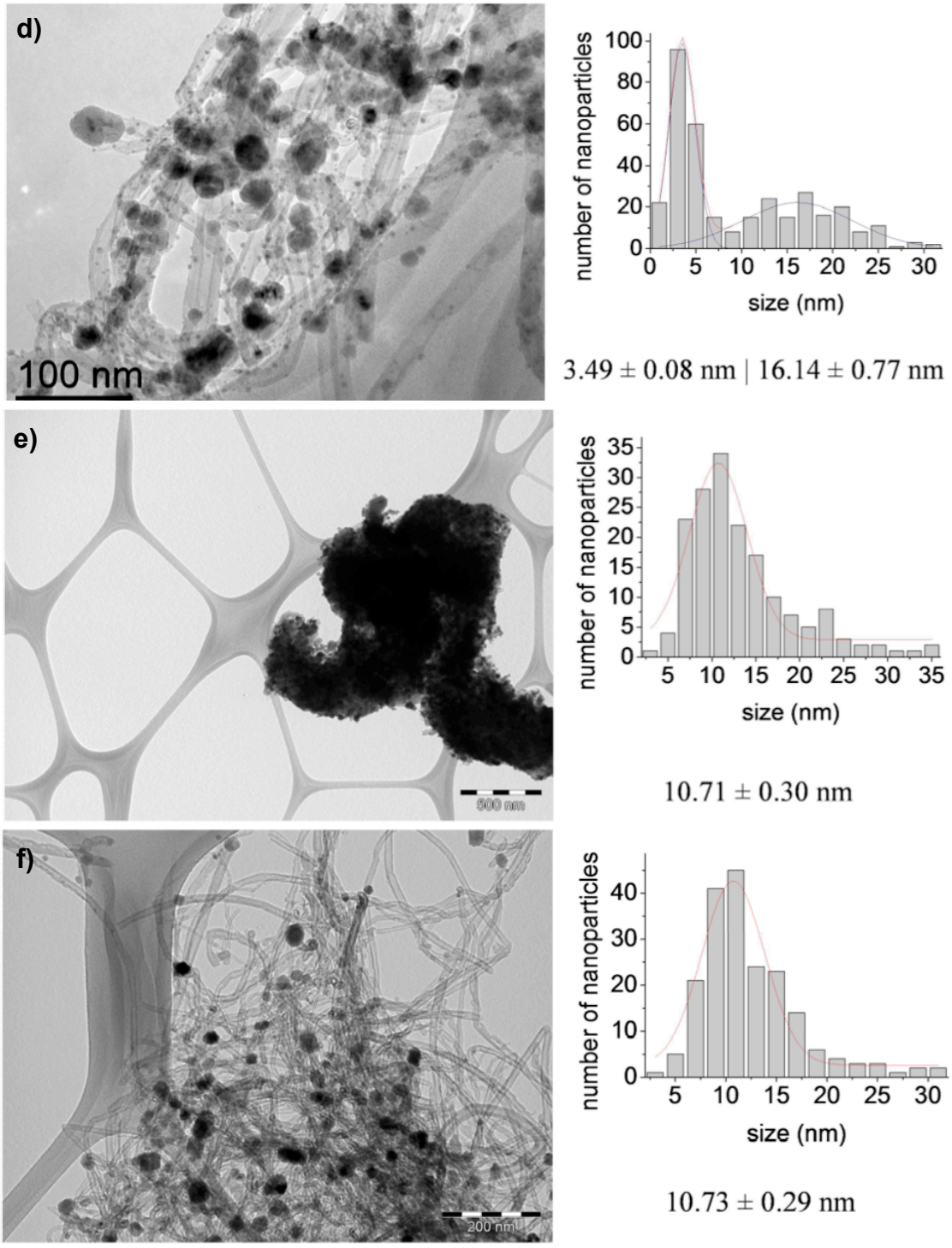

Figure 3 TEM micrographs and particle size distribution of a) pre-treated Ru-GO, b) pre-treated Ru-CNT, c) pre-treated Ru-Fe3O4/GO, d) pre-treated Ru-Fe3O4/CNT, e) pre-treated Fe3O4/GO and f) pre-treated Fe3O4/CNT

15.6 Recycling test

The most promising nanocatalyst, Ru-(Fe_3O_4/GO), was pre-treated and then employed in a recycling test. After each reaction cycle, the reactor was emptied by the top pipeline

leaving the catalyst inside and washed with fresh ethanol. During the recovery of the product, the catalyst was kept on the bottom of the autoclave using an external neodymium magnet as shown in Figure 4.

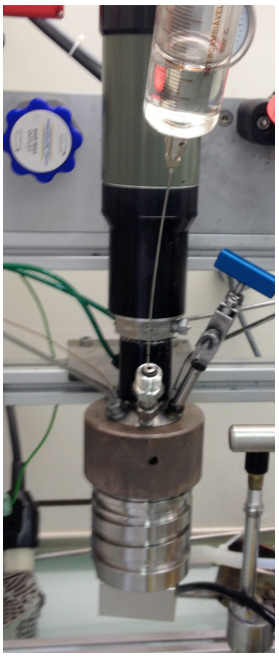

Figure 4 Example of magnetic recovery and recycle

After each recycle the catalytic activity decreased and we observed a loss of 20 % in the conversion from the fresh catalyst to the first recycle. After the second recycle, the decrease was less evident (see Figure 5).

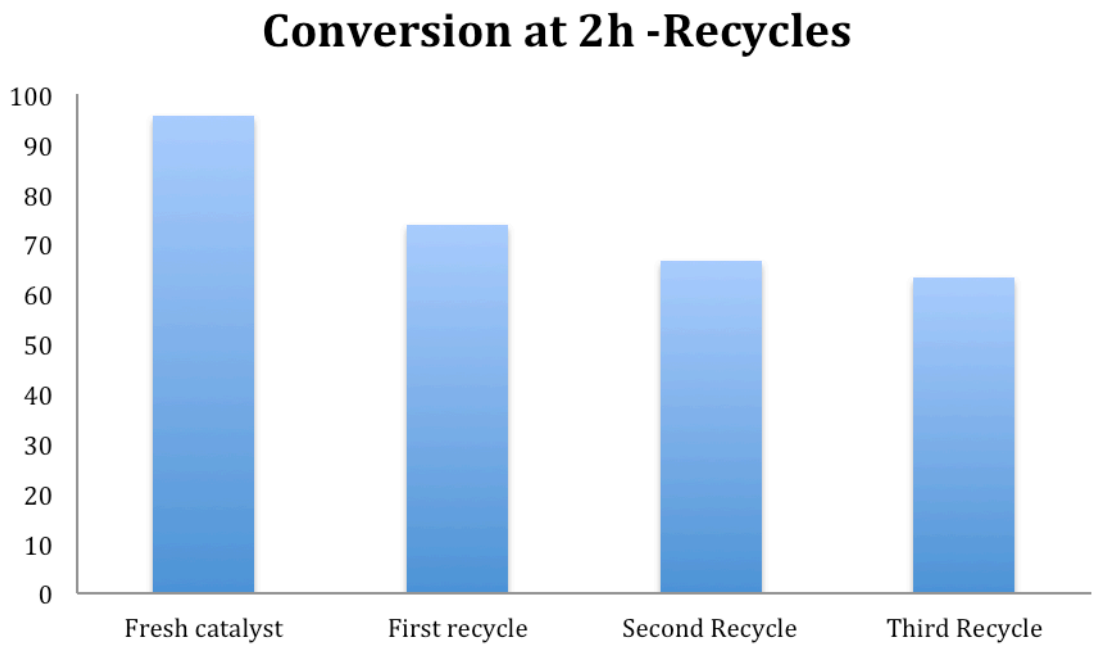

Figure 5 Histogram of Recycling test of 2%Ru-(30%Fe_3O_4-GO) HT

The TEM micrograph and particle size distribution of the pre-treated Ru-Fe_3O_4/GO after three recycles is reported in Figure 6 and showed a slight increase in nanoparticle size.

After the recycle experiment the metal particles of the Ru-Fe_3O_4/GO nanocatalysts showed a bimodal distribution centred at 2.87 nm and 14.14 nm.

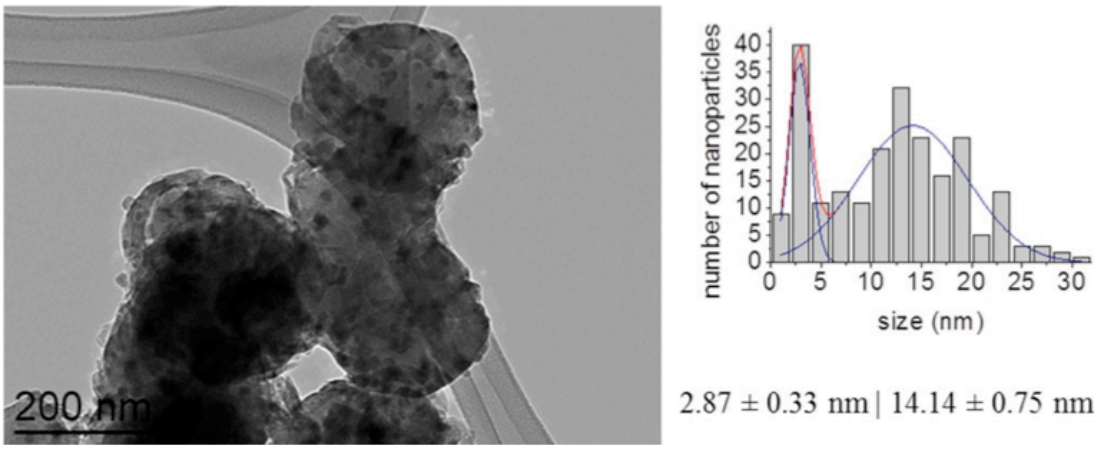

Figure 6 TEM micrograph and particle size distribution of pre-treated Ru-Fe3O4/GO after the third recycle

The leaching effect of these catalysts was evaluated by analysing the solution after 1 h of reaction. In more detail, the Ru-Fe_3O_4/GO catalyst was separated using an external neodymium magnet and washed with ethanol. The reaction solution was evaporated and analysed with ICP-OES showing a ruthenium content of 3 ppm and an iron content of 21 ppm that correspond to 25% and 6% of the original Ru and Fe. These results illustrate that the loss of catalytic activity is caused by leaching rather than by an increase in particle size.

15.7 Hydrogenation of other nitroaromatics

The most promising catalyst was also employed in the hydrogenation of other nitroaromatics such as 2-chloronitrobenzene (oCNB), 3-chloro-1-nitrobenezene (mCNB) and 1-nitro-4-phenyloxybenzene (4NPOB).

The reactions were carried out under the same conditions as the hydrogenation of 4-chloronitrobenzene.

Table 4 Selective Hydrogenation of different nitroaromatics at 60°C under 30 bar of H_2 using 100 mg of 2%Ru-(30%Fe3O4-GO) HT, 0,00254 mol of substrate and 50 ml of Ethanol

Entry	Nitroaromatics	Products	Time (min)	Yield (%)	TOF (h^{-1})	A (mol/g h^{-1})
1	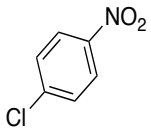	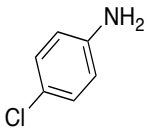	60	94,9	423	4,2
2	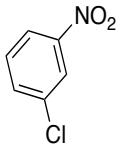	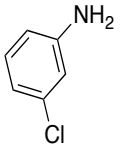	60	35,9	159	1,6
3	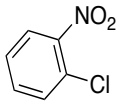	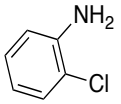	60	65,2	288	2,8
4	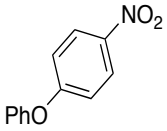	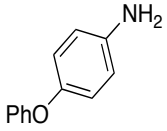	60	50	218	2,2

The hydrogenation of the isomers of chloronitrobenzene are dependent on the position of the chlorine as we can observe in Table 6. After 1 hour of hydrogenation, 4-chloronitrobenzene, 2-chloronitrobenzene and 3-choloro-1-1nitrobenzene showed respectively a yield of 94,9%, 35,9% and 65,2%. Moreover, the Ru-(Fe_3O_4/GO) catalyst also showed promising catalytic activity in the hydrogenation of 1-nitro-4-phenyloxybenzene, which has a more bulky functional group.

15.8 Conclusion

In conclusion, the remarkable catalytic performance of ruthenium carbon nanocatalysts are combined with their magnetic properties which guarantee an easy, efficient, clean recovery and recycle of the catalyst.

A marked effect of the support on catalytic performance was ascertained, and in particular, ruthenium on magnetic graphene oxide Ru-(Fe_3O_4/GO) showed the best catalytic activity and thanks to its magnetic properties it is easily recoverable from the reaction mixture. However, during the recycling test this catalyst showed a loss of catalytic activity, especially in the first recycle. Finally, this promising catalyst was also employed in the selective hydrogenation of other nitroaromatics confirming that these

ruthenium carbon systems are able to hydrogenate the nitro group of diverse substrates. This promising work has already been published by the authors.[12]

15.8 References

[1] X. Yan, J. Sun, Y. Wang and J. Yang, *Journal of Molecular Catalysis A: Chemical* **2006**, *252*, 17-22.
[2] X. Han, R. Zhou, G. Lai and X. Zheng, *Catalysis Today* **2004**, *93–95*, 433-437.
[3] V. L. Khilnani and S. B. Chandalia, *Organic Process Research & Development* **2001**, *5*, 257-262.
[4] H.-U. Blaser, H. Steiner and M. Studer, *ChemCatChem* **2009**, *1*, 210-221.
[5] M. Oubenali, G. Vanucci, B. Machado, M. Kacimi, M. Ziyad, J. Faria, A. Raspolli-Galetti and P. Serp, *ChemSusChem* **2011**, *4*, 950-956.
[6] A. Tijani, B. Coq and F. Figueras, *Applied Catalysis* **1991**, *76*, 255-266.
[7] a) M. Nesselberger, M. Roefzaad, R. Fayçal Hamou, P. Ulrich Biedermann, F. F. Schweinberger, S. Kunz, K. Schloegl, G. K. H. Wiberg, S. Ashton, U. Heiz, K. J. J. Mayrhofer and M. Arenz, *Nat Mater* **2013**, *12*, 919-924; b) J. Speder, L. Altmann, M. Baumer, J. J. K. Kirkensgaard, K. Mortensen and M. Arenz, *RSC Advances* **2014**, *4*, 14971-14978.
[8] a) G. Prieto, J. Zečević, H. Friedrich, K. P. de Jong and P. E. de Jongh, *Nat Mater* **2013**, *12*, 34-39; b) G. Prieto, J. D. Meeldijk, K. P. de Jong and P. E. de Jongh, *Journal of Catalysis* **2013**, *303*, 31-40.
[9] H. Gao and J. Zhao, *The Journal of Chemical Physics* **2010**, *132*, 234704.
[10] H. Vu, F. Gonçalves, R. Philippe, E. Lamouroux, M. Corrias, Y. Kihn, D. Plee, P. Kalck and P. Serp, *Journal of Catalysis* **2006**, *240*, 18-22.
[11] a) B. F. M. A. Solhy, J. Beausoleil, Y. Kihn, F. Goncalves, M.F.R Pereira, J.J.M. Orfao, J.L. Figueiredo, J.L. Faria, P. Serp, *Carbon* **2008**, *46*, 1194-1207; b) M. L. Toebes, F. F. Prinsloo, J. H. Bitter, A. J. van Dillen and K. P. de Jong, *Journal of Catalysis* **2003**, *214*, 78-87; c) M. L. Toebes, Y. Zhang, J. Hájek, T. Alexander Nijhuis, J. H. Bitter, A. Jos van Dillen, D. Y. Murzin, D. C. Koningsberger and K. P. de Jong, *Journal of Catalysis* **2004**, *226*, 215-225; d) A. J. Plomp, H. Vuori, A. O. I. Krause, K. P. de Jong and J. H. Bitter, *Applied Catalysis A: General* **2008**, *351*, 9-15.
[12] E. Bertolucci, R. Bacsa, A. Benyounes, A. M. Raspolli-Galletti, M. R. Axet and P. Serp, *ChemCatChem* **2015**, *7*, 2971-2978.

16. CONCLUSION

Two new sustainable and greener synthetic approaches to produce well-defined magnetic nanostructured catalysts were developed. These new precipitation and hydrothermal procedures permit to obtain good particle size and shape control. Both these innovative methodologies are characterized by:

- The use of aqueous ethanol as a solvent;
- The use of monomode or multimode microwave irradiation, which are highly energy efficient heating sources;
- The absence of polymeric stabilizers, which could lead to MNP surface passivation, decreasing both magnetic properties and catalytic activity;
- A single reaction step;
- Short reaction time.

The correlations between the obtained nanostructure characteristics and the main synthetic parameters (such as temperature, heating sources, pH, precursor concentration and reaction time) were deeply investigated. These relationships resulted fundamental in order to drive the nanoparticles synthesis toward nanocatalysts with the desired properties.

In particular maghemite nanoparticles characterized by an average diameter of 3-4 nm, a surface area of 62 m^2/g and magnetic saturation of 9.7 emu/g can be obtained with the precipitate method. On the other hand, magnetite nanoparticles with an average diameter of 14 nm, a surface area of 78.8 m^2/g and magnetic saturation of 45.88 emu/g can be obtained with the hydrothermal method.

Thanks to the versatility of these two methods and the correlations established between the nanosystems characteristics and the main synthetic parameters it was possible to prepare a wide range of bimetallic nanocatalysts and nanocomposite materials.

The bimetallic nanocatalysts based on Pd, RuO_x, Pt and Cu_2O showed well-defined morphologies and promising magnetic properties. These novel catalysts were employed in some strategic industrial reactions as:

- Hydrogenation of cinnamaldheyde to hydrocinnamaldheyde;
- Oxidation of 1-phenylethanol to acetophenone;
- Oxidation of hydroxymethylfurfural to furan dicarboxylic acid;

- Suzuki-Miyaura cross-coupling;
- Heck-Mizoroki cross-coupling;
- Cassar-Heck cross-coupling;
- Direct arylation of 1-methyl-1-H-imidazole and 4-iodioanisole;
- Gas-phase Ethanol oxidation/condensation;
- Hydrogenation of *p*chloronitrobenzene to *p*chloroaniline.

Among the magnetic palladium systems employed in the hydrogenation of cinnamaldheyde to hydrocinnamaldheyde, the Pd@γ-Fe_2O_3 catalyst showed the best catalytic activity giving a hydrocinnamaldehyde yield of 77% with a selectivity of 85%. This result is higher than those reported in literature for analogous palladium magnetic systems.[1] Unfortunately, this catalyst lost the 60% of its catalytic activity after the first reaction cycle due to poisoning or leaching, thus it is necessary to consider a regeneration stage and better understand the deactivation mechanism.

The magnetic ruthenium nanocatalysts RuO_x@γ-Fe_2O_3 were employed in the oxidation of 1-phenylethanol to acetophenone in aqueous media. This type of catalysts showed a low acetophenone yield (38%) due to the complex multiphasic system. Furthermore it was ascertained that the ruthenium (0) contained in commercial Ru/C and Ru/Al_2O_3 was more active than the oxidized species (oxidation state 3^+) contained in Ru2 catalyst.

Moreover the magnetic nanocatalysts Pd-, RuO_x- and Pt- based were employed in the oxidation of "green, renewable hydroxymethylfurfural to furan dicarboxylic acid. These three metals showed diverse activity leading to the formation of different partially oxidized products (DFF, FFCA or HFCA). More in details, the Pd6 (4.7%Pd@Fe_3O_4) catalyst showed the highest FDCA yield (49.9%), followed by the Pt1 (6.7%Pt@Fe_3O_4) and Ru2 (1.87%Ru@Fe_3O_4) catalysts with a FDCA yield of 41.7% and 8.3%, respectively. The ruthenium catalyst exhibited lower activity toward the oxidation of the aldehyde group to carboxylic acid as underlined by the higher FFCA yield. On the other hand Pd and Pt favored the oxidation of aldehyde group to carboxylic acid leading to higher FDCA and HFCA yields.

The magnetic palladium Pd6 catalyst was also employed in diverse cross-coupling reactions to evaluate its catalytic activity. In particular, for the Suzuki-Miyaura cross-coupling of *p*-bromoanisole with phenylboronic, the Pd6 catalyst showed a promising high catalytic activity, higher than that observed with commercial palladium on carbon. Instead, the Heck-Mizoroki cross coupling of *p*-bromoacetophenone with styrene and Cassar-Heck cross-coupling of the *p*-iodoanisole with phenylacetylene required a larger

amount of Pd6 catalyst to reach the same yield of commercial palladium on carbon, underlining that the magnetic nanocatalyst was less active for these cross-couplings. The Pd6 catalyst showed also a surprisingly higher activity in direct arylation of 1-methyl-1-H-imidazole and 4-iodioanisole, similar to those of traditional homogeneous systems. This last result is particularly interesting due to the easy, efficient and rapid separation of the catalyst from the reaction media.

Moreover, the copper oxide nanoparticles supported on magnetite or on alumina were employed in the gas phase ethanol oxidation/condensation, another interesting reaction in the field of green chemistry. The catalytic results underline that copper oxide supported on magnetite (Cu1, $Cu_2O@Fe_3O_4$ and Cu2, $Cu_2O@Fe_3O_4$) leads to a higher butyraldehyde yield following a more direct reaction mechanism, whereas copper oxide supported on alumina (Cu3, $Cu_2O@Al_2O_3$) gives a high butanol yield probably following the classic Guerbet mechanism. This is absolutely new evidence, newer reported in literature.

Finally, the ruthenium nanoparticles supported on different carbon nanostructures (Multiwall carbon nanotubes (CNTs), N-doped multiwall carbon nanotubes (NCNTs), Nanodiamond (Nd) and Graphene oxide (GO)) were employed in the hydrogenation of p-chloronitrobenzene to p-chloroaniline, showing encouraging results. In particular 0.77%Ru@GO and 1.13%Ru@Fe3O4@CNT showed the higher catalytic activity, 0.10 mol/g h and 0.14 mol/g h, respectively, underlining a positive effect of graphene oxide in the hydrogenation rate.

The ascertained good performances can be related to the reached accurate control of nanoparticle properties, thus opening the way to their application as electrostatic sensors and nanoconductors. As a consequence an extensive study of the effects of particle size and composition on magnetic and electrical properties was performed underlining that increasing the particle size the superparamagnetic effect decreased and the conductance resonance was shifted to higher frequency.[2] Furthermore a promoting effect of palladium nanoparticles on magnetic properties was ascertained.

16.1 References

[1] J. Yu, L. Yan, G. Tu, C. Xu, X. Ye, Y. Zhong, W. Zhu and Q. Xiao, *Catalysis Letters* **2014**, *144*, 2065-2070.

[2] a) A. M. R. Galletti;, E. Bertolucci;, Mirko Marracci, B. Tellini; and C. Visone, *Instrumentation and Measurement Technology Conference (I2MTC)* **2014**, pp. 464-467; b) E. Bertolucci, A. M. R. Galletti, C. Antonetti, M. Mirko, B. Tellini, P. Fabio and V. Ciro in *Chemical and Magnetic Properties Characterization of Magnetic Nanoparticles*, *Vol.* IEEE, Pisa, **2015**.

17. EXPERIMENTAL SECTION

17.1 Chemicals

Ethylene Glycol (Sigma Aldrich) CAS 107-21-1: it was used as received.

Polyvinylpyrrolidone (Sigma Aldrich) CAS 9003-39-8: it was used as received.

Sodium Alginate (Sigma Aldrich) CAS 9005-38-3: it was used as received.

Polyvinyl alcohol (Sigma Aldrich) CAS 9002-89-5: it was used as received.

Acetone (Carlo Erba) CAS 67-64-1: it was dried on Na_2SO_4 and then purified by distillation at atmospheric pressure. It was stored at room temperature under nitrogen.

Diethyl Ether (Carlo Erba) CAS 60-29-7: it was used as received and stored at room temperature.

Ethanol absolute (Carlo Erba) CAS: 64-17-5 it was used as received and stored at room temperature.

Isopropyl Alcohol (Carlo Erba) CAS 67-63-0: it was used as received and stored at room temperature.

Poly(N-vinyl-2-pyrrolidone) (Aldrich) CAS 9003-39-8: it was used as received and stored at room temperature.

Poly vinyl-alcohol (Aldrich) CAS 9002-89-5: it was used as received and stored at room temperature.

Sodium alginate (Aldrich) CAS 1344-28-1: it was used as received and stored at room temperature.

γ-Al_2O_3 (Chimet): product number 49, surface area 110 m_2/g. It was dried at 180°C for 5 h and then it was stored at room temperature under nitrogen.

Carbon Nanotubes (Arkema): they were used as received.

Carbon Nanodiamond (Aldrich): they were used as received.

Graphene: it was used as received from Prof. Philippe Serp laboratory.

$Ru(acac)_3 \cdot H_2O$ (Aldrich) CAS 14284-93-6: it was used as received and stored at room temperature.

$CuSO_4$ (Aldrich) CAS 7758-98-7: it was used as received and stored at room temperature.

$FeCl_3 \cdot 1{,}5\ H_2O$ (Carlo Erba) CAS 7705-08-0: it was used as received and stored at room temperature.

$Pd(OAc)_2$ (Aldrich) CAS: 3375-31-3 it was used as received and stored at room temperature, (% Pd = 48.1 %).

$Fe(OAc)_2$ (Aldrich) CAS 3094-87-9: it was used as received and stored under argon at room temperature.

Fe_3O_4 powder 50-100 nm CAS 1317-61-9: it was used as received and stored at room temperature

Fe_3O_4 powder <5μm CAS 1317-61-9: it was used as received and stored at room temperature.

Glucose (Sigma Aldrich) CAS 50-99-7: it was used as received

Sodium Gluconate (Sigma Aldrich) CAS 527-07-1: it was used as received

Sorbitol (Sigma Aldrich) CAS 50-70-4: it was used as received

Copper sulphate (Sigma Aldrich) CAS 7758-98-7: it was used as received

Sodium carbonate (Carlo Erba) CAS 471-34-1: it was used as received

Ascorbic Acid (Fluka): it was used as received.

$Cu_2(O_2CNEt_2)_4 \cdot NHEt_2$: it was used as received from Prof. Guido Pampaloni laboratory.

$[Pt_4(OAc)_8] \cdot HOAc$: it was used as received from Prof. Tiziana Funaioli laboratory.

Phenol (Fluka) CAS 108-95-2: it was used as received and stored at room temperature.

Cyclohexanone (Fluka) CAS 108-94-1: it was used as received and stored at room temperature.

Cyclohexanol (Fluka) CAS 108-93-0: it was used as received and stored at room temperature.

Chlorophorm (VWR International) CAS 67-66-3: it was vented before use

Cinnamaldehyde (Aldrich) CAS 104-55-2: it was purified by distillation and then stored at room temperature under nitrogen.

Hydrocinnamaldehyde (Aldrich) CAS 1866-31-5: it was used as received and stored at room temperature under nitrogen.

Cinnamyl Alcohol (Aldrich) CAS 104-54-1: it was used as received and stored at room temperature.

Hydrocinnamyl Alcohol (Aldrich) CAS 122-97-4: it was used as received and stored at room temperature.

Decalin (Sigma-Aldrich) CAS 91-17-8: it was used as received and stored at room temperature.

1- Phenylethanol (Sigma-Aldrich) CAS: 98-85-1: it was used as received.

Benzyl Alcohol (Sigma-Aldrich) CAS 100-51-6: it was used as received and stored at room temperature.

Acetophenone (Sigma-Aldrich) CAS 98-86-2: it was used as received and stored at room temperature.

1- chloronitrobenzene CAS 100-00-5: it was used as received and stored at room temperature.

NaOH (Carlo Erba) CAS: 1310-73-2: it was used as received and stored at room temperature.

Sodium sulphate (Baker) CAS: 7757-82-6: it was used as received

Barium hydroxide (Sigma Aldrich) CAS 12230-71-6: it was used as received

Ammonia (Sigma Aldrich) CAS 1336-21-6: it was used as received

HCl (Carlo Erba) CAS: 7647-01-0: it was used as received and stored at room temperature.

H_2SO_4 (Carlo Erba) CAS 7664-93-9: it was used as received and stored at room temperature.

HNO_3 (Carlo Erba) CAS 7697-37-2: it was used as received and stored at room temperature.

Acetic Acid (Baker) CAS 64-19-7: it was used as received and stored at room temperature.

Tetrahydrofuran (Baker) CAS 109-99-9: it was used as received and stored at room temperature.

4-iodoanisole (Sigma-Aldrich) CAS 696-62-8: it was vented before use.

Phenyl acetylene (Fluka) CAS 536-74-3: it was vented before use.

Potassium phosphate (Riedel-de-Haen) CAS 7778-53-2: it was use as received and stored at room temperature.

4-bronoanisole (Sigma Aldrich) CAS 104-92-7: it was vented before use

5-Hydroxymethyl -2-furaldehyde (Sigma Aldrich) CAS 67-47-0: it was used as received.

2,5 Furan dicarboxylic acid (Sigma Aldrich) CAS 3238-40-2: it was used as received

2,5 Furan dicarboxaldehyde (Sigma Aldrich) CAS 823-82-5: it was used as received

Styrene (Sigma Aldrich) CAS 100-42-5: it was distilled on CaH_2 before use
N-methyl-1-H-imidazole CAS 616-47-7: it was vented before use
Phenylboronic acid (Sigma Aldrich) CAS 98-80-6: it was vented before use
Dimethyl acetamide (Sigma Aldrich) CAS 127-19-5: it was used as received
CuI (Sigma Aldrich) CAS 7681-65-4: it was used as received
Dimethylformamide (Baker) CAS 68-12-2: it was vented before use
Dichloromethane (Sigma Aldrich) CAS 75-09-2: it was vented before use
Ethyl acetate (Sigma Aldrich) CAS 141-78-6: it was used as received
Petroleum (Sigma Aldrich) CAS 101316-46-5: it was used as received
5%Pd/C (Engelhand): it was used as received
5%Pd/Al2O3 (Sigma Aldrich): it was used as received
Toluene (Sigma Aldrich) CAS 108-88-3: it was vented before use
Methanol (Sigma Aldrich) CAS 67-56-1: it was vented before use
Naphthalene (Fluka) CAS 91-20-3: it was vented before use
Biphenyl (Sigma Aldrich) CAS 92-52-4: it was vented before use
Nitrogen, Argon, Hydrogen (Rivoira): analytical pure products and used as received.

17.2 Instrumentations

Ultraviolet-Visible absorption measurements (UV-Vis) were carried out with a UV-Vis spectrophotometer JASCO V-530 operating at room temperature.

Morphology and structure investigations were performed with high-resolution (TEM) images recorded with a JEOL- JEM 2010 with an accelerating voltage of 200KV. The particle size distributions were obtained by counting at least 300 particles onto the micrographs. The mean diameter (d_m) was calculated as $d_m = \Sigma\, d_i\, n_i\, / \Sigma n_i$ where n_i was the number of particles of diameter d_i. The counting was carried out on electron micrographs obtained starting from 50,000 up to 100,000 magnifications.

The BET surface area of the supports and of the supported catalysts was determined by nitrogen adsorption, using a single point ThermoQuest Surface Area Analizer Qsurf S1.

XPS measurements were performed with a VG Microtech ESCA 3000 Multilab, equipped with a dual Mg/Al anode. The spectra were excited by the unmonochromatised Al Kα source (1486.6 eV) run at 14 kV and 15 mA. The samples

were analysed as powders mounted on a double-sided adhesive tape. In order to avoid contact with air, the mounting on the sample holder was performed inside a glove bag filled with N_2 and then the holder was loaded inside the XPS machine in a N_2 atmosphere. The binding energies were calibrated with respect to the C1s set at 285.1 eV arising from the adventitious carbon. Peak resolution and quantitative analyses were performed with the software provided by VG.

pH analyses were made with the pH-meter Bench Top Hanna Instrument, pH209-209R.

The different synthetized iron oxide phases were identified using a Micro Raman spectroscopy (Raman Invia Renishaw) equipped with a CCD detector and a Leica microscopy using a x50 objective lens and holographic grating (1800 grooves mm-1). The samples were excited with 633 nm radiation from a 0,10 mW air-cooled He-Ne laser.

FT-IR spectra were recorded on the IR Perkin Elmer Spectrum One Spectrophotometer, using an Attenuated Total Reflectance, (ATR).

The X-ray-diffraction (XRD) pattern was measured with a Thermo ARL X´TRA powder diffractometer, operating in the Bragg-Brentano geometry and equipped with a Cu-anode X-ray source (Kα, λ =1.5418 Å), using a Peltier Si(Li) cooled solid state detector. The pattern was collected with a scan step of 0.18°, a scan rate of 0.5 °/min, an exposure time of 21.6 s/step, in the 18°- 80° 2θ range. The phase identification was performed with the PDF-4+ 2011 database provided by the International Centre for Diffraction Data (ICDD). The nanocrystalline sample was ground in a mortar and then put in a low-background sample holder for the data collection.



Figure 1 Microwave oven CEM Discovery S class

The microwave syntheses were performed in the CEM Discover S-class system. The instrument consists of a single-mode cavity. It works with continuous power generation and control of power supply and it is capable of supplying power in 1 W increments from 0 to 300 W. The system is equipped with a vertically focused IR temperature sensor.



Figure 2 Microwave over MARS 6

The microwave syntheses were performed in the MARS 6 microwave oven. The instrument consists of a multi-mode cavity. It works with continuous power generation and control of power supply and it is capable of supplying power in 1 W increments from 0 to 1800 W. The system is equipped with a vertically focused IR temperature sensor.



Figure 3 Parr autoclave

The autoclave syntheses were carried out in a 100 mL mechanically stirred Parr 4560 autoclave. The reactor is equipped with mechanical stirring and electrical heating. It has one high pipeline for liquid feeding, one low pipeline for gas feeding, an amperometer for pressure control and a thermocouple for temperature control.

The noble metal content was determined by inductively coupled plasma-optical emission spectrometers (ICP-OES) with a Spectro-Genesis instrument equipped with Smart Analyzer Vision software and weight percentages are reported in the first column. For the ICP-OES of the solid catalysts, each sample was heated over a heating plate in a porcelain crucible in the presence of aqua regia (2 mL) four times, dissolving the solid residue in 0.5 M aqueous HCl. The limit of detection calculated for Pd was 2 ppb.

Magnetization measurements were performed at room temperature on dried powder samples using a Vibrating Sample Magnetometer (VSM) of a Quantum Design PPMS instrument, applying the magnetic field from 90 KOe to zero.

Dielectric permeability was tested via spectroscopic analysis of the equivalent electrical properties of the samples. A capacitor was made by inserting each nanopowder or pellet between two copper plates and connected to an E4980A Agilent LCR meter. The

equivalent parallel conductance (Gp) and capacitance (Cp) values were estimated via an impedance spectroscopy technique.

Hydrogenation of cynnamaldehyde to hydrocinnamaldehyde was carried out using a gas-chromatograph Hewlett-Packard 5890, equipped with a FID detector and a PONA column (cross linked methyl silicon gum, 50 m x 0,2 m x 0,5 μm).

Oxidation of 1-phenyl ethanol to acetophenone was carried out using a gas chromatograph Perkin Elmer Auto System 8700, equipped with a FID detector and a DB1701 (95% methyl silicone e 5% phenyl silicone) column, 30m X 0.2mm X 0.5 μm.

Oxidation of HMF to FDCA carried out using an HPLC Perkin Elmer Flexer Series 200 equipped with an MPLC Polypore CA (4.6mm x 220mm x 10 μm) column and a RI detector. The reaction mixture was previously filtered with a PURADISC filter characterized by 0,2μm membrane in PTFE. HPLC analysis was performed at 60°C using H2SO4 0.005 M as eluent and a flow of 0.1 ml/min.

The cross-coupling reactions were carried out with a GLC analysis performed with a cromatograph Dani GC 1000 equipped with PTV injectors, a Dani DDS 1000 detector, and two columns: ATD35Alltech FSOT (30 m x 0.25 mm) and ATD1Alltech FSOT (30 m x 0.25 mm).

The cross-coupling products were analysed by NMR carried out at room temperature, 200 MHz and TMS as internal standard.

Oxidation/condensation of ethanol was analysed with an automatic sampling system for GC analysis. This was performed by using an Agilent-7890A instrument equipped with a thermal conductivity detector (TCD). Agilent chromatographic columns Carboxen-1000 packed and DB-FFAP (30m, 0,53mm) were used for product separation. Compounds were identified also by GC-MS.

Hydrogenation of *p*-chloronitrobenzene to *p*-chloroaniline was carried out by sampling the mixture each hour, and the products were analysed using a gas chromatograph (Perkin-Elmer Clarus 500, equipped with a stabilwax DA capillary column and FID

detector). The following temperature program was adopted: 80°C for 3 minutes, a ramp of 35°C /min until 225°C and a hold time of 10 minutes.

17.3 Synthesis of nanostructured iron oxides

Precipitation synthesis of iron oxides nanoparticles

In a typical experiment, FeCl3·1.5H2O (1g) and the proper amount of NaOH were dissolved in EtOH 96 wt% (44 mL) under stirring. As soon as the base was added the mixture became darker. The resulting mixture was treated by monomode microwave (CEM discovery S-class equipped with an 80 mL glass vessel) at 160°C for 15 minutes at 250W under inert atmosphere. At the end of the treatment, particles were collected using centrifuge at 1500 rpm for 5 minutes, washed three times with EtOH at 96 wt% (40 mL) and dried under vacuum for 12 h. They were stored under argon.

Hydrothermal synthesis of magnetite nanoparticles

In a typical experiment, the desired amount of $Fe(OAc)_2$ was dissolved in EtOH 96 wt% (44 mL). Then this solution was thermal treated by monomode microwave (CEM discovery S-class equipped with an 80 mL glass vessel) at 120°C for 15 minutes at 250W. At the end of this treatment, particles were magnetically collected using a neodymium magnet washed and dried under vacuum for 12 h. This approach was also investigated using different heat sources, such as multimode microwave (MARS.6 equipped with an 80 mL press vessel), a 100 mL Parr autoclave electrically heated, and the corresponding reaction conditions.

17.4 Synthesis of magnetic nanocatalysts

Synthesis of magnetite palladium nanocatalysts characterized by a hierarchical structure in which palladium particles are supported on magnetite

0.5g of maghemite or magnetite prepared following the new precipitate or hydrothermal methods and 0.05g of palladium acetate ($Pd(OAc)_2$) were dispersed in 44 ml of aqueous ethanol. Then the obtained dispersion was MW-irradiated at 120°C for 15 min. At the end of this treatment, the particles were magnetically collected and dried under vacuum.

Synthesis of magnetite nanocatalysts characterized by a complex structure in which metals (Pd, Ru, Pt, Cu) are intercalated in the magnetite structure

In a typical experiment, the desired amount of $Fe(OAc)_2$ and of the metal precursor (such as $Ru(acac)_3$, $Pd(OAc)_2$ $Cu(acac)_2$, $Cu_2(O_2CNEt_2)_4 \cdot NHEt_2$ or $[Pt_4(OAc)_8] \cdot HOAc$) were dissolved in EtOH 96 wt% (44 mL). Then this solution was thermal treated by monomode microwave (CEM discovery S-class equipped with an 80 mL glass vessel) at 120°C for 15 minutes at 250W. At the end of this treatment, particles were magnetically collected using a neodymium magnet washed and dried under vacuum for 12 h.

17.5 Preparation of magnetic nanocomposites

In a typical experiment, the desired amount of $Fe(OAc)_2$ and of the polymer (such as Poly(N-vinyl-2-pyrrolidone), Poly vinyl-alcohol or Sodium alginate) were suspended in EtOH 96 wt% (44 mL). Then this solution was thermal treated by multimode microwave (MARS.6 equipped with an 80 mL Teflon vessel) at 150°C for 15 minutes at 450W. At the end of this treatment, particles were magnetically collected using a neodymium magnet washed and dried under vacuum for 12 h.

17.6 Preparation of ruthenium and/or magnetic carbon nanomaterials

Synthesis of ruthenium nanoparticles over carbon nanomaterials

$[Ru(acac)_3]$ (78mg, 0.19 mmol) was dissolved in 44 ml of isopropanol. 1 g of carbonaceous support (FLG, CNT, NCNT or Nd) was then added to the solution and sonicated. The resulting dispersion was MW-irradiated at 180°C and 250 W for 12 minutes. At the end of the treatment the catalysts were recovered by centrifugation, washed three times with 40 ml of isopropanol and finally dried under vacuum at room temperature for 12 h. Ru-FLG: 0.8% Ru, Ru-CNT: 1.4% Ru, Ru-NCNT: 0.9%Ru.

Synthesis of magnetite nanoparticles over carbon nanomaterials

$[Fe(OAc)_2]$ (1g, 1.5 mmol) was dissolved in 44 ml of isopropanol. 1 g of carbonaceous support (FLG, CNT, NCNT or Nd) was then added to the solution and sonicated. The resulting dispersion was MW-irradiated at 180°C and 250 W for 15 minutes. The final product was magnetically recovered, washed three times with 40 ml of isopropanol and

finally dried under vacuum at room temperature for 12h. Fe_3O_4-FLG: 16.4 % Fe, Fe_3O_4-CNT: 15.8 % Fe, Fe_3O_4-NCNT: 10.2% Fe.

Synthesis of ruthenium and magnetite nanoparticles over carbon nanomaterials
$Fe(OAc)_2$] (1g, 1.5 mmol) was dissolved in 44 ml of isopropanol. 1 g of carbonaceous support (FLG, CNT, NCNT or Nd) was then added to the solution and sonicated. The resulting dispersion was MW-irradiated at 180°C and 250 W for 15 minutes. [$Ru(acac)_3$] (78mg, 0.19 mmol) was added and the dispersion was MW-irradiated again for 12 minutes at 180°C and 250W. The final product was magnetically recovered, washed three times with 40 ml of isopropanol and finally dried under vacuum at room temperature for 12h. Ru-Fe_3O_4-FLG: 0.6% Ru, 18.1 % Fe, Ru-Fe_3O_4-CNT: 1.0% Ru, 13.6 % Fe, Ru-Fe_3O_4-NCNT: 0.6% Ru, 30.3 % Fe.

Synthesis of copper oxide supported on alumina

The copper on alumina nanocatalysts were prepared following the same procedure. 1 g of support γ-alumina (γ-Al2O3) and 0,305 g of Cu2(O2CNEt2)4 □ 2NHEt2 were dispersed in 44 ml of ethanol, then the mixture was MW-irradiated at 120°C and 250W for 15 minutes. The final product was magnetically recovered, washed three times with 40 ml of propanol and finally dried under vacuum at room temperature for 12h

17.7 Preparation of copper nanoobjects

Synthesis of copper nanoparticles

$Cu(NO_3)_2 \cdot 3H_2O$ (80mg), Polyvinyl alcohol (0.1g) and ascorbic acid (1.3 g) were dissolved in ethylene glycol (40 ml) under stirring, and MW-irradiated at 140°C and 150W. After the MW treatment, the copper nanoparticles were formed as confirmed by the suspension colour, which turned from light blue to reddish due to the presence of free Cu^{2+} ions.

Synthesis of copper nanowires

The seed solution was prepared by dissolving sodium gluconate (2.5g) in 30 ml of water and adding 0.12 ml of NaOH 1M and 1.2 ml of $CuSO_4$ 10^{-2} M, then the mixture was treated with microwave at 80°C, 250W for 5 min. Meanwhile, the growth solution was prepared by dissolving sodium gluconate (1.9) in 6 ml of water and adding 1.2 ml of

$CuSO_4$ 10^{-2} M. Finally, the growth solution was added to the seed solution and treated with microwave at 80°C, 250W for 10 minutes.

17.8 Catalytic reactions

The selective hydrogenation of cynnamaldehyde to hydrocinnamaldehyde

A typical hydrogenation experiment was carried out at 100°C under 20 bar of hydrogen using 3.8 ml of cinnamaldehyde, the desired amount of palladium catalysts and 100 ml of decaline. The reaction was followed by a gas chromatography (Hewlett-Packard 5890, equipped with a FID detector and a PONA column (cross linked methyl silicon gum))

Oxidation of 1-fenilethanol

The oxidative reactions were carried out in Parr autoclaves magnetically stirred. In each reaction the autoclave was charged with 10 ml of water, 60 mg of 1- phenyl ethanol (0,5 mmol) and the ruthenium catalyst with a rate of 1-phenylethanol/ruthenium of 61. Subsequently, the autoclave was fluxed and pressurized with oxygen (10 atm) and maintained at 100°C for six hours. At the end of this treatment, the autoclave was rapidly cooled with ice to room temperature. The catalyst was recovered using an external neodymium magnet and the reaction mixture was pre-treated and analysed by gas chromatography. The pre-treatment consisted in the extraction of the unreacted reagent and products with 5 ml of ethyl ether three times and dehydration on sodium sulphate.

The selective oxidation of HMF to FDCA

Typical oxidation was carried out in a 40 ml Parr autoclave electrically heated and was followed using an HPLC Perkin Elmer Flexer Series 200 equipped with a MPLC Polypore CA column. In particular, the HMF and the magnetic catalysts were dispersed in 5 mL of H_2O to obtain a HMF/metal ratio of 50 and a final HMF concentration of 0.05 M and heated up to 140°C under oxygen pressure. At the end, the reactor was quenched at 0°C, the catalyst was magnetically collected and the reaction mixture was analysed through HPLC analysis.

The Suzuki-Miyaura cross-coupling

The Suzuki-Miyaura cross coupling of phenyl boronic acid (1.2 mmol), sodium carbonate (3.8 mmol), the magnetic palladium catalyst (3.5 mol % od palladium) and the internal standard biphenyl was carried out in a glass reactor previously vended. The vented ethanol (2 ml), water (2 ml) and *p*-bromoanisole (1 mmol) were then added to

the glass reactor and the mixture was heated up to 80°C. At the end of the reaction, the catalyst was magnetically collected with an external neodymium magnet. The obtained biphasic solution was then extracted 3 times with 10 ml of diethyl ether. The organic phases were dehydrated with sodium sulphate and concentrated under vacuum. Finally, the concentrated phase was purified through flash chromatography (the eluent was petroleum:toluen (85:15)).

The Heck-Mizoroki cross-coupling

The Heck-Mizoroki cross coupling of *p*-bromoacetophenone (1 mmol), sodium acetate (1.5 mmol) and the magnetic palladium catalyst (5 mol % od palladium) was carried out in a glass reactor previously vended. Vented dimethyl fromamide (5 ml) and distilled styrene (1.5 mmol) were then added to the glass reactor and the mixture was heated up to 130°C. At the end of the reaction, the catalyst was magnetically collected with an external neodymium magnet and the reaction mixture was diluted with 10 ml of chloromethane. The biphasic solution obtained was extracted 3 times with 15 ml of water to remove the dimethyl acetamide. The organic phases were dehydrated with sodium sulphate and concentrated under vacuum. Finally, the concentrated phase was purified by crystallization.

The Cassar-Heck cross-coupling

The Cassar-Heck cross coupling of *p*-iodoanisole (1 mmol), potassium phosphate (1 mmol) and the magnetic palladium catalyst (1 mol % od palladium) was carried out in a glass reactor previously vended. Vented propanol (2,5 ml), water (2,5 ml) and distilled phenyl acetilene (1.2 mmol) were added to the glass reactor and the mixture was heated up to 80°C. At end of the reaction, the catalyst was magnetically collected with an external neodymium magnet and the reaction mixture was diluted with 10 ml of water. The obtained biphasic solution was then extracted 3 times with 10 ml of AcOEt. The organic phases were neutralized with a sutured NaCl solution, dehydrated with sodium sulphate and concentrated under vacuum. Finally, the concentrated phase was purified through flash chromatography (the eluent was petroleum:toluen (8:2)).

Direct arylation of N-metil-1-H-imidazolo and p-iodoanisole

The direct arylation of *p*-iodoanisole (2 mmol), CuI (2 mmol), the magnetic palladium

catalyst (5 mol % od palladium) and the internal standard naphthalene was carried out in a glass reactor previously vended. The vented dimethylformamide (5 ml) and N-metil-1-H-imidazolo (1 mmol) were added to the glass reactor and the mixture was heated up to140°C. At the end of the reaction, the catalyst was magnetically collected with an external neodymium magnet and the reaction mixture was diluted with AcOEt (100 ml). The obtained solution was then treated with 100 ml of a saturated ammonium chlorine solution and left under stirring for 2 h. At this point, the water phase turned blue and was extracted 3 times with 50 ml of AcOEt. The organic phases were neutralized with a sutured NaCl solution, dehydrated with sodium sulphate and concentrated under vacuum. Finally, the concentrated phase was purified through flash chromatography, (the eluent was DCM:MeOH (95:5))

Oxidation/condensation of ethanol

The reactivity tests were performed by using a continuous-flow reactor that operated under atmospheric pressure. Typically, (0,02-0,2g) of catalyst was loaded as powder form. The inlet feed volume ratio was constant and set at 5% of ethanol, 23,81% of air and 71,19% of nitrogen. Downstream products were fed to an automatic sampling system for GC analysis. This was performed by using an Agilent-7890A instrument equipped with a thermal conductivity detector (TCD). Agilent chromatographic columns Carboxen-1000 packed and DB-FFAP (30m, 0,53mm) were used for product separation. Compounds were identified also by GC-MS.

The hydrogenation of 1-chloronitrobenzene to 1-chloroaniline

In a typical experiment, the autoclave was purged by three vacuum/argon cycles. The sonicated suspension of the nanocatalysts (100mg) in 25 ml of solvent was introduced in the autoclave and pre-treated at 110°C under 30 bar of hydrogen for 1h. A solution of the nitroaromatic compound (2,5 mmol) in 25 mL of solvent was then added to the autoclave and allowed to react under 30 bar of hydrogen at 60°C. The reaction was followed by sampling the mixture each hour, and the products were analysed by gas chromatography.